PROCEEDINGS OF THE 11TH MEETING OF INTERNATIONAL COLLABORATION ON ADVANCED NEUTRON SOURCES

KEK, TSUKUBA, OCTOBER 22-26, 1990

VOL.2

Cover Art
T. Sayama

Property of Jack M. Carpenter
Please return to IPNS Library
Building 360 - Room E101

KEK Report 90-25
March 1991
AMRD

Proceedings of the Eleventh Meeting of the

International Collaboration on Advanced Neutron Sources ICANS-XI

KEK, Tsukuba, Japan, October 22-26, 1990

Volume II

Instrument Workshop

Editors
M. Misawa
M. Furusaka
H. Ikeda
N. Watanabe

© National Laboratory for High Energy Physics, 1991

KEK Reports are available from:

Technical Information & Library
National Laboratory for High Energy Physics
1-1 Oho, Tsukuba-shi
Ibaraki-ken, 305
JAPAN

Phone:	0298-64-1171	
Telex:	3652-534	(Domestic)
	(0)3652-534	(International)
Fax:	0298-64-4604	
Cable:	KEKOHO	

Volume 2

Contents of Volume 2 ix

Instrument Workshop

Total Performance

Why total performance 637
N.Watanabe

Performance of chopper spectrometers 644
M.Arai, A.D.Taylor, S.M.Bennington, Z.A.Bowden, R.Osborn, M.Kohgi, K.Ohoyama, and T.Nakane

Improving the resolution of chopper spectrometer at pulsed neutron sources 655
J.M.Carpenter and D.F.R.Mildner

Small-angle neutron scattering at pulsed sources compared to reactor sources 673
R.P.Hjelm,Jr, P.A.Seeger, and P.Thiyagarajan

Total performance of small-angle machines at pulsed source 677
M.Furusaka, N.Watanabe, K.Suzuya, I.Fujikawa, and S.Satoh

Total performance of LAM-80ET 684
K.Inoue, T.Kanaya, K.Kiyanagi, S.Ikeda, K.Shibata, H.Iwasa, T.Kamiyama, and Y.Izumi

Summary of this session 702
P.A.Egelstaff

Recent Progress on Instruments

•Inelastic Scattering Instruments

First results from the UK-Japanese spectrometer MARI 705
A.D.Taylor, M.Arai, S.M.Bennington, Z.A.Bowden, R.Osborn, K.Andersen, W.G.Stirling, T.Nakane, K.Yamada, and D.Welz

IPNS chopper spectrometer improvements 711
J.M.Carpenter and C.-K.Loong

Optimization of a multi-disk chopper spectrometer for cold neutron scattering experiments 717
R.E.Lechner

Crosscorrelation method using a pulsed white polarized neutron beam 733
M.Kohgi, H.Fujimoto, K.Ohoyama, K.Yamada and M.Motoya

Recent progress on MAX 739
Y.Todate, H.Ikeda, K.Tajima, and S.Tomiyoshi

Progress with the PRISMA spectrometer 743
U.Steigenberger, M.Hagen, C.Petrillo and F.Sacchetti

Advances in crystal analyser spectroscopy at ISIS 752
C.J.Carlile, U.Steigenberger, J.Tomkinson, M.A.Adams, M.Prager, and R.Mukhopadhyay

Neutron scattering on ROTAX 774
H.Tietze, W.Schmidt, R.Geick, U.Steigenberger, and H.Samulowitz

Recent progress on eVS 790
J.Mayers, A.C.Evans and A.D.Taylor

•Elastic Scattering Instruments

Recent progress in TOP spectrometer 792
S.Itoh, T.Watanabe and Y.Endoh

Collimation and background reduction design for the time of flight neutron reflectometer SPEAR at LANSCE 799
W.A.Hamilton, G.S.Smith, and R.Pynn

First results from SANDALS - the small angle neutron diffractometer for amorphous and liquid samples at ISIS 809
A.K.Soper

Status of the new GLAD instrument at IPNS 820
R.K.Crawford, J.M.Carpenter, R.Dejus, J.R.Haumann, R.Kleb, D.G.Montague, D.L.Price, and S.Susman

Use of a semi-opaque beamstop for monitoring sample transmissions at GLAD 830
D.G.Montague, J.M.Carpenter, R.K.Crawford, R.Dejus, D.L.Price, and S.Susman

EXPERIMENTS using single neutron pulses 840
C.D.Bowman, P.A.Egelstaff, and H.G.Priesmeyer

Single crystal diffraction at ISIS 849
C.C.Wilson and D.A.Keen

Future ISIS single crystal instruments 861
C C.Wilson and W.I.F.David

Analysis of a drum chopper for use on a new small angle diffractometer at IPNS 873
R.K.Crawford, J.E.Epperson, P.Thiyagarajan, and J.M.Carpenter

New Components

•Polarizers and Thin Film Multilayer Devices

Optical neutron polarizers 890
J.B.Hayter

A double reflection multilayer monochlomator for cold neutron polarizing and small angle scattering experiments 899
T.Ebisawa, S.Tasaki, T.Akiyoshi, and N.Achiwa

Polarising filter tests at ISIS 906
R.Heap, P.W.Mitchell, J.Mayers and A.D.Taylor

Investigation and growth of multilayers 910
P.Boni, I.S.Anderson, R.Hauert, P.Ruterana, K.Solt, B.Farnoux, G.J.Herdman, J.Penfold, and O.Scharpf

Optimization of the transmission of a double-trumpet neutron beam compressor 919
R.E.Lechner and F.Mezei

Summary of this session 930
W.G.Williams

•Detectors

Area detector for small angle neutron scattering at KUR 932
Y.Maeda, M.Sugiyama and S.Uehara

Scintillation detector system in neutron-nucleus experiments 937
H.M.Shimizu, T.Adachi, and Y.Masuda

Neutron detectors at IPNS 943
R.K.Crawford, J.R.Haumann, and G.E.Ostrowski

An update on ISIS detectors 957
P.L.Davidson, M.W.Johnson and N.J.Rhodes

Several experiences of using Li-glass scintillators 971
N.Niimura, H.Hirai, K.Aizawa, K.Yamada, and F.Okamura

Summary of this session 975
R.K.Crawford and N.Niimura

•Sample Environments /Peripheral Equipments

Neutron diffraction study in pulsed high magnetic field 979
M.Motokawa, H.Nojiri, M.Uchi, S.Watamura, H.Kawai, and Y.Endoh

High pressure diffraction at ISIS 987
S.Hull, W.I.F.David, R.M.Ibberson and C.C.Wilson

Feasibility studies for high pressure neutron powder diffraction experiments 995
R.B.Von Dreele

Lanthanum nuclear polarization for T-violation experiment 1002
Y.Masuda, T.Adachi, S.Ishimoto, A.Masaike, K.Morimoto, and H.M.Shimizu

Neutron scattering at ultra-low temperatures 1010
K.Kakurai

Recent Progress on Data Taking and Analysis

A summary of the workshop on neutron scattering data analysis held at the Rutherford Appleton Laboratory in March 1990 1015
M.W.Johnson

Recent improvements of the parameterization of Bragg peak profile functions 1036
J.M.Carpenter, W.C.Dimm and F.J.Rotella

Correcting beam monitor & diffraction data for chopped delayed neutron backgrounds 1044
J.M.Carpenter, D.F.R.Mildner, J.W.Richardson, Jr., and W.C.Dimm

Machine control and online data analysis using PV-WAVE 1054
G.S.Smith, W.A.Hamilton, R.O.Nelson and G.P.Cort

Future strategy for computing at ISIS 1061
W.C.A.Pulford

(posters)

Measurements of two-dimensional antimagnetic spin wave by using chopper spectrometer installed in pulsed neutron source 1078
K.Yamada, M.Arai, A.D.Taylor, S.Hosoya, A.Sano, K.Nakajima, K.Ohyama, M.Kohgi, T.Nakane, T.Perring and Y.Endoh

Crystal analyzer type spectrometer LAM-D at KENS spallation thermal neutron source 1082
K.Inoue, K.Kanaya, Y.Kiyanagi, K.Shibata, K.Kaji, S.Ikeda, H.Iwasa, and Y.Izumi

Thermal neutron small-angle scattering spectrometer (WIT) 1095
N.Niimura, K.Aizawa, M.Hirai, U.Sangawa, and K.Yamada

Diffuse scattering studies on SXD 1099
C.C.Wilson, S.Hull and D.A.Keen

High precision structural refinement from time-of-flight single crystal data 1106
C.C.Wilson

Powder diffraction at ISIS 1114
W.I.F.David, S.Hull, R.M.Ibberson and C.C.Wilson

Helium-3 neutron polarisers 1122
W.G.Williams

A new polarized target for structure studies on biomolecules at GKSS 1135
M.Hirai, W.Knop, H-J,Schink, H.B.Stuhrmann, R.Wagner, J.Zhao, O.Scharpf, R.R.Crichton, M.Krumpole, K.Nierhaus, T.O.Niinikoski, and A.Rijllart

Engineering strain measurements using the NPD at LANSCE 1144
M.A.M.Bourke, J.A.Goldstone, and K.J.Lovell

List of participants 1153

Instruments Workshop

Total Performance

Recent Progress on Instruments
- Inelastic Scattering Instruments
- Elastic Scattering Instruments

New Components
- Polarizers and Thin Film Multilayer Devices
- Detectors
- Sample Environments/Peripheral Equipments

Recent Progress on Data Taking and Analysis

ICANS-XI International Collaboration on Advanced Neutron Sources
KEK, Tsukuba, October 22-26, 1990

Why Total Performance

N. WATANABE
National Laboratory for High Energy Physics
1-1 Oho, Tsukuba-shi, Ibaraki 305 Japan

ABSTRACT
The importance of total performance and, consequently, total optimization, of the entire system for neutron scattering experiments is discussed in terms of two examples using existing instruments.

I. INTRODUCTION

Why is total performance important? The reason is very clear: the quality of neutron scattering data or scientic information obtained depends exactly on the total performance of the entire system, including the accelerator, neutron source, neutron transport line, instrument (itself), sample environment, data taking and analysis system. Thus, total optimization becomes indispensably important. Even though a great deal of effort to optimize each component has been made, total optimization has not yet been well established.

First, let us list up what components have to be considered. Table I summerizes main components with their importance on total performance.

The accelerator system is the most expensive and important component of a spallation neutron facility and, in some cases, is shared with other facilities, such as the Japanese Hadron Project. An accelerator system used for a pulsed neutron source can be characterized by the time-averaged proton-beam power, $\bar{P}$; pulse width, τ_p; and repetition frequency, f, although it is often graded only by $\bar{P}$. The figure of merit of an accelerator, FOM_{acc}, is really expressed at the epithermal neuton region, such as $FOM_{acc} = \bar{P}$, within certain limits of f and τ. In the cold neutron region, however, the proton-beam power per pulse becomes much more important (discussed later) and, $FOM_{acc} = \bar{P}/f$. Although τp is important, as far as a synchrotron or a compressor ring is concerned, it is usually sufficiently short even for epithermal neutrons. It becomes important only when the macroscopic pulses from a proton linac are directly utilized. The stability of the proton beam or the reliability of an accelerator system is, of course, another important factor regarding the performance: the long-term duty cycle is strongly dependent on both the beam-break time and the shortened target life (beam time loss for a target exchange).

The performance of a neutron source is mainly determined by the target, moderator as well as coupling between them. The choice of a target material is most important: non-fissile (non actinide heavy metal), non-enriched (usually depleted) or enriched uranium. Although the neutron yield from these three are roughly 1:2:5, the fast-neutron background caused by delayed neutrons becomes much more severe than this order. There is strong limitation in the choice of target and moderator materials which depends on $\bar{P}$. The target life also depends on $\bar{P}$.

Table I Main Components of neutron facility with their importance on total performance

Components	Choice/parameters	Importance on total performance
Accelerator	Time-averaged proton-beam current ($\bar{I}_p$) or power ($\bar{P}$) Repetition frequency (f) $\bar{P}/f$ Pulse width (τ_p) Stability and reliability	Total neutron yield Bandwidth of neutron wavelength Especially important for cold neutron experiments Important only when long pulse from linac is directly used Target life, long-term duty cycle
Proton-beam injection schene	Horizontal/vertical	Determines target-moderator coupling (wing/flux-trap) Total number of neutron beams
Proton-beam delivery scheme	To single/multi TMRA'(s) (or target station(s))	Efficiency of proton-beam utilization and total facility gain
Target	Material (non-fissile, depleted U, enriched U)	Neutron yield, delayed neutron background
Target-moderator coupling	Wing or flux-trap	Slow neutron intensity, Number of neutron beams Fast neutron leakage
Moderator		
for cold neutrons	Material (liq. H_2, supercritical H_2, CH_4 at 20K or 100 K, etc) with/without premoderator, size (thickness), flat or groved	Fast-to-cold neutron conversion efficiency Pulse characteristics
for thermal neutrons	Material (H_2O, CH_4 at 100K, liq. H_2, etc), size and poisoning	Intensity and pulse width (resolution)
for epithermal neutrons	Material (mostly H_2O), size	Intensity and pulse width (resolution)
Moderator/reflector coupling	Coupled or decoupled	Slow neutron intensity, pulse width (resolution)
Reflector	Material (depends on moderator, coupling scheme and neutron energy used)	Slow neutron intensity, pulse width (resolution) Shielding
Target/moderator/reflector assembly (TMRA)	Number (single or multi,-dedicated to cold neutron source, thermal/epithermal neutron source, etc.)	Number of neutron beams totally avairable, More efficient proton beam utilization, Futher optimization for each TMRA.
Target station	Number (single or multi)	Number of neutron beams totally avairable, More efficient proton beam utilization, Futher optimization for each TMRA.
Beam collimator block		
inside void vessel (space)	With/without	Minimize background caused by high-energy neutrons and delayed neutrons when it exists
in bulk shield	Beam size, careful alignment	Best compromization between beam-intensity and background
Guide	Material (^{N}Ni, 58Ni, super mirror, etc.) Length	Transmittance and emittance, Beam size. Useful bandwidth of neutrons, resolution, space for instruments
	Distance between source and inlet of the guide	Beam acceptance
	Air gap on both side of tail culler	Transmission loss
Background supperession chopper	Stopping power Rise-up time, distance from the source	Background level Maximum incident neutron energy
Monochromating chopper	Chopper pulse width, distance from the source	Energy resolution
Overlap supperssion chopper		Bandwidth
Spectrometer	Sample position Analyzer and/or detector	Incident neutron solid angle (intensity) and resolution Resolution and detector/analyzer solid angle (detection efficiency)
Special sample environment	To be discussed elsewhere	
Layout in surrounding instruments	Avairable space	Minimum incident flight path length for high intensity requirement Maximum flight path length for scattered neutrons (resolution limit)
Experimental Hall	Size	Maximum total flight path length (resolution) Total number of instruments
Data taking system	To be discussed elsewhere	
Data analysis technique	To be discussed elsewhere	

There are several choices available for each component. For example, regarding the target station, one must decide which is the better; horizontal or vertical proton injection; a wing or flux-trap geometry in the target-moderator coupling; coupled or decoupled moderators; how many target stations or target-moderator-reflector assmblies (TMRA's); what is the optimal proton-beam delivery scheme; what combination of moderators with different characteristics; and what neutron-beam allocation are the optimal for various kinds of experiments. All of those should be considered on the basis of total performance. However, it is not easy to totally optimize so many components. When we construct a new facility or improve an existing one, we first have to establish a philosophy, a fundamental concept and a strategy under give boundary conditions. A preliminary thought of this kind concering JHP is given in ref. 1.

In our experience, the size of the experimental hall is one of the most important components. A finite size hall limits various possibilities for higher performance. There are very many components to be optimized totally, as listed in table I. In the existing instruments, only some parts have been optimized. We discuss in the next section two existing instruments as examples of how to consider whether something has been totally optimized or not.

II. EXAMPLES ON TOTAL PERFPRMANCE

The first example is a case which is favourable for KENS: i.e., the case of LAM-80ET, which has been fairly well totally optimized for high-resolution spectroscopy in the low-energy transfer range. The various parameters of this instrument are listed in Table II and are compared with those of IRIS, a corresponding instrument at ISIS. This table is a modified version of that which appears in ref. 4. LAM-80ET has large analyzer mirrors comprising small mica crystals; recently, IRIS has also been equipped with a new analyzer system comprising the mica crystals.[5] Although the number of fast neutrons produced at the KENS target is only 1/34 of that at ISIS, the total gain or the performance (resolution and data rate) is almost the same as shown in the table and Fig. 1[6,7]. The higher efficiency of LAM-80ET is mainly due to a higher conversion efficiency (from fast-to-cold neutrons) of the KENS solid methane moderator and larger solid angle of the analyzer mirrors. The advantages of LAM-80ET over IRIS are a better signal-to-background ratio and a larger energy window due to a lower repetition rate of neutron pulses (relatively large $\bar{P}/f$) in KENS (20 Hz). *Note that the cold neutron intensity per pulse in KENS is almost the same as that in ISIS (see Table II).* The energy window in IRIS is about ±300 μeV with $E_f \sim 0.832$ eV (the 004 reflection of mica crystal), and a full repetition rate of 50 Hz;[5] the corresponding value for LAM-80ET is about +1000, -500 μeV. The energy window of 300 μeV is just sufficient for measuring the tunneling spectrum in the above example; when a larger energy window is essential, however, 50 Hz is two high, and thinned out repetition using a chopper becomes indispensable while, of course, sacrificing intensity. Futhermore, LAM-80ET can simultaneously be used to measure different spectra with different E_f's by different reflections of mica crystal (006, 008,....). This increases the range of the Q-ω space simultaneously accessible with LAM-80ET. As a consequence, the relative gain of LAM-80ET to IRIS is effectively larger than the value listed in the table. However, there still exists an important mismatch in LAM-80ET: the instrument has a neutron guide, the cross section of which is 5×3 cm^2 in the first 3.5 m and 5×2 cm^2 in the succeeding part, and has no super mirror converging guide as is used in IRIS. If we were to have a similar guide as that used in IRIS (5×5 cm^2 guide and super mirror converging guide), we could expect an additional gain of about 2.8.

The next example is a case which is not favourable for KENS; i.e. the chopper spectrometer, INC, in KENS. Figure 2 shows time-of-flight (TOF) and energy spectra from a YbN sample at room temperature measured on INC, compared with the

Table II Comparison of the various parameters between LAM-80ET and IRIS

Componets	IRIS	Relative gain of LAM-80ET to IRIS	LAM-80ET
Proton beam Energy (MeV)	750		500
Time-averaged current (μA)	100		5
Protons per pulse	1.3×10^{13}		1.56×10^{12}
Repetition rate (Hz)	50		20
Fast neutron yield	1.72×10^{16}	1/34.4	5×10^{14}
Fast neutrons per pulse	3.4×10^{14}	1/13.6	2.5×10^{13}
Moderator	Liquid H_2 at 25K (decoupled)		Solid methane at 20K (decoupled)
Conversion efficiency from fast to cold neutrons (rerative values)	1	8	8
Cold neutrons per pulse (relative values)	**1**	**1/1.7**	**1/1.7**
Bandwidth Δλ (A)	2	(4)	8
Energy window (μeV) (with the 004 reflection of mica)	±300	(3.3)	+1000 -500
Guide tube gsin (relative value)	1	1/2.8	1/2.8
Analyzer mirror (mica)			
Reflectivity (relative value)	1	1	1
Solid angle (relative value)	1	9	9
Total gain		**0.75**	
Overall energy resolution (μeV) (with the 004 mica reflection)	**4.2**		**5.6**

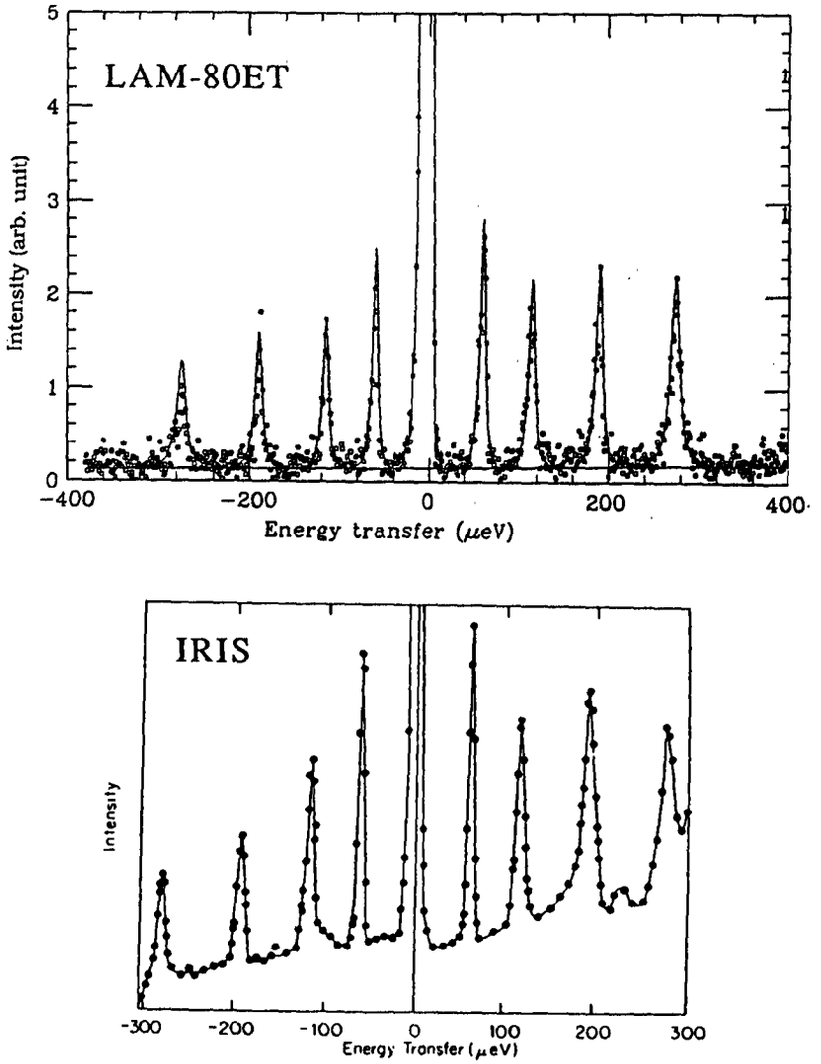

Fig. 1 Tunneling spectra of N-oxy γ-picoline measured on LAM-80ET (upper) and IRIS (lower) with E_f=0.832 μeV using the 004 reflection of mica crystals in analyzer system.

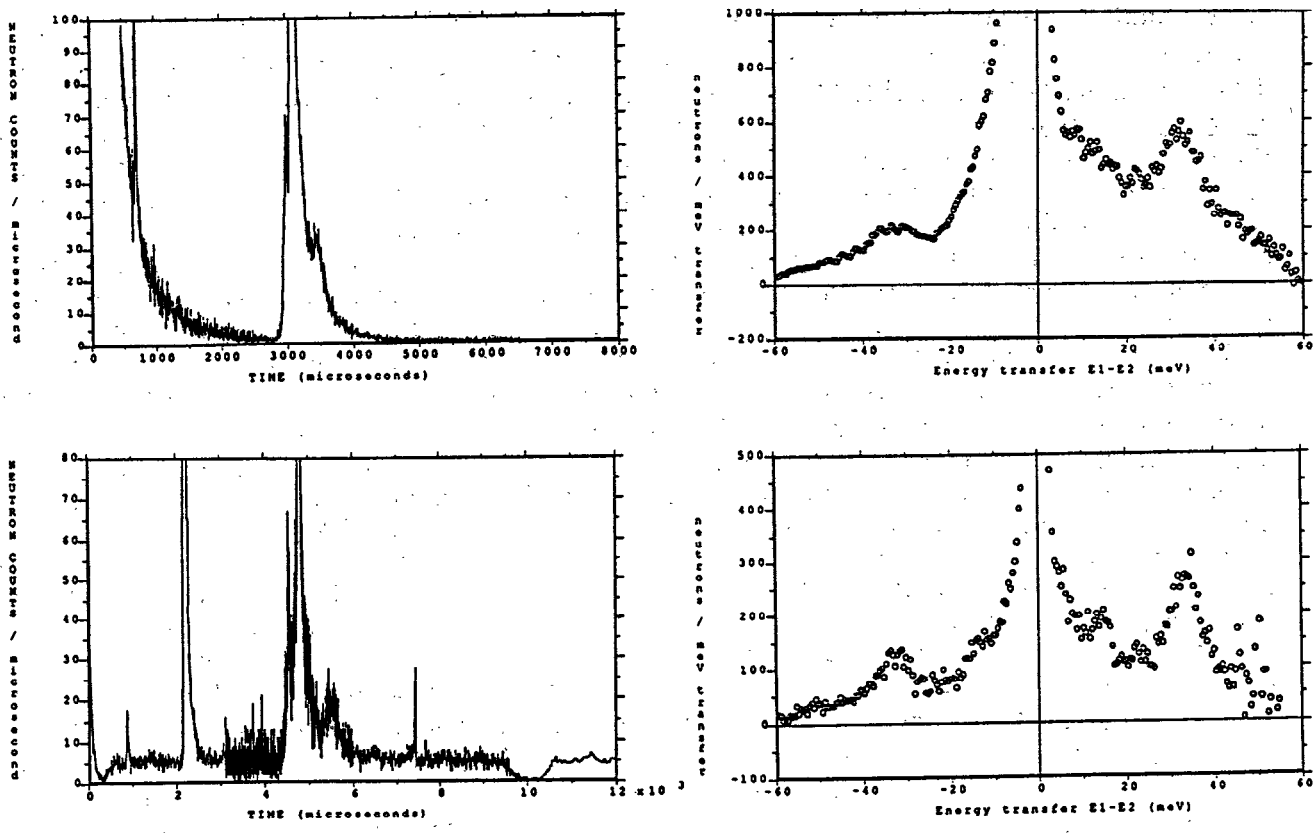

Fig. 2 TOF (left) and energy (right) spectra from YbN sample measured on INC (upper) and MARI (lower). Many peaks in the TOF spectrum measured on MARI are the sprious except for those appear between 4~6 msec.

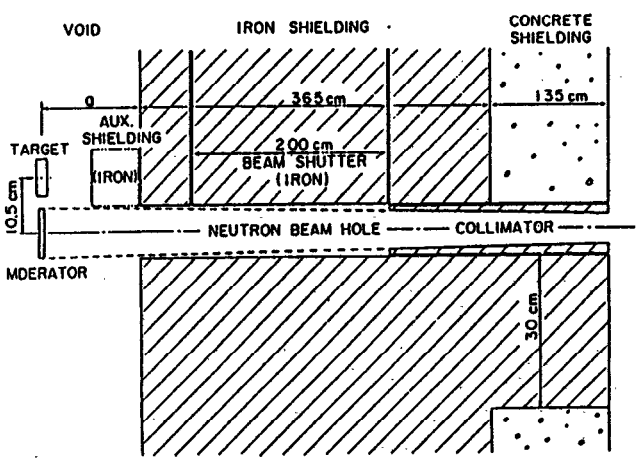

Fig. 3 Model target station used for the calculation of dose equivalent rate.

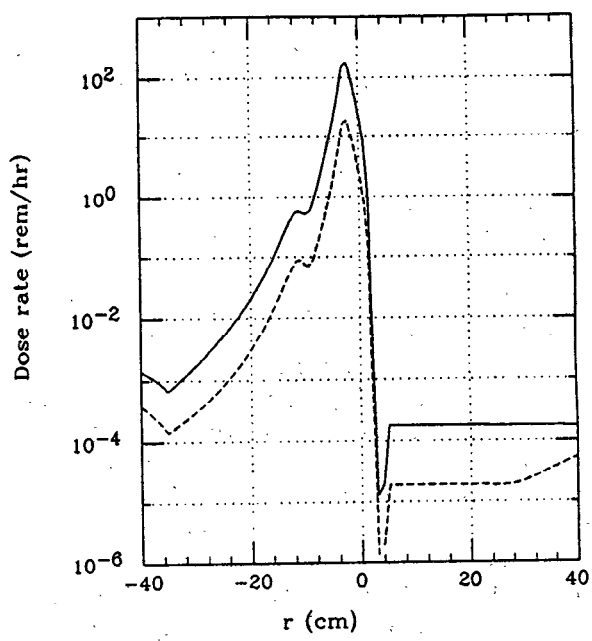

Fig. 4 Calculated dose equivalent rate at the exit of neutron beam hole: solid/dashed curves refer to without/with auxiliary iron block of 50 cm thick.

corresponding spectra from the same sample on MARI, a high-resolution chopper spectrometer in ISIS, by the same experimenter.[8] INC can provide almost the same data rate, with about a 10-times better signal-to-background ratio, but with much poor energy-resolution in a lower energy transfer range (20 ~ 30 meV), as in this case. We think that the better signal-to-background ratio in INC is due to better beam collimation in the bulk shield with a minimum void space between the souce and inner iron-collimator-block, as well as a lower repetition. The leakage of fast neutrons from a neutron-beam-hole is especially enhanced in the case that a large void space exists between the target and bulk shield. We performed a calculation on the dose equivalent rate, mainly concerning high-energy and fast neutrons, at the outer surface of the bulk shield around the neutron beam hole. High-energy neutrons produce fast neutrons and, eventually, epithermal neutrons when they are stopped. Therefore, the dose equivalent rate is a good measure of fast-neutron contamination in a slow neutron-beam. A model target station is shown in Fig. 3.[9] Figure 4 shows the calculated results. The dose equivalent rate is very high in the case of a void space with a=1 m. If we put an auxiliary iron block of only 50 cm thick inside the void vessel (as shown in Fig. 3), it is possible to decrease the dose equivalent rate by one order of magnitude, as shown by the dashed curve in Fig. 4. We actually experienced a higher background in various spectrometers when the previous tungsten target was replaced by the present depleted-uranium type. We overcame this by inserting a narrower beam collimator, stacked iron and B_4C picture frames (as used in ISIS) into the beam hole. The size of the aperture at the inner end of the collimator (about 1.7 m from the moderator) is 8 × 8 cm, which is smaller than the previous size (10 × 10 cm^2). Although the new collimator slightly limits the moderator viewed surface, the reduction in beam intensity is less than 10 %. We succeeded in reducing the background by one order of magnitude by this method. Note that even though the distance between the target and first iron shielding block in the present KENS facility is only 0.35 m (just reflector thickness), loose collimation resulted in a serious background problem. This means that the existence of a large void space between target and the inner surface of iron shielding makes the background problem more difficult.

INC has no burst (t_0) chopper. The large background at a smaller TOF is due to the lack of such a chopper; INC data shows the importance of a burst chopper.

The energy-resolution of INC is about 1.5-times as large as that of MARI, if INC views the same moderator as MARI, since INC has shorter flight-path lengths (about 1/1.5)for incident and scattered neutrons. To our regret, INC views a room-temperature moderator without poisoning, causing the greatest mismatch for INC, especially when the incident neutron energy is below 100 meV. The observed resolution (full width at half maximum) is much greater than the above value due to the longer pulse width of thermal neutrons from the room-temperture moderator. The longer exponential die-away tail of a thermal neutron pulse is the worst, making it difficult to characterize the inelastic scattering peak in this example. In the energy-transfer range (as in this example) the energy resolution of LAM-D in KENS is much better than INC. The resolution is the most important in a chopper spectrometer. If we could install INC at a beam hole viewing the solid methane moderator, it could provide much better data in this energy range. At the epithermal neutron region, however, INC is , of couse, reasonablly good: although it has almost the same data rate as dose MARI, it has 1.5-times the relaxed resolution. The spacial limitation is another important disadvantage for INC. The flight-path length for scattered neutrons at higher angles is only 1.3 m, since we were not allowed to dig a large hole in the floor to install a larger detector chamber, and there was no enough space for a horizontal detector arrangement due to the existing instruments on both sides.

III. CONCLUSION

As a conclusion we emphasize that there are very many mismatchs when we consider the total performance; in other words, there is still much room for improvements.

IV. ACKNOWLEDGEMENT

The auther is thankful to Dr. M. Kohgi for providing YbN data measured both on INC and MARI and to Dr. M. Misawa for further calculations of the dose equivalent rate around the neutron beam hole.

REFERENCE

1 Y. Kiyanagi and N. Watanabe; Proc. ICANS-XI (Tsukuba, Oct. 22-26, 1990) P-408
2 Y. Kiyanagi, N. Watanabe, M. Furusaka, H. Iwasa and I. Fujikawa : ibid, P-388
3 N. Watanabe : ibid, P-471
4 K. Shibata and T. Kamiyama : A summary of Performance on IRIS and LAM-80ET, TUNNEL 902, Proc. Japan-U.K. Collaboration on Neutron Scattering Research, KEK Report 90-17 (Dec. 1990) P-39
5 C. J. Carlile : The design of the IRIS inelastic neutron spectrometer and improvements to its Analyzer, ibid. P-1
6 C. J. Carlile : Tunneling measurements of Methane, Methle Pyridine and its derivatives, and Ammonia in Caesium in tercalated Graphite on IRIS, ibid. P-59
7 S. Ikeda et al., : Neutron scattering form N-oxy γ-picoline, ibid. P-42
8 M. Kohgi, private communication
9 N. Watanabe, M. Misawa and S. Ikeda : Technical problems in KENS-II design, Proc. Meeting on BSF Future Prospect-II (Mar. 11-12, 1983), KEK Int. 83-7 (1983) P-199 (in Japanese)

Q(R.Pynn): What is the $\Delta d/d$ for mica? What is this matched to- the full width of the pulse from the moderator or the leading edge of pulse? At what energy have the matching been done? Have you thought about other analyzer crystals for LAM-80, such as silicon?

A(N.Watanabe): We have no data on $\Delta d/d$ of mica crystal. I think $\Delta E_f/E_f$ in LAM-80ET using 002 reflection of mica is mainly determined by a finite angular uncertainty between sample and analyzer crystal (1cm x 1cm) rather than $\Delta d/d$ of mica itself.

C(W.G.Williams): Optimization is a useful concept but in practical situations we are always concerned with compromise. IRIS at ISIS is a good example. It does not need a 50 Hz source.

ICANS-XI International Collaboration on Advanced Neutron Sources
KEK, Tsukuba, October 22-26, 1990

Performance of Chopper Spectrometers

M.Arai[1], A.D. Taylor[2], S.M. Bennington[2], Z.A. Bowden[2], R. Osborn[2], M. Kohgi[3], K. Ohoyama[3] and T. Nakane[4]

[1]National Laboratory for High Energy Physics, Oho, Tsukuba 305 Japan
[2]Rutherford Appleton Laboratory, Chilton, Didcot, Oxon OX11 0QX, UK
[3]Tohoku University, Aoba, Aoba-ku, Sendai 980, Japan
[4]Matel. Res. Inst., Tohoku University, Katahira, Aoba-ku, Sendai 980, Japan

ABSTRACT
We discuss the performance of chopper spectrometers at pulsed neutron sources, with particular reference to results from MARI, HET and INC. Finally we suggest optimized parameters for several options on the performance.

1. Introduction

1.1. The Standard Spectrometer for a Pulsed Neutron Source

In a direct geometry spectrometer on a pulsed neutron source the incident neutron energy is monochromatized by a mechanical fermi chopper phased to the source. This is the natural type of spectrometer for inelastic scattering on a pulse neutron source. The wide dynamical range in Q-E space gives a unique opportunity for new science as we have shown in another report in this volume[1].

The overall performance of a chopper spectrometer on a pulsed neutron source requires the optimization of many aspects of its performance -- intensity, resolution, background, angular coverage, dynamic range etc. -- within the constraints imposed by the nature of the source (current, frequency etc..), the target/moderator system (material, coupling, geometry etc.), the beam line components available and the source geometry.

At present HET and MARI at the ISIS facility of Rutherford Appleton Laboratory in UK, LRMECS and HRMECS at the IPNS facility of Argonne National Laboratory in USA and INC at the KENS facility of National Laboratory for High Energy Physics in Japan are fully operational. The design parameters for these spectrometers are summarized in Table I. In this report we will give an overview of the performance of these spectrometers and concentrate on HET, MARI and INC, which have almost identical chopper systems, to discuss practical aspects of their performance and problems. We also give some suggestions for future optimizations.

	Proton Current (μA)	Moderator Target factor	Flux at moderator (n/eV.sr.100cm2.s)	Moderator Area (*100cm^2)	Chopper Transmiss	L1+L3 (cm)	Scattering Angle	L2 (cm)	ΔE/E	Intensity at Sample (n/cm^2/s	Int/ΔΩ (Counting rate)	Normlized by MARI
MARI	100	1	3.00E+12	0.64	0.8	1170	3°~135°	400	1.0%	2244	1.40	1.00
HET	100	1	3.60E+12	0.64	0.8	1170	3°~7°	400	1.0%	2693	1.68	1.20
							9°~29°	250			4.31	3.07
							134°~136°	400			1.68	1.20
INC	3	2	2.16E+11	0.64	0.8	820	5°~40°	250	1.5%	493	0.79	0.56
							40°~130°	130			2.92	2.08
LRMECS	14	2	1.01E+12	0.64	0.8	683	3°~120°	250	2.0%	4425	7.08	5.05
HRMECS	14	2	1.01E+12	0.64	0.8	1385	3°~	400	1.0%	538	0.34	0.20

Table I Current performance of chopper spectrometers. The calculation is for epithermal region.
Intensity at Sample =Flux.Mode*Mode.Area*Chop.Trans*ΔE/(L1+L3)^2
Int/ΔΩ = Intensity at Sample / L2^2

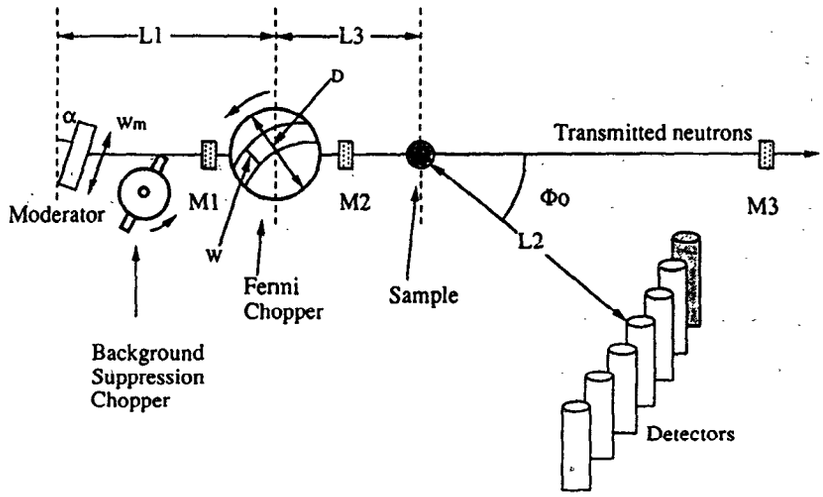

Fig. 1 Schematic diagram of a chopper spectrometer.

1.2. Outline of a Chopper Spectrometer

The structure of a chopper spectrometer is shown in Fig.1. Neutrons starting at time t_o at a moderator are monochromatized by a fermi chopper at distance L_1 which is phased to the neutron burst time. Fast neutrons are cut out by a background suppression chopper at an upstream position. The incident neutron spectrum is monitored by M_1, the monochromatized spectrum by M_2 and the transmitted spectrum by M_3. As the only moving components in the spectrometer are the choppers, enormous detector arrays can be easily arranged around the sample covering a wide range of scattering angles.

2. *Energy Resolution*

2.1. Conventional Expression for the Resolution

The resolution depends on the time width of the moderator pulse Δt_m, the time width of the chopper opening Δt_{ch} and the flight path lengths L_1,L_2 and L_3. A detailed derivation of the monochromatized pulse shape is given fully in reference (2). However it is quite helpful to illustrate the essence of the resolution for the present discussion.

The asymmetric moderator pulse shape can be described by a slowing down and storage component[3]. Propagating neutrons are transmitted through the chopper, when the energy (the slope in the Time-Length diagram in Fig. 2 is appropriate for the chopper opening at L_1. The chopper opening time width is very short (typically a few μs), giving a pin-hole camera effect in the time-length space. This reverses the image of the moderator pulse shape at the detecting point.

The actual pulse shape is obtained by the velocity integration of the various neutron energies which pass through the chopper. The calculation is achieved by a convolution of the moderator pulse function and chopper opening function. However in most cases the following equation[4,5] gives a reasonable estimate for the energy and momentum resolution especially in the slowing down region above the Maxwellian.

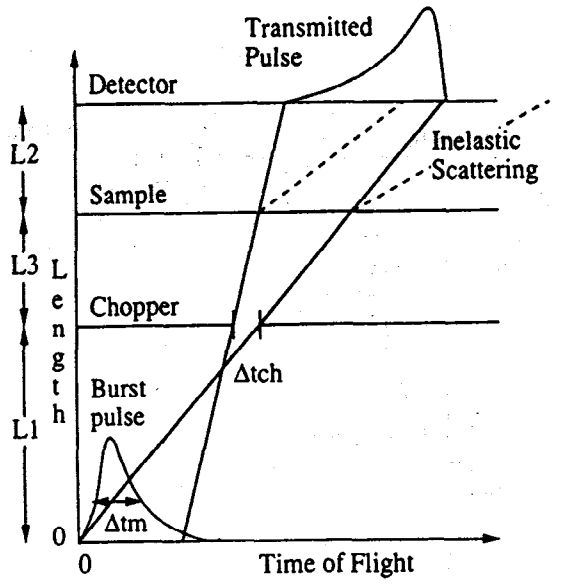

Fig. 2 Pin-hole camera effect on the pulse shape in time-length space.

$$\frac{\Delta\varepsilon}{E_i} = [\{2R_1[1 + \frac{L_1+L_3}{L_2}(1-\frac{\varepsilon}{E_i})^{3/2}]\}^2 + \{2R_2[1 + \frac{L_3}{L_2}(1-\frac{\varepsilon}{E_i})^{3/2}]\}^2]^{1/2} \quad . \quad (1)$$

$$\frac{\Delta Q}{Q} = \frac{2mE_i}{h^2Q^2}\{\frac{E_i}{4E_f}(\cos(\Phi_0) - \sqrt{\frac{E_f}{E_i}})^2(\frac{\Delta\varepsilon}{E_i})^2 + \frac{E_f}{E_i}\sin^2(\Phi_0)\,\Delta\Phi^2\}^{1/2} \qquad (2)$$

,where $R_1 = \Delta t_{ch}/t_{ch}$, $R_2 = \Delta t_m/t_{ch}$

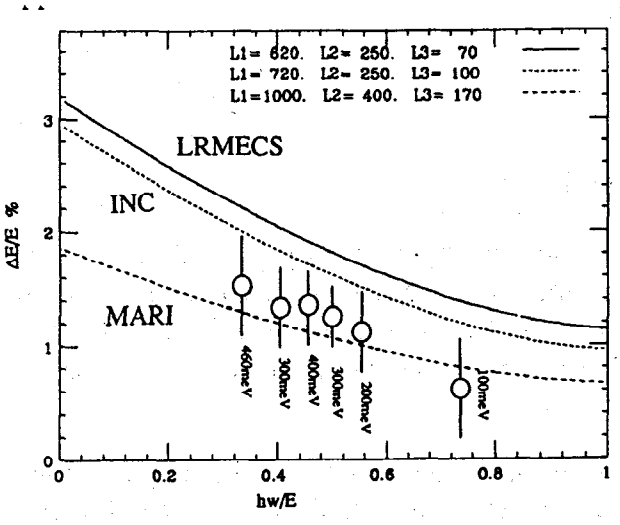

Fig. 3 Calculated energy resolution from eq. (1). Circles are the observation.

The moderator time width is described approximately by Δt_m [μs] ~1.8 /√E [eV] in the slowing down region. For resolution matching, the chopper opening time Δt_{ch} should be matched to the Δt_m. The length L_1 and L_2 are the dominant components for the overall energy resolution. Figure 3 shows the calculated energy resolution of the LRMECS, INC and MARI spectrometers.

2.2. Moderator Characteristics and Time Structure

The moderator characteristics are very important for the performance of a spectrometer at a pulsed neutron source. The time structure of the moderator pulse is directly reflected in the resolution of the spectrometer. The calculated time widths for several moderators are shown in Fig. 4 [6]. The deviation from the straight line described by Δt_m [μs] ~1.8 /√E [eV] reflects the contribution of the storage

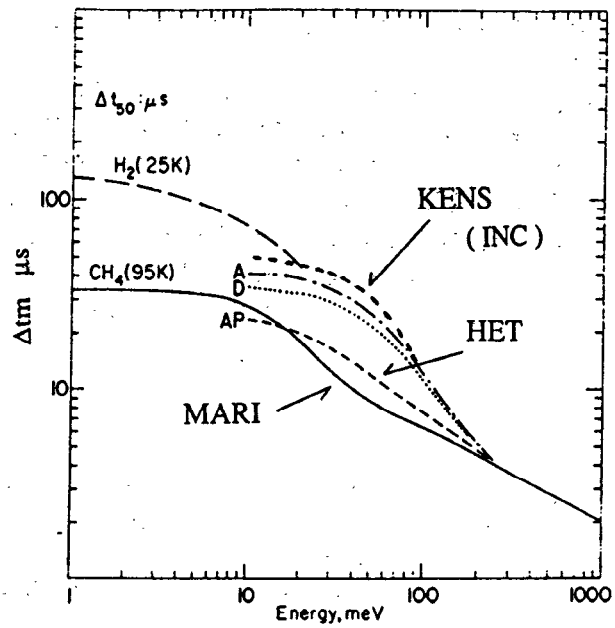

Fig. 4 Predicted FWHM of the moderator pulse shape as a function of energy.

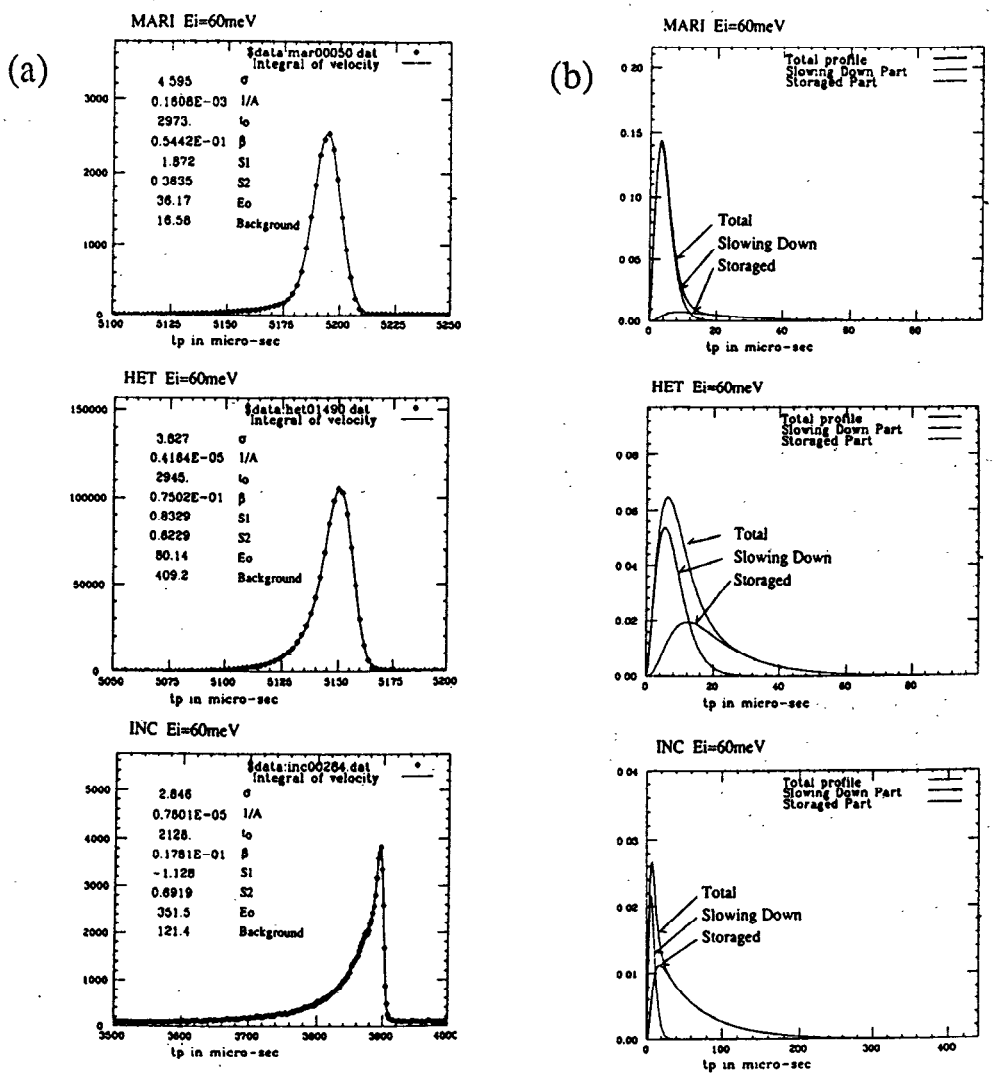

Fig. 5 (a) Transmitted pulse shape at the downstream monitor M3 for Ei=60meV. The line is a fit. σ, chopper opening time width; A, amplitude, other parameter's notation is the same as ref.3). (b) Expected moderator pulse shape at the moderator surface.

component. A poisoned or cooled moderator maintains good resolution in the low energy region by sacrificing some intensity.

Here we estimated the moderator pulse shape from the observed pulse shape at the downstream monitor M_3 shown in Fig. 5 (a). A deconvolution with a chopper window function (similar to a Gaussian) gives us a rough estimate of the moderator characteristics as shown in Fig. 5 (b). The MARI moderator is liquid CH_4 at 100K poisoned at 2.25cm depth. The HET moderator is ambient H_2O poisoned at 1.5cm depth. The INC moderator is ambient non-poisoned H_2O. The difference in poisoning has an enormous effect on the pulse shape and the resolution of the spectrometer.

2.3. Observed Resolution

In the epithermal region, the moderator pulse shape is dominated by the slowing down component. The pulse shape is close to symmetric so the observed pulsed shape gives a direct measure of the resolution of a spectrometer. Fig. 6 (a) shows the observation of spin waves in the one dimensional antiferromagnet $KFeS_2$ on MARI and the estimated energy resolution is plotted as circles in Fig. 3. The agreement between the observation and the calculation is good for various incident energies and we can see that the simple resolution equation (1) gives us a reasonable estimate of the resolution.

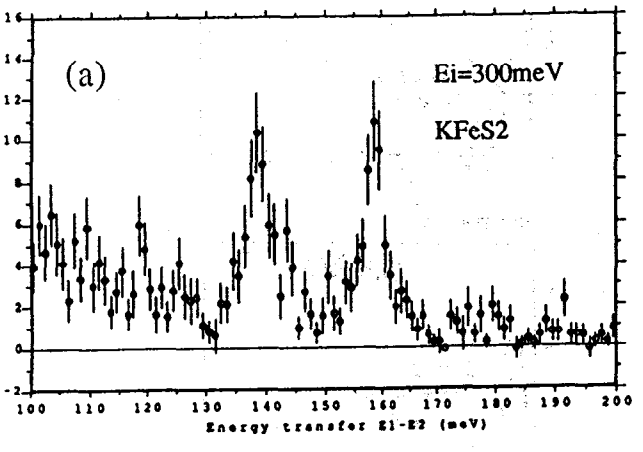

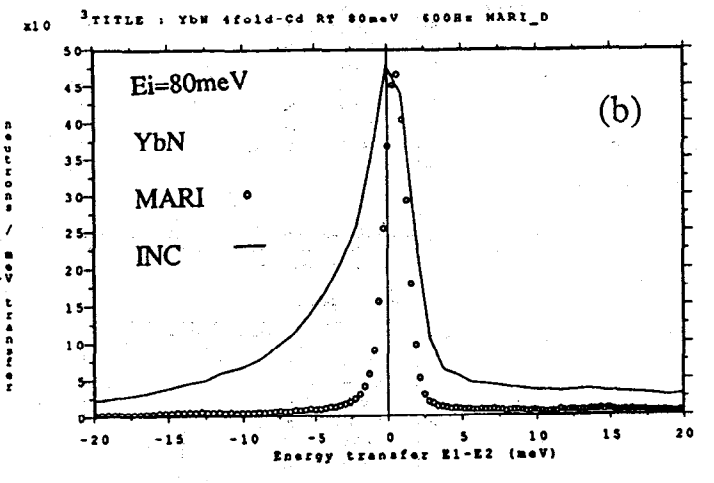

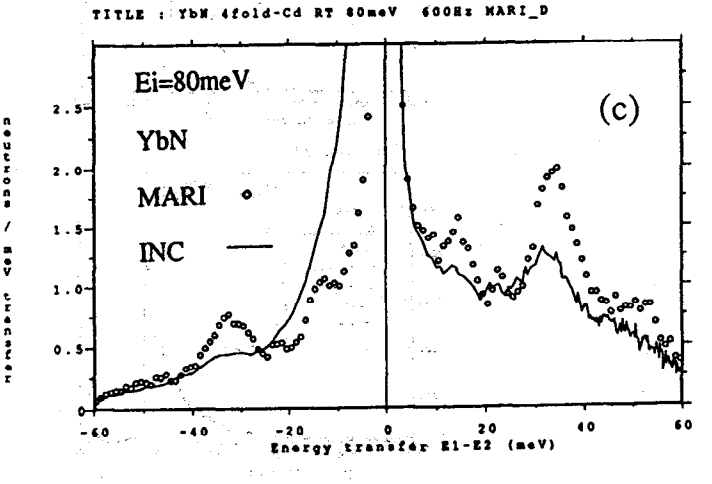

Fig. 6 (a) Spin wave excitation peak of 1D-antiferromagnet KFeS2 with Ei=300meV. (b) Comparison of the energy resolution at the elastic peak for Ei=80meV measured on YbN. Intensity was normalized at the peak. (c) Comparison at the inelastic region on YbN Ei=80meV. Intensity is normalized per detector solid angle.

When the incident energy is lower than the epithermal-Maxwellian cross-over energy, the storage component becomes the dominant part, and the moderator pulse

width increases rapidly as seen in Fig. 4. This effect is clearly shown in Fig. 6 (b) and (c) observed on the crystal field excitation of YbN with the incident energy of 80meV. The energy resolution is three times worse for INC than MARI at this energy, although only 50% worse at epithermal region.

The need for good resolution is illustrated by problems taken from the both extremes of these instruments energy range. At the low energy end, Fig. 7 (a) shows the spectrum of Tm:$YBa_2Cu_3O_7$ taken with Ei=20meV on MARI. The line width of the crystal field excitations was followed using the FWHM resolution of about 300μeV - with a 80μeV leading edge ! At high energy, HET required the 50meV resolution available at 2.14eV to observe the full inter-multiplet spectrum of Tm up to 1776meV, Fig. 7 (b). This high resolution has been crucial in enabling a wide range of science to be tackled by these spectrometers.

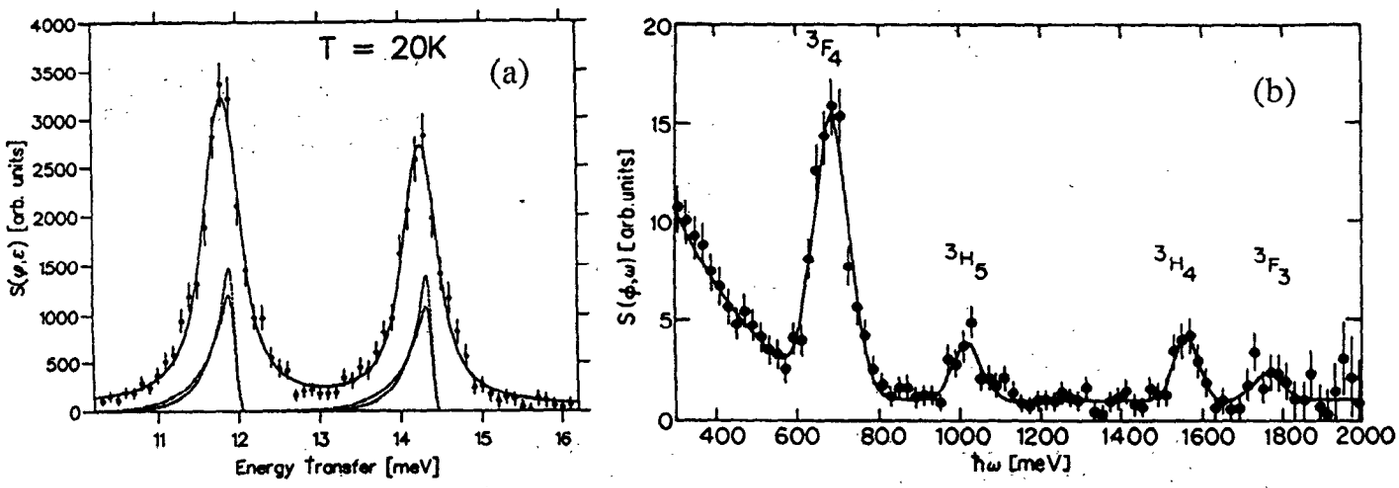

Fig. 7 (a) Measurement on Tm:YBa2Cu3O7 with Ei=20meV on MARI. (b) Measurement on Tm with Ei=2140meV on HET.

3. *Intensity*

From a practical point of view we should design a spectrometer to have reasonable intensity at the sample position. In Table I we estimated the neutron flux at the sample position from the calculated neutron flux at the moderator surface $\Phi_0(E)$[6], the moderator area M, chopper transmission T, flight path length L_1,L_2 and L_3 and the designed resolution ΔE. We obtain a value at the sample position close to observation for HET, MARI and INC by using the following equation[5].

$$\text{Intensity at sample}(E)=\Phi_0(E)*M*T*\Delta E/(L_1+L_3)^2 \qquad (3)$$

The flux at the sample is more or less similar among the spectrometers (several thousands neutrons/cm^2/s). This value is one order of magnitude smaller than that of the typical inelastic instrument in ILL. However a large number of detectors surrounding the sample can compensate the counting rate and provide one-day experiments as a typical measurement. The flux at the sample can be rapidly increased by a small relaxation in the energy resolution, so the optimization of the spectrometer performance is important. For example INC has 50% worse resolution than that of MARI. However the estimated counting rate per solid angle is only 50%

of that of MARI in spite of the large difference in proton current (30 times). This was confirmed by the measurement on YbN as shown in Fig. 6 (c).

4. Angular Coverage

Chopper spectrometers naturally lend themselves to wide angular coverage. The only difficulty is the cost of detectors ! In Fig. 8 we show the observable Q-E space for these spectrometers. HET has a very limited angular coverage both at the small (3° ~ 7°) and the high angle (134° ~ 136°), whereas MARI (3° ~ 135°), INC (5° ~ 130°) and LRMECS (3° ~ 120°) have a very wide angle coverage. An important feature of MARI and LRMECS is their equi-resolution over the angular range. INC has

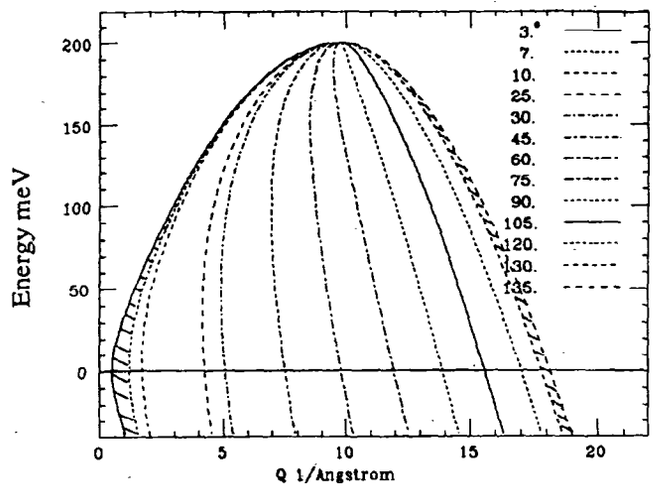

Fig. 8 Accessible Q-E space for Ei=200meV. The shaded area is for the HET 4m detector bank.

heterogeneous resolution from 40° to 135°. The wide angular coverage gives a full S(Q,E) measurement in one experiment, which is especially important to understand the dynamics and structure of non-crystalline materials. From our experience the equi-resolution angular coverage is very important in most experiments. Even when the scientific interest is concentrated at small angles as in magnetic scattering the phonon contribution can only be estimated from data at higher angles. If the energy resolution varied across the angular range this estimation would not work properly. Figure 9 shows the phonon contribution estimated from the high angle data under the magnetic scattering on $CeCu_2Si_2$ on HET.

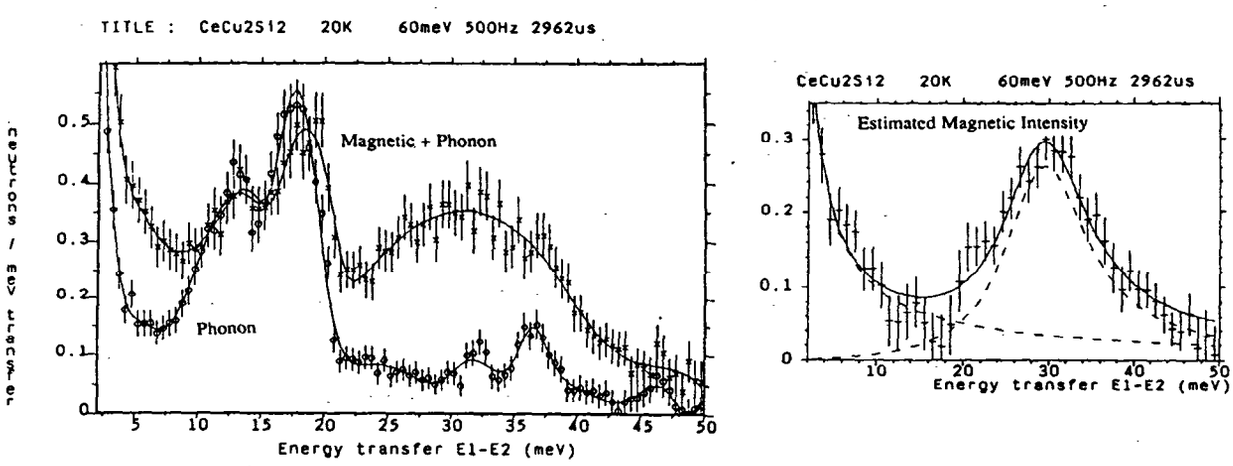

Fig. 9 Estimation of the magnetic scattering of CeCu2Si2 at small angles after subtraction of the phonon contribution using high angel data.

5. *Background*

5.1. Delayed Neutron Background

There are contradictory requirements in the choice of target material. Fissile material such as uranium produces twice as many neutrons as a non-fissile target such as tungsten or tantalum. However the accompanied delayed neutron background causes a lot of trouble in the data analysis and sometimes reduces the data quality. Figure 10 shows the observed data on g-SiO_2 from MARI with Ta and U targets under otherwise identical conditions. Here the data are normalized to an accumulated proton current of 10mAhrs. The signal was twice as intense with the U-target, but the background level was 30 times higher. (The background level for the Ta-target is about 0.1 count/min/detector. This value is close to the ideal intrinsic noise level for ^{3}He detectors.) The background level depends on the fast neutron cross-section of the sample, so that a simple subtraction of the empty cell data is not appropriate.

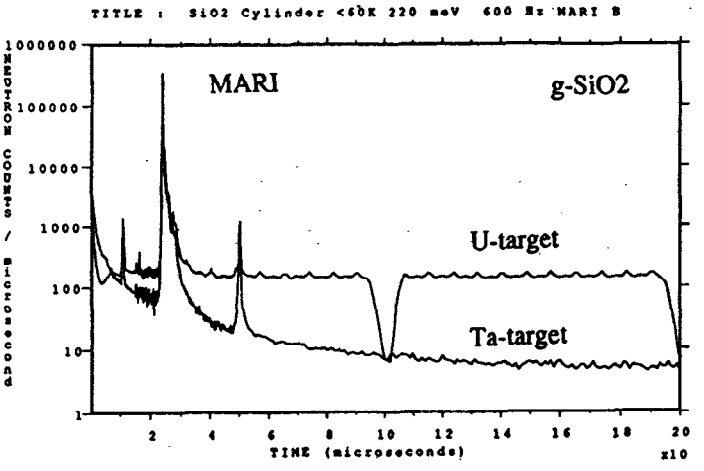

Fig. 10 Comparison of the background from g-SiO2 on MARI with a U-target and Ta-target under otherwise identical conditions. The central dip for the U-target is due to the background suppression chopper.

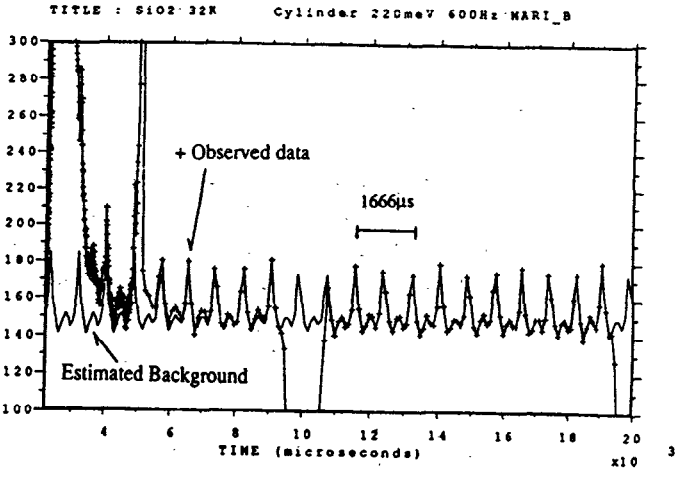

Fig. 11 Modulated delayed neutron background and estimated correction.

The modulated structure in the delayed neutron background depends on the chopper conditions such as frequency, phase and attenuating structure. Such a modulated background can be subtracted by averaging the long time background as shown in Fig.11. The background was averaged by folding the data in the long time region with the chopper periodicity of 1666.7μs (600Hz). The complete subtraction is difficult and sometimes the quality of low intensity data is diminished. The modulated background does not affect high energy excitation data, because the scattered intensity is concentrated in a small time-of-flight region. For low energy transfer measurements, however, the scattered intensity is spread over a wide range of time-of-flight and the signal can become comparable to the delayed neutron background. To some level we can diminish the delayed neutron background by a careful design of the collimator system. However since this background is a sample born background, it is difficult to avoid if we chose fissile material for the target.

In Fig.12 we compare the data for the same sample of YbN at MARI and INC. The signal-to-background (S/N) ratio is ten times worse in MARI. After taking into account the difference of the accelerator duty cycle (20Hz for INC and 50Hz for

MARI), the factor is still four, which may be attributable to differences of collimation system, or to reflector differences between KENS and ISIS.

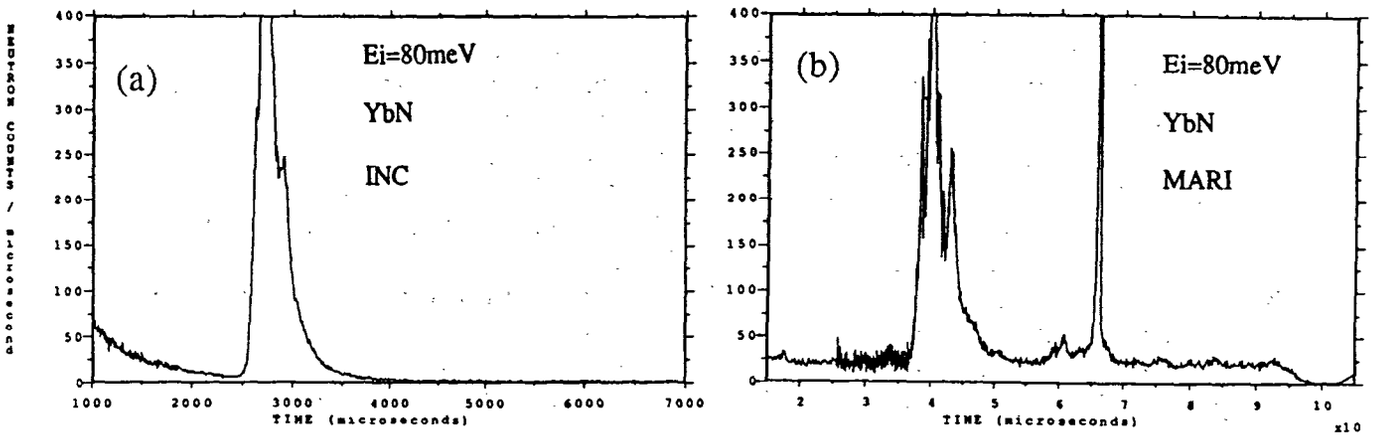

Fig. 12 Comparison of the data from the same sample of YbN for (a) INC and (b) MARI.

5.2. Background Suppression Chopper

A key device for these instruments is a background suppression chopper. HET and MARI are effective to energies over 2eV, whereas LRMECS, HRMECS and INC without a background suppression chopper are restricted to less than ~500meV due to the high background for many problems.

5.3. Spectrometer Born Background

Another background source is within the spectrometer itself where neutron can be scattered by internal components such as the sample cell, sample environment equipment, the vacuum chamber wall and the shielding around the sample itself. External background is normally broad in time (Fig. 11), whereas multiply scattered background from within the spectrometer can give very sharp and intense spurious peaks. Figure 13 shows an early measurement of the crystal field excitation of Tm:$YBa_2Cu_3O_7$ on MARI. The two peaks at higher energy transfer in Fig. 13 are the real excitation spectrum as shown in Fig. 7 (a). The first peak is spurious, produced by a multiple scattering from the flange of the cryostat above the sample. The elastic signal from the sample was further scattered by the flange and came to the detectors at a later time-of-flight, thus imitating an inelastic signal. Such processes are now suppressed by a strategically placed low albedo surface.

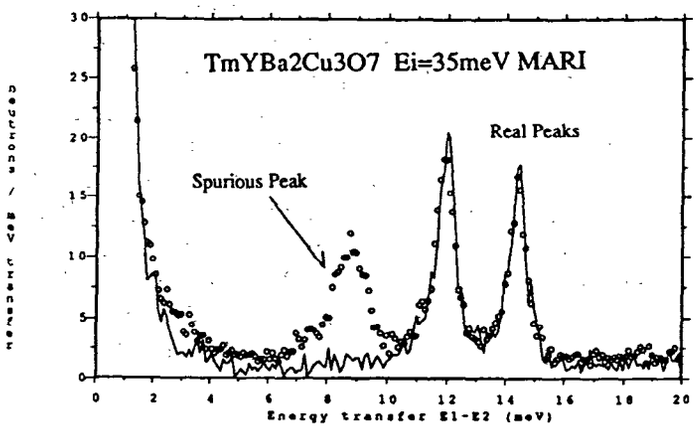

Fig. 13 Multiple scattering inside the spectrometer. The two peaks at higher energy transfer are the real excitations. The first peak is spurious.

A second example of internal background is coherent scattering from the thin aluminum membrane, situated downstream from the sample, which separates the spectrometer vacuum and sample vacuum. The baffle shields in the spectrometer shadow some detectors from this scattering but this is ineffective at the small angle region. The total flight path of this diffracted background is longer, again causing it to manifest itself as an apparent inelastic signal. It is present in an 'empty' spectrometer run, but sample attenuation make this effect difficult to estimate quantitatively.

6. *Conclusion*

There are no absolute criteria for the optimization of the performance of a chopper spectrometer, but the following rules of thumb are appropriate:

Intensity: It is important to obtain reasonable statistics in one day on a typical sample. On MARI 5000 n/cm^2/s should satisfy this criterion for a wide variety of science. From this starting position we tried to find optimized parameters for chopper spectrometers at other neutron sources, subject to typical geometrical constraints, i.e. $L_3/L_1=0.15$ and $L_2/(L_1+L_3)=0.4$.

In Table II, "High Resolution Option" corresponds to this condition. The last two columns show the expected intensity per unit solid angle normalized to that of MARI. By relaxing the resolution a little, we can achieve the similar statistics in spite of the considerably different proton current. In the "High Intensity Option" by relaxing the resolution by 50%, we can get 10 times higher intensity. The flux decreases proportionally to 1/(length)^3 but the resolution is proportional to 1/length. Therefore a careful design of the parameters can compensate the performance greatly.

Angular Coverage: Continuous angular coverage with equi-energy-resolution has been found to be practically very important. Even when the signal is concentrated at small angle, as with magnetic excitations, the high angle data with the same energy resolution is essential to estimate the non-magnetic contribution.

	Proton Current (μA)	Moderator Factor	Flux at moderator (n/eV.sr.100cm2.s)	Moderator Area (*100cm^2)	Chopper Transmiss	L1 (cm)	L3 (cm)	L2 (cm)	ΔE/E	Intensity at Sample (n/cm^2/s)	Int/ΔΩ	Local ratio normlized by MARI	Grand ratio normlized by MARI
High Resolution Option (for Maximum Proton Current and U-target)													
MARI	200	1	6.00E+12	0.64	0.8	969	145	388	1.0%	5000	3.33	1.00	1.00
INC	8	2	5.76E+11	0.64	0.8	663	99	265	1.5%	1500	2.13	0.64	0.64
LRMECS	14	2	1.01E+12	0.64	0.8	726	109	290	1.4%	2000	2.37	0.71	0.71
High intensity Option (for Maximum Proton Current and U-target)													
MARI	200	1	6.00E+12	0.64	0.8	611	92	244	1.6%	20000	33.51	1.00	10.07
INC	8	2	5.76E+11	0.64	0.8	444	67	178	2.3%	5000	15.85	0.47	4.76
LRMECS	14	2	1.01E+12	0.64	0.8	425	64	170	2.4%	10000	34.64	1.03	10.41
Low Background Option (for non-fissile target)													
MARI	200	0.5	3.00E+12	0.64	0.8	829	124	331	1.2%	4000	3.64	1.00	1.09
INC	8	1	2.88E+11	0.64	0.8	584	88	233	1.7%	1100	2.02	0.55	0.61
LRMECS	14	0.5	2.52E+11	0.64	0.8	558	84	223	1.8%	1100	2.21	0.61	0.66

Table II Some optimizations of a spectormeter for several options.
Intensity at Sample (Ei) =Flux.Mode*Mode.Area*Chop.Trans*ΔE/(L1+L3)^2
Int/ΔΩ = Intensity at Sample / L2^2. Constraint; L3/L1=0.15 and L2/(L1+L3)=0.4

Background: The background level is often dominated by the target material. The delayed neutron background can be critical in a direct-geometry inelastic spectrometer, but on the other hand a fissile target actually provides twice the intensity for diffractometers and other instruments without increasing their background significantly. So the choice of the target material for a facility is difficult. The last calculation in Table II the "Low Background Option (for non-fissile targets)" suggests that we obtain intensity by relaxing the resolution by small amount. It may be worthwhile to consider this option for a high intensity spallation neutron source, where the optimization of the target-moderator coupling with a non-fissile target give the system with long life-time and good reliability.

7. *Acknowledgement*

The experiments on MARI were carried out during the commissioning period in 1991 under the UK-Japan collaboration on neutron scattering research. We are indebted to Prof. N. Watanabe for his continued support of this collaboration.

References

1) A.D. Taylor et al., ICANS-XI MARI report.
2) C.-K. Loong, S. Ikeda and J.M. Carpenter, Nucl. Inst. Meth. Phys. Res. A260 (1987) 381
3) S. Ikeda and J.M. Carpenter, Nucl. Inst. Meth. Phys. Res. A239 (1985)536
4) C.J. Carlile, A.D. Taylor and W.G. Williams, Rutherford Appleton Laboratory Report, RAL-85-052
5) M. Arai, M. Kohgi, M. Itoh, H. Iwasa, N. watanabe, S. Ikeda and Y. Endoh, ICANS-X Proc. 297 (1988)
6) A.D. Taylor, Rutherford Appleton Laboratory Report, RAL-84-120, 1984

Q(R.Pynn): You mentioned many characteristics of spectrometers among which we have to choose in order to achieve total performance. Do you have any advice for us on how to make these choices?

A(A.D.Taylor): No. This is too hard a question to answer in general. However it is important not to be frozen into inaction by the large number of the options available. Your fourier analysis is, however, a helpful guide.

ICANS-XI International Collaboration on Advanced Neutron Sources
KEK, Tsukuba, October 22-26, 1990

IMPROVING THE RESOLUTION OF CHOPPER SPECTROMETERS AT PULSED NEUTRON SOURCES

J. M. Carpenter
Intense Pulsed Neutron Source, Argonne National Laboratory,
9700 South Cass Avenue, Argonne IL 60439
and
D. F. R. Mildner
Center for Analytical Chemistry
National Institute of Standards and Technology,
Gaithersburg MD 20899

The submitted manuscript has been authored by a contractor of the U. S. Government under contract No. W-31-109-ENG-38. Accordingly, the U. S. Government retains a nonexclusive, royalty-free license to publish or reproduce the published form of this contribution, or allow others to do so, for U. S. Government purposes.

ABSTRACT

We examine the relationships between intensity and resolution in pulsed-source chopper spectrometers, including the effects of Soller collimation, narrower rotor slits and higher rotor speeds. The basis is a simplified description of a spectrometer, approximately optimizing the rotor pulse and lighthouse effects. The analysis includes a new treatment of the angular distribution transmitted through a system consisting of a coarse collimator and a Soller collimator. The results encourage the prospect for a reasonably easily accomplished, higher resolution, optional configuration of the pulsed source chopper spectrometers at IPNS.

I. INTRODUCTION

All three chopper spectrometers[1] at IPNS[2] include Soller collimation between the incident beam monitor detector, which is immediately downstream from the chopper, and the sample. This is primarily a shielding device which has little impact on the resolution or intensity of the instrument.

Here we consider the Soller collimator as a device to narrow the angular distribution of the beam striking the sample, and thus to reduce that contribution (sometimes called the "lighthouse" or the "sweep time" effect) to the chopped-beam pulse width and to the resolution of the instrument. A similar effect can be obtained by narrowing the width of the slits in the chopper, though in this case the limit of what can be done approaches the pulse width due to the lighthouse effect. This can also be accomplished by increasing the rotor angular speed as has been done at the HET and MARI spectrometers[3] at ISIS, but this would require major modifications to the rotor systems of the IPNS instruments. The object of this work is to examine the effects on the intensity and the resolution caused by adjusting the Soller collimation and the chopper slit width,

optimizing the combined effects under the constraints of fixed rotor speed, rotor aperture, and moderator size.

In the process we find it necessary to calculate the angular distribution of neutrons transmitted by two overlaid collimating systems, one coarse (defined by the widths and separation of the moderator, the rotor aperture and the sample) and one fine (defined by the Soller collimator). The present work complements that of Loong, Ikeda and Carpenter[4] in this respect.

II. Intensity and Resolution

Figure 1 schematically represents the components of the spectrometer. Throughout, it is assumed that the collimator is wider than the penumbra of the beam formed by the source and the chopper. The time-averaged number of neutrons passing through the system per unit time is

$$I(E) = (2E_1/t_1)\, i(E)\, C\Delta\Omega f_R f_C \Delta t_R$$

$$= 2 i_{epi} C\Delta\Omega f_R f_C v_1 \Delta t_R / L_1, \qquad (1)$$

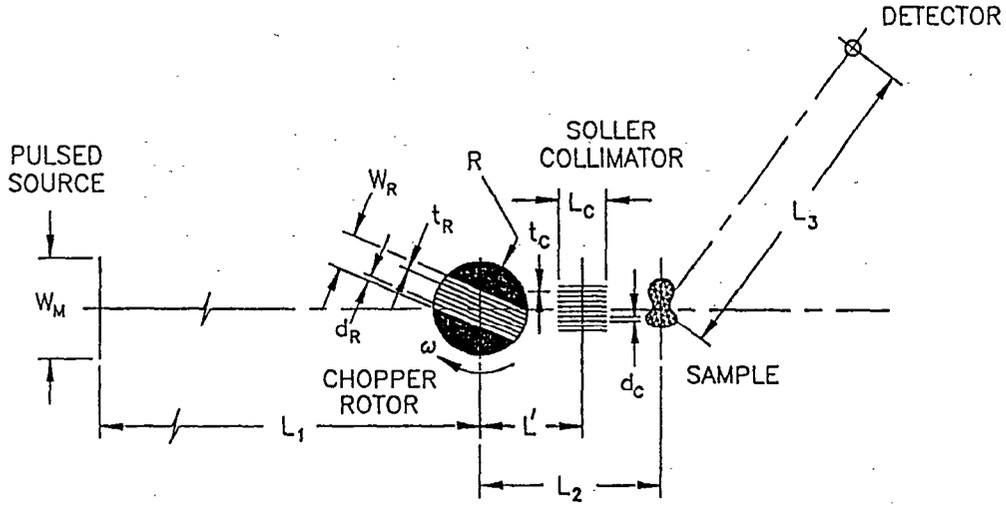

Figure 1: ***A schematic diagram of the time-of-flight chopper spectrometer on a pulsed neutron source. The pulsed source is the moderator of width W_M. The chopper of radius R is located a distance L_1 downstream and is rotating at an angular speed ω; it has an aperture of width W_R which includes numerous neutron-opaque slats of width t_R, spaced d_R apart. Located a further distance L′ downstream is a Soller collimator of length L_C with numerous neutron-opaque slats of width t_C, spaced d_C apart. The sample is located a distance L_2 from the rotor, and the detector is a distance L_3 from the sample.***

where i(E) is the time-averaged beam current per unit energy, that is, the number of neutrons per unit time, per unit energy, per unit solid angle, emitted from the entire moderator surface. $2E_1/t_1$ is the Jacobian $|dE/dt|$. $i_{epi} = Ei(E)$ is approximately constant with respect to E in the epithermal region. $C\Delta\Omega$ is the solid angle accepted from an average point on the moderator surface, C is a factor which represents the fraction of the source area viewed, f_R and f_C are the fractions of the areas of the rotor aperture and the collimator that are open,

and Δt_R is the rotor pulse width for a perfectly collimated beam. The subscript 1 refers to the beam from the moderator incident on the chopper rotor.

If there is no Soller collimator, the accepted solid angle is given by

$$C\Delta\Omega = H_R W_R / L_1^2, \tag{2}$$

where H_R and W_R are the height and width of the chopper aperture, and L_1 is the distance between the source and the chopper centerline. The more general situation represented by Figure 1 is rather complicated. The main burden of this work is to analyze this case.

Consider a Soller collimator whose angular divergence α_C is given by

$$\alpha_C = d_C / L_C, \tag{3}$$

where d_C is the width of the collimator slits of length L_C. Let the collimator divergence be very small, viz., $\alpha_C << W_M/L_1$ and $\alpha_C << W_R/L_1$, where W_M is the width of the source (moderator). The accepted solid angle is now

$$\Delta\Omega = H_R \alpha_C / L_1, \tag{4}$$

and the viewing factor is

$$C = \begin{cases} W_R/W_M & \text{if } W_R \le W_M \\ 1 & \text{if } W_R \ge W_M. \end{cases} \tag{5}$$

(See equation (A17) in the Appendix.)

The duration of the rotor pulse (the full width at half-maximum in a perfectly collimated beam) for neutrons of optimum speed is

$$\Delta t_R = d_R / (2R\omega), \tag{6}$$

where d_R is the rotor slit width, R is the radius of the slit package, and ω is the rotor angular speed. The fractions are

$$f_R = d_R/(d_R + t_R), \quad f_C = d_C/(d_C + t_C) \tag{7),(8}$$

where t_R and t_C are the thicknesses of the slats.

The energy transfer resolution (neglecting the effects of sample size, detector thickness, and time channel width) is[4]

$$\sigma_e^2 = (m^2/L_1^2)\{[v_1^3 + (L_2/L_3)v_2^3]^2\sigma_t^2 + [v_1^3 + ((L_1 + L_2)/L_3)v_2^3]^2\sigma_C^2\}, \tag{9}$$

where m is the neutron mass, v_1 and v_2 are the incident and scattered neutron speeds, and σ_e^2, σ_t^2, and σ_C^2 are respectively the variances of the energy transfer, moderator emission time and chopper pulse time distributions. L_2 and L_3 are the distances from the chopper to the sample, and from the sample to the detector, respectively.

In the epithermal regime, the standard deviation of the moderator emission time t is given by

$$\sigma_t = \sqrt{3}/(av_1), \tag{10}$$

where a is the constant in the moderator emission time distribution[3],

$$\phi(v,t) \propto t^2 e^{-avt}. \tag{11}$$

The chopper pulse variance is

$$\sigma_C^2 = \sigma_R^2 + \sigma_L^2, \tag{12}$$

where σ_R is the standard deviation of the (triangular) rotor pulse for neutrons of optimum speed in a perfectly collimated beam,

$$\sigma_R^2 = (\Delta t_R)^2/6. \tag{13}$$

σ_L is the contribution to the chopper pulse width due to the lighthouse effect,

$$\sigma_L = \sigma_\alpha/\omega, \tag{14}$$

where σ_α is the standard deviation of the angular distribution of the neutrons transmitted through the system.

It is shown in the Appendix that if there is no Soller collimator, the angular acceptance is

$$\Delta\alpha = \psi_0 + \psi_1 \tag{15}$$

and the variance of the distribution is

$$\sigma_\alpha^2 = (\psi_0^2 + \psi_1^2)/6, \tag{16}$$

where

$$\psi_0 = (W_M + W_R)/(2L_1) \tag{17}$$

and

$$\psi_1 = |W_M - W_R|/(2L_1). \tag{18}$$

On the other hand, if the Soller collimator completely determines the angular distribution, then

$$\Delta\alpha = \alpha_C = d_C/L_C \tag{19}$$

and

$$\sigma_\alpha^2 = (\Delta\alpha)^2/6 = \alpha_C^2/6, \tag{20}$$

where d_C and L_C are the width and length of the collimator slits.

The expressions for $\Delta\alpha$ and σ_α for a partially illuminated collimator are more complicated, and are set out below and in the Appendix. The full width at

half maximum (FWHM) is used as the estimate of resolution. The relationship between the FWHM and the standard deviation of the distribution of any quantity q is given by $\Delta q = \sqrt{(8\ln 2)}\sigma_q = 2.35\sigma_q$ applies if q has a Gaussian distribution; we use this relationship even though it is only approximately true.

III. APPROXIMATE OPTIMIZATION

The transmitted intensity is proportional to the product of the angular acceptance and the rotor pulse width,

$$I \propto \Delta\alpha\Delta t_R, \tag{21}$$

and the energy transfer resolution depends on the time and angular variances (see equations (9), (12) and (14))

$$\sigma_\epsilon^2 = A + B(\sigma_R^2 + \sigma_\alpha^2/\omega^2). \tag{22}$$

(We need not be explicit about the factors A and B here.) An approximate optimization results if we assume that the variances are related in identical proportion to the the full widths at half maximum, for example, as they are for triangular distributions (see equations (13) and (20), though neither of these is generally true). Then the greatest intensity for some given energy transfer resolution is attained when $\Delta t_R = \Delta\alpha/\omega$, or

$$\sigma_R = \sigma_\alpha/\omega. \tag{23}$$

The calculations performed as an initial approximation and for survey purposes assume this relationship. To the extent that it is incorrect, the calculated intensity is smaller than could actually be obtained for the same resolution, therefore a second pass optimization has to be performed, using the more accurate relationships. If the Soller collimation completely determines the angular distribution, and the neutrons are of optimum speed for the rotor, the expressions (13) and (20) are exact, and the optimization equation (23) is also exact.

IV. THE ANGULAR DISTRIBUTION OF ACCEPTED NEUTRONS

The angular distribution of neutrons transmitted through a partially illuminated Soller collimator depends in a complicated way upon the parameters of the system. However, ignoring the fine structure of the spatial and angular distribution, the angular distribution $P(\psi)$ can be expressed as

$$P(\psi) = F_R(\psi)F_C(\psi), \tag{27}$$

where $F_R(\psi)$ describes the angular distribution that would be transmitted through the rotor aperture from the moderator surface, and $F_C(\psi)$ describes the angular distribution that would be transmitted through a fully illuminated collimator slit which is assumed to be much smaller than the rotor aperture. Figure 2 illustrates the distributions $P(\psi)$, $F_R(\psi)$, and $F_C(\psi)$; these may be deduced from Figure A3 in the Appendix which shows the phase space diagram at the collimator center.

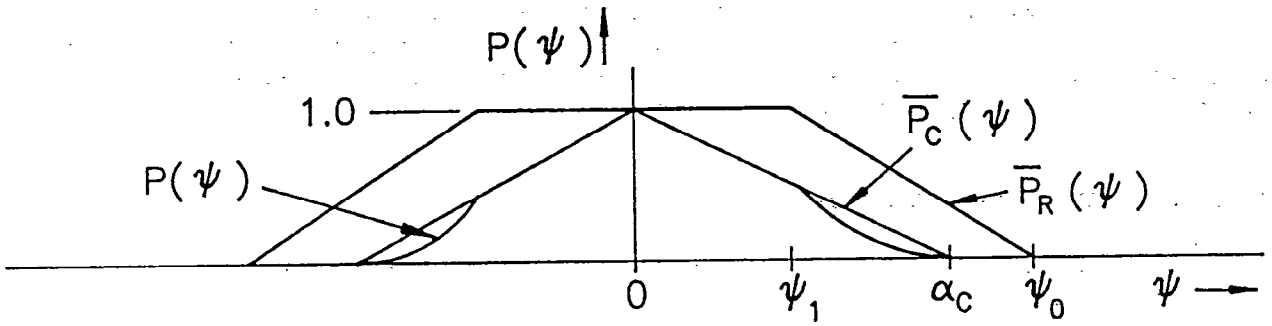

Figure 2: ***The angular distribution $\overline{P}_R(\psi)$ of neutrons transmitted through the rotor aperture from the moderator surface, and the angular distribution $\overline{P}_C(\psi)$ of neutrons that would be transmitted through a fully illuminated collimator slit. Their product $P(\psi)$ gives the angular distribution of neutrons transmitted through a partially illuminated collimator. The results shown are for the case $\psi_1 < \alpha_C < \psi_0$, and may be deduced from Figure A3 in the Appendix.***

In the Appendix we develop an expression for the number of neutrons passing through the system per unit time (equation (1)) in terms of the distributions given by the approximation (27), and introduce the viewing factor C (equations (5) and (A17)). The results give

$$\overline{P}_R(\psi) = \begin{cases} 1, & 0 < |\psi| < \psi_1 \\ (\psi_0 - |\psi|)/(\psi_0 - \psi_1), & \psi_1 < |\psi| < \psi_0 \\ 0, & |\psi| > \psi_0, \end{cases} \tag{28}$$

and

$$\overline{P}_C(\psi) = \begin{cases} 1 - |\psi|/\alpha_C, & 0 < |\psi| < \alpha_C \\ 0, & |\psi| > \alpha_C. \end{cases} \tag{29}$$

There are several cases for $P(\psi)$, depending upon the relative values of α_C, ψ_0, and ψ_1. Figure 2 is for the case $\psi_1 < \alpha_C < \psi_0$. The angular acceptance and the variance of the distribution are given by

$$\Delta\alpha = \int_{-\infty}^{\infty} P(\psi)\,d\psi \tag{30}$$

and

$$\sigma_\alpha^2 = (1/\Delta\alpha)\int_{-\infty}^{\infty} \psi^2 P(\psi)\,d\psi. \tag{31}$$

For $\alpha_C < \psi_1$, we have

$$\Delta\alpha = \alpha_C \tag{32}$$

and

$$\sigma_\alpha^2 = \alpha_C^2/6. \tag{33}$$

For this condition, the expression (20) is exact, and the optimization equation (23) is also exact for neutrons of optimum speed for the rotor.

For $\psi_1 < \alpha_C < \psi_0$,

$$\Delta\alpha = 2\{\psi_1(1 - \psi_1/(2\alpha_C)) + (1/(\psi_0 - \psi_1))[(\alpha_C - \psi_1)\psi_0 - (\alpha_C^2 - \psi_1^2)(1 + \psi_0/\alpha_C)/2 + (\alpha_C^3 - \psi_1^3)/(3\alpha_C)]\}, \quad (34)$$

and

$$\sigma_\alpha^2 = (2/\Delta\alpha)\{\psi_1^3(1/3 - \psi_1/(4\alpha_C)) + (1/(\psi_0 - \psi_1))[(\alpha_C^3 - \psi_1^3)\psi_0/3 - (\alpha_C^4 - \psi_1^4)(1 + \psi_0/\alpha_C)/4 + (\alpha_C^5 - \psi_1^5)/(5\alpha_C)]\}. \quad (35)$$

For $\alpha_C > \psi_0$,

$$\Delta\alpha = 2\{\psi_1(1 - \psi_1/(2\alpha_C) + (1/(\psi_0 - \psi_1))[(\psi_0 - \psi_1)\psi_0 - (\psi_0^2 - \psi_1^2)(1 + \psi_0/\alpha_C)/2 + (\psi_0^3 - \psi_1^3)/(3\alpha_C)]\}, \quad (36)$$

and

$$\sigma_\alpha^2 = (2/\Delta\alpha)\{\psi_1^3(1/3 - \psi_1/(4\alpha_C)) + (1/(\psi_0 - \psi_1))[(\psi_0^3 - \psi_1^3)\psi_0/3 - (\psi_0^4 - \psi_1^4)(1 + \psi_0/\alpha_C)/4 + (\psi_0^5 - \psi_1^5)/(5\alpha_C)]\}. \quad (37)$$

No simple analytic expressions relating the angular acceptance $\Delta\alpha$ and the variance σ_α^2 of the angular distribution can be obtained for these last two conditions.

In the limit of very large α_C, equations (36) and (37) become the simple results already known for the case with no Soller collimator,

$$\Delta\alpha = \psi_0 + \psi_1 \quad (15)$$

and

$$\sigma_\alpha^2 = (\psi_0^2 + \psi_1^2)/6. \quad (16)$$

V. Calculations

We have performed several calculations all of which correspond to the flight path lengths of the HRMECS instrument[1] at IPNS. The thickness of the collimator blades is neglected so that $f_C = 1$. Table I shows the cases calculated.

Cases 1 and 2 correspond to current IPNS rotor technology[1]; case 3 represents HRMECS with a chopper similar to that[5] currently proposed for the Los Alamos Neutron Scattering Center (LANSCE) chopper spectrometer; case 4 is for HRMECS with a chopper similar to that of the HET spectrometer at ISIS. All cases were computed with the approximate optimization condition (23) for small rotor slit spacings, for which a Soller collimator is appropriate for optimum

intensity. For larger rotor slit spacings, highest intensity demands no Soller collimator, and the calculations do not include the effect of Soller collimation.

Figure 3 illustrates the results of these calculations for case 1, that of the HRMECS instrument with a standard 3" x 4" rotor of radius 77 mm at a frequency of 270 Hz and an incident energy E_1 of 500 meV. Shown in this Figure are the time-averaged neutron intensity $I(E_1)$ transmitted per unit time, the optimized collimation α_C, the chopper pulse FWHM Δt_C (including the lighthouse effect, and given by equation (12)), the FWHM energy transfer resolution for elastic scattering $\Delta\epsilon_{el}$, and the FWHM

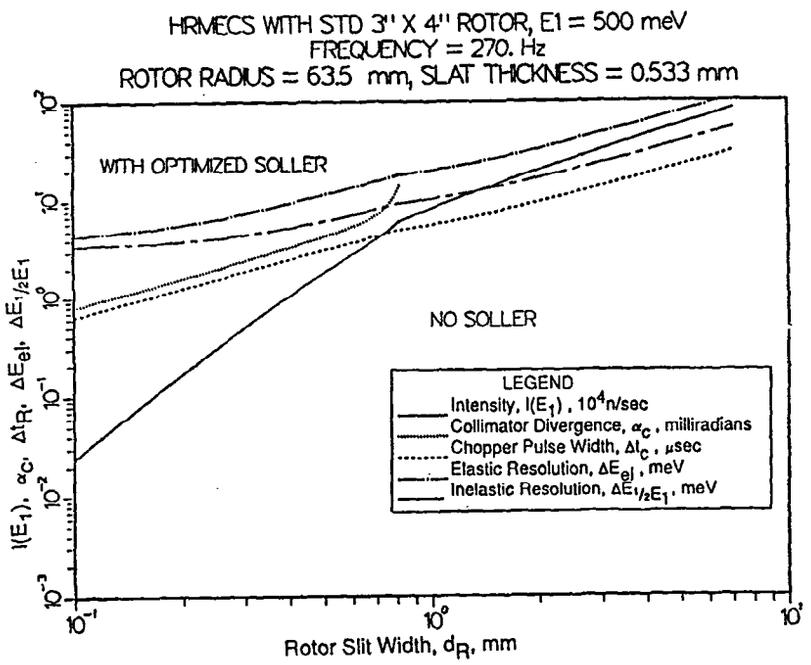

***Figure 3:** The results of the optimized intensity calculations as a function of rotor slit width d_R for the HRMECS instrument with a 3" x 4" rotor of radius 77 mm at a frequency of 270 Hz and an incident energy E_1 of 500 meV. Plotted are the time-averaged neutron intensity $I(E_1)$ transmitted per unit time, the collimation α_C the chopper pulse FWHM Δt_C, the FWHM energy transfer resolution for elastic scattering $\Delta\epsilon_{el}$, and the FWHM energy transfer resolution for loss of one-half the incident energy $\Delta\epsilon_{(1/2E1)}$.*

energy transfer resolution for loss of one-half the incident energy $\Delta\epsilon_{(1/2E1)}$, all plotted as functions of the rotor slit width d_R. Also shown on Figure 3 are plotted points which correspond to calculations for the currently-used Soller collimator of HRMECS, namely α_C = 11.6 mrad, and for the rotor slit widths of the normal and high-resolution rotors without the optimization condition. As the rotor slit width approaches zero, the chopper pulse width approaches its limit Δt_L defined by the lighthouse effect, the energy transfer resolutions approach their minimum values, but also the transmitted intensity approaches zero. For larger slit widths, all these values increase.

TABLE I

The specifications for different rotor types used in the calculations. W_M is the moderator width, E_I the incident energy, ν the rotor frequency, R the rotor radius, W_R and H_R the width and height of the chopper aperture, d_R the rotor slit width, and t_R the rotor slat thickness.

Case	Rotor Type	W_M, mm	E_I, meV	ν, Hz	R, mm	W_R, mm	H_R, mm	d_R, mm	t_R, mm
1	IPNS	100.	500.	270.	63.5	76.2	101.6	1.02	0.533
2	IPNS	100.	500.	270.	77.0	50.8	101.6	1.57	0.533
3	LANSCE	100.	500.	600.	50.0	43.2	66.0	0.80	0.660
4	ISIS	100.	500.	600.	50.0	47.0	47.0	0.76	0.380

The other three cases of Table I give results which are similar in form to those shown in Figure 3, though the range over which the Soller collimation is required for the other cases depends on the rotor slit width d_R. The relative intensities for each case should be compared at fixed resolution. Figure 4 represents the same data for case 1 as a function of the elastic energy transfer resolution to facilitate such a comparison. This is possible because the resolution and the rotor slit width are related monotonically. From such figures for each case we have generated Table II which shows the relative intensities at different energy transfer resolutions.

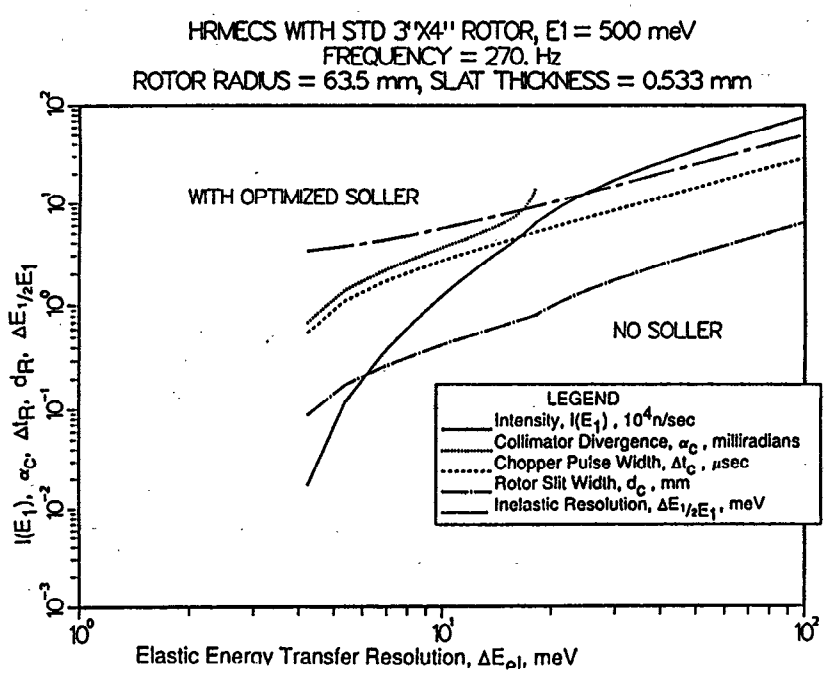

Figure 4: The results of the optimized intensity calculations as a function of the elastic energy transfer resolution $\Delta\epsilon_{el}$ for the HRMECS instrument with a 3" x 4" rotor of radius 77 mm at a frequency of 270 Hz and an incident energy of 500 meV (similar to Figure 3).

TABLE II

The relative intensities at 500 meV (in units of 10^4 cm^{-2} sec^{-1}) for the four different rotor types given in Table I for elastic energy transfer resolutions of 10, 12.5, 15 and 20 meV.

Case	Rotor Type	$\Delta\epsilon_{el}$ = 10 meV	$\Delta\epsilon_{el}$ = 12.5 meV	$\Delta\epsilon_{el}$ = 15 meV	$\Delta\epsilon_{el}$ = 20meV
1	IPNS	1.25	2.1	3.4	8.3
2	IPNS	0.84	1.7	2.7	6.0
3	LANSCE	1.3	2.0	2.8	4.2
4	ISIS	1.3	1.8	2.2	3.4

Recognizing that the condition (23) is only approximate, we have searched for higher intensity conditions with fixed resolution. For example, Figure 5 shows the results for the 270 Hz rotor with a 3"× 4" aperture (case 1) for elastic resolution of 10. meV (2 % of the incident energy for 500. meV incident energy), which is comparable to HET. The approximate optimization gives about the same intensity as the refined optimization, since the intensity varies rather slowly around the optimum. Various choices of α_C and d_R that give the same resolution also give almost the same intensity. The intensity and the approximately optimized and refined parameters for this energy transfer resolution are given in Table III. The results for energy transfer resolutions of 12.5 and 15. meV for elastic scattering for the same rotor are given in Table III. The Figures from which these results are derived are similar in shape as those shown in Figure 5. For comparison, Table III also gives the intensity and the parameters for the present HRMECS arrangement, for which the elastic resolution is calculated to be about 20. meV. (The calculated results for the present arrangement are close to observed values.) The Table also gives parameters for HRMECS with a 600 Hz rotor similar to that for the ISIS HET spectrometer, and with no Soller collimator. All these results include the effect of the partial open area of rotor slit package, $f_R = d_R/(d_R + t_R)$.

The intensity loss for 12.5 meV resolution compared to present rotor design is only about a factor of 3.5, which is now nearly compensated by the increased intensity available from the IPNS booster target[6]. The parameters appear to be feasible. The reason that the intensity loss is not greater is that the source pulse width, the rotor, and lighthouse contributions to the resolution are not perfectly optimized in the present HRMECS. The resolution improvement accomplishable by the present method is relatively easy compared to the alternative of replacing existing choppers with magnetic-bearing choppers. It requires only a new rotor and slit package of the same type now in use, and a new Soller collimator. The new arrangement could easily be introduced as an option among other instrument configurations.

Comparing the results of Figure 4 (for HRMECS with a standard, 270 Hz rotor and optimized Soller collimator) with those for HRMECS with an ISIS-style, 600 Hz rotor, we see that for the same resolution, the standard rotor provides the same or <u>better</u> intensity for given resolution. This is because the aperture of the standard rotor is larger than that of the ISIS rotor. This conclusion must be

TABLE III

The calculated transmitted intensity $I(E_1)$ at an incident energy E_1 of 500 meV and the rotor and collimator parameters (chopper pulse width Δt_C, rotor pulse width Δt_R, rotor slit width d_R and Soller collimation α_C) for both the approximately optimized and the refined cases for the HRMECS rotor design (270 Hz), optimized for different energy transfer resolutions $\Delta\epsilon_{el}$ and $\Delta\epsilon_{1/2El}$ with the HRMECS flight path arrangement. Also shown are the present arrangement for HRMECS, and that for the 600 Hz HET rotor with the HRMECS spectrometer design.

	$\Delta\epsilon_{el}$ meV	$\Delta\epsilon_{1/2El}$ meV	$I(E_1)$ n/sec	Δt_C μsec	Δt_R μsec	d_R mm	α_C mrad
Approx. opt.(1)	10.0	5.63	1.24	2.70	1.99	0.428	3.63
Refined opt.(1)	10.0	5.63	1.29	2.70	2.19	0.473	3.15
Approx. opt.	12.5	6.76	2.31	3.47	2.56	0.551	4.93
Refined opt.	12.5	6.76	2.38	3.47	2.82	0.606	4.25
Approx. opt.	15.0	7.92	3.70	4.23	3.12	0.671	6.57
Refined opt.	15.0	7.92	3.80	4.23	3.44	0.740	5.45
HERMECS #	20.1	10.4	8.22	5.76	4.73	1.02	11.6
With HET chopper*,	9.3	5.34	1.27	2.49	2.02	0.760	----

(1) corresponding to Figure 5
present arrangement
* with no Soller collimator

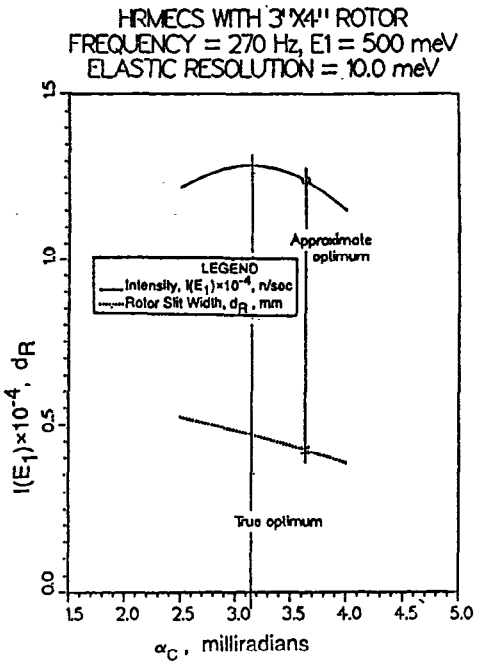

Figure 5: The results of the more refined optimization for an elastic energy transfer resolution $\Delta\epsilon_{el}$ of 10.0 meV for the HRMECS 3" x 4" rotor of radius 77 mm at a frequency of 270 Hz with an incident energy E_1 of 500 meV (similar to Figure 3), showing the intensity $I(E_1)$ transmitted and the rotor slit width d_R as a function of the collimation α_C.

tempered, however, by the realization that sample size contributions to the resolution are not accounted for in these comparisons; these are smaller in the case of the ISIS rotor, but can be focussed out for special conditions.

Finally, we repeat that all calculations assume that the collimator open fraction $f_C = 1$, that is, we have ignored the thickness of the collimator blades (thus we have avoided being specific about the length of the collimator and the width of the slits). In practice, we caution that this factor must be included in final design calculations; it can readily be introduced at the stage represented by Figure 5, as a factor on the intensity given there.

VII. Conclusions

We have further developed the relationships between the resolution and intensity for time-of-flight chopper spectrometers, including the effect of Soller collimation. The angular distribution is determined coarsely by the size of the moderator and the rotor aperture, together with the distance separating them, and is resolved finely by the Soller collimation. The placing of additional collimation between the chopper and the sample reduces the angular distribution of the beam striking the sample, and hence reduces the lighthouse contribution to the instrumental resolution. We have considered the effects of adjusting this collimation and the chopper slit width, assuming a fixed rotor speed, rotor aperture and moderator size, and have optimized the rotor pulse and the lighthouse effect for the best intensity. The transmitted intensity is

proportional to the product of the angular acceptance and the rotor pulse width. The energy transfer resolution depends on the root of the sums of squares of the rotor pulse width and the lighthouse effect (the angular acceptance of the system divided by the rotor angular speed). The greatest intensity for some given energy transfer resolution occurs when these two quantities are equal.

We have derived new expressions for the angular distribution of a beam formed by a coarse collimator system overlaid by a fine Soller collimator, assuming that the collimator slit width is much less than the widths of the moderator and the rotor aperture. Slightly different expressions are obtained depending on the relative sizes of the moderator and the rotor aperture. This distinction determines whether the collimator lies in the umbra of the beam (the source is fully observable through the rotor aperture), or whether the center of the beam in penumbra (the source is partially obscured by the rotor aperture). We have considered the optimized conditions for no collimation present, for Soller collimation placed between the rotor and the sample, and when the collimation is only partially illuminated. We show that small rotor slit spacings require appropriate Soller collimation for optimum intensity, whereas for large rotor slit spacings the highest intensity requires no Soller collimation.

VIII. APPENDIX

The angular and spatial distribution of neutrons transmitted through a collimating system in two dimensions can be usefully described in terms of diagrams in the phase space consisting of the positions and directions of trajectories at their crossing of a reference screen, which will be placed at the collimator center. Figure A1 illustrates the definitions of relevant quantities. A neutron which leaves from the point (z',ψ') in the source phase space, at a position z' in the source plane and in direction ψ' relative to the reference axis, crosses a reference screen at a distance L along and normal to the reference axis of the beam at a point (z,ψ) in its phase space given by

$$z = z' + L\psi'$$

$$\psi = \psi' \qquad \text{(A1)}$$

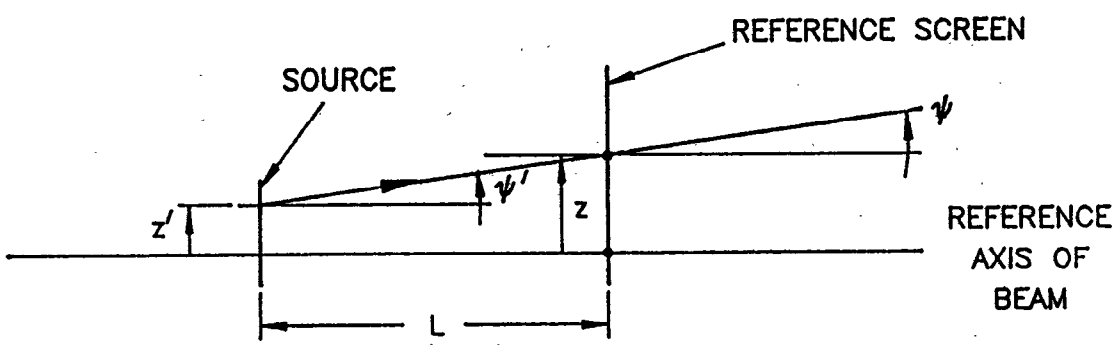

***Figure A1:** A neutron leaves the source from a point (z',ψ') in the source phase space, where z' is the distance from the reference axis of the beam, and ψ' is the direction relative to that axis. The neutron traces a path which crosses a*

reference screen placed a distance L along and normal to the reference axis at a point (z,ψ) in the reference plane phase space, such that $z = z' + L\psi'$ and $\psi = \psi'$.

In the case under consideration, we need to describe the combined effect of a finite, isotropic source (the moderator), a finite aperture (the chopper), and a Soller collimator. Figure A2 shows the horizontal plane of the geometry of the collimation system considered in this paper. The reference screen is taken as the collimator centerline, and Figure A3 shows the corresponding phase space acceptance diagram. Everything is represented and calculated in the sense of small angle approximations, and for the purpose of this Appendix in two dimensions.

The areas inside the parallelograms are regions of the phase space that are illuminated by the source and accepted through the system. The large shaded parallelogram where $P_R(z,\psi) = 1$ represents the region illuminated by the finite source that is accepted through the rotor aperture, and the small parallelograms where $P_C(z,\psi) = 1$ represent the region that is accepted through the Soller collimator. Altogether, the region illuminated and accepted by the system depicted in Figure A2 is the region common to both the large and the small parallelograms.

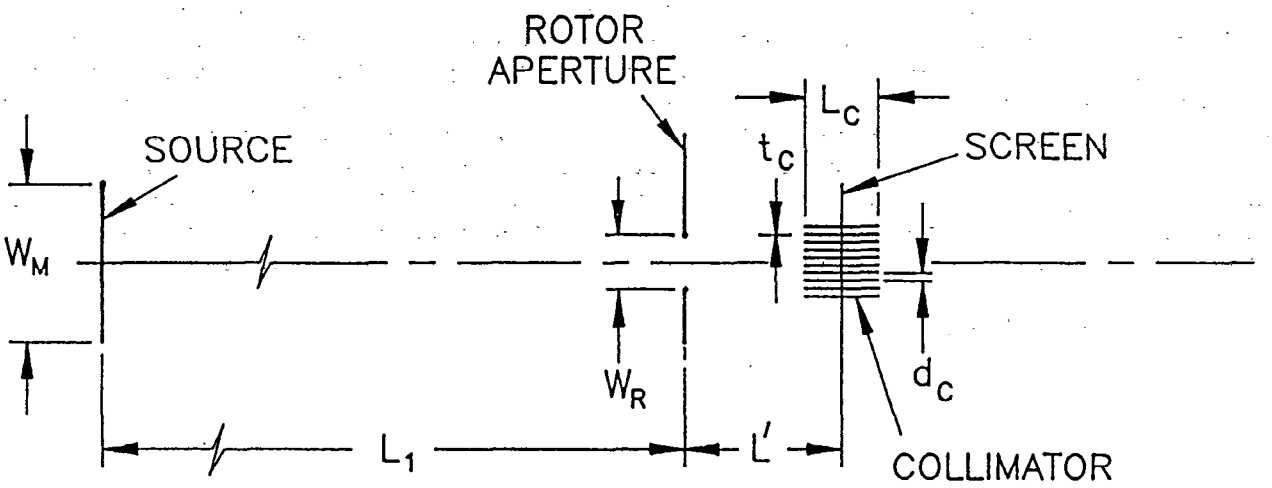

Figure A2: A schematic diagram of the horizontal plane of the geometry of the collimation system. The moderator has a width W_M. The chopper has an aperture width W_R and its centerline is located L_1 downstream. The Soller collimator of length L_C has slits of width d_C and slats of width t_C, and its centerline is located a further distance L' beyond the chopper. The reference screen for Figure A3 is taken as the collimator centerline.

The lines $z = (L_1 + L')\psi \pm W_M/2$ represent the boundaries of the region in phase space illuminated by the moderator. The lines $z = L'\psi \pm W_R/2$ represent the boundaries of the region transmitted by the rotor aperture. These lines cross at $\pm W_R/2 = L_1\psi \pm W_M/2$. That is,

$$\psi_0 = \pm (W_M + W_R)/(2L_1) \tag{17}$$

and

$$\psi_1 = \pm \left|W_M - W_R\right| / (2L_1). \tag{18}$$

The lines $z = \pm L_C\psi/2 \pm d_C/2 + n(d_C + t_C)$ represent the boundaries of the region in phase space transmitted by the nth collimator slit. For each collimator slit, these lines cross at $\psi = 0$ and at $\psi = \pm \alpha_C = \pm d_C/L_C$ (equation (3)). An integration over z for the regions depicted in Figure A3 will give the distributions $\bar{P}_R(\psi)$, $\bar{P}_C(\psi)$ and $P(\psi)$ defined by equations (27).

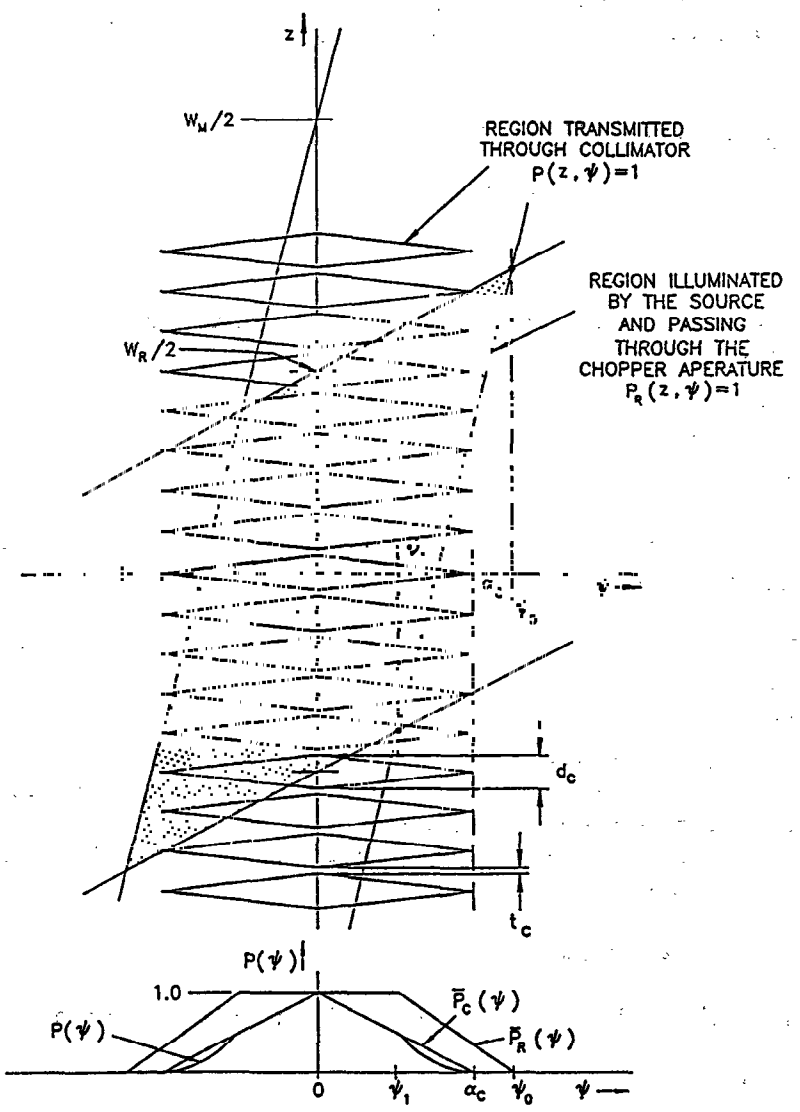

Figure A3: The phase space acceptance diagram at the collimator centerline for the geometry depicted in Figure A2. The large shaded parallelogram where $P_R(z,\psi) = 1$ represents the region illuminated by the moderator of width W_M, and transmitted by the rotor aperture of width W_R placed at a distance L_1 downstream from the moderator and a distance L' before the collimator. The small parallelograms where $P_C(z,\psi) = 1$ represent the regions transmitted through each collimator slit of width d_C and length L_C. Those regions common to both correspond to rays transmitted through the system.

If the angular current density on the source plane is $\phi_s(z',\psi')$, then the number of neutrons passing through the system per unit time is

$$I = \int \phi_s(z',\psi')\ P_R(z,\psi)\ P_C(z,\psi)\ \delta(z - z' - (L_1 + L')\psi)\ \delta(\psi - \psi')\ dz d\psi dz' d\psi', \tag{A2}$$

where the delta functions represent the transformation (equation (A1) from the phase space at the source to that at the reference screen. Performing the integrals gives

$$I = \int \phi_s(z - (L_1 + L')\psi,\psi)\ P_R(z,\psi)\ P_C(z,\psi)\ dz d\psi. \tag{A3}$$

Assuming that the source angular current density is uniform and isotropic (constant) within the region $(z' = z - (L_1 + L')\psi,\ \psi)$ for which $P_R \neq 0$ and $P_C \neq 0$,

$$I = \phi_s \int_{\text{all } z,\psi} P_R(z,\psi)\ P_C(z,\psi)\ dz d\psi. \tag{A4}$$

If W_M is the width of the source, we can write

$$\phi_s W_M = i_s, \tag{A5}$$

where i_s is the two dimensional version of the usual three dimensional beam current function. Then

$$I = (i_s/W_M) \int_{\text{all } z,\psi} P_R(z,\psi) P_C(z,\psi) dz d\psi. \tag{A6}$$

There is essentially no approximation so far.

When the collimator slit width $d_C << \text{Min}[W_M, W_R]$ (the usual case), $P_C(z,\psi)$ varies on a small scale with respect to z, in comparison to $P_R(z,\psi)$. We define the collimator slit angular distribution

$$\bar{P}_C(\psi) = \int_{-d_C/2}^{d_C/2} P_C(z,\psi)\ dz/d_C \tag{A7}$$

which is the integral for a single slit of width d_C and normalized so that $\bar{P}_C(\psi = 0) = 1$. Provided that the collimator exit is wider than the penumbra of the beam formed by the source and the rotor aperture,
$W_R + (W_R + W_M)(L' + L_C/2)/L_1$. Hence we may replace $P_C(z,\psi)$ in (A4) with its average value $f_C\bar{P}_C(\psi)$. Then

$$I = \phi_s f_C \int P_R(z,\psi)\ \bar{P}_C(\psi)\ dz d\psi, \tag{A8}$$

where f_C is the fraction of the area of the collimator which is open,

$$f_C = d_C/(d_C + t_C), \tag{A9}$$

and t_C is the thickness of the collimator slats.

We now introduce the rotor aperture angular distribution

$$\bar{P}_R(\psi) = \int_{\text{all } z} P_R(z,\psi)\ dz/W, \tag{A10}$$

which is normalized to a width W which is yet to be chosen. Then

$$I = \phi_s f_C W \int_{all\ \psi} F_R(\psi)\ F_C(\psi)\ d\psi \tag{A11}$$

so that finally,

$$I = i_s f_C (W/W_M) \int_{all\ \psi} F_R(\psi)\ F_C(\psi)\ d\psi. \tag{A12}$$

We now choose W so that $F_R(\psi)$ has the convenient property

$$F_R(\psi)_{max} = 1. \tag{A13}$$

Two cases can be distinguished, $W_R \leq W_M$ and $W_R \geq W_M$, depending on the relative widths of the rotor aperture and the moderator. With reference to Figure A3, we note that the maximum occurs for $\psi = 0$. Then when $W_R \leq W_M$

$$F_R(\psi = 0) = \int P_R(z, \psi = 0) dz/W = W_R/W, \tag{A14}$$

and when $W_R \geq W_M$

$$F_R(\psi = 0) = \int P_R(z, \psi = 0) dz/W = W_M/W. \tag{A15}$$

Therefore to provide in $F_R(\psi)$ the property (A12),

$$W = \begin{cases} W_R \text{ if } W_R \leq W_M \\ W_M \text{ if } W_R \geq W_M. \end{cases} \tag{A16}$$

Hence, from equation (A12), the viewing factor C in equation (1) of the text is

$$C = \begin{cases} W_R/W_M \text{ if } W_R \leq W_M \\ 1 \quad\quad \text{ if } W_R \geq W_M. \end{cases} \tag{A17}$$

The distinction between the two cases corresponds to whether or not the taking of the absolute value in (18) of the text represents a change in sign of $W_M - W_R$. Otherwise stated, the distinction corresponds to whether a point at the center of the beam lies in the penumbra of the beam (the source is partially obscured by the rotor aperture), or whether the center is in the true umbra of the beam (the source is fully observable through the rotor aperture).

IX. REFERENCES

1. D. L. Price, J. M. Carpenter, C. A. Pelizzari, S. K. Sinha, I. H. Bresof, G. E. Ostrowski, "The IPNS Chopper Spectrometers", Proc. 6th Int. Coll. Advanced Neutron Sources, Argonne, 1982, ICANS-VI, ANL-82-20, 207-214.

2. G. H. Lander and D. L. Price, "Neutron Scattering with Spallation Sources", Physics Today 38 (1985) 38-45.

3. A. D. Taylor, B. C. Boland and Z. A. Bowden, "HET: The High Energy Inelastic Spectrometer at ISIS", Proc. ICANS-IX (Villigen, Switzerland, 1986), SIN report, 349-364 (1987).

4. C.-K. Loong, S. Ikeda and J. M. Carpenter, "The Resolution Function of a Pulsed-Source Neutron Chopper Spectrometer", Nucl. Instr. and Meth. A260 (1987) 381-402.

5. J. M. Carpenter, R. K. Crawford, R. Kleb, C.-K. Loong, G. E. Ostrowski, D. L. Price, M. Nutter, R. Pynn, R. A. Robinson, S. K. Sinha, J. M. Rowe, P. Sokol and A. D. Taylor, LAUR 87-2582 (1987).

6. A. E. Knox, J. M. Carpenter, J. L. Bailey, R. J. Armani, R. N. Blomquist, B. S. Brown, D. R. Henley, A. G. Hins, B. A. Loomis, A. W. Schulke and H. R. Thresh, "Progress on the IPNS Enriched Uranium Booster Target", Proc. ICANS-IX (Villigen, Switzerland, 1986) SIN report, 557-589 (1987).

This work was performed under the auspices of the U.S. Department of Energy, Division of Materials Sciences, Office of Basic Energy Sciences, under Contract W-31-109-ENG-38.

ICANS-XI International Collaboration on Advanced Neutron Sources
KEK, Tsukuba, October 22-26, 1990

SMALL-ANGLE NEUTRON SCATTERING AT PULSED SOURCES COMPARED TO REACTOR SOURCES

Rex P. Hjelm, Jr.*, Philip A. Seeger*, and P. Thiyagarajan†
* Los Alamos Neutron Scattering Center, Los Alamos National Laboratory, Los Alamos, New Mexico 87545 USA. † Intense Pulsed Neutron Source and Chemistry Divisions, Argonne National Laboratory, Argonne, Illinois, 60436 USA

Abstract: Detailed comparisons of measurements made on small-angle neutron scattering instruments at pulsed spallation and reactor sources show that the results from the two types of instruments are comparable. It is further demonstrated that spallation instruments are preferable for measurements in the mid-momentum transfer domain or when a large domain is needed.

Introduction

Small-angle neutron scattering (SANS) instruments at pulsed sources use time-of-flight (TOF) to measure the magnitude of the momentum of each counted neutron, rather than monochromate the incident beam. This is necessary, as the time-averaged flux at pulsed spallation sources is low, and every available neutron must be used. The methods of data acquisition and reduction for TOF-SANS are new and some aspects are still under development, and we need to demonstrate that data obtained using these new techniques are reliable, and that measurements taken on the two classes of instruments are comparable. We present here some results of some measurements designed to meet this objective, in which detailed comparisons are done between measurements on standard samples at TOF instruments with SANS instruments at reactors. In this paper we will show that the answers obtained from the two types of instruments are the same, with the caveat that there are some minor differences that may be due to incoherent scattering, multiple scattering, and instrument resolution. We hope that as a result of this work experimenters will be aided in planning measurements and in making good choices as to which type of instrument might be more suitable for a particular measurement.

Results

A blend of d-polystyrene (48%) with h-polystyrene

Small-angle scattering from a blend of 48% deuterated polystyrene is expected to exhibit $I(Q) \sim Q^{-2}$, characteristic of a Gaussian coil. In Figure 1 we show the results of data taken on two TOF-SANS instruments: the Low-Q Neutron Diffractometer (LQD) at the Los Alamos Neutron Scattering Center, Los Alamos National Laboratory and the Small-angle Neutron Diffractometer (SAD) at Argonne National Laboratory; and two reactor-based instruments: the 30M SANS at Oak Ridge National Laboratory, and D-11 at the Institut Laue-Langevin.

Measurements on LQD and SAD were taken with instrument fixed geometry. The SAD measurement was taken with the detector off-axis. In each case data acquisition and reduction was done by standard methods and are described elsewhere [1-4]. Two geometries were used on the reactor instruments: 19 and 7 M sample to detector distances on the 30-M SANS, and 10 and 2.5 M on D-11. Measurements on the 30-M instrument were done by F. Bates and G. Wignall.

All data are placed in a scale of absolute differential scattering probability per unit solid angle, $dP/d\Omega$ (division by sample thickness will give $d\Sigma/d\Omega$ (cm^{-1}), the macroscopic differential cross section per unit volume per unit solid angle). This was done by determining a calibration constant for each instrument. For the reactor instruments, a primary standard, water, was used [5,6]. Secondary standards with cross sections derived from the reactor instruments were used to calibrate the TOF instruments. In the case of SAD this was an irradiated aluminum standard Al-4, the absolute intensity of which was determined on the Oak Ridge 30 M instrument [6]. For LQD calibration was done using the polystyrene blend discussed here and also a silica gel sample; the absolute intensity values for which were determined on D-11.

The absolute SANS intensities (shifted by factors of two for comparison in figure 1) from each measurement are identical, on the average. Since calibration of the TOF instruments was done using results from the reactor based instruments, there is no surprise that the intensity agrees. That the two TOF instruments agree very well, does show that the determination of a

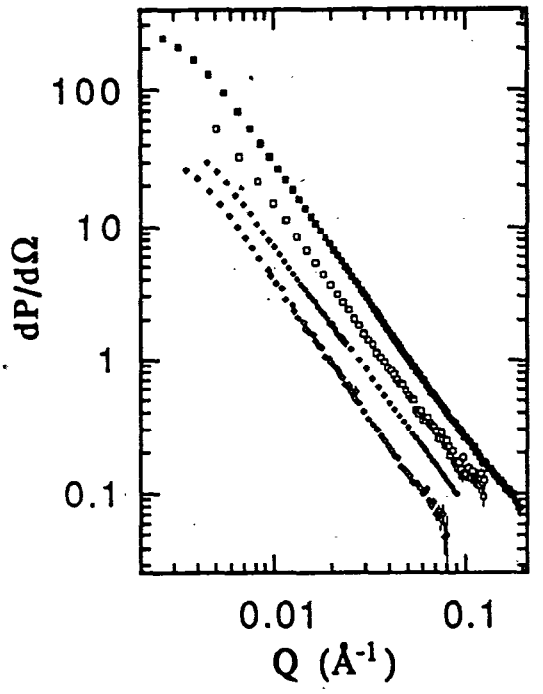

Figure 1. *Polystyrene Blend:*
■, LQD; □, SAD; ◆, D-11;
✧, 30-M SANS

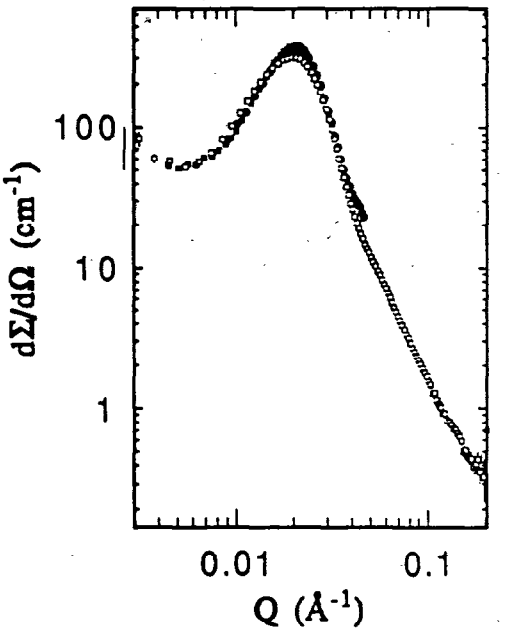

Figure 2. *Vycor Glass:*
■, D-11, 10M; ●, D-11, 5M; □ LQD

calibration constant for these instruments can be done in a straightforward manner, even though the two TOF instruments are very different in design and neutron source characteristics [1,7]

These data (figure. 1) show the large Q-domain accessible using TOF instruments on a single measurement—larger than that available on the reactor instruments, even with two camera settings. In principle, data can be obtained on LQD over the domain $0.002 < Q < 0.5$ Å^{-1}, and $0.005 < Q < 0.3$ on SAD. Realization of this range depends on a number of factors, including scattering intensity, counting times, incoherent scattering and the range of incident neutron wavelength used. These limit the domain of useable data in this instance to $0.003 \leq Q \leq 0.2$ Å^{-1} on LQD and $0.005 \leq Q$ 0.12 Å on SAD.

The slopes of the double log plots for the TOF data are -2 to within experimental error. The slopes of the lines for the reactor-SANS data are slightly smaller. We are not sure of the reasons for the difference but suspect that effects from incoherent scattering may play a role here. George Wignall (private communication) reports that a value of 0.4 cm^{-1} (0.04 in Figure 1) has been subtracted from the ORNL data to obtain a line on the double log plot with slope -2.

In the data taken one LQD there is a deviation form the $I(Q) \sim Q^{-2}$ power law at the lowest Q values . It is likely that in this domain $Q^{-1} \approx R_g$, the radius of gyration of the polymer; thus we are observing a cross-over into a Guinier region. There also may be some effects from multiple scattering [8] due to the large incident neutron wavelengths used to obtain very low Q data. This points out a potential disadvantage of TOF-SANS at very low Q, as limits in instrument length (if

a frame overlap chopper is not used) requires the use of long wavelength neutrons in order to obtain data in this region.

A Sample of Vycor glass:

The porosity of this vycor glass leads to a correlation peak at $Q \simeq 0.02$ Å^{-1}. In Figure 2 we compare data taken at D-11 and LQD. The D-11 data are taken at sample to detector distances of 10M and 5M using 10Å neutrons. Data on LQD were taken with a proton beam current on target of 60μA. The results give some further interesting comparisons between LQD and D-11.

Scattering measurements (expressed in figure 2 as $d\Sigma/d\Omega$ (cm^{-1})) taken on the two instruments are essentially the same, given that for a peaked function the instrument resolution becomes a factor in the result. In the example in Fig. 2 data, from LQD were reduced using all time channels. This gives the maximum Q-range for the measurement. When this procedure is used the precision in Q for LQD (sample to detector distance $\cong$ 4.3M) is similar to D11 at 5M, as evidenced by the similarity in curve shape and height. However, resolution of a TOF instrument is dependent on the TOF-channels used in data reduction [2]; thus, had only longer TOF-channels been included, a narrower peak in the region about $Q \approx 0.02^{-1}$ would have resulted.

The data acquisition time for this experiment and its transmission on LQD was 30 minutes. To achieve the same statistics (0.45%) in an equal width Q-bin (0.001 Å^{-1}) at a single value of Q (0.030 Å^{-1}) at D - 11 would take 9 minutes at the 5 - m position. Thus it took more than 3 times as long to get a data set at LQD, but the Q - range obtained is nearly 4 times as wide. In this example, the extended range allows determination of the power-law slope above $Q = 0.045$ Å^{-1} . When a constant (incoherent contribution) of 0.14 cm^{-1} is subtracted, the slope of -3.360±0.006 extends to the highest values of Q measured.

Conclusions:

From these examples, we conclude that the results of scattering measurements taken at TOF-SANS and reactor-based SANS instruments are comparable. Small differences can perhaps be better understood, and thus corrected. The current generation of small-angle instruments on pulsed spallation sources is competitive at moderate Q and may be faster when a wide range of Q is required. It appears, however, that present high flux reactor-based instruments are superior for measurements at very low-Q or over a narrow range of Q.

Acknowledgements

This work was performed under the auspices of the Office of Basic Energy Sciences, U. S. Department of Energy, under contract no. W-7405-ENG-32 to the University of California.

References:

1. Crawford, R.K., Epperson, J.E., Thiyagarajan, P., and Trow, F. (1987), eds, *Instrumental Techniques and Data Analysis at Pulsed Source SANS Instruments*, IPNS Note 46, Argonne National Laboratory, Argonne Illinois, USA
2. Hjelm, R. P. Jr (1988). *J. Appl. Cryst.* **21**, 618 - 628.
3. Hjelm, R. P. Jr & Seeger, P. A. (1989). *Advanced Neutron Sources 1988, Institute of Physics Conference series* **97**, edited by D. K. Hyer, pp. 367 - 387. Bristol, IOP Publishing.
4. Seeger, P.A. and Hjelm, R.P. Jr. (1991), *J. Appl. Cryst.* (in press)
5. Jacrot, B., and Zaccai, G. (1981), *Biopolymers*, **20**, 2413-2426.
6. Wignall, G.D., and Bates, F.S. (1987), *J. Appl. Cryst.*, 20, 28-40.
7. Seeger, P. A., Hjelm, R. P. Jr, & Nutter, M. J. (1990), *Mol. Cryst. Liq. Cryst.*, 180A, 101 - 117.
8. Copley, J.R.D. (1988), *J. Appl. Cryst.*, **21**, 639-654

Q(R.E.Lechner): Which kind of "incoherent back ground" were you referring to in your comparison of small angle scattering instruments, where you claim that this background is larger at reactors than at pulsed sources? Should not the ratio of coherent to incoherent scattering be independent of the instruments? Could it be that the compared instruments at pulsed sources are better shielded than at the reactors?

A(R.Pynn): We do not really understand yet why the pulsed source SANS data seem to be so much better than data from reactors. Perhaps it has to do with wavelength dependence of incoherent scattering. Remember that larger values of Q are measured with shorter wavelength neutrons at pulsed sources, so the incoherent contribution varies as a function of Q. We need to do more work to understand both the incoherent & inelastic scattering contributions to SANS for both reactors and pulsed sources.

C(N.Watanabe): I agree to your argument that simple statement "performance of SANS is proportional to average source flux" is too naive. My argument yesterday is just for simple comparison.

Q(N.Niimura): We should think that transmission and scattering measurement should be carried out simultaneously by developing the detector system for SANS.

A(R.Pynn): I agree with you. That means of course that we have to find a way of inter-calibrating the detector we use for transmission measurements and the one we use to measure scattering. Or perhaps we could develop a detector with a large enough dynamic range to measure both transmission and scattering.

ICANS-XI International Collaboration on Advanced Neutron Sources
KEK, Tsukuba, October 22-26, 1990

Total Performance of Small-Angle Machines at Pulsed Source

M. Furusaka, N. Watanabe, K. Suzuya*, I. Fujikawa and S. Satoh
National Laboratory for High Energy Physics, Tsukuba 305, Japan
*Institute for Materials Research, Tohoku University, 2-1-1 Katahira, Sendai 980, Japan

Abstract

The total performance of a small-angle neutron-scattering (SANS) instrument is discussed in terms of the incident neutron intensity and solid angle covered by the detector system. Although the time-averaged neutron intensity is very low at a pulsed source compared with that at a reactor, there is a considerable gain in intensity for a SANS instrument at a pulsed source, even in the small-Q region when incident neutrons with a wide range of wavelengths are used together with a detector system covering a wide solid angle. A small/medium angle diffractometer, WINK, at KENS is described, which was designed so as to take full advantage of a wide incident-neutron spectrum and a nearly 4π-solid-angle detector.

Introduction

In terms of the "total performance", what parameters should be considered for a SANS instrument, especially one at a pulsed neutron source? Very often, in optimizing a SANS instrument, only the resolution and intensity relationship (in terms of incident neutron collimation and resolution of a detector system) has been discussed; the use of monochromatic neutrons has been implicitly assumed. In the case of a pulse source, it is essentially important to utilize neutrons of a wider range of wavelength, especially with smaller wave numbers, $k=|\mathbf{k}|$, together with a wide solid-angle detector system. There has been no established way for optimizing a collimator system used in a polychromatic neutron beam. In this paper, the optimization of a SANS instrument is discussed in terms of various parameters, such as the period of neutron bursts, the incident neutron intensity/spectrum and the solid angle covered by a detector system.

Intensity optimization

In the optimization of various parameters, one must first know the boundary conditions. From an experimental point of view, the relevant parameters are the required Q-range, especially a minimum Q (Q_{min}), Q-resolution ΔQ. In this paper all of the parameters are discussed (not in terms of wavelength (λ)) in the wave number (k).

One of the possible scenarios used in choosing a suitable collimation system from the required Q_{min} is shown in the following. From the fundamental equation, we can write,

$$Q = 2k_z \sin(\frac{\varphi}{2}) , \tag{1}$$

where, k_z is the z-component of a wave number vector along the beam direction, and φ is the scattering angle. Then, dQ can be expressed as

$$dQ = 2 \sin\frac{\varphi}{2} dk_z + k_z \cos\frac{\varphi}{2} d\varphi . \tag{2}$$

Usually, the angular uncertainty which is determined by the finite size of a sample and resolution elements of a detector system is sufficiently smaller than the incident beam collimation, i.e.,

$$(\Delta\varphi^f_{x,y})^2 \ll (\Delta\varphi^i_{x,y})^2 . \tag{3}$$

Then, using $\Delta k_{x,y} = k_z \Delta\varphi_{x,y}$, ΔQ can be expressed to a convolution approximation,

$$\Delta Q = \left[(2 \sin\frac{\varphi}{2} \Delta k_z)^2 + (\cos\frac{\varphi}{2} k_z \Delta\varphi_x)^2 + (\cos\frac{\varphi}{2} k_z \Delta\varphi_y)^2 \right]^{1/2}$$
$$= \left[(2 \sin\frac{\varphi}{2} \Delta k_z)^2 + (\cos\frac{\varphi}{2} \Delta k_x)^2 + (\cos\frac{\varphi}{2} \Delta k_y)^2 \right]^{1/2} . \quad (4)$$

A relative resolution $R = \Delta Q/Q$ is expressed as

$$R = \frac{\Delta Q}{Q} = \left[(\frac{\Delta k_z}{k_z})^2 + (\frac{1}{2} \cot\frac{\varphi}{2} \Delta\varphi_x)^2 + (\frac{1}{2} \cot\frac{\varphi}{2} \Delta\varphi_y)^2 \right]^{1/2} . \quad (5)$$

In the case of a reactor, since k_z is constant, the first term is independent of Q. The second and the third terms are proportional to $\cot(\varphi/2)$, i.e. inversely proportional to Q at smaller angles.

In the case of a pulsed source, the following condition generally holds:

$$\varphi \Delta k_z \ll \Delta k_{x,y} . \quad (6)$$

Therefore, the first terms of eqs. (4) and (5) are negligible compared to the other terms.

ΔQ at Q_{min} (ΔQ_{min}) is determined by the required resolution, R, as $\Delta Q_{min} = Q_{min} \times R$ (typically $R \approx 0.1$). A suitable collimator system can be chosen according to ΔQ_{min}. If a relaxed resolution, R^* (say $R^* \approx 0.3$), can be acceptable at the lower angle part of the detector system, Q can be extended to $Q_{min}^* = Q_{min} \times R/R^*$ with the same incident collimator system.

The components in eq. (4) must be nearly equal from the condition of resolution matching. Using eq. (4) the required $\Delta k_{x,y}$ for ΔQ_{min} is expressed as

$$\Delta k_{x,y} \approx \frac{1}{\alpha} \Delta Q_{min} . \qquad \alpha = \begin{cases} \sqrt{2} : \text{pulsed source} \\ \sqrt{3} : \text{reactor} \end{cases} \quad (7)$$

The values of α can be easily understood from eq. (4). Using the smallest available kz (k_z^{min}), $\Delta\varphi_{x,y}$ is given by

$$\Delta\varphi_{x,y} = \frac{\Delta k_{x,y}}{k_z^{min}} = \frac{1}{\alpha} \frac{\Delta Q_{min}}{k_z^{min}} . \quad (8)$$

The neutron intensity at the sample position is discussed in terms of $\Delta\varphi_{x,y}$. When an isotopic sample is assumed, the neutron intensity observed in ΔQ at Q is expressed as

$$I^{obs}(Q)\, \Delta Q = \int_{k_z^{min}}^{k_z^{max}} dk_z\, I^0(k_z)\, \eta(k_z, Q)\, V\, N\, Att(k_z, Q) \frac{d\sigma}{d\Omega}(Q) \frac{\Delta\Omega(k_z, Q)}{\Delta Q} \Delta Q, \quad (9)$$

where, k_z^{max} is the largest k_z available, $I^0(k_z)$ the incident neutron intensity at the sample position, $\eta(k_z, Q)$ the detector efficiency, V the volume of a sample, N the number density, $Att(k_z, Q)$ the sample attenuation, $d\sigma/d\Omega$ the scattering cross section, and $\Delta\Omega(k_z, Q)/\Delta Q$ the solid-angle covered by the detector system in ΔQ for a fixed k_z. Since the V, N, $Att(k_z, Q)$ and $d\sigma/d\Omega$ in the integral are sample dependent, only the other factors are considered here. Our goal is to maximize the function F(Q) in the following form at a specified Q range:

$$F(Q) = \int_{k_z^{min}}^{k_z^{max}} dk_z\, I^0(k_z)\, \eta(k_z, Q) \frac{\Delta\Omega(k_z, Q)}{\Delta Q} . \quad (10)$$

$I^0(k_z)$ can be derived from the phase space density of neutrons at the moderator (Maier-Leibnitz, H. 1966). The phase space density is expressed as

$$\frac{\Delta^6 n}{\Delta V_p} = \frac{\Delta^6 n}{\Delta k_x \Delta k_y \Delta k_z \Delta x \Delta y \Delta z \cdot \hbar^6}, \tag{11}$$

where n is the number of neutrons in the phase-space volume, V_p; $k_{x,y,z}$ the x,y and z (beam direction) components of **k**; Δk_x, Δk_y and Δk_z the corresponding resolution elements; and Δx, Δy and Δz the resolution elements in real-space.

The intensity, $I(k_z)$, at the sample position through a unit area for given $\Delta k_x \Delta k_y \Delta k_z$ is expressed as (Alefeld B. and Kollmar A., 1985),

$$I(k_z)\,\Delta k_z = \frac{\phi k_z^3}{2\pi k_T^4} e^{-\frac{k_z^2}{k_T^2}} \cdot \Delta k_x \Delta k_y \Delta k_z, \tag{12}$$

with

$$k_T = \frac{\sqrt{2 m k_B T_N}}{\hbar}. \tag{13}$$

In the above ϕ is the time-averaged neutron flux of the Maxwellian part, m the neutron mass, k_B the Boltzman constant and T_N the effective neutron temperature; $I(k_z)$ is assumed to have only the Maxwellian part ; the slowing down part is neglected for simplicity. It is not so difficult to add the slowing part afterwards. $I(k_z)$ is shown in Fig. 1.

$I^0(k_z)$ is expressed by replacing $\Delta k_{x,y}$ with $\Delta\varphi_{x,y}$,

$$\begin{aligned} I^0(k_z)\Delta k_z &= \phi \frac{k_z^3}{2\pi k_T^4} e^{-\frac{k_z^2}{k_T^2}} \cdot \Delta\varphi_x \Delta\varphi_y \Delta k_z \\ &= \phi \frac{k_z^3}{2\pi k_T^4} e^{-\frac{k_z^2}{k_T^2}} \cdot \left(\frac{\Delta Q_{min}}{\alpha\, k_z^{min}}\right)^2 \Delta k_z. \end{aligned} \tag{14}$$

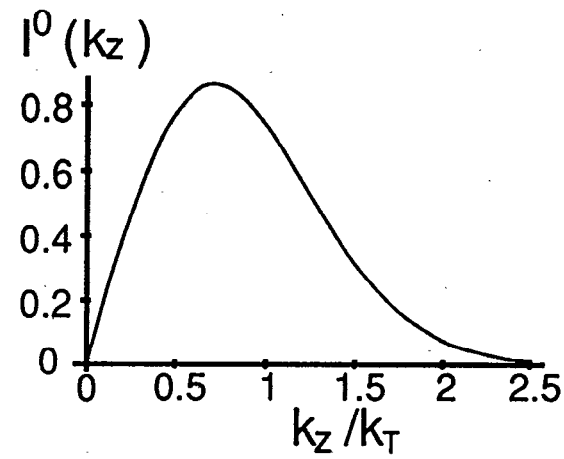

Fig. 1. Normalized spectrum, $I(k_z)$, at the sample position for a given $\Delta k_x \Delta k_y \Delta k_z$ resolution element. Only the Maxwellian part of the spectrum is shown as a function of k_z in units of k_T.

The importance of using a detector system with a large solid-angle is often overlooked in SANS instruments. The relation between solid-angle covered by a detector system and observed intensity is now discussed.

The solid angle subtended by a detector, $\Delta\Omega(\varphi)$, is expressed as

$$\begin{aligned} \Delta\Omega(\varphi) &= 2\pi \sin\varphi\, \Delta\varphi \\ &= 4\pi \sin\frac{\varphi}{2} \cos\frac{\varphi}{2} \Delta\varphi, \end{aligned} \tag{15}$$

where, φ is the scattering angle. Using the relations $Q = 2k_z \sin(\varphi/2)$ and $\Delta\Omega(k_z, Q)/\Delta Q$ for a fixed k_z is expressed as

$$\frac{\Delta\Omega(k_z, Q)}{\Delta Q} = \frac{2\pi Q}{k_z^2}, \quad (Q \le k_z). \tag{16}$$

$\Delta\Omega(k_z,Q)/\Delta Q$ is shown in Fig. 2. by a dashed line denoted by "Ideal".

F(Q) in eq. (10) can be expressed by using eqs. (12) and (15),

$$F(Q) = \int_{k_z^{min}}^{k_z^{max}} dk_z \frac{\phi k_z}{2\pi k_T^4} e^{-\frac{k_z^2}{k_T^2}} \Delta\varphi_x \Delta\varphi_y \, \eta(k_z, Q)\, Q$$

$$= \int_{k_z^{min}}^{k_z^{max}} dk_z \frac{\phi k_z}{2\pi k_T^4} e^{-\frac{k_z^2}{k_T^2}} \left(\frac{\Delta Q_{min}}{\alpha\, k_z^{min}}\right)^2 \eta(k_z, Q)\, Q. \qquad (17)$$

Figure 3 gives the useful bandwidth in k_z for measurements at Q, which is determined by k_z^{min} and k_z^{max} in eq. (17) for both the reactor and pulsed source. The limits for $\Delta Q/Q = 0.1$ (long-dashed line) and $\Delta Q/Q = 0.3$ (short-dashed line) in the case of the pulsed source are shown in Fig. 3.

For the case of an instrument at a reactor, if $\Delta Q_{min}/Q_{min} = 0.1$ is required at Q_{min}, Δk_z becomes $0.1/\sqrt{3}\ k_z^{min} = 0.058\ k_z^{min}$. Therefore, integration over k_z should be taken from k_z^{min} to $k_z^{max} = k_z^{min} + \Delta k_z$ with $\Delta k_z = 0.058\ k_z^{min}$. A typical useful bandwidth in k_z is indicated by the short line with arrows outside in Fig. 3.

For the case of a pulsed source, integration can be carried out from k_z^{min} (or from cutoff at $Q=2k_z$), up to the line defined by $\Delta Q/Q = 0.1$. A typical integration path in the low-Q region is indicated by a thin horizontal arrow in Fig. 3.

Numerical integrations of eq. (17) for a pulsed source were performed and the Q dependences of F(Q) are shown in Fig. 4 for different values of k_z^{min} (= 0.2, 0.4, 0.6 and 1 Å^{-1}). Rapid drop of F(Q)'s beyond Q = 2 Å^{-1} is due to the fact that only the Maxwellian part of the spectrum was assumed for $I^0(k_z)$. If the slowing-down part of the spectrum is taken into account, F(Q)'s keep almost the peak values in a higher Q region.

The calculations were performed under the condition that $\Delta Q/Q \leq 0.1$, even at Q_{min} with $\Delta Q_{min} = 10^{-3}$ Å^{-1}. Similar calculations for a reactor instrument for the same values of k_z^{min} are also shown by dashed straight lines in Fig. 4.

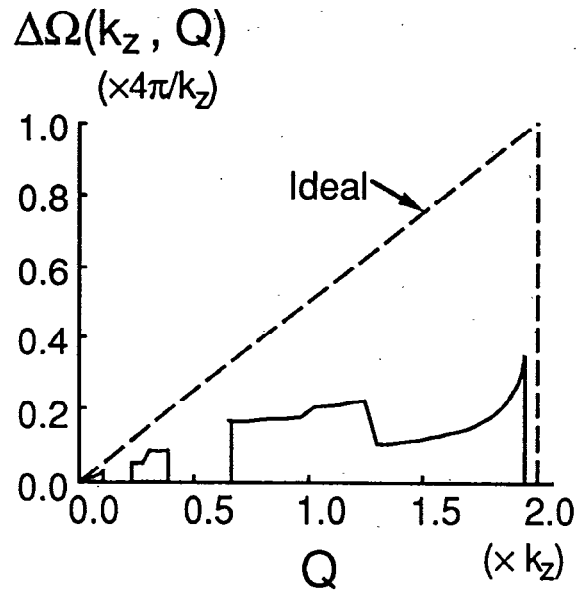

Fig. 2. $\Delta\Omega(k_z, Q)/\Delta Q$ as a function of Q for an ideal 4π solid-angle detector system for given kz (dashed line). The same function for WINK is also shown by thick solid curves.

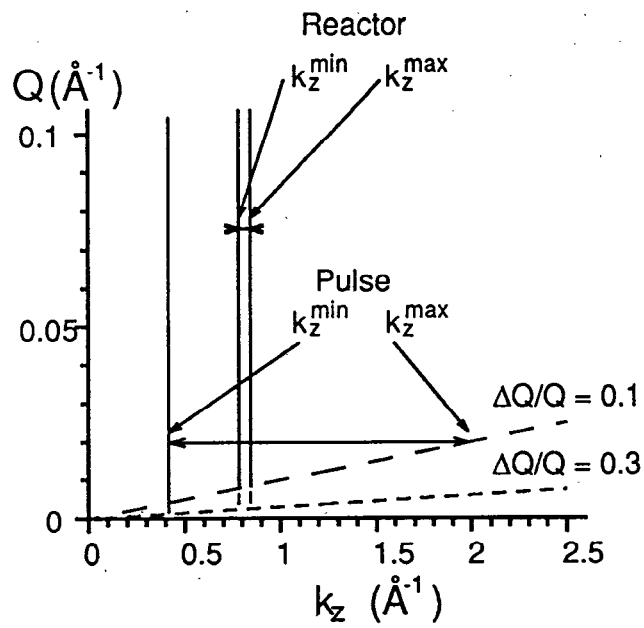

Fig. 3. Integration paths in a k_z-Q space.

In the case of a pulsed source, F(Q) increases drastically with decreasing k_z^{min}. This is because, a relaxed incident-collimation can be used with a smaller k_z^{min} to realize the same ΔQ_{min}. Under real experimental conditions, many difficulties arises when very small k_z is used: for example, a sample attenuation becomes serious at very small k_z and a measurement of transmission becomes difficult. A practical limit would lie around $k_z^{min} \approx 0.3$ Å^{-1} or $\lambda \approx 20$ Å.

In contrast, F(Q) for a reactor depends weakly on k_z^{min}. This is because, although $\Delta\varphi$ can be relaxed by using a smaller k_z^{min}, Δk_z should also be reduced as $\Delta k_z/k_z^{min} \approx 0.1$.

If only the first time-of-flight (TOF) frame is used, k_z^{min} for a pulsed source is expressed as

$$k_z^{min}\,(\text{Å}^{-1}) = \frac{2\pi}{3956}\cdot\frac{L\,(m)}{T\,(sec)}, \tag{18}$$

where L is the total flight-path length and T the period of neutron bursts. In order to obtain a lower k_z^{min}, L should be as short as possible and T as long as possible over a realistic range. A smaller k_z^{min}'s can, of course, be realized by taking the second or third TOF frame, while sacrificing the bandwidth (smaller k_z^{max}); in general, though, this is not realistic. On the other hand, a smaller k_z^{min} can also be realized by thinning (reducing) the repetition of the neutron bursts while sacrificing ϕ. In this case, there is appreciable gain under certain conditions.

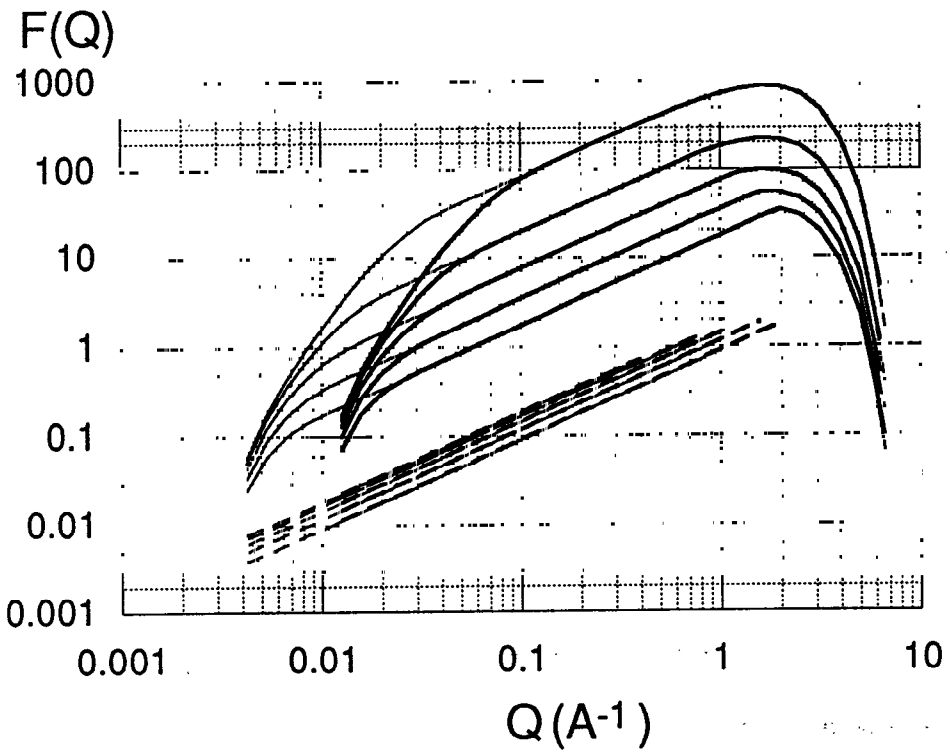

Fig. 4. Calculated F(Q) for k_z^{min} = 0.2, 0.4, 0.6, 0.8 and 1.0 Å^{-1}, from top to bottom for each type of plot. The solid curves are for a pulsed source with ΔQ_{min} = 0.001 Å^{-1}; $\Delta Q/Q \leq 0.1$ (thick lines) and ≤ 0.3 (thin lines), and dashed lines for a reactor source for $\Delta Q/Q \leq 0.1$ (thick lines) and for $\Delta Q/Q \leq 0.3$ (thin lines).

New small/medium-angle diffractometer WINK

As shown in the preceding sections, in constructing an ideal SANS instrument at a pulsed neutron source, the following conditions must be satisfied: i) period of neutron pulses as long as possible, ii) total flight path length as short as possible, and iii) detector solid angle as large as possible.

We designed and built a new small/medium-angle diffractometer, WINK, as shown in Fig.5, which satisfied the above conditions as much as possible. Unfortunately, there are many restrictions: for example, the beam line must be shared by three instruments! Actually, we built the WINK between two existing instruments: a low-energy inelastic spectrometer (LAM-40) and a high-resolution powder diffractometer (HRP). These three instruments share the same neutron beam (C4) viewing directly the solid methane moderator at 20K.

At KENS, the accelerator is operated at 20 Hz, which allows us a 50 msec bandwidth without reducing neutron pulses by a chopper. Since the total flight path-length is 11.3 m due to spatial limitations, k_z^{min} becomes 0.36 Å^{-1} (17.5 Å in wavelength). A tail-cutter is located at about 1.2 m upstream of the sample position, far from the moderator, for technical reasons. The frame overlap is, therefore, not negligible. We have a plan to install another tail-cutter just outside the biological shield. The sample position is 9 m from the moderator and the scattered flight-path-length is 2.3 m, which is much shorter than a desired length (about 4 to 5 m). We utilize a natural collimation between the moderator and the sample. The sample size was designed to be 20 mm by 20 mm. The detector arrangement at the small-angle position (L_2 = 2.3 m, φ = 1.5°~8.4°), which is installed inside the vacuum scattering chamber, is shown in Fig. 6. A similar detector arrangement is used at the

medium-angle position (L_2 = 1.1 m, φ = 12°~19°). The beam size of WINK is shown by a small square and the beam for HRP by a large rectangle, both shown in the center of the detector bank in Fig. 6. Conventional ^{3}He detectors of 1/2'-diameter are used at a lower-angle part, while at other angles 1'-diameter detectors are used. In order to squeeze as many detectors as possible into a compact space, detectors are slanted by 20 degrees, as shown in the figure. We have just installed them. Many high-angle detectors can be placed around the sample chamber, as shown in Fig. 5. The $\Delta\Omega(k_z, Q)/\Delta Q$ realized in WINK is shown by curves in Fig. 2. Even with the present detector arrangement, only 15-40% of the solid angle is covered, because of geometrical constraints.

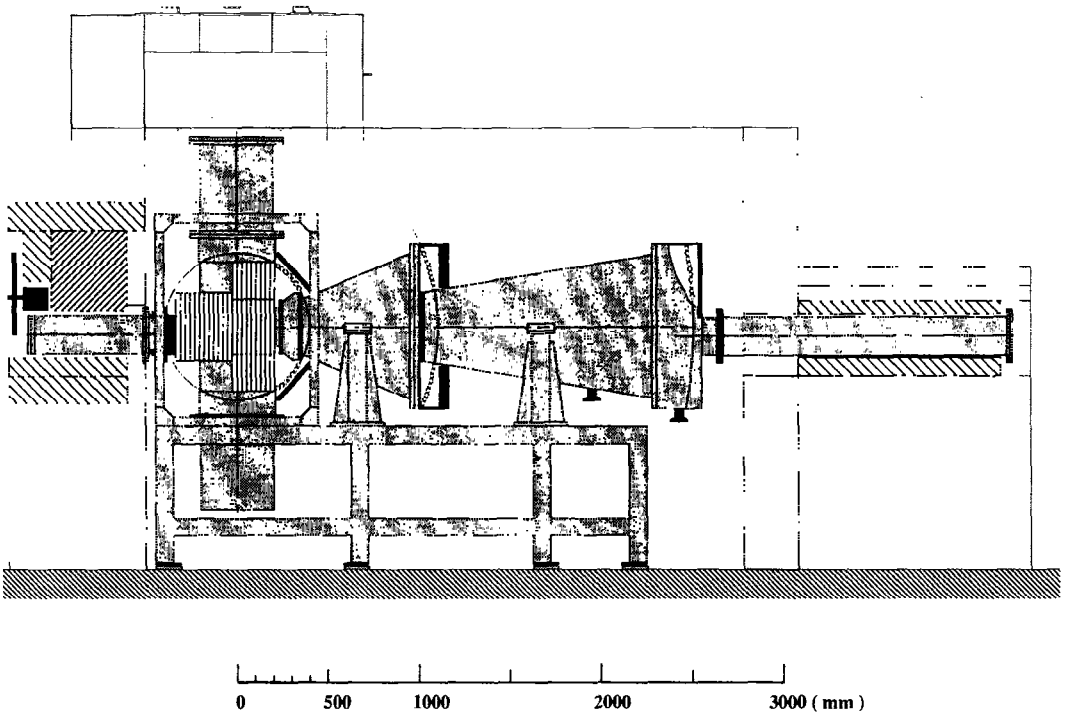

Fig. 5. Side view of WINK.

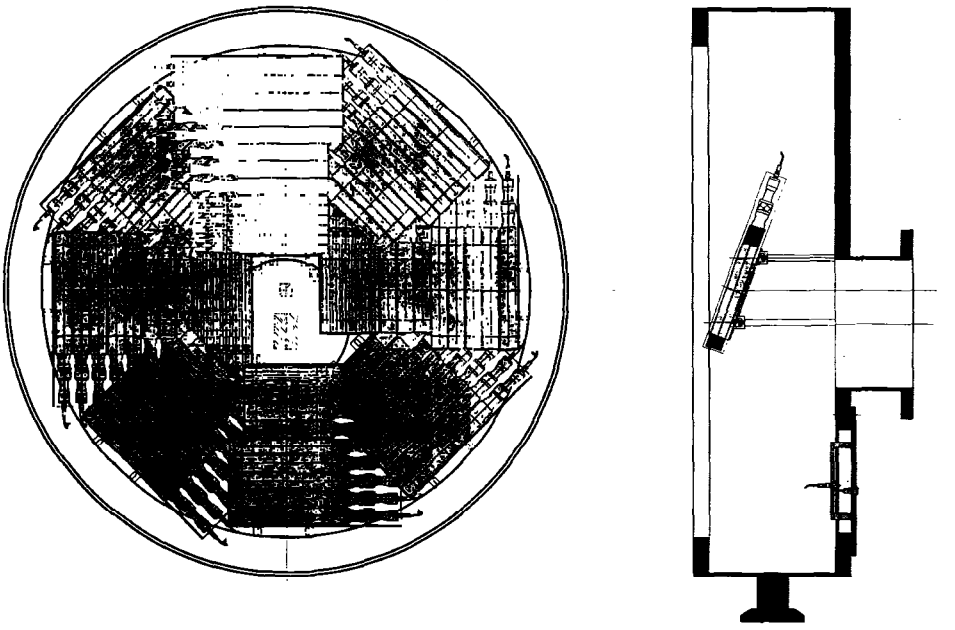

Fig. 6. Detector arrangement of a 2.3 m detector bank of WINK.

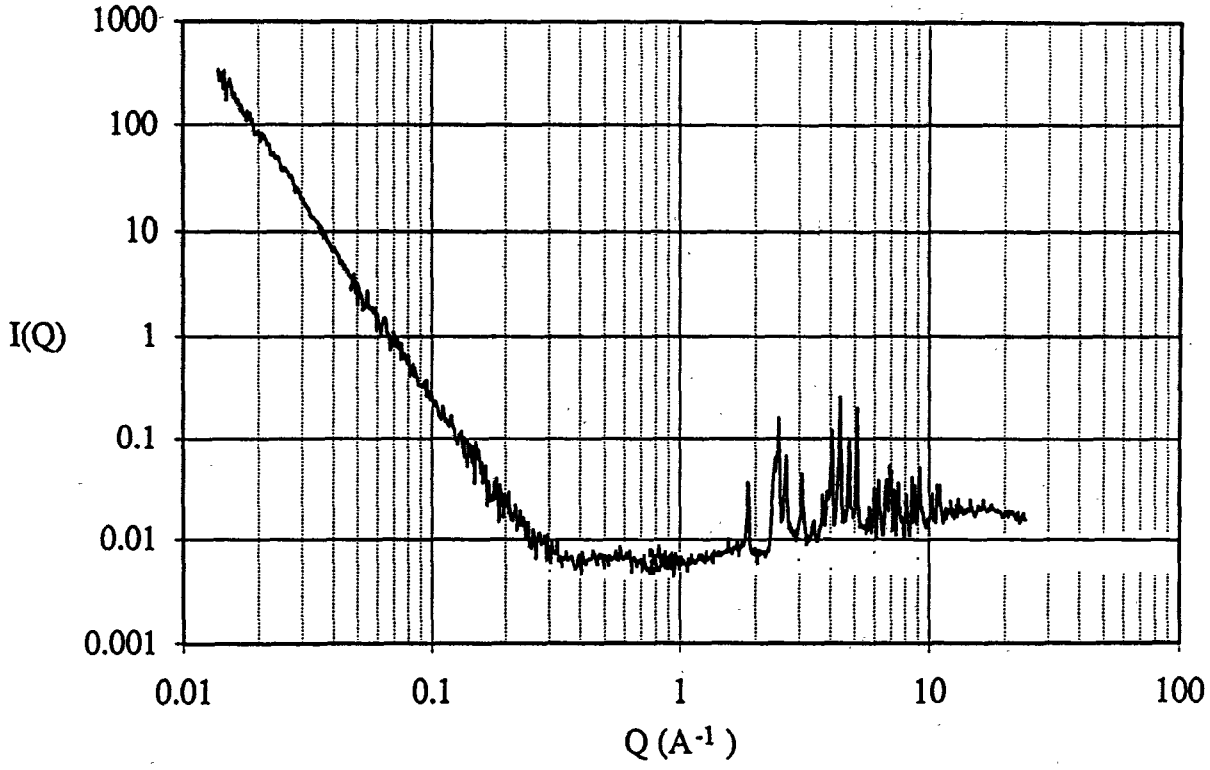

Fig. 7. Scattering spectrum from SiC fine powder measured by WINK instrument with only four detectors.

A preliminary scattering spectrum obtained from SiC fine powder using only one detector at each of four different scattering angles in about four hours is shown in Fig. 7. The Q-range covered by this instrument is sufficiently wide (Q = 0.015 - 20 $Å^{-1}$), as can be expected, and the dynamic range is almost 5 decades.

We are now constructing a high-angle detector bank as well as a sample changer. Only one fourth of the data-acquisition electronics is available now and a prototype data analysis software is under development. The instrument is expect to be completed within FY 1991.

Conclusions

From a total performance point of view, the utilization of neutrons with a wide k range, (especially that of small k_z^{min}), together with a detector system of a wide solid-angle coverage, plays essential roles in the case of a SANS instrument at a pulsed source.

WINK will be a hopefully ideal-like SANS instrument regarding the above points of view. However, there are many mismatches due to the various constraints: narrow space, beam shared with two other instruments, and so on.

References

Maier-Leibnitz H., Nukleonik **8** (1966) 61.

Alefeld B. and Kollmar A., Proc ICANS-VIII (1985) 385, (Rutherford Appleton Laboratory Report RAL-85-110, 1985).

Q(A. D. Taylor): How does the resolution change with angle impact on the data analysis?

A(M. Furusaka): The higher is the scattering angle, the better is the relative resolution $\Delta Q/Q$ owing to the $\cot(\varphi/2)$ term. Only data from the small-angle part affect the analyzed scattering function.

ICANS-XI International Collaboration on Advanced Neutron Sources
KEK, Tsukuba, October 22-26, 1990

Total performance of LAM-80ET

Kazuhiko Inoue[1], Toshiji Kanaya[2], Yoshiaki Kiyanagi[1], Susumu Ikeda[3], Kaoru Shibata[4], Hirokatsu Iwasa[1], Takashi Kamiyama[4], and Yoshinobu Izumi[o,5]

1)Department of Nuclear Engineering, Faculty of Engineering, Hokkaido University, Sapporo, Hokkaido 060, Japan
2)Institute for Chemical Research, Kyoto University, Uji, Kyoto-fu 611, Japan
3)BSF, National Laboratory for High Energy Physics, Tsukuba-shi, Ibaraki-ken 305, Japan
4)Institute for Material Research, Tohoku University, Sendai, Miyagi-ken 980, Japan
5)Macromolecular Research Laboratory, Faculty of Engineering, Yamagata University, Yonezawa, Yamagata-ken 992, Japan

Abstract

Application of mica in the crystal analyser of time-of-flight spectrometer installed in a pulsed cold neutron source is a new approach in high resolution neutron spectroscopy. We constructed a new set of mica crystal analysers for the neutron spectrometer at KENS (KEK), that gave a desirable performance of energy resolution accompanying by a surprisingly sharp rise shape of resolution function. The latter characteristic was especially indicative of the usefulness of mica crystal analyser in the quasielastic neutron scattering studies of localized random motions in condensed matters.

I. INTRODUCTION

Quasielastic neutron scattering is a very useful method to study diffusive motion or the relaxation process in molecular science and in many other fields. Measurements of quasielastic scattering often require a wide energy transfer range of several orders of magnitude in addition to a relatively wide momentum transfer range. It is easily seen that the design of a single quasielastic spectrometer which has the capacity to cover such a wide energy transfer range is beyond reach. Therefore, adopting a single design philosophy, we designed three quasielastic spectrometers which can be complementary devices, and installed them at the KENS spallation cold neutron source at the National Laboratory for High Energy Physics (KEK), Tsukuba.

During the past decade we have been engaged in developing the KENS spallation cold neutron source and a high resolution quasielastic spectrometer in addition to a conventional resolution one using the pulsed cold source. Our previous studies revealed the 20 K solid methane moderator to be the most adaptable to the modest capacity accelarator-based cold neutron source of the KENS-I size. Using the pulsed cold source, we have been accumulating basic data on the performance of the quasielastic spectrometer.

Based on our accumulated information, we then constructed a pulsed cold neutron source of the KENS-I' size. Several years of successful operation have proved that the 20 K solid methane cold source is still adaptable even for the neutron source of the KENS-I' size. Furthermore, our data has revealed that the crystal analyser type time-of-flight spectrometer, combined with the pulsed cold source, is the simplest but most suitable device for quasielastic scattering because of its flexibility of performance.

This paper describes the design and the performance of the LAM-80ET, which is an improved version of the LAM-80 having the special feature of a wide energy window. The design considerations of the instrument are discussed in section II, and the description of spectrometer and the practical performance are given in sections III and IV. Finally, a short remark of the method of data analysis is given in section V.

II. Design considerations

In order to carry out quasielastic neutron spectroscopy using the pulsed cold source, it is most desirable that the neutron pulse emitted from the cold source be utilized directly for energy analysis using the time-of-flight technique without any auxiliary device for narrowing the pulse width. As to accompanying secondary energy analysing devices, there are several options. Our early results suggested that a wide acceptance angle crystal analyzer mirror is the most suitable one. Therefore, we adopted the arrangement of devices shown in fig. 1.

In the case of time-of-flight measurements, the high resolution required is attained by selecting appropriately the length of a neutron flight path to the width of the neutron pulse, the Bragg angle and the material of the analyser mirror. An appropriate selection of these combinations enabled us to design a high resolution spectrometer with high intensity. Neutron guide tube was used for the purpose of the high intensity.

II.1 Scattered neutron spectrum

If the design parameters of the spectrometers are appropriately selected, the time spectrum of the scattered neutrons from the sample at a scattering angle θ is simply expressed as follows.

$$\eta(t;\theta)=\mathrm{const}\int\int\phi[E_1,t-l_2/(2E_2/m)^{1/2}]\sigma(E_1\rightarrow E_2,\theta)R(E_2)dE_1dE_2 \quad (1)$$

where $\phi(E_1,t_1)$ is the incident neutron flux at time t_1 into the sample, $\sigma(E_1\rightarrow E_2,\theta)$ is the incoherent differential scattering cross section, $R(E_2)$ is the energy resolution function of the crystal analyser mirrors, m is the neutron mass, and l_2 is the average flight path length of the scattered neutrons.

The quantities measured are the energy transfer, ε, and the scattering vector, Q, defined by

$$\varepsilon = E_1 - E_2, \quad (2) \quad \text{and} \quad Q = k_1 - k_2, \quad (3)$$

where k_1 and k_2 are the wave number vectors of the incident and the scattered neutrons, respectively, and Q^2 is given as follows,

$$Q^2=(2m/h^2)[E_1+E_2-2(E_1E_2)^{1/2}\cos\theta]. \quad (4)$$

II.2 Time-of-flight measurement

The time and energy spectrum, $\phi(E_1,t_1)$, of the neutrons impinging on the sample depends on the neutronic performance of the pulsed cold source. Since we needed precise information about the time structure of the neutron pulse emitted from the cold moderator, we measured the time structure by a thermica monochromator for the 20 K methane cold moderator and the pulse data were corrected for the monochromator resolution using the QUESA-40 code. Fig. 2 shows the pulse width at half-maximum, Δt_z, as a function of neutron wavelength after the correction of the resolution. A tremendous increase of pulse width occurs in the cold neutron wavelength range.

The energy resolution, ΔE_1, in the time-of-flight experiments is given by

$$\Delta E_1=2E_1\Delta t_z/t_1. \quad (5)$$

Using the data shown in Fig. 2, we can assess ΔE_1 as a function of the flight path length, l, for 4 and 6Å wavelength neutrons as shown in Fig. 3. From the figure, the length of the neutron flight path and the desired energy resolution in the case of the 20K methane pulsed cold source can be detemined. Because of the spatial limitation in the experimental hall, the length of the flight path is fixed to about 30m, and we obtain a resolution of 10μeV. This assessment is based on the QUESA-40 code.

II.3 Analyser mirror

To attain the desired resolution and high efficiency, it is necessary to match the energy resolution in time-of-flight measurement, ΔE_1, for the energy resolution of the analyser mirror, ΔE_2, according to eqs. 1 and 2. The design of the analyser mirror which fulfills the above requirements is as follows: a large number of small mica crystal pieces are mounted on a surface with special curvatures so that all pieces satisfy the same Bragg condition. Moreover, the flight path lengths from the sample to the counter via each crystal piece must be almost the same so as not to sacrifice the energy resolution ΔE_1 due to variance of t_2. To fulfill the latter condition, a relatively long distance from the sample to the crystal piece and from the crystal piece to the counter is needed. To decide the dimensions of the analyser mirror, many factors are involved.

The resolution function of the mirrors $R(\theta_B)$ is calculated by the following equation,

$$R(\theta_B)=\int\int\int p(r,\Sigma,S)|r-\Sigma|^{-2}|\Sigma-S|^{-2}\delta[\theta_B-\theta_B(r,\Sigma,S)]drd\Sigma dS, \quad (6)$$

where $\theta_B(r,\Sigma,S)$ is the Bragg angle determined by the positions r, Σ and S, and $p(r,\Sigma,S)$ is a factor representing efficiency due to the projection of each plane and the mosaicness of the crystals. The

integrations are performed with respect to the volume of the sample, the surface of the mirror and the plane of the diaphragm.

Fig. 4 shows a typical calculated results of $R(\theta_B)$ by eq. 6 for the case of the average Bragg angle of 80° and a 14 mm diameter and 80 mm height cylindrical sample. The result indicated that the angular spread of the Bragg angle $\Delta\theta_B$ is about 0.36°.

The energy resolution of the analyser mirror is estimated by the following expression,

$$\Delta E_2 = 2E_2[(\cot\theta_B \Delta\theta_B)^2+(\Delta\tau/\tau)^2]^{1/2}. \quad (7)$$

Here $\Delta\tau$ is the variance of the reciprocal lattice vector, τ, due to the limitation of the number of lattice planes contributing to the reflection. In our case, the second term in the brackets in the rhs of eq. 7 may be small enough to neglect as compared with the first term.

II.4 Overall resolution

Fig. 5 shows the variance of incident and scattered neutron energies ΔE_1 and ΔE_2 as a function of the Bragg angle calculated by eqs. 5 and 7 for the case of a flight path length 30m.

The overall energy resolution of the spectrometer is assessed by

$$\Delta\varepsilon = 2E[(\Delta t_z/t_1)^2 + (\cot\theta_B \Delta\theta_B)^2 + (\Delta\tau/\tau)^2]^{1/2}. \quad (8)$$

Here $E_1=E_2=E$ for quasielastic scattering.

Fig. 6 shows overall energy resolution of the spectrometer as a function of the Bragg angle for the case of flight path length 30 m. The highest resolution is attained for the backscattering condition of the analyser mirror, as seen in fig. 6. However, in this condition, the intensity of the scattered neutrons is seriously sacrificed due to the narrow band width, ΔE_2. An optimal condition is achieved by matching ΔE_1 to ΔE_2. The optimal condition for the desired performance can be found around the point where the two curves cross, as shown in fig. 5.

III. Description of spectrometer

The LAM-80ET utilizes a LAM-type analyser mirror, of which the structural frames supporting the crystal pieces were fabricated according to the same design method described previously. The average distance from the sample to the counter diaphragm via the mirror crystal is 120 cm.

III.1 High resolution machine

Fig. 7 shows the configuration of the LAM-80ET. The spectrometer is installed at the C-2 neutron guide hole, of which the distance from the cold source is about 26 m. As seen in the figure, there are eight identical mirrors, each containing 400 mica crystal pieces of 12mmx12mmx 3mm in size. Each analyser mirror is mounted at four fixed angles: ±15°, ±51.7°, ±78° and ±118°. Thus, the scattering angle of the analysers can cover the region from 15° to 118°. The set of analyser mirrors is housed in an evacuated container surrounded by neutron shields made of borated resin and cadmium sheets. Moreover, each analyser mirror has its own inner shields, as shown in fig. 7.

Fig. 8 shows bird's-eye view of the array of analysers, which

consists of eight analysers and eight helium counters. Scattering sample is placed at the center. Shieldings and diaphragms are not drawn.

Ⅲ.2 Sample container

A cylindrical shape was adopted for the scattering sample, to assure identical geometrical conditions for every analyser mirrors. The typical dimensions of the sample are 14 mm diameter and 80 mm height. These dimensions were determined by the optimization condition calculated between the energy resolution and the counting efficiency. This type of sample container proved to be very useful for liquid samples, and it could be utilized for the spectrometer at a wide temperature range of from 20 K to ambient temperature. However, a plate shape was adopted for the scattering sample in a tunneling experiment, as shown in Fig. 9, and it was utilized for the spectrometer at a wide temperature range of from 5 K to ambient temperature, in which a Heritoran was used as the cryostat.

Ⅲ.3 Data acquisition system

The system consits of three parts, that is, microcomputer, time analyser, and read/write as in the LAM-40 spectrometer. Fig. 10 shows the flow chart of the data acquisition system of the LAM-80ET.

Ⅳ. Performance

Ⅳ.1 Resolution

Fig. 11 shows diffraction peaks of mica and related crystals measured at the Bragg angle of 87° at the outlet of 31 m cold neutron guide in KENS. The peak shapes of mica are excellent for the higher order reflections from second to fifth but those of pyrolytic graphite are not as good as mica crystals for three values of mosaic spread.

Moreover, as can be seen from fig. 11, the background signal by stray neutrons scattered from the crystal is very faint in the case of mica. The reflections of mica from second to fifth are available for analysing the energy of scattered neutrons. Table 1 compiles the resolution (FWHM) of the spectrometer for each analysing energy. Here I_K is the relative intensity of the elastic peaks for each analysing energy for KENS condition.

Fig. 12 shows the measured spectra from vanadium using mica analyser of LAM-80 for E_3 and E_5 analysing energies. The shapes of the spectra indicates the usefulness of mica crystal analyser in the measurements of faint quasielastic spectrum accompanying with a strong elastic peak.

The LAM-80ET adopts the mirror of four times large size compared with that of the LAM-80. This means that the intensity gain is four times and generally the resolution is much worse. However, there is a solution, in which the intensity gain is four times compared with that of the LAM-80 but the resolution of the LAM-80 is conserved. Fig. 13 shows the typical results of the resolution function for each reflection from mica. The solid lines are the vanadium runs by the LAM-80 and the points are those obtained by the LAM-80ET. From this figure, we can see that the resolution for the LAM-80ET is almost the

same as that for the LAM-80.

IV.2 Intensity

Fig. 14 shows a comparison between the intensities obtained by using the LAM-80 and the LAM-80ET. The scattering sample was vanadium at ambient temperature. The intensity was normalized by monitor counts. We can see that the total intensity for the LAM-80ET is now eight times compared with the LAM-80 for each reflection from mica.

IV.3 Application

The LAM-80ET has been applied to study a tunnelling phenomenon, a sol-gel transition, a low energy excitation in amorphous polymers, and others. As a typical example, fig. 15 shows the tunnelling spectrum of N-oxy γ picoline measured by the LAM-80ET at 5K. The energy resolutions for these experiments are about 5 (down) and 16 μeV (up), respectively. Fig. 16 shows the temperature dependence of the tunnelling spectra of the same sample. We can easily seen that the tunnelling phenomena is observed the temperature goes down. Furthermore, a preliminary experimemnt for the energy resolution of 1 μeV has been tryed. Fig. 17 shows a typical result for N-oxy γ picoline using the (002) reflection. The measuring time was about 17 hours. Moreover, the counting rate and the resolution of the LAM-80ET have been confirmed to be comparable to those of IRIS at RAL (see Table 2).

V. Data analysis

As seen from eq.1, the measured neutron spectra are not simply related to the cross section of the sample as in the case of direct geometry facilities. Instead, they are expressed as the results of complex double convolution integrals related to the scattering function, the time structure of incident neutron pulse and the resolution of the analyser mirror. We are developing a data reduction program (QUESA-80ET code) for the determination of the scattering functions from measured spectra which consists of procedures for curve fitting of the spectra and hypothesis testing of the assumed scattering functions.

The measured spectrum is compared with calculated one in the data analysis by using QUESA-80ET code. The time-of-flight spectrum of scattered neutrons is actually expressed as a form of double integrals with respect to E_1 and E_2. In QUESA-80ET code, however, integration for the time-of-flight spectrum $\eta(t,\theta)$ is simply performed as follows

$$\eta(t,\theta) = \text{const} \int Y(t,\varepsilon)\, S(Q,\varepsilon)\, d\varepsilon, \qquad (9)$$

where $S(Q,\varepsilon)$ is the scattering function, Q is the average scattering vector and $Y(t,\varepsilon)$ is the effective resolution function given by

$$Y(t,\varepsilon) = \int \phi(E_2+\varepsilon, t-l_2/(2E_2/m)^{1/2})\{E_2/(E_2+\varepsilon)\}^{1/2} R(E_2)\, dE_2. \qquad (10)$$

For data analysis of quasielastic scattering, it is essential that multiple scattering corrections be assessed as accurately as possible by considering energy transfer and angular dependency. Some computer codes have been written for the multiple scattering calculations.

Information about neutron pulse structure is necessary to calculate the effective resolution function $Y(t,\varepsilon)$. Fig. 18 shows a

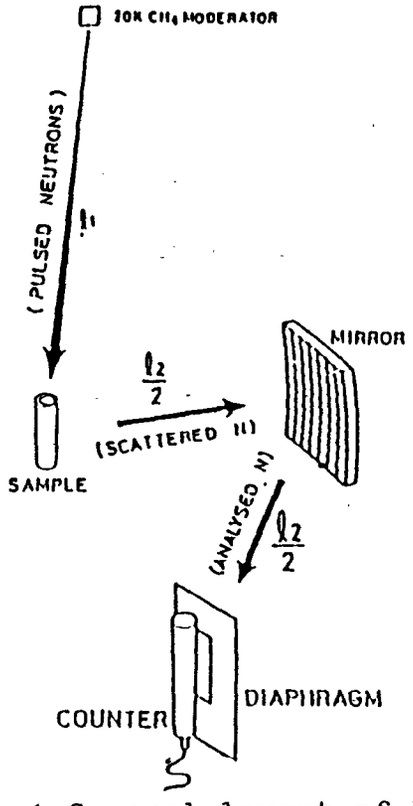

Fig.1 General layout of LAM

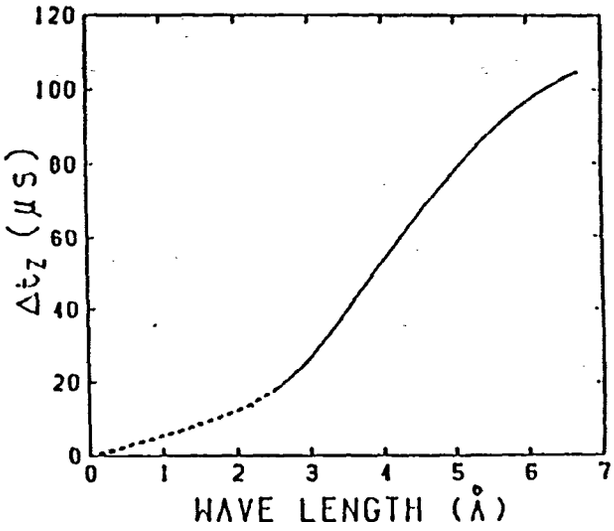

Fig.2 Measured pulse width as a function of wavelength

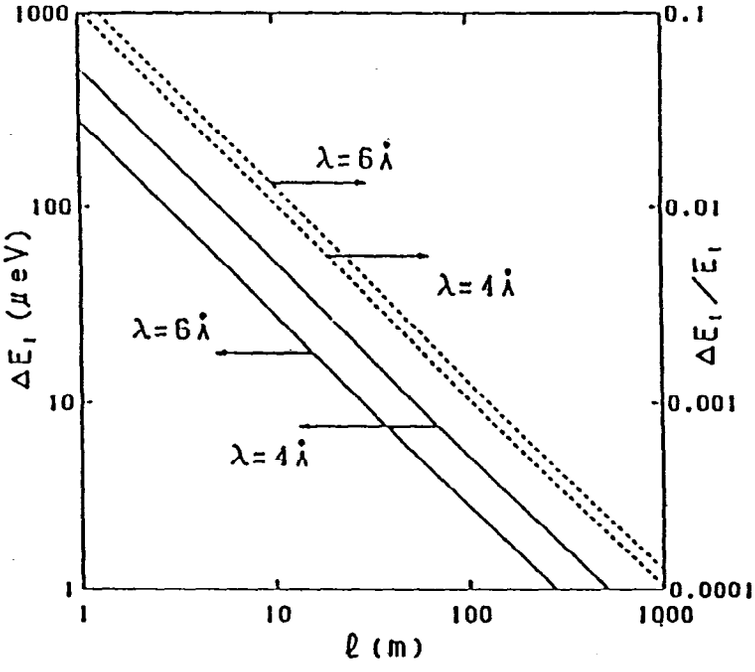

Fig.3 Total flight path length required for specified energy resolution.

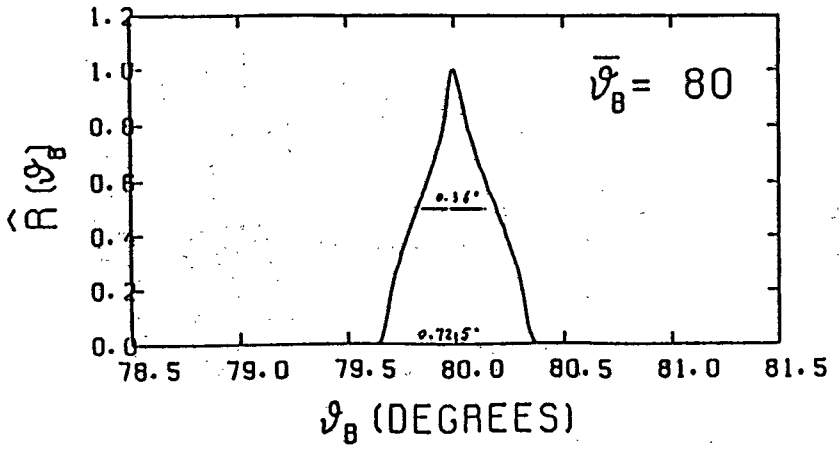

Fig. 4 A typical calculated result of $\hat{R}(\theta_B)$.

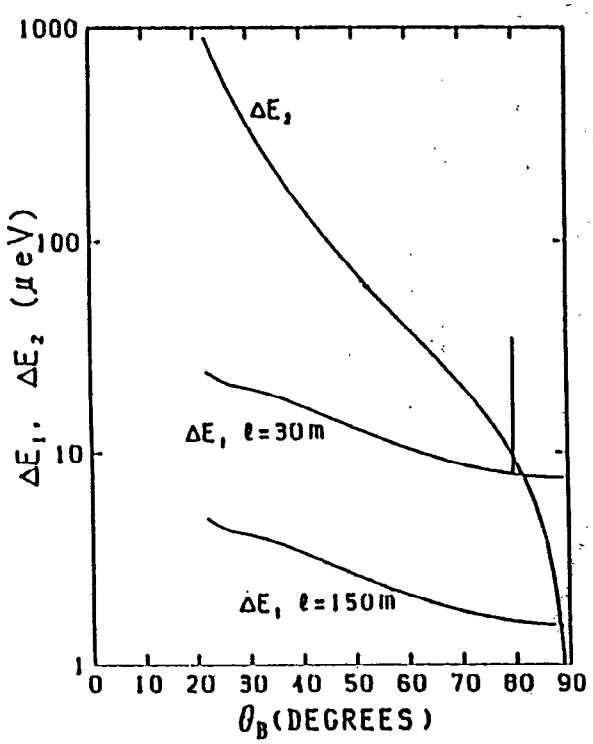

Fig.5 Partial energy resolutios as a function of the Bragg angle.

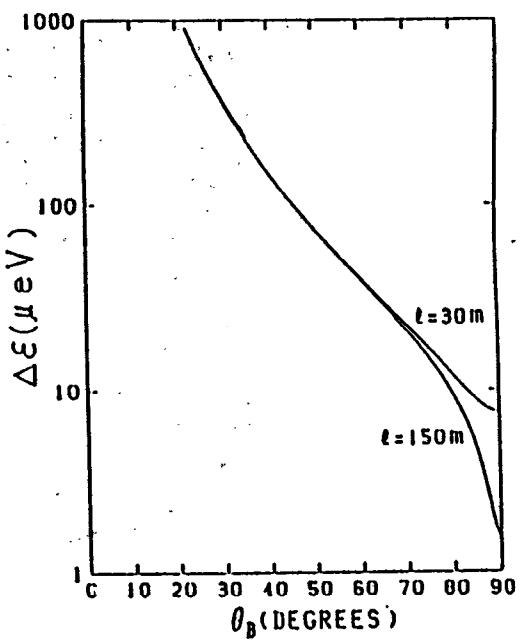

Fig.6 Overall energy resolutions

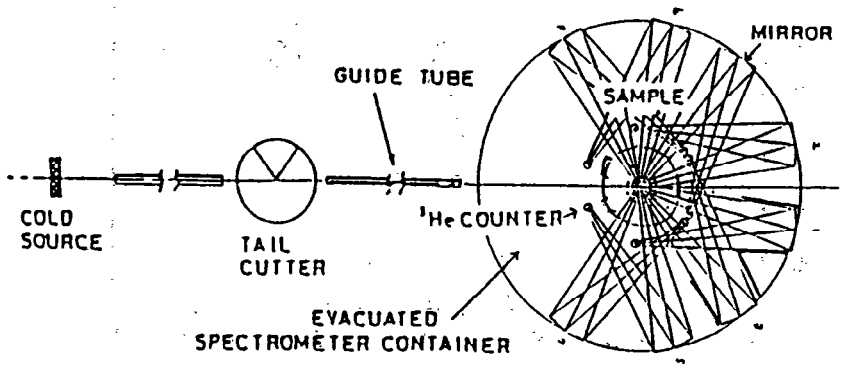

Fig. 7 The configuration of the high resolution quasielastic spectrometer (LAM-80ET)

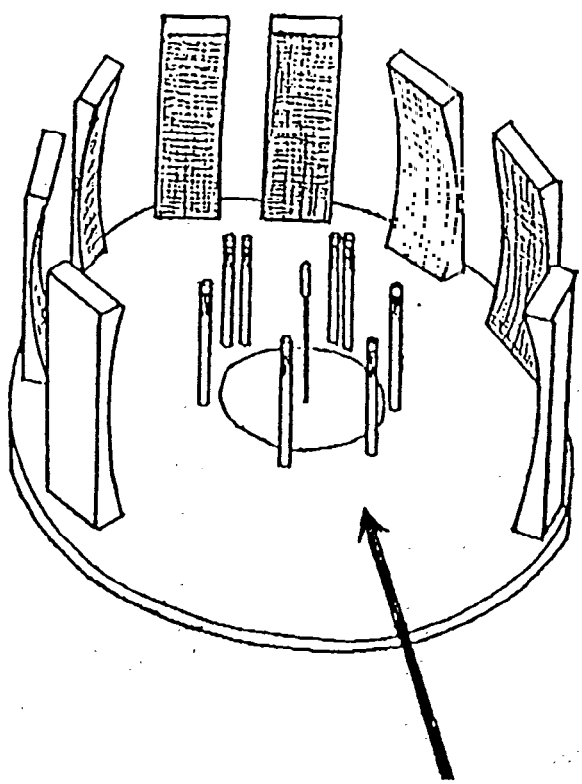

Fig. 8 Bird's-eye view of the LAM-80ET

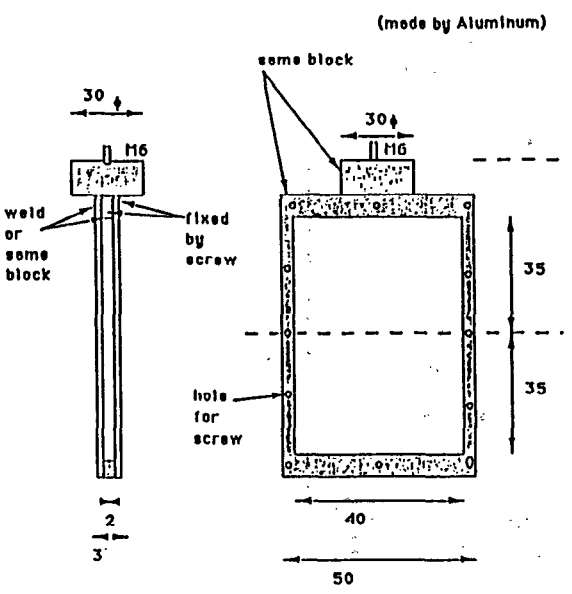

Fig. 9 Sample container for a tunneling experiment

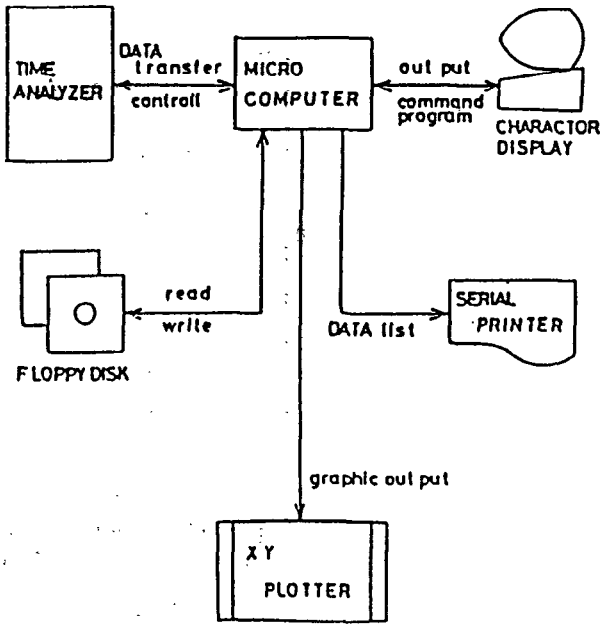

Fig. 10 Data acquisition system

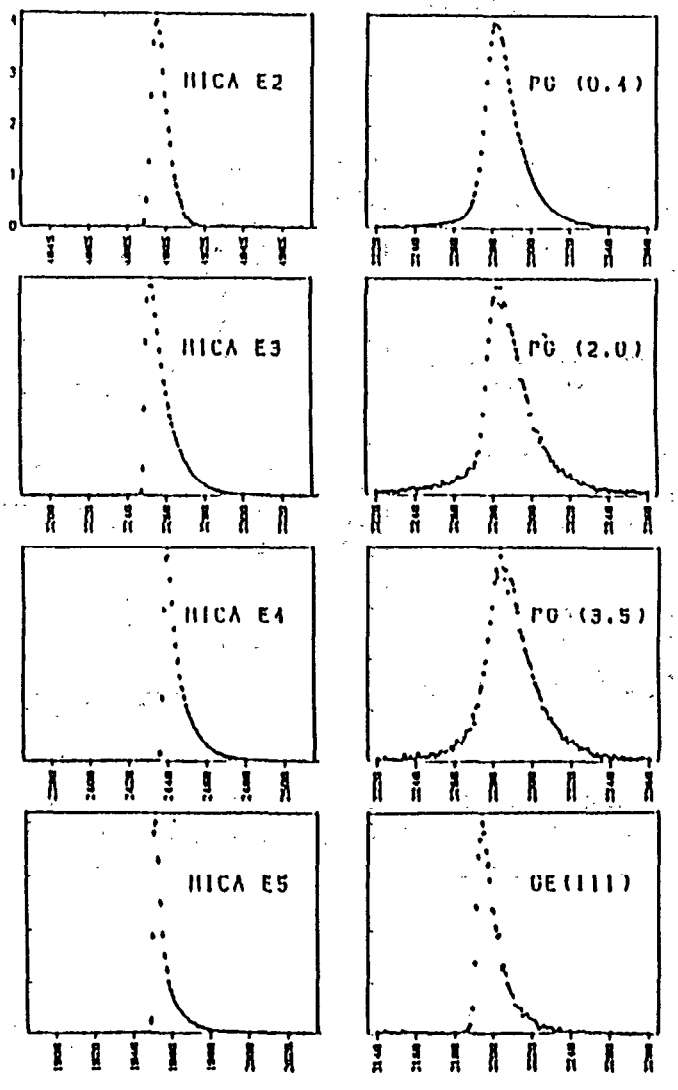

Fig. 11 Diffraction peaks of mica and related crystals

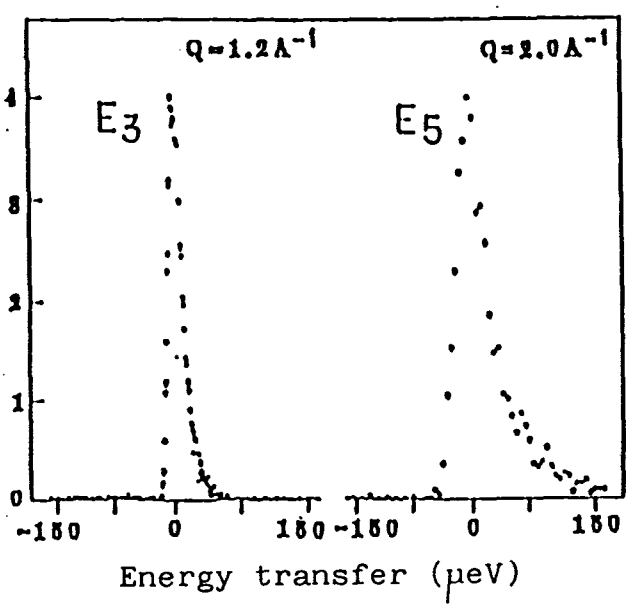

Fig. 12 Neutron scattering spectra from vanadium

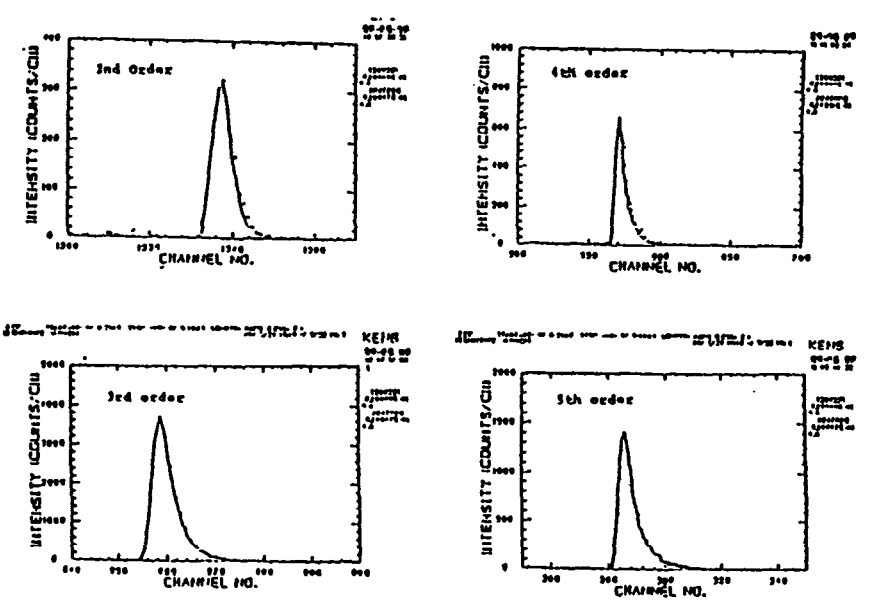

Fig. 13 A comparison between the resolution function of the LAM-80 (solid line) and the LAM-80ET (points) for each reflection.

Table 1. Parameters for each reflection

K	E_K(mev)	$\Delta \varepsilon_K$(μeV)	I_K
1(002)	0.20	1.2	
2(004)	0.83	5.5	0.08
3(006)	1.86	16	1.0
4(008)	3.31	31	0.32
5(0010)	5.18	39	0.74

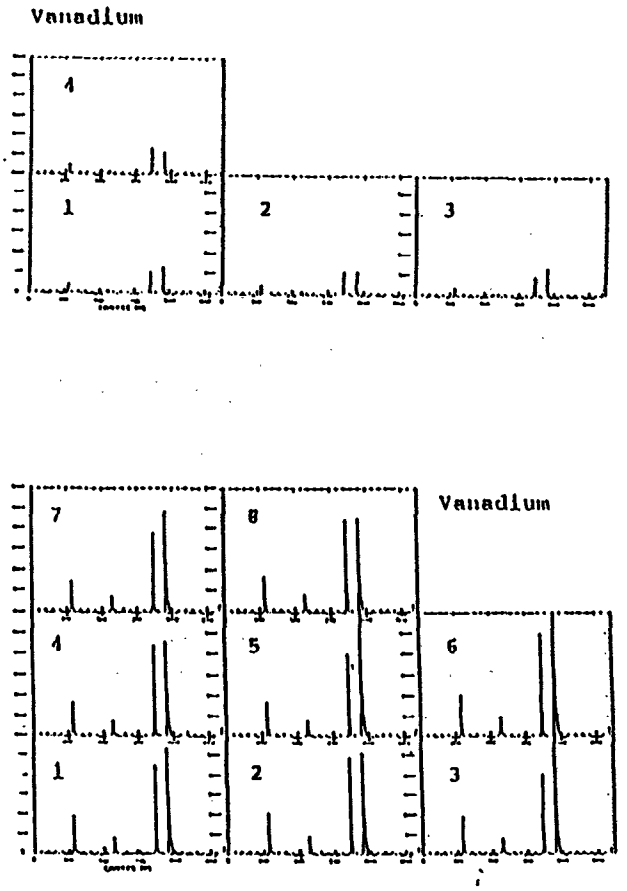

Fig. 14 A comparison between the intensities obtained by using the LAM-80(up) and LAM-80ET(down).

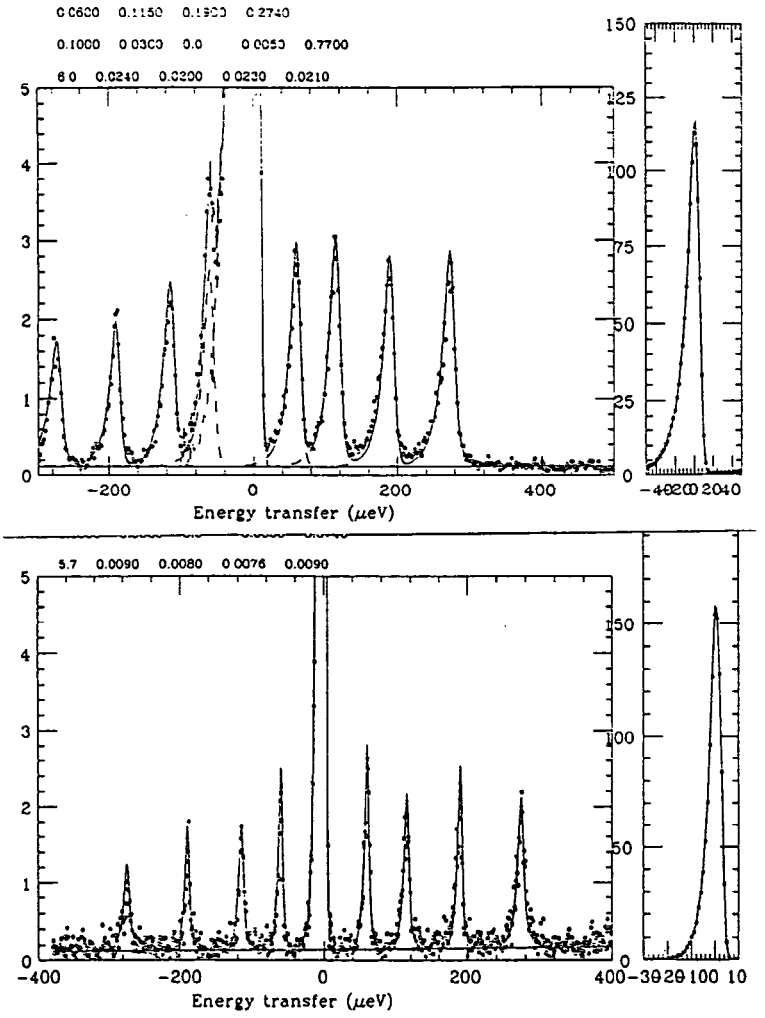

Fig. 15 Tunnel spectra of N-oxy γ picoline.
The energy resolutions are 16μeV (up) and 5μeV (down), respectively.

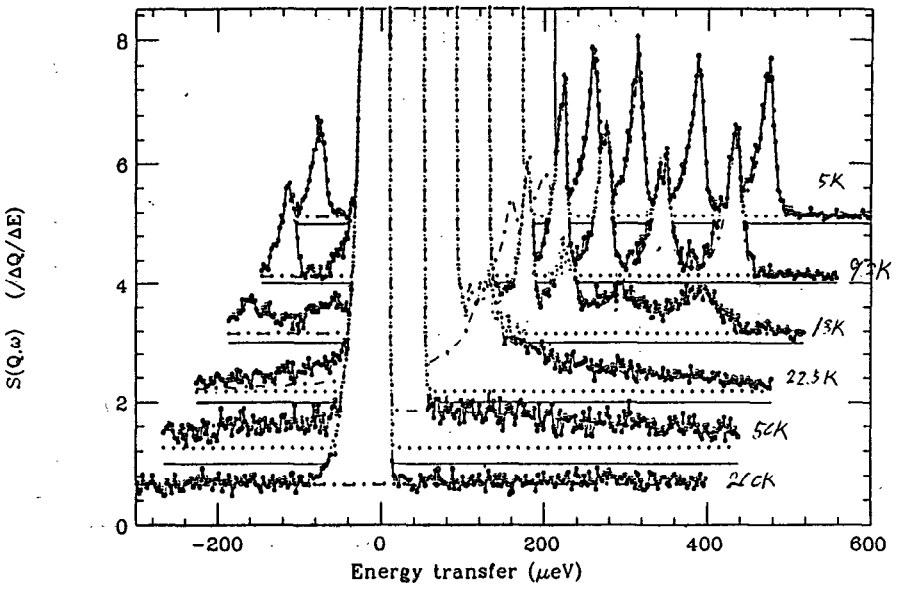

Fig. 16 Temperature dependence of the tunnel spectra of N-oxy γ picoline: the temperature cooresponds to 5, 9.2, 13, 22.5, 50 and 200K, respectively.

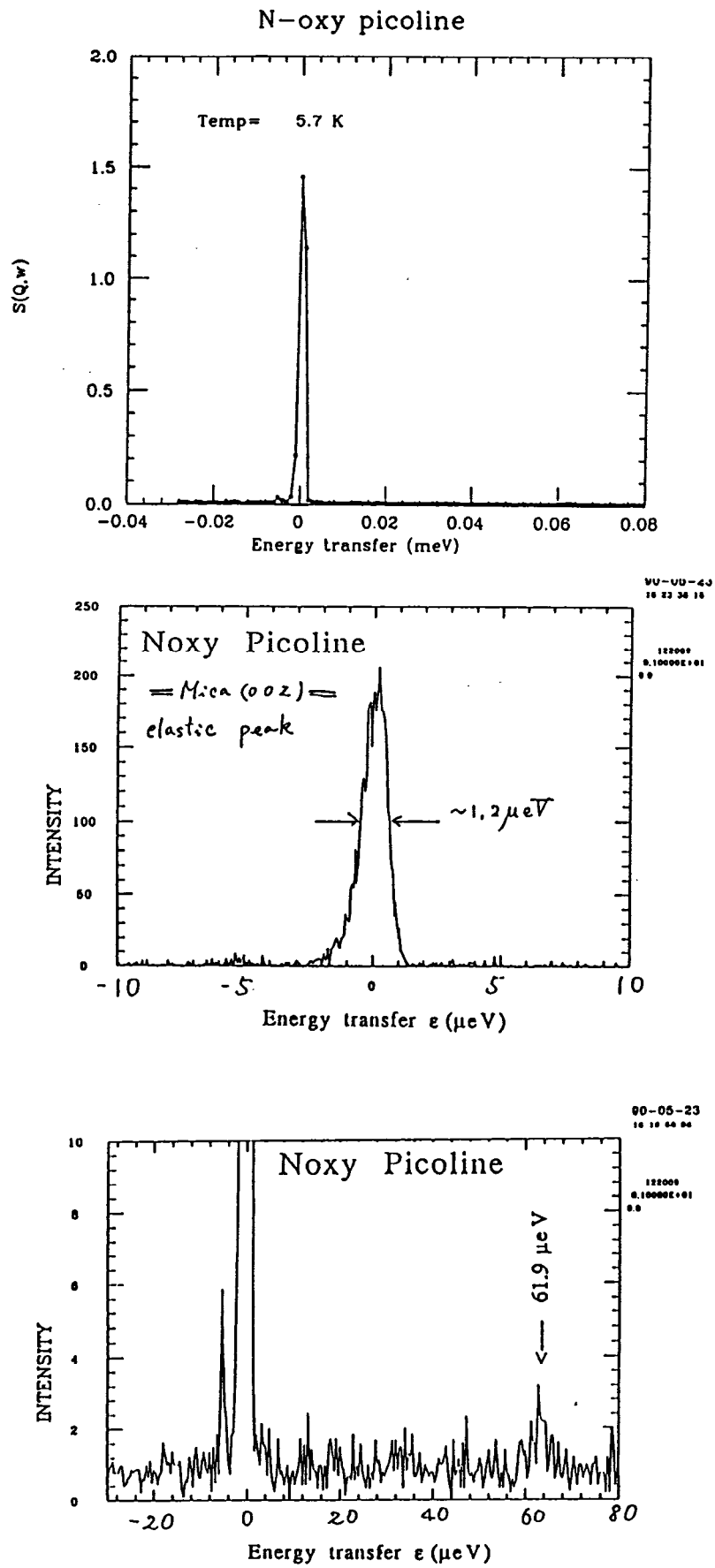

Fig. 17 Tunnel spectrum of N-oxy γ picoline. The energy resolutions is about 1μeV.

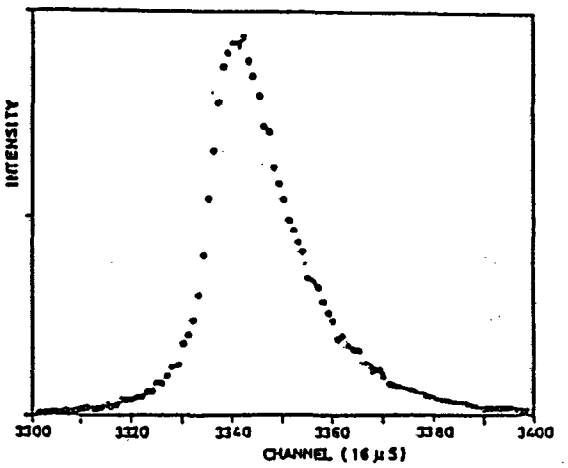

Fig. 18 Pulse structure at the place of LAM-80ET.

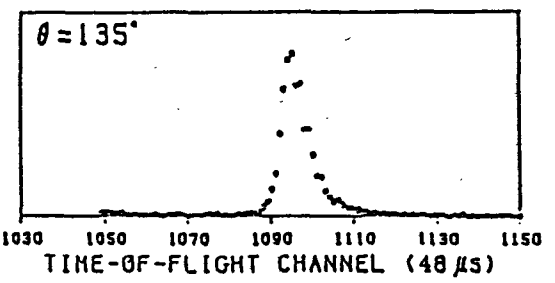

Fig. 19 Scattered spectrim from vanadium.

Table 2. A comparison of total performance between IRIS and LAM-80ET

POSITION	ITEM		IRIS	Relative Gain of IRIS against LAM-80	LAM-80ET
Source	Proton Beam	Energy (MeV)	750.	1.7	500.
		Current (μA)	100.	20.	5.
		Proton per pulse (p.p.p.)	1.3×10^{13}		1.2×10^{12}
		frequency (Hz)	50.		20.
	Moderator	Materials	Liquid H_2	1/8	Solid CH_4
		Temperature (K)	25.		20.
		Type	Cd decoupled		decoupled
		sub total		4.25	
Guide	Chopper	Window Δλ (Å)	2.		8.
		Frequency (Hz)	50.~10. (62.' disc at 6.4m)	1.	20.
	Guide Tube	Cut off (Å)	1.5		4.
		Option	Super Mirror Converging Guide	2.8	None
	Beam Size at Sample Position	(^{H} mm × ^{W}mm)	35.×25.		50.×20.
		sub total		2.8	
Spectrometer	Flight Path	L1 (m) (Source to Sample)	36.54		26.3
		L2 (m) (Sample to Counter)	1.47 (0.83+0.63)		1.2 (0.60+0.60)
	Analyzer Mirror	Area (^{H}cm × ^{W}cm)	(6.×225.)		(49.×16.8)×8
		Solid Angle (Sr)	0.196	1/9	1.83
		Crystal	P.G.	3.0	Mica
		Reflection Index	(002),(004),(006)		(002),(004),(006), (008),(0010)
		Bragg Angel (θ_B)	87.5		80.
		Type	Vertical Energy Focussing		Horizontal Energy Focussing
		sub total		1/3	
Total Gain				4.0	

preliminary data of pulse structure of cold neutrons from pulsed source at the outlet of 30 m guide tube. Fig. 18 shows the spectrum from vanadium and it is used to confirm the accuracy of the calculated effective resolution function in the case of $\varepsilon = 0$. As seen from eqs. 9 and 10, Y(t,0) has a pulse shape which equals exactly to the one of elastically scattered neutrons.

VI. Conclusion

The LAM-80ET described herein has demonstrated a satisfactory performance, and it has also shown the usefulness of the 20 K methane pulsed cold source. This instrument can be used effectively to study diffusive phenomena in detail by quasielastic scattering.

We are very much indebted to the many persons who have contributed to the performance of the LAM-80ET. It is a great pleasure to thank, in particular, Prof. N.Watanabe, Dr. A.Inaba, Dr. T.Takeda, and Dr. C.J.Carlile.

References

1. T.Springer, Springer tracts in modern physics., vol. 64 (Springer, Berlin, 1972).
2. T.Springer, Topics in current physics, vol. 3 (Springer, Berlin, 1977).
3. G.E.Bacon, Neutron scattering in chemistry (Butterworths, London, 1977).
4. M.Bee, Quasielastic neutron scattering (Adam Hilger, Bristol and Philadelphia, 1988).
5. Y.Ishikawa, KENS Report-IV, National Laboratory for High Energy Physics Report, Tsukuba, Japan (1983).
6. K.Inoue, Y.Kiyanagi, H.Iwasa and Y.Sakamoto, Nucl.Instr. and Meth., 178,459(1980).
7. K.Inoue, Y.Kiyanagi and H.Iwasa, ibid., 192,129(1982).
8. K.Inoue, Y.Ishikawa, N.Watanabe, K.Kaji, Y.Kiyanagi, H.Iwasa and M.Kohgi, ibid., A238,401(1985).
9. S.Ikeda, N.Watanabe, S.Satoh, M.Furusaka and K.Inoue, KENS Report-VI,24(1985/1986).
10. K.Inoue, K.Nishida, H.Iwassa, T.Akaba and F.Hiraga, KENS Report-VI,210(1985/1986).
11. K.Inoue,S.Ikeda,Y.Kiyanagi,K.Shibata,T.Kanaya,H.Iwassa,H.Niizeki, K.Kobayashi and T.Yoshihara, KENS Report-VII,17(1987/1988).

Q(A.D.Taylor): What is the width of the INELASTIC tunneling feature in N- Oxy-γpicoline taken with 1 μeV resolution.

A(Y.Izumi): The S/N of the data in the present preliminary experiment is insufficient to estimate the width.

Q(R.Pynn): Is the secondary spectrometer evacuated?

A(Y.Izumi): Yes, it is evacuated by a rotary pump to 10^{-3} mmHg.

REPORT OF SESSION ON "TOTAL PERFORMANCE"

P. A. Egelstaff

The phrase "total performance" has become a key one at this meeting, although in this session we were concerned only with its interpretation for neutron scattering instruments. Our program says "The performance of an instrument should be characterized as a whole system including accelerators, neutron source, instrument itself, sample environment, data acquisition and analysis system, etc." If we use this idea to characterize an instrument, then weaker sources have a chance to be competitive with the stronger sources because the instrument is assessed from the point of view of the experimentalist and the use he or she wishes to make of the data.

The six speakers discussed different instruments from this point of view. Drs. Watanabe and Izumi discussed LAM-80ET and how it had been improved and optimized to give a total performance similar to IRIS on a much stronger source. Very large mica crystal analysers were developed and used on LAM-80ET. Dr. Taylor discussed the present status of MARI and showed how its design had been optimized. Examples of early data were shown, and he felt that MARI could cover the work done by HET and LRMECS in one package. Later he spoke of the advantages of using two target assemblies on one source. Dr. Carpenter discussed how the resolution of pulsed source choppers could be improved and hence improve total performance. He used HRMECS as an example and described the improvement possible with the new design. Dr. Pynn discussed how small angle scattering instruments on reactors and pulsed sources should be compared, and emphasized the advantages of the wider Q range and wavelength scanning available at a pulsed source. From the point of view of total performance LQD was comparable to D11. Dr. Furusaka also discussed small angle scattering work at a pulsed source, and he reviewed the effects of varying path length, moderator temperatures, and other parameters on performance. Intensity at low Q should be optimized to improve total performance.

The six speakers discussed numerous different parameters, and while a full report of their

ideas cannot be given it is useful to list the items they considered in two categories. These are list A of hardware items and list B of data quality matters.

A Hardware Items to be Considered

Accelerator Parameters

Target and moderator parameters

Local Shielding and Voids

Geometrical Parameters, e.g. collimation, beam size, paths, etc.

Devices e.g. choppers, guides, crystals, filters, etc.

Detectors, etc.

Backgrounds, including crosstalk, spurious effects, etc.

Other spectrometer parameters

Costs and labour

B Data Quality Concerns

Intensity per variables of interest (e.g. time)

Signal/Background ratio, and absolute background

Background from expt. components (e.g. Al windows)

Resolution per variables of interest

Experimentally adjustable parameters (compared to fixed parameters)

Quality of instrumental checks

Ancillary Equipment - installation and operation

Convenience of operation; data taking and analysis

Costs and labour

With the help of such lists the concept of 'total performance' may be discussed in greater detail. First the experimentalist should define an ideal matrix [B] for each experimental case under

consideration. Let one of these matrices be called $[B^1]$. A "good total performance" would then consist of adjusting the matrix [A] in order to cause a given [B] to move significantly towards $[B^1]$. There maybe several roughly equivalent ways of doing this, and if so the one selected should minimize the costs and labour. The best example of this approach given in this session was the description of the development of LAM80ET. However in the other instrument sessions other examples were given, such as the design of SANDALS.

At the end of the Total Performance session the speakers formed a panel to discuss this topic. A wide ranging discussion was held, and some of the points made follow. It is easier to succeed when a few parameters stand out as being more important than the others (so that matrices [A] and [B] are small). Also new technical improvements which permit a bigger range of some parameters can alter an established picture, for example new guides, very large monochromators, better reflectors, etc. One speaker called for improved chopper designs for pulsed sources which would allow the more intense (but wider) pulses from large hydrogenous moderators to be exploited more effectively. Some radical questions were proposed, such as "when is it better to spend money on instruments, moderators etc. to improve total performance rather than on the purchase of higher power accelerators?" It was agreed that the concept of total performance should be explored further and ways of applying it to various experiments clarified. Finally it was suggested that a follow up session be included in the next ICANS meeting.

ICANS-XI International Collaboration on Advanced Neutron Sources
KEK, Tsukuba, October 22-26, 1990

FIRST RESULTS FROM THE UK-JAPANESE SPECTROMETER MARI

A D Taylor*, M Arai*, S M Bennington*, Z A Bowden*, R Osborn*, K Andersen+, W G Stirling+, T Nakane°, K Yamada° and D Welz°

*ISIS Facility, Rutherford Appleton Laboratory, Chilton, Didcot, Oxon OX11 0QX, UK
+Department of Physics, Keele University, Keele, Staffordshire
°Tohoku University, Aoba-ku, Sendai 980, Japan

ABSTRACT
The commissioning and preliminary scientific results from the MARI spectrometer at ISIS are reviewed.

I. INTRODUCTION

The MARI spectrometer is funded by the Japanese Ministry of Education, Science and Culture (Monbusho) as part of the UK-Japan Collaboration in neutron scattering. This collaboration, initiated in 1986, was the creation of the late Professor Yoshikazu Ishikawa. The name of the spectrometer, MARI, is the Japanese for 'Truth' and also the name of his daughter. It is appropriate that Professor Ishikawa's pivotal role in the UK-Japanese collaboration should be remembered in this way. The spectrometer was inaugurated by his widow, Mrs Hiroko Ishikawa, in a moving ceremony at the Rutherford Appleton Laboratory on 16 November 1990.

Figure 1. Dr Paul Williams (Director RAL), Mrs Hiroko Ishikawa and Sir Mark Richimond (Chairman SERC) at the MARI Inauguration.

The design concept (see Figure 2) is based on the highly successful HET spectrometer at ISIS and shares much of its technology. A 30 cm rotating nimonic chopper is used to attenuate fast neutrons produced at the moment when the protons hit the target. Subsequently, a monochromatic beam is produced by phasing a high speed Fermi chopper to the pulsed source. A wide variety of choppers (interchangeable with HET) are available with characteristics optimised for incident energies from 20 to 2000 meV. The beam at the sample position is 50 x 50 mm^2 with an intrinsic resolution of 1%. The vertical detector array is divided into a low angle bank and eight higher angle windows which together give an extensive and continuous angular coverage from 3° to 135°. The low angle bank (3 -12°) has a complement of 128 high pressure helium detectors in an octagonal array. The higher angle windows have three strips each containing 32 detectors arranged where appropriate on the Debye-Scherrer cone. Currently the full low angle array and the central strip of each window are installed. The highest angle window (120-135°) has its full complement of 96 detectors. Further detectors will be obtained as funds become available.

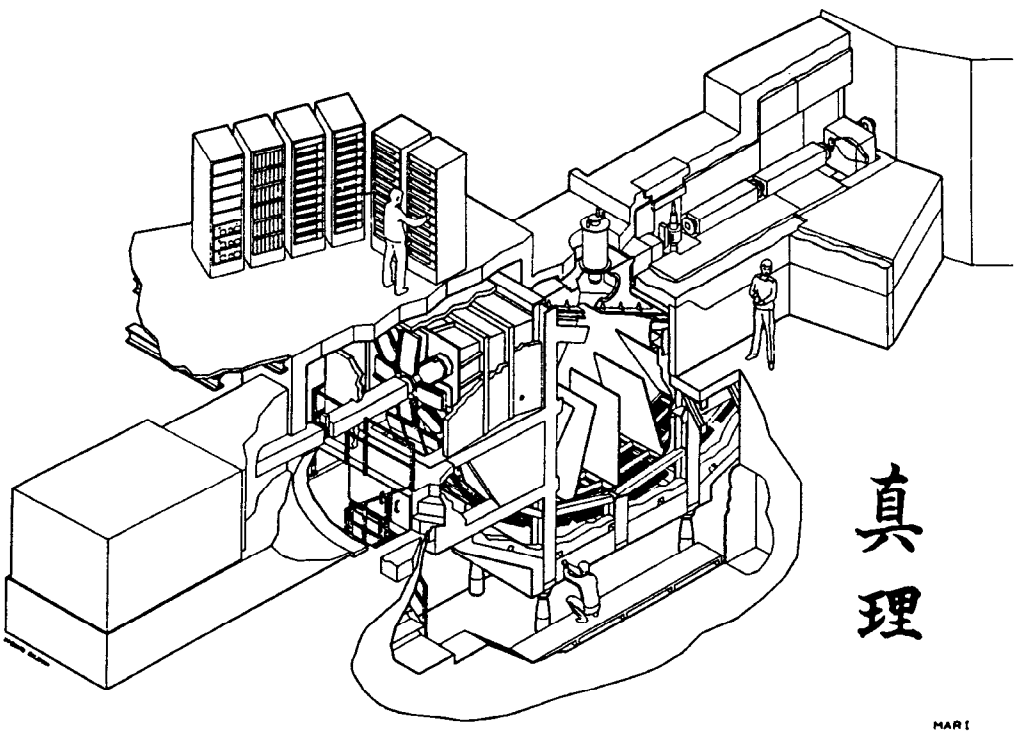

Figure 2. Schematic layout of the MARI spectrometer

After completion of the installation late in 1989, a hectic three-cycle commissioning phase began. Initial backgrounds were soon reduced to the levels attained on HET and the characteristics of MARI were thoroughly explored. This phase has been highly successful, due to the dedication and hard work of the excellent MARI team, and the spectrometer was made available for scheduling for the latter half of 1990. Proposals were considered by three Experiment Selection Panels (ESPs): Liquids and Amorphous Systems, Excitations and Momentum Distributions, and Molecular Spectroscopy, reflecting the broad appeal of the latest ISIS spectrometer. The ESPs showed excellent judgement in selected a broad and balanced programme for an already significantly oversubscribed instrument. The first six months of the experimental programme have borne out the fact that MARI is a world class instrument, destined to make a significant impact in condensed matter science.

II. EARLY RESULTS

The advantages of having MARI view the 100 K liquid methane moderator were confirmed. The monochromatic lineshape is significantly improved in the 50 -150 meV region and incident energies down to 20 meV are now possible with good flux. Such low incident energies provide excellent absolute resolution for studying low energy excitations such as the crystal field

transitions in doped superconductors. The pairing mechanism in these ceramic superconductors has been explored by studying the temperature dependence of the linewidths of these transitions, Figures 3(a) and 3(b).

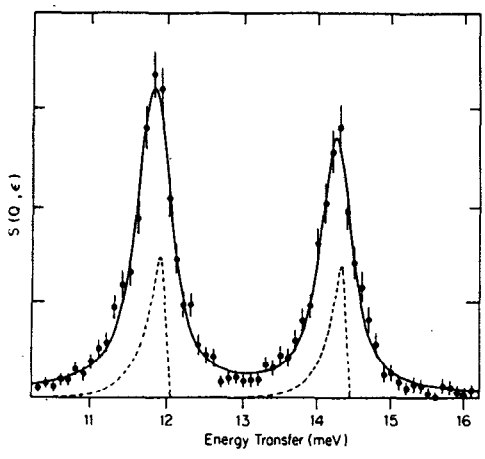

Figure 3(a). Γ_4 and Γ_2 transitions in $Tm:YBa_2Cu_3O_{7-x}$, measured at 20K on MARI. The dashed line represents the instrument resolution.

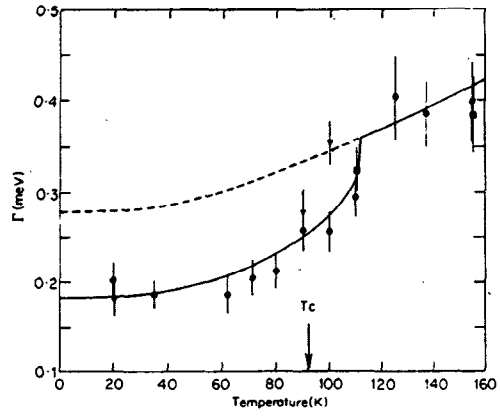

Figure 3(b). Variation of linewidth with temperature of the Γ_4 transition in $Tm:YBa_2Cu_3O_{7-x}$.

The advantage of the wide and continuous angular cover available on MARI is well illustrated by a commissioning experiment on helium. Final state interactions in Bose condensed ^4He provide a severe test of our understanding of this simple fluid. These manifest themselves as an oscillatory behaviour in the constant Q width of the dynamical structure factor $S(Q,\epsilon)$ and have been observed by triple-axis spectroscopy, but with poor resolution. Previous measurements using the high angle bank on HET required a different incident energy for each Q. Although the resolution was excellent, there was some difficulty in interpolating to constant Q from the limited available angular range and since many energies were required, statistics were poor for any given data set. A single measurement on MARI using an incident energy of 250 meV provided an $S(Q,\epsilon)$ surface (Figure 4(a)) from which constant Q data ranging from 4 to 16 $Å^{-1}$ have been obtained with high accuracy, in which the oscillatory behaviour can clearly be observed (Figure 4(b)).

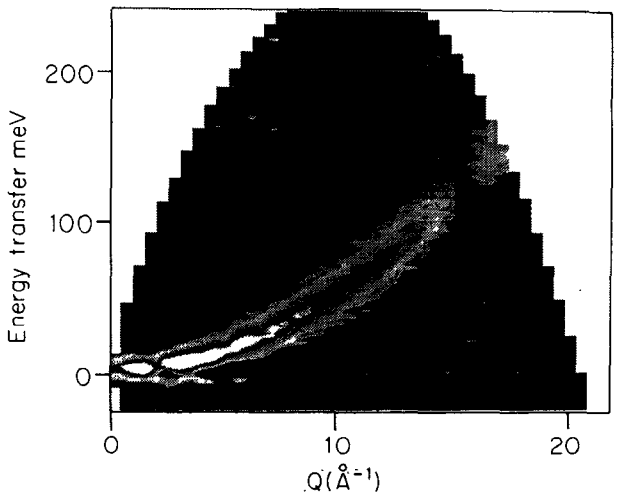

Figure 4(a). The $S(Q,\epsilon)$ surface for He at 1.5K accessible with 250 meV neutrons.

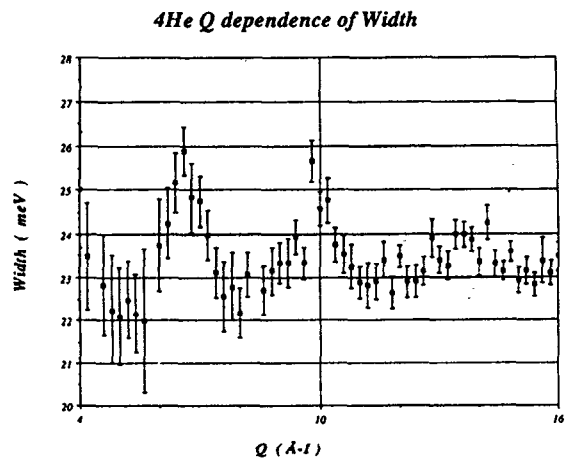

Figure 4(b). Oscillations in the width of the structure factor in He at 1.5K.

III. RANDOM NETWORK GLASSES

In the absence of a regular lattice, the dynamical structure factor gives unique insight into the correlations between structure and dynamics in glassy materials. Pioneering studies at Argonne National Laboratory's IPNS facility have until now represented the state of the art in this field. The superiority of MARI in resolution and intensity should provide high quality data which may prompt new extensions of the theory and aid a better microscopic description of non-crystalline materials.

During commissioning, a preliminary S(Q,ϵ) measurement was made on the tetrahedral oxide glass SiO_2. These data, obtained in only a day, are shown in Figure 5(a) on an absolute scale. Integration over energy at constant momentum transfer gives the static structure factor S(Q) and a good check of the quality of the data through this zeroth sum rule, Figure 5(b). The average vibrational density of states obtained from these data are also shown, in Figure 5(c). Fine structure is seen around 50 and 150 meV, suggesting the existence of the saturated non-bridging oxygen on the cluster surface. These results bode well for future high statistics experiments which will probe the Q dependence of these excitations and lead to a sophisticated discussion of the microscopic behaviour of such random network glasses.

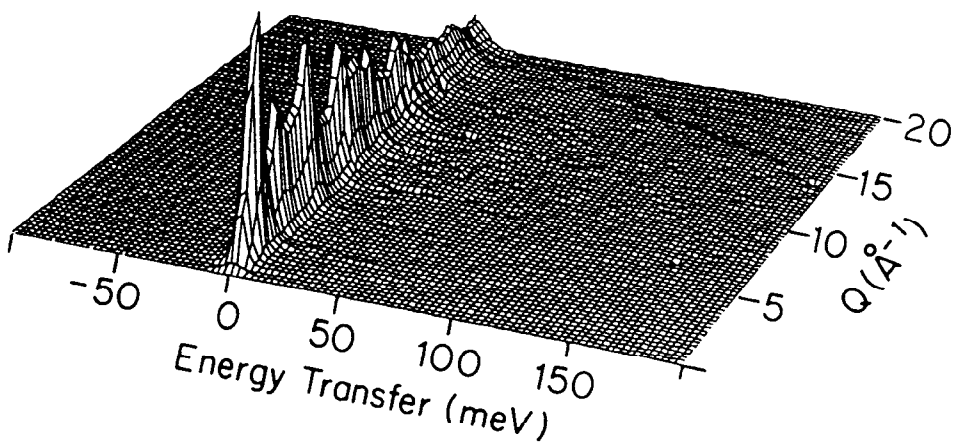

Figure 5(a). The S(Q,ϵ) surface for SiO_2.

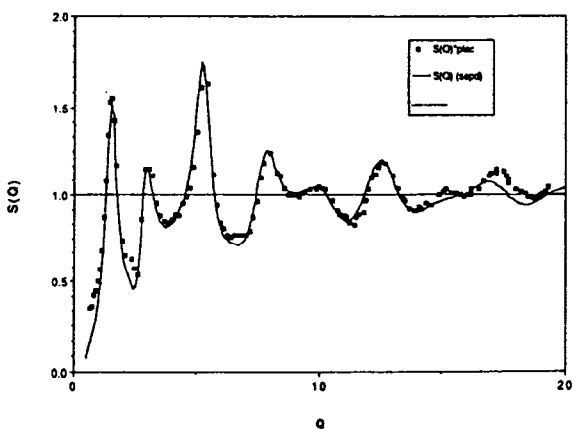

Figure 5(b). S(Q) for SiO_2.

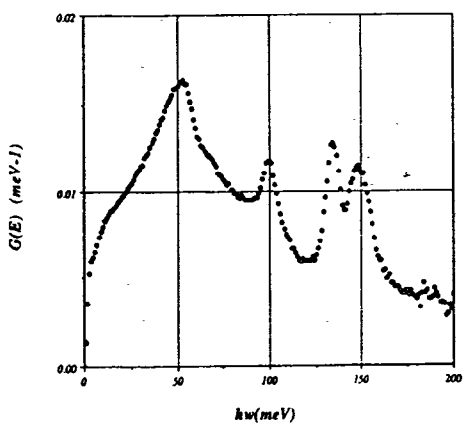

Figure 5(c). Density of states of G(ϵ)for SiO_2.

IV. LOCAL MODES IN LUH

MARI looks certain to have a significant impact on many aspects of vibrational spectroscopy including the study of the local modes in metal hydrides. Until now, these studies have been constrained as both HET and TFXA offer only a limited Q range at any one spectrometer setting. MARI has the momentum transfer range to follow accurately the rise and fall of intensity due to the Debye–Waller factor and hence to help determine the assignment of observed features. In rare earth – hydrogen systems such as $LuH_{0.1}$, the effects of the hexagonal lattice anisotropy on short range order and the vibrational spectrum of hydrogen can now be studied. Figure 6 gives data from MARI and indicates the more limited range available on HET and TFXA.

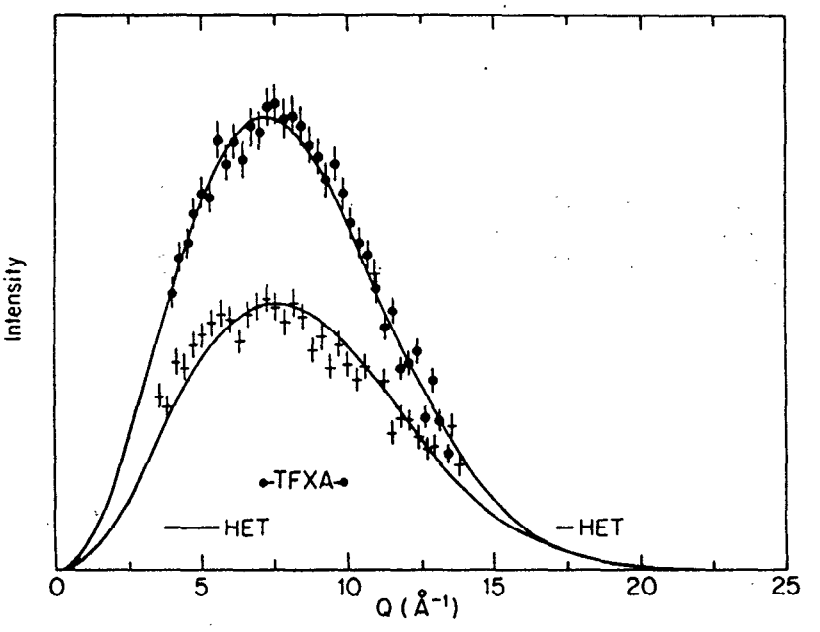

Figure 6. The variation of intensity with Q for the 100 meV and 134 meV modes in $LuH_{0.1}$. The more restricted range of both HET and TFXA are indicated.

V. ANTIFERROMAGNETISM

The potential of time–of–flight spectrometers for the study of excitations in low dimensional systems has been well illustrated by the first MARI experiment on single crystals. The covalent chains of iron–centered, edge–sharing sulphur tetrahedra in $KFeS_2$ order antiferromagnetically in one dimension. Earlier magnetic measurements implied that the spin–wave spectrum would be very steep. This was indeed found to be the case with the spin wave dispersion extending to more than 200 meV, Figure 7. The one dimensional nature of the problem means that all of the detectors in the MARI low angle bank can be summed together. The entire dispersion surface was mapped out using several incident energies in only a few days.

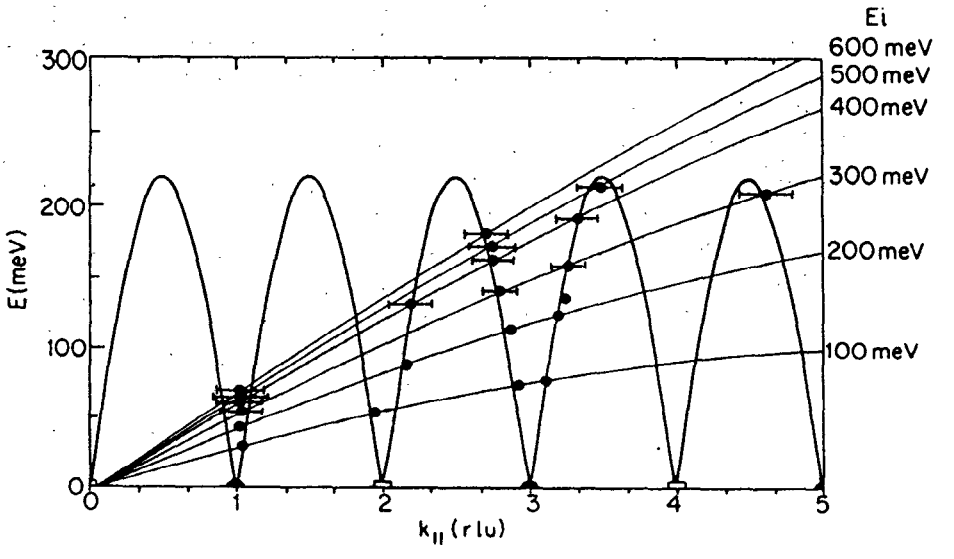

Figure 7. The dispersion of the antiferromagnetic spin waves in the quasi–one–dimensional system $KFeS_2$. For a crystal of volume 3 cm^3, each scan was collected in 1 mA–hr.

In the two-dimensional S = 1 antiferromagnet La_2NiO_4, well defined spin waves were observed to energies above 100 meV (Figure 8). With the appropriate crystal orientation, the two dimensional nature of the scattering could be exploited to great effect by directing the rod-like scattering into the horizontal bank. These detectors were summed to give the signal and **simultaneously** the vertical part of the array could be summed to give a measure of background.

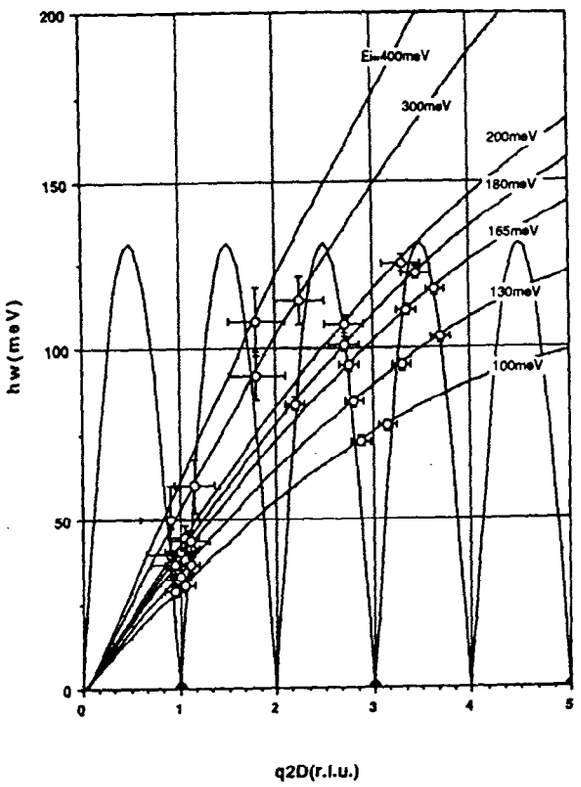

Figure 8. The dispersion of the antiferromagnetic spin waves in the two dimensional system La_2NiO_4.

Acknowledgement

We would like to thank all the support staff at ISIS for their excellent contributions to the MARI project.

Q(N.Watanabe): What was the major difference in resolution between HET and MARI for measuring crystal field line broadening in Tm 1-2-3 compound? I think there is no difference in moderator pulse width for E_i~25 meV.

Was there any advance in scientific results with MARI compared to HET?

A(A.D.Taylor): At low energies, the resolution is comparable. The large solid angle at low angles on MARI provides a significant intensity increase, however, on MARI. At this time, HET was fully scheduled: available for test experiments.

Q(R.Pynn): What type of detectors do you use on MARI?

A(A.D.Taylor): 2.5cm diameter, 30cm long 10atm, ^3He from Reuter-Stokes.

Q(R.Pynn): How does MARI compare with IN4 & IN1?

A(A.D.Taylor): IN4 always—will always win—if all you care about is intensity. For resolution, MARI is competitive down to, say, 20 meV. If you can use IN1, do so. If not (because of energy, resolution, S/N) use HET / MARI. For 1 and 2D systems, MARI is very effective even at 50 meV.

Q(H.Tietze): Does the vertical scattering plane of MARI have any influence on the resolution and performance of the instrument with respect to an assumed horizontal scattering plane?

A(A.D.Taylor): No basic influence on resolution, however, worse background from top in lighting and sample environment, which is in general designed vertical for horizontal scattering plane.

ICANS-XI International Collaboration on Advanced Neutron Sources
KEK, Tsukuba, October 22-26, 1990

IPNS Chopper Spectrometer Improvements

J. M. Carpenter and C.-K. Loong
Argonne National Laboratory
9700 S. Cass Avenue
Argonne, IL 60439

Abstract

We report the status of the IPNS chopper spectrometers and describe a number of projects underway and planned for their improvement.

I. Status of IPNS Chopper Spectrometers

Three chopper spectrometers are working at IPNS, the Low Resolution Medium Energy Chopper Spectrometer (LRMECS), the High Resolution Medium Energy Chopper Spectrometer (HRMECS) and the Pulsed High Energy Neutron Inelastic Chopper Spectrometer (PHENICS). LRMECS and HRMECS are general purpose machines and have operated as user instruments since 1982. Built in 1986, PHENICS was designed explicitly for and is used mostly for deep inelastic scattering, that is momentum distribution studies, and is equipped with a dedicated dilution refrigerator to enable studies of quantum fluids; it is operated by a Participating Research Team. Table I summarizes the essential features of the IPNS instruments as defined in Figure 1.

Table I
IPNS Chopper Spectrometer Parameters

Instrument	d_1, m	d_2, m	d_3, m	$\Delta E/E_0$	ϕ
LRMECS	7.0	1.1	2.5	6-8 %	-10° to -2°, 2° to 120°
HRMECS	12.7	1.1	4.0	3-4 %	-20° to -1°, 1° to 20°, 87° to 140°
PHENICS	12.6	1.0	2.5	4-5 %	57° to 62°,
			3.8	3-4 %	135° to 145°

Choppers are available which nearly optimally provide neutrons with incident energies between 5 meV and 2 eV and are fully interchangeable among the instruments.

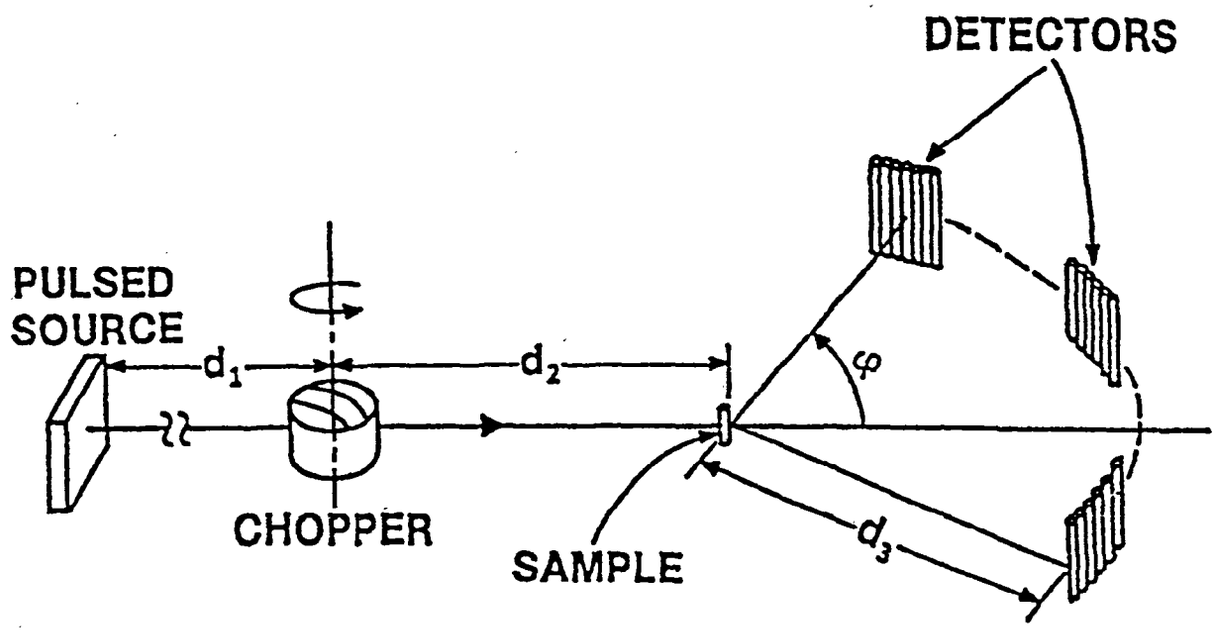

Figure 1. Schematic diagram of a pulsed source chopper spectrometer.

II. T_0 Choppers

The intense flash of fast neutrons that occurs at the time of the accelerator pulse (T_0) increases the background of neutrons in the scattered neutron detectors and is principally responsible for the personnel radiation background around the monochromating ("E_0") choppers. To reduce these effects, we are installing auxiliary "T_0" choppers before the E_0 choppers which are phased to be closed at the time of the prompt fast neutron pulse and open rapidly to pass the desired neutrons.

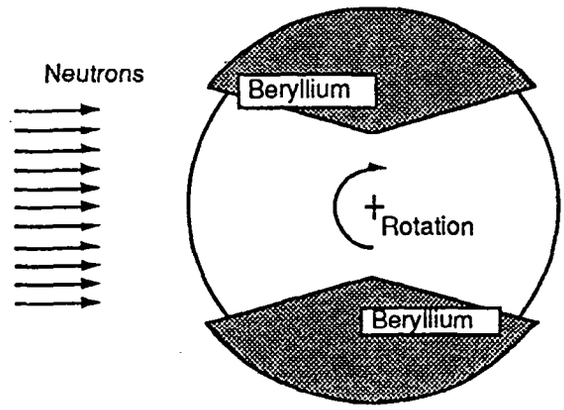

Figure 2. Schematic drawing of a T_0 chopper.

The drive, control and support systems of our T_0 choppers are of basically of the same design as those of the E_0 choppers, but the choppers have a wide, tapered, keyhole-shaped opening, as shown in Figure 2. For choppers of this form the fraction of the beam area that is open is a trapezoidal function of the time, although the fraction of the beam that penetrates the chopper is a more complicated function. Figure 3. illustrates the action of the T_0 choppers. For the case

shown the E_0 chopper is rotating at 210 Hz and the T_0 chopper is turning at 90 Hz, optimal for 100 meV neutrons which the system is phased to select.

T_0 choppers also reduce the number in the incident beam of fast and epithermal delayed neutrons which are emitted continuously between source pulses. These can pass through the Boron fiber-Aluminum slats in the E_0 choppers twice each revolution, and contribute to the background during the useful time interval at the detectors, roughly 3000- 6000 microseconds.

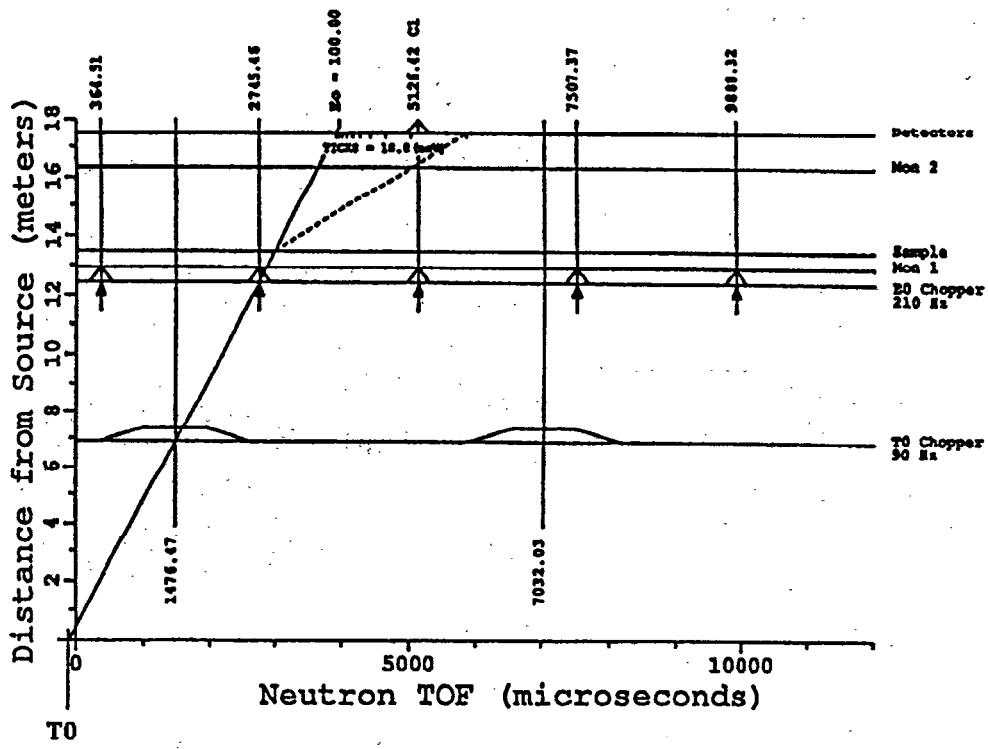

Figure 3. "Neutron time schedule" showing the action of a "T_0" chopper in HRMECS.

III. LRMECS

Figure 4 shows the present configuration of the Low Resolution Medium Energy Chopper Spectrometer. In our recent efforts we have moved the E_0 chopper about 1 meter farther from the source to provide space for the T_0 chopper and have improved the shielding around the E_0 chopper. We have begun design of an optional high resolution chopper and accompanying tighter (20' divergence) Soller collimator along the lines described elsewhere in these Proceedings, to provide energy transfer resolution $\Delta E/E_0 = 3. - 4.$ % in LRMECS. The same new chopper will be able to be used in HRMECS.

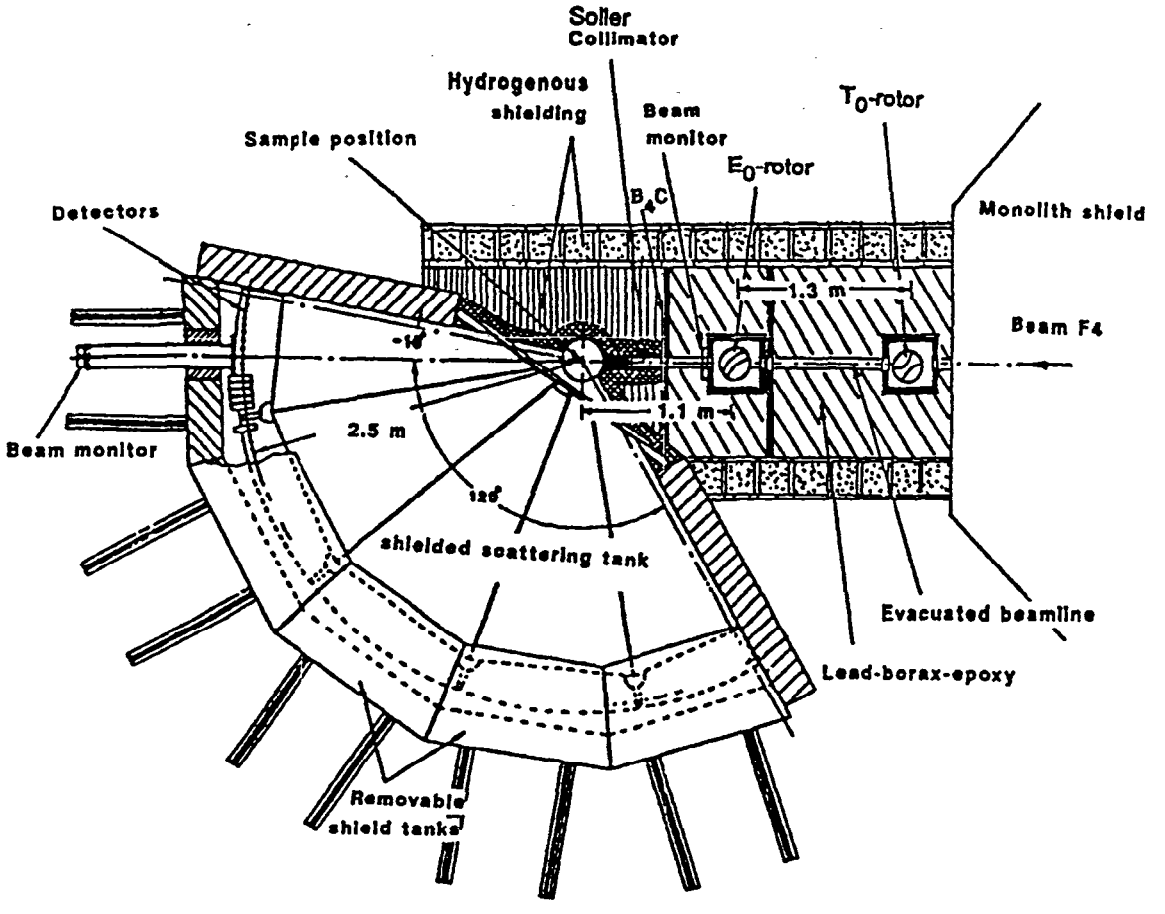

Figure 4. The Low Resolution Medium Energy Chopper Spectrometer.

IV. HRMECS

Figure 5 shows the configuration of the High Resolution Medium Energy Chopper Spectrometer. The intermediate angle flight path between 20° and 85° does not exist; efforts are underway to install the intermediate angle flight path. We have provided a well shielded position for a T0 chopper and work is underway on its design and fabrication. The high resolution chopper and optional tighter (20' divergence) Soller collimator will provide optional energy transfer resolution $\Delta E/E_0 = 1.5 - 2$ % in HRMECS.

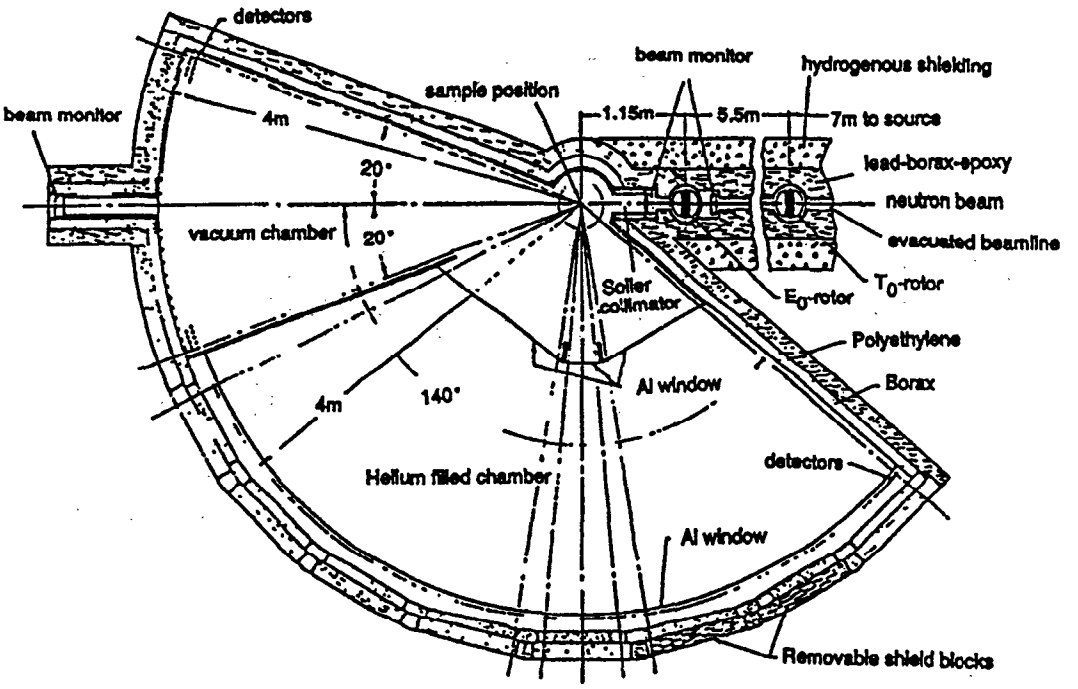

Figure 5. The High Resolution Medium Energy Chopper Spectrometer.

V. PHENICS

Figure 6 shows the present configuration of the Pulsed High Energy Neutron Inelastic Chopper Spectrometer. The sample position is equipped with a dedicated ^{3}He dilution refrigerator. The T_0 chopper has been in routine operation for more than one year. The low angle, 60° detector bank has recently been installed, which has mainly been used (without the E_0 chopper) for diffraction analysis of cryogenic polycrystalline samples and enables deep inelastic scattering studies of hydrogenous materials.

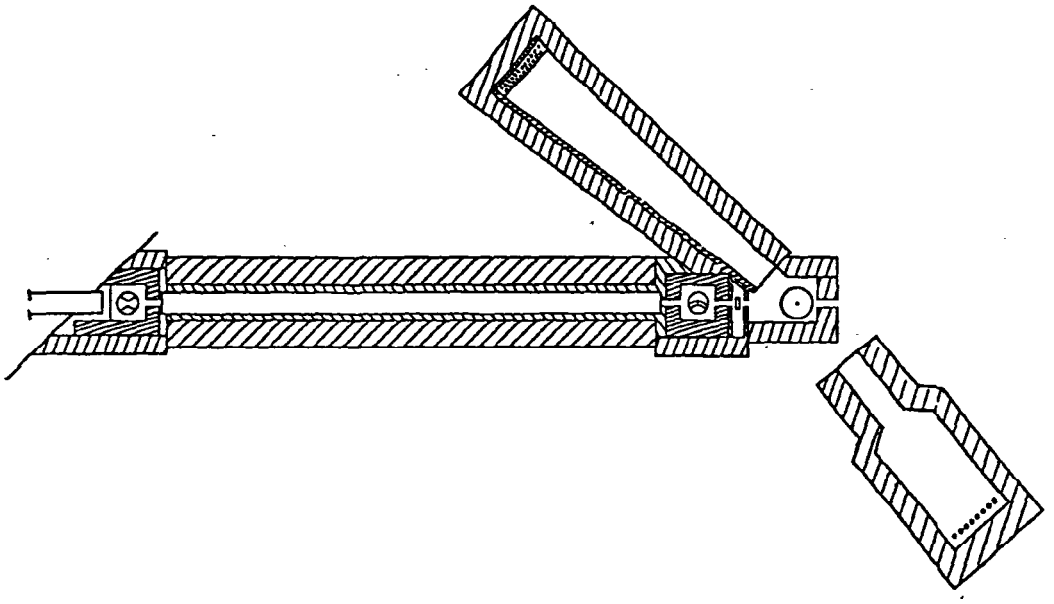

Figure 6. The Pulsed High Energy Neutron Inelastic Chopper Spectrometer.

VI. Summary of IPNS Chopper Spectrometer Improvement Projects

We are designing and preparing to install optional tighter Soller collimators in LRMECS and HRMECS to provide higher energy transfer resolution in those instruments when needed. A T_0 chopper has been installed in PHENICS which operates routinely and provides considerable improvement in the personnel and detector backgrounds. T_0 choppers are being designed and will be installed in LRMECS and HRMECS. The design of the long-needed intermediate angle flight path for HRMECS has been completed; the new flight path will be ready for installation in about one year. New VAX station computers are being installed to replace the PDP11-34 Data Acquisition Computers in all the chopper spectrometers. We are evaluating high speed, magnetic bearing choppers to replace our present 270 Hz, hard bearing designs sometime in the future.

VII. Acknowledgement

This work was performed under the auspices of the U. S. Department of Energy, Division of Materials Sciences, Office of Basic Energy Sciences, under contract W-31-109-Eng-38.

ICANS-XI International Collaboration on Advanced Neutron Sources
KEK, Tsukuba, October 22-26, 1990

OPTIMIZATION of a Multi-Disk Chopper Spectrometer for Cold Neutron Scattering Experiments

R. E. Lechner
Hahn-Meitner-Institut, Postf. 390128, D-1000 Berlin 39

ABSTRACT
The optimization with respect to intensity and resolution of the new multi-disk chopper time-of-flight spectrometer NEAT at the Hahn-Meitner-Institut (HMI) is discussed. In this discussion the following instrument variables and parameters are relevant :
- incident neutron wavelength and its range
- chopper revolution rate ("tangential" speed of disks)
- pulse widths of the two principal choppers and their ratio
- lengths of flight path between pricipal chopper disks and from sample to detectors
- total solid angle covered by the detectors
- transmissions of various spectrometer components.

It is shown, that a careful choice of parameter values, together with the minimization of neutron flux losses within the spectrometer, should allow to increase the intensity by at least an order of magnitude for given incident neutron flux and given energy resolution, as compared to existing spectrometers of the same type. The solution chosen for NEAT will provide a variable energy resolution at the detectors, which for elastic scattering is calculated to be in the range of $2\mu eV \leq \Delta(\hbar\omega) \leq 2meV$.

I. INTRODUCTION

In January 1985 the journal Physics Today presented on its frontpage a photograph of the Institut Laue-Langevin's neutron guide hall showing at its center the blue-coloured neutron shielding of the multi-chopper time-of-flight spectrometer IN5. This instrument /1/ is known to be one of the most successful high-resolution cold-neutron spectrometers for the study of low-energy excitations in condensed matter. About one year earlier (in 1984) we had decided at the Hahn-Meitner-Institut (HMI) in Berlin to build a new instrument of this kind for the same class of neutron scattering experiments. Obviously in this context the question arose, in which way such a spectrometer could be further improved regarding energy resolution and intensity. An answer to this question will be given in the present paper, with reference to the multi-chopper time-of-flight spectrometer NEAT under construction at the HMI.

II. SPECTROMETER Principle and Optimization

Let us start by briefly discussing the spectrometer principle as illustrated in Fig. 1 for the case of IN5. The left-hand side of the figure schematically shows the geometrical arrangement: Four chopper disks rotating around a horizontal axis are aligned along a neutron guide. The first (Ch1) and the last chopper (Ch4) are used to define the desired incident-neutron wavelength λ_0 by an appropriate phasing of their windows with respect to each-other. The remaining two choppers (Ch2 and Ch3) have additional filter functions required to achieve the monochromatization of the pulsed neutron beam and to avoid overlap in time of scattered neutron spectra due to consecutive chopper pulses. The nickel-coated glass guide connecting the choppers permits a transport of the neutrons from the first chopper to the sample (S) with very little loss in solid angle. At the sample the neutrons are scattered and then counted by a large number of detectors (D), set up at a distance of about 4m from the sample and at scattering angles from close to 0° up to about 132°.
The right-hand side of Fig. 1 represents - again schematically - a time-of-flight/flight-path diagram of the spectrometer for $\lambda_0 = 6$Å as an example. It illustrates the role of each chopper disk: Ch1 creates a "white" pulse which on its way quickly spreads in time, since it contains the rather large spectrum of neutron wavelengths (1Å $\lesssim \lambda_0 \lesssim$ 20Å) provided by the combination of a cold source moderator and a slightly curved neutron guide. At the location of Ch4 consecutive pulses would largely overlap each-other, because the faster neutrons of each pulse would have overtaken the slower ones of the corresponding previous pulse, by the time they arrive there. Therefore a pre-selection, narrowing down the wavelength band, is performed at an earlier stage by Ch2, in order to make the final monochromatization by Ch4 possible. Thus nicely tailored monoenergetic neutron pulses are leaving periodically Ch4 to be scattered at S. Scattering however transforms the pulses back into wide wavelength distributions reflecting the dynamics of the scattering system. The corresponding time distributions are generally so broad, that a new overlap problem arises at the detectors for spectra belonging to consecutive pulses. This problem can be circumvented by reducing the chopper pulse frequency with the aid of Ch3, running at a lower revolution rate. The corresponding time-of-flight period P3 is an integer multiple of the original value P.
The brief description of the IN5 lay-out given above represents a possible (and successful) solution for a multi-disk chopper t.o.f. spectrometer. The question, how the performance of such an instrument can be further improved, is answered by optimizing the spectrometer with respect to intensity and resolution. For this purpose three basically different, but to some extent interrelated problems must be considered:
i) Determination of optimum instrument parameter values on the basis of the fundamental relations between intensity and resolution on the one hand and spectrometer variables and parameters on the other.
ii) Effect of boundary conditions (mainly due to space and budget restrictions) on the possible choice of parameter values.
iii) Technical feasibility and optimization of spectrometer components, especially regarding their transmission.

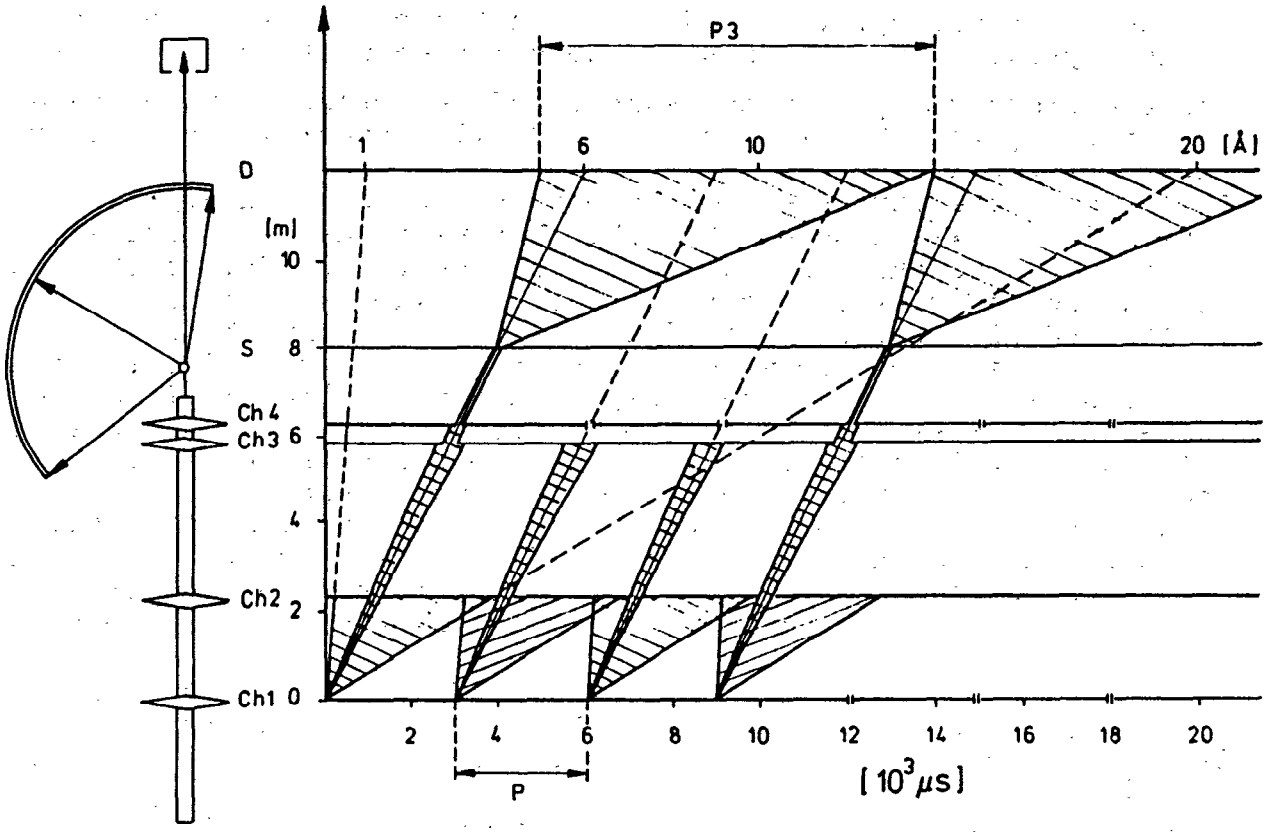

Fig. 1
Schematic drawing of the principle of a multi-chopper time-of-flight spectrometer (example: IN5). Left-hand side: four chopper disks (Ch1 to Ch4) aligned along a neutron guide directing the beam to the sample S in the center of a large detector array D. Right-hand side: time-of-flight/flight-path diagram for $\lambda_0 = 6$Å. The positions on the flight-path axis corresponding to the different chopper disks, to the sample and to the detectors are indicated by horizontal lines. P is the period defined by the time elapsing between consecutive neutron bursts of Ch1. P3 is the period of the frequency reduction chopper Ch3. The hatched areas indicate the regions covered by neutron pulses, as they spread in time during their flight.

III. FUNDAMENTAL Spectrometer Relations

For the discussion of the basic formulae governing the relation between intensity, energy resolution and spectrometer parameters /2/, it is sufficient essentially to consider the two principal choppers which define the monochromatic neutron pulse. In the example of Fig. 1 these are the disks Ch1 and Ch4. Ch2 has no influence on intensity and resolution, because its pulse frequency, phasing and opening time are chosen such, that they do not prevent any neutrons of the wavelength band, to be selected by Ch4, to pass by the latter. For similar reasons Ch3 does not affect the resolution; it merely reduces the intensity by the same factor, by which it divides

the pulse frequency. This reduction factor can however be expressed by an approximation in terms of the selected neutron wavelength λ_0 and the distance L_{SD} between sample and detectors. Thus no parameter directly related with Ch2 and Ch3 will appear in the spectrometer relations.
In deriving the formulae a number of assumptions and approximations were made. It was assumed that the mean width of each chopper window is equal to the inner width of the neutron guide, at the location where the disk is rotating. This is exactly true in the case of IN5 and also for one set of windows of the NEAT choppers. Since the border lines of the windows are oriented in radial directions, all windows have trapezoidal shape, deviating slightly from the rectangular cross-section of the neutron guide. As a consequence all neutron pulses created by single chopper disks have close to (but not exactly) triangular shape in time. These distributions have been approximated by Gaussians, in order to simplify their convolutions and the determination of the resulting widths in the resolution calculation. In fact, even if the single chopper pulses had exactly triangular shape, this would be a very good approximation.
The duration of the time-of-flight period, $P3 = N \cdot P$, is equal to the flight time of neutrons with the maximum wavelength λ_{max}, that is to be observed. P3 is therefore proportional to λ_{max} and to L_{SD}. λ_{max} is usually chosen roughly proportional to λ_0; exact proportionality is not possible, since for given P only discrete values of P3 are allowed, N being an integer. The choice of N is dictated by the necessity to reduce the frame-overlap of scattered neutron spectra; nevertheless the value of N is not unique, since it depends to some extent on experiment-specific requirements. Therefore, in order to simplify the study of the general behaviour of intensities as a function of instrument parameters, P3 was replaced by a continuous function proportional to the product $\lambda_{max} L_{SD}$.
Further approximations concern the neglection of attenuation factors due to losses in the neutron guide (imperfections of alignment and reflectivity, gaps in the reflecting guide walls) and losses by absorption and scattering in the material encountered along the neutron flight path (rest gas, windows, sample holder and detector walls). This is justified, because such attenuation factors have relatively little effect on the optimum choice of instrument parameter values; they are minimized independently by the available technical means (see below). For the same reason finally the effect of sample geometry (e.g. orientation) on the resolution has been neglected.
On the basis of the above assumptions and approximations the relations for the intensity and the energy resolution were obtained /2/. The intensity I at the sample position, i.e. the number of neutrons hitting the sample per cm^2 and second, is given by

$$I = \emptyset(\lambda_0) \cdot F \cdot h^2 / (m^2 \cdot \lambda_{max}) \qquad (1)$$

where $\emptyset(\lambda_0)$ is the differential neutron flux at the "monochromatic" wavelength λ_0 to be selected by the last chopper. We define $\emptyset(\lambda_0)$ as the number of neutrons arriving at the first chopper per unit of beam area, time and wavelength. This differential flux is already integrated over the beam divergence allowed for by the guide. The factor F contains those spectrometer parameters, which are

relevant for the intensity :

$$F = \tau_1 \cdot \tau_2 \; / \; (\; L_{12} \cdot L_{SD} \;) \qquad (2)$$

Here τ_1 and τ_2 are the "opening times" of the first and the last chopper, respectively, i.e. the full-width-at-half-maximum (FWHM) of the neutron pulses at the locations of these choppers. L_{12} and L_{SD} are the lengths of the neutron flight paths between the two principal choppers and from the sample to the detector, respectively; h is Planck's constant and m is the neutron mass.

The energy resolution $\Delta(\hbar\omega)$ of the spectrometer is the apparent FWHM in energy (at the detectors) of the spectrometer's response to a δ-function peak in the double-differential neutron scattering cross-section :

$$\Delta(\hbar\omega) = \Delta t_d \cdot h^3 \; / \; (\; L_{SD} \cdot m^2 \cdot \lambda^3 \;) \qquad (3)$$

Here λ is the wavelength of scattered neutrons; Δt_d, the time spread (FWHM) of the resolution-broadened δ-function, is given by:

$$\Delta t_d = (\; A^2 + B^2 + C^2 \;)^{1/2} \; / \; L_{12} \qquad (4)$$

with

$$A = \delta L \cdot \lambda \cdot L_{12} \cdot m \; / \; h \qquad (5)$$

$$B = b \cdot \tau_1, \text{ where } b = (\; L_{2S} + L_{SD} \cdot \lambda^3 \; / \; \lambda_0^{\,3}) \qquad (6)$$

$$C = c \cdot \tau_2, \text{ where } c = (\; L_{12} + L_{2S} + L_{SD} \; \lambda^3 \; / \; \lambda_0^{\,3} \;) \qquad (7)$$

The term A is due to the uncertainty δL in the length of the flight path, caused by beam divergence, finite sample size and detector thickness; the terms B and C represent the contributions of the chopper system, where L_{2S} is the distance from the second of the two principal choppers (Ch4 in Fig.1) to the sample; the other parameters have already been defined above.
We note, that calculations related to the same subject have been published earlier in a theoretical treatment of the resolution function of a two-rotor neutron velocity selector /3/. The resulting formulae for intensity and resolution differ however from ours.

IV. OPTIMIZATION of Intensity and Resolution

We wish to maximize the intensity I for any desired value of $\Delta(\hbar\omega)$ within the accessible range of energy resolutions, for a given pair (λ_0, λ) of neutron wavelengths. At a cold neutron guide neutron flux is available within the approximate limits $1\text{Å} \leq \lambda_0 \leq 20\text{Å}$ and scattered neutrons are then observable roughly in $1\text{Å} \leq \lambda \leq 24\text{Å}$. Intensity and resolution, given by expressions (1) to (7), are theoretically amenable to optimization via the variation of the spec-

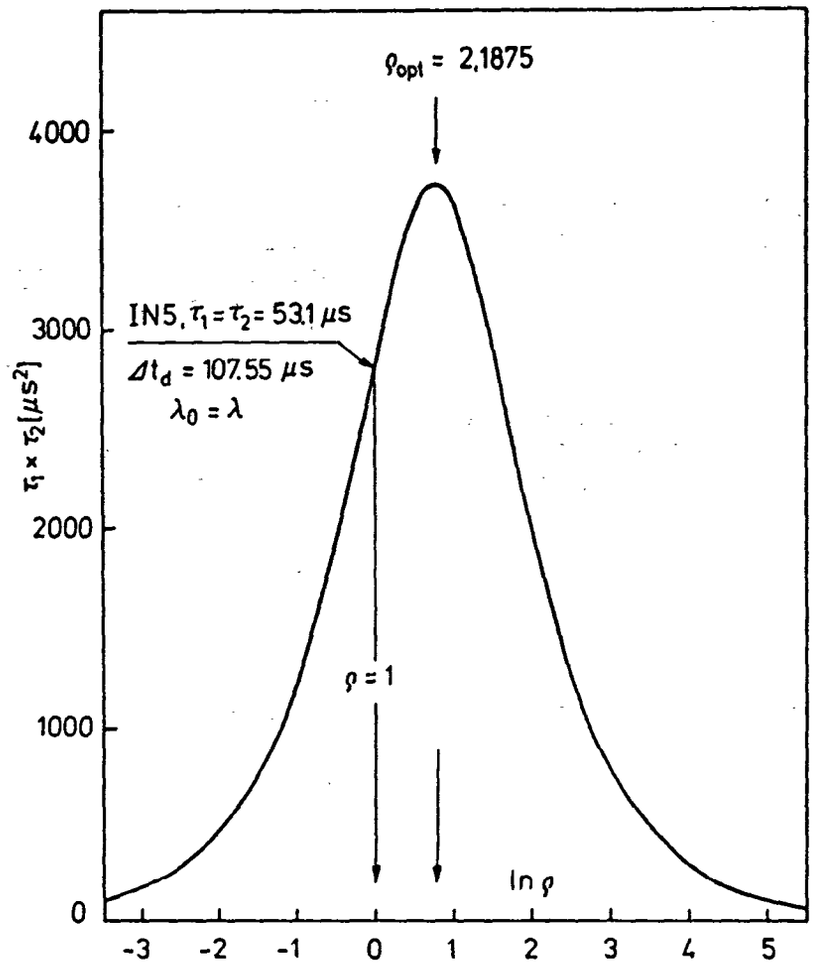

Fig. 2
The product of the chopper burst times $\tau_1 \cdot \tau_2$ as a function of $\ln\rho$, where $\rho = \tau_1/\tau_2$, is peaked at $\ln\rho_{opt}$; $\tau_1 \cdot \tau_2$ is proportional to the intensity at the sample. Example: spectrometer IN5 for elastic scattering ($\lambda_0 = \lambda$), for fixed time resolution at the detectors, Δt_d = 107.55 μs.

trometer parameters $L_{12}, L_{2S}, L_{SD}, \delta L$, τ_1 and τ_2. In practice there are of course some restrictions due to (sometimes trivial) boundary conditions. It is immediately evident, that the flight-path uncertainty δL and the distance L_{2S} from the last chopper to the sample should be minimized. This improves the resolution without any loss in intensity. To decrease δL one has to reduce the sizes of sample and detectors. In the case of L_{2S} the possibility of minimization depends on the required range of scattering angles and on the space needed for sample environment and shielding. Values of the order of 1cm for δL and 1m for L_{2S} (1.2m in the case of NEAT) have been realized.
In choosing values of the parameters L_{12}, L_{SD}, τ_1 and τ_2 we have to keep in mind, that the highest possible resolutions generally require long distances and short pulse widths (see eqs. (3) to (7)). Furthermore it is desirable to have access to a large range of

energy resolutions, which means that at least some of these parameters must be variable. In the case of the spectrometer NEAT L_{12} has been fixed for theoretical and for practical reasons at the value of 12.1m, whereas L_{SD} is variable within certain limits (L_{SD} = 2.5m for about 400 He-3 detectors and $4m \leq L_{SD} \leq 7.5m$ for a two-dimensional multidetector); τ_1 and τ_2 can be varied by factors of up to 80. Some technical details concerning the choppers will be given in the next Section.

The question of optimization can now be asked in two ways :
i) which set of spectrometer parameter values will maximize the intensity I for a given value of the resolution $\Delta(\hbar\omega)$?
ii) which set of spectrometer parameter values will minimize the resolution width $\Delta(\hbar\omega)$ for a given intensity I ?
Both questions have the same answer, namely the following simple condition for the optimum of the ratio $\rho = \tau_1/\tau_2$ of the two chopper opening times /4/ :

$$\rho_{opt} = (L_{12} + L_{2S} + L_{SD}\lambda^3/\lambda_0^3)/(L_{2S} + L_{SD}\lambda^3/\lambda_0^3) \qquad (8)$$

This relation covers all elastic and inelastic scattering experiments. We note, that it is independent of the flight-path uncertainty δL and of the pulse widths, τ_1 and τ_2. An analogous expression, but for the special case of elastic scattering only ($\lambda = \lambda_0$), has been mentioned previously by another author /5/.

Let us now study the intensity according to eq. (1) and see, how this behaves as a function of ρ, when the resolution is kept constant. Since the intensity does not depend on the flight-path uncertainty δL, we will neglect the term A in the expression (4) for Δt_d. As an example we will first consider the spectrometer IN5 for $\lambda \equiv \lambda_0$ (L_{12} = 6.25m, L_{2S} = 1.286m, L_{SD} = 3.977m). Assuming a chopper velocity of 15000 revolutions/minute, the chopper opening times are $\tau_1 = \tau_2 = 53.1\mu s$ for $\rho = 1$. The time spread Δt_d at the detectors, obtained from eqs. (4) to (7) (with A=0) is then 107.55μs. (This corresponds to a possible conventional mode of operation of the chopper system). We will keep Δt_d fixed at this value, while ρ is varied. Since all parameters in the expressions (1) and (2), except for τ_1 and τ_2, have been fixed, it suffices to consider the product $\tau_1 \cdot \tau_2$, which is proportional to the intensity I at the sample. Starting from eqs. (4) to (7), the function $\tau_1 \cdot \tau_2$ can be expressed in terms of ρ :

$$\tau_1 \cdot \tau_2 = L_{12}^2 \cdot \Delta t_d^2 \;/\; (b^2 \cdot \rho + c^2 \cdot \rho^{-1}) \qquad (9)$$

Plotted as a function of $\ln\rho$, the intensity represented by $(\tau_1 \cdot \tau_2)$ is peaked at the optimum opening time ratio $\rho = \rho_{opt}$, given in eq. (8), as can be seen in Fig. 2. Furthermore $\tau_1 \cdot \tau_2$ is perfectly symmetric about this value which is ρ_{opt} = 2.1875 in our example. In the case of the chopper system considered (with equal beam widths and windows for both principal choppers) the phasing requirement only permits the use of integer ρ values. It is therefore more interesting to examine $(\tau_1 \cdot \tau_2)$ at $\rho = 2$. This is so close

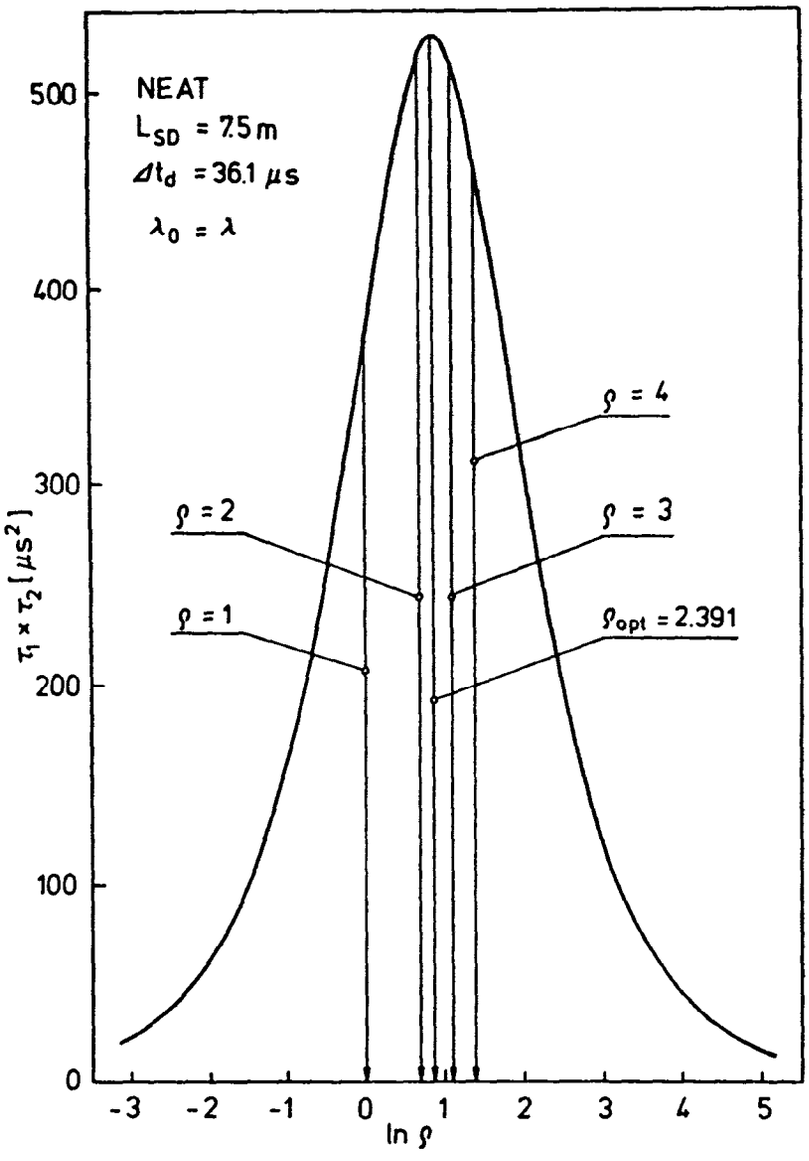

Fig. 3
Product of the chopper burst times $\tau_1 \cdot \tau_2$ as a function of $\ln\rho$ for the spectrometer NEAT with $\lambda_0 = \lambda$, sample-detector distance L_{SD}= 7.5m and time resolution Δt_d= 36.1 μs.

to the peak, that the intensity gain is almost the same as for ρ_{opt}, namely about 32% (gain factor: 1.32), as compared to the conventional example of operation mentioned above, with $\tau_1 = \tau_2$ at 15000 revolutions/minute. This means that in our example about 32% can be gained in intensity at the sample, with no loss in energy resolution at the detectors, if the first chopper is rotated at 9242 rev./min and the last chopper at 18484 rev./min rather than both at 15000 rev./min. It is interesting to note, that this gain is independent of the wavelength λ_0 and of the flight-path uncertainty δL. If the latter is also taken into account, the

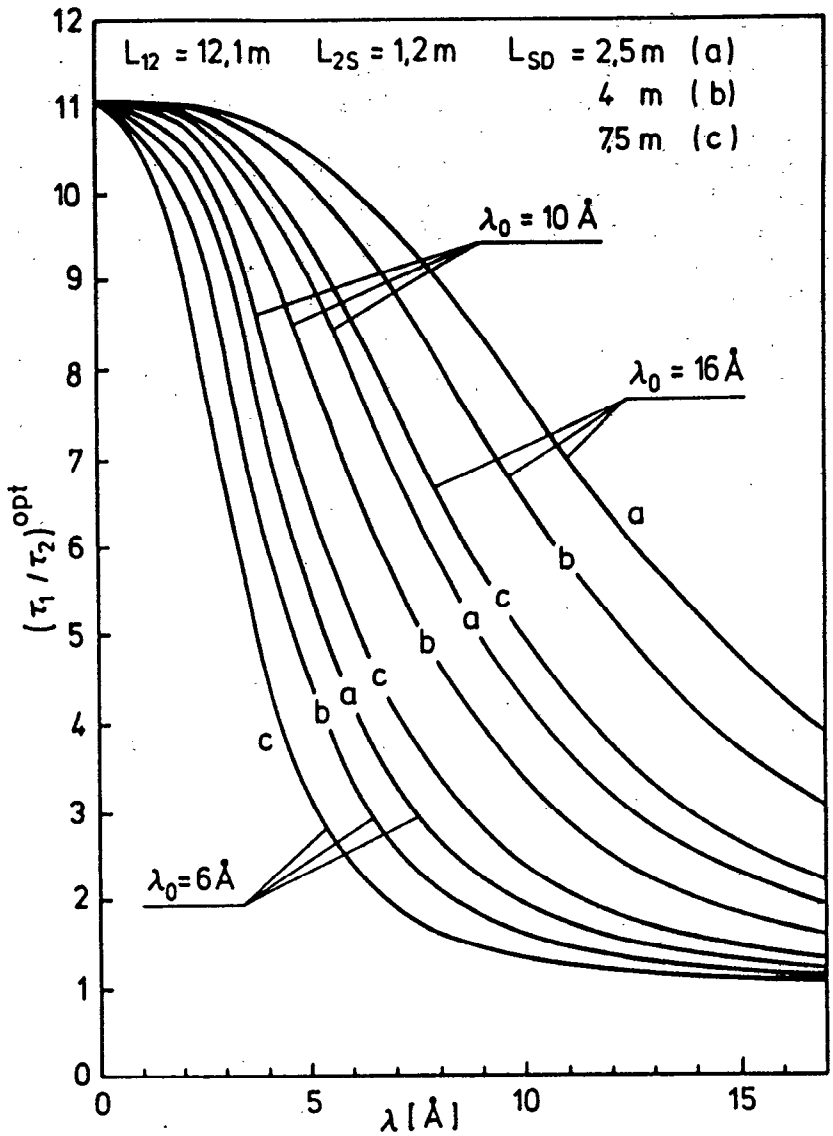

Fig. 4
Optimum burst-time ratio $\rho_{opt} = (\tau_1/\tau_2)^{opt}$ of the spectrometer NEAT as a function of scattered neutron wavelength λ, with incident neutron wavelength λ_0 and sample-detector distance L_{SD} as parameters. L_{12} = distance between the two principal choppers, L_{2S} = distance from the last chopper to the sample.

intensity curve shown in Fig. 2 is only renormalized, but neither changes shape nor peak position.

A similar calculation carried out for the spectrometer NEAT (L_{12}= 12.1m, L_{2S}= 1.2m, largest sample-detector distance L_{SD}= 7.5m) in the case of elastic scattering yields the curve of Fig.3. Here the best possible time resolution at the detector - when, as before, the term A is neglected - corresponds to Δt_d = 36.1μs. The integer value closest to ρ_{opt}=2.391 is ρ=2. In this case the intensity gain

relative to the case $\rho=1$ is about 38% (gain factor: 1.38), at the same energy resolution.

The behaviour of the optimum opening time ratio ρ_{opt} in the general case of inelastic neutron scattering is illustrated for NEAT in Fig. 4. Here ρ_{opt} is plotted for three different sample-detector distances (L_{SD}= 2.5m, 4m and 7.5m) as a function of the scattered neutron wavelength λ, with λ_0 as a parameter. It is easily seen, that the limiting value of ρ_{opt} at $\lambda=0$ is $(L_{12}+L_{2S})/L_{2S}$, which is independent of L_{SD} and λ_0. For $\lambda \rightarrow \infty$ ρ_{opt} tends towards 1, independently of all parameters.

To conclude this Section, we consider an example of inelastic scattering on the spectrometer NEAT, with λ_0=10Å, λ=6Å, L_{SD}=7.5m. This corresponds to E_0~0.8meV, E~2.2meV, $\hbar\omega = E-E_0$~1.4meV, where E_0 and E are the energies of incident and scattered neutrons and $\hbar\omega$ is the energy gain of the latter. In this case ρ_{opt}=5.291 and at the closest integer value, ρ=5, the intensity gain factor is ~2.74.

V. CHOPPERS, Neutron Guide and Detectors

One of the origins of the limitation in energy resolution of a chopper time-of-flight spectrometer is the limit of mechanical resistance of the disk material, since highest resolution (corresponding to minimum values of τ_1 and τ_2) is obtained at maximum chopper velocity. The latter is effectively doubled, if the first and last (single disk) choppers (Ch1 and Ch4 in Fig. 1) are replaced by counter-rotating pairs of disks /6/. NEAT has therefore been provided with this feature. The disks are made of a high-strength aluminium alloy and magnetic bearings are used, in order to achieve high phasing stability and reliability in operation.

In addition, in order to further improve the resolution, we have foreseen the possibility to use a built-in opening time ratio of ρ=2, especially at the highest velocity of both principal choppers (20000 rev./min), since this value of ρ is an excellent choice for low-energy-transfer experiments, where the highest resolution is needed (see Sec. IV). The (ρ=2)-operation at highest resolution is achieved using a double-trumpet beam compressor /7/ at the last chopper (pair). This reduces the beam width at this location by a factor 2, while the flux integral over the beam cross-section is essentially conserved. On the other hand, in the lower-resolution regime, ρ can also be varied by changing the chopper velocities and/or by using different chopper windows. Fig. 5 shows a schematic illustration of the last pair of chopper disks; each disk has three different pairs of windows, the narrowest ones of which have the same width as the guide; in the lower part of the figure the disks are shown, looking at their faces opposite to the respective chopper drives. A particular pair of windows is selected by an appropriate choice of the phase relationship between the members of the chopper pair. If windows larger than the guide are used, the eqs. related to the resolution given above have to be modified slightly, since the Gaussian convolution approximation mentioned in Sec. III is then not applicable. This subject will however not be treated here.

Since the transmission of every chopper enters into the final intensity, we have chosen to use very thin disk choppers with open windows (transmission = 1) produced by cutting slits into the disk

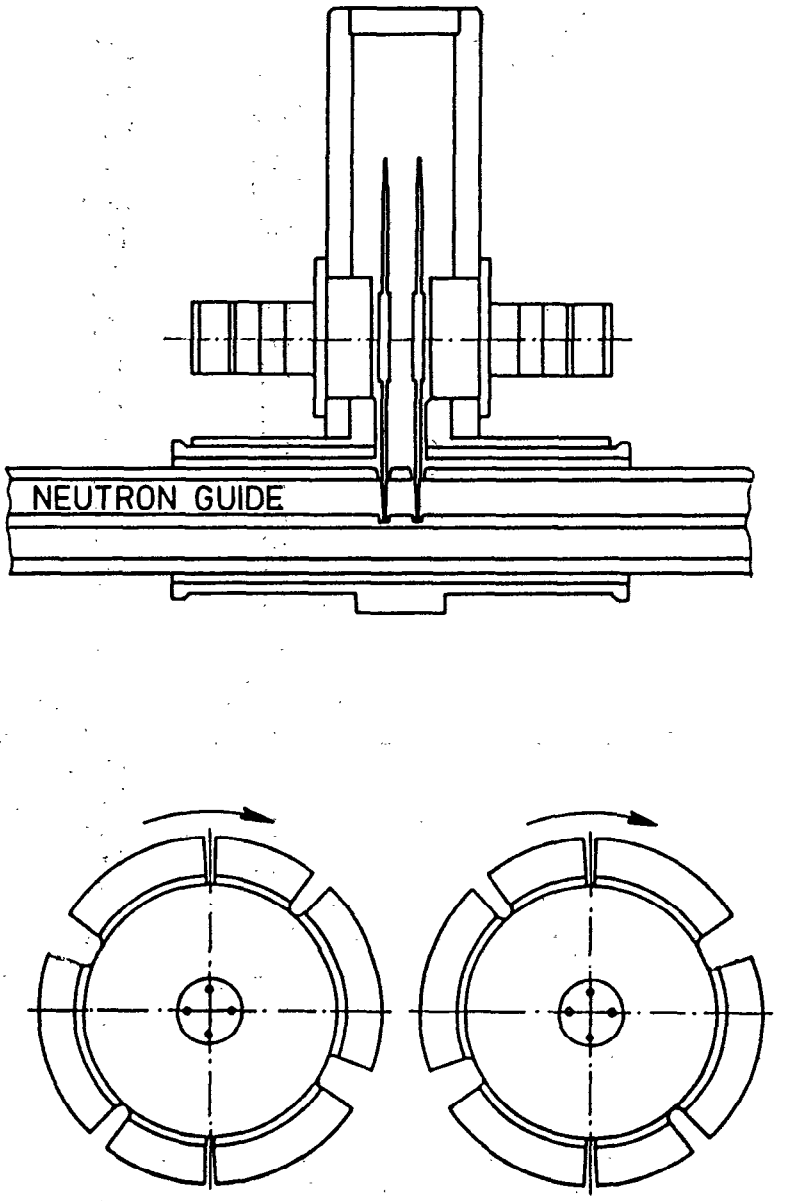

Fig. 5
Schematic drawing of the last pair of chopper disks of the spectrometer NEAT. Above: vertical cut showing, how the disks are placed in slots within the upper part of a divided neutron guide. Below: each disk has 3 different pairs of windows; arrows indicate the sense of rotation; the face opposite to the chopper drive is shown for each disk.

edges. These disks run in narrow slots (transmission better than 0.99) cut perpendicularly to the beam into the neutron guide (Fig. 6). In order to avoid unnecessary losses, it is important to minimize gaps (i.e. interruptions) in the neutron guide, which are needed for inserting chopper disks and other components, such as vacuum windows, shutters and monitors. The intensity loss V due to

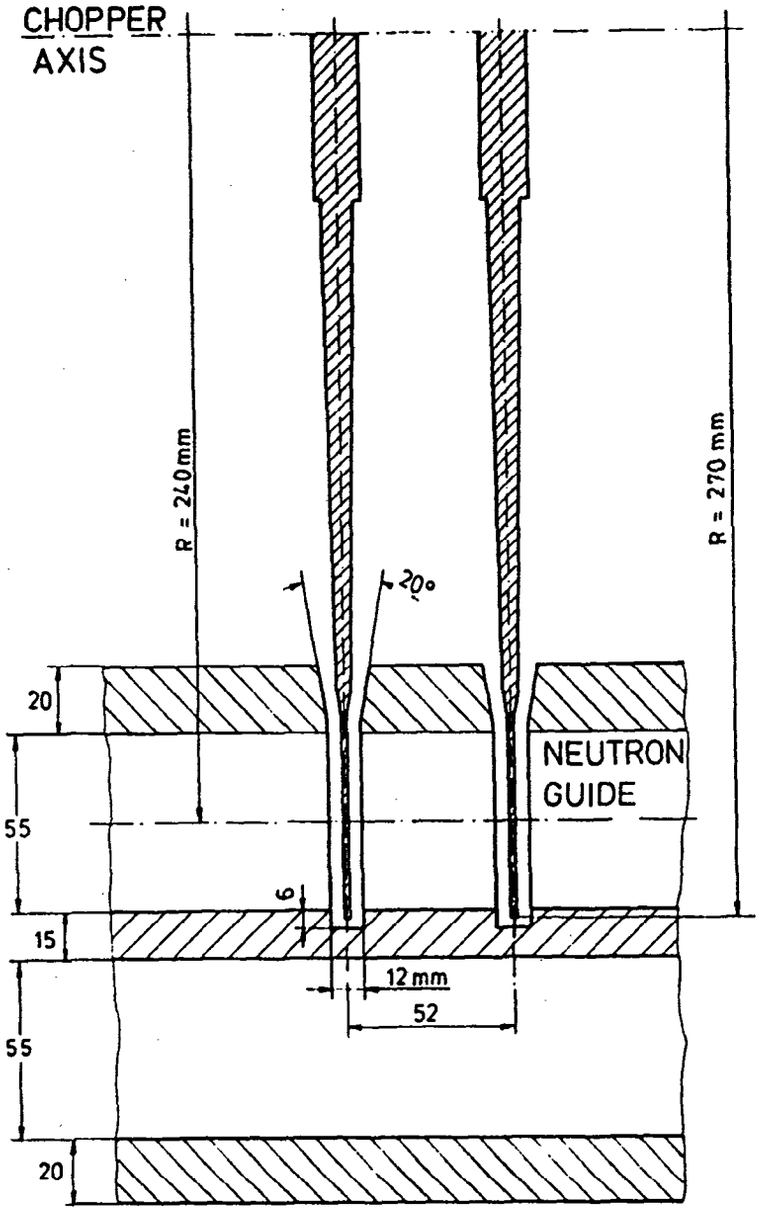

Fig. 6
Vertical cut of neutron guide, drawn to scale, with slots in which the chopper disks are running. The widths of the slots in beam direction, as wellas the thickness of the disks are made as small as possible, in order to minimize intensity losses.

a guide gap is related to the beam divergence and is therefore wavelength dependent. It can easily be shown that V, expressed as a percentage of the neutron flux, is given by

$$V = 100 \cdot G \cdot tg\gamma_c (W+H-G \cdot tg\gamma_c/2) \;/\; (2WH) \qquad (10)$$

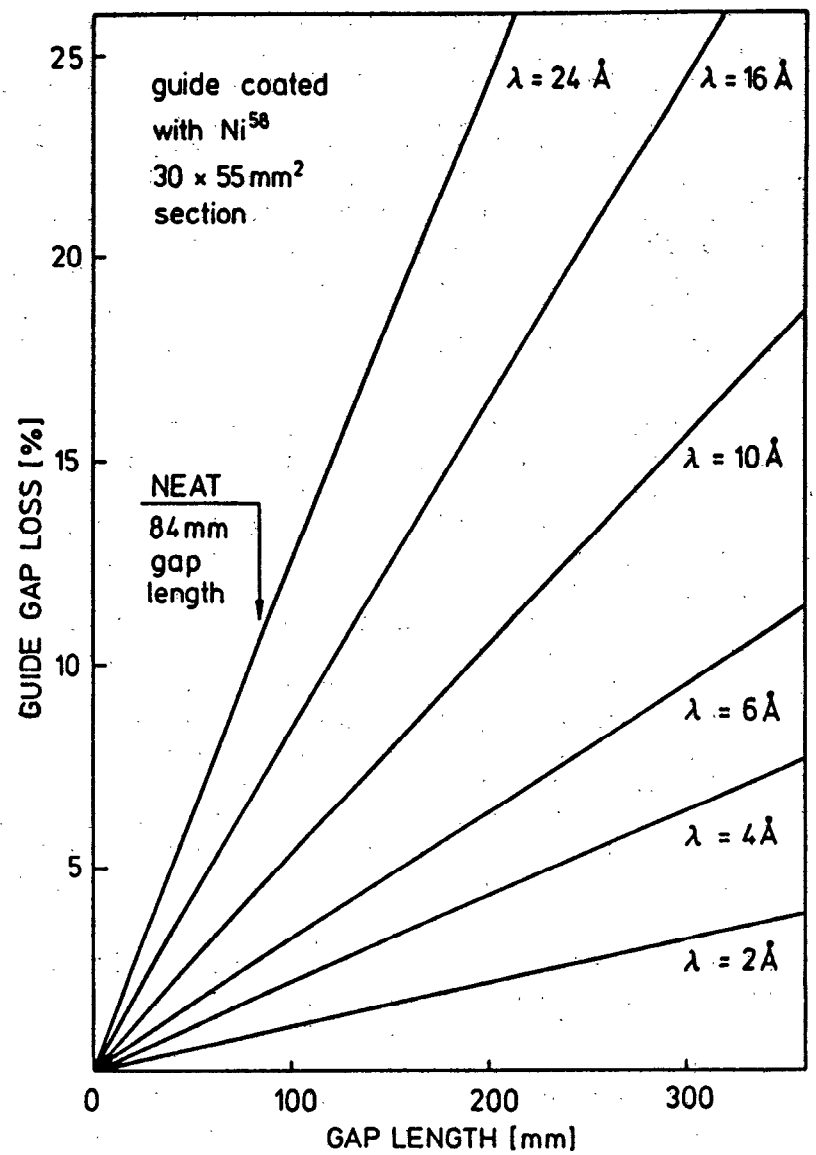

Fig. 7
Percentage of intensity loss due to interruptions in the neutron guide (guide gaps) as a function of the gap length, with the neutron wavelength λ as a parameter. The curves apply to the Ni-58 coated neutron guide section (with parallel walls) of the spectrometer NEAT (beam cross-section: 30 X 55 mm^2).

where
G = gap length in beam direction
γ_c = critical angle of total reflection of the material used for coating the neutron guide (Ni-58 in the case of NEAT)
W = inner width of the guide (beam width)
H = inner height of the guide (beam height)
For geometries occurring in practice V is an almost linear function of G. In Fig. 7 this is shown for a number of different neutron

wavelengths for the parallel-walled guide of NEAT. An arrow points at the value of the total gap length (84mm) in the case of NEAT, which is due to the insertion of 7 chopper disks with minimized thickness; here the fact, that a beam compressor is used at the last chopper pair, was neglected. The corresponding flux loss is, for instance, about 2.7% at $\lambda = 6$Å and about 4.5% at $\lambda = 10$Å. For the same wavelengths the theoretical loss values in the case of IN5 (4 chopper disks, total gap length 80mm, but smaller beam cross-section) are 2.9% and 4.8%, respectively. Much larger loss percentages are expected in the case of the spectrometer MIBEMOL /6/, where the total gap length related to the use of 6 chopper disks amounts to 300mm.

Last, not least, the connection between resolution, intensity and detector budget needs some consideration. Roughly speaking the total efficiency of the spectrometer increases with the total solid angle Ω_t, that can be covered with detectors, the energy resolution improves with increasing sample-detector distance L_{SD}, whereas the total cost of the detectors is proportional to $(\Omega_t \cdot L_{SD}^2)$. Obviously some compromise has to be made. For the 400 Helium-3 detectors of the spectrometer NEAT we have chosen a distance L_{SD} of 2.5m, which is fairly modest as compared to IN5 (where L_{SD} is about 4m). This was done, in order to increase the total solid angle by a factor of about 2.5 for the given number of detectors. Thus an intensity gainfactor of 2.5 is obtained at fixed resolution, since we have nevertheless conserved the energy resolution (for given chopper pulse widths) by choosing a relatively large distance of L_{12}=12.1m between the principal choppers (see eqs. (3) to (7).

Another interesting feature of NEAT is the addition of a large two-dimensional position-sensitive detector (surface $1m^2$) with variable distance, $4m \leq L_{SD} \leq 7.5m$, in order to be able to reach larger distances for highest-resolution experiments. This multidetector can be used at all scattering angles from 0° (small-angle-scattering) up to 134°. It increases appreciably the accessible range of $\Delta(\hbar\omega)$ and thus the flexibility of the spectrometer; e.g. for elastic scattering energy resolutions over three orders of magnitude ($2\mu eV \lesssim \Delta\hbar\omega \lesssim 2000\mu eV$) will be available.

VI. CONCLUSION

In the present paper we have discussed the optimization of a multi-disk chopper time-of-flight spectrometer regarding intensity and resolution. Our considerations have led to the concept of an improved version of this type of instrument. It has been the basis for the development of the new spectrometer NEAT, which is being installed at the Hahn-Meitner-Institut in Berlin.

For the evaluation of the improvement achieved it is useful to consider intensity gain factors at constant energy resolution. Obviously it is not possible to define one single factor describing the total gain for all experiments, since gain factors depend on the incident and scattered neutron wavelengths and on a number of instrument parameters varying from case to case. One can however obtain some insight by summarizing the pertinent results discussed in Sections IV and V :

1. In an example of elastic scattering using $\rho=2$ (rather than the conventional value $\rho=1$) we obtained a typical gain factor 1.38,

whereas in an example of inelastic scattering the gain factor was 2.74.

2. Once a chopper disk runs at the highest possible velocity, a further reduction in the neutron pulse width - for instance by a factor 2 - is always possible by simply reducing the width of the (parallel-walled) neutron guide and that of the chopper window by the same factor. Obviously this method (used in the spectrometer IN5) causes a corresponding intensity loss. This kind of loss is avoided to a large extent in the spectrometer NEAT with the aid of a double-trumpet beam-compressor /7/ with real-space reduction factor ß=2. The avoided loss corresponds to a gain factor of about 1.7; it is smaller than 2, because the transmission of the beam-compressor is somewhat short of 1.

3. In similar fashion we claim to introduce an additional intensity gain factor of 2, if the single disk chopper is replaced for the purpose of a further pulse-width reduction by a pair of counter-rotating disks /6/, turning at the same velocity (rather than employing the detrimental method of pulse-width reduction, which consists in throwing away half of the beam).

4. The minimization of neutron guide interruptions (total gap length of 84mm in the case of NEAT) also permits to decrease intensity losses; for instance at λ= 10Å a factor of 1.12 is gained as compared to a case with a gap length of 300mm (MIBEMOL).

5. As compared to IN5, where slots were cut into the absorber coating but not into the aluminium disk itself, we gain a factor of about 1.08 by the use of open chopper windows.

6. As compared to IN5 we have shortened the sample-detector distance for the 400 single detectors, but increased the distance between the principal choppers; by doing this we gain a factor 2.5 in intensity due to the corresponding increase in solid angle subtended by the detectors, while the resolution is kept (roughly) constant.

Combining the above gain factors, we achieve - at fixed energy resolution - a total intensity gain factor of about 13 in the example given for elastic scattering and about 26 in the inelastic scattering example. Thus we may conclude by stating, that the concept presented here represents an improvement by at least an order of magnitude over the design of the spectrometer we have realized almost twenty years ago.

As a final remark I should like to note, that the concept of NEAT described above was developed in 1984/85 at the Hahn-Meitner-Institut. Design work began in 1985. At the time of writing the present paper (end of 1990) most of the components are completed and the spectrometer is being installed at the BER-II reactor. In 1988 I have communicated the essential points of this concept to our colleagues at the N.I.S.T. Labs. in Gaithersburg (USA), who had expressed interest in building a similar instrument. We have been informed , that this is now under way /8/.

Acknowledgement

Thanks for continuous support of the NEAT project are due to H. Dachs, F. Mezei and H. Stiller.

References

/1/ F. Douchin, R. E. Lechner and R. Scherm, unpublished (1973)
R. Scherm, Jül-295-NP, KFA Jülich (1965)
Due to heavy service responsibilities, which the authors had at the time, the development of the time-of-flight spectrometer IN5 is only (somewhat scantily) documented in several internal reports :
F. Douchin, R. E. Lechner and Y. Blanc, ITR 26/73, ILL Grenoble (1973).
R. E. Lechner, F. Volino, A. J. Dianoux, F. Douchin, H. Hervet and G. C. Stirling, ISR 8/73, ILL Grenoble (1973).
See also: Guide to Neutron Research Facilities at the ILL High-Flux Reactor, eds. H.Blank and B. Maier (Dec.1988)p.52.

/2/ R. E. Lechner, in Proc. Workshop on Neutron Scattering Instrumentation for SNQ, Maria Laach, Sept.3-5,1984; eds. R. Scherm and H. Stiller, Jül-1954(1984)p.202.

/3/ R. J. Royston, Nucl. Instr. Meth. 30(1964)184

/4/ R. E. Lechner, in "Neutron Scattering in the 'Nineties",IAEA Vienna (1985)p.401.

/5/ R. M. Brugger, in "Thermal Neutron Scattering", ed. P. A. Egelstaff, Academic Press, London and New York (1965)p.54.

/6/ S. Hautecler, E. Legrand, L. Vansteelandt, P. d'Hooghe, G. Rooms, A. Seeger, W. Schalt and G. Gobert, in "Neutron Scattering in the 'Nineties", IAEA Vienna (1985)p.211.

/7/ R. E. Lechner, in "Advanced Neutron Sources 1988" (Proceedings of the ICANS X Meeting, Los Alamos 1988), ed. D. K. Hyer, Inst. of Physics Conference Series Number 97, Bristol and New York (1989)p.843.
R. E. Lechner and F. Mezei, "Optimization of the Transmission of a Double-Trumpet Neutron-Beam Compressor", contribution to the present Proceedings of the ICANS XI Meeting, Tsukuba 1990.

/8/ J. C. Copley, Nucl. Instr. & Meth. in Phys. Res. A291(1990)519.

Q(J.M.Carpenter): What range of wavelength do you expect to use?
A(R.E.Lechner): Between 1 and 16Å. Intensity goes to zero for $\lambda = 0.8$ Å.

ICANS-XI International Collaboration on Advanced Neutron Sources
KEK, Tsukuba, October 22-26, 1990

Crosscorrelation Method Using a Pulsed White Polarized Neutron Beam

M. Kohgi, H. Fujimoto, K. Ohoyama, K. Yamada and K. Motoya*
Department of Physics, Faculty of Science, Tohoku University, Sendai 980, Japan
*Department of Physics, Faculty of Science, Saitama University, Urawa 338, Japan

The application of the crosscorrelation method on a pulsed white polarized neutron beam is discussed. The key to the method is to modulate the polarization of the incident neutron beam according to a pseudorandom binary sequence and to count the scattering events by using a two dimensional time analyzer. Based on this technique, the measurement of spin wave excitations in the ferromagnetic Heusler alloy Cu_2MnAl was performed on the PEN spectrometer at KENS, KEK. The experimental result shows that the combination of the pulsed white polarized neutron beam with the crosscorrelation method with polarization modulation is quite promising for the study of the magnetic response in various materials.

I. Introduction

Polarized neutron technique is a powerful tool for studying magnetism. It has been mainly developed for the monochromatic polarized neutron beams in steady state reactors. In implementing the polarized neutron technique at a pulsed neutron beam, it is especially important to utilize as many neutrons as possible, that is, to polarize incident neutrons in a broad energy band and to utilize all of them. The combination of the filter type polarizer and the crosscorrelation method at pulsed neutron sources is expected to be a good approximation to it.

Crosscorrelation methods were firstly applied to neutron spectrometry at steady state reactors, where the monochromatic incident neutron beam is modulated in time according to a pseudorandom binary sequence (PRBS) using a disk type chopper[1] or a spin flipper chopper[2]. The conventional TOF spectrum is recovered by crosscorrelation of the count rate at detector with the modulating sequence. This method was soon applied to the unpolarized white neutron beam in a pulsed reactor using a classical statistical chopper[3]. The technique can be extended to polarized white neutron beam in pulsed neutron source, where the polarization of the incident neutron beam is modulated by using a spin flipper chopper whose driving current is modulated according to a PRBS.[4] The aim of the present work is to show the feasibility of this technique.The principle of the method is briefly described in the next section.

II. Principle of the Method

The polarization of the pulsed incident neutron beam is modulated by using a spin flipper coil whose driving current is modulated according to a PRBS $\{S_i\}$ of period L, where $S_i = 0$ or 1, which correspond to the neutron polarization anti-parallel or parallel to the guide field, and $S_{i+L} = S_i$. The sequence $\{S_i\}$ has the following auto correlation function:

$$a_j = \sum_{i=1}^{L} s_i \cdot s_{i+j-1} = \begin{cases} K & (j=1, L+1, \ldots) \\ cK & (\text{otherwise}) \end{cases} \qquad (1)$$

where $K = \sum_{i=1}^{L} s_i$, and $c = \frac{K-1}{L-1}$.

The polarization modulation is so controlled that the PRBS pattern shifts by a step cyclically at each sequential counting frame triggered by the neutron burst. The procedure continues until one cycle shift of the PRBS is finished, and then it repeats a new sequence of the counting of scattered neutrons. In this way, the scattered neutron events are counted in a two-dimensional time analyzer, one time label of which is the total TOF t_m, and the other is the counting frame number j (=1,···,L) which corresponds to the shift number of the PRBS. Then, the count rate $I_{j,m}$ is expressed as:

$$I_{j,m} = \sum_{i=1}^{L} \{ I^p_{i,m} \cdot (\frac{1-P_i}{2} + P_i s_{i+j-1}) + I^a_{i,m} \cdot (\frac{1+P_i}{2} - P_i s_{i+j-1}) \} + b_m$$

$$= \frac{1}{2} \sum_{i=1}^{L} P_i \cdot I^d_{i,m} \cdot (2s_{i+j-1} - 1) + \frac{1}{2} T_m + b_m, \qquad (2)$$

where P_i is the absolute value of the polarization of neutrons at the incident time channel i, and $I^d_{i,m} = I^p_{i,m} - I^a_{i,m}$ and $T_m = \sum_{i=1}^{L} (I^p_{i,m} + I^a_{i,m})$ with

$$I^p_{i,m} = \int_{t_i}^{t_i+\Delta t} dt_1 \int_{t_m}^{t_m+\delta t} dt \ \sigma_p(t_1, t) \text{ and } I^a_{i,m} = \int_{t_i}^{t_i+\Delta t} dt_1 \int_{t_m}^{t_m+\delta t} dt \ \sigma_a(t_1, t). \qquad (3)$$

$I^P_{i,m}$ and $I^a_{i,m}$ correspond to the count rates at the total time of flight channel (t_m, $t_m+\delta t$) for the incident neutrons with parallel and anti-parallel polarization, respectively, and with incident time within (t_i, $t_i+\Delta t$). σ_a and σ_p represent the corresponding cross sections:

$$\sigma_p(t_1, t) = J \left(\frac{d^2\sigma^{++}}{d\Omega dE'} + \frac{d^2\sigma^{+-}}{d\Omega dE'} \right),$$

$$\sigma_a(t_1, t) = J \left(\frac{d^2\sigma^{--}}{d\Omega dE'} + \frac{d^2\sigma^{-+}}{d\Omega dE'} \right), \qquad (4)$$

where the signs indicate the spin states of incident and scattered neutrons, and $J = \partial E'/\partial t$. b_m is the instrument background. In Eq.(3), the effects of the incident neutron pulse shape, the spin-flipper pulse shape and other time uncertainties are not included for the sake of simplicity. Such effects can be included by convoluting appropriate shape functions.

The crosscorrelation of the count rate $I_{j,m}$ with the PRBS pattern gives:

$$C_{k,m} = \sum_{j=1}^{L} s_{j+k-1} I_{j,m} = \sum_{j=1}^{L} s_{j+k-1} [\sum_{i=1}^{L} \{ \frac{1}{2} P_i \cdot I^d_{i,m} (2s_{i+j-1} - 1) \} + \frac{1}{2} T_m + b_m]$$

$$= (1-c) K \cdot P_k \cdot I^d_{k,m} + \frac{1}{2}(2c-1) K \sum_{i=1}^{L} P_i \cdot I^d_{i,m} + K(\frac{1}{2} T_m + b_m). \qquad (5)$$

The first term in the right hand side of Eq.(5) is proportional to the spectrum $I^d_{k,m}$. The second and third terms depend only on the total TOF channel number m, and give otherwise flat background. Therefore, the first term can be easily discriminated from the others. The recovered value $I^d_{k,m}$ gives direct information on the magnetic inelastic scattering with incident time t_k and total TOF t_m.

III. Experiments

As an example of the application of the present technique, the observation of spin wave scattering from a ferromagnet is described here. If the magnetization of the ferromagnet is parallel to the scattering vector, the cross section of spin wave scattering is described as:

$$\frac{d^2\sigma^{\pm\mp}}{d\Omega dE'} \propto \delta(\hbar\omega \mp E_q), \tag{6}$$

where the upper and lower signs correspond to the spin wave creation and annihilation processes, respectively. Therefore, it is possible to observe the spin wave scattering by this technique with no use of spin analyzer in the scattered beam.

A neutron spin flipper system and a two dimensional time analyzer were constructed for the present work. The flipper coil is made of aluminum wire (diameter 0.6 mm) and its size is 7 x 4 x 1 cm^3. The inductance of the coil was about 100 μH. The direction of the field (along the longest edge of the coil) is perpendicular to both the neutron beam and the guide field in which the coil is placed. The guide field inside the coil is canceled by using another coil which is wound on the flipper coil along its second longer edge. The intensity of the driving current for the flipper coil is controlled to be proportional to the $1/t$ relation, where t is the time from each neutron burst, so that a 180 degree flip of the neutron spin is ensured for any incident neutron energy. The maximum current was about 3 A. The current is then switched on and off according to a PRBS. The time constant of the flipper coil circuit was τ=3 μs. The timing of switching is given by a module which generates the PRBS pattern which shifts by one step at each frame of neutron burst. The scattered neutron events are counted in the memories in the two dimensional time analyzer system according to their total time of flight and frame number.

The polarized neutron scattering experiments were carried out on the PEN spectrometer at the spallation neutron source KENS at KEK. The spectrometer produces polarized white neutrons by passing the neutrons through a dynamically polarized proton filter. Typical neutron polarizations obtained by the spectrometer are 90 % at 100 meV and 70 % at 1 eV. Details of the spectrometer are described elsewhere.[5)]

The experimental setup is shown schematically in Fig.1. The sample was a single crystal of ferromagnetic Heusler alloy Cu_2MnAl, the size of which is 3 x 2 x 0.8 cm^3. The sample position from the neutron source was 6.98 m. The crystal was so oriented that the [111] reciprocal lattice

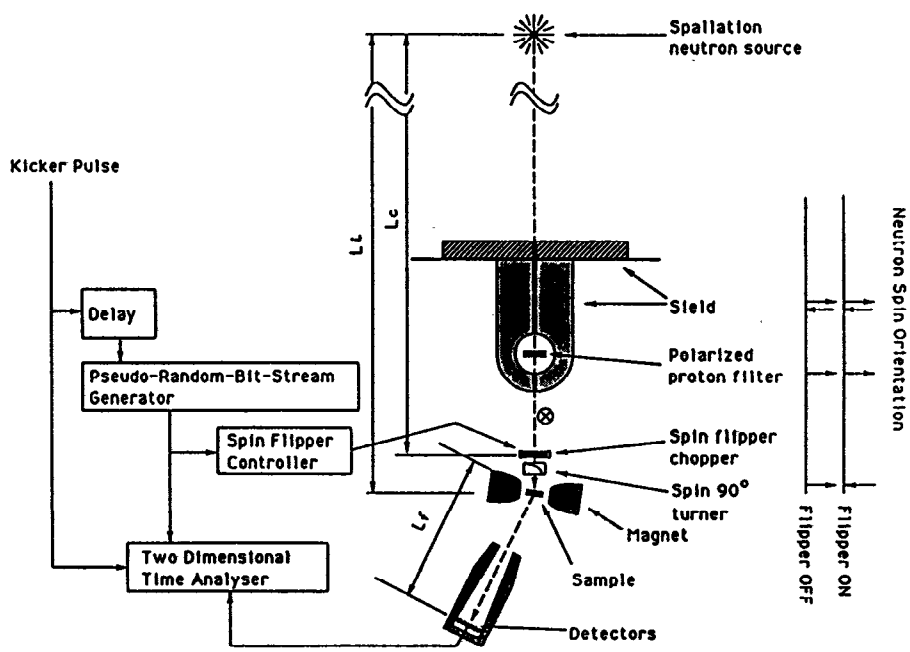

Fig.1 Experimental setup of the crosscorrelation method at the KENS pulsed neutron source.

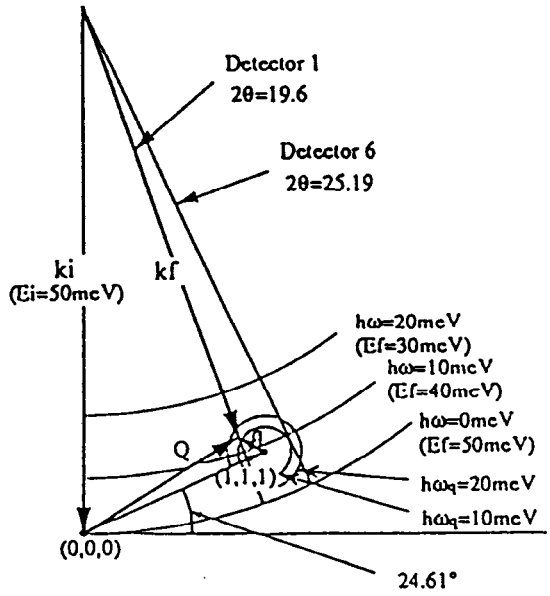

Fig.2 Scattering configration in the reciprocal space. Only the case of the neutrons with the incident energy of 50 meV is shown.

vector coincided with the scattering vector of neutrons with initial and final energies of 50 and 42 meV, respectively, for the detector with the scattering angle of 21.8 degrees. The scattering configuration is shown in Fig.2. A magnetic field of 1 T was applied to the sample along the reciprocal lattice vector. Therefore scattering with an energy loss of about 10 meV is expected to be observed on the dispersion surface of the spin wave excitation, that is, $D(\kappa-\tau)^2$, where D is the spin wave stiffness constant (175 meVÅ^2 for Cu_2MnAl), κ is the scattering vector and τ is the (111) reciprocal lattice vector. Since the magnetization of the sample is almost parallel to the scattering vector, only those incident neutrons whose polarization is parallel to the magnetization are scattered. Therefore, the difference spectrum around $\hbar\omega$~10 meV corresponds to the spin wave creation process. The flipper coil was placed 53 cm upstream from the sample. The polarization of incident neutrons with the energy from 33 to 78 meV was modulated by the spin flipper according to a PRBS of 31 steps after a delay of 1635 μs from neutron burst. The time unit of the sequence was 30 μs. The scattered neutrons were detected by six ^{3}He detectors which are placed at a distance of 1.5 m from the sample and separated each together by about 1 degree. As an example, Fig.3 shows the raw data $I_{j,m}$ with the frame number j=15 at the detector 3 (2θ=21.8 degrees).

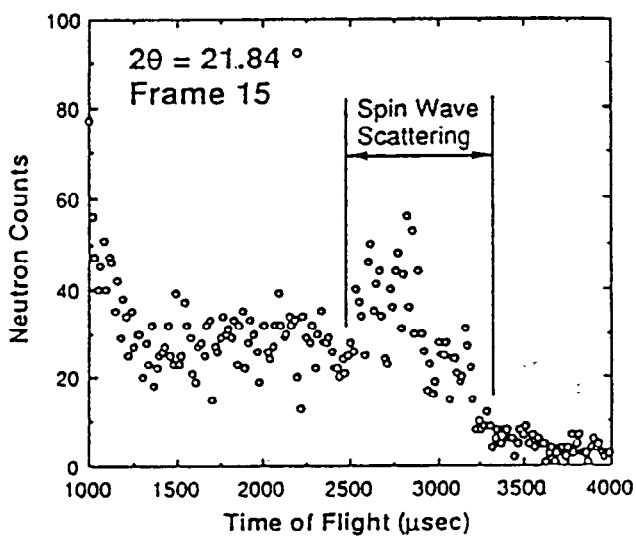

Fig.3 Raw data at scattering angle of 21.84 degrees and frame number of 15.

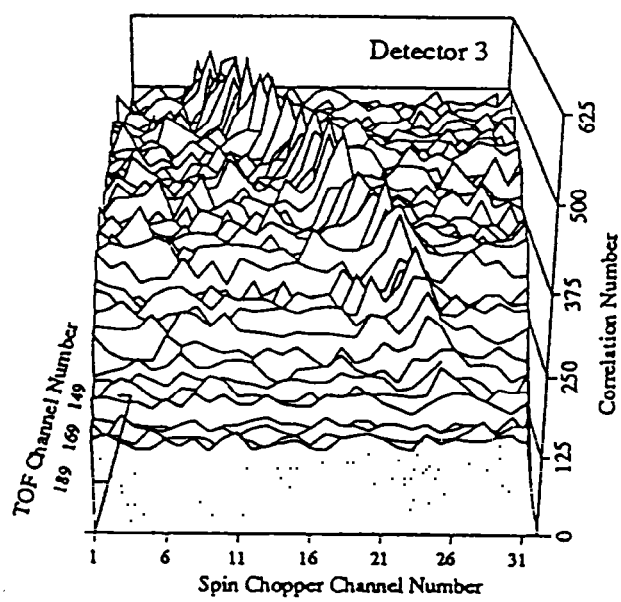

Fig.4 Result of the crosscorrelation of the count rates at the detector 3 (2θ=21.84°).

Fig.4 shows the correlation number $C_{k,m}$ obtained from crosscorrelation of the count rate $I_{j,m}$ at the detector 3 with the PRBS patterns. The channel width for total TOF was 16 μs. The spin chopper channel number k of $C_{k,m}$ corresponds to the incident time t_1 at the sample with the relation $t_1 = 6.98/6.45\cdot(1635 + 30\,k)$ μs. The ridge-like increase of the correlation number seen in the figure comes from the spin wave scattering. In order to see this more clearly, the data at total TOF from

170 to 174 channels are plotted as a function of energy transfer in Fig.5. Since their loci of the inelastic scans in the scattering plane are close each together and cross the dispersion surface twice, the scattering is expected to occur at two energy transfers, that is, around 5 and 14 meV. Although the energy resolution is not high and the counting statistics are rather low, a clear peak at around 5 meV and a hump at around 14 meV are visible in the figure. The reason that only the peak at 5 meV is distinct is due to the difference of the temperature factors between the two peaks. The solid line shows the result of a simulation of the spin wave scattering in the present configuration. In the simulation, neutron pulse shape at the moderator and time uncertainty at the spin flipper were taken into account. It can be seen that the observed spectrum is in good agreement with that of the simulation. Nearly the same results were obtained for the other data with total TOF from about 140 to 200 channels. This means that the spin wave scattering was observed with incident neutrons whose energies ranged from about 40 to 70 meV. It is in good agreement with our expectations under these scattering conditions. Almost same results are obtained for the other detectors. Of course, their positions of the spin wave ridges are shifted according to their scattering angles.

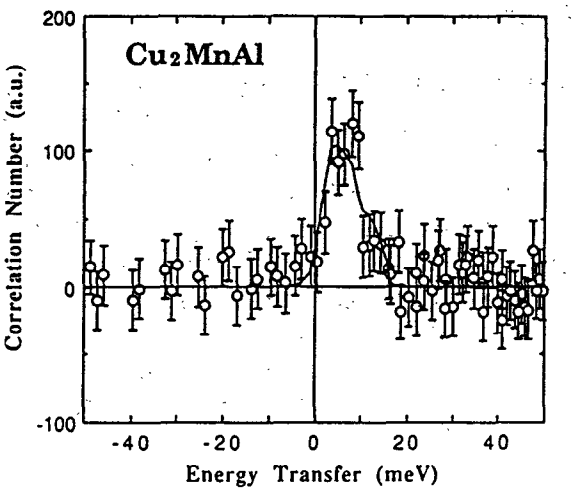

Fig.5 Example of spin wave spectrum of Cu_2MnAl obtained by the crosscorrelation method. Solid curve shows the result of the simulation.

IV. Discussion

The result of the present experiment shows that the combination of pulsed polarized white neutron beam with the crosscorrelation method with polarization modulation is quite promising for the study of the magnetic excitations or fluctuations in various magnetic materials. The resolution of the present spectrometry is determined by incident neutron pulse shape, spin flipper pulse shape and neutron flight lengths. Therefore, it can be discussed on the same basis as in the case of the conventional chopper type spectrometer. In the present experiment, the energy resolution dE/E_i was about 12 % at the incident and final energies of 50 and 40 meV, respectively. However, there is no difficulty to improve the resolution to the order of a few % if neutron source intensity permits; for example, if the time unit of modulation sequence, incident and final flight lengths are chosen to be moderate values of 10 μs, 11 m and 4 m, respectively, the resolution is expected to be 2 %.

In the present experimental configuration, no spin analyzer was used in the scattered beam. Therefore, the present technique is applied only for the measurement of spin wave excitations in ferromagnet. The equipment with spin analyzer in the scattered beam gives the full power to the technique. It allows the measurement of all kind of magnetic excitations such as the spin wave excitations, paramagnetic spin fluctuations, or crystal field excitations. The technique to make difference between spectra of vertical and horizontal field arrangements is also useful in this case. By using a broad energy band spin analyzer in the scattered beam, the crosscorrelation technique allows a dense mapping in momentum-energy space of magnetic dynamical response in a single measurement, as demonstrated by the present experiment. The spin analyzer should, of course, work in a energy band as wide as that of the polarizer. The dynamically polarized proton filter, however, is not suitable for this purpose because it is technically difficult to cover wide solid angle in the scattered beam. Therefore, although the energy band available is not so wide as the polarized proton filter, the resonance absorption filter would be a better choice in the thermal and epithermal energy region. In order to obtain results with good resolution an intense pulsed neutron source is required of course.

In summary, the technique using the crosscorrelation method with polarization modulation in pulsed polarized white neutron beam has been shown to be feasible. The combination of the technique with intense pulsed neutron source and broad energy band polarizer provides a unique and powerful tool in the study of the dynamics in magnetic materials.

References

1) F. Gompf, W. Reichardt, W. Glaser and K.H. Beckurts, Neutron Inelastic Scattering (proc. Symp. Copenhagen, 1968) 2, IAEA, Vienna (1968)417.
2) L. Pál, N. Kroó, P. Pellionisz, F. Szlávik and I. Vizi, ibid. 407.
3) N. Kroó, P. Pellionisz, I. Vizi, G. Zsigmond, G. Zhukov and G. Nagy, IAEA Symp. on Neutron Inelastic Scattering (1972), IAEA/SM-155/F-6.
4) R. Cywinski and W. G. Williams, Nucl. Instr. and Meth. 228(1985)406.
For the principles of the crosscorrelation method, see also the references herein.
5) M. Ishida, Y. Ishikawa, S. Ishimoto, M. Kohgi, A. Masaike, Y. Masuda, K. Morimoto and T. Nakajima, Proceedings of the Eighth Meeting of the International Collaboration on Advanced Neutron Sources, RAL-85-110(1985)612.

Q(W.G.Williams): What is the rise time for switching on the spin flipper and how does this compare with the typical flipper on time?

A(M.Kohgi): The inductance and resistance of our flipper coil circuit is about 100μH and 30Ω,respectively. Therefore, the time constant of the circuit is t=3μsec. There is no technical difficulty to decrease the value to about 1μ sec. For faster spin chopper, see, for example, Y.Itoh and S. Takahashi, Nucl. Instr. Method 221 (1984) 490.

ICANS-XI International Collaboration on Advanced Neutron Sources
KEK, Tsukuba, October 22-26, 1990

Recent progress on MAX

Y.TODATE, H.IKEDA†, K.TAJIMA†† and S.TOMIYOSHI*

Department of Physics, Faculty of Science,
Ochanomizu University, Otsuka,Bunkyo-ku,Tokyo 112
†National Laboratory for High Energy Physics, Oho, Tsukuba 305
††Department of Physics, Faculty of Science and Technology,
Keio University, Hiyoshi, Yokohama 223
*Institute for Materials Research ,Tohoku University, Sendai 980

Introduction

Crystal analyser spectrometer MAX at KENS can observe collective excitations such as phonons and magnons in single crystals by means of TOF method. Excitation spectrum along a desired direction of the sample crystal can be measured using fifteen independent analyser-detector systems[1-5]. In practical use, the energy transfer range is 1meV to 150meV depending on the Q region to be covered. The energy resolution $\delta E/E_f$ is about 0.1 and can be adjusted by inserting Sollar collimators before and/or after the analyser. MAX exhibits its better performance in several tens meV energy transfer region. This energy region is not so easy to observe using a triple-axis spectrometer at a medium power steady reactor. MAX is now being used mainly to investigate magnetic excitations. Dispersion relations of the magnetic excitations in various magnetic materials have been determined. Advantages in the application of MAX to the low-dimensional systems should be noted[4,5]. All the scans made by the detectors of MAX are constant-q when the incoming neutron beam is set parallel to the direction in which the system has no correlation, i.e. the direction perpendicular to the plane (chain) of the two- (one-) dimensional material. Furthermore, better experimental condition is found in the case of low-dimensional systems because the strong restriction on the TOF scan due to the periodicity of the $S(Q,\omega)$ is relaxed.

Improvements

In order to improve the signal-to-noise ratio (S/N), the counting rate and the flexibility of the spectrometer, several modifications have been made. During the past few years S/N of the spectrometer has been improved significantly. Furthermore, new inpile collimator with sintered B_4C arrays has been inserted in order to eliminate the fast neutron background. We have improved the counting rate by focusing the neutron beam reflected by the analyser crystals. Small pieces of pyloritic graphite (5 cm x 0.6 cm) are aligned on a holder which has appropriate vertical curvature so as to focus the reflected beam to the small area on the ^{3}He counter. Note that we can obtain a better counting rate without sacrificing S/N because it is not necessary to enlarge the aperture of the counter shielding box. Moreover, the vertical slit Sollar collimators are still useful for these vertically curved analyser mirrors. The size of the analyser mirrors is enlarged to 7 cm (height) x 10 cm (length) from 5 cm x 10 cm. Consequently, without increasing the background or sacrificing the resolution, we have obtained more than 2 times higher counting rate than the previous flat ones. In order to obtain more flexibility, the direction of the rotation of the detector arms has been changed from counterclockwise to clockwise. (Analyser arms are rotated clockwise.)

Resolution of spectrometer

Resolution characteristics of MAX have been investigated in detail. Analytical resolution function was derived and examined experimentally. The derivation is based on the formalism of Cooper and Nathans [6], Komura and Cooper [7] and Windsor and Heenan [8]. Since, as is usual, Gaussian distributions were assumed for all the broadenings which occur due to the finite angular collimations, the mosaic of the analyser crystal, the time distribution of the neutron pulse and the time broadenings due to the finite sample size or gate width, the resolution function can be expressed analytically in terms of a Gaussian form in the 4-dimensional (Q, ω) space. Derivation of the resolution function of MAX and

the so-called resolution matrix is shown in reference 9. Here we only give a useful expression for the energy width which can be derived from the resolution function:

$$(\Delta\hbar\omega)^2 = 4E_I^2\left[\left(\frac{\tau}{T_I}\right)^2 + \left(\frac{E_F}{E_I} + \frac{L_F}{L_I}\sqrt{\frac{E_I}{E_F}}\right)^2 \cot^2\theta_A\,(\Delta\Theta_A)^2\right]$$

where

$$\tau^2 = \tau_m^2 + \tau_s^2 + \tau_c^2$$

and

$$(\Delta\Theta_A)^2 = \frac{\alpha_2^2\alpha_3^2 + \alpha_3^2\eta_A^2 + \eta_A^2\alpha_2^2}{\alpha_2^2 + \alpha_3^2 + 4\eta_A^2}$$

α_2 and α_3 corresponds to the divergence angle of the collimator placed between sample to analyser and analyser to detector respectively and η_A is the mosaicness of the analyser crystal. The time distribution (width τ_m) of incident neutron pulse is a function of wavelength. τ_s gives the time broadening due to the finite sample size. τ_c is chosen so that the corresponding Gaussian has the same standard deviation as the actual distribution caused by the finite time channel width. Usually τ_m is the largest compared with τ_s and τ_c. Parameters α_2, α_3 and η_A in the analyser part were determined so as to reproduce the observed energy width. We have plotted in Fig. 1(a) the observed energy width of incoherent elastic scattering from Vanadium for various collimations. The calculated widths using eq.(1) are indicated by solid lines in the figure. Figure 1(b) is a graph of calculated energy width as a function of E_F and $\hbar\omega = E_I - E_F$. In the figures the nominal aperture angles of the Sollar collimators are denoted as 20', 30', ... ("B" : without the Sollar collimator).

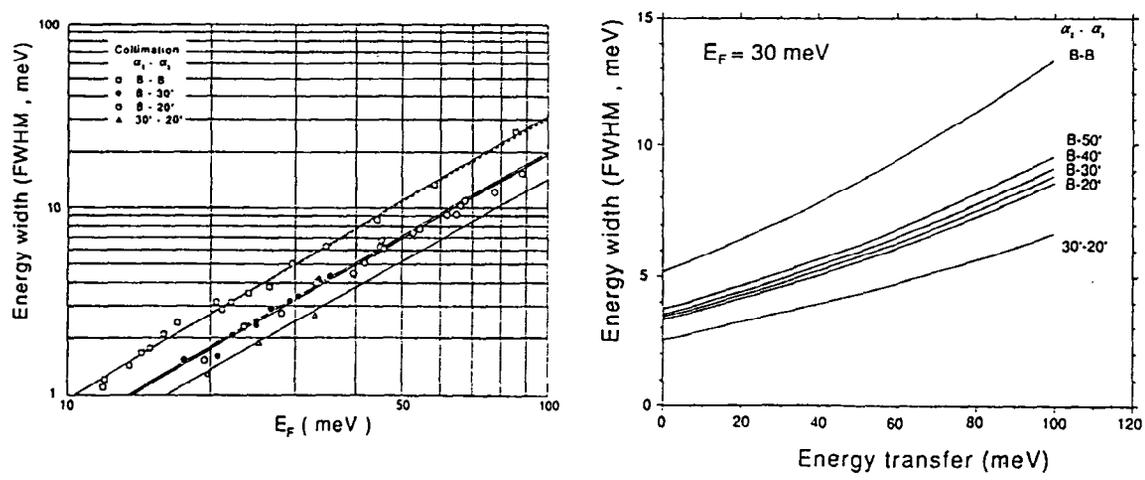

(a) (b)

Fig. 1 Energy resolution of MAX for various collimations. (a) shows the observed energy widths as a function of E_F at $\hbar\omega=0$. The solid lines are the corresponding calculations described in the text and the dotted line expresses the $E_F^{3/2}$ dependence[9]. (b) is calculated as a function of $\hbar\omega$ in the case of E_F=30meV.

We have also measured the spatial shape of the resolution at the elastic position by using Bragg scattering from a small perfect Ge single crystal. A spatial map of the intensity was drawn by rocking the sample and the analyser. Good agreement was obtained in both volume and spatial orientation of the resolution ellipsoid. By using the resolution function the effect of the spectrometer configuration on the resolution can be estimated. The volume of the resolution ellipsoid for the configuration of clockwise rotation of the detector arms (present configuration of MAX) is larger than the previous counterclockwise rotation or "W-configuration". However, present configuration has more flexibility. Note that the direction of the longer axis of the ellipse projected on to the scattering plane is always close to the direction of k_F in the present configuration as shown in Fig. 2(b).

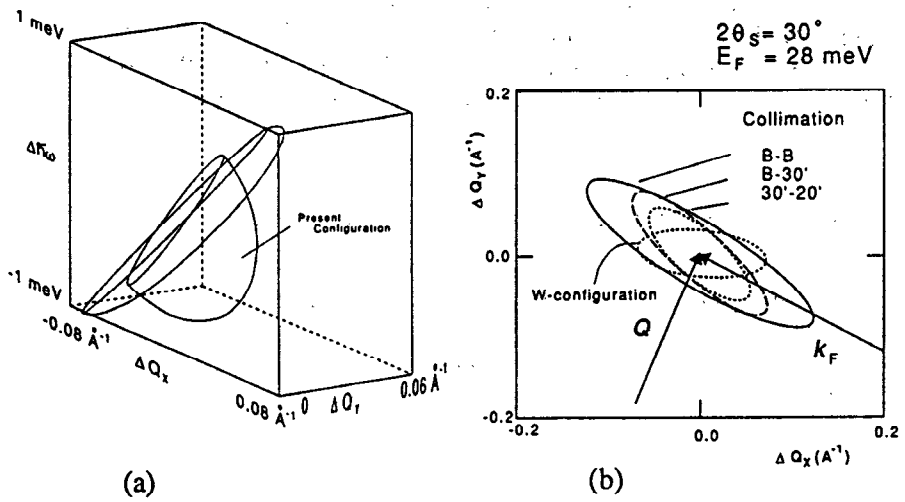

Fig. 2 Calculated resolution ellipsoids. (b) is the projected ellipses on to the scattering plane, where ΔQ_X is parallel to $-k_I$.

The resolution function derived analytically is useful for qualitative discussion of the instrumental resolution characteristics. Occasionally, however, observed peak shapes do not have the symmetric Gaussian form because the incident neutron pulse has a highly asymmetric time distribution. The resolution function derived above cannot reproduce this asymmetry. Employing the neutron pulse shape function proposed by Ikeda and Carpenter[10], numerical calculation of the resolution function was performed. It has been found that ,without any other adjustable parameters, observed incoherent elastic profile is well reproduced by a Monte Carlo calculation as shown in Fig.3. We are now extending this calculation to the inelastic scattering.

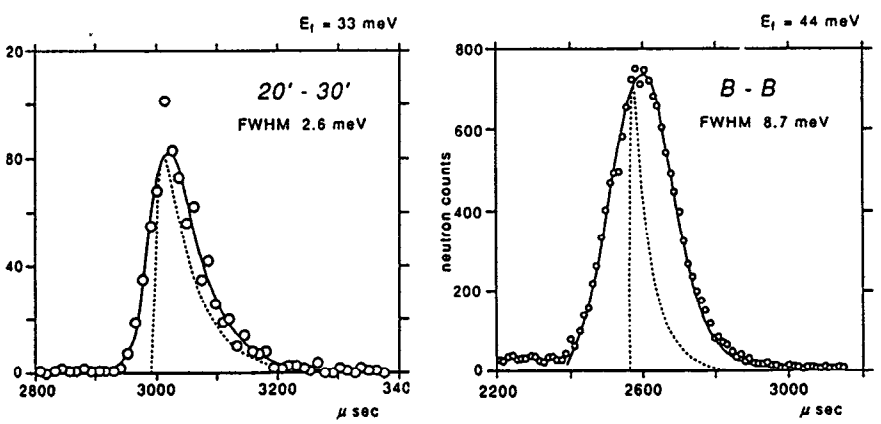

Fig. 3 Observed and calculated incoherent elastic peak profiles. Dotted lines represent the incident neutron pulse.

References

1) K.Tajima, Y.Ishikawa, K.Kanai, C.G. Windsor and S.Tomiyoshi: Nucl. Instrum. & Methods **201** (1982) 491.
2) K.Tajima, Y.Ishikawa, K.Kanai, S.Tomiyoshi and Y.Todate: Physica B**120** (1983) 136.
3) Y.Todate, Y.Ishikawa, K.Tajima, S.Tomiyoshi and H.Takei: J. Phys. Soc. Jpn. **55** (1986) 4464.
4) Y.Todate, H.Ikeda, F.Shibata, K.Tajima and Y.Endoh: J. Phys. Condens. Matter **1** (1989) 5895.
5) K.Tajima, Y.Todate and H.Ikeda: Physica B **156&157** (1989) 301.
6) M.J. Cooper and R. Nathans: Acta. Crystallogr. **23** (1967) 357.
7) S. Komura and M.J. Cooper: Jpn. J. Appl. Phys. **9** (1970) 866.
8) C.G. Windsor and R.K. Heenan: Nucl. Instrum. & Methods **171** (1980) 115.
9) Y.Todate, K,Tajima, H.Ikeda and S.Tomiyoshi : Jpn. J. Appl. Phys. **29** (1990) 1220.
10) S. Ikeda, J.M. Carpenter: Nucle. Instrum. & Methods **A239**(1985)536.

Q(U.Steigenberger): Which improvements do you plan to increase the flexibility of MAX.
A(Y.Todate): N/A

Q(H.Tietze): Did you try to factorize the influence of the sample, i.e. its size, mosaicity etc., on the resolution function of MAX?
A(Y.Todate): The sample size effect is included in the resolution function, but the mosaicity is not.
Q(H.Tietze): What about the Q-resolution of MAX?
A(Y.Todate): ΔQ is about $0.1 Å^{-1}$ at $Q = 2 Å^{-1}$.

ICANS-XI International Collaboration on Advanced Neutron Sources
KEK, Tsukuba, October 22-26, 1990

Progress with the PRISMA spectrometer

U.Steigenberger and M.Hagen
ISIS Science Division, Rutherford Appleton Laboratory
Chilton, Didcot, Oxon. OX11 0QX, U.K.

C.Petrillo and F.Sacchetti
Istituto di Struttura della Materia del CNR
Frascati, Roma, Italy

Abstract
The PRISMA spectrometer is an indirect geometry multi-analyser instrument at the ISIS spallation neutron source, which is intended for the measurement of coherent excitations in single crystal samples. A brief description of the present status of the instrument is given and in light of this description aspects of the current spectrometer design which limit its use are discussed. Possible developments which may overcome these limitations are outlined.

I. Introduction

The development of the PRISMA spectrometer at ISIS is a joint project between the Italian Consiglio Nazionale delle Richerche and the United Kingdom Science and Engineering Research Council. The participating laboratories in this project are the ISIS Facility at the Rutherford Appleton Laboratory, U.K. and the Istituto di Struttura della Materia, Frascati, Italy. The name PRISMA is derived from the acronym Progetto dell'Istituto di Struttura della Materia. PRISMA is designed for the measurement of coherent excitations (phonons, spin waves etc.) in single crystal samples. An original design for such a spectrometer at ISIS was given by Andreani et. al. [1] and a recent description of the actual spectrometer and its initial performance has been given by Steigenberger et. al. [2].

The installation and commissioning of PRISMA was started in 1987 and since the middle of 1989 the spectrometer has been available for scheduled experiments at ISIS. However it is not the intention of this paper to describe these experiments but instead to discuss areas of the spectrometer design where we have, during commissioning and the recent experiments, identified the need for improvement. In section II we give a brief description of PRISMA, which is required in order to facilitate the discussion of improvements. For a more detailed description the reader is referred to ref. [2]. The improvements described in section III have already been, at least in part, implemented and we include a discussion of their initial performance, while those described in section IV are still under consideration. Finally section V contains a brief conclusion.

II. Spectrometer Description

PRISMA is an indirect geometry multianalyser spectrometer. The sample is exposed to a

polychromatic neutron beam and the final energies of the detected neutrons (after scattering from the sample) are determined by an array of analyser-detector arms. From the total time of flight of the detected neutrons and a knowledge of their final energy the incident energies can be calculated. On PRISMA we have an array of 16 analyser-detector arms which are very closely spaced (2° apart) mounted on a single scattering arm which can rotate by ±120°. A schematic diagram of this arrangement is shown in figure 1. All of the analyser and detector angles can

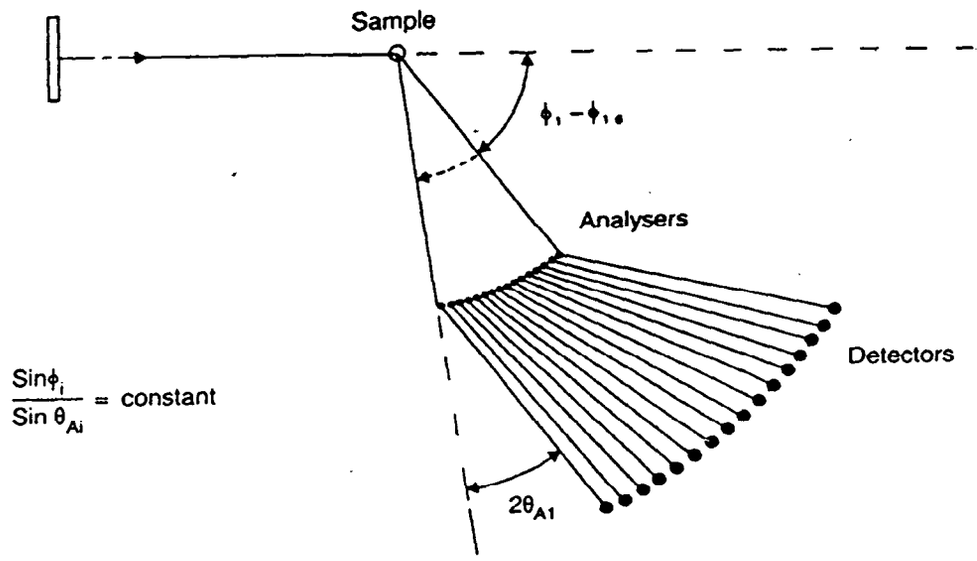

Figure 1: A schematic diagram of the PRISMA spectrometer.

be moved individually subject to the condition that the detector arms do not collide. In figure 2 we show how the wavevector transfer $\mathbf{Q} = \mathbf{k}_i - \mathbf{k}_f$ varies during a measurement on PRISMA. A high symmetry direction in the crystal is aligned parallel to $\mathbf{k}_i$. Since $\mathbf{k}_f$ is fixed in direction and length for a particular detector the wavevector transfer scans along the direction given by the dashed line in figure 2 as a function of the length of $\mathbf{k}_i$ (ie. time of flight). It is possible for all of the analyser detector systems to measure along this same direction (ie. the dashed line) if they have different values of $|\mathbf{k}_f|$. The condition for this situation is that the Bragg angle θ_A of the analyser crystal and the scattering angle ϕ for each analyser-detector system are related by the equation :

$$Q_\perp = \frac{\pi}{d_A}\frac{\sin\theta_A}{\sin\phi} \tag{1}$$

where $Q_\perp$ is the component of the wavevector transfer perpendicular to the direction of the incident neutron beam and d_A is the d-spacing of the analyser crystal planes. The energy transfer measured in each analyser detector system is therefore given by :

$$E = \frac{\hbar^2}{2m}\left(Q_\parallel^2 - 2(Q_\perp \cot\phi)Q_\parallel - Q_\perp^2\right) \tag{2}$$

Since the scattering angles ϕ are different for each of the analyser detector systems the energy transfers measured at a given wavevector on the dashed line in figure 2 are different and the spectrometer performs a net of scans in the $(E, Q_\parallel)$ plane.

III. Recent Developments

It is always desirable in a scattering experiment to have the background as small as is practical, and this is especially true for inelastic scattering where the cross-sections for phonons etc.

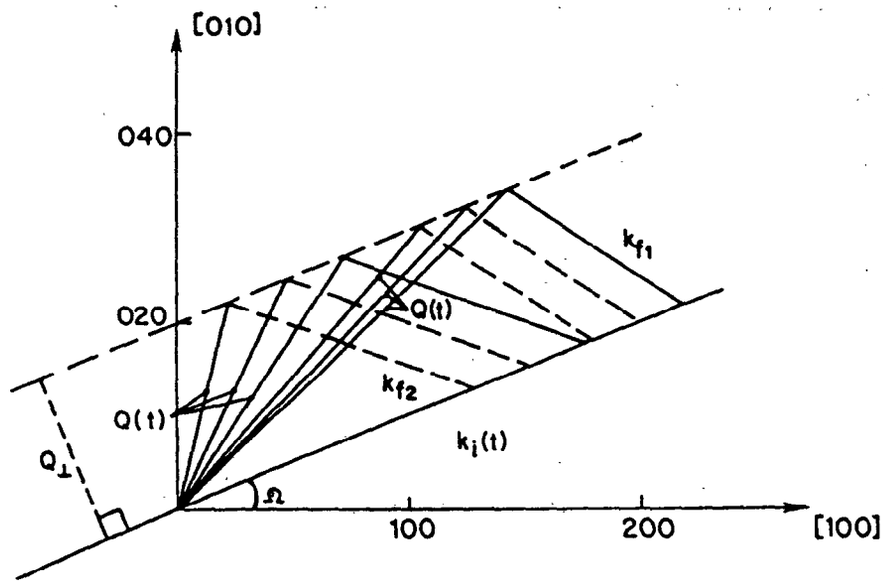

Figure 2: The vector triangles in reciprocal space representing the wavevector transfers in a scattering measurement on PRISMA.

are $\approx 10^{-5}$ those for Bragg scattering. On PRISMA we have found that the background (with a non-hydrogenous sample) for scattering angles $\phi \geq 40°$ is about 25 counts/meV transfer/day with ISIS running at 100μA proton current and a U^{238} target. This background originates from 3 approximately equal sources. There is an ambient background, with the beam on but no sample (or sample environment equipment) of ≈ 8 counts. It should be noted that these counts are neutronic and that the electronic background is considerably less than this level. The remaining $\frac{2}{3}$ of the background is associated directly or indirectly from the sample. We have discovered that when the direct path from the sample to the detector via the analyser is blocked by absorber but the sample is in position then the background is increased by a further 8 counts above the ambient. This presumably arises from the effect of scattering (predominantly Bragg) by the sample into the surrounding shielding. The remaining 8 counts therefore arises from direct scattering from the sample via the analyser to the detector. This background is flat as a function of energy transfer. We presume it arises from elastic incoherent scattering both at the sample and at the analyser.

For scattering angles $\phi < 40°$ the background was found to increase rapidly with decreasing scattering angle. A significant part of this increase was discovered to be due to neutrons with energies $E > 270$ meV (which is the absorption edge of Cd). Much of the shielding around the detectors on the scattering arm is Cd since this shielding must be thin. This latter point will be discussed further in section IV. In order to reduce the background at low ϕ we have recently installed a background chopper in the incident beam line. This chopper limits the wavelength band which is seen by the sample. This is achieved by blocking the incident neutron beam at $t \approx 0$, i.e. the time when the proton pulse hits the target with a block of nimonic material. The size of the nimonic block is such that it covers completely the aperture of the beam for a time period of about 255μs at a chopper frequency of 50Hz. The effect on the incident spectrum is shown in figure 3. Here the ratio of two normalised monitor spectra is plotted (monitor with chopper / monitor without chopper) as a function of incident energy. The reduction in the number of neutrons with energies greater than 500meV is clearly visible. The chopper is

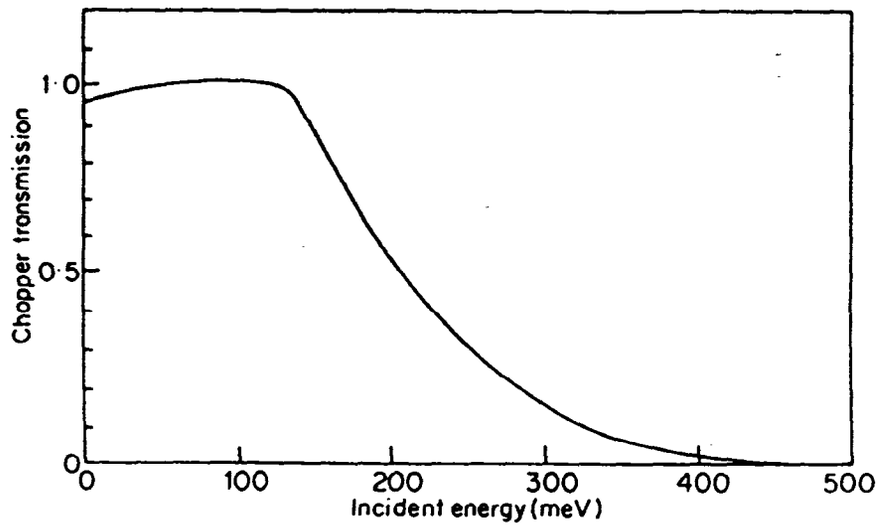

Figure 3: The chopper transmission spectrum.

additionally equipped with a tailcutter disk (12mm thick, 90% Mg, 10% Cd) which blocks the very low energy neutrons between 6667μs and 20000μs when running at 50 Hz. As the chopper has two nimonic blocks separated by 180°, an alternative option is to spin it at 25Hz. This doubles the time during which the nimonic part covers the beam, although such a mode would require the removal of the tailcutter disk.

As well as reducing the background, work is also being carried out on increasing the measured intensity for certain experiments by having the different analyser crystals available. At present on PRISMA we are using cylindrical Ge crystals with a $[1\bar{1}0]$ axis perpendicular to the scattering plane as analysers. This allows us to employ the (111), the (400) and the (220) reflections for analysis. The virtue of using the (111) reflection lies in the fact that second order contamination is absent due to the zero structure factor of the (222) reflection in the diamond crystal structure. The structure factors of the (220) and (400) reflections are twice that for the (111) reflection but have the disadvantage of second order contamination.

We are planning to have available a second set of analyser crystals of highly oriented pyrolytic graphite (HOPG). The high reflectivity of HOPG will allow us to gain a significant increase in measured intensity for experiments where the desired energy transfer range will not be contaminated by second order reflection from the analysers. HOPG is available from the Union Carbide corporation in two forms, one with mosaic spread 0.4° and one with mosaic spread 0.8° in various thicknesses. The choice of which form to use to maximise intensity without degrading resolution depends upon the effective collimation of the spectrometer after the sample. In order to be sure that we optimise our intensity we have performed test measurements on PRISMA using two samples provided by Union Carbide. Sample #A had a mosaic spread of 0.4° and was 2mm thick, and sample #B had a mosaic spread of 0.8° and was 4mm thick. We masked the samples to have identical surface area in the polychromatic beam on PRISMA and positioned one detector to view the sample at a scattering angle corresponding to a neutron energy of 15 meV. The results are shown in figure 4 for both sample #A and sample #B. Clearly the line width in energy is the same for both samples but the reflectivity of sample #A is higher by nearly 50%.

We have also compared the HOPG #A sample with a Mica analyser and one of the present Ge analyser crystals (c.f. figures 5a-c) for similar energies. The d-spacings of the Ge (111)

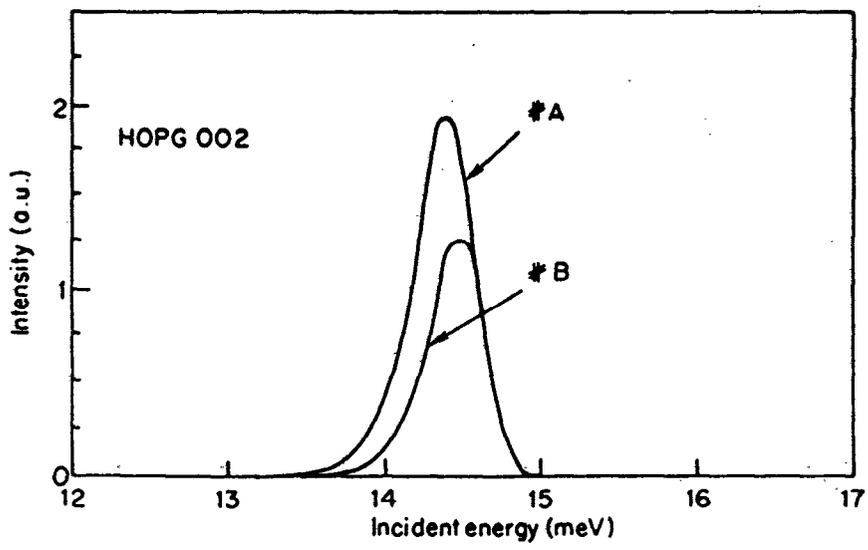

Figure 4: The relative reflectivity of two highly oriented pyrolitic graphite crystals is shown for neutrons with an energy of 15 meV. Sample #A had a mosaic spread of 0.4° and sample #B a mosaic spread of 0.8°.

reflection of 3.266 Å, the HOPG (002) reflection of 3.355 Å and the Mica (003) reflection of 3.334 Å are all quite similar (the possible usefulness of this similarity will become more apparent in the next section. Mica is a 2-dimensionally layered aluminia-silicate and the lattice constant perpendicular to the layers is around 10 Å depending on the exact chemical composition. We have used thin sheets of natural amber Mica, tightly packed to give an overall thickness of 3mm. As can be seen from figure 5b the resolution for the Mica (003) reflection at an analysing energy of 27 meV is about 1.29 meV and lies in between the values of 1.56 meV for the Ge (111) reflection and 1.0 meV for the HOPG (002) reflection. Although the measurements were performed for very similar settings of the spectrometer angles, it is not possible to make a comparison of the absolute reflectivities, because of the different sample geometries. However, the intensity difference between HOPG and Mica is too large to be explained by geometry alone hence Mica must have a lower reflectivity. Our interest is not therefore primarily in using the (003) reflection but the possibility of using the (001) reflection. At present the minimum analysing energy that can be used on PRISMA is 18 meV (again this point is discussed further in section IV). The use of Mica (001) would, for the same range of $2\theta_A$ angles available at the moment lower this minimum limit to 2 meV. Although correspondingly it will of course lower the upper limit as well. However the possibility of such low analysing energies is attractive for certain low energy transfer experiments. A careful evaluation of possible problems such as, the lower reflectivity, contamination from the (002) reflection or linewidth effects from using energies in the range of the Maxwellian of the methane moderator is required.

IV. Possible Future Developments

In order to obtain a densely packed net of scans in the $(E, Q_{\|})$ plane the analyser-detector systems are close together at only 2° separation. This can be compared with the much wider angular separation on the very similar spectrometer MAX at the KENS spallation source [3]. However the small angular separation on PRISMA leads to two serious restrictions. Firstly, as was alluded to in section II, the measuring configuration described can only be used if the detector arms are in an arrangement where they do not collide. This depends upon the

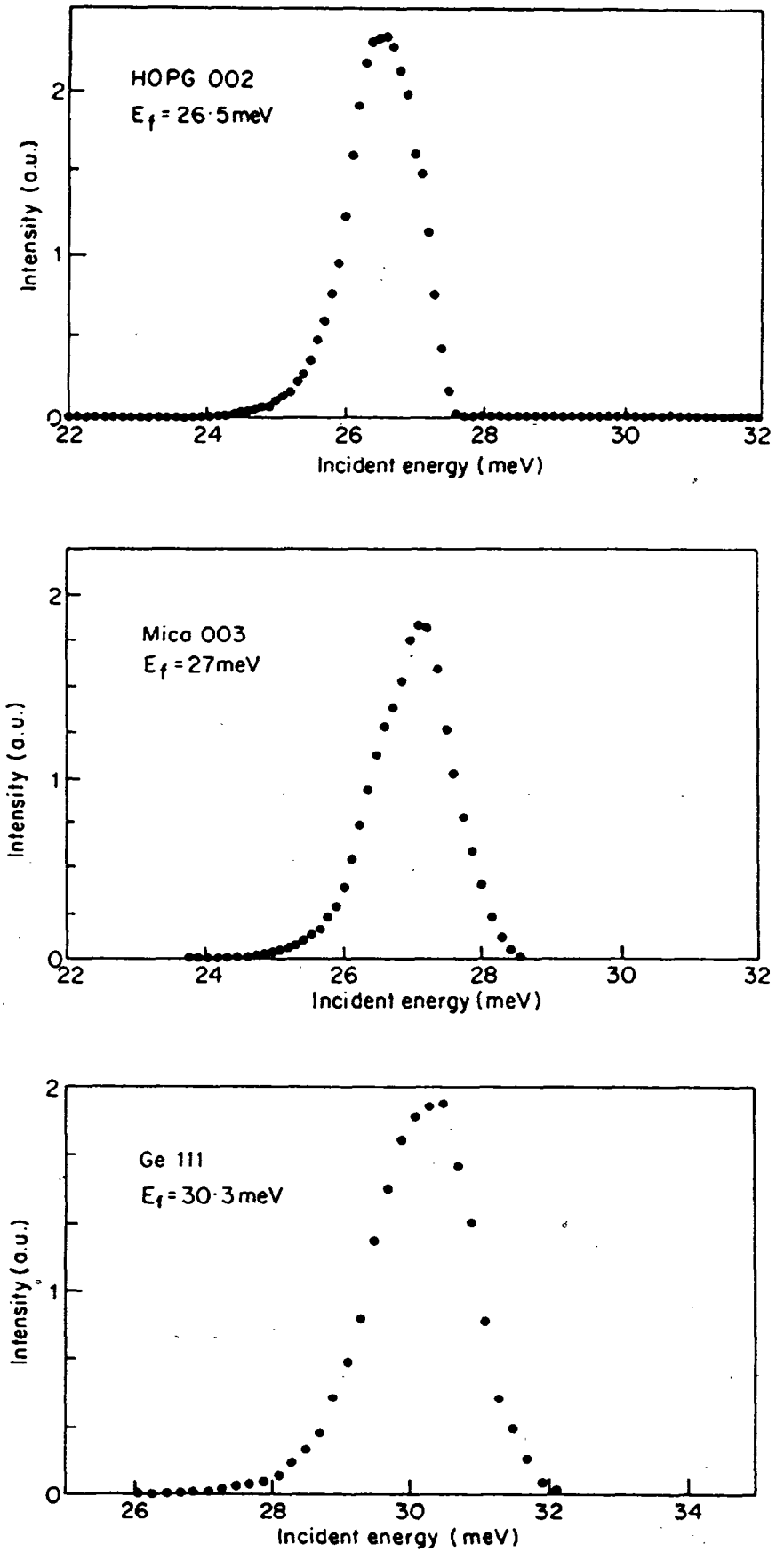

Figure 5: The measured scattering from analyser crystals of (a) HOPG (002), (b) Mica (003) and (c) Ge (111) at energies of 26.5, 27 and 30 meV respectively.

distances involved as well as the angular separation. On PRISMA the sample-analyser and analyser-detector distances are 573mm and 170mm respectively and each arm is 12mm across. Further to this there is an overall maximum $2\theta_A$ angle for any detector of 38° set by the shape of the frame supporting the arms. For the Ge (1,1,1) analysing planes this means a minimum analysing energy of 18 meV. These limitations impose severe restrictions on the E range accessible for small values of |Q|. In figure 6 we show the available range using Ge (1,1,1) analysers for two cases, (i) where only one detector is used and the remaining 15 are driven as far out of the way as possible and (ii) where all 16 detectors are used. It should be noted that

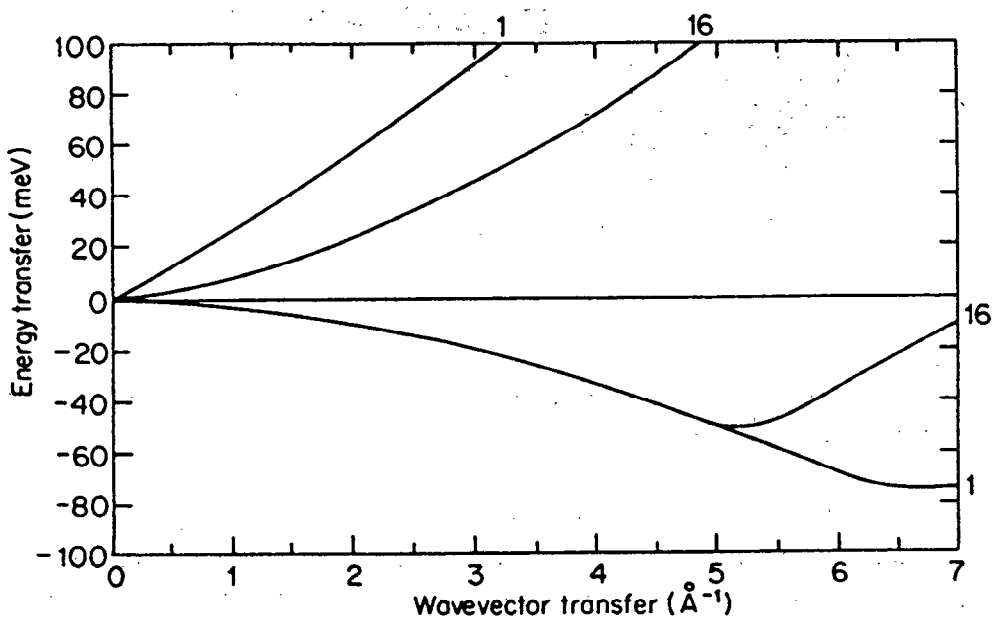

Figure 6: The possible minimum and maximum energy transfers are shown as a function of the magnitude of the wavevector transfer for the cases of 1 and 16 analyser-detector systems in use, as described in the text.

this figure applies to |Q| and that in a single crystal experiment where a particular direction as well as magnitude is required the situation may well be worse.

The second side effect of the small angular separation is that the shielding around each detector arm must be small in order to allow the arms to approach each other as close as posssible. On PRISMA we have 1mm of Cd around each detector arm. Around the whole array of arms there is a further "shielding box" of B_4C and Cd but this is not as preferable as having a significant amount of shielding around each individual detector.

These constraints could be overcome by the use of a double-bounce analyser system as schematically indicated in figure 7. In such an arrangement a change of the analyser energy would not require the detector to move. Furthermore, increasing the angular separation between the detector arms would enable us also to improve substantially the shielding around the detectors. Of course, the double reflection will lead to loss of intensity. However, by a suitable choice of analyser material this can be minimized. Obviously these intensity considerations exclude the combination Ge/Ge and mean that an HOPG/HOPG combination would be best. However an alternative combination of Ge(111)/HOPG(002) which profits from the absence of second order contamination due to the first Ge crystal without the loss of reflectivity of a second Ge crystal may also be a possibility. Although the outcoming beam from such an analyser is not parallel to the incoming beam its deviation for analyser energies greater than

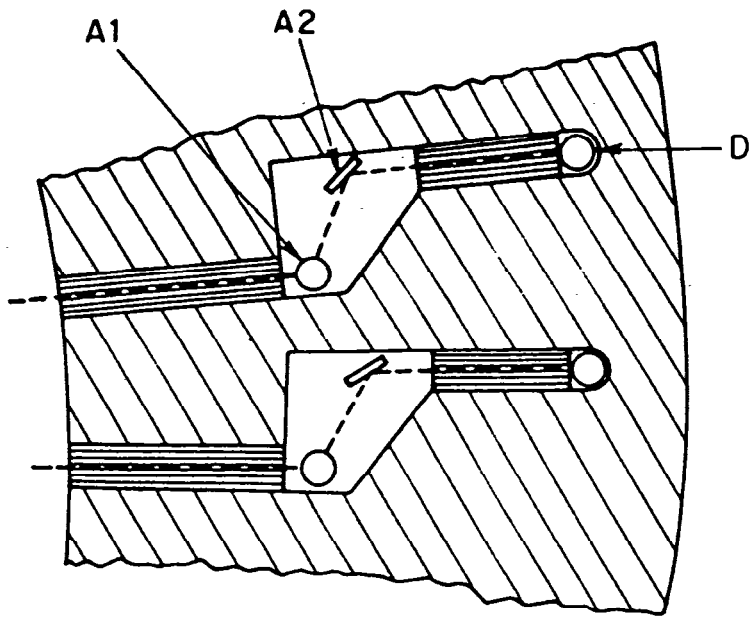

Figure 7: A schematic diagram of a double-bounce analyser system. A1 and A2 indicate the two analyser crystals and D the detector.

4 meV is less than 3°. We have started a research and development programme to study the feasibility of these ideas. The prototype of a double-bounce analyser should be ready by the end of next year and we plan to study a series of combinations of analyser crystals.

V. Conclusion

The PRISMA and MAX spectrometers have both shown that measurements of phonon or spin wave dispersion relations are quite feasible at pulsed neutron sources. This does not mean, however, that these particular spectrometers necessarily represent the ultimate design for instruments to carry out such measurements. In this paper we have described a number of ideas for improving and expanding the capabilities of the PRISMA spectrometer. These ideas are at different stages of development and their effectiveness remains to be assessed. However such is the usefulness of the information from the measurement of coherent excitations that they are certainly worth pursuing.

Acknowledgement

Our thanks go in particular to the ISIS chopper group for their support and to our colleagues at ISIS for many useful discussions.

References

[1] C.Andreani, C.J.Carlile, F.Cilloco, C.Petrillo, F.Sacchetti, G.C.Stirling and C.G.Windsor, Nucl. Inst. and Meths. in Phys. Res., A254, 333 (1987)

[2] U.Steigenberger, M.Hagen, R.Caciuffo, F.Cilloco, C.Petrillo and F.Sacchetti, Nucl. Inst. and Meths. in Phys. Res. B (in press)

[3] K.Tajima, Y.Ishikawa, K.Kanai, C.G.Windsor and S.Tomiyoshi, Nucl. Inst. and Meths. in Phys. Res., 201, 491 (1982)

Q(H.Tietze): The 30meV phonon in D_2O is only poorly separated from the elastic central line. Is that resolution of PRISMA dominated by the sample or by the instrument itself?

A(U.Steigenberger): In that case the resolution is limited by sample properties, because of disordering in the D_2O-sample.

Q(N.Watanabe): Is the D_2O sample the single crystal?

Do you think the liquid CH_4 moderator has advantage than a room temperature moderator for typical PRISMA experiments? Is time structure of neutron pulse important?

A(U.Steigenberger): Yes, the D_2O sample is a single crystal.

The time structure of the neutron pulse has certainly an influence on the resolution of the instrument. On the other side, resolution appears to vary so rapidly as a function of time of flight due to other effects that we are not too concerned about the contribution from the neutron pulse width.

Q(H.Tietze): Do you think of using a Si-multi-layer crystal as a tiny device for double analysers on PRISMA or would the intensity obtained from double-Si-analysers be too weak?

A(U.Steigenberger): It is thought of wing PG together with the existing Ge-analysers, which will them be moved independently.

Q(P.A.Egelstaff): Could you expand your statement that 1μeV resolution with 20Å neutrons is available on ISIS? For example if we wished to study the quasi-elastic peak for a polymer and its width was 1μeV, should we go to the ILL or to ISIS? Some data on counting rates, energy ranges and experimental times would be useful.

A(U.Steigenberger): For Mica 002 the energy transfer range is 90 meV, which is an order of magnitude larger than that of IN10, the lutedine data were taken in 12 hours. Of course the flux at $\lambda = 20$Å is much bigger at ILL, in particular because the ISIS moderator was not designed to provide neutrons at this wave length.

ICANS-XI International Collaboration on Advanced Neutron Sources
KEK, Tsukuba, October 22-26, 1990

Advances in Crystal Analyser Spectroscopy at ISIS

C J Carlile, U Steigenberger, J Tomkinson,
M A Adams, M Prager* and R Mukhopadhyay[x]

ISIS Pulsed Neutron Facility
Rutherford Appleton Laboratory
Chilton
Oxfordshire OX11 0QX
UK

Permanent addresses *IFF, KFA Julich, Germany, [x]BARC, Trombay, India.

Abstract

A review of the development of crystal analyser spectrometers on reactors and pulsed sources is given for both incoherent and coherent inelastic spectroscopy. The status of and developments on the three operational instruments IRIS, TFXA and PRISMA at ISIS are given. Particular attention is paid to the improvement of resolution and background in present and future generation instruments.

Introduction

Crystal analyser spectrometers have a fundamental advantage over direct geometry spectrometers because of the opposite handedness of the Q,ω locii as shown in figure 1. This means that, when studying cold samples in their excitational ground state, the neutron energy loss technique can still be employed, giving access to large energy and momentum transfer ranges, yet maintaining the instrumental resolution. The resolution can thus be decoupled from the energy transfer and the final analysed neutron energy can be very low

if high resolution is required. Since neutrons of the analyser energy need not be present with any intensity in the incident beam the development of synthetic long wavelength analysers, such as Langmuir Blodgett films, with d-spacings beyond that of natural crystalline materials, could be considered in the future.

A disadvantage of the technique however is that the full white beam travels into the spectrometer and falls onto the sample and its environment. This generates a neutron population within the analyser tank which is, perhaps, a hundred times higher than on a similar performance direct geometry spectrometer. The effect becomes more severe the higher the ratio of energy transfer range to resolution width. The problem can be overcome despite early pessimism expressed in an IAEA panel meeting in 1969:

H A Mook	"Perhaps you could use a time-of-flight spectrometer with the flight path first, then use a crystal to analyse the neutrons..."
B N Brockhouse	"I think it would be very difficult to work in the main beam with a single crystal analyser ..."
G Dolling	"It should be pointed out that you really are making things hard for yourself when you put your specimen in the main beam".

However it does mean that collimation of the incident and scattered beams must be effective and that internal shielding must be well defined and universal. Also the crystal used as the analyser itself must have a very high contrast for the desired energy neutrons compared with other energies in the incident beam. In practice this means that the ratio of the coherent elastic cross section to the sum of the coherent inelastic and incoherent cross sections must be minimised.

A significant bonus however on white beam crystal analyser instruments is that a diffraction pattern of the sample can be recorded simultaneously with the inelastic spectrum. This aids the diagnosis of structural phases when studying complex materials with multiple phase transitions and hysteresis effects such as displayed by liquid crystals. It also allows structural parameters to be linked to spectroscopic observations in the study of samples uniquely prepared in beam such as intercalates, or those which are undergoing transformations in time.

Early Instrumentation

The so-called beryllium filter spectrometer is the archetypal crystal analyser instrument. Set against the triple axis spectrometer and the direct geometry chopper time of flight instruments on reactor sources it developed a tarnished reputation to the extent that it almost attained the status of a term of abuse! This was largely due to the poor resolution, caused by the wide band pass of the filter and the poor definition of the incident energy, and the increasingly higher background as the energy transfer increased, mainly due to coherent inelastic scattering in the monochromator. Attempts to improve its performance, such as by using a chopped white-beam to sort the incident neutron energy by time of flight or by the use of filter difference techniques had only limited success.

Quasielastic and Tunnelling

The first high precision instrument in the crystal analyser class was the backscattering machine developed firstly at Munich and then at Jülich before emerging at ILL as IN10. This instrument generates its white beam (over a 30μeV window) by Doppler shifting the Bragg reflection from a silicon monochromator using a mechanical piston, and analyses the scattered beam with a very large area silicon analyser mirror in exact backscattering geometry, giving an energy resolution of 1μeV. This concept has been extended to higher momentum transfers with the design of IN13 which uses a similar geometry to IN10 but employs CaF_2 as monochromator and analyser. The white beam scan over 450μeV, is achieved by temperature cycling the monochromator.

The backscattering principle was applied to pulsed sources in the design of the IRIS spectrometer where the incident white beam is naturally present at the end of a long incident flight path. The analyser consists of a large array of graphite crystals ($1350cm^2$) in a geometry close to backscattering, giving a resolution of 15μeV over an energy transfer range of 3meV. The decision not to go to exact backscattering in the instrument design eliminated the need for a beam modulation chopper before the sample, a device used on IN10 to discriminate against neutrons scattered directly into the detector from the sample. This decision increased the expected count rate on IRIS by a factor of 4 (2.5 x 1.5) since the saving in the instrument budget was used to increase the graphite area by 50% and the chopper transmission would have been 40%. The instrument is shown schematically in figure 2.

At KENS, the development of such a high resolution instrument followed a different path involving firstly a graphite analyser instrument with an 80° take-off angle (LAM 40) followed later by a near-backscattering instrument with a 160° take-off angle (LAM 80). This has been further developed with the addition of mica analysers and the instrument is now known as LAM 80 ET.

Molecular Spectroscopy

On pulsed sources, the first appearance of a crystal analyser machine was at IPNS where a copper analyser at relatively low take-off angles was used with limited success, largely because of the moderate resolution due to the $\cot\theta$ term and the difficulty of achieving effective focussing. At KENS a fundamental improvement in the design was achieved by the realisation that a simple focusing geometry could be built which allowed the resolution line width to be preserved and the intensity to be enhanced. This geometry is shown in Fig 3. The parallel arrangement of the sample, analyser and detector bank ensures that the time of flight of neutrons from the sample to the detector is independent of the neutron energy selected at different points on the analyser. This concept has been extended in the design of the time focusing crystal analyser spectrometer TFXA at ISIS as shown in Figure 4 to include separate recording of individual detector elements and a subsequent merging in software.

Coherent Excitations

A different developmental direction again of the crystal analyser technique has led to the design of instruments on pulsed sources able to study coherent excitations in single crystals. The first such instrument was the constant-Q spectrometer installed at the Harwell linac. This utilised a large monolithic flat single crystal of germanium as an analyser, placed after the sample. Different points on the analyser select different final energies thus generating a 'constant-Q' scan in reciprocal space. At LANSCE this concept has been further developed with the separation of the analyser into a number of individually controllable cylindrical analyser crystals still with the overall geometry of a flat plate. The mosaic spread of each crystal has been separately selected in an attempt to equalise the resolution width across the scan.

At KENS a variation on this theme led to the development of a multiple analyser crystal spectrometer MAX. This idea is more flexible than the constant-Q design and enables a scan along a particular reciprocal lattice direction to be measured in one setting of the instrument. This has been further refined in the building of the joint Anglo-Italian instrument PRISMA at ISIS with its 16 individually controllable analyser detector arms. It is shown in Figure 5. Recently the rotating collimator has been replaced by a t-zero nimonic chopper to reduce further the flux of fast neutrons onto the sample.

Using a single rotating analyser and a linear position sensitive detector, the ROTAX spectrometer is being built at ISIS by a team from the University of Würzburg. ROTAX is an ambitious attempt to create the flexibility of a triple axis instrument on a pulsed source spectrometer and installation will begin in 1992.

Instrument Performances & Future Developments

IRIS

The present (January 1991) characteristics of IRIS are listed in Table 1. A set of resolutions from 1μeV to 50μeV can be accessed, each with an increasing range of Q. The energy transfer ranges with each resolution is limited by the adjacent analyser reflections. A beryllium filter, cooled to 25K, has been developed for use with the graphite (002) reflection which will increase the energy transfer range to approximately ~10meV, determined by the limit of transmission down the curved neutron guide. Furthercommissioning work is needed before this option comes into service fully.

The underlying broad feature beneath the elastic line from graphite has been positively identified as being due to thermal diffuse scattering from the analyser itself. There are two ways to minimise this. The first involves the use of collimating blades between the analyser and the detector. Unfortunately this solution will also reduce the Bragg intensity and will not affect the relative level of TDS directly under the Bragg line itself. More promising is to reduce the phonon population by cooling the analyser. Tests on IRIS show that there is a linear fall in TDS intensity with temperature down to 50K as shown in Fig 6 for an offset angle from the Bragg reflection of 4°. As a consequence a helium cooling loop is to be installed on the graphite analyser with a design temperature of 25K. When this is operational in mid-1991 the

Table 1: The Characteristics of IRIS (Jan 1991)

Analyser Reflection	Analyser λ Å	Analyser E_f meV	Energy Resolution μeV	Energy and Momentum Transfer Ranges
Mica 002	19.8	0.208	1	250 μeV to ~ 100 μeV 0.09 to 0.7 $Å^{-1}$
Mica 004	9.9	0.83	4.2	300 μeV to ~ 300 μeV 0.18 to 1.4 $Å^{-1}$
Mica 006	6.6	1.87	11	1 meV to -1 meV 0.26 to 1.88 $Å^{-1}$
PG 002	6.7	1.835	15	3 meV to -1 meV 0.25 to 1.85 $Å^{-1}$
PG 004	3.35	7.28	50	5 meV to -4 meV 0.5 to 3.7 $Å^{-1}$

background from TDS sources should improve by an order of magnitude.

Additional valves and filters have been installed in the vacuum system of the analyser tank in order to ensure that vacuum oil vapour does not condense on the graphite and intercalate between the layers.

Interestingly tests of CaF_2 on HRPD also point towards TDS effects being the cause of a similar undiagnosed broad background on IN13.

A recent major development on IRIS has been the realisation of the mica analyser array with an area of ~1500cm^2. This provides a resolution of 11μeV for the (006) reflection with a more clearly defined "moderator edge" than occurs in graphite. This suggests that mica is much more perfect, in terms of

$\Delta d/d$, than graphite and the instrument is clearly mismatched at this distance (38m) from the moderator. The optimum distance for matching is yet to be determined but at 60m the resolution would further improve by 50%.

Despite this mismatch the effective count rate from the mica (006) array is only slightly less than 50% of the count rate from the graphite (002) array. Since mica is 100 times cheaper than graphite a large area array is quite feasible. Plans are in hand to double the present area to $3000cm^2$ in the coming months.

The use of the (004) reflection at an analysing energy of 830μeV (λ = 9.9Å) gives an improvement of elastic resolution to 4.2μeV. The intensity of the elastic line is only about 2.5 times lower than for the (006) reflection and is quite feasible to use. Run times of the order 6-10 hours are necessary.

The (002) reflection gives a resolution of 1.0μeV over a wide energy transfer range, as shown in Figure 7. The practical use of this option has been limited up to now because of the 50Hz pulse repetition rate on ISIS. A second pulse leaves the moderator before the 20Å neutrons destined for the mica (002) reflection reach the band pass chopper at 6.4m. Accordingly a second band pass chopper is presently being installed at 10m which should be operational for the first cycle of 1991. The use of 20Å neutrons should then be routine. It does appear that we have underestimated the intensity of long wavelength neutrons in our incident spectrum and the 10 metre chopper should improve the general background in the spectrometer even when working at shorter wavelengths. Because of the low Q range observed ($0.07Å^{-1}$ to $0.7Å^{-1}$) this will facilitate the measurement of translational diffusion. Its use for tunnelling spectroscopy is still to be explored - the low Q will be a disadvantage in this case. Plans to study crystal field excitations where the low Q is a positive advantage are in hand.

Mica, as an analyser, offers great promise which has yet to be fully realised. Little is known about its neutron reflecting properties and more development work is required. The value of $\Delta d/d$ for the various chemical isomorphs is unknown and the optimum thickness for maximum reflectivity and minimum background has not been explored. A full survey of the various varieties has yet to be carried out. Nevertheless it is clearly a material worthy of more study. Interestingly it is now being considered as a long wavelength monochromator for IN6 in order to improve the resolution.

On the data analysis side progress has been made in the implementation of maximum entropy techniques for the deconvolation of inelastic spectra. Using the MEMSYS code developed at Cambridge we have been able to deconvolute features in the tunnelling spectrum from lutidine using the graphite (002) analyser data which have subsequently been experimentally observed using the mica (004) analyser. This data, in turn, has been deconvoluted to reveal further structure which, once again has been confirmed in measurements on IN10 using an offset monochromator. In order to obtain reliable results the resolution function of the instrument must be known precisely, as well as its variation with energy transfer. The data and deconvolutions are shown in figure 8. Obviously, until much more experience has been accumulated, the use of the maximum entropy technique will be initially used as a guide to further, higher resolution measurements. However, once confidence has been generated, and the results accepted by the community, it will find universal acceptance in the field of inelastic spectroscopy.

TFXA

The time focussing crystal analyser spectrometer TFXA illustrated in figure 4, has been operational for over five years. During that period it has undergone continous development within the limits imposed by the monolithic design of the analyser shielding tank. It has been established that thick samples may be used, with scattering probabilities as high as 40% of the incident beam, without seriously compromising the spectral quality. The original graphite analysers have been replaced by a more relaxed mosaic spread set of greater thickness. This has increased the detected count rate by a factor of 4. The original detector bank has been replaced with high pressure squashed 1.2cm helium-3 tubes which has improved the instrumental resolution. At the same time substantial reductions in background have been achieved. The quality of the spectra generated on TFXA has moved molecular spectroscopy beyond a threshold and into a region where individual modes can be well-resolved and the effects of lattice modes and multiphonon events can be quantified. This is illustrated in figure 9 where the spectrum from the 72 atom molecule nicotinamide adenine dinucleotide at 30K is shown. As a consequence of this improved spectral quality much recent progress has been made in implementing an iterative data fitting algorithm CLIMAX which uses a generalised molecular force field model to refine the dynamical model of the molecule and its crystalline surroundings. Molecular spectroscopy with neutrons has entered a stage in the quantitative analysis of data which resembles that experienced by powder diffraction in the late 1970's with the advent of Rietveld refinement.

A major development on TFXA in the forthcoming few months will be the installation of a prototype mica analyser replacing one of the graphite analyser arrays. Higher order contamination will be removed with a cooled polycrystalline graphite filter in place of the present beryllium filter. Using the mica (004) reflection it is expected that the resolution of the instrument at energy transfers up to 100meV will improve by approximately 50%.

Separate papers in this conference deal with the PRISMA and ROTAX projects and the reader is referred there for more details.

Future Plans for New Instruments

Operational experience in the past few years has put us in a strong position to capitalise on the advances achieved with the first generation instruments and their developments. It is clear that high resolutions can be obtained quite readily on pulsed source instruments and that scientific advances follow such improvements in resolution. Equally well the original designs were somewhat conservative being designed without the benefit of today's experience.

Therefore in laying down plans for future instruments the direction is clear. We must further improve resolution and range. The improvement of intensity, for its own sake, is of limited value.

Accordingly plans have been drawn up to separate the high and medium resolution options of IRIS into two instruments on twin guide tubes from the same beam hole. IRIS-2 will be a spectrometer which seeks to optimise the use of mica with resolutions improved by a factor of 2 and employing very large area analysers in order to utilise to the full the plentiful supply of cold neutrons from the hydrogen moderator. IRIS-1 will contain the cold graphite analysers, increased in area by a factor of two. The space released by the present mica analyser will be used to install a large position sensitive diffraction detector for long d-spacing diffractometry up to 30Å with high intensities and a resolution $\Delta d/d$ of 2.5×10^{-3}.

Molecular spectroscopy will be further advanced by the construction of an instrument, Cassandra, having 0.3% resolution in energy transfer, a factor of 3 better than currently available, over a range from 5 meV to 100meV. Cassandra will use a large area mica analyser in near backscattering geometry on the end of a 60 metre long curved supermirror guide.

The experience gained on PRISMA in the last two years is already indicating the scientific value of surveying coherent excitations over a two-dimensional net. Tests of a prototype dog-leg double analyser, currently in the design stage, will indicate the optimum layout for PRISMA-2 which it is hoped to define by 1992.

Acknowledgements

We are grateful to Professor R E Hester of York University, Dr F Fillaux, CNRS, Thiais and Dr R N Silver, LANL for the use of their results prior to publication.

Figure Captions

Fig 1. The Q,ω locii for direct and inverted geometry spectrometers with a defined energy, either E_i or E_f, of 1.8meV as a function of neutron energy transfer $E_i - E_2$. The dashed line is the locus for an inverted geometry instrument and the full line is that of a direct geometry machine.

Fig 2. A cut away view of IRIS the backscattering instrument at ISIS showing its dual arrays of graphite and mica analysers.

Fig 3. The time focusing geometry for the crystal analyser spectrometer first implemented at KENS.

Fig 4. A schematic view of TFXA the time-focused crystal analyser spectrometer at ISIS.

Fig 5. The 16 analyser-detector instrument PRISMA at ISIS.

Fig 6. The effect of cooling on the thermal diffuse scattering from graphite around the (002) reflection. The crystal has been offset 4° from the Bragg position. The inset shows the integrated intensity in the phonon "wings" as a function of temperature.

Fig 7. The observation of 1μeV resolution on IRIS using the mica (002) reflection at an analysing wavelength of 19.8Å. Note the wide energy transfer range.

Fig 8. Data and deconvolutions of tunnelling spectra in 2,6 lutidine on IRIS and IN10: (a) Data and deconvoluted image from PG(002) analyser (b) Data and deconvoluted image from Mica (004) analyser (c) Deconvoluted image as in (b) and data from IN10.

Fig 9. The molecular spectrum of nicotinamide adenine dinucleotide at 30K measured on TFXA.

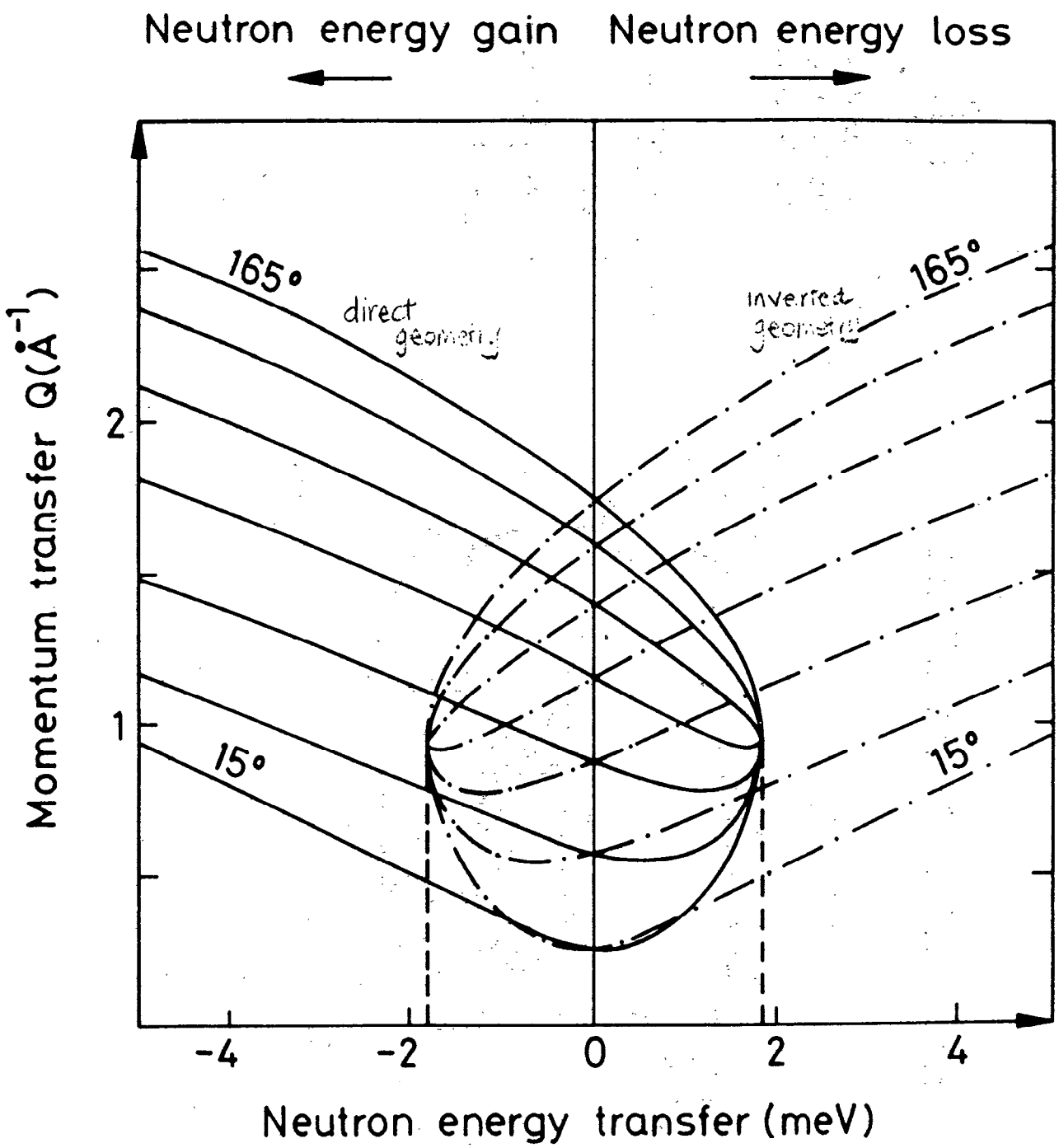
Neutron energy gain
Neutron energy loss
Momentum transfer Q(Å^{-1})
2
1
165°
15°
direct geometry
inverted geometry
165°
15°
-4
-2
0
2
4
Neutron energy transfer (meV)

FIGURE 1

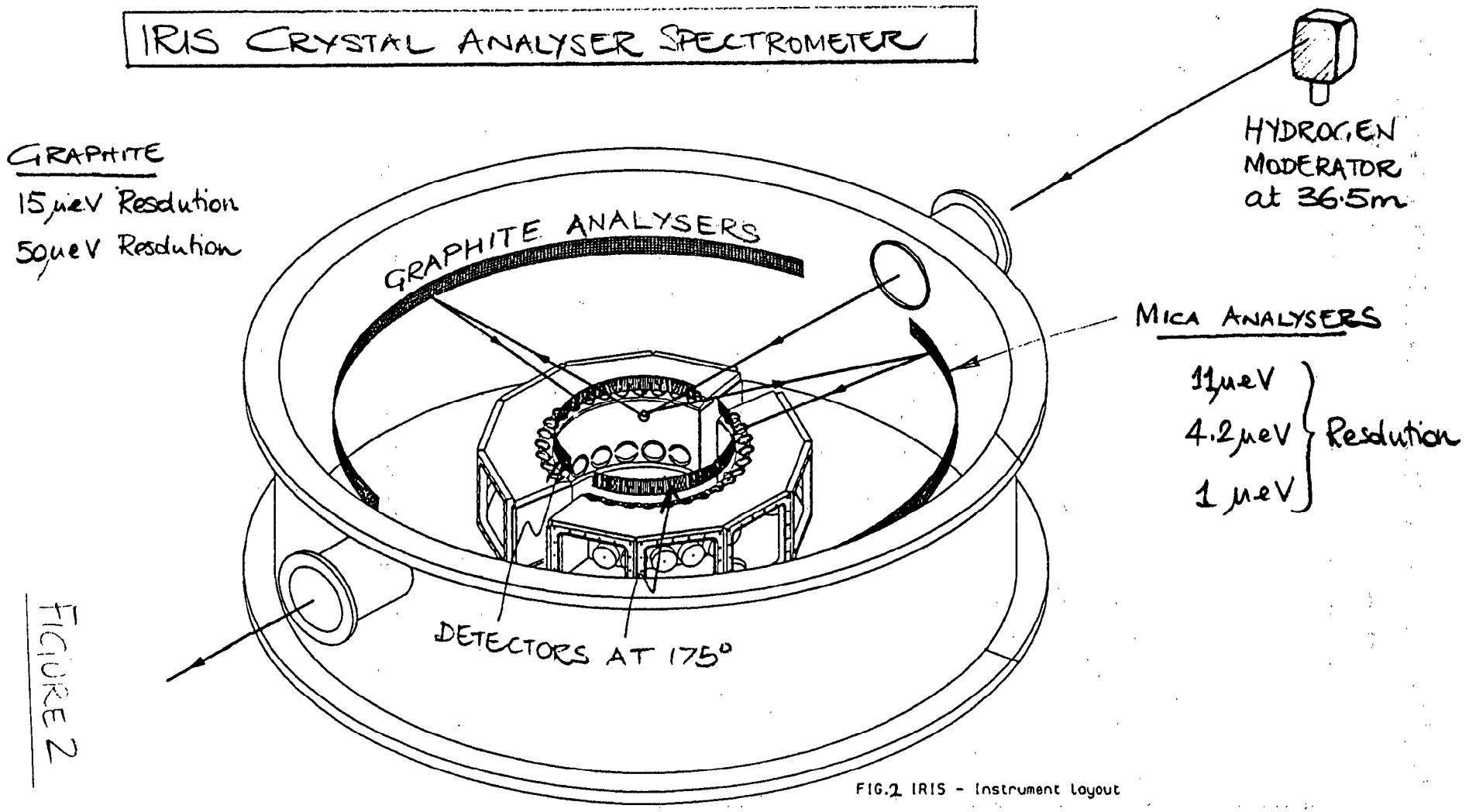

FIG.2 IRIS - Instrument layout

FIGURE 2

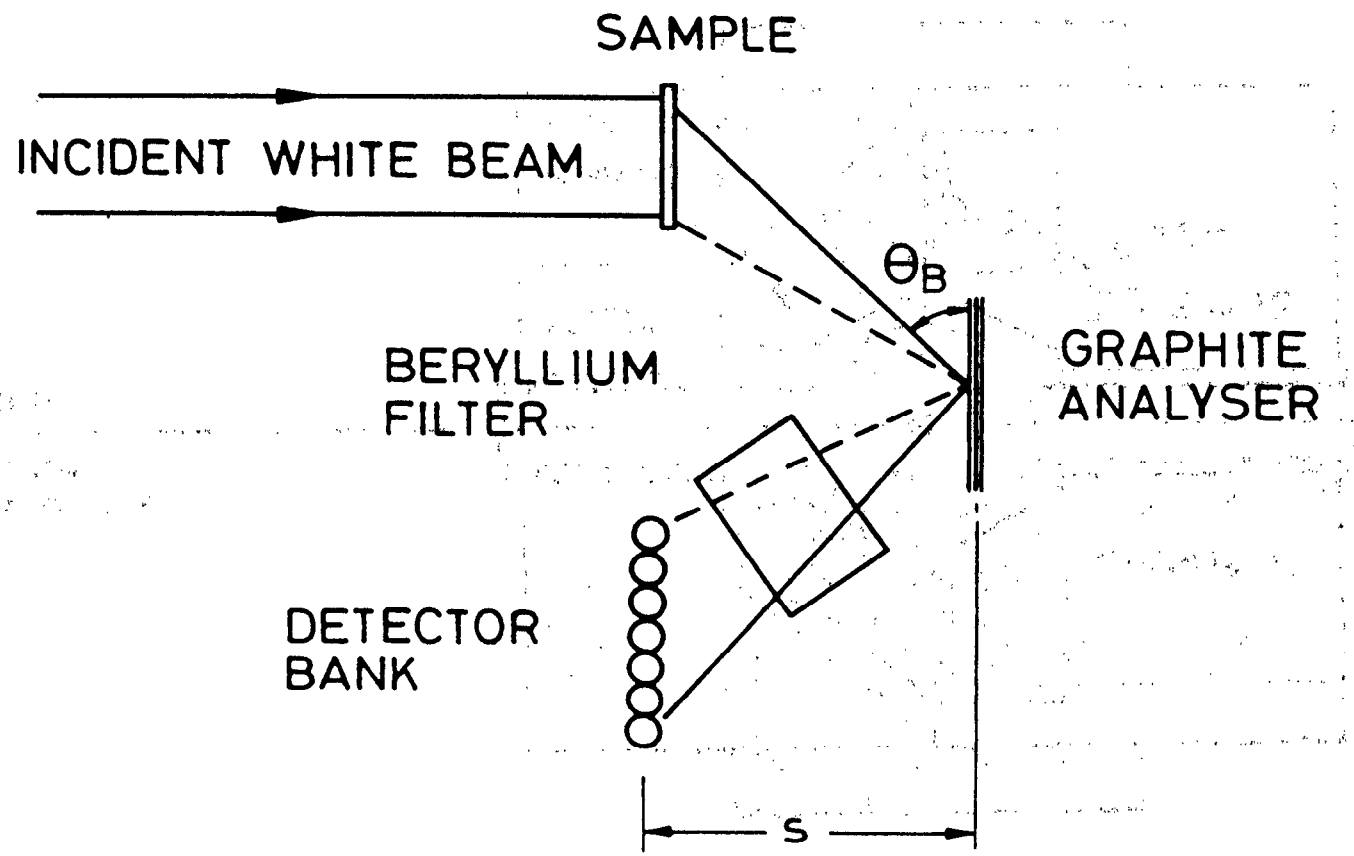
SAMPLE
INCIDENT WHITE BEAM
Θ_B
BERYLLIUM FILTER
GRAPHITE ANALYSER
DETECTOR BANK
S

FIGURE 3

TIME FOCUSSED CRYSTAL ANALYSER SPECTROMETER

$\Delta E/E \sim 1.5\%$ $E_1 = 5$ meV to 2000 meV

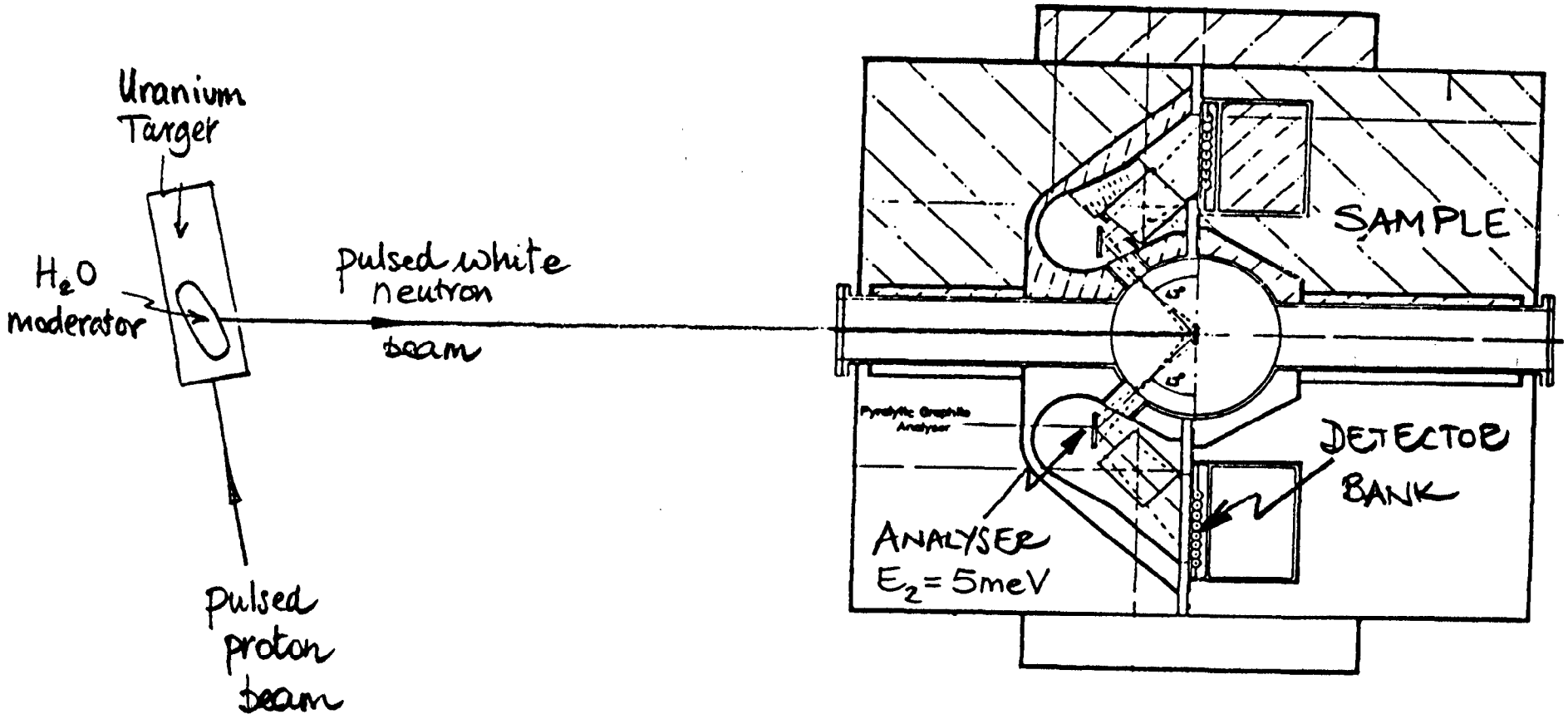

FIGURE 4

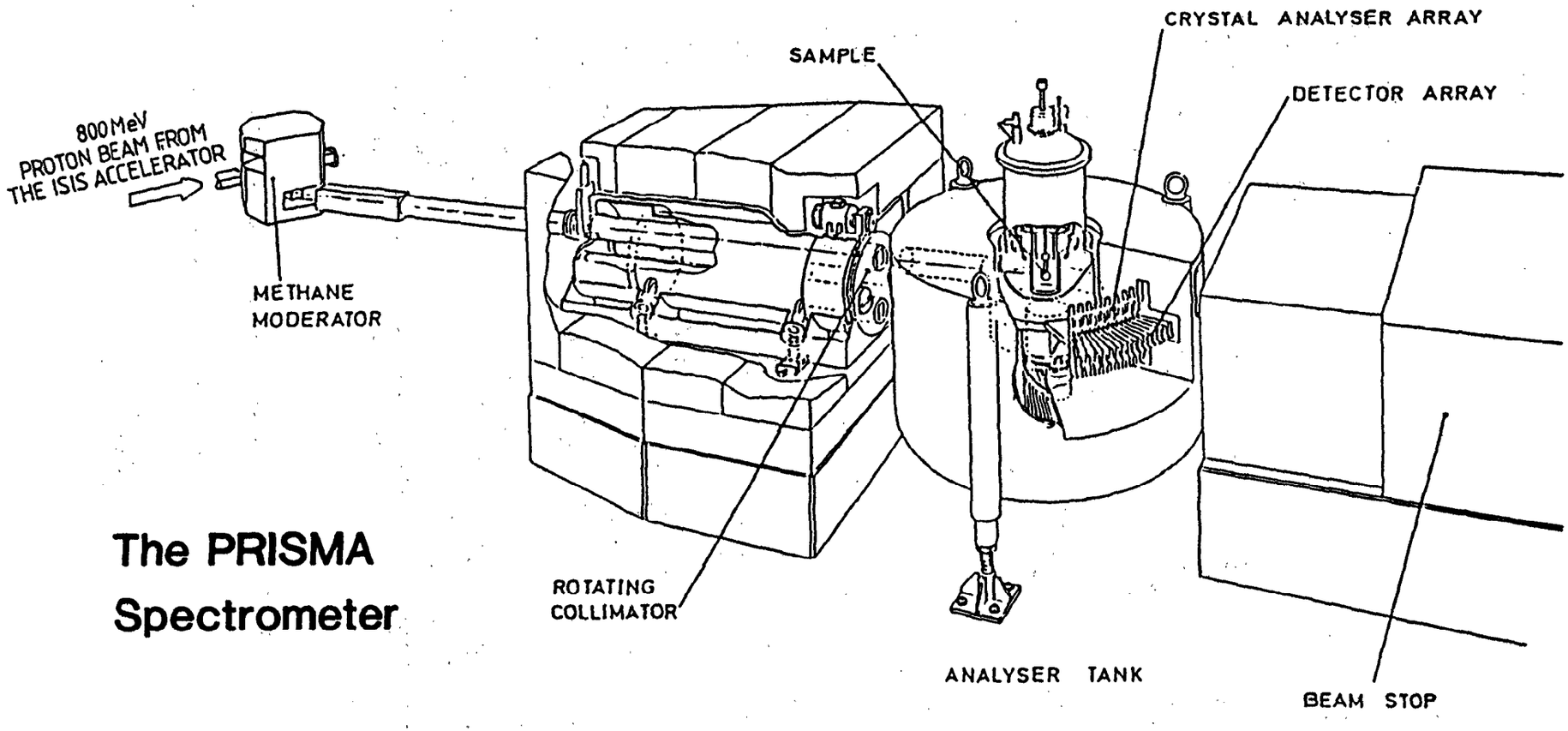

The PRISMA Spectrometer

FIGURE 5

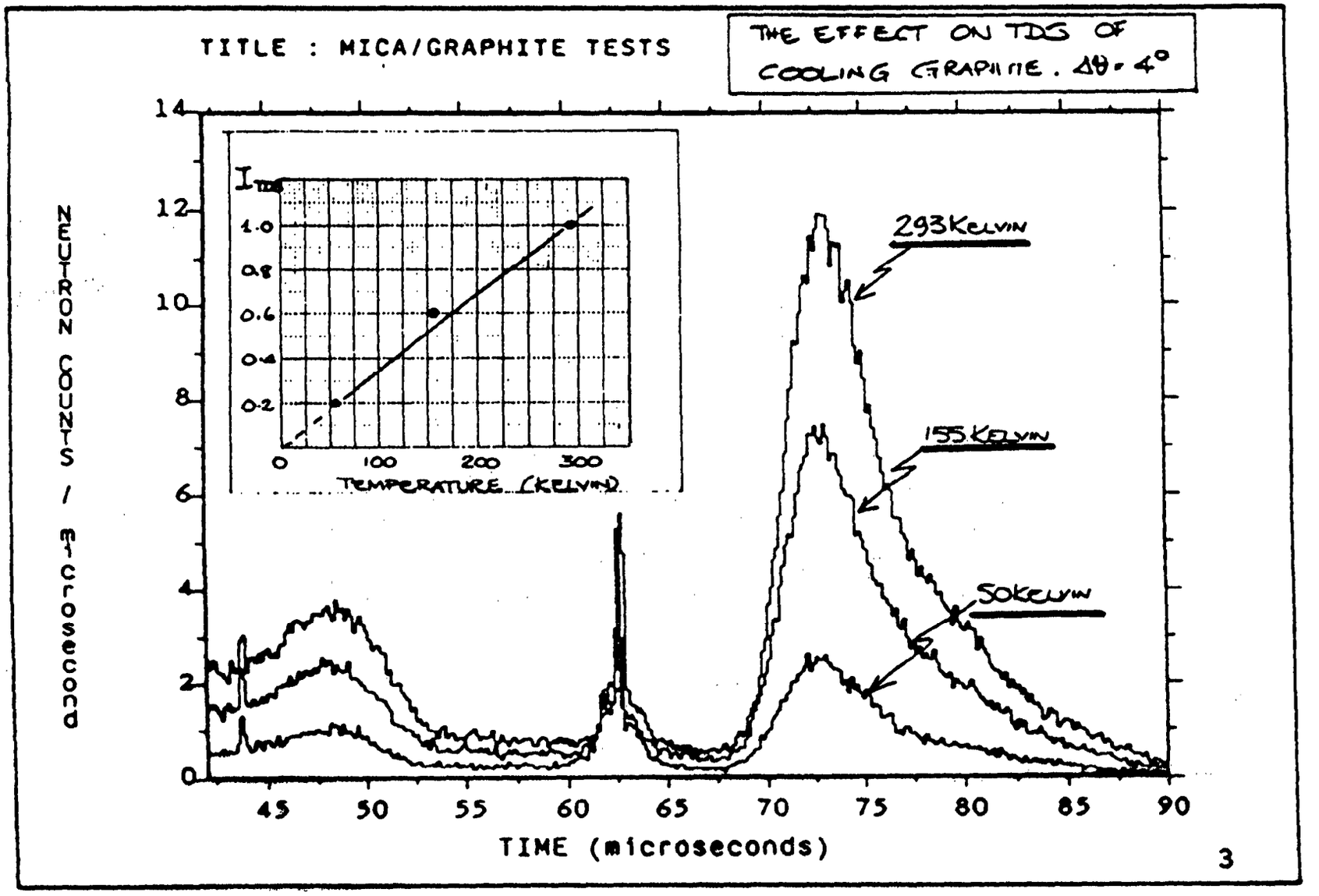
TITLE : MICA/GRAPHITE TESTS
THE EFFECT ON TDS OF COOLING GRAPHITE. Δθ = 4°
293 KELVIN
155 KELVIN
50 KELVIN
NEUTRON COUNTS / 5 microseconds
TIME (microseconds)
TEMPERATURE (KELVIN)
0
100
200
300
0.2
0.4
0.6
0.8
1.0
0
2
4
6
8
10
12
14
45
50
55
60
65
70
75
80
85
90
3

FIGURE 6

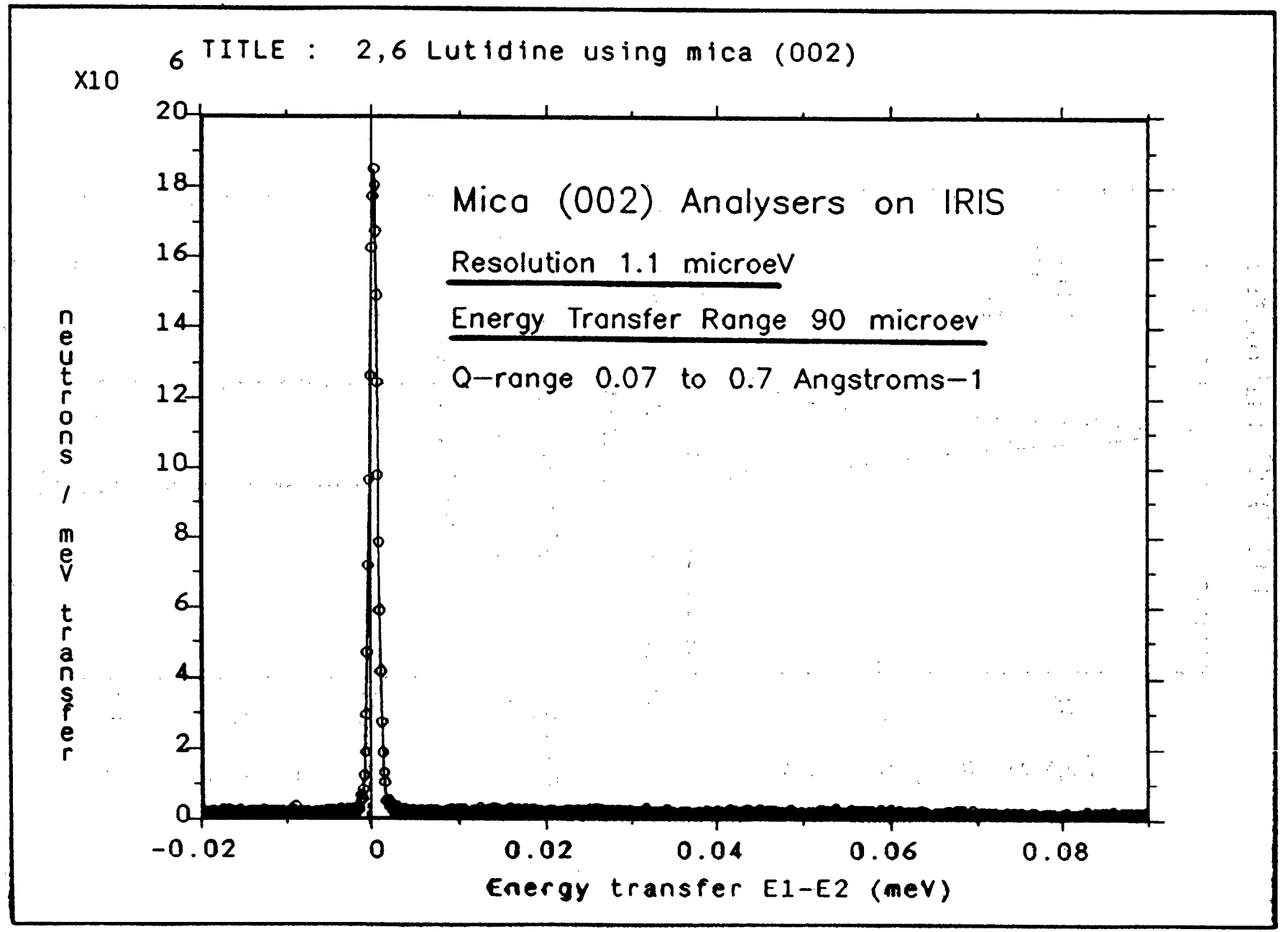
TITLE : 2,6 Lutidine using mica (002)
X10 6
Mica (002) Analysers on IRIS
Resolution 1.1 microeV
Energy Transfer Range 90 microev
Q-range 0.07 to 0.7 Angstroms-1
neutrons / mev transfer
Energy transfer E1-E2 (meV)
20
18
16
14
12
10
8
6
4
2
0
-0.02
0
0.02
0.04
0.06
0.08

FIGURE 7

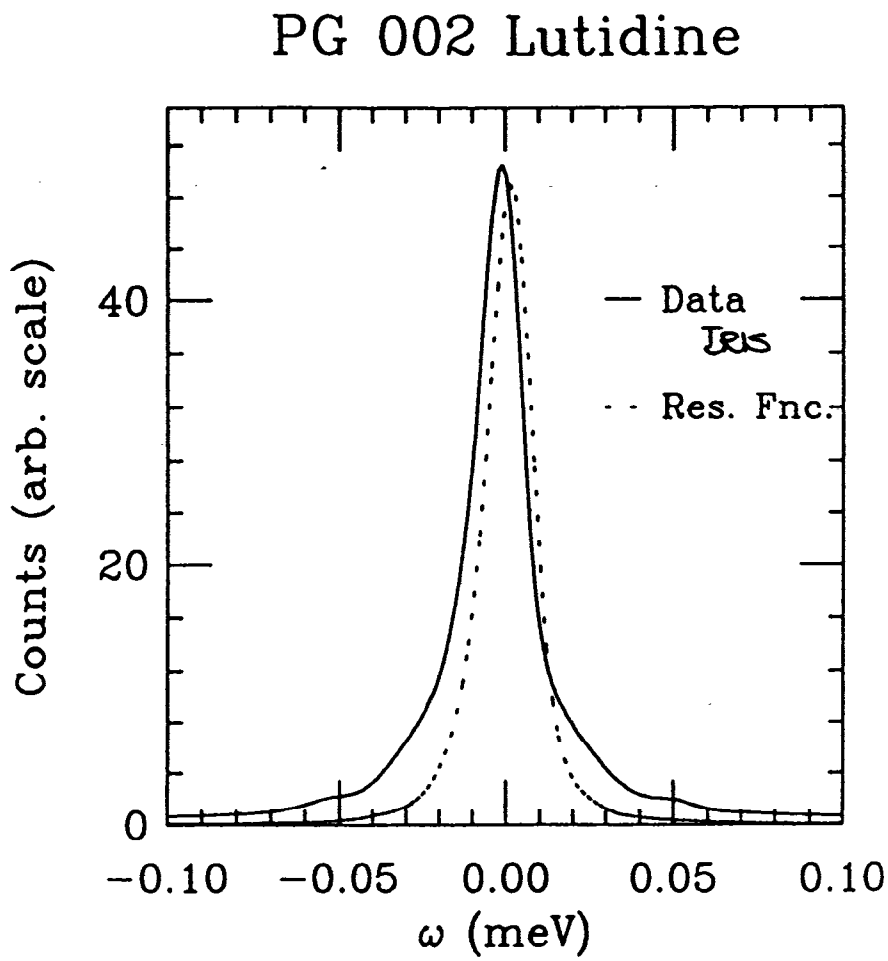

FIGURE 8(a) Lutidine PG002

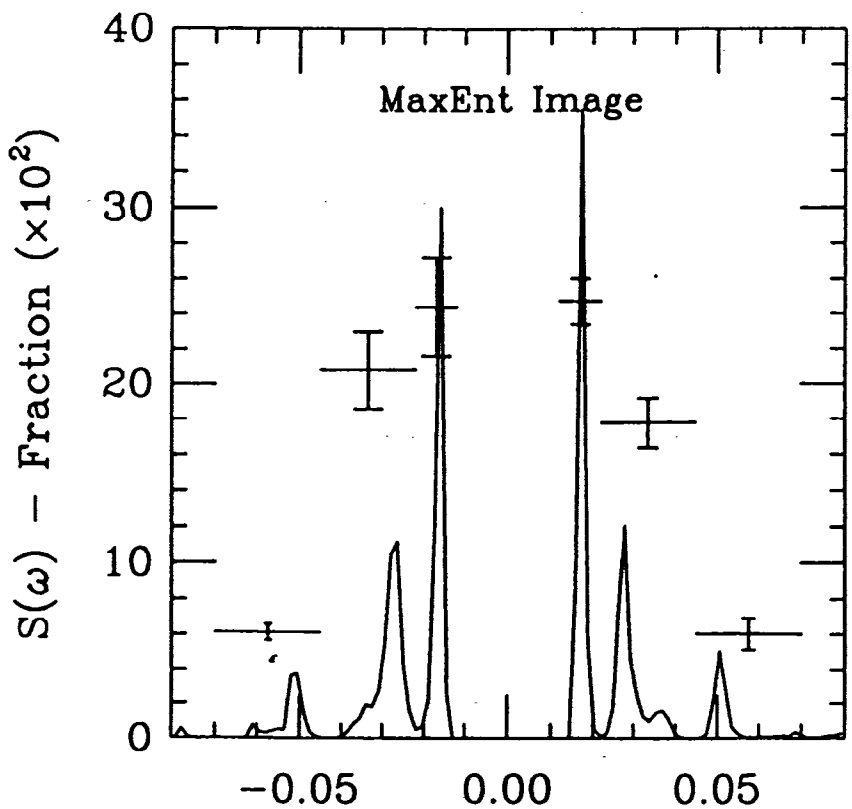

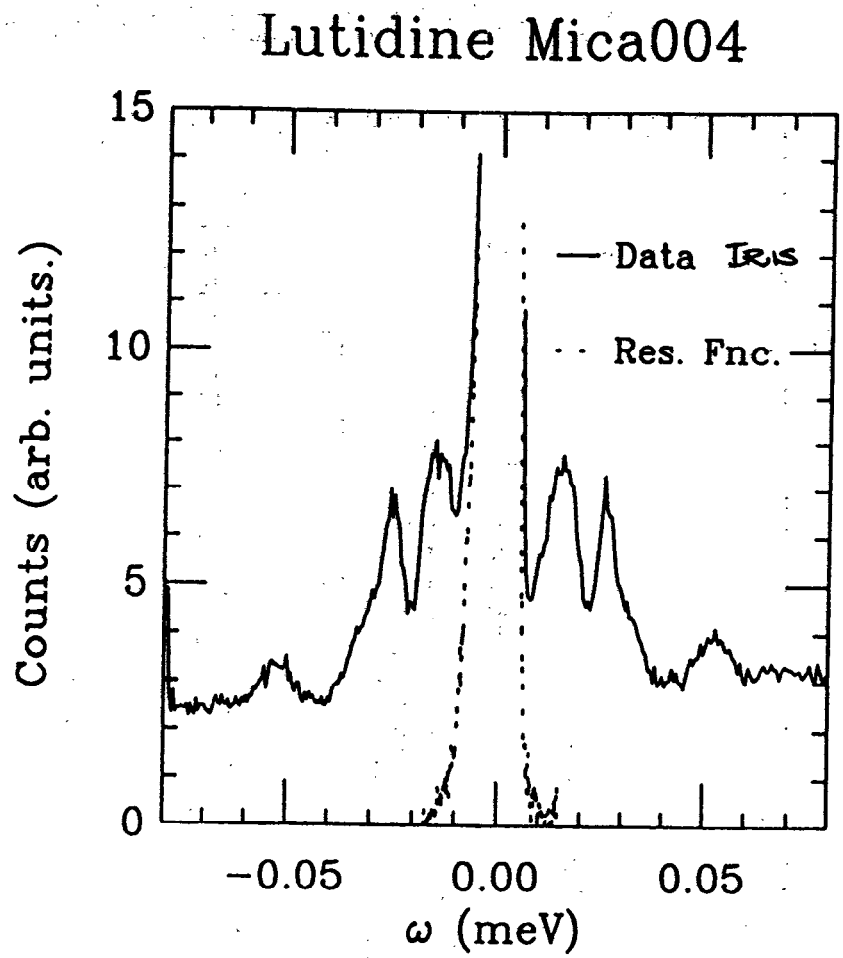
Lutidine Mica004
Data IRIS
Res. Fnc.
Counts (arb. units.)
15
10
5
0
−0.05
0.00
0.05
ω (meV)

FIGURE 8(b)

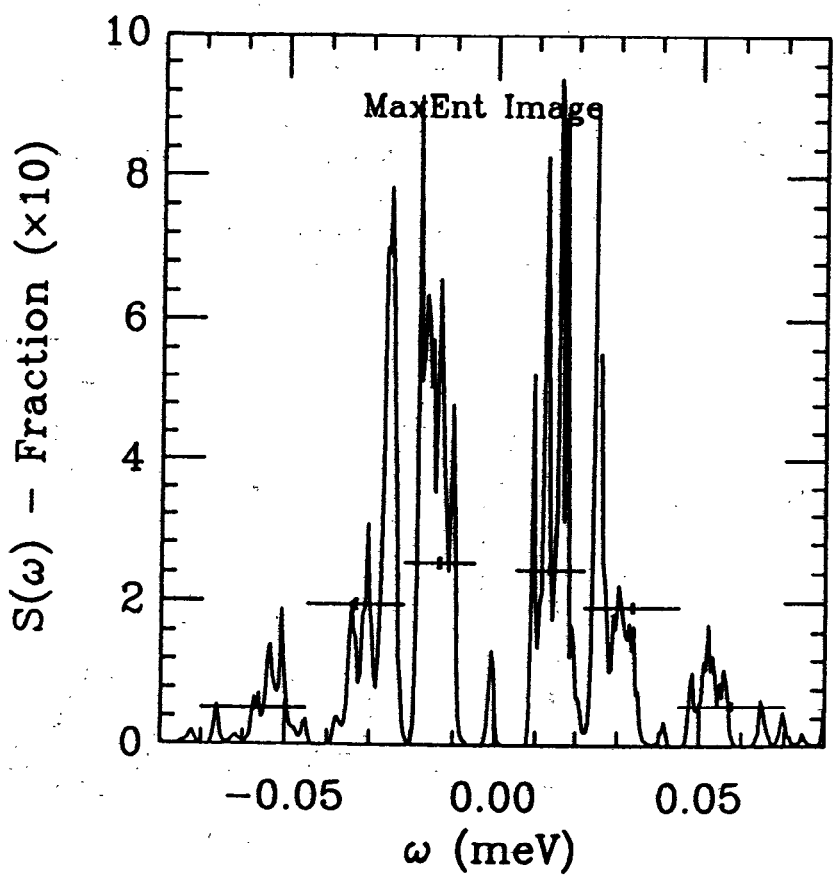
Lutidine Mica004
MaxEnt Image
S(ω) - Fraction (×10)
10
8
6
4
2
0
−0.05
0.00
0.05
ω (meV)

Lutidine Mica004

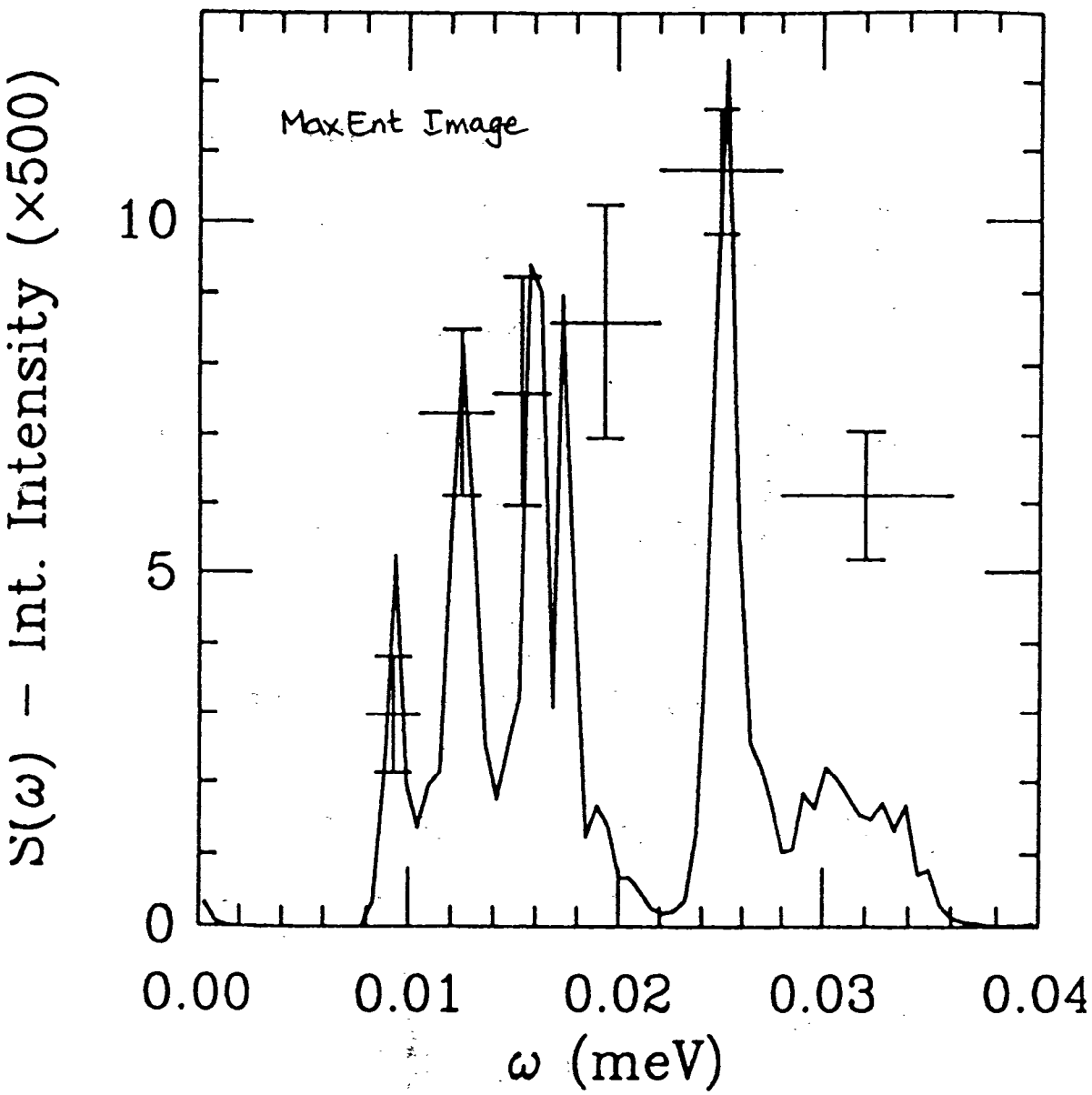

FIGURE 8(c)

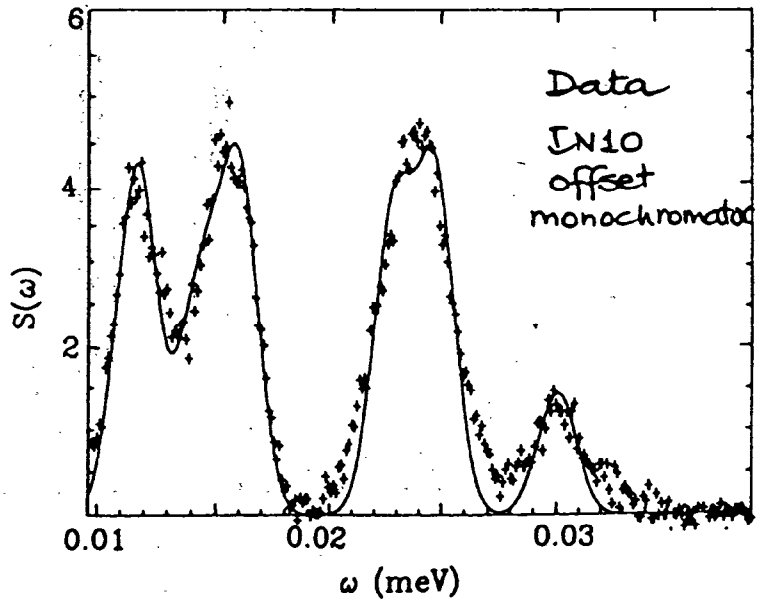

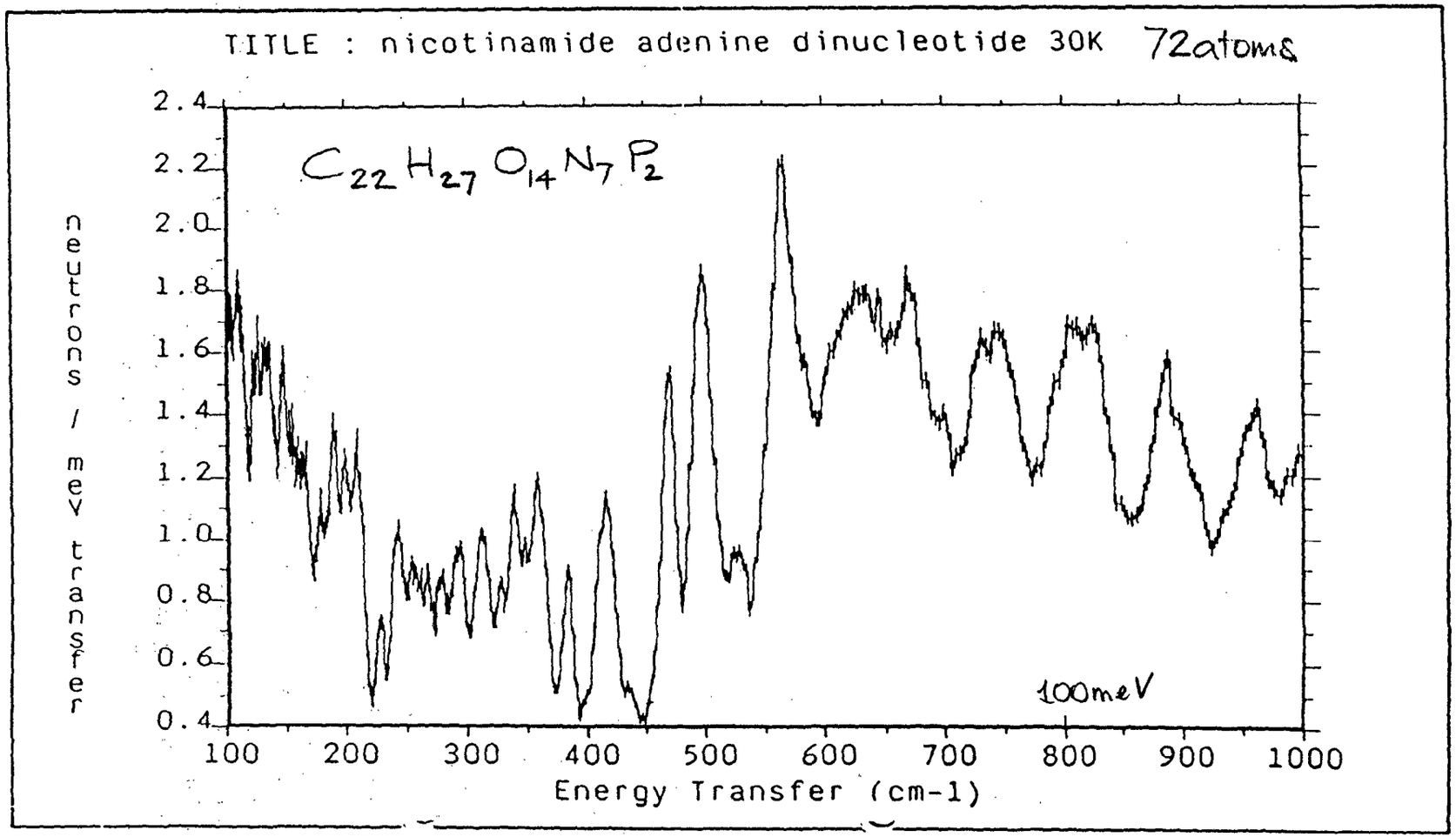
TITLE : nicotinamide adenine dinucleotide 30K
72atoms
$C_{22}H_{27}O_{14}N_7P_2$
100meV
neutrons / mev transfer
2.4
2.2
2.0
1.8
1.6
1.4
1.2
1.0
0.8
0.6
0.4
100
200
300
400
500
600
700
800
900
1000
Energy Transfer (cm-1)

FIGURE 9

ICANS-XI International Collaboration on Advanced Neutron Sources
KEK, Tsukuba, October 22-26, 1990

NEUTRON SCATTERING ON ROTAX

H. Tietze [a,b], W. Schmidt [a], R. Geick [a], U. Steigenberger [c], H. Samulowitz [d]

a) Physikalisches Institut der Uni Würzburg, Am Hubland, 8700 Würzburg, F.R.G.
b) IFF der KFA Jülich, Pf 1913, 5170 Jülich, F.R.G.
c) Neutron Division Rutherford Appleton Lab., Chilton, U.K.
d) HEWATT GmbH, Am Hahnenkreuz 46, 5190 Stolberg-Dorff, F.R.G.

Successful coherent inelastic and elastic neutron scattering on ROTAX !

ROTAX is an inverted time-of-flight spectrometer for neutron inelastic scattering of single crystals at ISIS. Its particular technical highlight is the performance and utilisation of its nonuniformly rotating crystal analyser, which is time synchronised with the neutron source. However, the parameters determining a particular mode of operation or time-of-flight scan through (Q,ω)-space are, in general, kept free with respect to the individual demand of the experimentalist. The user of the instrument may thus program his personal particular scan, providing much more flexibility and versality for an inelastic coherent scattering experiment at a pulsed spallation source taking advantage of the time structure and utilising not only the average neutron flux.

At realistic conditions of the geometry and neutron optics, prototypes of the ROTAX spectrometer have been critically andfirmly tested on the S9 test beam facility at ISIS, in order to confirm and prove the ability and stability of the technical design of the ROTAX-analyser drive.

Throughout this paper we shall concentrate on the results of these test experiments with the ROTAX analyser drive, particularly on elastic and inelastic neutron scattering at an aluminium single crystal, where acoustic phonons have been measured directly in longitudinal and transverse polarisation. Precursory alignment of the test apparatus will be explained and the intensity performance of the ROTAX "lighthouse mode" will be discussed in comparison to the PRISMA-mode of a non-spinning idle analyser as used in conventional TOF-X spectrometers.

I. Introduction

ROTAX stands for rotating analyser crystal spectrometer which is a highly flexible time-of-flight neutron spectrometer of inverted geometry with one single crystal analyser. By means of a user defined, programmable non-uniform rotation of the analyser crystal several types of scans in (Q,ω)-space can be performed [1], e.g. const.-energy or const.-$\vec{Q}/Q$ scans. The scope of the instrument will be neutron inelastic scattering investigations on collective excitations of single crystalline samples. In some sense ROTAX will compete with triple axis spectrometers at reactor thermal beam lines and of course with conventional TOF-crystal analyser spectrometers installed at pulsed spallation sources, e.g. with the Constant-Q spectrometer at LANCE [2] and with the high-symmetry spectrometers MAX at KENS [3] and PRISMA at ISIS [4,5]. As discussed earlier [6] the major advantage of ROTAX in comparison to the above mentioned spectrometers is to provide the user with an instrument with a much higher degree of flexibility in the choice of scans. Thus, ROTAX will quite considerably improve the work in the field of single crystal collective excitations at pulsed sources. Set-up and optimisation of ROTAX scans with respect to the analyser-motor performance have been discussed earlier [7]. A detailed description of technical ROTAX concept, the electronic control of the regulation loop, the feed-back, logic and hardware configuration is also given in [7].

The basic idea of the instrument is to analyse by Bragg reflection all the neutron energies being scattered during one ISIS pulse from a sample placed in a white pulsed beam. During the neutron flight time between the moderator and the sample, the neutron pulses will disperse in energy and time (cf. fig.1).

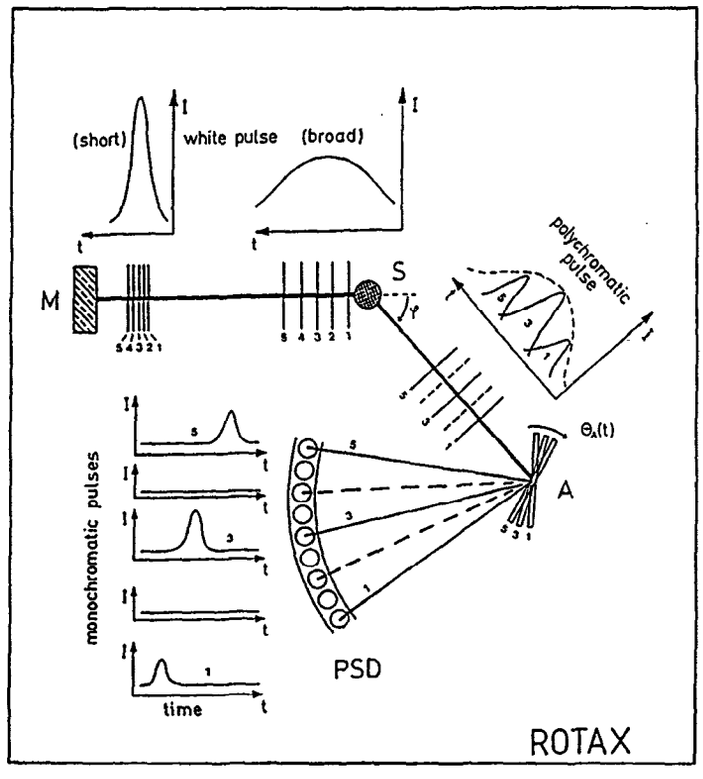

Fig. 1. Schematic diagram of ROTAX and neutron the pulse propagation.
M: moderator, S: sample, A: analyser, PSD: detector.

According to the scattering function of the sample, the neutrons will then be scattered within a certain solid scattering angle ϕ into polychromatic sequences of neutron packages, which will reach the analyser crystal consecutively after a well defined time-of-flight. If the analyser crystal is then positioned at the appropriate time to a Bragg angle $\Theta_A(t)$ corresponding to the scattered neutron energy, it will scatter this particular neutron package into a wide angle position sensitive detector. The scattering equations involved have been determined earlier [1]; the scattering angles ϕ and $\Theta_A(t)$ and the total time-of-flight t_0 determine the energy and momentum transfer of the neutrons unambigously. In order to detect several (ideally all) of the scattered neutron energies, it is essential to turn the analyser crystal in an accelerated, non-uniform spinning mode which must be synchronised with the time structure of the neutron pulses. There is not one general function of analyser motion, but it rather varies from one scan through (Q,ω)-space to another depending on the initial scan parameters as being defined by the experimentalist.

II. Experimental set-up

The ISIS test beam facility on the S9 beam line viewing the solid methane moderator has been used to perform first neutron scattering experiments with a provisional prototype of the ROTAX spectrometer. The purpose of these test experiments was to basically demonstrate the capability and flexibility of the ROTAX principle. It was further to firmly test the prototype and our technical concept of the heart of ROTAX, the control of its synchronised analyser motor. Minimum effort was put on all the other spectrometer components of the test assembly, such as beam collimation, shielding, goniometer drive and automatisation, data aquisition and detector electronics, in order to keep them as simple and as cheap as possible.

An aluminium single crystal has been used as a sample for the tests and was placed with its (001) scattering plane directly into the white pulsed neutron beam at L_i = 12.08 m incident flight path. A cylindrically shaped Germanium single crystal of 1.2 cm diameter and 5 cm height has been used as Bragg-analyser of the scattered neutron energies. It was mounted on the ROTAX analyser motor shaft, well balanced and well oriented with its <110> crystallographic axis parallel to the rotational motor axis. Its nutation amplitude has been measured to be less than 20 μm. 10 ^{3}He gas tube counters, grouped in two arrays of 5 counters each, have been used as neutron detectors combined with standard RAL data acquisition electronics. The two detectors arrays and the ROTAX motor equipped with the Ge-analyser was then mounted on a double pivoting arm centered around the sample position. The reason for grouping the detectors within two arrays was to achieve sufficient angular resolution within each array in order to demonstrate the essential capability of ROTAX: i.e. to scan at least two time channels (or neutron energies) quasi-simultaneously within one frame of the neutron pulses. Fig. 2 illustrates schematically the geometric set-up, whereas the essential geometric parameters are compiled in tab. 1. As part of detector tests, one unit of the high resolution ^{6}Li-glas szintillator detector bank JULIOS [8] has been used to specify details for the final detector decision for ROTAX. The JULIOS bank and its total data aquisition electronics was a loan from the powder diffractometer SV7 at the DIDO reactor at KFA Jülich, and it was especially equipped with a suitable time analysis system of at least 12 μsec time resolution in an adjustable 8 bit wide time window.

Tab. 1.: Test beam parameters as used for ROTAX test assembly:

sample	Al single crystal	analyser plane:	
		Ge-(400)	d_A=1.414 Å
sample shape	cylindrical 3.7 cm ∅, 4.8 cm height	Ge-(220)	d_A=1.999 Å
		distances:	
sample orientation	<100> x <010> in scattering plane	moderator to sample	L_i=12.08 m
		sample to analyser	L_a=0.595 m
		sample to detector (He)	L_f=0.585 m
analyser	Ge single crystal	sample to detector (Julios)	L_f=0.368 m
analyser shape	cylindrical 1.2 cm ∅, 5 cm height	beam size at sample	3.5 x 3.5 cm^2
		primary collimaion	natural in-pile
analyser orientation	<100> x <011> in scattering plane	secondary collimation	none
		range of:	
analyser mosaicity	$\eta \approx 1°$	scattering angle ϕ:	0° - 100°
		analyser angle Θ_A:	-20° - 110°

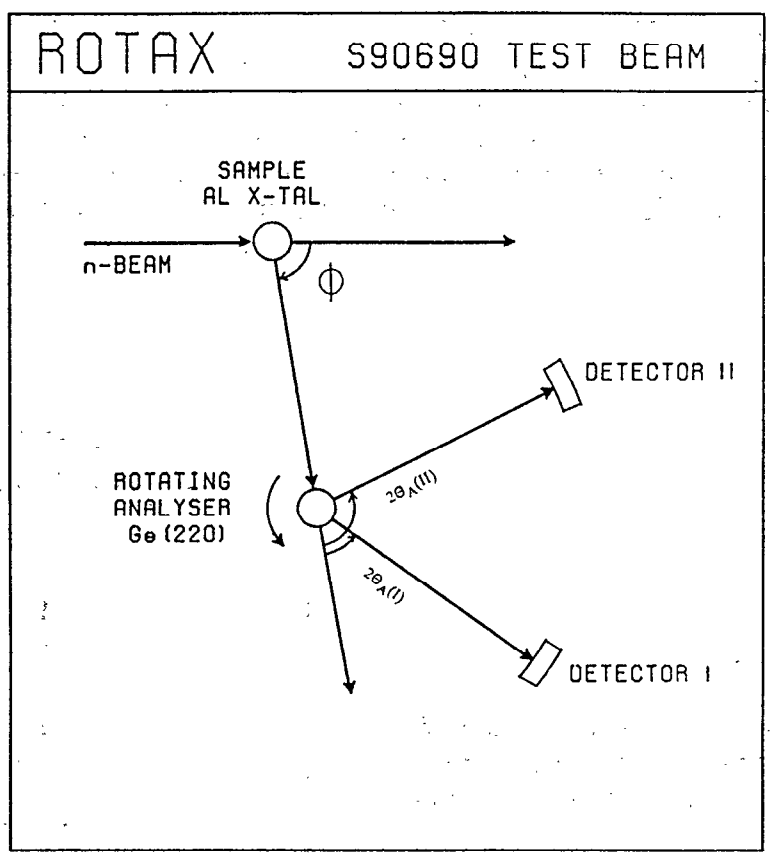

Fig. 2: geometric set-up of ROTAX test assembly.

III. Calibration, Alignment and Background

Mechanical uncertainties and misaligments in the spectrometer flight paths and especially in the angular setting of the scattering angle ϕ and detector angle $2\Theta_A$ with mechanical protractors, had to be determined and gauged. The in-pile neutron flight path was determined by resonance absorption technique, where an auxiliary detector was put to the sample position to measure the incident time-of-flight of the 4.280 eV and 10.360 eV neutron energies being absorbed by a lead foil, placed directly in the white incident beam. The secondary flight paths could be measured directly with sufficient accuracy. Hence, the effective scattering angle ϕ as well as the detector angle $2\Theta_A$, were obtained straight foreward from neutron Bragg diffraction:

$$2\,d\sin\theta = \lambda = \sqrt{K_0 / E} = \sqrt{2K_0 / m_n}\;\; t_0 / L_0 \qquad (1)$$

with $K_0 = h^2/2m_n = 81.8054$ Å^2·meV, L_0 and t_0 the total flight path and total time, $m_n = 10.4541$ meV·msec^2·m^{-2} the neutron mass and E, λ the neutron energy and wavelength. d is the lattice spacing of the Bragg plane under consideration and θ the half of the Bragg scattering angle. Thus, ϕ is gauged by Bragg diffraction from the Al-sample ($\theta = \phi/2$), whereas the detector angle $2\Theta_A$ is gauged by placing the Ge-analyser on top of the ROTAX motor into the direct neutron beam ($\theta = 2\Theta_A/2$). This diffraction mode of ROTAX was also used to lign-up the Al-sample and Ge-analyser crystal and to determine the offset values and zero setting of the ϕ- and $2\Theta_A$- circles, respectively (cf. fig. 3).

The Bragg pattern of a Ni-powder sample has been used to calibrate and normalise the efficiency of the different ^{3}He-gas tube counters. Some rather poor shielding of approx. 2 mm B_4C and 0.3 mm Cd sheets has been used to protect the detectors against strange irradiation from the air scattering of the primary beam and against the albedo of surrounding material, namely the steel ground plate, which was illuminated by the sample's Bragg star under some obscured scattering angles. Still, there was a lot of fairly isotropic background intensity in the serious spectra.

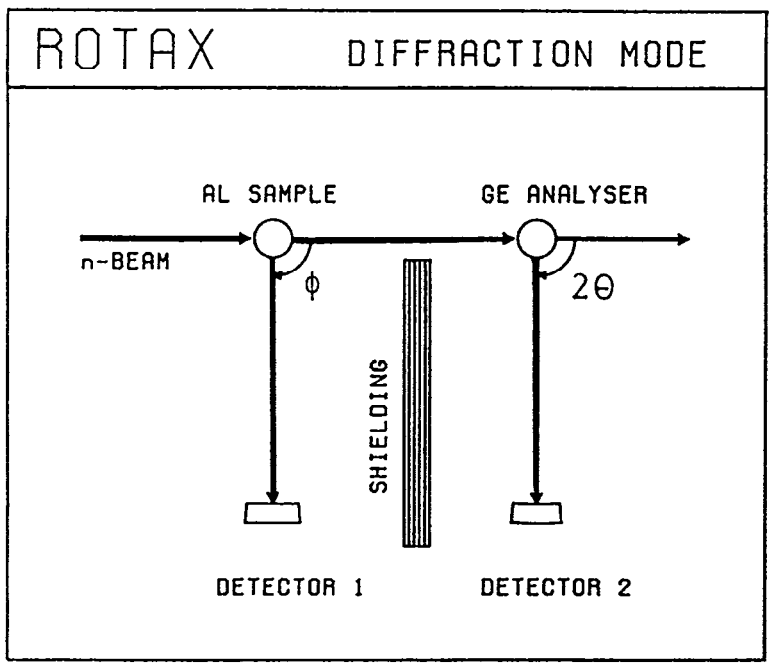

Fig. 3: set-up of ROTAX diffraction mode for spectrometer calibration and aligment.

IV. Mode of Operation

The flexibility of ROTAX is to almost arbitrarily choose the type of time-of-flight scan in (Q,ω)-space. In our previous papers [1,6,7,9,10] two particular ROTAX-scans, namely the const.-energy and the const.-ψ scan, where the direction of momentum transfer $\vec{Q}/Q$ is fixed, have been discussed in detail. Regarding the corresponding motor performance and motor dynamics, the const.-energy mode of operation is, in general, much more power consuming and more difficult to perform reliably than, for instance, the const.-ψ scan mode. Therefore and in a first step, the const.-ψ mode has been applied for all inelastic scans performed in the test experiments considered here. This is, however, by no means the end of phantasy; in fact, many other scan modes are, in principle, conceivable. For comparison with the corresponding PRISMA-mode of operation measurements with an oriented, but non-spinning idle analyser have also been done parallel to all of the basic "lighthouse modes".

The const.-ψ mode is most adapted to measure excitations in longitudinal polarisation, where the reduced wave-vector $\vec{q}$ is parallel to the momentum transfer $\vec{Q}$. The time-of-flight parabola of energy vs. momentum transfer intersects naturally the extended dispersion scheme of an excitation, e.g. a phonon (cf. fig. 4). The excitation spectrum can be obtained from several Brillouin zones simultaneously and the appropriate choice of scan-parameter ψ will uniquely define a desired point (ω_0,Q_0). Of course, the same point (ω_0,Q_0) can also be scanned in const.-energy mode, for instance, but then there is only one intersection of the dispersion curve with the TOF-frames. This situation may change for transverse polarisation (fig. 5), where the constant.-energy scan mode may be advantageous from that point of view.

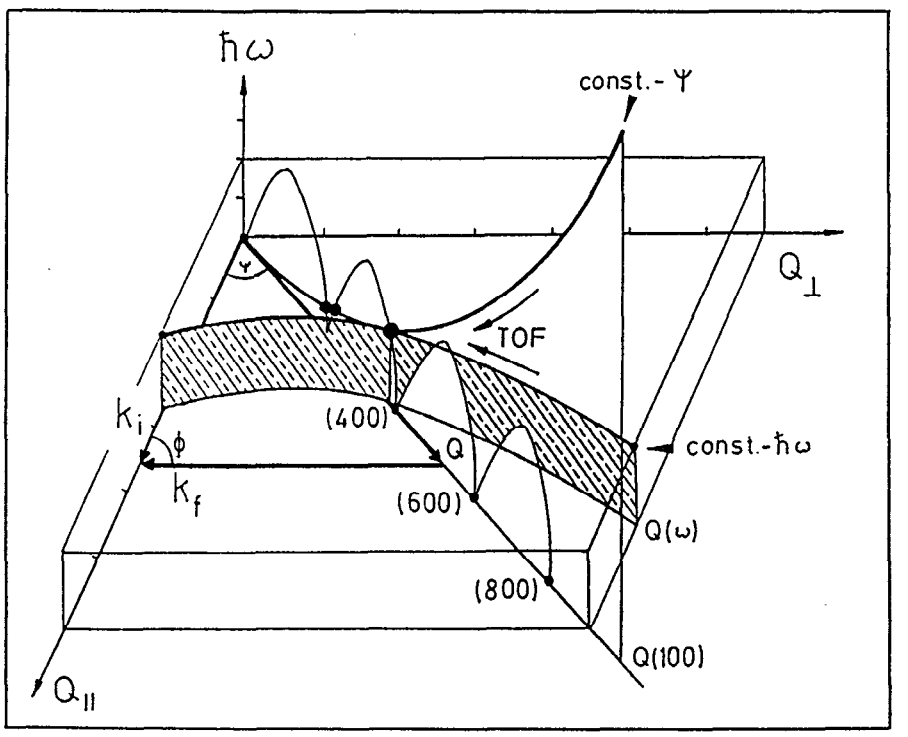

Fig. 4: Time-of-flight curves in (Q,ω)-space for a const.-ψ and const.-$\hbar\omega$ scan. The dots indicate the intersection of const.-ψ parabola with an assumed longitudinal acoustic phonon dispersion as discussed in text.

Fig. 5: Time-of-flight curves in (Q,ω)-space for a const.-ψ and const.-ħω scan. The dots indicate the intersection of const.-ħω hyperbolic with an assumed transverse acoustic phonon dispersion as discussed in text.

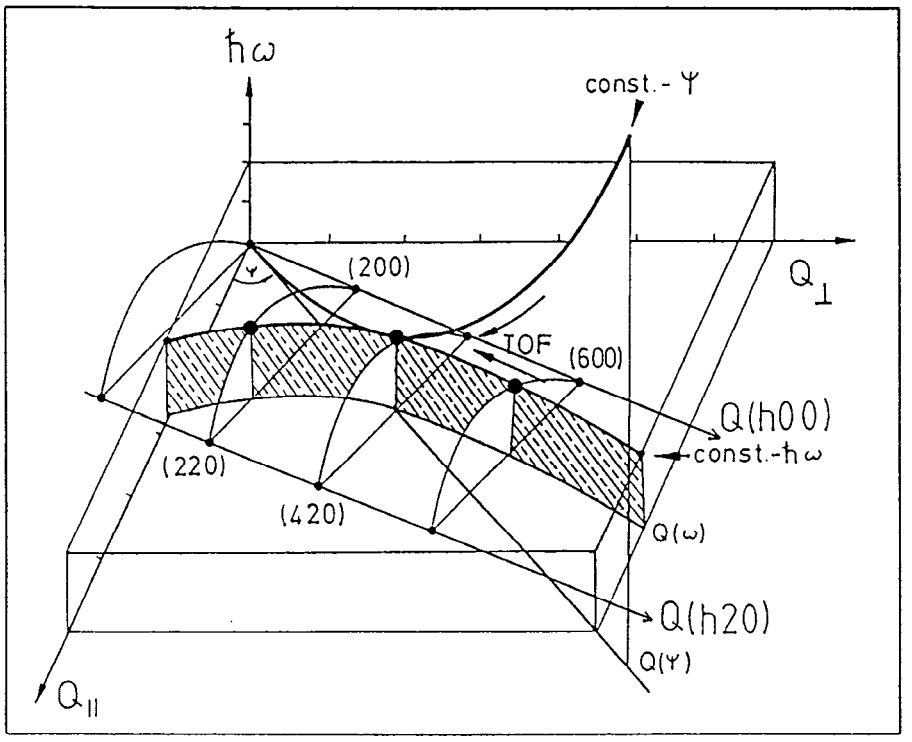

V. Elastic scattering

Elastic scattering from the Al-Bragg peaks of the <100>-zone has been performed at a scattering angle of ϕ = 76.6°. All Bragg reflections of the same crystallographic zone will occur at the same angle ϕ, however, their Bragg energies are different. Hence, these Bragg peaks are to be observed at different time channels of total neutron time-of-flight. On conventional TOF-X spectrometers with one idle analyser, only one of these Bragg peaks can be observed in due course, if the analyser angle is set properly to this Bragg energy. For comparison purposes we have done this with our test assembly as well, using the Ge-(400) reflection at $2\Theta_A = 52.6°$ to display the Al-(400) Bragg peak on the detector (fig. 6). We may call this mode the "PRISMA mode" of ROTAX, because this is exactly what PRISMA at ISIS or MAX at KENS would do on each single one of their plenty analyser arms. We have had one arm only, equipped with one analyser crystal on the S9 test assembly, however, the ROTAX principle enforced us to do more with it: By setting both arms of the two detector arrays to angles of $2\Theta_A(I) = 33.6°$ and $2\Theta_A(II) = 52.6°$ the Al-(600) and Al-(400) Bragg reflections could be observed simultaneously (fig. 7). In fig. 7 the intensities obtained from both detectors arms has been added to one file, just to clarify and simplify the presentation of the figure. ROTAX, i.e. the Ge-analyser crystal, has been spinned for elastic scattering in order to catch the two Al-Bragg energies of 117 meV and 52 meV, respectively. Both, the Ge-(400) and the Ge-(220) reflections have been used and of course, this does only affect the motor performance and dynamics, not the obtained neutron scattering intensity at the detector.

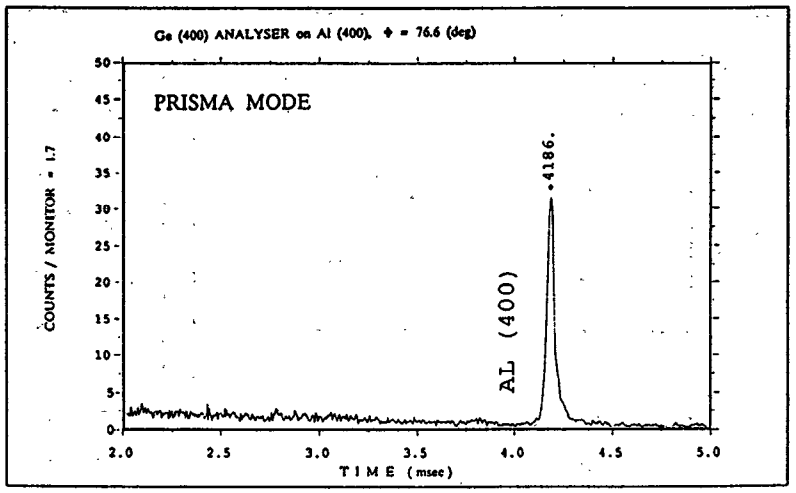

Fig. 6: Al-(400) Bragg peak as observed with Ge-(400) analyser plane in PRISMA mode at $\phi = 76.6°$ scattering angle.

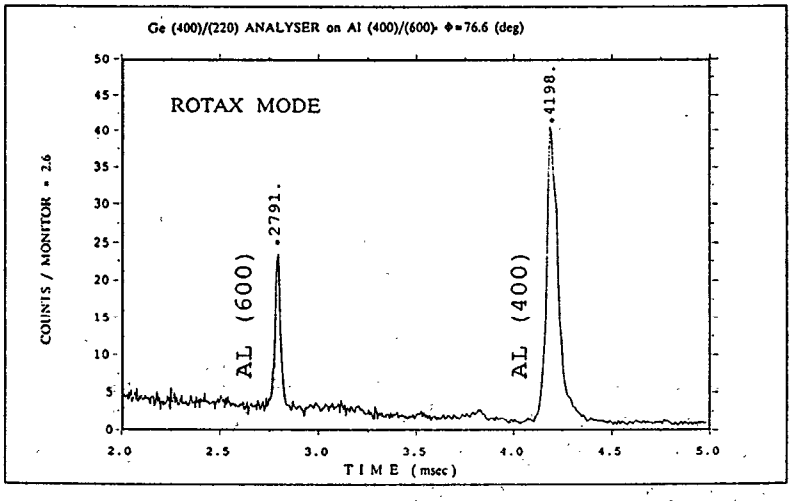

Fig. 7: Al-(400) and Al-(600) Bragg peaks as observed either with Ge-(400) or Ge-(220) analyser plane in ROTAX elastic lighthouse mode at $\phi = 76.6°$ scattering angle.

In case of elastic scattering, there is no difference between const.-energy and const.-ψ scans with respect to the motor performance. However, the motor dynamics depends significantly on the appropriate choice of analyser reflection plane. The particular scan discussed here, performed much better when using the Ge-(220) reflection as analyser, because of its lattice spacing of $d_A = 1.999$ Å, where the average rotation frequency of the analyser is much more adapted to the ISIS pulse repetition frequency. Hence, the mean square acceleration of the analyser is less when using Ge-(220) instead of Ge-(400) reflection. Fig. 8 illustrates these two cases of motor dynamics and performance. The required and the actually achieved values for $\Theta_A(t_A)$ at the time t_A, when neutrons arrive at the analyser, and its derivatives $d\Theta_A/dt_A$, $d^2\Theta_A/dt_A^2$ are plotted, the dashed lines mark the desired time channels for the Al-Bragg energies of 117 and 52 meV, respectively. There is no general rule to determine the optimum analyser reflection. It rather depends on the experimental condition and required parameters, such as sample scattering angle ϕ, neutron energies to be scanned, actual motor performance and reliability under the terms of strict synchronisation with the neutron source, intensity considerations etc. Therefore, it is essential also to look at the actual angular decoder values of the analyser's motor and to permanently monitor these values in the data aquisition system of ROTAX.

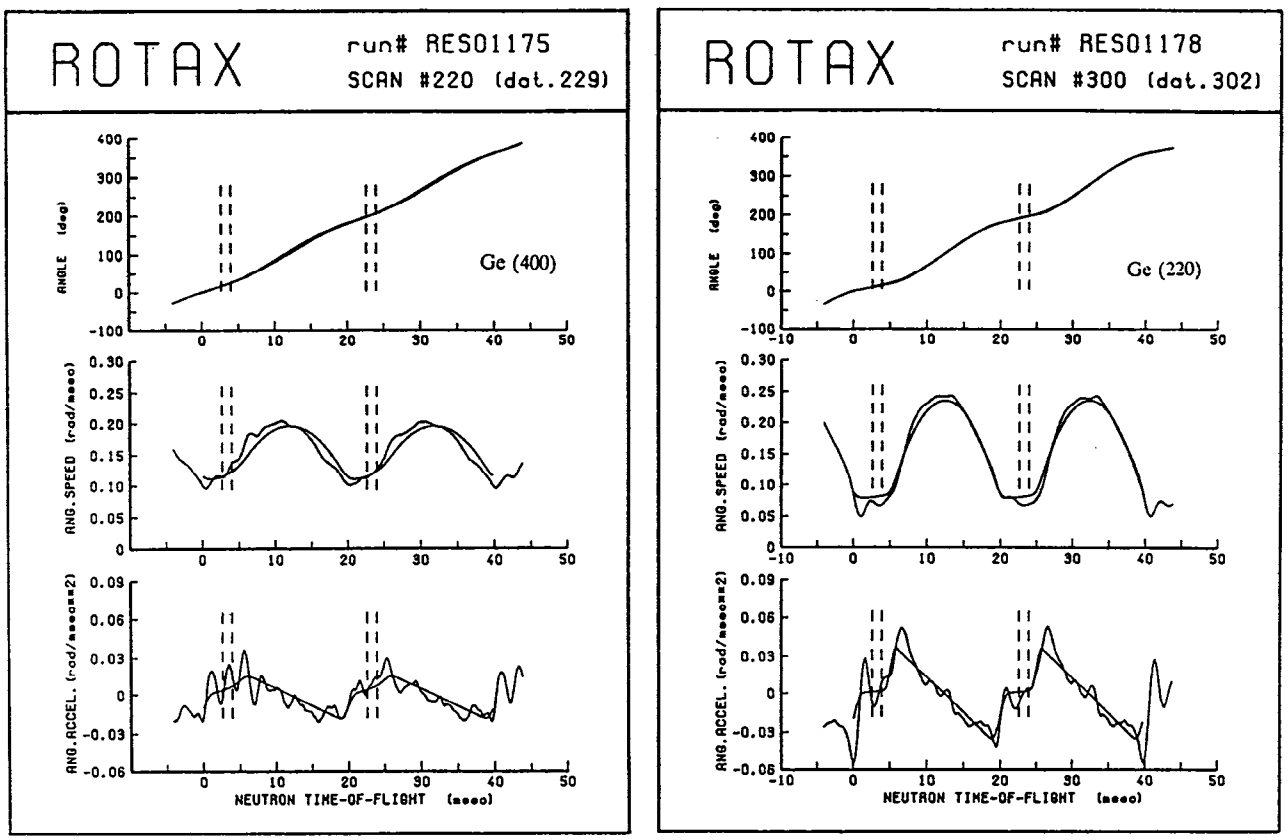

Fig. 8: ROTAX motor performance to the Al-(400)/(600) Bragg scans of fig. 7, a) with Ge-(400) and b) with Ge-(220) analysing plane. The analyser angle Θ_A and its derivatives is plotted for 1 motor revolution in the time of 2 ISIS cycles. The dashed lines indicate the time channels of interest for the (400) and (600) Bragg energies of aluminium.

When using the Ge-(220) plane, the range of $2\Theta_A$ is naturally smaller than for the Ge-(400) plane. In fact, it was possible to cover the range of $2\Theta_A$ between 15° and 60° with the JULIOS szintillator bank and to catch three Al-Bragg lines, namely the Al-(400), (600) and (800) reflection, simultaneously, i.e. within one shot.

VI. Inelastic Scattering

ROTAX is primarily dedicated to inelastic scattering, thus it is essential to demonstrate its capability in this field as well. The longitudinal acoustic phonons LA[100] of aluminium have been measured by means of const.-ψ scans in energy loss for the neutrons, i.e. $k_f<k_i$. Fig. 9 illustrates the experimental condition: in the upper part of the figure the alimunium LA[100] dispersion [11] is plotted together with the const.-ψ TOF-parabolas for various values of the parameter ψ. The effective position of the two detector arrays is indicated. In the lower section of fig. 9 the Q-space with the Brillouin zone of the actual Al-lattice is shown together with the scattering triangle for the elastic and inelastic condition.

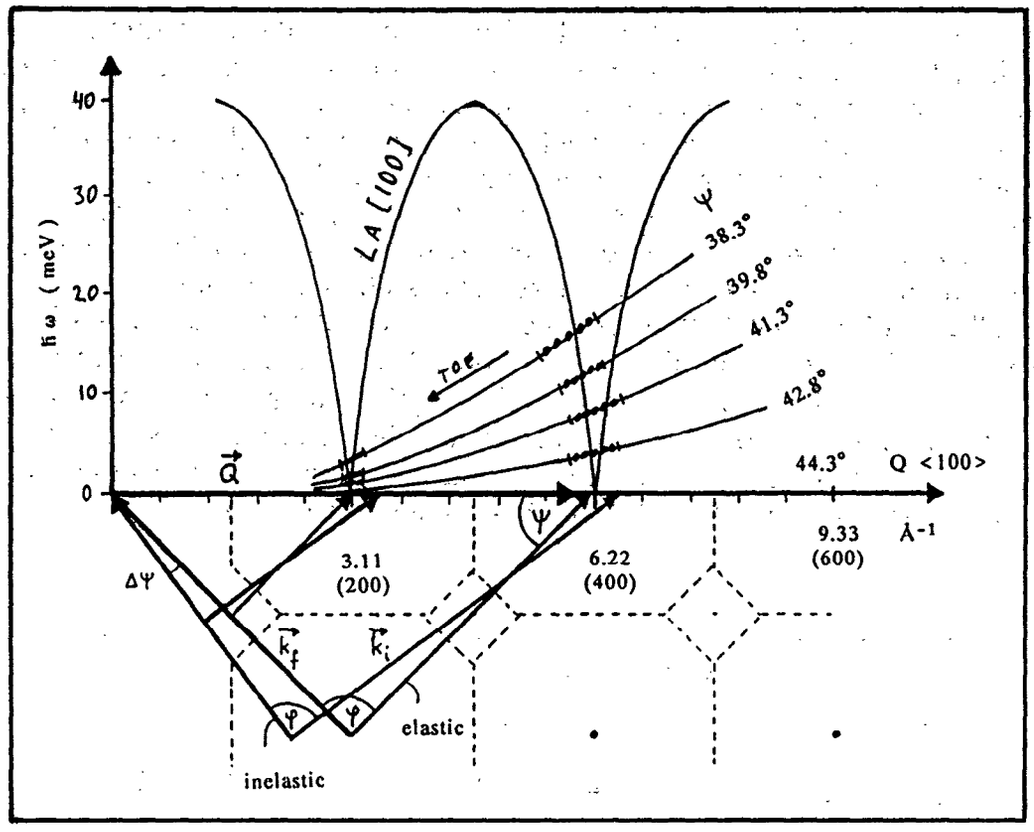

Fig. 9: LA[100] phonon dispersion of aluminium, Q-space and ROTAX const.-ψ parabolas of the test experiment discussed in text.

For const.-ψ scans the obtained energy transfer $\hbar\omega$ in terms of scattering angle ϕ and scan parameter ψ is given by [1]:

$$\hbar\omega = \frac{\hbar^2 Q^2}{2 m_n} \frac{\sin(2\psi + \phi)}{\sin\psi} = \frac{\hbar^2 Q^2}{2 m_n} (\cos 2\psi + \operatorname{ctg}\phi \sin 2\psi) \qquad (2)$$

Thus, we obtain:

$$2\psi + \phi \begin{cases} < 180° & \text{inelastic scattering, energy loss of the neutrons} \\ = 180° & \text{elastic scattering} \\ > 180° & \text{inelastic scattering, energy gain of the neutrons} \end{cases}$$

At a scattering angle ϕ = 91.4° LA[100] phonons of aluminium have been observed in the (200) and (400) Brillouin zones at const.-ψ varying between ψ = 44.3° and ψ = 38.3° in step of $\Delta\psi$ = 1.5°. A typical result is shown in fig. 10, where we present a multi-plot of the unfiltered original raw-data without any background correction or monitor normalisation, just as obtained directly from each of the nine detector spectra (in fact, counter #1 was idle). Counter #2-#5 were grouped in detector array II at an angular position of $2\Theta_A(II)=99.4°$, whereas the others were grouped in detector array I at $2\Theta_A(I)=44.5°$ (cf. fig. 2). Apparently, there is the isotropic elastic incoherent scattering at time channels of 9.8 msec and 4.9 msec total time-of-flight due to the Al-(200) and Al-(400) lines, respectively. This isotropic

incoherent elastic line originates from the fluorescense of the germanium crystal when it is irradiated by the very intense Bragg peaks of the aluminium sample. From either these elastic lines phonon scattering intensity is seen to emerge very clearly in both detector arrays. In fact, the phonon at 4.8 msec measured in the (400)-Brillouin zone is characterised by $\hbar\omega$ = 4 meV energy transfer and $\vec{q}$ = 0.04 reduced wavevector, the other one at 9.2 msec, measured in the (200)-Brillouin zone, is found at $\hbar\omega$ = 1 meV and $\vec{q}$ = 0.01. All other peaks, bumps and hubbles of intensity shown in the spectra in fig. 10 are due to background scattering, because of weak shielding and the albedo of the steel ground-plate mentioned above. Real inelastic scattering on ROTAX has, in fact, to fulfill a 4-fold coincidence, because the incident and final neutron energy as well as the detector position and appropriate analyser Bragg angle at the desired time t_A of neutron arrival at the analyser must all fit together according to the scattering laws of energy and momentum conservation. In general, background scattering does not fulfill all these requirements at once.

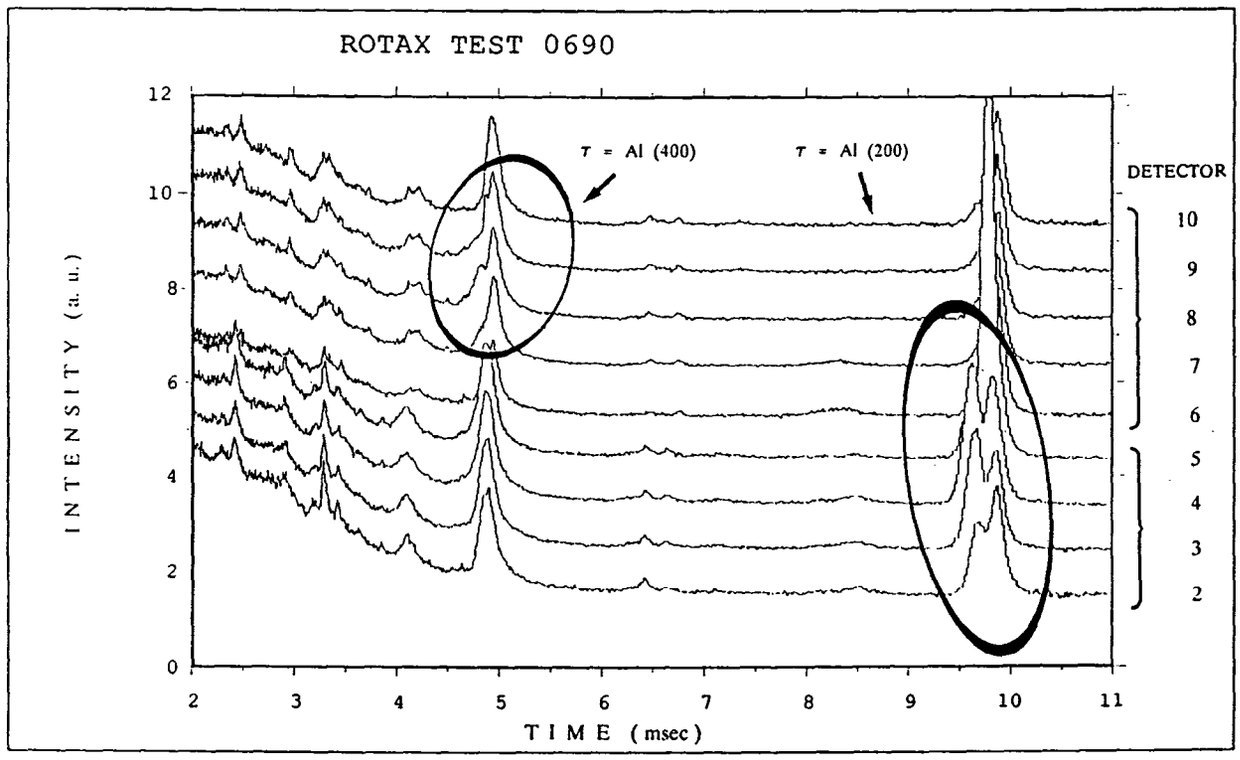

Fig. 10: Raw-data TOF-spectra of two Al-phonon lines of a const.-ψ=42.8° scan with Ge-(220) at ϕ=91.4° scattering angle.

Although in energy loss of the neutrons, inelastic scattering occurs prior to elastic scattering, because of two reasons: a) the analyser is spinning with increasing Θ_A, hence decreasing analysing final energy, b) inelastic scattering occurs from accordingly more energetic and thus faster incident neutrons. A more distinct presentation of the experimentally observed phonon lines is given in figs. 11 and 12: fig. 11 shows a window of the original TOF-spectrum for the 4 meV phonon together with an according

background spectrum as obtained from a $2\Theta_A$-offset scan. Fig. 12 presents the 1 meV phonon more pronounced and in addition to the incoherent elastic line plotted in a scale of energy transfer. The elastic line immediately disappears, if the Al-crystal is rocked to another position in ψ, where the Bragg beam of divergence α_1 does no longer hit the analyser crystal. In fact, this condition is fulfilled and consequently no such incoherent scattering has been found for higher energy transfers or reduced values $\psi<42°$, where $\psi<\psi_{el}-\alpha_1/2$ for $\psi_{el}=(180°-\phi)/2$ (cf. eq. 2 and fig. 13).

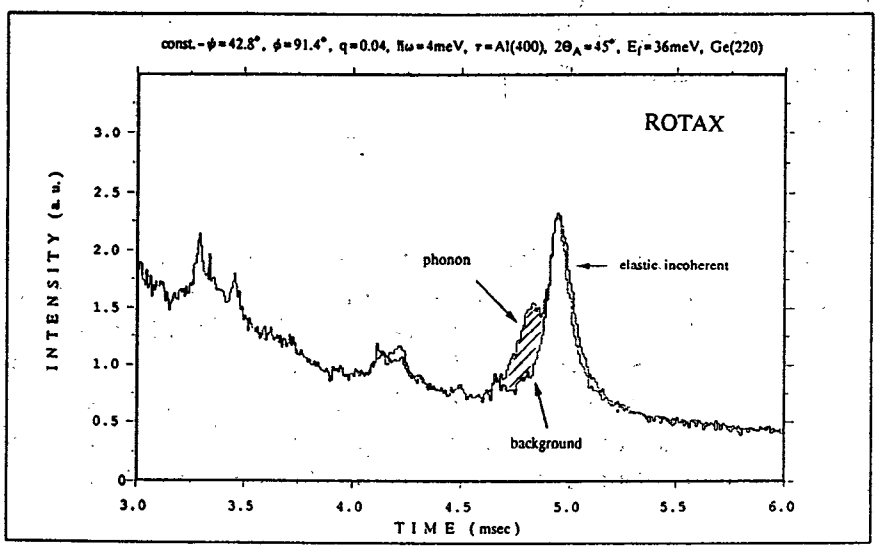

Fig. 11: The $\tau=(400)$, $q=0.04$, $\hbar\omega=4$meV LA[100] phonon of fig. 10 together with a $2\Theta_A$-offset background scan.

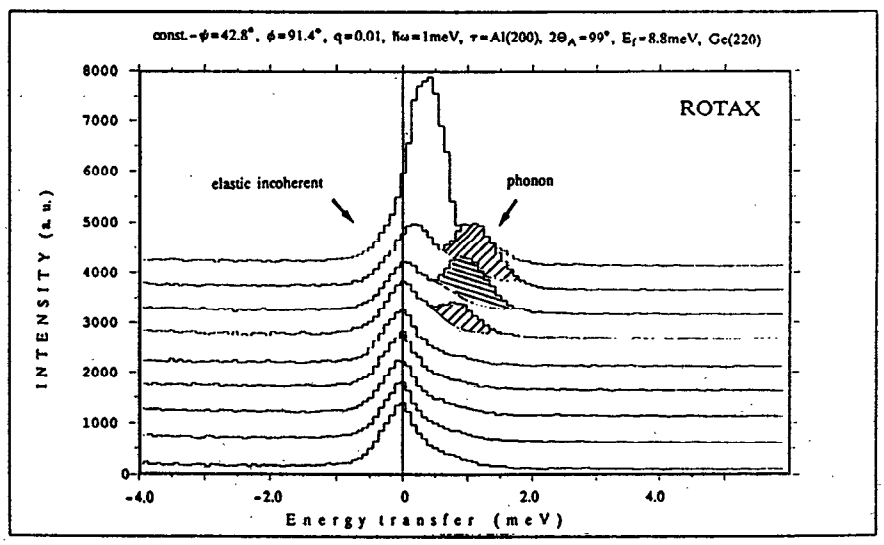

Fig. 12: The Al-(200) incoherent elastic scattering and the $q=0.01$, $\hbar\omega=1$meV phonon of fig. 10.

It is not possible to obtain all these longidutinal phonon modes in the "PRISMA mode" directly. Therefore no PRISMA-type scan of the measurements discussed above can be given for purposes of comparison. This, however, may be regarded as an illustrative example of the advanced scan flexibility on ROTAX!

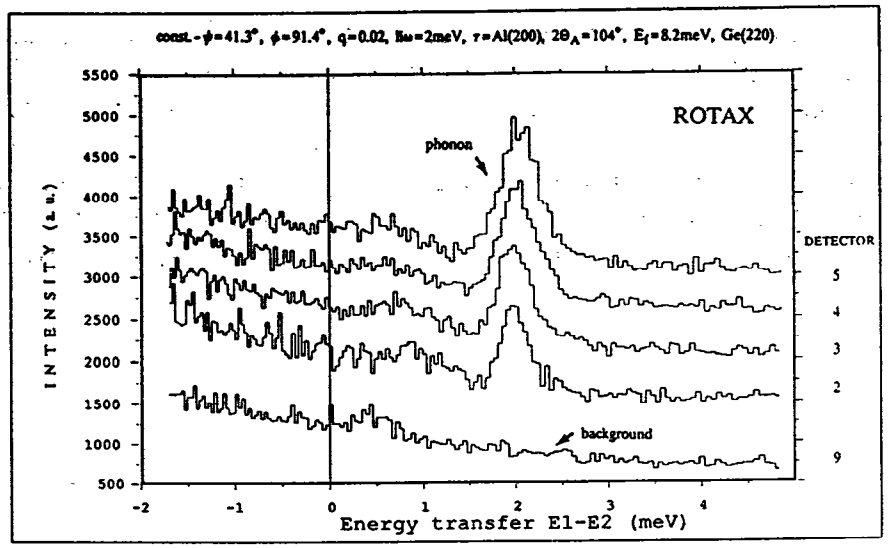

Fig. 13: The $\tau=(200)$, $q=0.02$, $\hbar\omega=2$meV phonon of aluminium without an accompanying elastic incoherent line; scanned with const.-ψ = 41.3° at ϕ = 91.4° scattering angle. The Ge-(220) analyser plane was used.

Anyhow, to give an idea about the competition of a ROTAXed "lighthouse mode" versus the "PRISMA mode" of operation, we shall give in the following an example of a tranverse TA[100] phonon scan (cf. fig. 5) of aluminium, taken at $\tau=(410)$ for wavevector $\vec{q}=0.5[010]$ and $\hbar\omega=25.4$ meV. In figs. 14 and 15 the inelastic scattering intensity of this zone boundary phonon is plotted vs. energy transfer as obtained from the PRISMA and ROTAX mode, respectively. The intensity has been normalised to the monitor count- rate and corrected for background scattering in either case.

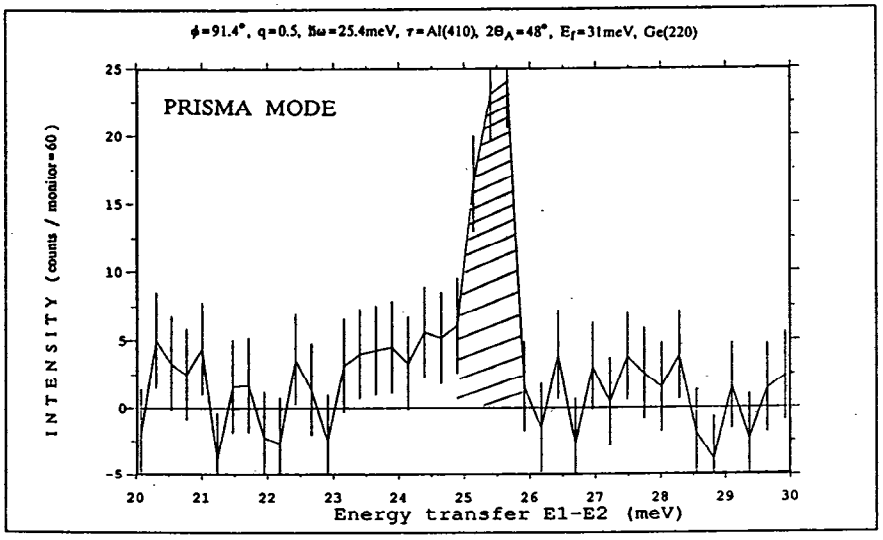

Fig. 14: The TA[100] zone boundary phonon of aluminium at $\hbar\omega$ = 25.4 meV. PRISMA mode at ϕ = 91.4° scattering angle with Ge-(220) analyser.

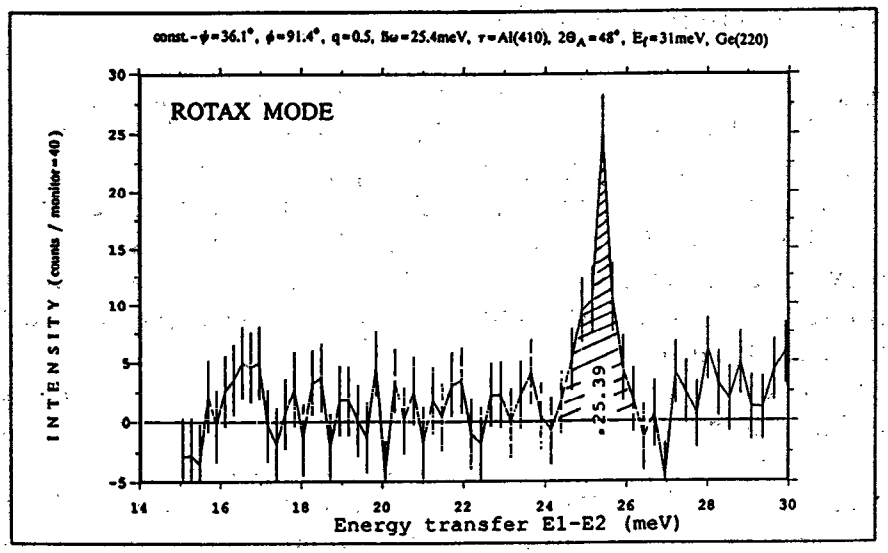

Fig. 15: The TA[100] zone boundary phonon of aluminium at $\hbar\omega$ = 25.4 meV. ROTAX const.-ψ=36.1° mode at ϕ = 91.4° with Ge-(220)

Apparently, ROTAX performes about equally with PRISMA under the same experimental condition. Further, the actually achieved motor performance should not be omitted for this particular example. The required and achieved values of the analyser Bragg angle Θ_A and its derivatives are plotted in fig. 16 for one motor revolution in the time of two neutron frames. Of course, the accurate setting of the analyser Bragg angle is of striking importance for the intensity obtained on ROTAX, whereas the accurate performance of the angular speed is of importance for the ROTAX motor regulation government and the angular acceleration is the dominant factor for the torque and power of the motor. The dashed lines in fig. 16 again indicate the desired time channel of best achievable accuracy and, of course, there is only one such time channel of interest for this particular scan, because there is only one excitation line in every neutron frame to be measured.

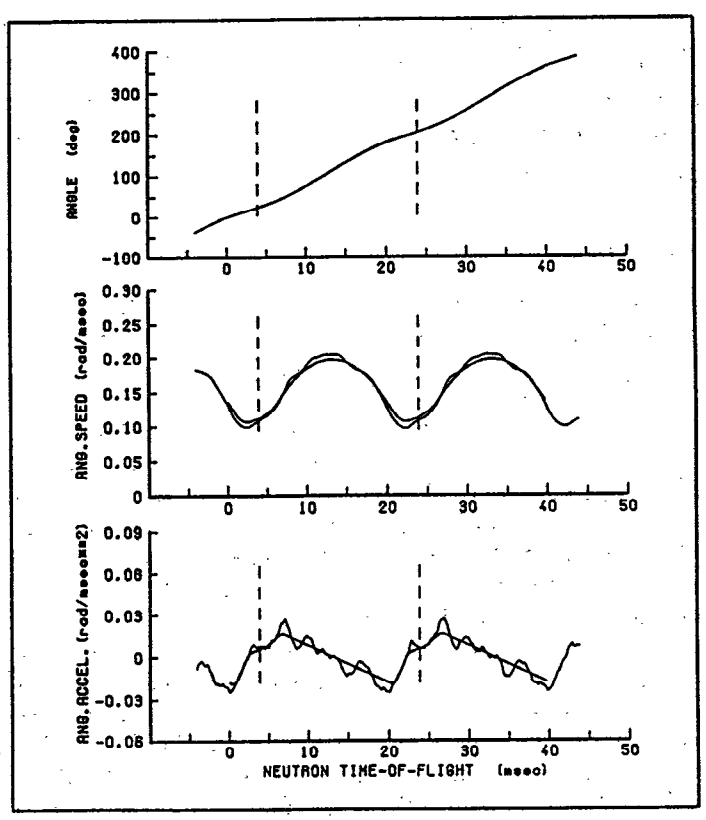

Fig. 16: ROTAX motor performance to the transverse phonon scan of fig. 15. The analyser angle Θ_A and its derivatives is plotted for one motor revolution in the time of 2 ISIS cycles. The dashed line indicates the time channel of interest.

VII. Concluding remarks

After more than four years of research, design and development of the fundamental technical devices for ROTAX, i.e. the control unit for its spinning analyser drive, we were able to demonstrate the principle proof on the basic capability and performance of the instrument under realistic neutron scattering conditions. In a two-phase test experiment on the S9 test beam facility at ISIS this success has been achieved with a provisional assembly of the ROTAX spectrometer and with a prototype of the motor control unit. Only minimum effort has been put to background suppression, full detector furnishment, software comfort and experimental elegance, and still phonons have been measured successfully with sufficient intensity and peak-to-background ratio within reasonable counting times. Although the technical development of ROTAX is by no means complete and finished yet, further improvements already being under construction will enhance the reliability and accuracy of the ROTAX drive considerably, we are now in the position to say without any doubt: ROTAX is working and it will fulfill its promisses! We shall now enter the "concrete phase", starting the design and installation of the spectrometer and its bulky components at its finally desired position behind the anglo-italian PRISMA spectrometer on the N2 beam line at ISIS. We expect to become operational in early 1993.

Acknowledgment

We want to thank all those who have contributed to the success reported above; namely Mr. A J Chappell, Mr. A F Gilleard, Mr. E M Mott and Mr. S M Spurdle (RAL) for their help in the preparation period and their support during the test experiments on S9 at the Rutherford Appleton Laboratory. We also want to thank the ISIS computing group and further, Dr. C J Carlile (RAL) and Dr. C Petrillo (CNR Frascati, Italy) for providing the excellent Al-sample and Ge-analyser crystals. We acknowledge Mr. E Jansen and Mr. R Skowronek (KFA Jülich) for their assistance with the JULIOS szintillator bank, which has been borowed from the Institute of Mineralogy of the Univ. of Bonn, F.R.G. - This work has been performed under the terms of the "Rutherford-Würzburg" collaboration agreement and it has been funded by the German Federal Minister for Research and Technology (BMFT) under contract number 03-Ge2-Wue.

References

[1] Geick R and Tietze H, Nucl. Inst and Meth. A **249**, 325 (1986)
[2] Robinson R, Eckert J and Pynn R, Nucl. Inst. and Meth. A **241**, 312 (1985)
[3] Tajima K, Ishikawa Y, Kanai K, Windsor C G and Tomiyoshi S, Nucl. Inst. and Meth **201**, 491 (1982)
[4] Andreani C, Carlile C J, Cilloco F, Petrillo C, Sacchetti F, Stirling G C and Windsor C G, Nucl. Inst and Meth. A **254**, 333 (1987)
[5] Steigenberger U, Hagen M, Caciuffo R and Sacchetti F 1990 RAL-90-004 and Nucl. Inst. and Meth. to be published 1990
[6] Tietze H and Geick R, Proc. ICANS IX 1986 CH-Villigen, SIN-rep 3-907998-01-4, 389 (1987)
[7] Tietze H, Schmidt W, Geick R, Samulowitz H and Steigenberger U, Proc. WONSDA II, to be published in IOP Conf. Series 1990
[8] Jansen E, Schäfer W, Szepesvary A, Will G and Kurz R, Physica B **156**, 584 (1989) and references therein
[9] Schmidt W, Tietze H and Geick R, Physica B **156**, 554 (1989)
[10] Tietze H, Schmidt W and Geick R, Physica B **156**, 550 (1989)
[11] Stedman R and Nilson G, Phys Rev. **145**, 492 (1966)

Q(I.M.Thorson): What angular tolerance are you achieving at present?
A(H.Tietze): The present 0.5°, although 0.1° is required and we see how to achieve this.

ICANS-XI International Collaboration on Advanced Neutron Sources
KEK, Tsukuba, October 22-26, 1990

RECENT PROGRESS ON eVS

J Mayers, A C Evans* and A D Taylor

ISIS Facility, Rutherford Appleton Laboratory, Chilton, Didcot, Oxon OX11 0QX, UK
* Department of Physics, University of Warwick, Coventry, CV4 7AL

ABSTRACT
The development of eVS at ISIS is reviewed.

I. INTRODUCTION

The electron volt spectrometer (eVS) is dedicated to measuring atomic momentum distributions in condensed matter. At sufficiently high energy and momentum transfers the impulse approximation is valid and the scattering is identical to that which would be obtained from a free gas of atoms, with a momentum distribution identical to that of atoms in the target system. The neutron scattering cross-section is then related in a simple way to the atomic momentum distribution function by conservation of energy and momentum, as in 'billiard ball' collisions. These 'Deep Inelastic Neutron Scattering' measurements are possible only on pulsed neutron sources such as ISIS, which have sufficient intensities at the neutron energies required for the impulse approximation to be valid. eVS is an inverse geometry spectrometer, where the filter difference technique is used to analyse the energy of scattered neutrons at energies greater than 4 eV. This enables energy transfers between 10 and 30 eV and momentum transfers greater than 100 $Å^{-1}$ to be obtained.

The technique is particularly valuable for the investigation of hydrogen potentials in, for example, hydrogen bonds or metal hydrides. It gives direct information on the hydrogen wavefunction, which is complementary to the information on energy eigenfunctions obtained by conventional neutron spectroscopic techniques. A preliminary measurement on the anisotropy of the proton momentum distribution in a single crystal of $KHCO_3$, has given very promising results, despite the non-ideal instrument geometry [1]. The rms momentum components parallel and perpendicular to the hydrogen bond were found to be significantly different and were in excellent agreement with calculations using a potential derived from previous neutron spectroscopic measurements.

The time-of-flight scans for the measurements on $KHCO_3$ are shown in Figure 1. In the impulse approximation the neutron scattering function $S(Q,\epsilon)$ is peaked along the 'recoil line', $\epsilon = Q^2/(2M)$ where M is the atomic mass. This corresponds to scattering from a stationary atom with conservation of energy and momentum. The atomic motion Doppler broadens $S(Q,\epsilon)$ into a function of width $\simeq pQ/M$, at constant Q, where p is the rms atomic momentum. The recoil line and the measured FWHM of $S(Q,\epsilon)$ are also shown in Figure 1. The position at which the scans cross the recoil line determine the energy and momentum transfers at the peak position. It can be seen from this that an energy transfer of $\simeq$ 20 eV and momentum transfer of 50 $Å^{-1}$ were obtained at the highest scattering angle. These values are respectively 100 and 10 times greater than those obtainable on reactor sources and should ensure that the impulse approximation can be used with confidence.

Typical time-of-flight scans are illustrated in Figure 2 It can be seen that the hydrogen peak (the left hand peak) is well separated from the peak obtained from K, C, O and Al atoms in the sample and sample holder. This easy separation of the hydrogen scattering is one of the advantages of the technique. As the scattering angle increases, the hydrogen peak moves to higher energy transfers (and hence shorter times since eVS is an inverse geometry instrument).

It is anticipated that many of the experiments during the next year will measure the anisotropy of the proton momentum distribution in single crystals. eVS has been redesigned for such

measurements. Two banks of detectors at ±45° allow for the simultaneous measurement of the distribution of momentum components along directions separated by 90°, with good resolution. More sophisticated data analysis should facilitate the measurement of the shape of the atomic momentum distribution, rather than simply mean momentum components.

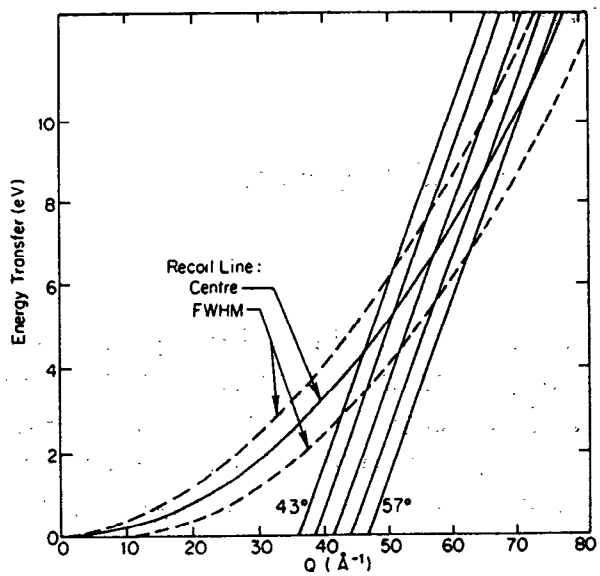

Figure 1. Time-of-flight loci from the 4.906 eV Au resonance analyser used in the momentum distribution measurements on a single crystal of $KHCO_3$.

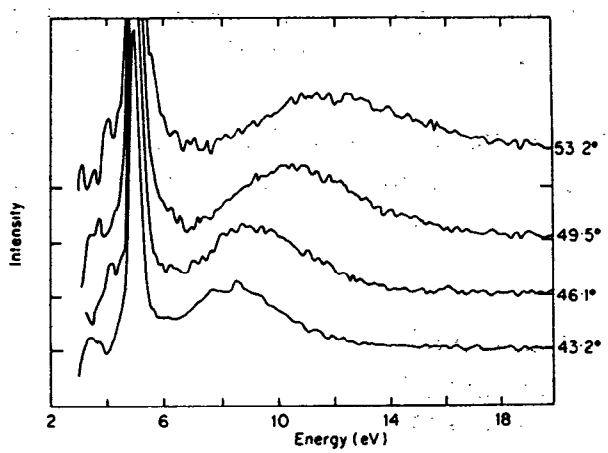

Figure 2. Recoil scattering from $KHCO_3$ with momentum transfer along the hydrogen bond. Scattering from hydrogen occurs at high energies/short times and is well separated from that due to heavier atoms.

References

[1] P Postorino, F Fillaux, J Mayers, J Tomkinson and R S Holt
Anisotropy of the Proton Momentum Distribution in Single Crystal $KHCO_3$
J Chem Phys 1990 (in press)

ICANS-XI International Collaboration on Advanced Neutron Sources
KEK, Tsukuba, October 22-26, 1990

Recent progress in TOP spectrometer

S.Itoh, T.Watanabe and Y.Endoh
Department of Physics, Tohoku University, Sendai 980, Japan

ABSTRACT

We have continuously improved the polarized cold neutron spectrometer which is named TOP. Several methods for polarized cold neutron experiments can be considered, and in the depolarization measurement we have currently obtained the excellent results. In the present development, we modified the spectrometer for the purpose of the achievement of small angle neutron scattering (SANS) experiment to the practical level.

I. Introduction

The TOP spectrometer (Time-of-flight spectrometer with Optical Polarizer) was constructed at the pulsed cold neutron source (KENS) at the National Laboratory for High Energy Physics (KEK) to study mesoscopic magnetism in 1980[1),2)], and the wide mesoscopic scale is covered by various methods. We are aiming to obtain complementary informations over the wide scale.

To investigate the magnetic structure of the mesoscopic system, polarized cold neutrons are advantageous, and we can consider several methods using the TOP spectrometer as follows;

SANS	
integrated intensity	(already established)
scattering function	(present development)
polarization analysis	(under construction)
Reflection	(under construction)
Depolarization	(already established)

In the previous TOP spectrometer, the depolarization method has been achieved to the practical level and the excellent results have been obtained for the studies of magnetization process of ferromagnets or spin glass[3)]. In the SANS experiments, we obtained good results for the studies where the integrated intensities were discussed, for instance, the study of helical spin structure[4)], however, the scattering functions could not be discussed due to poor resolution. Therefore we decided to modify the

spectrometer using a position sensitive detector (PSD) system and improved both resolution and total counting rate. We mainly report the development of the SANS system.

II. Overall layout

The typical SANS system where the resolution and the intensity are optimized consists of the moderator, the sample and the ditector[5]. In the TOP spectrometer, there exist a neutron guide tube and a polarizer between the moderator and the sample. Neutrons are propagated by total reflection in the guide tube and the polarizer. Since the divergence of neutron beams propagated by total reflection are not changed, the moderator surface can be replaced by the outlet of the polarizer. On the basis of the optimization for the geometry mentioned above, we modified the TOP spectrometer introducing a PSD system. PSD's adopted in our development are 1/2 inch in diameter and 24 inches in effective length with ^{3}He of 10 atm in pressure. Three PSD's are parallely arranged and essentially one-dimensional measurements are aimed, since the measurements of the magnetic scattering are mainly performed and the magnetic scattering occurs one-dimensionally for an applied field. The positional resolution at PSD's is 1.1 cm and the width of a timing channel in the time analyzer is 1.536 msec.

The overall layout of the TOP spectrometer is displayed in Fig.1. The polarizer and the spin flipper were already established[1),2)]. We mainly designed a new scattering chamber to minimize the air scattering effect, so that we can assemble the detecting system in the vacuum chamber at 0.01 Torr in pressure.

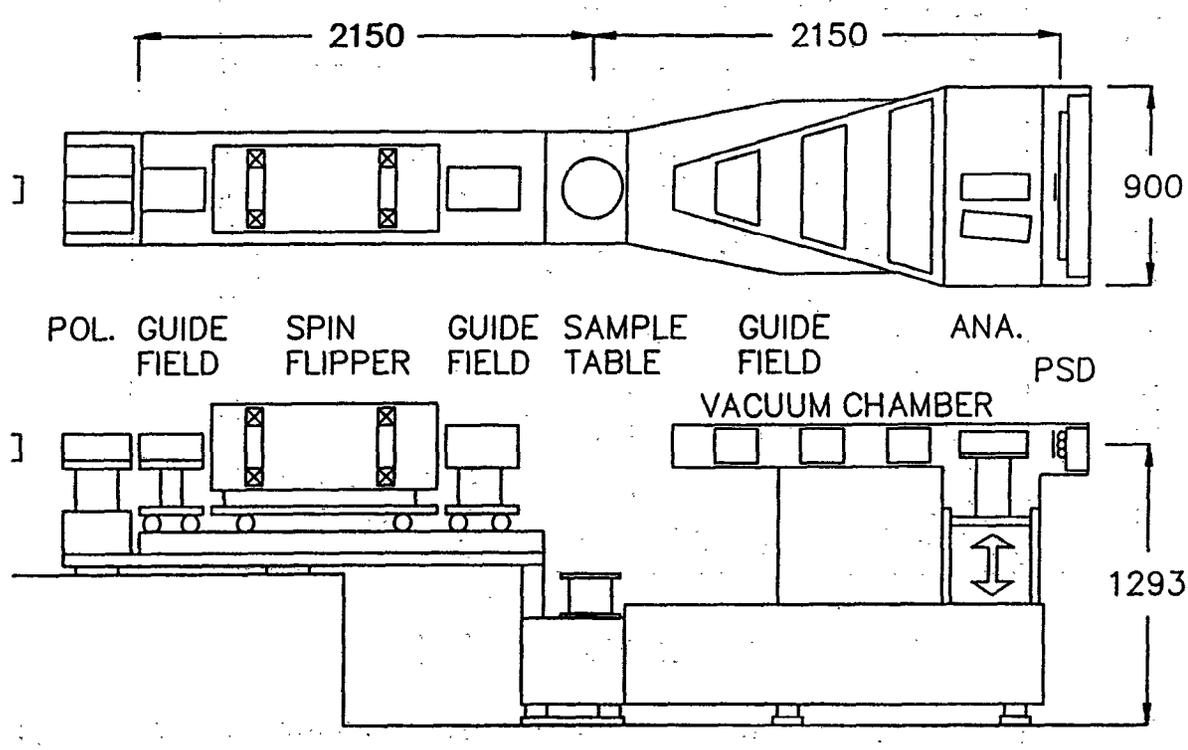

Fig.1 Schematic drawing of the TOP spectrometer.

We also mounted preamplifires, polarization handling devices such as spin analyzers and guide magnets with a uniform field of 30Oe, a mechanical elevator for setting the analyzers, and a beam stopper system in front of PSD's in the compact scattering chamber. We mounted two analyzers for transmitted beams and for scattered beams. The analyzer for scattered beams is mounted at one position of 5°, 6°, 7° and 8° in the scattering angle. Two analyzers are on a table and the reflecting angle of neutrons within the analyzer is set by rotation of the table. The analyzers are removed downward in the experiment without analyzers.

Moreover, we developed data acquisition system in the introduction of PSD system, which was already reported[6].

III. Characteristics of SANS system

First we estimate the Q-range and its resolution in the SANS experiment with the typical experimental condition. In the typical condition, the ranges of the scattering angle and the wavelength are ϕ=1.0~8.1° and λ=3~9Å, respectively, and their resolutions are $\Delta\phi$=14mrad and $\Delta\lambda$=0.19Å, respectively. Figure 2 shows the calculated Q-range and its resolution ΔQ for the typical condition. The Q-range between 0.012 and 0.29 $Å^{-1}$ is covered, practically 0.02~0.28 $Å^{-1}$ is covered. ΔQ shows weak dependence on scattering angle ϕ and λ, and ΔQ=0.01 for 9Å in wavelength.

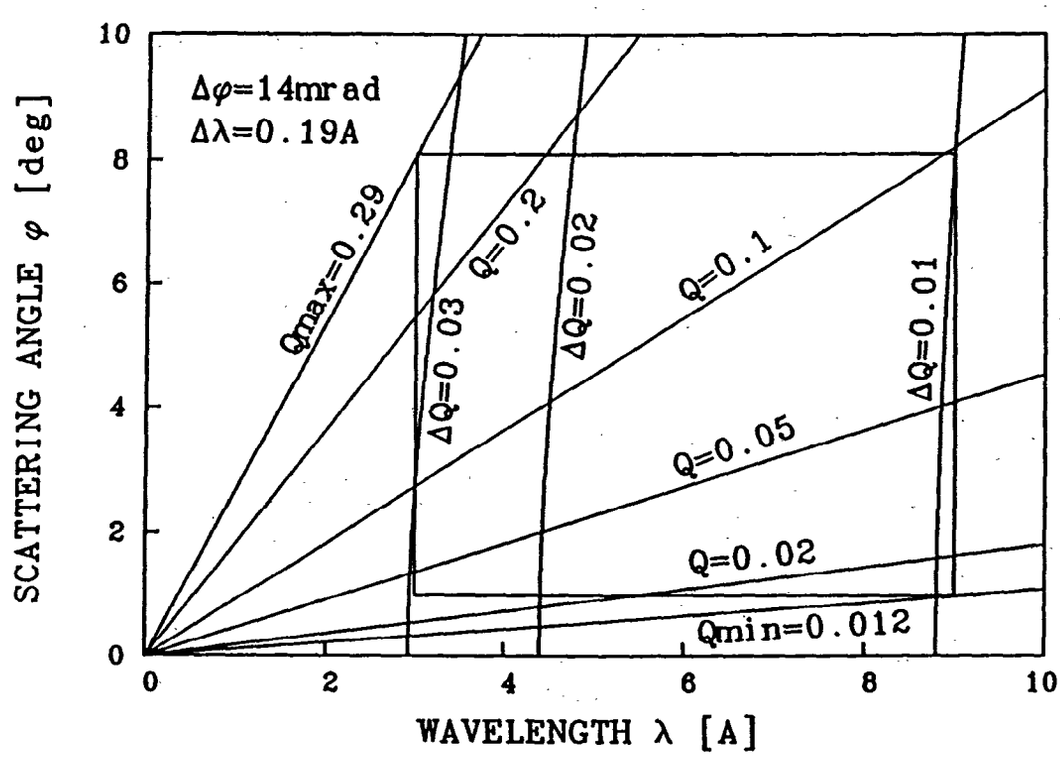

Fig.2 The Q-range and its resolution ΔQ calculated for the typical experimental condition. The inside region of the rectangle is available.

Next, Figure 3 shows the intensity against the positional channel of PSD's, integrated over the timing channels and reduced to the intensity at the sample position. The sample is H_2O of 1mm in thickness. The divergence of the incident beams is 7mrad both vertically and horizontally. The divergence is corresponding to the collimation determined by the area of the polarizer outlet and the beam cross section of the sample.

Additionally we also improved the polarization using supermirrors. The quality of polarized neutrons consists of polarizing efficiency of the polarizer P_P, that of the analyzer P_A and the flipping efficiency of the spin flipper f. Figure 4 shows the polarizing qualities $P_P P_A$ and f determined by the measurement of transmitted beams. The flipping efficiency f is almost unity in the whole range of wavelengths. The polarization efficiency $P_P P_A$ in the present development is greater than that of the previous TOP spectrometer. In the measurement, the analyzer was the supermirrors for the present status and the previous type mirrors[2)] for the previous status, and the polarizer was the previous type mirrors for each status. The principle of the previous type mirrors is based on the spin-dependent total reflection. Therefore the difference of $P_P P_A$ between the present TOP and the previous TOP is the difference between the supermirrors and the previous type mirrors. We are planning to use a supermirror polarizer in no distant future.

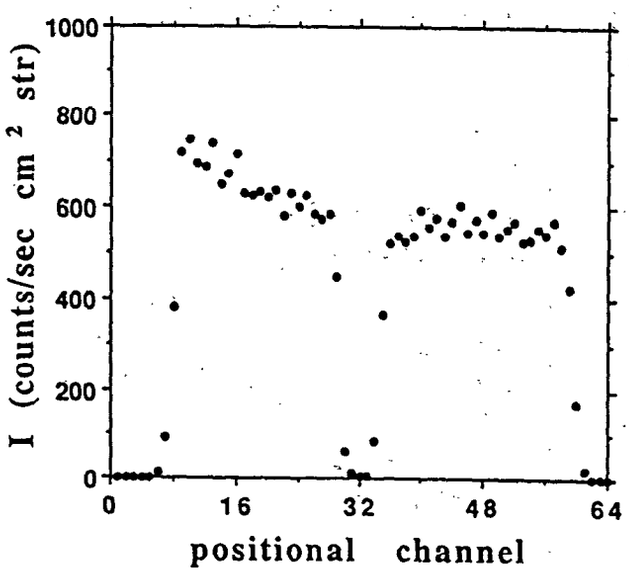

Fig.3 Normalized intensity against the positional channels of PSD's, integrated over the timing channels and reduced to the intensity at the sample position.

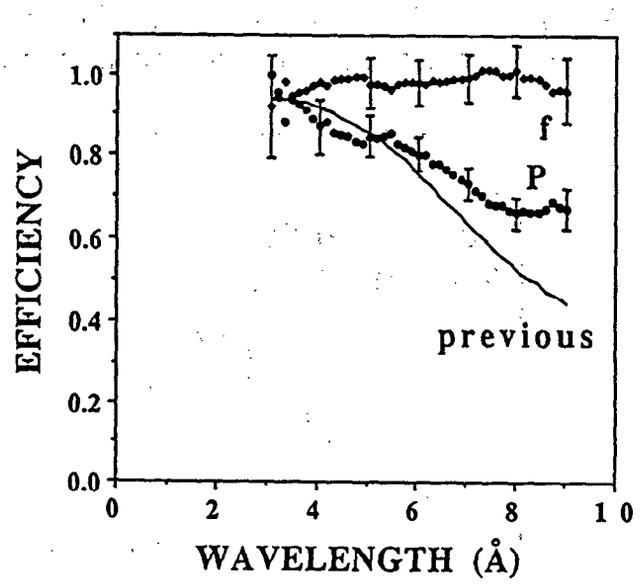

Fig.4 Wavelength dependence of the polarizing efficiency $P_P P_A$ and the flipping efficiency f. The solid line is the polarizing efficiency of the previous TOP spectrometer.

IV. Demonstration

Now we demonstrate an example of the SANS experiment. Figure 5 shows the scattering intensities from a cobalt ferrofluid[7]. The beam cross section is $1cm^2$ and the sample thickness is 1mm. It spent about 2 hours to measure each scattering curve. The shoulder on the intensity is corresponding to the interparticle correlations. Ferrofluids are colloidal suspensions of ferromagnetic particles of about 100Å in diameter and a suitable system for polarized SANS experiments.

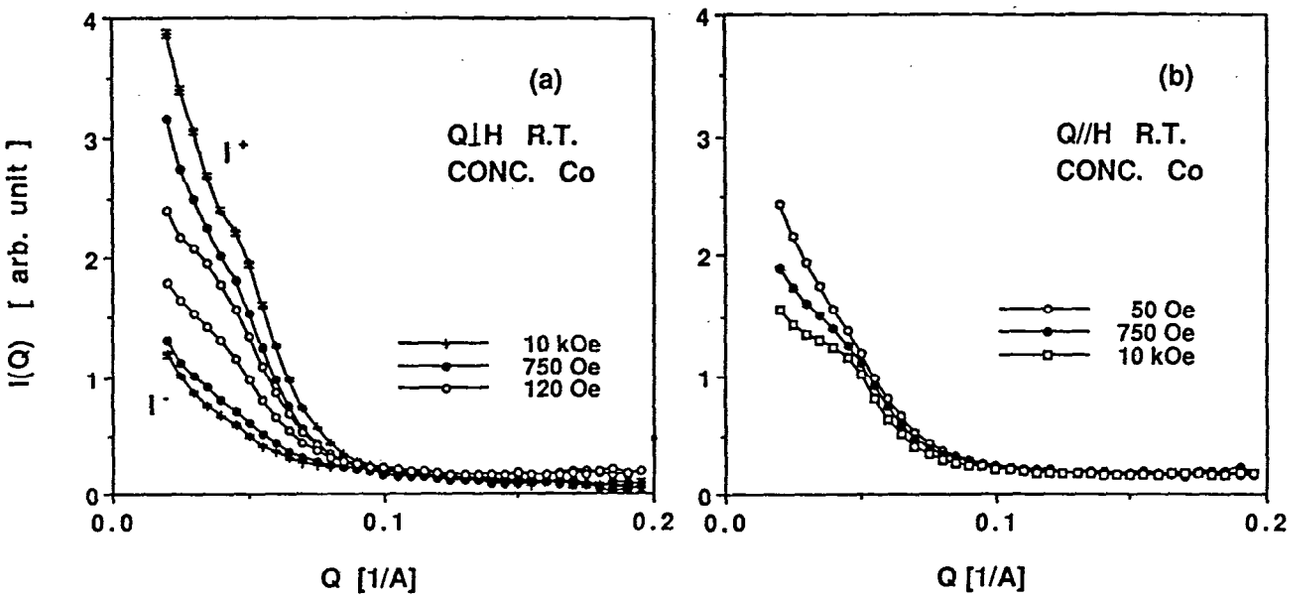

Fig.5 The observed scattering intensities from a cobalt ferrofluid. It spent about 2 hours to measure each scattering curve.

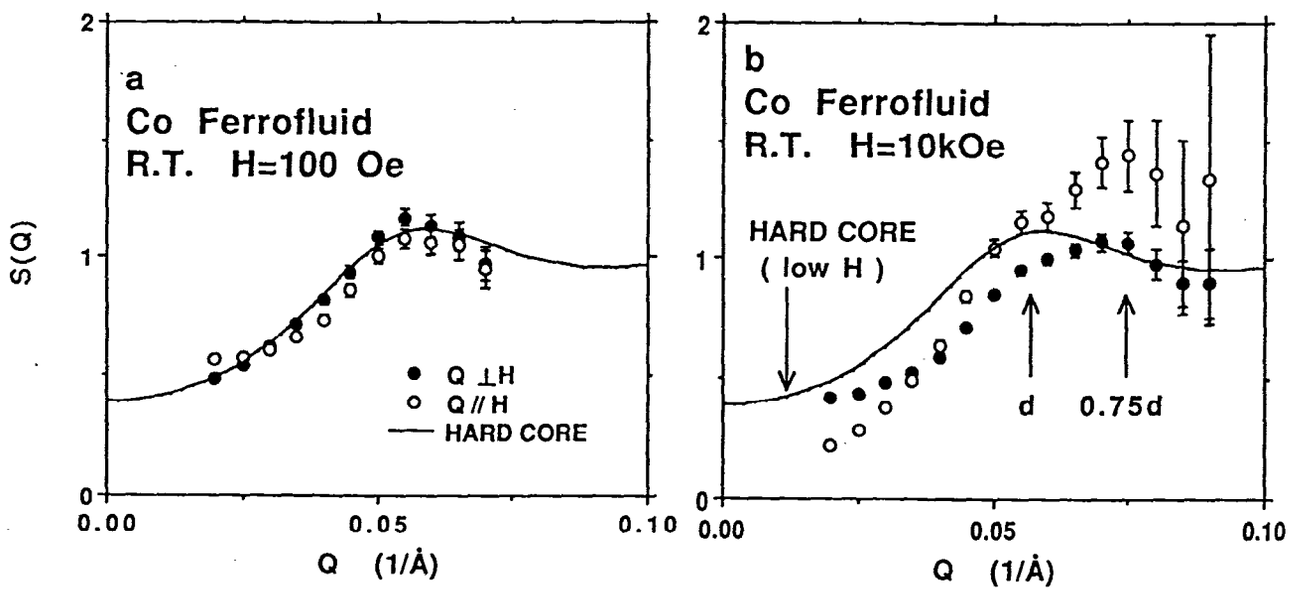

Fig.6 Distinguished structure factors under Q⊥H (closed circle) and Q//H (open circle). The interparticle correlations are isotropic under the weak external field of 100Oe (a) and anisotropic under the strong field of 10 kOe (b).

The structure factors distinguished from the intensities are shown in Fig.6. The interparticle correlations are isotropic under 100Oe but anisotropic under 10 kOe. First, the structure factors under the weak field are well approximated to random distribution of spherical particles, so-called Percus-Yevick approximation[8]. The solid line in Fig.6 is the calculation for the parameters of the volume fraction including surfactants η=0.11 and the diameter d=90Å which are experimentally determined. Next, the structure factors are anisotropic under the strong field and each structure factor has a main peak in the position corresponding to the particle-particle distance 0.75d and a shoulder corresponding to d. This result indicates that the particles are aggregated densely and the aggregation is stretching along the strong filed.

V. Conclusion

We have continuously improved the TOP spectrometer. The SANS experiments have achieved to the practical level by the present development and we have obtained excellent results. By the depolarization method, excellent results have been currently obtained as in the past.

Our next step is the development of the polarization analysis of the SANS system and the reflection method. In the present status of polarization analysis of SANS, the smallest scattering angle is 5°. If the analyzer can be placed at the position of smaller angle, for instance 2°, polarization analysis will work for the strong small angle scattering. Further developments are required and it is now under construction. The reflection method was listed above as another possible experiment using polarized neutrons. This method is known to be useful for studies of surface magnetism. Well-collimated beams are required for the realization of this method, it is also under construction. After these construction, we will achieve our purpose.

References

1) Y.Endoh, Y.Sasaki, H.Ono, S.Mitsuda and S.Ikeda, Physica 120B (1983) 45.
2) Y.Endoh, S.Ikeda, S.Mitsuda and H.Fujimoto, Nucl. Instr. Meth. Phys. Res. A 240 (1985) 115.
3) S.Mitsuda and Y.Endoh, J. Phys. Soc. Japan 54 (1985) 1570; S.Mitsuda, Y.Endoh and H.Yoshizawa, to be published.
4) M.Ishida, Y.Endoh, S.Mitsuda, Y.Ishikawa and M.Tanaka, J. Phys. Soc. Japan 54 (1985) 2975.
5) P.A.Seeger, Nucl. Instr. Meth. 178 (1981) 157; D.F.Milder and J.M.Carpenter, J. Appl. Cryst. 17 (1984) 249.
6) Y.Endoh, S.Itoh and S.Mitsuda, Proceedings of ICANS-IX (Villigen,1986)457.
7) R.Pynn, J.B.Hayter and S.W.Charles, Phys. Rev. Lett. 51 (1983) 720.
8) J.K.Percus and G.J.Yevick, Phys. Rev. 110 (1958) 1.

Q(J.B.Hayter): Does the polarization efficiency drop at longer wavelength because of depolarization effects somewhere in the instrument (perhaps in the Drabkin flipper)? Normally, it is easier to obtain good efficiency at long wavelength, unless q is small enough that (q/λ) becomes very small.

A(S.Ito): For the Soller type magnetic mirrors, spin dependent critical wavelengths $\lambda_c^{\pm} \sim (b \pm p)^{-1/2}$ exist, neutrons are polarized in the range of $\lambda_c^{+} < \lambda < \lambda_c^{-}$. If we could ideally choose as $b = p$, $\lambda_c^{-} \rightarrow \infty$, however, λ_c^{-} becomes finite because of the difference between b and p. Therefore beam is depolarized by the neutrons in other spin state.

Q(R.Pynn): Why does the polarization decrease with wavelength on TOP?

A(S.Ito): N/A

ICANS-XI International Collaboration on Advanced Neutron Sources
KEK, Tsukuba, October 22-26, 1990

Collimation and background reduction design for the time of flight neutron reflectometer SPEAR at *LANSCE*

W.A. Hamilton, G.S. Smith & R. Pynn
Manuel Lujan, Jr Neutron Scattering Center (*LANSCE*)
Los Alamos National Laboratory, NM 87544, USA

ABSTRACT
The effectiveness of neutron reflection measurements as a probe of surface and interface characteristics depends on the dynamic range of wave vector transfers over which the reflectivity can be measured, and upon the resolution possible within that range. We discuss some aspects of the design and our experience of the performance of the Surface ProfilE Analysis Reflectometer SPEAR at *LANSCE* with respect to collimation, wave vector transfer range and resolution and suppression of background.

I. INTRODUCTION

The reflection coefficient for neutrons (illustrated schematically in figure 1) is related to the profile of the neutron scattering length density, β, normal to the reflecting surface. For low reflectivities the relation reduces to the relatively simple form [1,2]:

$$R \approx \frac{[4\pi]^2}{Q_R^4} \left| \int_{-\infty}^{\infty} \frac{d\beta}{dz} \exp[iQ_R z]\, dz \right|^2 \qquad (1)$$

In which the reflectivity is proportional to the modulus squared of the Fourier transform of the gradient of the β profile and falls off as the fourth power of the reflection wave vector transfer perpendicular to the reflecting surface or interface. $Q_R = 4\pi\sin\theta/\lambda$, where θ is the angle of incidence and λ is the

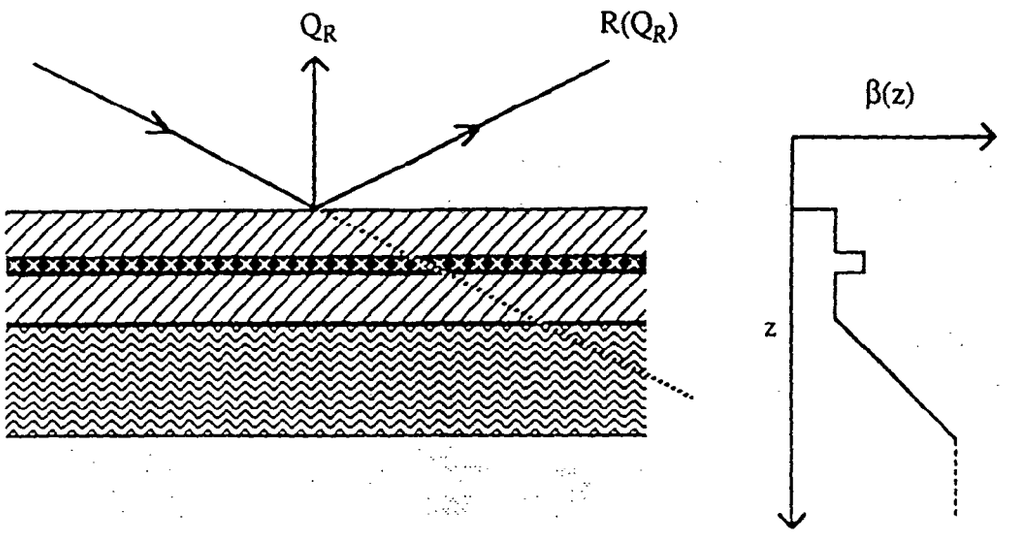

Figure 1. A schematic illustration of a reflectivity measurement. We wish to infer the scattering length density profile $\beta(z)$ from measurements of the reflectivity R as a function of the scattering vector Q_R.

neutron wavelength. Neutron reflectivity experiments measure the specular reflection as a function of Q_R, yielding information about the composition and density gradients at surfaces and interfaces.

As equation (1) makes clear, the information available from a neutron reflection experiment depends largely the dynamic range in Q_R over which the reflectivity can be measured. The maximum value of Q_R essentially determines the depth resolution of the technique. Firstly, this will be limited by available neutron wavelengths and scattering angles. Secondly, since reflectivity falls so rapidly with increasing scattering vector, instrumental backgrounds form various sources can combine to limit the minimum reflectivity, and hence maximum Q_R. Finally, the ultimate limits to the useful Q_R range are determined by sample dependent effects, such as incoherent scattering from the bulk [3].

II. SPEAR at *LANSCE*

On November 2-3, 1987, a workshop was held at the Los Alamos National Laboratory to discuuss the design criteria for a time of flight reflectometer based on the spallation neutron source at the Manuel Lujan, Jr Neutron Scattering Center (*LANSCE*) [4]. A feature that was overwhelmingly supported at the meeting was a vertical scattering plane, which allows reflection measurements from unconstrained liquid surfaces. Given the design restrictions associated with necessarily horizontal samples a number of measures were suggested to maximize the accessible range of Q_R. It was decided that the instrument should view a cold moderator to make available a large a range of neutron wavelengths as possible. Also, since backgrounds associated with spallation neutron production are intense, tight collimation of the neutron beam within the bulk biological shield was advised. Since the level of shielding required

necessarily fixes the incident angle upon a liquid surface, it was further decided that , the instrument should provide two independently operable beams at different angles to the horizontal. Thus allowing a choice of high and low angles of incidence and a consequent flexibility in Q_R ranges depending on the reflecting strength of samples.

The configuration of SPEAR as built on flight path 9 at *LANSCE* [5] is shown in Figure 2. The instrument views the liquid hydrogen moderator. Maintained at 20K, produces observable neutron flux to about 50 Å, well beyond the range necessary for reflection experiments. The moderated neutrons are collimated into two beams within the LANSCE target's bulk biological shield. These beams are inclined downward at angles of 1.5° and 1.0° to the horizontal and converge at a common sample position 8.73 m downstream from the moderator. A specially designed mercury shutter allows the beams to be operated either independently or simultaneously. As defined by the in-shield collimation the vertical angular full width of neutron illumination at the sample position of the beams is 0.15° and 0.1°, 10% of the nominal angles of incidence on a horizontal sample, with a horizontal divergence of 0.25°. The standard detector position is a further 3.65 m downstream from the sample. The moderator to detector distance of the instrument is therefore 12.38 m. At the *LANSCE* source's 20 Hz repetition rate this leads to a first frame overlap wavelength of 16.0 Å.

III.T_0 FLASH AND FRAME OVERLAP BACKGROUND SUPPRESSION

Equipment in the beam handling area between the bulk shield and the sample position is used to further tailor the beams' wavelength composition and horizontal collimation, and to suppress background contributions.

The first component encountered in this region is a T_0 chopper, located in a heavily shielded cave just outside shutter exit, about 4.5 m from the moderator. This device rotates to bring a 300 mm Nickel alloy (Inconel) slug into the beam paths during the initial flash of high energy neutrons and gamma rays from the spallation target, blocking them from the instrument cave proper. Altering the rotation direction and phasing of the chopper with respect to the neutron pulse allows the chopper to be opened as soon as desired after the flash for either beam. Typically we set the chopper to open at about 3 ms, admitting neutrons with wavelengths greater than 1 Å.

The fast neutrons eliminated by this chopper are a particularly significant background at short times, since they can be moderated in the instrument cave shielding and scatter into the detector arriving at the same time as neutrons reflected from the sample, overwhelming a weak reflection signal from short wavelength neutrons at high wave vector transfers. Our measurements of cave backgrounds show a background reduction by about three orders of magnitude when this chopper is in operation.

A further advantage of this chopper is that is enables direct measurement of the incident illumination upon the sample at short wavelengths using the same detector as we use for reflection measurements. Without the chopper it proved impossible to shield a normal ^{3}He tube detector sufficiently to prevent saturation due to the flash, from which the detector took 5 to 10 ms to recover, without blocking the moderated neutron signal altogether. This made a direct incident beam spectrum

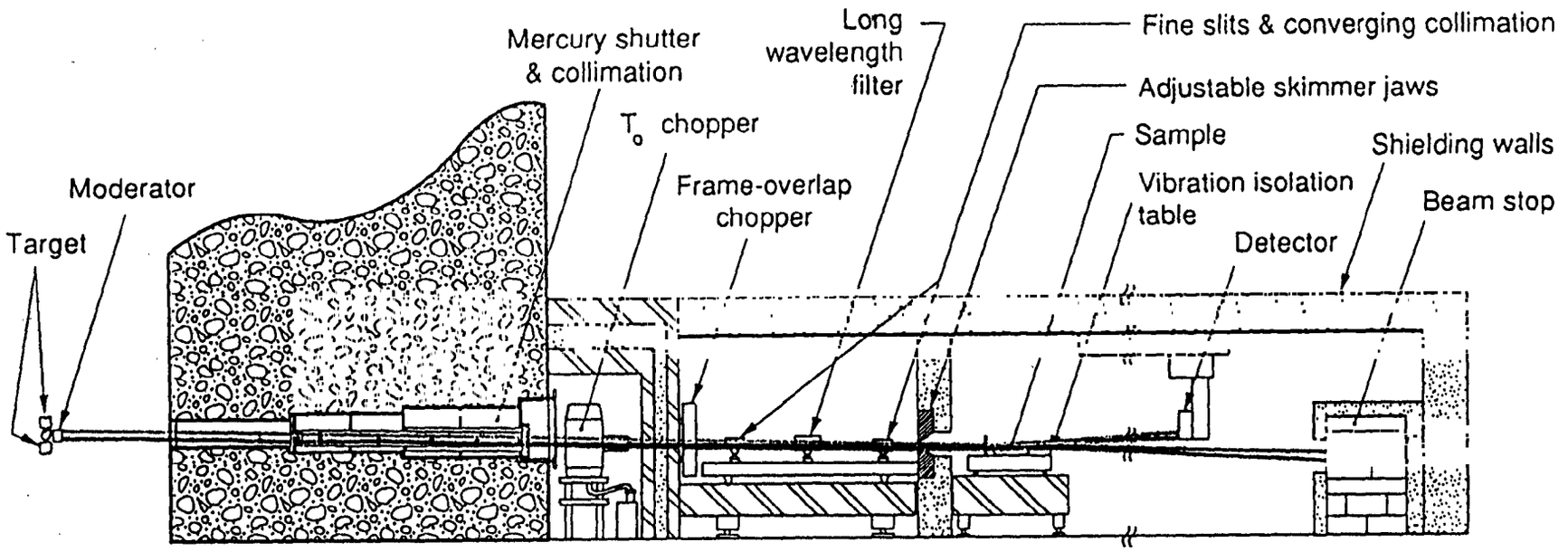

Figure 2 Physical layout of the Surface ProfilE Analysis Reflectometer SPEAR at *LANSCE*. The operation of the moderator, bulk shield collimation system, the T_0 chopper, the frame overlap chopper and mirrors, and detector are discussed in the text.

impossible for wavelengths below about 3 Å, and this region had to be measured with a less sensitive monitor detector. This introduced errors due to efficiency corrections between detectors into our determination of the reflection coefficient in this region. With the frame overlap chopper even our rather more fragile linear position sensitive detector can be used in the direct beam path with only cadmium slits in the beam handling area and at the sample position to reduce the neutron signal to suitable rates. Measurement of the incident illumination over the range 1 to 3 Å, increases our the reliably normalizable dynamic range range in Q_R at a given angle of incidence by a factor of three.

The neutron beams leave the enter the instrument cave proper from the T_0 chopper cave passing through narrow channels in the heavy shielding wall, and encounter a frame chopper mounted on the far side of that wall at the midpoint of the beam line (6.19 m). This chopper consist of a lightweight neutron absorbing disc (Boral backed by Cadmium) with two opposing 90° segments removed. Rotating at one half of the source repetition rate this chopper admits neutrons from either 0-16 Å or 16-32 Å depending on its direction of rotation. This has two effects. Primarily, this increases by a factor of two the range of Q_R accessible in measurements at a single angle, and allows us to measure reflectivities from a horizontal sample down to wave vector transfers of 0.007 $Å^{-1}$ using the 1.0° beam. It is also reduces frame overlap contamination of the reflected beam signal. Frame overlap contamination is a critical problem for time of flight reflection measurements since the falloff in intensity at longer wavelengths is offset to a large extent by the rise in reflectivity (at least until total reflection is reached at the critical value of Q_R). While this has a favorable consequence in that it evens out count rates and hence statistics across Q_R range of a reflection measurement, it also allows relatively few slow neutrons from a previous pulse reflected since they reflect very strongly from the sample to result in a signal comparable to that from the weak reflection of many more faster neutrons from the current pulse, when they arrive at the detector at the same time (1/v cross section contributions to detector efficiencies also work to exacerbate this problem). The frame overlap chopper acts as our first line of defence against this effect, blocking cross talk between the reflection signals the neutrons from two time frames.

As it happens, the hydrogen moderator is efficient enough that the 1-16 Å reflection signal can also be affected by frame overlap contamination from at least the beginnings of the 32-48 Å wavelength band admitted at the same time by the chopper. The simplest way to eliminate this final long wavelength contamination is to take advantage of their high reflecivity to filtering them out of the beam. We use a set of Nickel film on Silicon mirrors set at a relatively high angle (~3°) such that neutrons beyond 32 Å are totally reflected out of the beam onto the sample.

IV. BULK SHIELD COLLIMATION AND INSTRUMENT RESOLUTION

The choice of a vertical scattering plane and the use of neutrons of wavelengths of tens of Å has consequences not usually encountered in conventional neutron scattering. Our collimation, to a first approximation a geometric optics system of the simplest kind, has had to be designed to take into account gravitational "aberration" effects which become significant in our 16-32 Å frame.

Since we deal with such small angles of incidence ($\theta < 2^{\circ}$) the acceptance of most samples is small, of order a millimeter or so. Effectively acting as a narrow slit, this strongly defines the collimation of the neutrons In order to reduce background in the instrument we decided to do as much initial collimation as possible within the bulk shield. In the absence of gravitational affects neutrons the small acceptance of the sample would (with slight corrections for non-zero sample acceptances) allow us to define the angular spread ($\Delta\theta$) of the neutron beam upon the sample with a system of collimating slits converging to the sample position. A schematic of the actual situation is shown in Figure 3. Slow neutrons will actually fall appreciably away from a line of sight path in the time it takes them to travel from the moderator to the sample - a 32 Å neutron travels at 124 ms^{-1} and would fall 24 mm below the sample. To reach the sample slower neutrons need to start out at an angle above the direct path and from lower down on the moderator and these paths are blocked by line of sight collimation. This will cause us to lose illumination at longer wavelengths and will also cause the collimation angle to vary drastically with angle becoming tighter as a greater fraction of the paths are blocked eventually cutting off altogether. (This collimation variation is the main reason that this "gravitational filtering" of long wavelength neutrons was rejected as a solution to the 32-48 Å frame overlap contamination, in favour of the Nickel on Silicon reflection filters mentioned in the previous section.) To allow such paths the

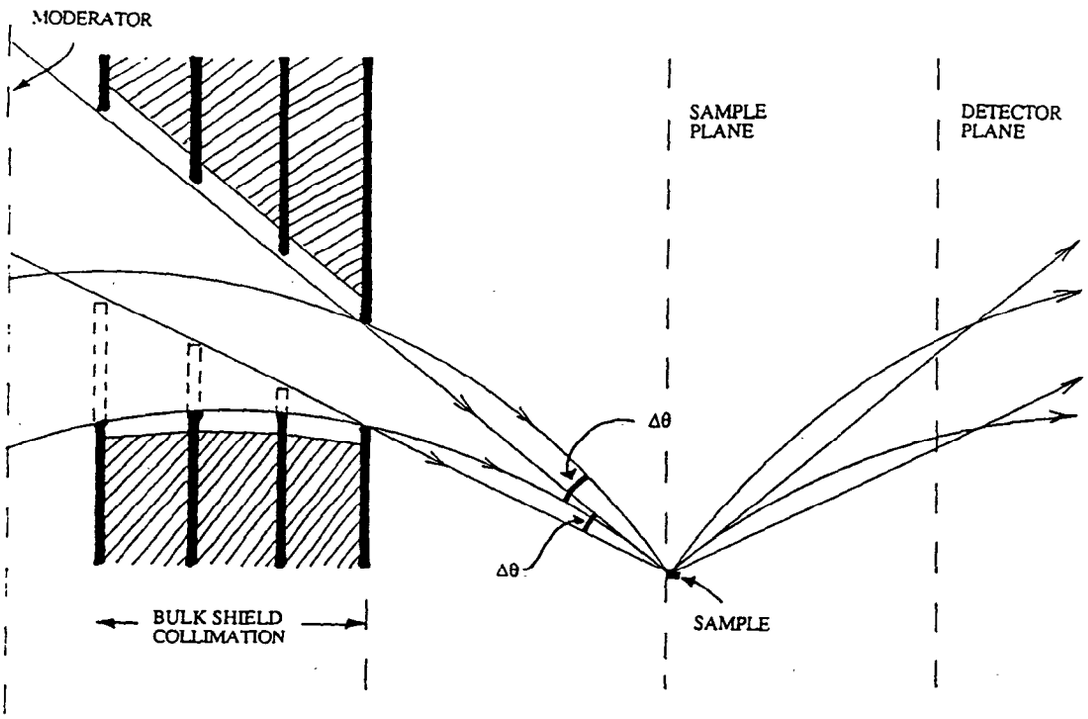

Figure 3. Gravitational effects on slow neutron trajectories (the vertical scale is exaggerated), showing the necessary breaking away of the bulk shield collimation elements to allow longer wavelength neutron to reach the sample position.

lower half of the collimation system has to break away from the line of sight path as it nears the moderator. At the entrance to the our collimation about 1 m from the moderator the slit edges of the collimation system have to be 7 mm below the fast neutron line of sight paths to allow a full angular spread, $\Delta\theta$, of 32 Å neutrons to reach the sample unimpeded.

One obvious consequence of the noticeably parabolic trajectories followed by longer wavelength neutrons is that they are incident upon the the sample at a higher angle of incidence than the line of sight collimation. At the 4.47 m separation between the exit slit of our collimation system and our sample position the center of the incident angle distribution is higher than the nominal line of sight value up by 0.08°, representing a +5% shift in Q_R for the 1.5° beam incident upon a horizontal sample. Another consequence of this higher angle of incidence is that when the slower reflected neutrons leave the sample they are initially aimed higher on the detector plane than the nominal straight line reflection trajectory. However, en route to the detector they will fall back towards and eventually cross its level as far from the sample as the sample is from the collimator exit (independent, to first order, of the angle of incidence upon the sample). Thus, if the collimation exit to sample distance were the same as the sample to detector distance, the reflected beam position on the detector plane would be essentially independent of wavelength. On SPEAR this was not quite realized, the distances are 4.47 m and 3.65 m respectively, resulting in a slight shift upward over the nominal postion on the detector of 1 mm for the reflection of 32 Å neutrons. Both these effects are easily dealt with in software when the reflection signal is normalized to the incident spectrum (as are related effects: a slight amount of gravitational focussing due the increase in angle, and an effective increase in the sample's acceptance).

SPEAR's current detector is an Ordela 1202N linear position sensitive detector with a resolution of 2 mm FWHM and an active length of 200 mm [6]. We acquired this detector mainly to enable the measurement of diffuse scattering from rough surface and interface samples and to allow us to measure and correct for instrument backgrounds by measuring in the off specular region simultaneously with our specular reflection measurement. For many good quality (flat) samples the detector has provided us with an unexpected bonus, allowing relatively high resolution measurements to be made without further collimating the incident beam and suffering a consequent loss of incident intensity.

Since our reflection plane is vertical this is the usual orientation of the detector allowing us to determine angles from the sample position 3.65 m away with a resoltion of ~0.03° FWHM. Data collected from by this detector is usually displayed by our analysis software as a two dimensional colour image. Figure 4 shows a typical data set, in this case reflection showing interference fringes from a thin film of Nickel on a Sapphire substrate. With angle on vertical scale and time of flight horizontally, the figure clearly shows that we can resolve features in wave vector transfer across the width of the beam, with the interference minima clearly crossing at an oblique angle. In fact, for many samples, such as this one, which show very little diffuse scattering and no significant broadening of the beam due to ripples on the sample surface, we can assume to a good approximation that all the scattering we see is specular, relative to the mean plane of the sample. If this is so the angular structure of the beam is undistorted by reflection from the sample and angular relations across the beam relate directly to relations of angles of incidence. In which case reflection features are aligned in directions of constant

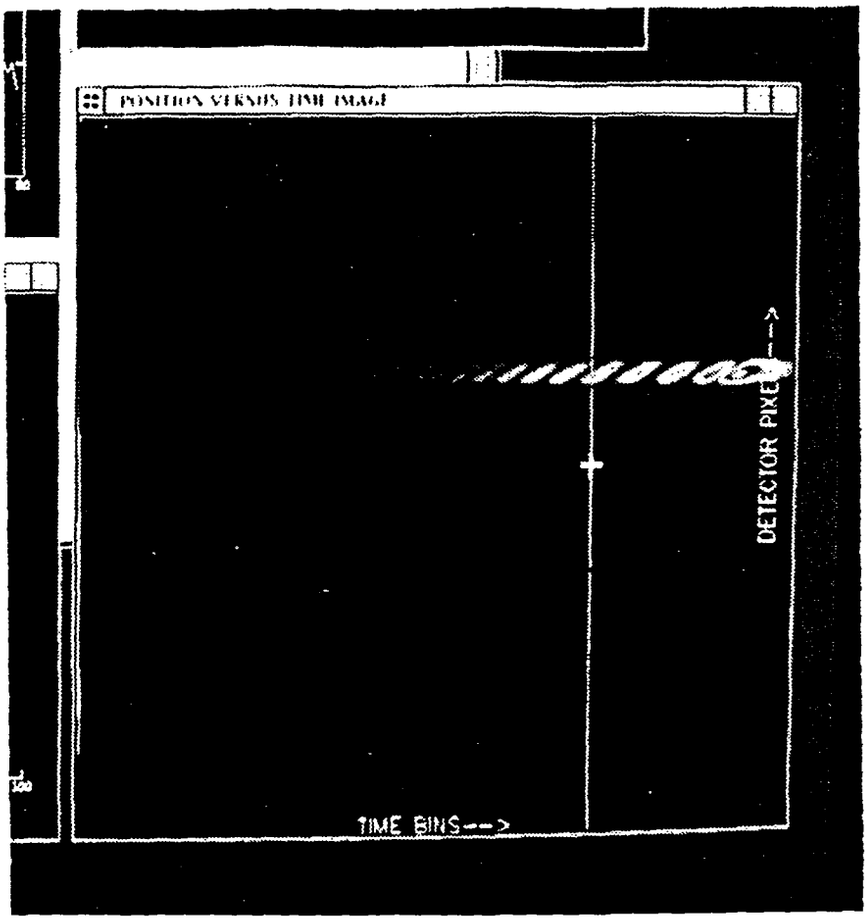

Figure 4. Reflected beam signal display from the SPEAR data acquisition system. The 0.15° collimated incident beam is clearly modulated by finer constant Q_R structure upon reflection, representing higher resolution reflectivity information.

$Q_R = 4\pi\sin\theta/\lambda$. Since $\sin\theta$ is proportional to height on the detector and λ is prortional to the time of flight these are lines of constant height/T, which is what we observe to be the case. (The gravitational shifts mentioned in the previous section distort this relation slightly).

This observation has meant that in general we have needed to do very little fine collimation beyond the bulk shield for good quality samples. Using the postion sensitive detector and the constant Q_R transform outlined above, we are able to determine the reflectivity to a resolution, typically $\Delta Q_R/Q_R$ ~1-2%, limiteded mainly by the angular resolution at the detector (determined by the detector resolution, the sample acceptance and the sample detector separation) and the wavelength resolution (determined by the neutron pulse width and the time of flight binning), and largely independent of our incident beam collimation.

V. CONCLUSION

We have presented some of the design features of the neutron reflectometer SPEAR. Using a T_0 and frame overlap choppers we have shown that background can be significantly reduced allowing measurements of much lower reflectivities. We have found that we can make routine use of neutrons up to 32 Å on pulsed source instrument by proper design of a collimation system which allows for gravitational effects on slow neutron trajectories. Finally, for many samples the use of a position sensitive detector enables us to make reflectivity measurements at good resolution and high incident intensity using a relatively coarsely collimated beam.

References

1. J. Lekner, *Theory of the Reflection of Electromagnetic and Particle Waves*, Martinez Nijof, Dordrecht, Holland (1987).
2. T.P. Russell, *X-ray and Neutron Reflectivity for the Investigation of Polymers*, Materials Research Reports, to be published.
3. J. Penfold, *Instrumentation for Neutron Reflectivity, Workshop on Methods of Analysis and Interpretation of Reflectivity Data at Argonne National Laboratory 23-25 August 1990*, to be published in Physica B.
4. *A Neutron Reflectometer for LANSCE ?, Report of a Workshop held at the Los Alamos National Laboratory November 2-3 1987.*, ed. D.K. Hyer, Los Alamos National Laboratory Conference Report, LA-11301-C (1988).
5. *Condensed Matter Research At LANSCE*, ed. D.K. Hyer, Los Alamos National Laboratory Publication, LALP 90-7 (1990).
6. Product Summary, Oak Ridge Detector Laboratory, Oak Ridge, Tennessee (1989).

Q(M.Furusaka): What is the type of detector you use?

A(R.Pynn): An ORDELA linear PSD with a nominal positional resolution of about 1.5mm.

Q(W.G.Williams): At what wavelength does the gravity correction become significant? Our calculations at RAL suggested gravity effects could be ignored at $\lambda<10$Å.

A(R.Pynn): I would agree. We can just see the correction towards the end of the first frame, around the 14Å mark.

ICANS-XI International Collaboration on Advanced Neutron Sources
KEK, Tsukuba, October 22-26, 1990

First Results from SANDALS – the Small Angle Neutron Diffractometer for Amorphous and Liquid Samples at ISIS

A K Soper

Neutron Science Division, Rutherford Appleton Laboratory, Chilton, Didcot, Oxon, OX11 0QX, U.K.

Abstract. SANDALS is a liquids and amorphous diffractometer which uses the broad epithermal flux of neutrons available at a pulsed neutron source. It exploits the fact that the Placzek or inelasticity correction in diffraction data from liquids is minimized at small scattering angles and high incident neutron energies. At the same time it measures the structure factor, S(Q), over a broad range of wave vector Q and this enables the pair correlation function to be evaluated more reliably than on conventional diffractometers. The physical constraints on the design of such an instrument are fairly severe: any vacuum windows and apertures in the neutron beam must not be seen by the small angle detectors, in order to keep backgrounds as low as possible. Only boron carbide can be used for the collimator apertures because traditional absorbers such as cadmium are transparent over the broad range of energies used by the instrument. And there is a minimum requirement to have the resolution $\Delta Q/Q$ in the range 1-4% for most liquids experiments. Three modules of 20 zinc sulphide scintillator detectors, out of a possible complement of 90 modules, have been run for a trial period. A further group of 15 modules is currently being installed. The instrument fulfilled all its design specifications, with backgrounds at the 1% level compared to scattering from a standard vanadium scatterer. A significant effort has gone recently into evaluating the absolute stability of the detector. Some of the initial results using hydrogen/deuterium substitution on molecular liquids are presented.

1. INTRODUCTION

After a long design and construction period SANDALS began operation in December 1989, albeit with only 3% of its full complement of detectors in place. This was the culmination of several years of design studies and some tests with a prototype detector. In the course of this period the basic specification for the instrument, which was extremely stringent as originally proposed [1], was modified slightly so as to ensure that the likely count rate at ISIS would be competitive with or exceed the capabilities at equivalent facilities worldwide. This would be in addition to the unique features of SANDALS as a small angle diffractometer. The result is a compromise between the ideal instrument as originally envisaged and the requirements of most users who would be unable and unwilling to spend more than a few days at a time running an experiment. The initial results indicated that this compromise is not severe and the instrument has already demonstrated its potential to map out partial pair correlation functions over a range of state conditions in a relatively short time. As further detectors are added it will become increasingly powerful in this regard and in the future there is a very real likelihood that the sample preparation and data analysis stages will become the rate limiting factors.

A key element of the design of SANDALS and of other high count rate pulsed neutron diffractometers of its type is the construction of large solid angle banks of detectors. For SANDALS the solid angle of the detectors in the scattering angle range 3° to 41° is 40% of its theoretical value of 1.5sr because the engineering constraints imposed by other factors in the design simply prevent it being made any larger, yet this already presents a major project to install and monitor the performance of the ~1800 individual detector elements involved. The use of ^{3}He proportional counters was ruled out early on partly for reasons of cost, but also because they would not make optimal use of the epithermal neutron flux. Instead a major effort has gone into developing a zinc sulphide scintillator detector which can be made twice as efficient as ^{3}He and can also be packed much more compactly into the available space. All the indications are that the performance of this detector is excellent in terms of quiet count, deadtime, efficiency, and γ-sensitivity, but as with any new design unexpected difficulties, primarily associated with the detector, stability were encountered. This was partly a result of the very stringent requirements imposed on a liquids diffractometer of this type. As a result the completion of the first bank of detectors has been delayed by about 9 months while a full analysis of the stability question has been conducted. It is now believed that the main elements of the problem are understood and construction of the next batch of 15 modules is proceeding rapidly.

A review of the background which lead to the present SANDALS instrument was given in the previous ICANS proceedings [2]. In this paper the underlying design principles are reviewed with the main part of the article concentrating on the early commissioning runs. In addition the results of some of the first user experiments are described.

2. DESIGN CONSIDERATIONS

ISIS is a 50Hz pulsed neutron source. On a methane moderator the neutron spectrum has declined to about 1/10th of its peak intensity in the maxwellian at a wavelength of about 5Å, which corresponds to a time-of-flight of 1260μs per m. Therefore in order to avoid serious frame overlap problems without the use of either a filter or a frame overlap chopper (both of which have the effect of reducing the incident flux significantly) the maximum allowable total flight path from source to detector is limited by the 20ms window to about 15m. The present SANDALS has been designed around this constraint, although there is nothing to prevent the flight path being increased in the future, with the inclusion of a chopper, in order to improve the resolution. It is unlikely the final flight paths can be increased very much without a substantially increased detector cost.

The second major constraint was the resolution. Although the structure peaks from a liquid or amorphous material are generally quite broad, the resolution is normally expressed (and obtained) as a ratio in $\Delta Q/Q$ so that the true resolution, ΔQ, gets *broader* at large Q. Therefore if the structure factor persists to large Q, as occurs very often in molecular liquids and amorphous solids the instrument resolution can become a significant factor in determining the true width and shape of peaks in the pair correlation function. Normally the ideal resolution for a liquids diffractometer is

in the region of 1-2% , but in SANDALS this has been set to 2-4% for most angles because to make it much smaller results in a factor of 20 or more reduction in count rate. However there is some provision for changing the beam defining apertures to alter the resolution to a lower value if so needed.

The requirement for resolution couples strongly with the collimator design. Since energies as high as 100eV are to be used for diffraction on SANDALS, the collimator can be made only of materials with significant absorption at epithermal energies, like boron carbide. Special emphasis was placed on ensuring that a series of beam defining rings along the collimator could not be seen directly by the small angle detectors. In this way the background from collimator scattering has been held to a minimum. Since the resolution function at small angles is dominated by the angular divergence of the incident beam, the viewed area of moderator and the sample size are important factors when calculating the resolution and these in turn control the rate of decrease in the collimator aperture with increasing collimator length.

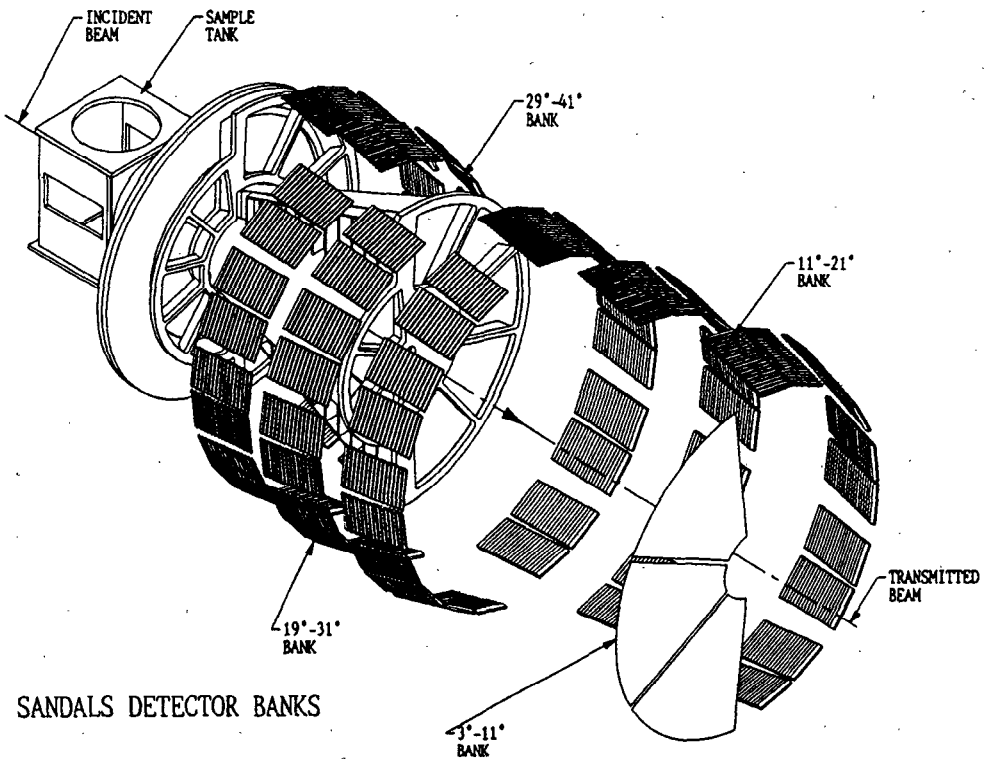

Figure 1. Drawing of the SANDALS vacuum tank and detector array. The beam enters at the top left and leaves at the bottom right. The detectors are arranged on the surface of a cylinder corresponding to a constant resolution trajectory. The odd shaped vacuum tank allows a continuous span in scattering angle from 3° to 41°

Obviously optimising the count rate has been a major item in the final design, in order to be able to exploit fully the scientific opportunities for looking at the state dependence of *partial* structure factors. In addition provision has been made to allow significant amounts of shielding between detector modules and to have a continuous coverage of detector angles from 3° to 41°. The same design also has a continuous variation in resolution over this angular range. Furthermore the resolution is nearly constant resolution for the angular range 11° to 41°: this will greatly assist in experiments

which attempt to determine the inelasticity correction by comparing diffraction data at different scattering angles, and also for experiments where anomalous dispersion near a resonance is attempted. There is provision for further detectors at larger angles should the demand arise in the future. An outline drawing of the instrument in completed state is shown in figure 1.

3. SANDALS DETECTORS

As described above the zinc sulphide scintillator detectors form the backbone to the design of SANDALS. The detectors are grouped into modules of 20 detectors each, and each detector consists of a zinc sulphide scintillator/glass sandwich which views the neutrons scattered by the sample. Each detector is viewed by two photomultiplier tubes via an air coupled light guide made from silvered milar film. The whole unit, consisting of 20 scintillator sandwiches, 20 light guides, and 21 photomultiplier tubes is housed in mold made from boron carbide powder and expoxy resin, with provision for attachment of the associated wiring at the back of the module. The modules are mounted on the circumference of a cylinder of radius 0.8m about the transmitted beam, by means of a large steel and aluminium frame, figure 2. The entire detector array and vacuum tank are housed in a blockhouse made from 300mm thick wax tanks.

The signal cables from each module are fed out through holes in the blockhouse to racks of electronics, where the signals are first amplified and discriminated and then fed to an encoder units which looks for coincidences between neighbouring phototubes and generates an appropriate computer address. The rest of data acquisition electronics and computer hardware is identical to that found on the other ISIS neutron spectrometers.

Evidence that this system of neutron detection is successful is shown in figure 3, where the diffraction pattern from sintered magnesium oxide is shown for the initial batch of 60 detectors (3 modules). The uniformity from one detector to another is generally very good, as is the signal to noise ratio in the Bragg peaks. Note that the Bragg peaks all occur at short times of flight because the scattering angle is small and in the range 11° to 21°. In addition it will be noted that the resolution is almost the same across this angular range, even though the value of $\cot\theta$, which dominates the resolution at small angles (2θ is the scattering angle), changes by a factor of 2 in the same region.

A difficulty which had not been anticipated was the large amount of heat produced by the crates of electronics: coupled with an unusually hot summer the temperature immediately above the crates often rose above 40°C at times with a diurnal variation of up to 15°C. As a result a significant temperature instability was observed. This was cured by installing temperature compensation in all the relevent electronic modules. A further step to be executed early in 1991 will be to install air conditioning both inside the blockhouse and around the sensitive electronics. Other sources of instability possibly associated with mains supply fluctuations have also been investigated. Obviously since most liquids or amorphous materials experiments rely on comparison of sample scattering to a standard scatterer it is imperative that good detector stability is achieved.

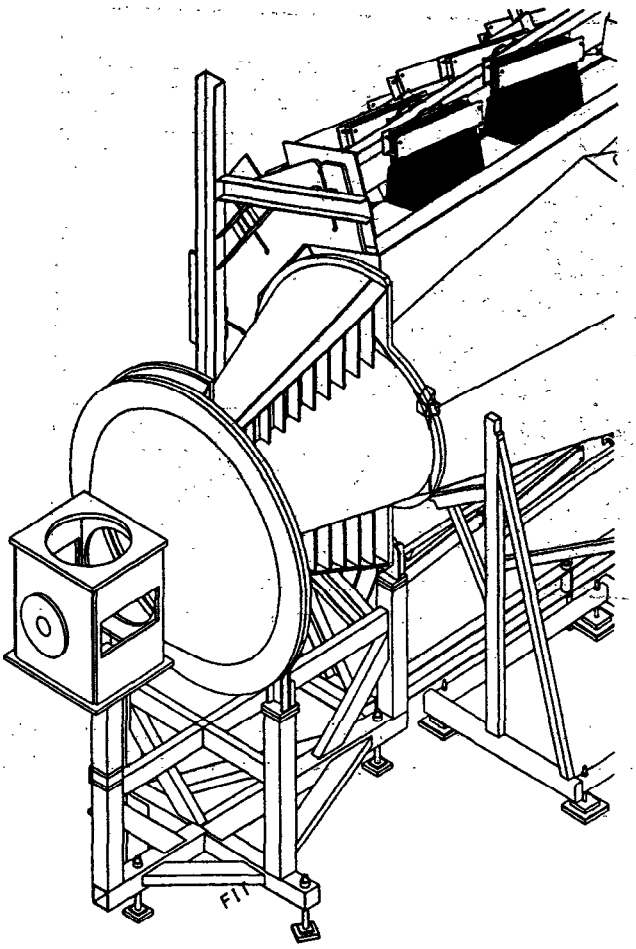

Figure 2. Drawing of part of the mounting for the SANDALS detector modules. The sample vacuum tank is shown at the bottom left mounted on a steel frame. This is where the neutron beam enters. In the middle are the conical-shaped vacuum and argon-filled flight paths and at the top are the scintillator modules (shaded black) in their support frame

4. NEUTRON BACKGROUND

For all three modules the beam on, no sample background was extremely good, and lay at the 1-3% level, compared to the scattering from a standard vanadium rod, over a very wide energy range (see figure 4). A slight turn up is seen at the lowest energies, and this arises from the intrinsic quiet count of ~15 counts per minute of these high efficiency detectors. It is expected that this quiet count can be reduced with an improved discrimination system

5. COUNT RATE

The measured C-number (see [2] or the ATLAS Manual [3] for the definition of C-number) for the first three modules is shown plotted in figure 5. The measured numbers have been scaled by a factor of 6 to correspond to the situation when installation of 1/5th of the detectors is completed early in 1991. For comparison the D4 diffractometer

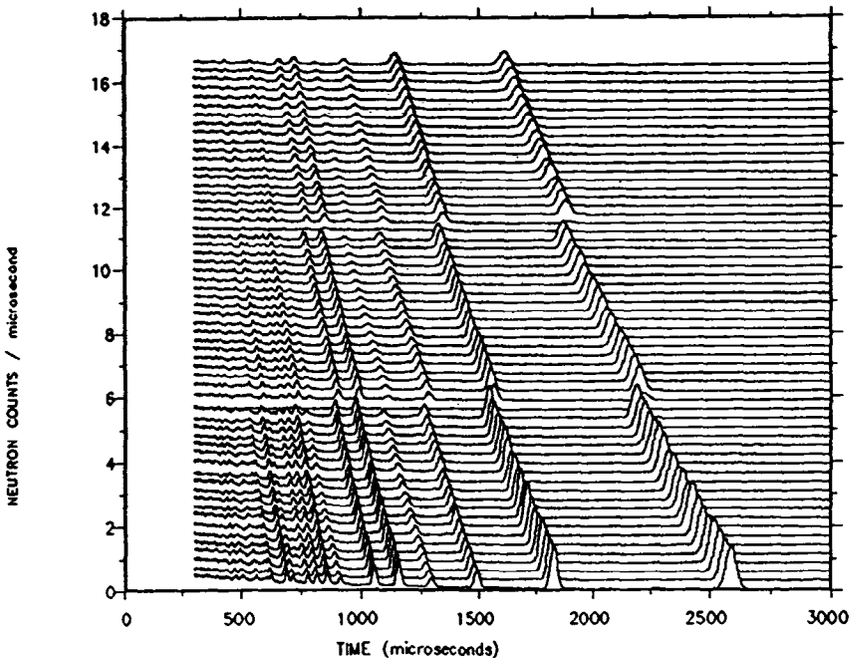

Figure 3. Diffraction pattern from sintered magnesium oxide showing 60 SANDALS detectors in operation simultaneously. The steps in the lines of peaks correspond to the different flight paths for each module

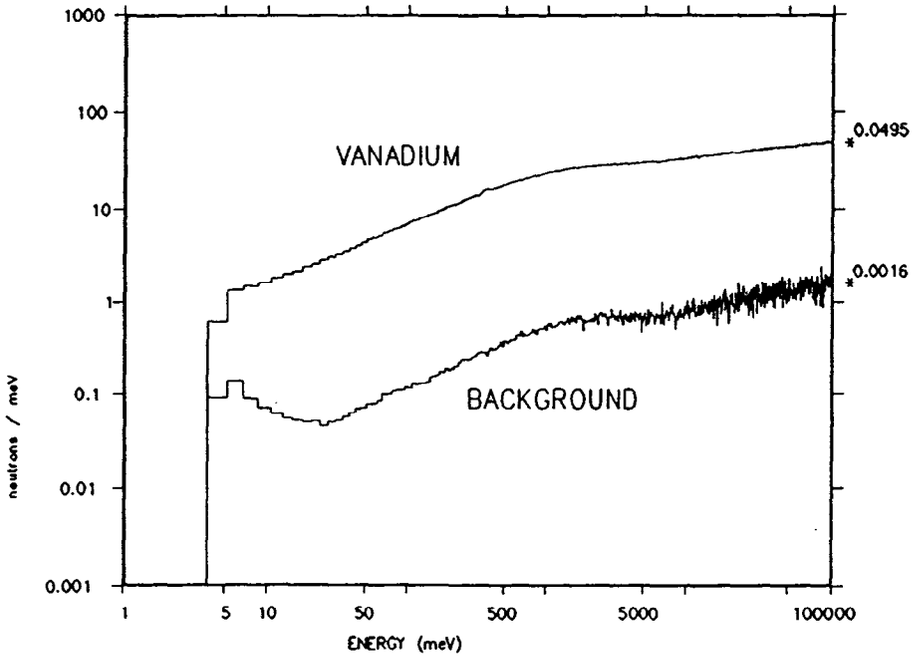

Figure 4. Background on SANDALS compared to the scattering from vanadium at a scattering angle of 12°. Note that even at 100eV the background is still 3% . This is much better than has been achieved on other ISIS diffractometers.

at ILL has a C-number of 53 n/0.05Å^{-1}/s/cm^{3}V over the wave vector range 0.4Å^{-1} to

17Å^{-1}. The measured numbers appear to be below the expected count rate by about a factor of 2, but this is a function of the detector set up. The method of coincidence used to determine if a neutron event has occurred is extremely good at discriminating against bad events, but it maybe that the discrimination is too severe at present.

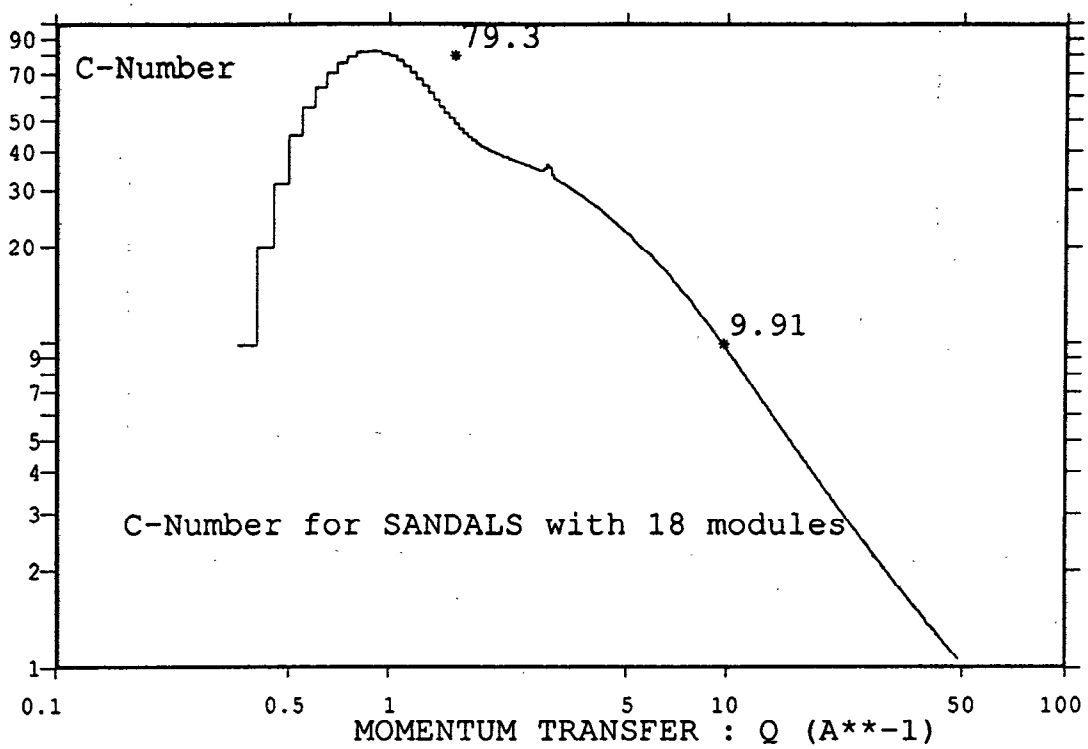

Figure 5. Measured count rate for SANDALS scaled up to the 18 modules which are to be installed shortly

6. RESULTS FOR SILICA AND WATER

Figure 6 shows the pair correlation function obtained from SANDALS data taken on two sheets of silica, each 3mm thick. The Si-O and O-O distances can be clearly identified in this curve, and the width and height of the main peaks is in good agreement with that obtained elsewhere [4]. The data were recorded in 6 hours on SANDALS and the transform procedure [5] used all the data out to Q=50Å^{-1} and included the resolution function in the calculation.

For water this was a standard hydrogen/deuterium substitution experiment in which the H-H, O-H and O-O partial structure factors were extracted. The data was recorded at the rate of 1 sample per 24hrs. The oscillations in the O-O function (see figure 7) appeared to damp out quicker than had been expected from earlier work and this leads to a slightly broader main peak in g(r), but otherwise the agreement with the earlier reactor work was extremely good, with coordination numbers entirely as expected.

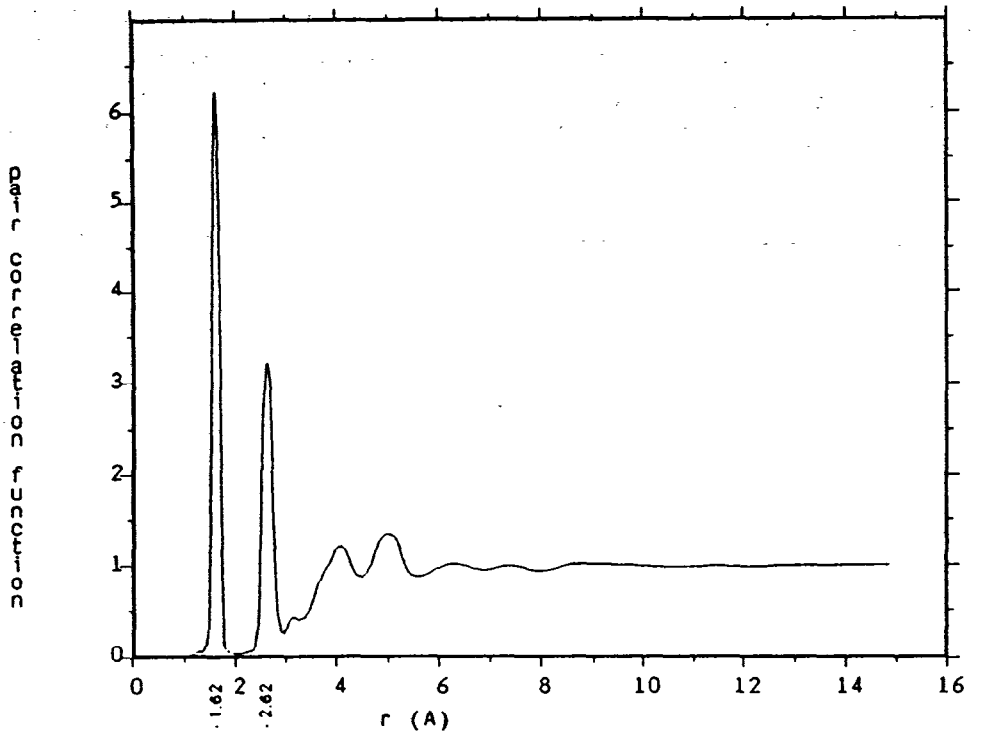

Figure 6. Pair correlation function obtained from the SANDALS data on Silica. Note the sharpness and height of the first two peaks, even though all the data has been accumulated at scattering angles below 20°.

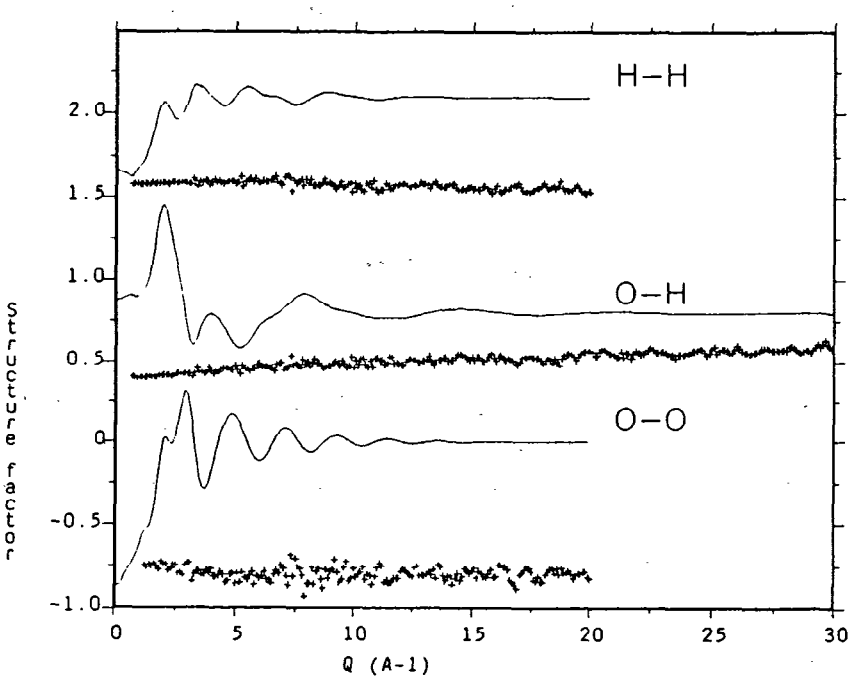

Figure 7. Minimum noise [5] fits to the measured partial structure factors for water as measured on SANDALS. The crosses show the residual between data and fit.

7. THE FIRST USER RESULTS

To date four user experiments have been completed on SANDALS. These include a study of the structure of water in dimethyl sulphoxide (DMSO) solutions, the structure of water and the distribution of cations in tetramethylammonium (TMA) chloride solutions, the structure of water in ethylene glycol solutions ("anti-freeze") as a function of lowering the temperature, and most recently the structure of superheated water up to 175°C. All involved the use of the H/D substitution method to extract partial correlation functions. Where there are more than two components present this method still extracts three correlation functions, but the partials are themselves composite correlation functions, consisting of a weighted sum of several correlations. For this reason the H-H function is the easiest to interpret.

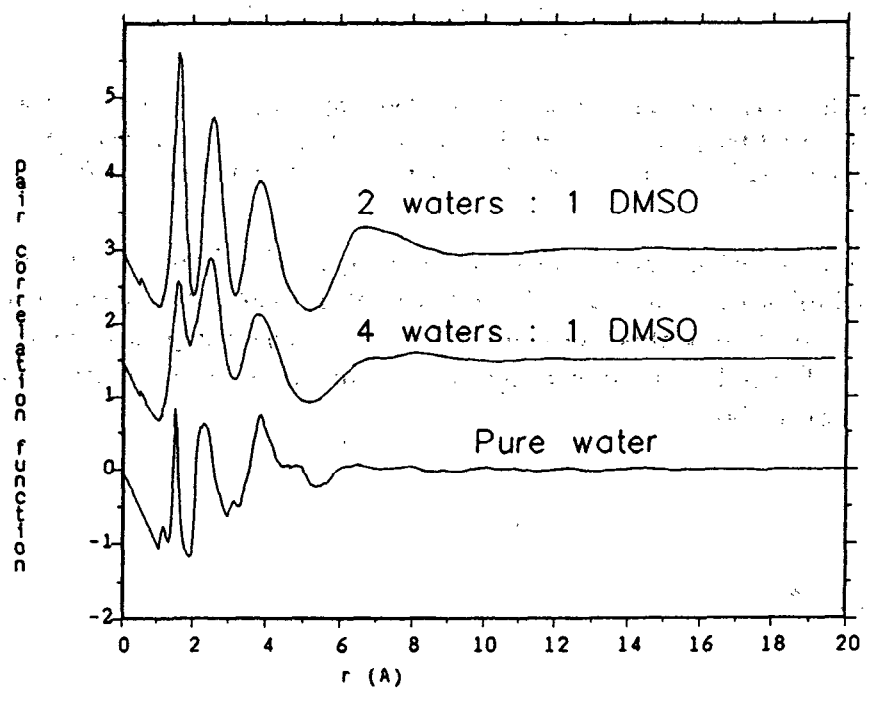

Figure 8. H-H correlation for two concentrations of DMSO in water compared to the same function for bulk water. A general broadening and shift of the peak at 2.4Åcan be seen at the highest concentration.

For the DMSO solutions the main result was that this molecule apparently forms stronger hydrogen bonds with water than water does to itself: the g(r) functions remain quite structured at high concentrations but there is a shift in the peak at 2.4Åto larger r values as the concentration increases, figure 8. This is what would be expected if the oxygen on the DMSO formed 2 or 3 hydrogen bonds with the water, leaving fewer water molecules bonded to themselves. This result is in direct contrast to what was found for TMA, methanol [6] or ethylene glycol, where the tetrahedral water structure is preserved even at high concentrations.

The ethylene glycol solutions also revealed an iteresting result. At the lowest temperature, 160K, the solution is expected to become a mixture of a glassy ethylene

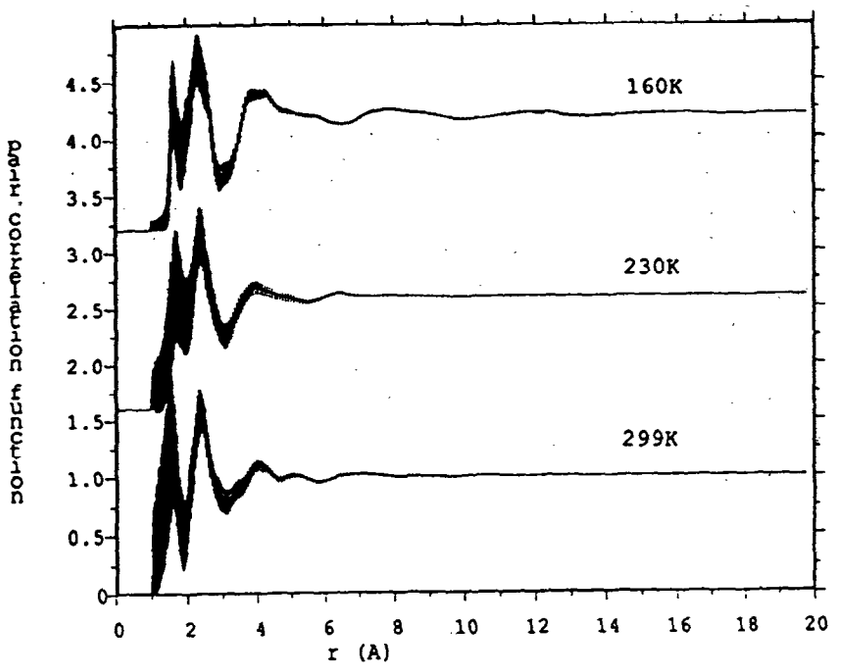

Figure 9. The H-H correlation function in concentrated ethylene glycol solutions as a function of temperature. In the lowest temperature phase (166K) the freezing does not appear to affect the short range significantly but does introduce a long range correlation out to and beyond 20Å

glycol/water mixture, with excess water appearing in the form of ice. In fact the diffraction data indicated that most of the water was frozen, by virtue of the Bragg peaks which appeared, but this does not affect the short range proton correlations very significantly, figure 9: the long range order appears as an oscillation in the pair correlation function to large r.

8. CONCLUSION

The initial results on SANDALS described here give an indication of the powerful and exciting science that will be possible as the detector banks are completed. It is already clear that the instrument is performing up to design characteristics, with a particular emphasis at present on ensuring the detector stability is adequate for the likely counting statistics. The number of user derived experiments will increase steadily as expertise at operating the instrument and performing the data analysis increases, and it is likely that the time taken to acquire datasets will become less. Hence it is hoped to realize the aim expressed long ago of mapping out the pair correlation function as a function of state conditions. This serves as an extremely stringent test of the computer simulation models. It is likely that the full power of small angle diffraction from liquids and amorphous materials will only be realised when methods like Reverse Monte Carlo [7] can be incorporated into the data analysis.

Acknowledgments

The development of SANDALS would not have been possible without the considerable assistance from a large number of people, in particular K. Brine, B. Holsman, S Spurdle and A F Gilleard of the ISIS design team, P L Davidson, N J Rhodes and E Mott of the ISIS detector group, and B C Boland and R Hall of the ISIS operations groups. Invaluable support and advice have been received from P A Egelstaff, J Penfold, J L Finney, A D Taylor, M W Johnson, W S Howells, A C Hannon and many others of the ISIS team.

References

1 W S Howells, A C Wright, R N Sinclair, and J C Dore, SERC internal report, Appendix to NBRC 9–85, 1985

2 A K Soper, *Advanced Neutron Sources 1988*, ed. D K Hyer, IOP Conference Series No. 97, p353, 1989

3 A K Soper, W S Howells, and A C Hannon, *ATLAS – Analysis of Time-of-Flight Diffraction Data from Liquid and Amorphous Samples*, Rutherford Appleton Laboratory Report RAL-89-046, 1989

4 D J Grimley, A C Wright, and R N Sinclair, J. Non-Cryst. Sol. **119**, 49, 1990

5 A K Soper, Proceedings of a Workshop on Neutron Scattering Data Analysis 1990, to be published by IOP

6 A K Soper and J L Finney, Proceedings of a Symposium on *Hydrogen Bond Physics* Il Ciocco, Italy, 1990, to appear in J. Mol. Struct.

7 R L McGreevy, Proceedings of a Workshop on Neutron Scattering Data Analysis 1990, to be published by IOP

Q(P.A.Egelstaff): SANDALS will give a lot of new and exciting information on amorphous samples; can you tell us of the ideas the U.K. amorphous materials group may have for exploiting this instrument?

A(J.L.Finney): The major demand immediately is in studying partial paircorrelations in hydrogenous systems, eg, aqueous solutions of ions and molecules TMACl, DMSO, ethyleneglycol as functions of temperature and pressure. As the detector component increases, we expect a major increase in work probing structural changes as a function of state point.

ICANS-XI International Collaboration on Advanced Neutron Sources
KEK, Tsukuba, October 22-26, 1990

Status of the New GLAD Instrument at IPNS*

R. K. Crawford, J. M. Carpenter, R. Dejus, J. R. Haumann, R. Kleb,
D. G. Montague,[§] D. L. Price, and S. Susman
Argonne National Laboratory, Argonne, IL 60439.
[§]On leave from Willamette University, Salem, OR.

ABSTRACT

The complete flight path for the new glass, liquids, and amorphous materials diffractometer (GLAD) at IPNS is now in place, and 160 linear-position-sensitive detectors have been installed. This paper discusses the final instrument configuration and calibration of the instrument. Some of the development of instrument components and data analysis software utilizing the GLAD prototype, which operated for ~ 2 years prior to the installation of GLAD, are also discussed.

I. INTRODUCTION

The new Glass, Liquids, and Amorphous Materials Diffractometer (GLAD), which was been described in detail at an earlier ICANS meeting,[1] has recently been installed at IPNS. In order to develop various components and techniques for the instrument, a prototype flight path with 55 linear-position-sensitive detectors (LPSDs) was operated on the GLAD beamline during 1988-1989. This report summarizes the experience obtained with the prototype flight path for that instrument, the current status of the final version of the instrument, and the status of the data analysis software.

II. INSTRUMENT STATUS

The main vacuum tank arrived at IPNS in December, 1989. The prototype flight path was removed and the final flight path, evacuated scattering chamber, detectors, and shielding were installed during Spring, 1990. The first measurements with a sample in the new flight path were made in July, 1990. Figure 1 shows what GLAD looks like in relation to the adjacent instruments,

*Work supported by U.S. Department of Energy, BES, contract No. W-31-109-ENG-38.

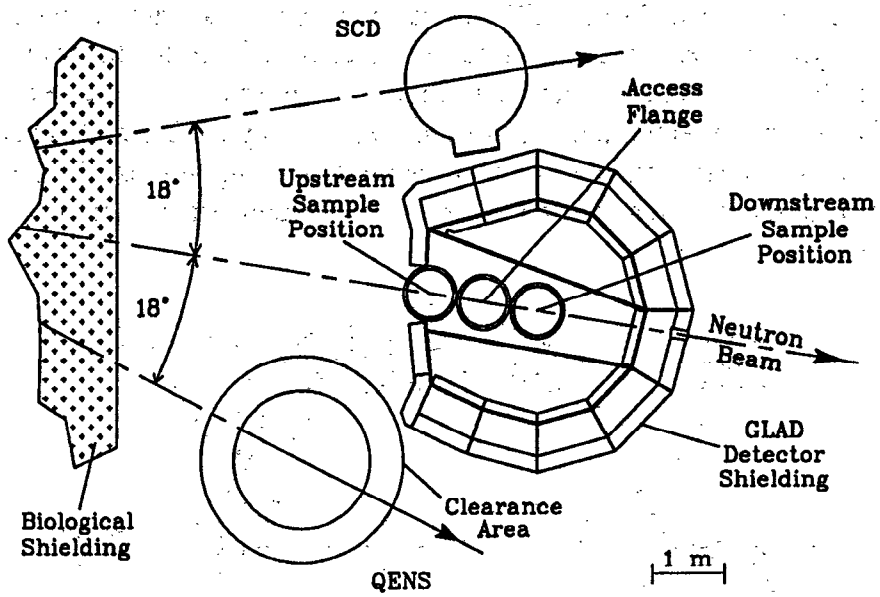

Figure 1. Schematic of the final layout for GLAD in relation to the adjacent instruments SCD and QENS.

QENS and SCD. GLAD has two sample positions, an upstream position 9.0 m from the moderator for the highest resolution measurements and a downstream position 10.5 m from the moderator, which provides higher data rates at some sacrifice in resolution. Crossed converging soller collimators focused on the forward detector bank provide the final collimation for the thermal and epithermal neutrons used by GLAD. With this collimation scheme the sample size does not contribute significantly to the resolution,[2] so samples up to ~2.5 x 2.5 cm^2 can be used at the upstream position. A series of massive apertures upstream from the soller collimators serves to define the beam, and is the primary collimation for those higher-energy neutrons for which the soller collimators become transparent. The last of these massive apertures can be adjusted to control the beam size to minimize the amount of background when smaller sample sizes are used. The flight path is evacuated and the detectors are located outside this vacuum, viewing the sample positions through thin Al windows.

The evacuated flight path, soller collimators, and detector modules are shown in Fig. 2, which also indicates the locations of the detectors near the inner edges of the modules. When the upstream sample position is used this detector locus is approximately the focusing locus for the soller collimators,[2] although some compromises have been made at the higher scattering angles in order to optimize the total resolution. All of the GLAD detectors are LPSDs, and there are 160 LPSDs mounted in 4 detector modules in the final version of GLAD at this stage. Each of these LPSDs is a cylindrical gas-proportional-counter, 1.11 cm inside dia x 60 cm active volume, filled with 10 atm of ^3He, and encoded into 64 segments by charge-division encoding. These 160 LPSDs completely fill three detector modules at low angles and partially fill a fourth module at the higher angles. These modules are indicated in Fig. 2. In order to cover as small scattering angles as possible, the LPSDs in the forward detector module extend through the path of the direct beam. A small B_4C "beam attenuator", described in detail elsewhere,[3] is located in the beam upstream from these LPSDs (see Fig. 2) to absorb enough of the direct beam to protect these LPSDs from

significant overload. The currently-installed detectors cover scattering angles from -9° to +47° for the upstream sample position and from -17° to +95° for the downstream sample position, with the negative sign implying scattering angles measured clockwise from the direct beam when viewed from above, as in Fig. 2. Angular coverage is continuous over these ranges except for the small gaps between the detector modules and the portions excluded by the beam attenuator at very-small scattering angles. The beam attenuator obscures the scattering angles $|2\theta| < 1.7°$ when the upstream sample position is used and $|2\theta| < 3.4°$ when the downstream sample position is used.

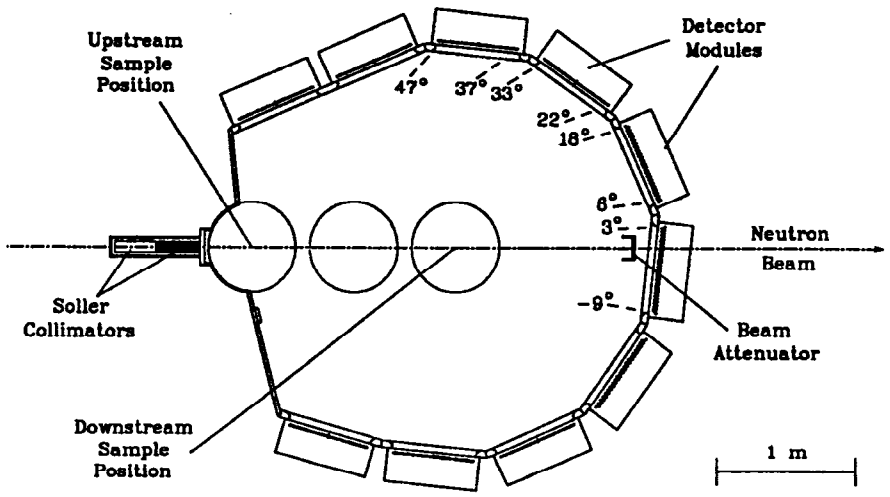

Figure 2. GLAD evacuated scattering chamber and detector modules. The limiting scattering angles, relative to the upstream sample position, are shown for the four detector modules now installed. The remaining six planned detector banks are also shown in their correct locations, but with no angle indications. The actual detector modules holding the banks of LPSDs are similar to the one shown in Fig. 3. The soller collimators and the beam attenuator which protects the LPSDs at small angles from the direct beam are also shown.

For incident neutrons having a wavelength of 0.1 Å, the currently-installed LPSDs will produce a maximum Q of 50.5 $Å^{-1}$ and 92.6 $Å^{-1}$ for the upstream and downstream sample positions respectively, although the quality of the data over this full Q range remains to be seen. Within the next 3-4 years the remainder of the 10 detector modules will be filled, raising the total to 408 LPSDs and providing angular coverage from -76° to +95° for the upstream sample position and -134° to +150° for the downstream position. As shown in the figure, the locations of the detector modules on the two sides of the flight path are not symmetric, so that when the full complement of detectors is installed the scattering angles not covered on one side of the flight path will be covered on the other.

Prior to the installation of GLAD, the IPNS powder diffractometers SEPD and GPPD were used for diffraction studies of amorphous materials. The intensity of the incident neutron beam for GLAD is approximately twice that at SEPD and four times that at GPPD. Furthermore, GLAD detectors will eventually cover several times the solid angle spanned by those on SEPD or GPPD, so the demands on the TOF data acquisition system are much more severe for GLAD than on the previous instruments. The new FASTDAS system[4] has been developed to respond to these higher instantaneous and time-averaged counting rates on GLAD.

As part of the correction procedures for analyzing diffraction data for glasses and liquids it is important to measure the sample attenuation characteristics. Considerable effort was expended to develop a transmission monitor[3] for this purpose as well as to improve the accuracy and response of the incident beam monitor.[5] Results of such transmission measurements are described elsewhere in these proceedings.[3]

III. TESTS USING THE PROTOTYPE FLIGHT PATH

Configuration

The final tests with the prototype flight path were completed in December 1989. Measurements were made on various samples and calibrants, including vanadium, SiO_2, polyethylene, diamond powder, intercalates and zeolites, iridium and hafnium, germanium, nickel, and beryllium. Figure 3 shows schematically the prototype flight path arrangement including the variable aperture, beam monitor, soller collimators, sample chamber, B_4C beam attenuator, and the

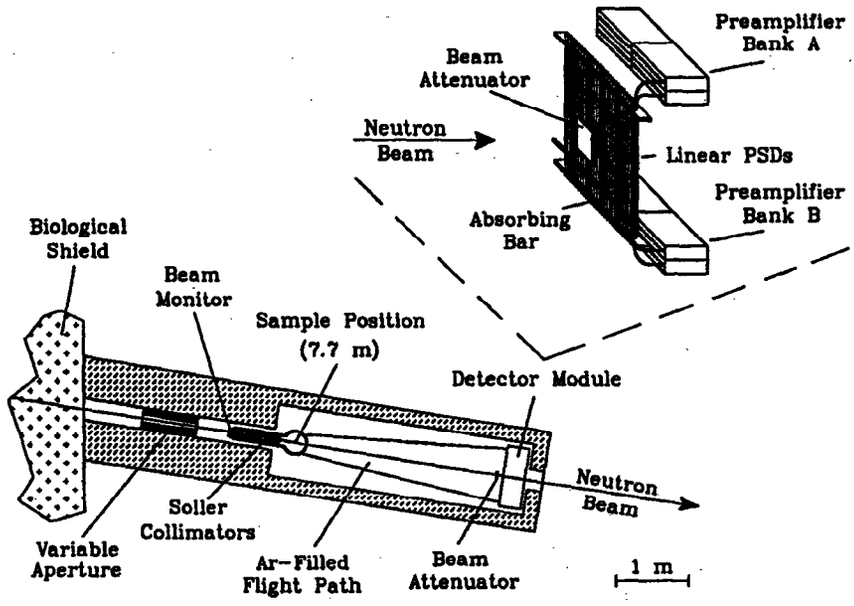

Figure 3. The prototype GLAD flight path in use during 1988-1989. The inset to the figure shows details of the detector module along with the relative locations of the beam attenuator and the absorbing bar used in calibrating the LPSDs. Each detector module in the final version of GLAD is identical to this except for some details of the positioning of the LPSDs within the individual modules.

single detector module. The path between the sample chamber and the detectors on this prototype instrument was not evacuated. Instead it was filled with a low pressure flow of Ar gas to force out the air and water vapor which would otherwise be in the scattered neutron flight path and would produce a large background due to scattering from the main beam. The sample position was at 7.7 m from the moderator and the detector module was centered on the direct beam at 10.7 m from the moderator. This module was protected from the direct beam by a beam attenuator, and contained a complement of 55 LPSDs of the same type as are now in the final instrument. Each of these

LPSDs had charge sensitive preamplifiers top and bottom, and the positions of the detected neutrons were determined by the charge-division method. The detectors were placed for complete area coverage in such a way that the active area of each tube was not shadowed by an adjacent detector. The position encoding resolution was about 1.4 cm, so the data were binned in 2-segment groupings for a total of 1540 individual detection areas of ~1 cm x 2 cm. Angular coverage in scattering measurements ranged from a lower limit of about 2°, limited by background near the penumbra of the beam of high energy neutrons, to a maximum of ~8° at the tops and bottoms of the end detectors. The range of time-of-flight (TOF) values used for most measurements was 200 μs to 12,000 μs, which corresponds to a wavelength range from 0.07 Å to 4.4 Å.

Calibration

The prototype flight path was very useful for developing techniques for both angle and wavelength calibration of GLAD. For angle calibration the most useful samples have been diamond powder and several different intercalation compounds. Additional angular calibration is available from the measured instrument geometry and from the flood-pattern measurements with an absorbing bar at various positions in front of the LPSDs. Figure 4 shows the results for diffraction from a powder sample of stage-2 cesium-intercalated graphite. The figure includes data from all of the segments as a function of TOF for one of the LPSDs at the end of the detector array. Each trace

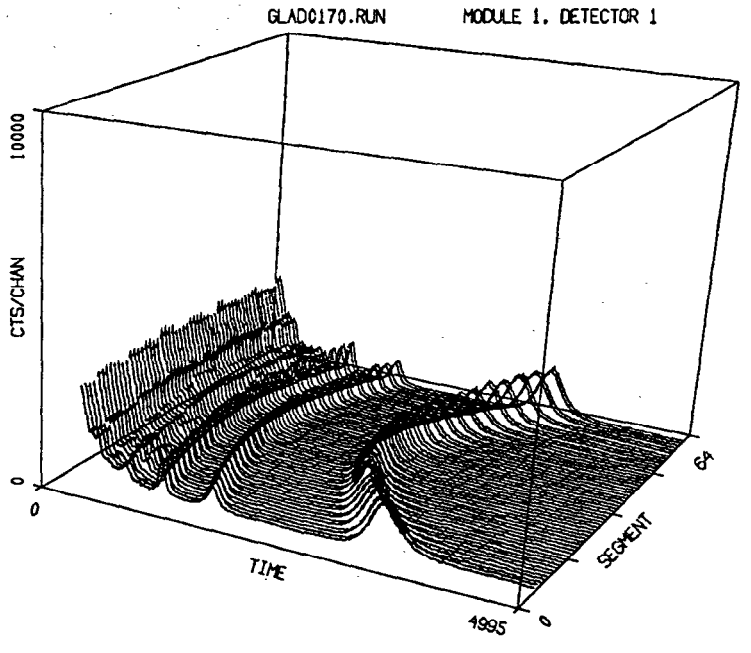

Figure 4. Bragg peaks from a powder sample of stage-2 cesium-intercalated graphite illustrating the "diffraction rings" for the LPSD centered at 6.1°. The maximum scattering angle is 8.0° for the end segments of this detector.

in the figure gives the detector response for a single segment of ~1 cm length from a single LPSD. However since pairs of such segments were grouped together during the histograming process, each independent TOF histogram corresponds to a ~2 cm length of the LPSD and appears as a double trace in the figure. The central segments in this figure correspond to a scattering angle of ~6.1°

and the end segments correspond to scattering angles of ~8.0°. At least four Bragg peaks are clearly observed for each segment, and for the end segments these occur at 754 μs, 1163 μs, 1726 μs, and 3515 μs. The peak at 3515 μs corresponds to Bragg scattering which occurs at a d-spacing of 9.33 Å for this sample, indicating that the average scattering angle for the end segments of this LPSD is 7.97°. The angle-TOF correlation of the Bragg peak positions is clearly evident as "diffraction rings" in the data displayed in this manner.

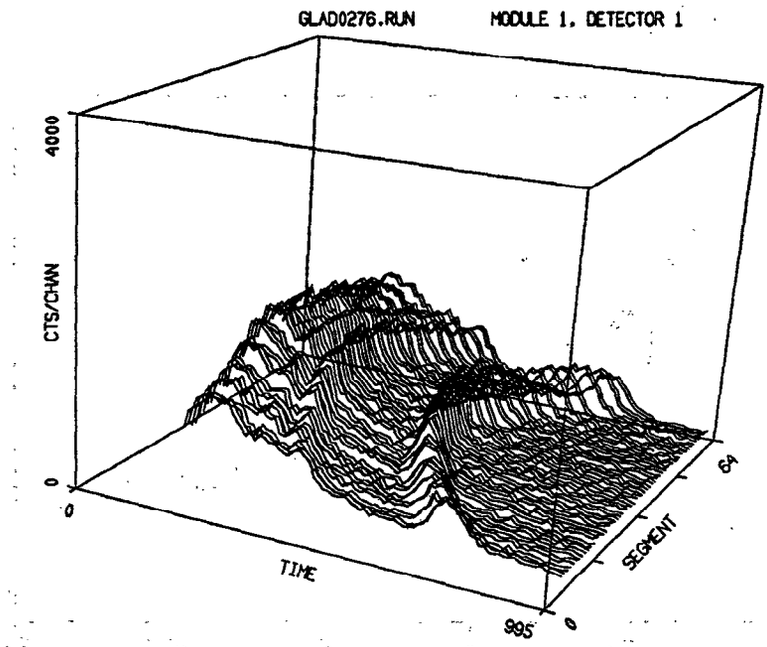

Figure 5. The use of diamond powder as a scatterer for angle calibration purposes.

Figure 5 illustrates the scattering measured for diamond into one of the end LPSDs for TOFs from 200 μs to 1000 μs. The peak positions yield the angle calibration and the widths the resolution. Most of the peak widths indicated in the figure reflect the range of scattering angles sampled by these two paired LPSD segments, rather than any intrinsic timing resolution. Note that the TOF range is about one-sixth of that in Fig. 4 and the "diffraction rings" are still very clear. We obtain a single segment resolution ($\Delta Q/Q$) at $Q = 0.5$ Å^{-1} of about 0.075 at the center of the detector and 0.10 near the top of the detector. The differences here are primarily due to the geometrical effects of the rectangular segment shape. The resolution is nearly twice as broad at the top and bottom of the central LPSDs of the array as compared to the center of the end LPSD because of this geometrical effect.

On SEPD and GPPD, angular data are time-focused into eight separate detector groups before the data are histogramed and stored into a run file, so for these instruments final wavelength and angle calibration is done for these eight focused detector banks rather than for the individual detectors. On GLAD, angular data are not time-focused into groups before the data are stored in a run file, although separate detector segments at the same scattering angle may be grouped together on-the-fly. Thus on GLAD it is necessary to calibrate every segment for wavelength-vs-TOF as well as for angle. We have had to rely on nuclear absorption resonances and Bragg scattering from crystalline materials to determine the wavelength of the incident neutrons as recorded by TOF in the individual segments. Figure 6 shows the TOF spectrum obtained in one of the LPSD segments

when an iridium foil was placed in the incident beam and an "isotropic" scatterer (polyethylene) was placed at the sample position. The three lowest energy resonances of iridium are at energies of 0.656, 1.303, and 5.36 eV (wavelengths of 0.353, 0.251, and 0.124 Å respectively), and these are clearly observed in the figure as depressions at approximately 960, 680, and 330 μs respectively. Measurements have also been made using hafnium foils, oriented nickel and germanium single crystals, and nickel and beryllium polycrystals as incident beam filters to provide a range of wavelength calibrations up to 4 Å.

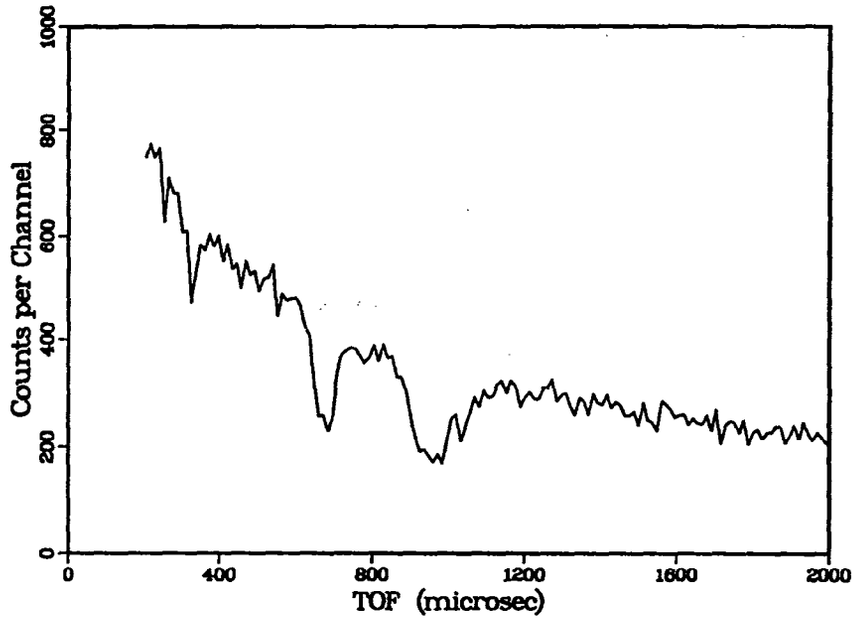

Figure 6. The use of iridium as an absorber for wavelength calibration purposes.

Scattering Data

Results measured on this prototype flight path for the S(Q) for a 0.37 cm plate and a 0.9 cm rod of SiO_2 are shown in Fig. 7, where they are compared with similar data from SEPD. Data reductions for the GLAD temporary flight path data utilized the GLAD analysis software discussed below. The measurements with the prototype GLAD flight path extend the Q-range down to near 0.1 $Å^{-1}$, while the upper limit of Q is 4.2 $Å^{-1}$ for 0.2 Å incident neutrons. Measurements were also made with the SiO_2 rod in the vanadium foil ("Howe") furnace and in an 8 kbar aluminum pressure cell as a test of the data analysis programs. Measurements on a smaller SiO_2 rod (0.4 cm) were also performed. Although they were limited by the scattering from the argon gas, these results indicated that the sensitivity of the small-angle detector array was good.

IV. ANCILLARY EQUIPMENT

Provision has been made on the final GLAD instrument for rapid evacuation of the total scattering chamber. Apparatus has been designed and assembled to provide automated control of sample environments. A 10-position, room-temperature sample changer has been constructed and

tested, and a 5-position, low temperature (10 K to 300 K) sample changer is in the final stages of assembly and calibration. High pressure capability is provided by a hydraulic system fitted with an 8 kbar aluminum cell or with an 8 kbar Rene-41 cell intended for work at elevated temperatures. The pressure system has been tested and is being calibrated. As mentioned above, a high-temperature (300 K to 1300 K) vanadium foil furnace has been tested in the prototype flight path. Preliminary indications are that experimental data obtained using this furnace are contaminated by secondary scattering from the furnace mounts, so this problem is under study.

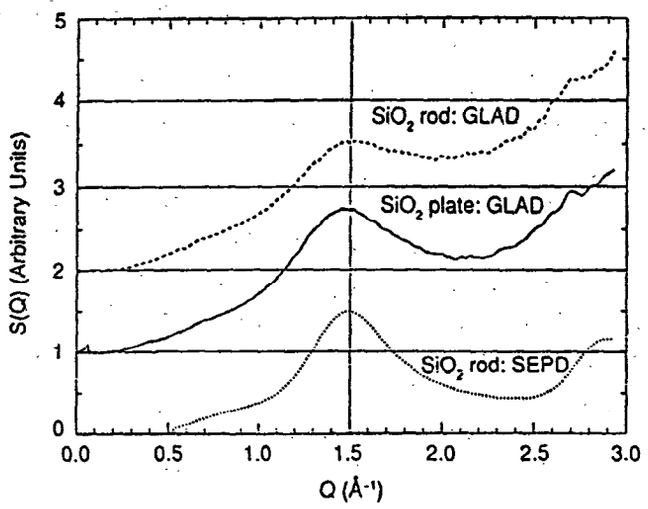

Figure 7. Comparison of SiO_2 scattering results measured on SEPD and on GLAD.

V. ANALYSIS SOFTWARE

A large effort has been devoted to the development of efficient and structured computer programs for the analysis of scattering from amorphous and liquid materials at IPNS. The programs have been developed on the VAX series of computers using VAX FORTRAN (Digital Equipment Corporation, Maynard, MA, USA), commercial NAG-library routines (Numerical Algorithms Group Ltd, Oxford, UK), and other library routines developed locally at Argonne. Plotting routines utilize either CA-DISSPLA Version 11.0 (Computer Associates International, Inc., Garden City, NY, USA) or the IPNS GPLOT GKS-based graphics routines.[6]

An experiment on GLAD is started by first setting up a run file which contains information about how LPSD segments are grouped together and how the TOF histograms are organized. There are virtually no restrictions on how this may be achieved; for example, detector segments may be grouped into Debye-Scherrer cones (preferable for isotropic scattering) and the time fields may be chosen with a channel width which is proportional to the TOF. In addition the run file contains calibration information concerning scattering angles, distances, etc. which are needed in the subsequent data analysis. The run files are large (up to ~12 Mbyte = 24,000 blocks on the VAX), and even though the packing density of data on mass storage devices is increasing steadily, the amount of data generated by GLAD will be enormous by any standard. A typical experiment will encompass several run files generated in a short period of time, which will be the case, in particular,

when one of the automatic sample changers is used. Hence, efficient programs must be available for analyzing the data and compressing it to more manageable sizes. The raw run files will be archived on secondary mass storage devices (currently 8-mm tapes holding about 2 Gbytes each) after the first-step analysis.

The analysis may be divided into several distinct tasks. The first step is carried out by the INTENSITY program. This program reads the "raw" data from the binary run files and examines the detector grouping and the TOF histograming at the time of data collection. The program then re-groups the data as the user chooses (e.g. redundant information may be grouped together after checking for spurious behavior) and normalizes the scattering to the incident beam spectrum and subtracts background scattering. The conversion from TOF to wavelength is also made in this program. The converted data are stored in a file as a function of scattering angle and wavelength.

The next step is to calculate the correction coefficients which are applied to the data subsequently by the STRUCTURE FACTOR program. The CORRECTIONS program calculates the absorption corrections for the reference scatterer (typically vanadium), the sample, and the container by the method of Paalman and Pings,[7] and calculates the multiple scattering by the method of Blech and Averbach.[8] At present, the corrections assume either a cylindrical sample geometry or a flat plate sample geometry. However, corrections for other geometries are under development, some of them based on routines developed at ISIS[9] in the UK. Experiments utilizing special environments place high demands on reliable correction routines, and much future work will be devoted to this subject.

The STRUCTURE FACTOR program applies the corrections to the data and normalizes to the reference run. The inelasticity (Placzek) corrections[10] are also calculated and applied in this program. Each detector group is still treated separately, and the output contains the structure factor for every group (each at a slightly different angle) as a function of the scattering vector Q which has been calculated from the wavelength and the scattering angle.

The TRANSFORM program typically combines the data (flux or counting-statistics weighting) from the different detector groups into a "single" structure factor S(Q) which will cover a range from approximately 0.1 - 40 $Å^{-1}$ or higher when the full complement of detectors at high angles is installed in GLAD. Then, the structure factor is transformed into real-space via the Fast Fourier Transform technique. Various real-space correlation functions may be calculated which then can be analyzed in terms of bond-lengths, coordination numbers, vibrational amplitudes, etc. A program for fitting overlapping peaks, which accounts for the broadening introduced by the finite upper integration limit, also is available.

Acknowledgments

The efforts of the following in the design and construction of GLAD are gratefully acknowledged: D. Bohringer, T. Bush, M. Faber, J. Jorgensen, D. Leach, G. Ostrowski, J. Richardson, A. Schulke, and K. Volin. The efforts of the following students from Willamette University are also acknowledged: D. Bloom, R. Colleran, D. Gipp, B. Haagensen, and L. Moen.

References

1. R. K. Crawford, D. L. Price, J. R. Haumann, R. Kleb, D. G. Montague, J. M. Carpenter, S. Susman, and R. J. Dejus. Advanced Neutron Sources 1988, Proceedings of the 10th Meeting of the International Collaboration on Advanced Neutron Sources (ICANS X), held at the Los Alamos National Laboratory, Oct. 3-7, 1988. Institute of Physics Conference Series Number 97, IOP Publishing Ltd, New York. pp 419-426 (1989).
2. A. C. Nunes. Nucl. Instr. and Meth. 119, 291-293 (1974).
3. D. G. Montague, J. M. Carpenter, R. K. Crawford, R. Dejus, D. L. Price, and S. Susman. "Use of a Semi-Opaque Beamstop for Monitoring Sample Transmissions at GLAD", these proceedings.
4. R. K. Crawford and J. R. Haumann. IEEE Trans. Nucl. Sci. NS-37, 72-81 (1990).
5. R. K. Crawford, J. R. Haumann, and G. E. Ostrowski. "Neutron Detectors at IPNS", these proceedings.
6. T. G. Worlton. Proc. DECUS Spring Symp., 105-117 (1988).
7. H. H. Paalman and C. J. Pings, J. Appl. Phys. 33(8), 2635-2639, (1962).
8. I. A. Blech and B. L. Averbach, Phys. Rev. 137(4A), A1113-A1116, (1965).
9. A. K. Soper, W. S. Howells, and A. C. Hannon, Rutherford Appleton Laboratory, RAL-89-046, (1989).
10. M. Misawa, D. L. Price, and K. Suzuki, J. Non-Cryst. Solids, 37, 85-97, (1980).

ICANS-XI International Collaboration on Advanced Neutron Sources
KEK, Tsukuba, October 22-26, 1990

Use of a Semi-Opaque Beamstop for Monitoring Sample Transmissions at GLAD*

D. G. Montague,§ J. M. Carpenter, R. K. Crawford, R. Dejus, D. L. Price, and S. Susman
Argonne National Laboratory, Argonne, IL 60439.
§On leave from Willamette University, Salem, OR.

ABSTRACT

Accurate corrections for many types of measurements made on time-of-flight neutron diffractometers require data on the macroscopic transmission cross-section of the sample used, and this data must span the entire wavelength range covered by the instrument. This report describes a transmission monitor consisting of a semi-opaque beamstop in front of a portion of the array of position-sensitive detectors used for diffraction measurements on the GLAD prototype. The semi-opaque beamstop was made of a molded B_4C-epoxy plate pierced by several small-diameter holes which transmitted a small fraction of the beam, and the segments of the position-sensitive-detectors directly behind these holes served as several independent beam monitors. This arrangement was used on the GLAD prototype flightpath to measure the transmissions of a number of samples, and results of these tests are reported and discussed. Based on these results, a similar transmission monitor has been incorporated in the final GLAD instrument.

I. INTRODUCTION

Accurate corrections for measurements made on neutron diffractometers require data on the transmission cross-section of the samples used. This is necessary because tabulated values of the total cross-sections do not reflect either the sample structure or inelastic scattering, which are unknown until each sample has been completely characterized. This report describes a transmission monitor consisting of a B_4C plate with small diameter holes placed in front of the ^3He linear-position-sensitive detectors (LPSDs) on the prototype flight path for the Glass, Liquid, and Amorphous Materials Diffractometer (GLAD) instrument at IPNS.

*Work supported by U.S. Department of Energy, BES, contract No. W-31-109-ENG-38.

Transmission cross-section measurements are described by Windsor[1] for flat plate samples whose extent is larger than the area of the neutron beam. The process involves the determination of the neutron intensity; that is, background corrected counts in a detector divided by the counts in an incident monitor counter, for a sample in the beam and for the sample out. The attenuation of neutrons by materials in the beam is given by

$$I(\lambda) = I_o(\lambda)\, e^{-\sum_i N\, \sigma_i(\lambda) t_i} \tag{1}$$

where the index i represents the various attenuators in the path, such as aluminum windows, gases in the flight path, as well as the sample itself. The symbol $I(\lambda)$ represents the number of counts per unit wavelength, corrected for background, in the downstream detector, normalized for the number of incident neutrons per unit wavelength. Thus when the normalized intensity for the sample in is divided by the normalized intensity for the sample out, we have:

$$\frac{I(\lambda)_{\text{sample in}}}{I(\lambda)_{\text{sample out}}} = e^{-\sigma_T(\lambda) t_s N_s} \tag{2}$$

where N_s and t_s are the number density and thickness of the sample and $\sigma_T(\lambda)$ is the total wavelength-dependent cross-section, scattering plus absorption, of the sample. Then

$$\sigma_T(\lambda) = \frac{1}{t_s N_s} \ln\{I(\lambda)_{out}/I(\lambda)_{in}\} \tag{3}$$

where we have neglected any gas displaced by the sample. In the ideal case[1] the result does not depend on detector efficiency, geometry, or the incident flux distribution. When the sample is not flat or does not cover the entire beam and/or the beam profile is not uniform, the expansion becomes:

$$\frac{I(\lambda)_{\text{sample in}}}{I(\lambda)_{\text{sample out}}} = \frac{\int_{A_1} f(x,y)\, dx\, dy + \int_{A_s} f(x,y)\, e^{-\sigma_T(\lambda) t_s(x,y) N_s}\, dx\, dy}{\int_{A_T} f(x,y)\, dx\, dy} \tag{4}$$

where A_T is the total cross-sectional area of the beam, A_1 the area not obstructed by the sample, A_s the area subtended by the sample, and f(x,y) is the incident neutron beam profile. The length of path through the sample may vary across the sample, depending on the sample geometry. To carry this further, it is necessary to make specific assumptions about the beam profile function f(x,y) and the sample shape $t_s(x,y)$.

II. EXPERIMENTAL ARRANGEMENT

The GLAD instrument recently installed at IPNS is described in a separate report in these proceedings.[2] The prototype flight path used for development of this instrument during 1988-1989,

is also described in that report. This prototype flight path, which was used for the transmission measurements described here, is shown in Fig. 1. The neutrons from the liquid methane moderator were scattered from a sample at 7.7 m from the moderator, and were detected by a detector bank consisting of 55 closely-packed gas-proportional counter LPSDs. Each of these cylindrical LPSDs had a 1.11 cm inside dia x 60 cm active volume, encoded into 64 segments per LPSD. The position identification was accurate to about 1.4 cm, so the data were binned in 2 cm groupings. This detector bank was centered on the direct beam at a position 3.0 m downstream from the sample, and was protected from the full effects of the direct beam by a "beam attenuator" placed just upstream from the detector bank (Fig. 1). This report describes the measurements made with the LPSD segments behind the beam attenuator in the path of the direct beam.

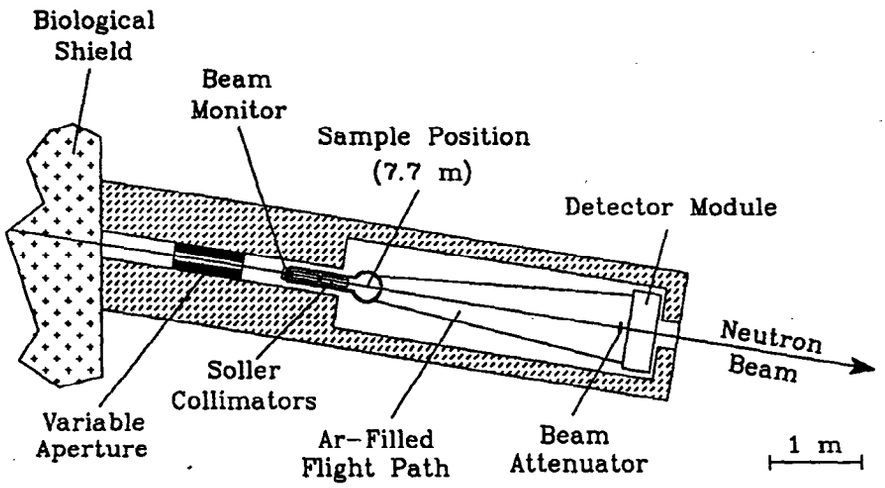

Figure 1. Layout of the prototype GLAD flight path.

There are thermal, epithermal, and higher energy neutrons leaving the moderator "promptly" after the 450 MeV protons strike the target. There are also delayed thermal, epithermal, and higher energy neutrons coming from the moderator with a similar energy spectrum but with essentially no time correlation to the incident proton pulse. This delayed neutron intensity is nearly constant over the full TOF frame.[3,4] Since the soller collimator blades were more-or-less transparent to high-energy neutrons, the penumbra of the high-energy neutrons was primarily determined by the massive apertures upstream from the soller collimators, and was measured to be ~14 cm x 14 cm. The beam divergence permitted by the converging soller collimators determined the much smaller penumbra of the thermal and epithermal neutrons, which was about 4 cm x 4 cm.

The beam attenuator was a slab of natural B_4C, 17 x 17 cm^2 x 1.3 cm thick, with five 0.15 cm diameter holes parallel to the incident neutron beam. The block was made by casting a mixture of B_4C granules and epoxy in a form containing five small rods perpendicular to the face. These holes transmitted enough of the lower-energy neutrons to allow them to be differentiated from the delayed, high-energy neutrons, while keeping the overall count rate sufficiently low to avoid saturating the detection system. This attenuator and its relation to the detector array is shown in Fig. 2. The width and height of the attenuator were chosen to fully cover the penumbra of the high-energy neutrons. The 1.3 cm thickness of the attenuator block was chosen to provide enough attenuation of the medium energies to permit the thermal and epithermal neutrons transmitted

through a pinhole to be discriminated from those transmitted through the absorbing material. (A 1.3 cm thickness of the B_4C-epoxy mix has a transmission of about 5% for neutrons of wavelength 0.1 Å.) The fast delayed neutrons in the incident beam passed through the B_4C beam attenuator with little or no attenuation, but the detectors had low efficiency for detecting these neutrons.

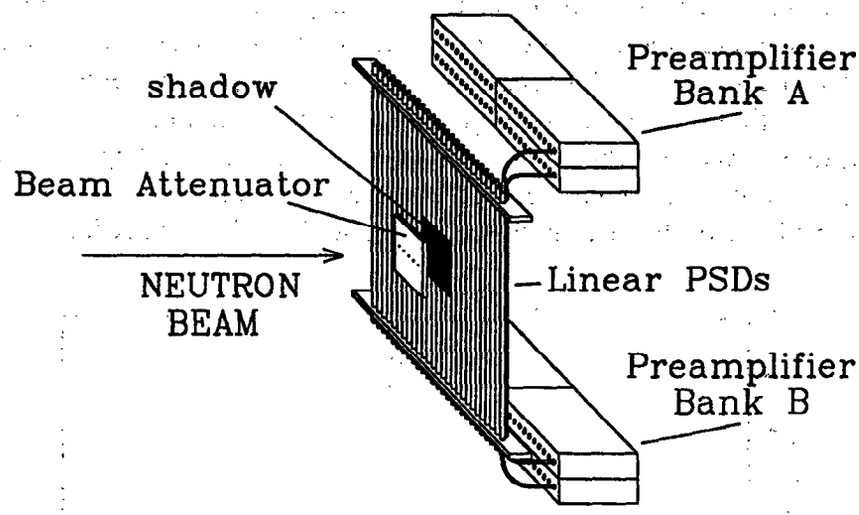

Figure 2. Beam attenuator in front of the detector array.

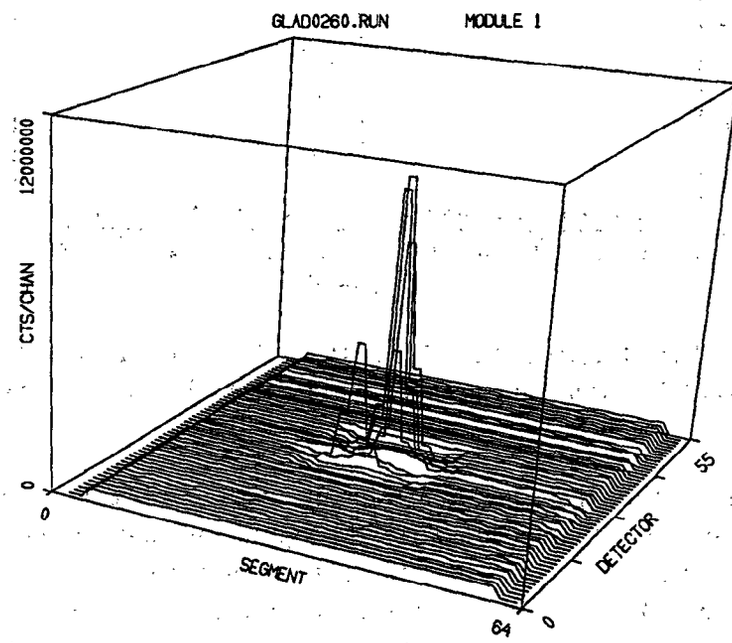

Figure 3. Sum over the time spectra from 200-15000 μs for each segment in the entire 55-LPSD array, with a polyethylene scattering sample. The depressed region in the center is the shadow of the beam attenuator, and the 5 peaks are due to the neutrons transmitted through the pinholes in this beam attenuator, which were in front of 5 of the LPSDs.

III. RESULTS

Figure 3 shows the sum of counts in each segment of the LPSD array for a 0.31 cm thick polyethylene plate sample, with the holes in the beam-attenuator located approximately 0.5 cm below the center line of the LPSD array. All segments of all 55 LPSDs are shown; the vertical scale represents the sums of all counts over the TOF range 200 μs to 15,000 μs. Since the total number of neutrons scattered by the sample into each segment is nearly independent of position, this view shows the shadow of the B_4C beam attenuator as a depressed region at the center of the display. The peaks within this depressed region are due to the neutrons transmitted through the pinholes in the beam attenuator. The LPSDs behind the pinholes have large numbers of counts in the segments near the holes, although the widths of these peaks is much greater than would have been predicted on the basis of the measured detector resolution of 1.4 cm fwhm.

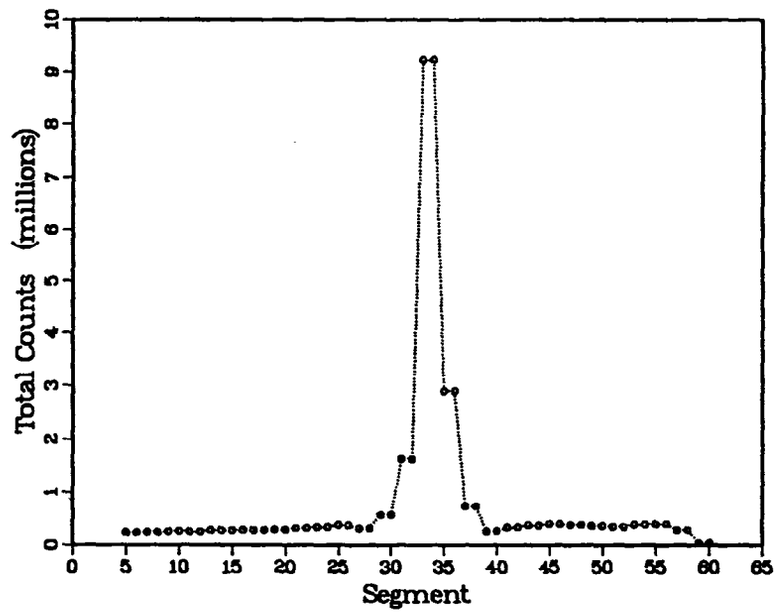

Figure 4. Details of the peak for detector 27 from Fig. 3. The peak is centered behind the pinhole in the beam attenuator in front of this LPSD. Adjacent segments have the same values because of the way the data were grouped.

Figure 4 shows one of these peaks in greater detail. Pairs of adjacent segments were grouped together in the histograming so that separate TOF histograms were collected for each 2-cm-long grouping, and the figure shows the sums over the TOF range of 200 μs to 15,000 μs for each of these groups (as in Fig. 3). Because there were two segments per group and Fig. 4 displays a point for each segment, adjacent points correspond to the same group and thus have the same total number of counts. It can be seen that 6 of the 2-cm-long groups have counts significantly above the surroundings. Examination of the time dependence for each segment of the LPSDs shows that the spread in the position determination is much greater for TOFs near 200 μs than for those longer than 1500 μs. The measured position resolution of 1.4 cm is valid even for the segments behind the pinholes for the longer TOFs, but for these segments for TOFs less than about 600 μs, the high instantaneous intensities lead to pulse-pileup which produces errors in the position encoding, and this is what has led to the broad peaks seen in Figs. 3 and 4. This extreme broadening is not

observed in the segments at the top and bottom of the same LPSDs at the same TOF values, since these segments are not exposed to such high data rates. It appears that the pileup effects have not been large enough to cause data to be lost, so the correct spectrum transmitted through the pinhole can be recovered by summing over all the adjacent groups for which there are significant numbers of counts (6-10 groups, centered behind the pinhole).

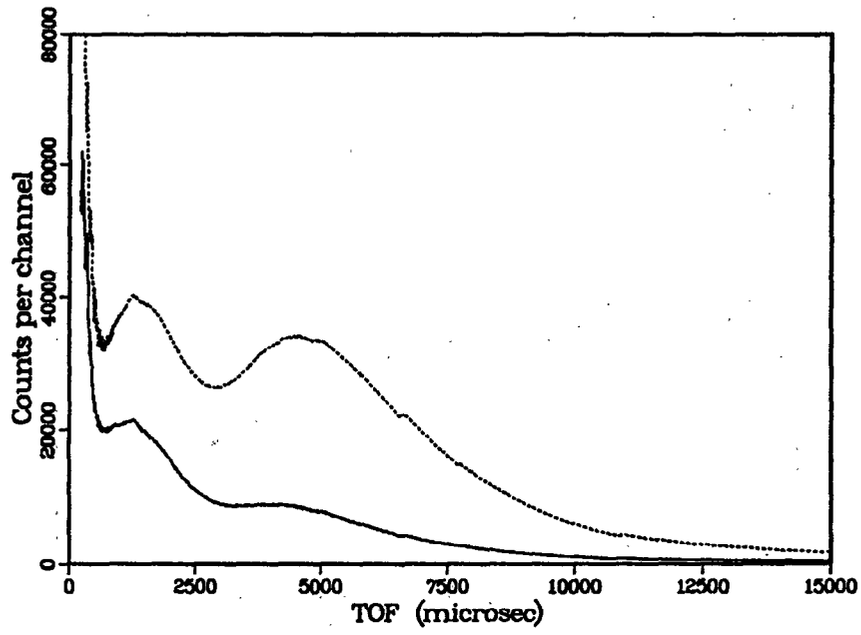

Figure 5. TOF spectra from segments 33-34 of the same LPSD as in Fig. 4. Solid line is for a polyethylene sample, dashed line is for no sample.

Figure 5 gives the time dependence of the counts for the 2-segment group behind the pinhole, which is the one with the most counts in Fig. 4. Data collected with a polyethylene sample (same data as for Figs. 3 and 4) and with no sample are shown. Incident beam monitor data were used to normalize both spectra to the same total number of neutrons incident on the sample position. Since this was a rather thick sample of polyethylene, its transmission was only ~30% as can be seen from the figure. The figure also shows significant distortion of the spectral shape below TOF values of ~1500 μs for both curves. This is due to the misencoding discussed above. Thus such a "single-group" measurement would not be expected to yield accurate sample transmissions at TOF values below ~1500 μs.

As noted above, a more accurate "transmission monitor" can be "constructed" by summing the 10 middle segments of detector 27 (or of any of the other LPSDs behind the pinholes in the beam attenuator). Figure 6 shows a comparison of spectra measured by the incident beam monitor as shown in Fig. 1 and the "transmission monitor" which is constructed by summing the 10 middle segments of detector 29 in a different data run. These measurements were made with no sample in the sample position, and were corrected for the efficiencies of the upstream monitor and the LPSD involved. The agreement is very good for wavelengths longer than 1 Å, except at the longest wavelengths shown, where background subtraction is a problem for the transmission-monitor data. The disagreement below 1 Å is partially due to some penetration of epithermal neutrons through the 1.3 cm thickness of B_4C and epoxy, but may also be due in part to some additional pulse-pileup

effects which result in more extreme position misencoding or in actual detector dead-time. Some of the differences may also be real spectral differences due to the fact that the two monitors were located ~4 m apart along the line of the beam, with the soller collimators, several Al windows, and ~3 m of Ar gas between them.

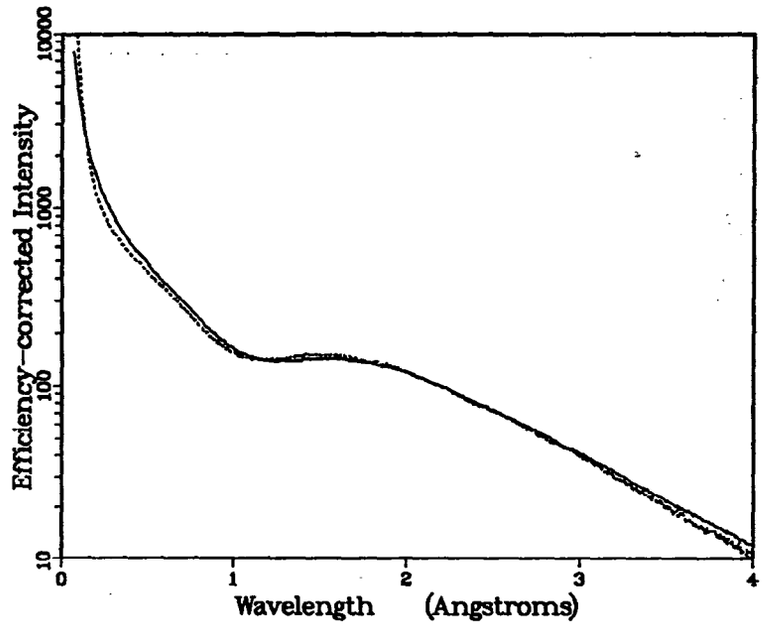

Figure 6. Comparison of the response of the incident beam monitor (solid line) and the transmission beam monitor (dashed line) described in the text. Both have been corrected for their wavelength-dependent detector efficiencies and have been arbitrarily scaled to match near the Maxwellian peak.

In order to correct for the background it is necessary to subtract a term from the intensity for both the sample and the empty sample holder measurements. The long-TOF data from the LPSD segment behind the pinhole were used to determine the delayed-neutron background. The proportion of fast delayed neutrons relative to the thermal and epithermal neutrons of interest changes rapidly with position across the detector bank, since the spatial profile of the former is determined by the upstream beam apertures while that of the latter is determined by the soller collimators. Hence adjacent LPSDs or adjacent segments of the same LPSD which were not behind pinholes could not be used to determine this background. Uncertainty in this background correction currently limits the usefulness of this transmission monitor to wavelengths below ~5 Å.

Figures 7, 8, and 9 show results for transmission cross-sections σ_T measured as a functions of wavelength. Since there were 5 pinholes in the beam attenuator, 5 independent transmission measurements were made concurrently in different LPSDs. Data from 3-5 of these independent measurements are shown in the figures. The solid lines are values from Sears[5] in the case of vanadium and SiO_2, and the values for polyethylene, CH_2, were constructed from H_2O data[6] modified using data from Sears[5]. Errors on the experimental points, calculated using the method of reference 1, are on the order of 2% or less for the vanadium and polyethylene data and somewhat greater for the SiO_2 data. The present measurements yield numbers in reasonable agreement with the cross-sections estimated in this manner. At the long-wavelength end of the measurements a leveling of the measured vanadium cross-section is observed; this is the region of low statistics

beyond 2.0 Å where the background subtraction has the largest effect. For the short-wavelength end the measured cross-section again falls below the tabulated values; this is due to the penetration of neutrons through the B_4C beam attenuator and possibly also to pulse-pileup effects.

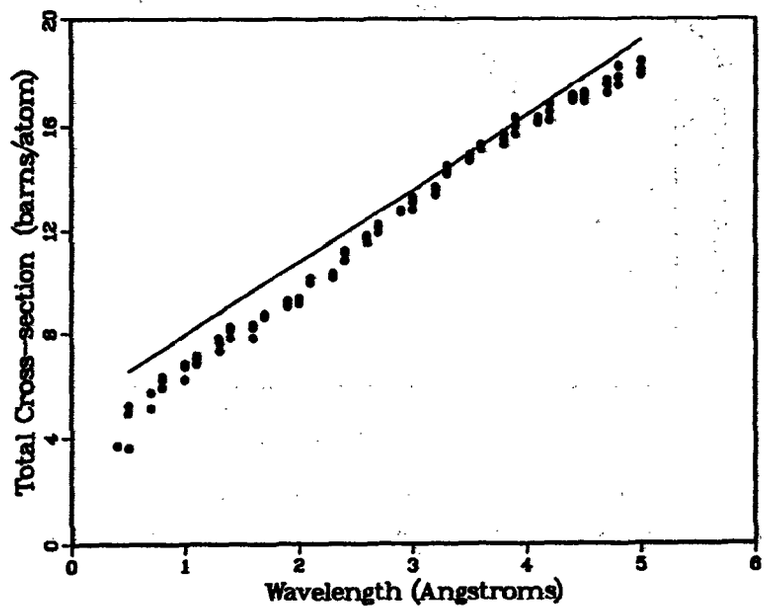

Figure 7. σ_T **for vanadium. The solid circles represent independent concurrent measurements from three of the different LPSDs behind pinholes in the beam attenuator, while the line represents the estimated value.**

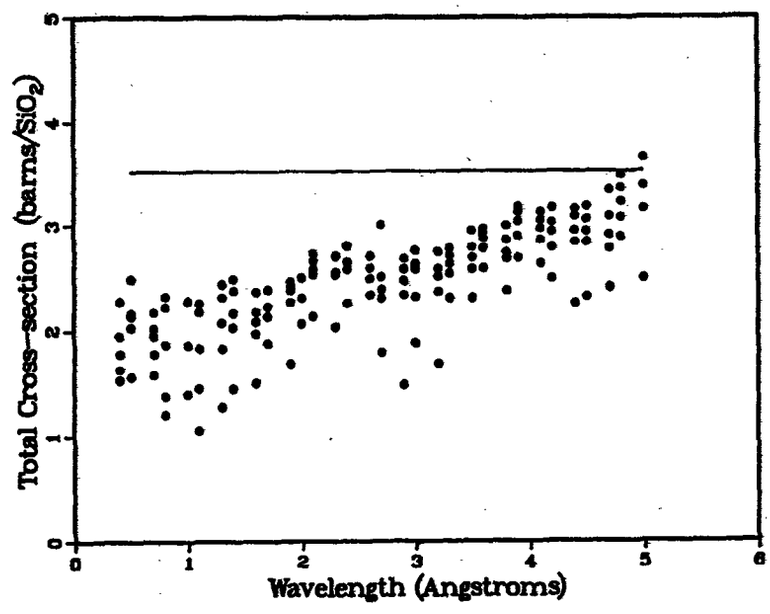

Figure 8. σ_T **for SiO_2. The solid circles represent independent concurrent measurements from all five different LPSDs behind the pinholes in the beam attenuator, while the line represents the estimated value.**

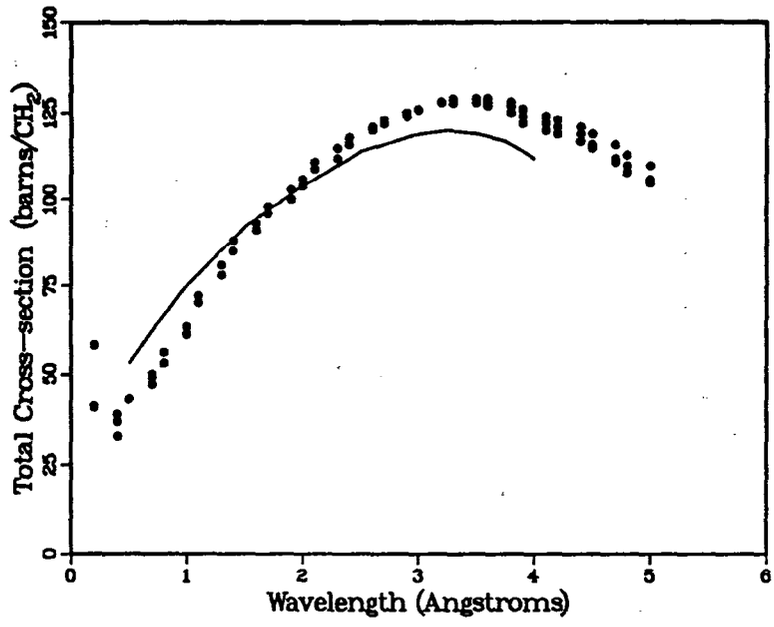

Figure 9. σ_T for polyethylene. The solid circles represent independent concurrent measurements from three of the different LPSDs behind pinholes in the beam attenuator, while the line represents the estimated value.

IV. CONCLUSION

It is seen that reasonable results are obtained from transmission measurements made in the GLAD prototype. Problems still remaining include: (1) Accurate determination of the high-energy neutron background was not possible. (2) The prototype scattering flight path was filled with argon gas with an unknown, and not well controlled mixture of air and water vapor. (3) The count rate was high, especially at short times due to the initial burst of high energy neutrons, leading to pulse-pileup and dead-time effects. (4) The size and shape of the pinholes and the thickness of the B_4C beam attenuator have not yet been optimized. Nevertheless, the method works sufficiently well that a similar "transmission monitor" scheme will be used in the newly-installed final version of GLAD, and development will continue in an effort to reduce the effects of these remaining problems.

References

1. C. G. Windsor. Pulsed Neutron Scattering, Taylor and Francis, London (1981). pp 394-399.
2. R. K. Crawford, J. M. Carpenter, R. Dejus, J. R. Haumann, R. Kleb, D. G. Montague, D. L. Price, and S. Susman. "Status of the New GLAD Instrument at IPNS", these proceedings.
3. J. M. Carpenter. Nucl. Instr. and Meth. 175, 287-292 (1980).
4. J. E. Epperson, J. M. Carpenter, P. Thiyagarajan, and B. Heuser. Nucl. Instr. and Meth. A289, 30-34 (1990).
5. V. F. Sears. Methods of Experimental Physics: Neutron Scattering, vol. 23A, ed. K. Sköld and D. L. Price, Academic Press, Orlando (1986). p 521.

6. D. J. Hughes and R. B. Schwartz. Neutron Cross Sections, 2nd Edition, BNL 325, Brookhaven National Laboratory, Upton, NY (1958).

Q(A.D.Taylor): Are the GLAD detectors in the spectrometer vacuum, or behind a thin window.

A(R.K.Crawford): Detectors are outside vacuum.

Q(R.Pynn): What size pin holes do you use? Could you use this semi-opaque beam stop for TOF SANS measurements?

A(R.K.Crawford): Pinholes are ~0.7 mm dia. In principle this technique can be used for SANS, but in practice detector resolution is usually not good enough to present some cross-talk with the scattering.

ICANS-XI International Collaboration on Advanced Neutron Sources
KEK, Tsukuba, October 22-26, 1990

EXPERIMENTS Using Single Neutron Pulses

by C.D. Bowman*, P.A. Egelstaff‡ and H.G. Priesmeyer$^{\phi}$

*Physics Division, Los Alamos National Laboratory
‡Physics Department, University of Guelph
$^{\phi}$Institute of Pure & Applied Nuclear Physics, University of Kiel

ABSTRACT
The combination of intense neutron pulses from the LANSCE or ISIS sources with modern detectors of neutron currents, has allowed work to begin on exciting new experiments using single neutron pulses. To illustrate this field we shall describe three applications which make use of the transmission of neutrons through a sample as a function of their energy. The three examples are (i) the measurement of the temperature along the body of a projectile after launching, (ii) a strobo-scopic study of the warming cycle of a jet engine at full power and (iii) the study of phase transitions under extreme conditions. To prepare for experiments of this kind a 40 m special flight path is being built at LANSCE, and preliminary experiments to demonstrate the method have been made with an existing 10 m path.

I. INTRODUCTION AND DESCRIPTION OF THE METHOD

The advent of pulsed neutron sources driven by high powered accelerators, has opened up the possibility of doing both transient and stroboscopic measurements with neutrons (e.g. Egelstaff[1]). These experiments would require good data to be taken with a single neutron pulse, either because one pulse represents the whole experiment or because we wish to compare the data taken with the first pulse to that taken with each subsequent pulse.

Over the past year sources such as LANSCE or ISIS have provided proton pulses of about 3 μC each, which is on the lower limit of usefulness. In 1991 it is expected that LANSCE will deliver 5 μC pulses at 20 Hz, and for single shots may deliver a 10 μc pulse. Thus it is worthwhile preparing some test experiments which will help define the fields in which single pulse experiments could be useful and which would clarify the experimental methods.

Figure 1 shows a sketch of the apparatus that would be used. Sufficient neutrons must be absorbed by the Li-glass scintillators during the transit of the pulse, that smooth current variations occur in the photo-multiplier circuits which may be digitized and recorded. At present flux levels this requirement restricts the measurement technique to the transmission method. A burst of fast neutrons would be moderated in a light water slab, and a beam of resonance and thermal neutrons would be collimated on to the chosen sample. On passing through the sample the neutron beam intensity is changed by the events in progress there, and this information is carried to the end of the flight path where it is recorded by the Li-glass photomultiplier system. One advantage of this method is that, due to the flight times of the neutrons, the information impressed on the neutron beam in time Δt is expanded to $(L_2/L_1)\Delta t$ at the detector, (where L_1 and L_2 are the distances from the moderator to the sample and to the detector respectively).

The transmission (T) of a sample is defined as the ratio of the intensity of the beam with the sample

present to that in the absence of a sample. In the resonance region dips in the curve of T vs neutron energy, can occur due to neutron absorption resonances. A possible energy range for these effects is 1 to 100 eV, but the exact range of usefulness will vary from case to case. For example in the case of Ta there are 9 resonances between 60 and 20 eV, which may be used to measure the temperature of a sample as a function of time. The width of the resonance has two components, first nuclear absorption and scattering and secondly Doppler broadening due to the nuclear velocities. We are interested in the latter effect which is given by the formula:

$$\Gamma_D = \sqrt{4E_R\, k_B T/A} \qquad (1)$$

where E_R is the resonance energy, T the sample temperature and A the atomic weight of the nucleus. It can be seen that Γ_D is large for high values of E_R and/or temperature and in many cases will be the dominant component. For example at 40 eV in Ta at room temperature the value of Γ_D is 0.15 eV compared to a nuclear width of only 0.05 eV. In such cases the resonance width technique will provide a temperature measurement deep inside a sample in a time of about 1 μsec.

The thermal neutrons in the pulse have longer wavelengths (λ) and are sensitive to Bragg reflections from the sample. They are found when the Bragg condition is satisfied:-

$$\lambda = (2d/n) \sin \theta_B \qquad (2)$$

where d is the interplanar spacing, n the order of reflection and θ_B the Bragg angle. A strong Bragg reflection will remove neutrons from the beam and hence reduce the transmission: an effect which increases as θ_B (or λ) increases. Because the maximum value of θ_B is π, this effect switches off as λ increases past the point where $\theta_B = \pi$ for any choice of d. The rises in T at these points provide information on the positions and widths of the Bragg reflections, and hence a range of structural information. For simple structures (e.g. fcc) there would be a range of suitable Bragg reflections, and each reflection would be covered in about 50 μsec with separations between reflections of 0.5 to 3 ms.

By using both of these techniques a range of experiments are possible, and some selected examples will be described here. Stroboscopic measurements are possible on several time scales, successive resonances occur on a 5 μsec scale, while successive Bragg reflections occur on a 500 μsec scale. In contrast at 50 Hz or 20 Hz, successive pulses would occur at 20 or 50 ms respectively. If a sample is moving, one could build neutron absorbers into its structure at specific points to act as markers, and so define both its position relative to the beam and its bulk velocity. In favourable cases the bulk velocity might be determined by the resonance method, since there is an additional bulk shift in the resonance energy due to the component of velocity along the neutron beam. A similar shift would occur in Bragg peak positions but maybe harder to observe.

Thus there are a large number of simple observations that may be made in this field, and both the experiments and the observational methods need to be chosen with care in order to exploit the technique properly.

II. MEASUREMENT OF THE TEMPERATURE ALONG THE AXIS OF A PROJECTILE AS A FUNCTION OF TIME AFTER FIRING

A simple sketch of the geometry which might be used in this case is shown in figure 2. A special projectile is envisaged which might be 30 cm long and 1 cm x 5 cm cross section, with a 0.2 mm thick Ta strip dividing the 1 cm section down its centre (this projectile would be strip shaped and its rotation would be prevented, for simplicity, in this demonstration). If the projectile crossed the beam at an average velocity of 1 cm/μsec the data of interest would be impressed on the beam in ~30 μsec. However if the sample were

4 metres from the moderator and the total neutron flight path was 40 metres, the data would be spread out to 300 μsec at the detecting station. Each resonance in Ta would need about 1 eV of energy to define the transmission dip, and at 40 eV this would be covered in 0.7 μsec at the sample and 7 μsec at the detector. We note also that in this experiment, and in similar ones, the neutron itself is the detector at the site of explosion/projectile/etc and is unharmed, while the fragile detection apparatus for the neutron is ~30 m away and is also unharmed.

In order to determine the exact time of the passage of the projectile across the beam and its exact velocity (if normal to the beam), the projectile would be equipped with ^{10}B markers which would produce additional characteristic dips in the neutron transmission curve. For example if the ^{10}B rings are 0.5 cm wide and deep, a nearly triangular transmission dip of 95% would be seen at 40 eV having a width of ~0.7 eV. By tipping the projectile to an angle of 13° away from the normal, a 2 eV transmission dip shift would occur and the two methods of measuring projectile velocity could be compared.

Several measurements might be made with the starting length, ℓ, being varied. In this case a picture of the temperature profile in space and time can be built up. It is hoped that the conditions of any experiment of this type could be controlled so that the temperature profile could be calculated theoretically and compared to the experimental results. If successful a program of this kind would establish the base for more ambitious experiments.

Projectiles are used also for experiments with shock waves. In this case the time scale for the initial shock is too short for these techniques, but temperature measurements after the shock may be useful. There are two time scales, first there is a shock die-away time of ~10 μsec, and temperature measurements synchronized to follow the shock by 1 μsec steps would be useful. Secondly there is a residual effects recovery period of about 1 msec, and temperature measurements at 10 μsec intervals to 100 μsec, followed by intervals of 100 μsec to 1 msec could be informative. Such data appear to be difficult to obtain by other methods, but relatively straightforward by this method.

III. STROBOSCOPIC MEASUREMENTS ON A ROTOR UNDER STRESS

Another example of a stroboscopic study with neutron pulses may be provided by experiments on rotating systems: in this case a continuous stream of pulses is used unlike the single pulse of the previous section. To illustrate this field we shall consider the stresses in a jet engine as it accelerates to full power, and hence maximum stresses, and subsequently as it warms to its maximum temperature while operating at full power. Figure 3a is a sketch showing an impeller blade attached to the rotor. The neutron beam should be directed in successive experiments at points of high stress in the rotor (e.g. near the root of the blade or near the centre of rotation). At first, some demonstration experiments would be done with a simple rotor, and if successful with increasingly realistic set-ups. The rotational frequency and neutron pulse frequency should be simply related so that a time sequence for a chosen point on the rotor is obtained. Resonance widths and positions would be measured to determine temperatures and velocities, while structural data would be obtained from widths and shifts of Bragg reflections.

Figure 3b shows the time structure for a 20 Hz neutron beam. The resonance data (for temperature) is obtained first, followed at about 5 ms by the thermal neutron structural information. These data are repeated at 50 ms intervals. One might take one second of such data, and repeat it at one minute intervals for example. Normally it would be possible to make such measurements for only one point on the rotor at one time. Thus the whole program would consist of a number of runs, starting the rotor from rest, each looking at a different site. If the rotor is taken close to its limit, suitable safety precautions would be built into the set-up and these would include heavy shielding. Consequently there would be an advantage to the transmission method of detection since it requires relatively small entrance and exit windows for the neutron beam.

IV. A DEMONSTRATION EXPERIMENT

In order to demonstrate the practicality of this technique, Priesmeyer et al[2] have carried out a demonstration experiment. They used a stationary sample of iron 2.5 cm thick and a beam area at the sample of 5 cm x 2.5 cm. The charge in the pulse was only 3 μC, and the distances from source to sample or detector were 8 m and 11.7 m respectively. With this set-up they obtained the data shown in figure 4 with a single pulse. The thermal neutron wavelength region is shown from 1.5 to 5 Å, and six Bragg reflections are observed clearly in 8 ms at the detector. The rising character of the overall intensity follows the Maxwellian shape of the thermal neutron distribution. Taking this and the instrumental resolution into account, the d-spacing in iron was determined to a precision of ~5 x 10^{-3} = $\Delta d/d$ in ~100 μsec (e.g. at the 211 reflection). If the charge in the pulse were increased to 10 μC or greater it would be possible to decrease the sample width from 2.5 to 1 cm, and with more optimum path lengths to improve the precision and with longer paths to improve the time resolution. It is hoped that such improvements will be possible with a new set-up under construction at LANSCE.

V. CONCLUSIONS

Experiments with a single neutron pulse are theoretically possible[1] at LANSCE or ISIS and three kinds of experiments were described in this paper. In addition a demonstration run at LANSCE in which the d-spacing of iron was measured to a precision of 0.5% in 100 μsec was described. This has opened the door to some new and exciting fields of research. With longer flight paths, an improved sample installation and pulses of ~10 μC many such experiments appear to be possible. A number of other areas, in addition to those described above, may be considered. They include — transient methods with pulsed electric or magnetic fields, and phase changes in geological minerals (e.g. olivine which has a phase change at ~10^5 atm, as a test case) using pulsed pressure fields.

An initial series of test experiments is required in order to establish these methods and to define their current limits. It is hoped that such a program may be commenced with a new long flight path installation at LANSCE.

References

1. Egelstaff P.A. "New Directions in Neutron Diffraction", ICANS-VII, p. 271, Report AECL 8488, Ed. Schriber, S.O., (1984).
2. Priesmeyer H.G., Bowman C.D., Yuan V.W., Seestrom S.J., Wender S.A., Richardson R., Wasson O.A., Xzu X. and Egelstaff P.A. Unpublished Memo entitled: Fast Transient Diffraction at LANSCE (1989).

Figures

1. The layout for single pulse experiments. A 10 μC proton pulse strikes the neutron production target, and fast neutrons are moderated to resonance and thermal energies in the moderator. They are collimated onto the sample, and after passing through it the beam diverges to a large detector array at about 40 m from the moderator. For initial tests a single detector may be placed at ~10 m from the moderator.
2. The geometry for a projectile experiment. A special projectile would be made with a 0.2 mm thick Ta strip along its axis for temperature measurements and ^{10}B markers for velocity measurements. The distance ℓ would be varied for different shots.

3a. A sketch of a rotor showing blades attached and two possible points at which stress and temperature measurements would be desirable.

3b. The time structure of the information obtained in single pulse sequence-experiments on rotors. Each arrow marks a set of either temperature or structural data.

FIG. 1

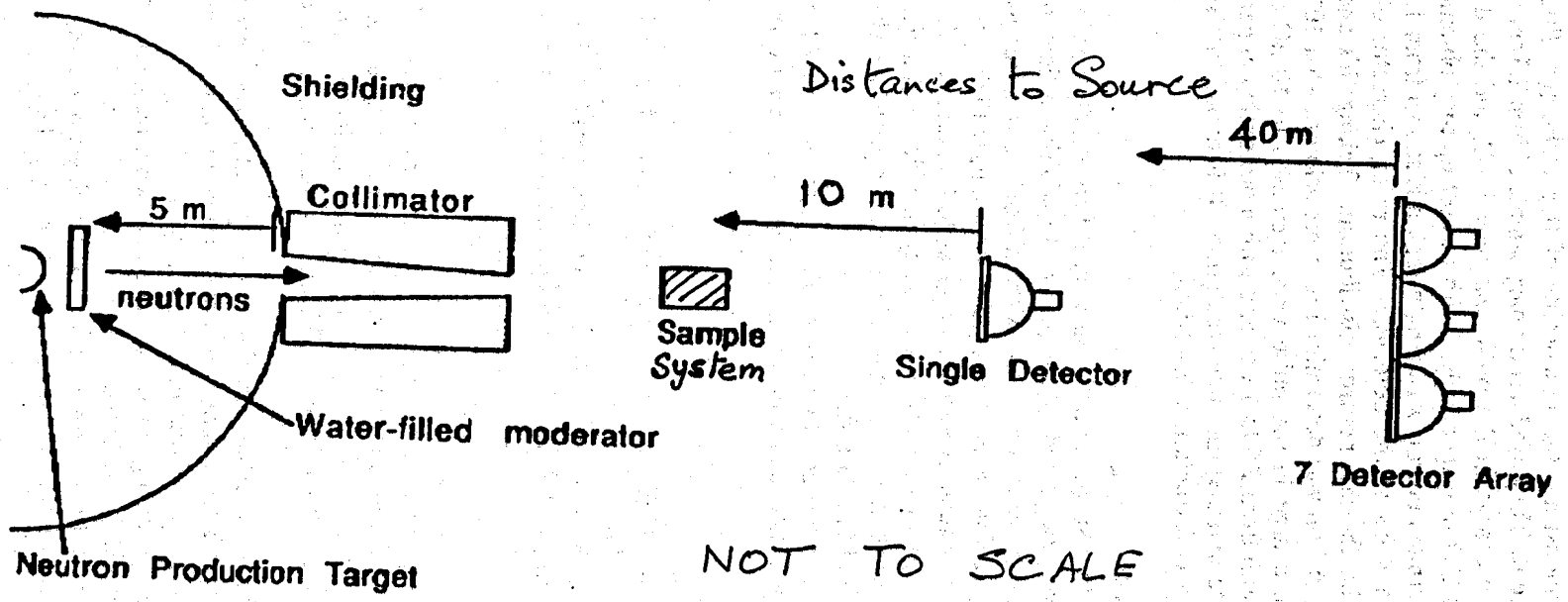
Shielding
Distances to Source
40 m
5 m
Collimator
10 m
neutrons
Sample System
Single Detector
Water-filled moderator
7 Detector Array
Neutron Production Target
NOT TO SCALE

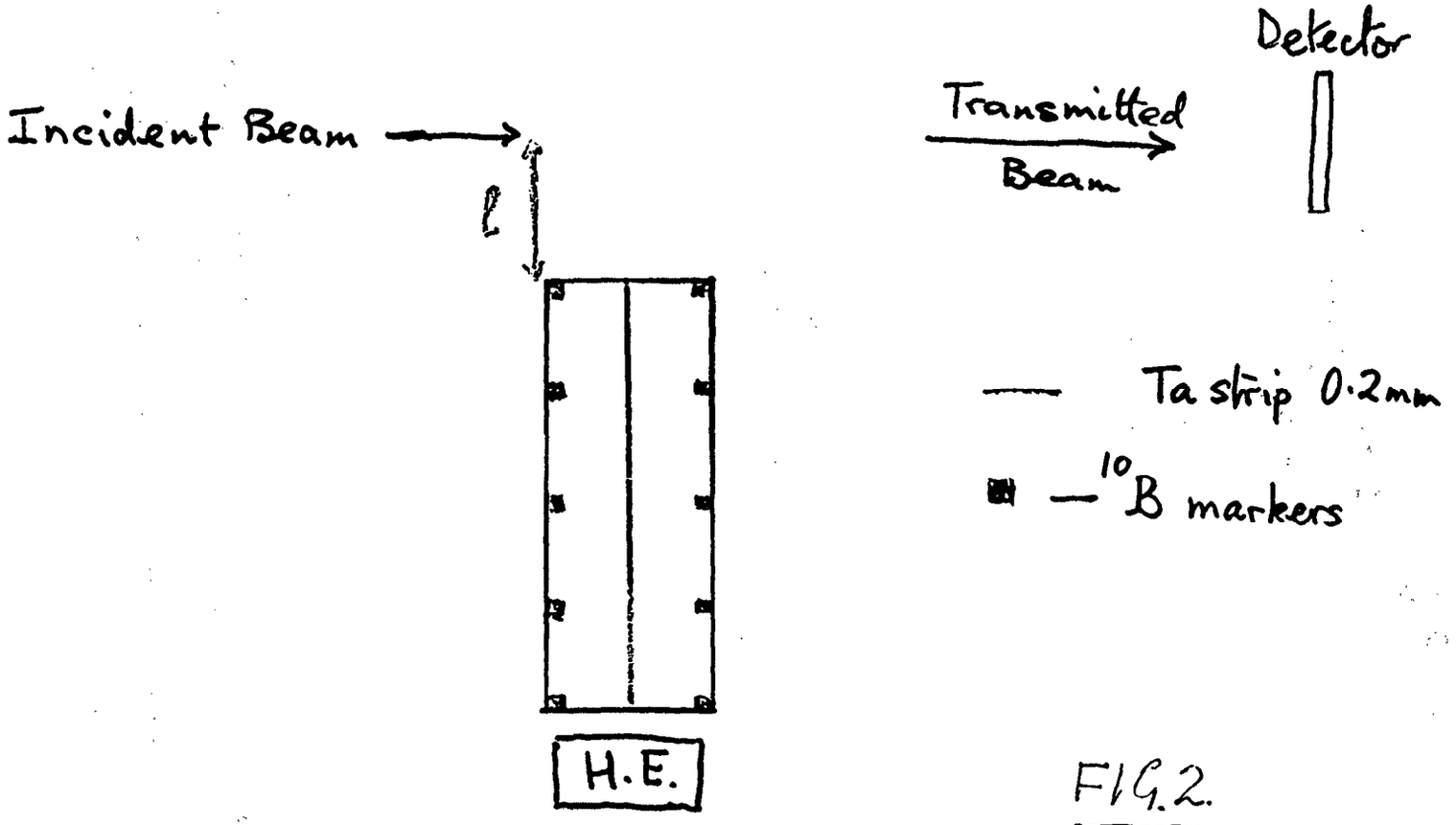
Incident Beam
l
H.E.
Transmitted Beam
Detector
Ta strip 0.2mm
^{10}B markers

FIG. 2.

3 (a)

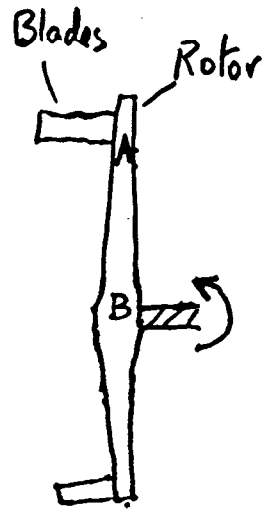

Points of measurement marked A and B

3(b)

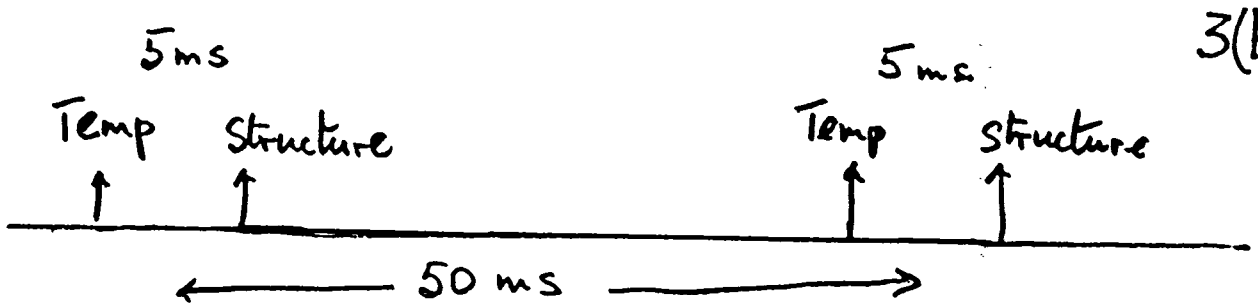

FIG 4

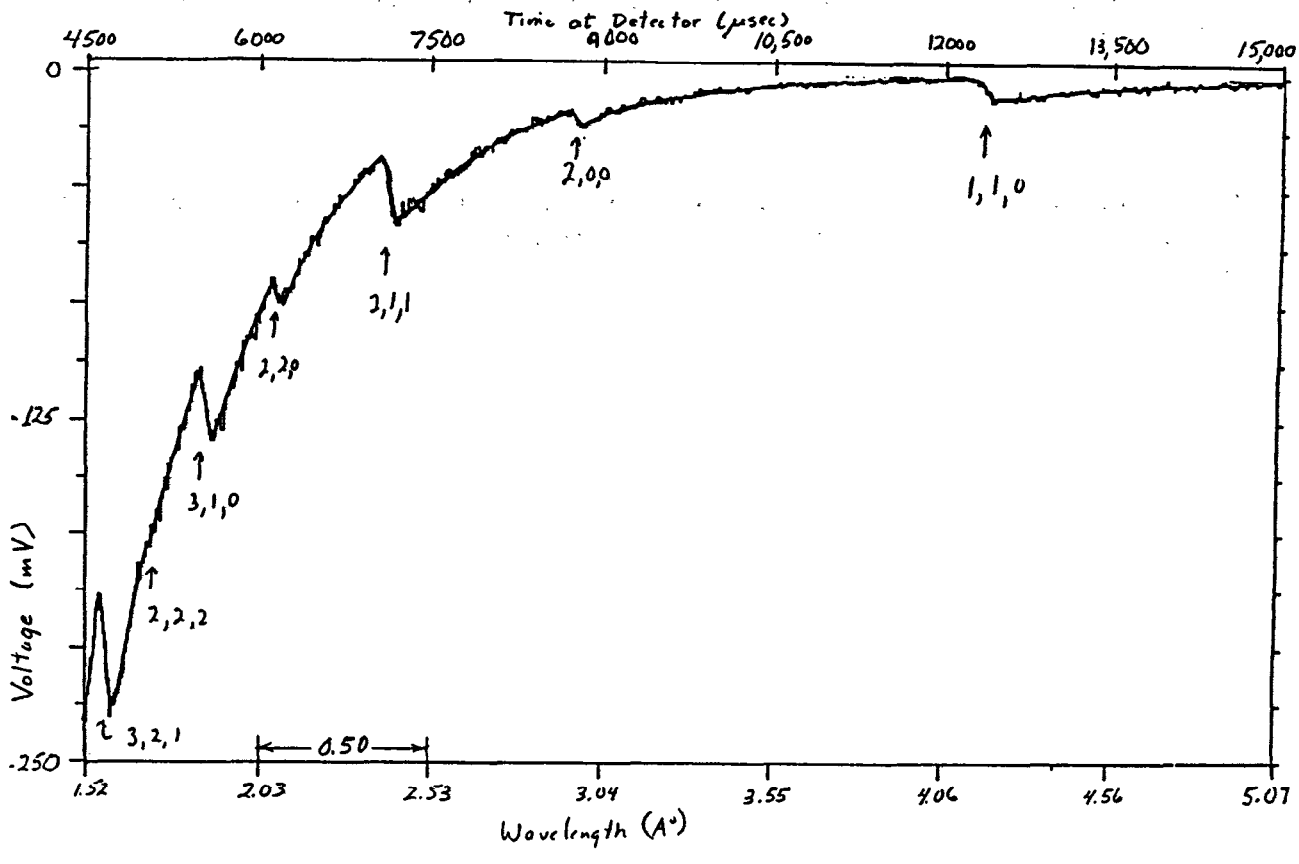
Time at Detector (μsec)
4500
6000
7500
9000
10,500
12000
13,500
15,000
0
-.125
-.250
Voltage (mV)
3,2,1
2,2,2
3,1,0
2,2,0
2,1,1
2,0,0
1,1,0
0.50
1.52
2.03
2.53
3.04
3.55
4.06
4.56
5.07
Wavelength (A°)

4. Experimental data obtained with a single 3 μC pulse at LANSCE in the thermal neutron region. The sample was a block of iron 2.5 cm thick, and the d-spacing may be determined from any of the indexed steps in the transmitted intensity (assuming the crystal structure is known). The overall shape of the intensity vs wavelength curve is due to the Maxwellian shape of the thermal neutron intensity distribution.

Q(J.M.Carpenter): Does the method really profit from use of analog detectors, sacrificing quantum statistical accuracy? Would not it do to use a stack of low-efficiency pulse counters?
A(P.A.Egelstaff): N/A

ICANS-XI International Collaboration on Advanced Neutron Sources
KEK, Tsukuba, October 22-26, 1990

Single crystal diffraction at ISIS

C C Wilson and D A Keen
ISIS Facility, Rutherford Appleton Laboratory, Chilton, Didcot, Oxon OX11 0QX, UK.

ABSTRACT
The ISIS Single Crystal Diffractometer SXD is a time-of-flight Laue instrument. The utilisation of large area position-sensitive detectors along with the pulsed nature of the ISIS beam makes SXD an ideal instrument for reciprocal space surveying, measuring large volumes in a single scan. The development of detectors for SXD will be described along with data processing strategies, and illustrations given of the scientific programme.

I. INTRODUCTION

There is a rich variety of information available from single crystal diffraction at a pulsed neutron source. The utilisation of both the time-of-flight technique to sort the white beam and large area position-sensitive detectors makes it possible to access large volumes of reciprocal space in a single measurement. The ISIS Single Crystal Diffractometer SXD (Figure 1; Forsyth and Wilson, 1990) is just such a time-of-flight Laue instrument. The main features of SXD are evident from this figure and the parameters given in Table 1. The ability of such an instrument to probe reciprocal space volumes is illustrated in Figure 2. The combination of a time-sorted wavelength range (providing two Ewald sphere surfaces at $1/\lambda_{max}$ and $1/\lambda_{min}$) and the large scattering locus subtended by the detector, allows the area shown in Figure 2 to be accessed *in a single measurement*. Of course, the detector also has height, and a full 3-dimensional reciprocal space volume is accessed on SXD.

It is clear from the above that SXD is an ideal instrument for the surveying of reciprocal space. This capability has particular relevance in the study of incommensurate structures, phase transitions and diffuse scattering. In these fields the time-of-flight Laue technique is extremely powerful. However, the characteristics of the data collected on such an instrument can also have certain advantages in more routine structural work. For example in the treatment of wavelength dependent effects and in obtaining high precision refinements from very high $\sin\theta/\lambda$ data.

II. DETECTORS

The requirements for an efficient detector for single crystal diffraction at a pulsed spallation neutron source such as ISIS are rather stringent. The technique of Laue time-of-flight diffraction produces a very large amount of information accessible in principle to an area detector at one time. The polychromatic nature of the incident beam allows many Bragg reflections (> 1000 in many cases) to diffract simultaneously into a 300 x 300 mm^2 active area during an ISIS pulse. Since SXD is situated close to the moderator (L_1 = 8 m) this leads to a high flux and large count rate requirements. With much of the ISIS flux being at fairly short wavelengths in the epithermal region, it is clear that a PSD installed on the instrument must have good response to neutrons with wavelengths down to say 0.2 Å. Finally, some of the effects being looked for in single crystal diffraction, such as satellite reflections, require good resolution in all three dimensions, two spatial and one time.

In order to exploit the possibilities of SXD one therefore requires a PSD with good pixel resolution (at worst 5 mm), fast count rate (dead time ~1 μs), linearity of response and stability. The original detector developed for SXD is the Anger camera (Forsyth, Lawrence and Wilson, 1988; Wilson and Zaleski, 1990). In addition, more recent developments of fibre-optic encoded PSDs have led to the provision of prototype modules of this design on SXD with great success.

Figure 1 – Plan view of SXD. Note the provision of large area PSDs subtending a large scattering angle at the sample.

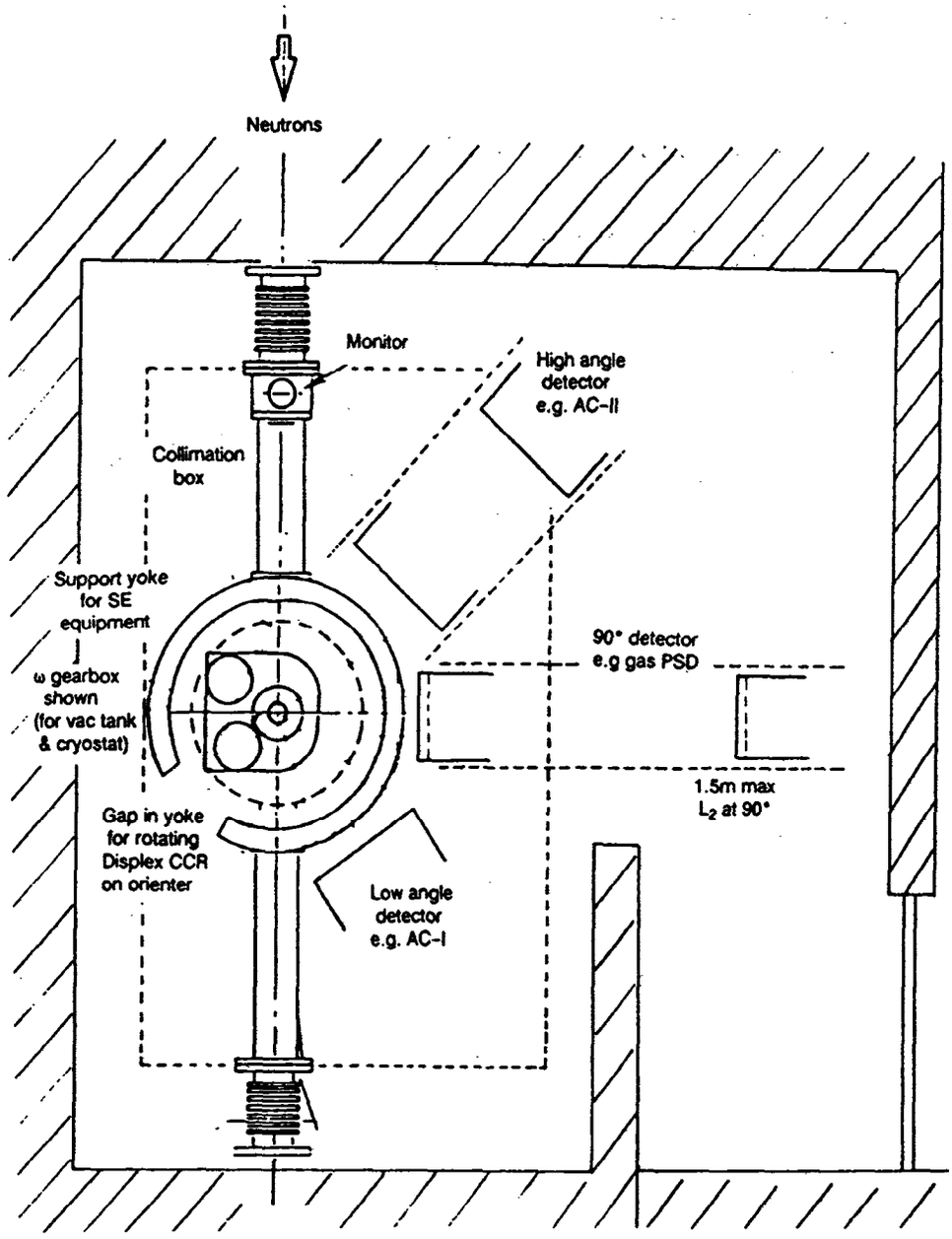

TABLE 1 – SXD instrument parameters

Laue time-of-flight diffractometer
Primary flight path $L_1 = 8$m from 316K H_2O moderator
Sample-detector distance $L_2 = 0.2$–1.5m (longest at 90°)
Wavelength range 0.25–8Å
$\sin\theta/\lambda$ range 0.02–2.5Å^{-1}

Detectors
Position-sensitive detectors

Fibre-optic encoded ZnS module, 80 x 80 mm^2, 5mm resolution
Anger camera I, ZnS scintillator, >300 x 300mm^2, 7–8mm resolution
Anger camera II in testing, ZnS scitnillator, >350 x 350mm^2, 5mm resolution
ORDELA ^{3}He gas detector, 250 x 250mm, 2–8mm resolution

Resolution, $\Delta d/d = 10^{-2} - 5.10^{-3}$

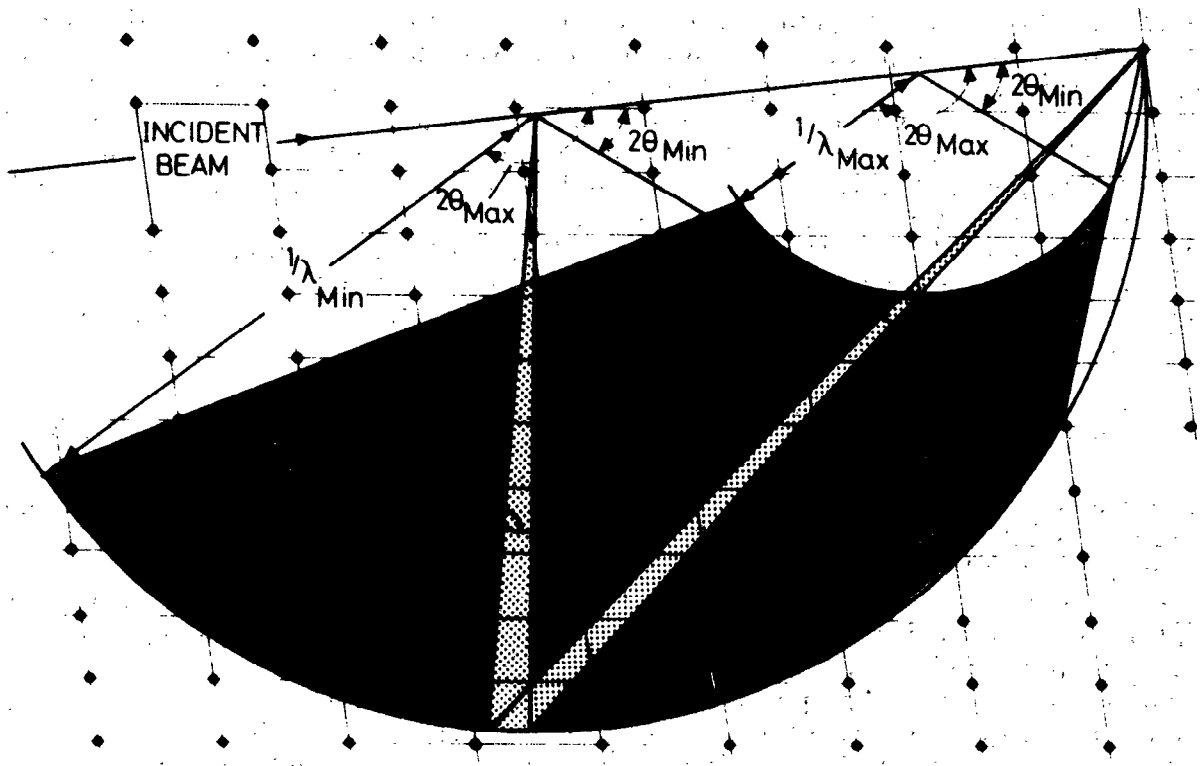

Figure 2 – Single crystal time-of-flight geometry

Anger Camera

The basic concept of this type of PSD (Anger, 1957) is that a single piece of scintillator is used to detect events. The light produced from an event is dispersed into an array of PM tubes (Figure 3) and the analogue signals of these tubes are used to derive electronically the position of the detected neutron. These detector coordinates would produce a 2D array of data were only positional information required but the addition of time-of-flight information on SXD produces a full 3D data set.

Figure 3 – General design of the neutron Anger camera.

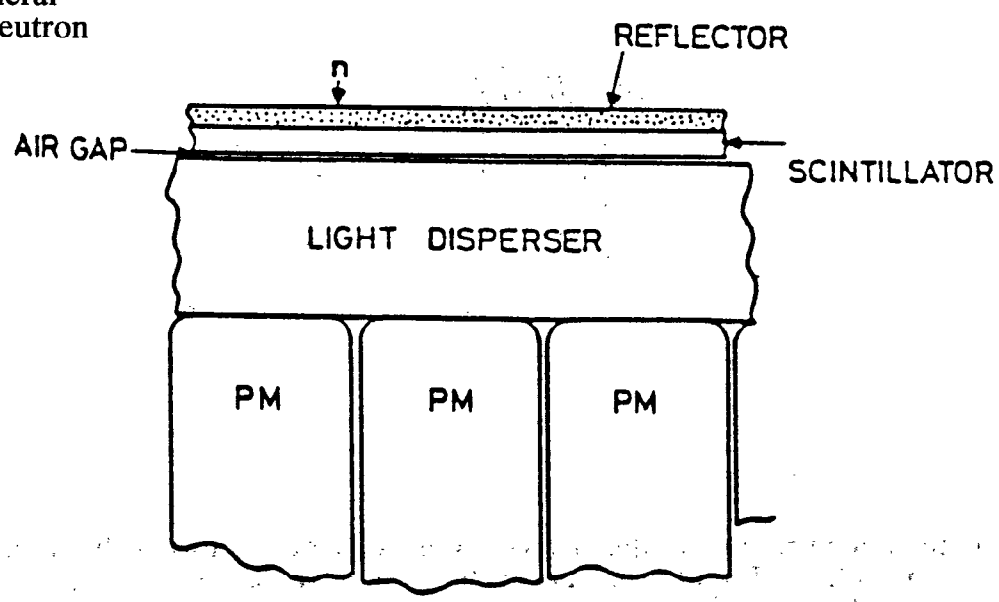

In the course of early commissioning of the Anger camera system, it was concluded that the available resolution was limited by the amount of light available from the optics, and also that the high γ sensitivity of the ^{6}Li-doped glass scintillator was causing considerable noise problems. Both of these problems can be overcome by the use of ^{6}Li loaded ZnS plastic scintillator, and it was found to be straightforward to modify the electronics to encompass the different dynamic response of this type of scintillator. The testing of the new AC-ZnS system was very successful. The resolution obtained from the prototype system is some 6-7 mm, but at present the count rate in the encoding electronics is rather slower than expected, a problem which is under investigation. With this caveat, however, it is the successful commissioning of the AC-ZnS system (Wilson and Zaleski, 1990) which has recently enabled the SXD scientific programme to begin in earnest.

The prototype fibre-optic ZnS PSD

The problems encountered with the Anger camera, and the re-examination of detector parameters in the light of experience on SXD, has prompted the examination of a new type of detector which is simpler both in concept and construction and is also less expensive to build. The fibre-optic ZnS PSD installed on SXD is a prototype constructed by the Neutron Detector group at ISIS (Davidson, Mott, Rhodes and Johnson, 1989). Basically the detector, shown schematically in Figure 4, consists of an array of 5 x 5 mm^2 pixel elements arranged on a ceramic grid, fibre-optic encoded to a set of phototubes. Physically, these pixel elements comprise inverted pyramids, abutted to form an array. The scintillator, a single, continuous piece of ~ 0.4 mm thick ^{6}Li-doped ZnS plastic, is supported some 0.1 mm above the base of these pyramids, with a group of optical fibres at each pyramid apex to collect the light and transmit this to the PMTs. In the prototype there are 16 x 16 pixels in X and Z, requiring 32 phototubes, giving an active area of some 80 x 80 mm^2. It has been shown that, by judicious choice of discriminator levels, this system can be made virtually insensitive to γ noise.

Figure 4 - General design of the prototype fibre-optic encoded ZnS PSD

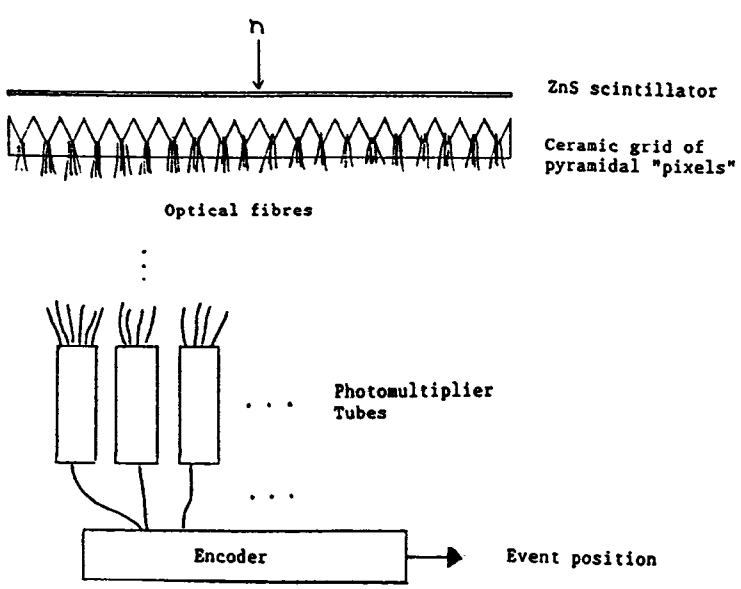

The commissioning results on this detector were very satisfactory with parameters found as illustrated in Table 2. The performance of this prototype detector has been excellent, and in spite of its small size, it has contributed significantly to the early stages of the SXD user programme.

TABLE 2 - ZnS fibre-optic PSD performance

Active area	80 x 80 mm^2 (typically subtending 20x20° at the sample)
Pixel resolution	5 mm x 5 mm
Linearity	Excellent to 0.1 mm
Quiet counts/detector noise	4 counts/cm^2/hour
Detector response	Smooth (flat) to < 10% and stable
Signal-to-background	> 4000:1 in (2 2 2) of SrF_2
Short wavelength response	(0 0 24) of SrF_2 observed at d = 0.24 Å, $\sin\theta/\lambda = 2.1 Å^{-1}$, $Q = 26.4 Å^{-1}$
Dead time	2-3 μs
Stability and reliability	Robust, easy to install and operate.

Gas detector

In addition to the in-house detectors described, we have purchased a 2D ^3He gas PSD from ORDELA Inc. at Oak Ridge to supplement the detector array. This detector is still being commissioned, but should give spatial resolution in the range 2-8mm as a result of parallax caused by finite thickness of the gas volume. The availability of several detectors improves the flexibility of SXD and, in addition, provides PSDs to support the increasing programme of high resolution single crystal studies on HRPD.

III. SXD SOFTWARE: THE DUAL ROLE OF THE INSTRUMENT

The trouble with large volumes of reciprocal space is that in examining them, one obtains large volumes of diffraction information (scattered intensity measurements). SXD typically operates with several thousand detector elements (a single Anger camera has 64x64 pixels = 4096 detector elements), which when combined with a few hundred time channels, essential of course within the framework of the time-of-flight technique, tends to give rather large data histograms, each of which is typically accumulated in less than an hour. Hence a major requirement for the efficient exploitation of the technique is the availability of a flexible software package for data analysis and display (Forsyth et al, 1986).

SXD is designed, as far as possible, in accordance with standard 4-circle geometry, and is probably best defined as a "restricted 4-circle" diffractometer. As a consequence, the diffraction geometry can be defined by the equation of Busing and Levy (1967),

$$h_L = \Omega \chi \Phi \mathbf{U} \mathbf{B} h$$

where

h_L is the diffraction vector in the laboratory Cartesian system;
Ω, χ and Φ are the matrices defining the diffractometer settings;
U and **B** are matrices describing the sample;
h is the reciprocal lattice vector.

It is clear from this that once the UB matrix for the sample has been determined, the problem is well-defined and the data processing can be made fairly automatic. The SXD software package is illustrated in Figure 5, showing the central role of the UB matrix.

The dual purpose of SXD is evident in the portion of this Figure beyond UB matrix refinement. The left-hand path "Structural Refinement" is routine crystallographic work, involving the extraction of structure factors and subsequent least squares refinement, while the right-hand side "Reciprocal Space Surveying" attempts to exploit the special ability of a time-of-flight Laue diffractometer such as SXD to sample large reciprocal space volumes.

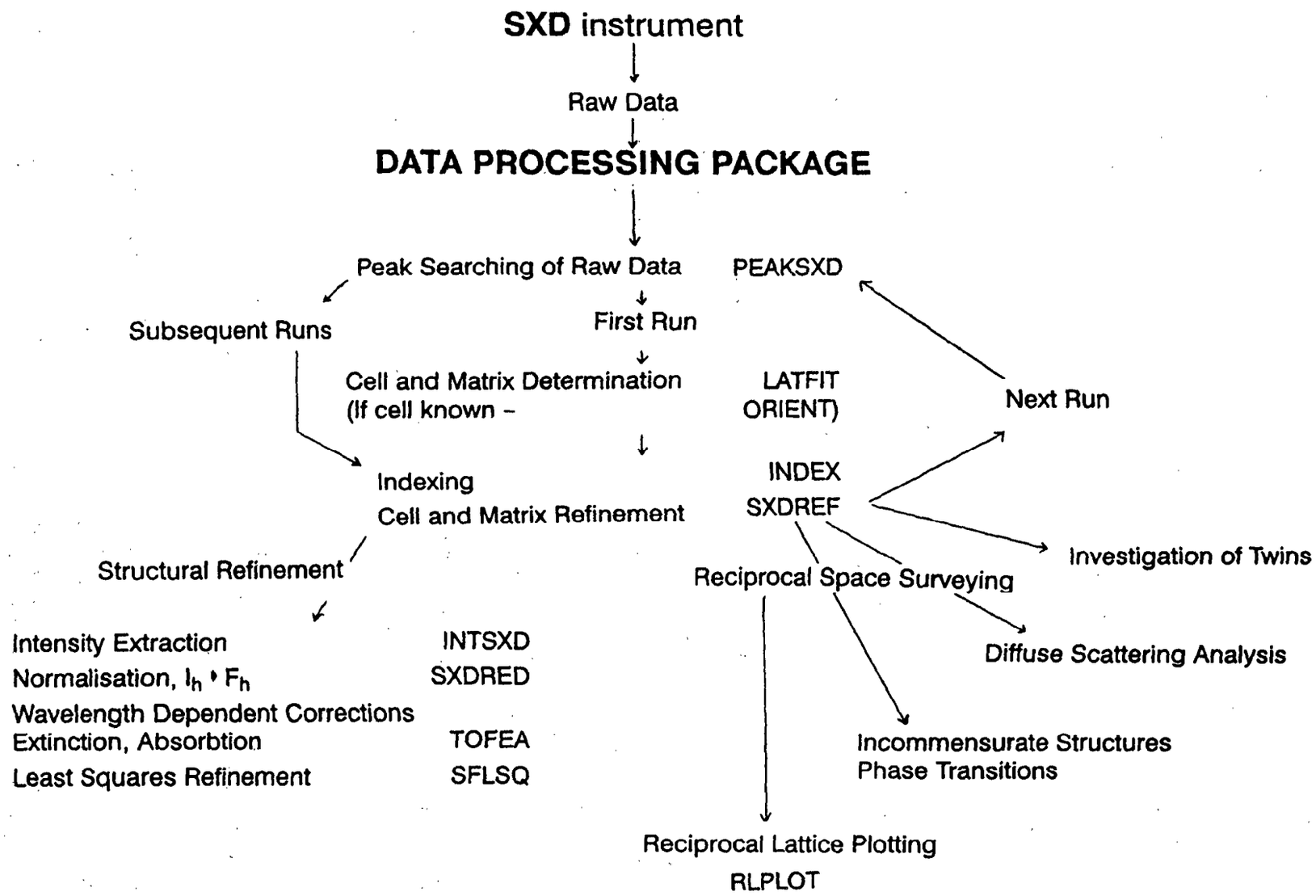

Figure 5 – The SXD data processing package.

IV. STRUCTURAL REFINEMENT

The extraction of structure factor information from an SXD data set proceeds in two stages. Given the provision of an accurate UB matrix from the earlier stages of the software package, integrated intensities are extracted from the raw data using Wilkinson's modification of the $\sigma(I)/I$ method (Wilkinson, 1986; Wilkinson et al, 1988). Once a reliable set of integrated intensities has been extracted from the raw data, these are reduced to structure factors. This reduction includes calculation of the coefficients for the evaluation and subsequent refinement of wavelength and path length dependent absorption and extinction corrections, using routines from the Cambridge Crystallographic Subroutine Library (CCSL; Brown and Matthewman, 1987). Structure factor refinement is then carried out within the framework of CCSL using the least squares program SFLSQ.

Structure and disorder in schultenite

One of the first examples of successful "routine" structural refinement carried out on SXD is the study of $PbHAsO_4$ (Wilson, Cox and Stewart, 1990). Lead hydrogen arsenate, occurring naturally as the mineral schultenite, undergoes a paraelectric–ferroelectric phase transition at 313 K, manifest in a lowering of crystal symmetry from P2/c to Pc and a gradual ordering of the hydrogen bonded H atom onto one of two disordered sites. The separation of these H...H disordered positions along with the O...O separation in the hydrogen bond have great bearing on the nature of the H potential. A structure determination performed at room temperature on SXD using a sample provided by the British Museum clearly revealed the presence of this H atom, previously unlocated by X-rays, and its 50:50 occupancy over two disordered sites (Figure 6). The separation of the two hydrogen sites (0.388(19) Å) is in good agreement with that in related materials. The provision of such details in hydrogen bonded systems is a good example of the structural refinement aspect of the SXD programme. The data for this study extended to $\sin\theta/\lambda$ of > $1Å^{-1}$, relatively high for such materials. This high resolution data allowed the refinement of the small distortion of the heavy atom lattice in the Pc phase. Further examination of these effects is in progress.

Figure 6 – High symmetry structure of $PbHAsO_4$, showing hydrogen atom disorder.

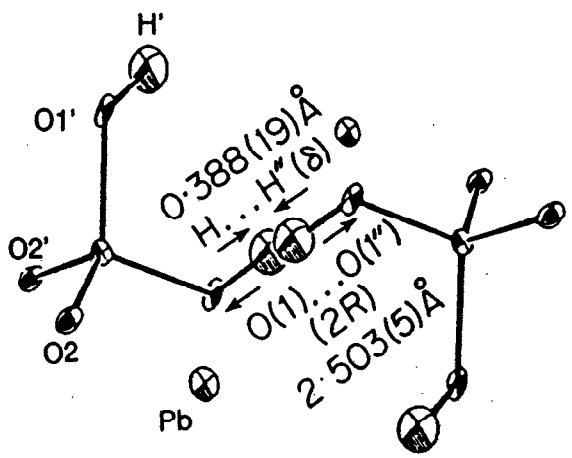

Wavelength dependent extinction and anharmonic thermal vibrations in strontium fluoride
The study of anharmonic thermal vibrations in SrF_2 (Forsyth, Wilson and Sabine, 1989) provided a rigorous test of the precision available from SXD. The data, from a heavily extinguished sample, provided a good example of the application of variable wavelength extinction corrections in CCSL. The extinction corrected data yielded an R-factor of 4.4% on those reflections expected to exhibit the effects of anharmonic vibrations of the fluorine atoms. The application of a third order anharmonic term, β_F, in the flourine potential led to a reduction in R-factor to 2.2%, and a value of $\beta_F = -4.19(30)\ 10^{-19}$ J Å^{-3}. this value was in good agreement with, but more precise than, the earlier $\beta_F = -3.95(46)\ 10^{-19}$ J Å^{-3} of Cooper and Rouse (1971). The improved precision is a consequence of the high $\sin\theta/\lambda$ value of 1.7 Å^{-1} reached on SXD (compared to 0.9 Å^{-1} in the earlier study).

V. RECIPROCAL SPACE SURVEYING

The other aspect of SXD, indicated on the right hand side of Figure 5, is to fully exploit the reciprocal space volumes accessed by the instrument in a single measurement. The ability to probe routinely those regions of reciprocal space *between* Bragg peaks lends the time-of-flight Laue technique great power in the study of incommensurate structures, phase transitions and diffuse scattering. Examples of the use of SXD in these cases are discussed below.

The simplicity of reciprocal space surveying on SXD again arises from the straightforward application of equation (1). In this case, one chooses a Q region (i.e. a set of indices $h_{min} < h < h_{max}$, $k_{min} < k < k_{max}$, $l_{min} < l < l_{max}$) within which one wishes to probe, with application of the equation as written giving the necessary detector coordinates to allow the data to be accessed. In the SXD package this is accomplished within the RLPLOT routines. Of course a mapping of reciprocal space points onto detector coordinates will never be exact and interpolation is adopted within the extraction program. Increased flexibility is also available within RLPLOT from the optional ability for performing detector and/or incident flux normalisation.

Diffuse scattering from Yttria-stabilised Zirconia
Within the cubic structure of Zirconia (ZrO_2), which is stabilised at ambient temperature by the presence of >9mol% Yttria (Y_2O_3), oxygen vacancies exist to maintain electrical neutrality. While the structure of ZrO_2/Y_2O_3 is fluorite, within the crystal there occur vacancy-free regions which cause a slight tetragonal distortion of the cubic lattice. This effect will give rise to coherent diffuse peaks at systematically absent Bragg peak positions. In addition, there is some ordering of vacancy pairs within the structure, giving rise to superlattice diffuse peaks in positions away from the Bragg peaks.

Figure 7 shows data collected on SXD from a single crystal of ZrO_2-9.4%Y_2O_3 (Hull et al, 1990). The sample was aligned with $<1\bar{1}0>$ vertical, allowing access to (hhl) reflections in the equatorial plane of the detector. The figure shows this (hhl) section, and clearly shows Bragg and diffuse scattering from this material. The sharp reflections such as (113) and (224), with h,k,l all even or all odd, are allowed in the cubic space group. Others, such as (114) and (116), are the diffuse Bragg peaks due to the distortion of the cubic lattice. There is also some diffuse scattering in the regions away from the Bragg peak positions, the observation of which is made easier by the surveying capability of SXD. These superlattice peaks are those caused by vacancy clustering. The measurement of diffuse scattering to the high Q values accessible on SXD (note the observation of the (1,1,10) diffuse peak) is important for the reliable modelling of the structural disorder causing this intensity.

Figure 7 – Bragg and diffuse scattering in the (hhl) plane of yttria-stabilised zirconia, ZrO_2–9.4%Y_2O_3. Note the high Q reached in this measurement, with the (1,1,10) diffuse peak clearly visible.

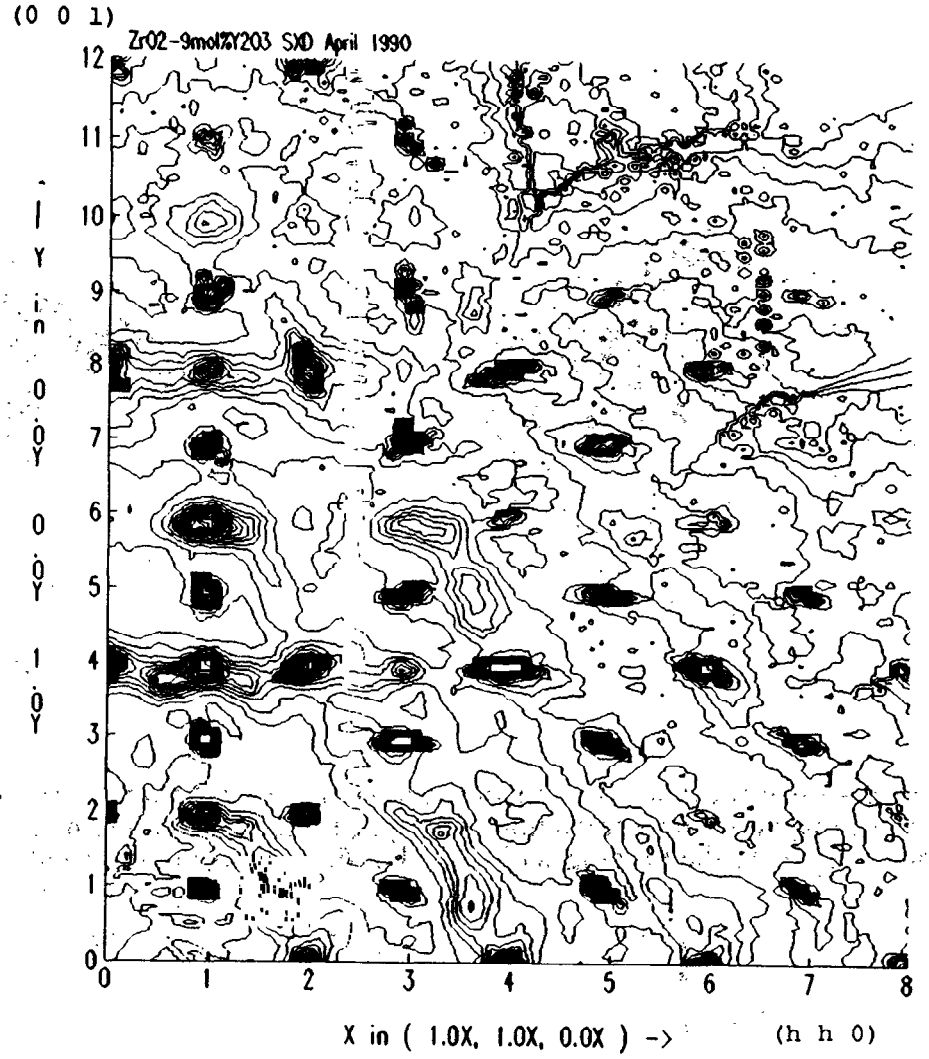

Magnetic phase transition in Holmium

The low temperature diffraction pattern of Holmium is rich in magnetic structure. The reciprocal space scanning properties of SXD can be used to follow phase transitions such as that in Ho (at around 133K) in a particularly simple way. By retaining the crystal and detector geometry fixed in one orientation it is possible to measure the temperature dependence of many reflections simultaneously. Satellite reflections, their positions and intensities, can be examined in any direction in reciprocal space. In an experiment such as the one in this example, one SXD histogram is frequently sufficient to give all the required data under one set of sample conditions.

In this experiment (Stirling et al, 1990), the region around (00l) was examined in the temperature range 150 → 14K. The magnetic phase transition gives rise to incommensurate reflections at (0,0,l±q) which can clearly be seen to appear as the temperature is lowered from 150K to 120K. Figures 8a and 8b show the (0kl) reciprocal lattice plane of Ho measured above and below the magnetic phase transition, clearly demonstrating the appearance of incommensurate satellite peaks. The temperature variation of the (00l) row clearly showed the satellites to move closer to the Bragg peaks and lock-in at $q = 1/6c$. In addition to these measurements around (00l), full scans of the (h0l) plane were carried out at a series of temperatures in the magnetically ordered region. These surveying scans, carried out rapidly and conveniently on SXD show, as expected, no evidence of squaring of the magnetic satellite structure (Figure 9).

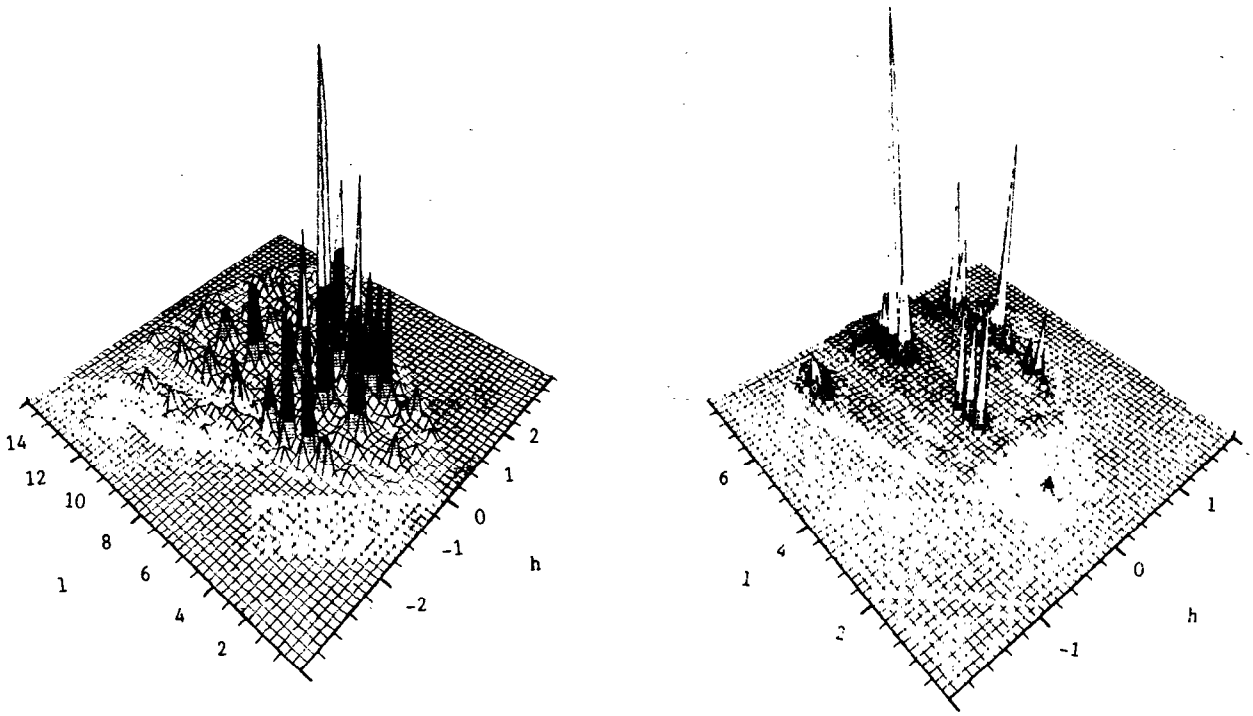

Figure 8 – Reciprocal lattice plots of sections of the (0kl) plane in Ho above (left) and below (right) the magnetic phase transition. The appearance of satellites in the low temperature phase is apparent. Note the Q–ranges displayed in these plots are different.

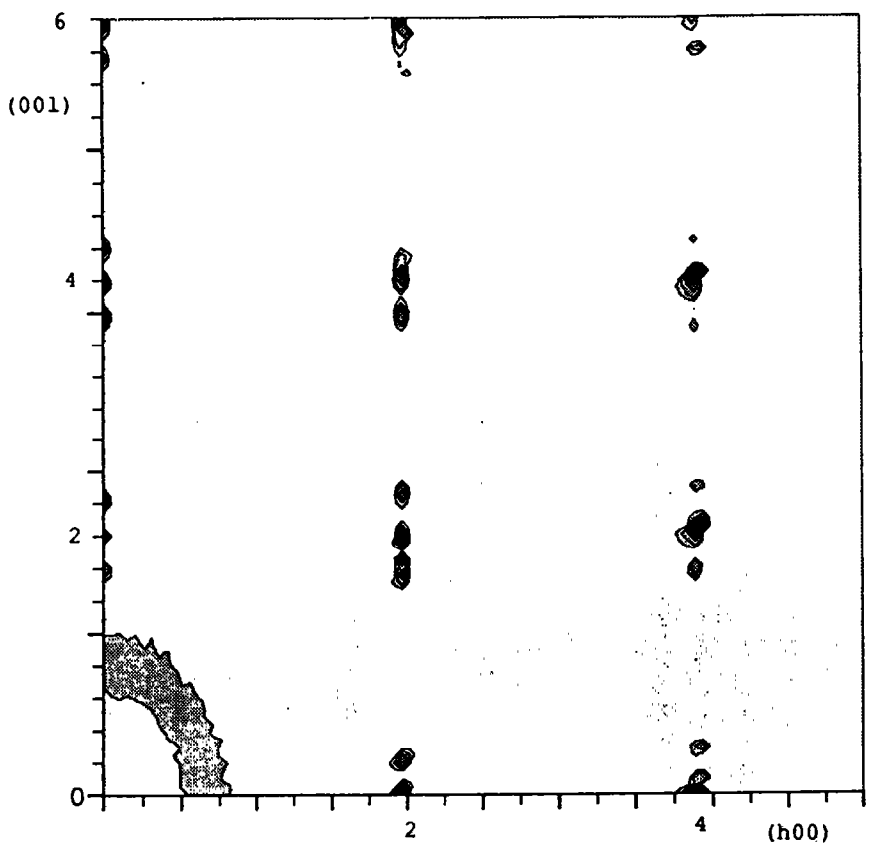

Figure 9 – A projection of the (h0l) plane in Ho at 120K showing the one dimensional nature of the incommensurate vector *q*, along *c*.

Ferroelastic domains in $LiKSO_4$

Lithium potassium sulphate undergoes several phase transitions, at temperatures varying from 940 to 38 K. These transitions have been characterised by several techniques, but for most of the phases only preliminary single crystal neutron scattering data are available. In both phase V below 198 K and phase VI below 38 K there is a ferroelastic domain structure leading to a broadening and splitting of certain peaks in the diffraction pattern. The study of this material on SXD should allow the measurement of peak shape in all reciprocal space directions and hence lead to a greater understanding of the symmetry changes involved in the paraelastic–ferroelastic phase transition. The profile of the $(1\,\bar{2}\,0)$ reflection of $LiKSO_4$ at 60K is shown in Figure 10. As can be seen from this, peak broadening and splitting is observed, showing the symmetry to drop at least to orthorhombic and possibly to monoclinic in phase V.

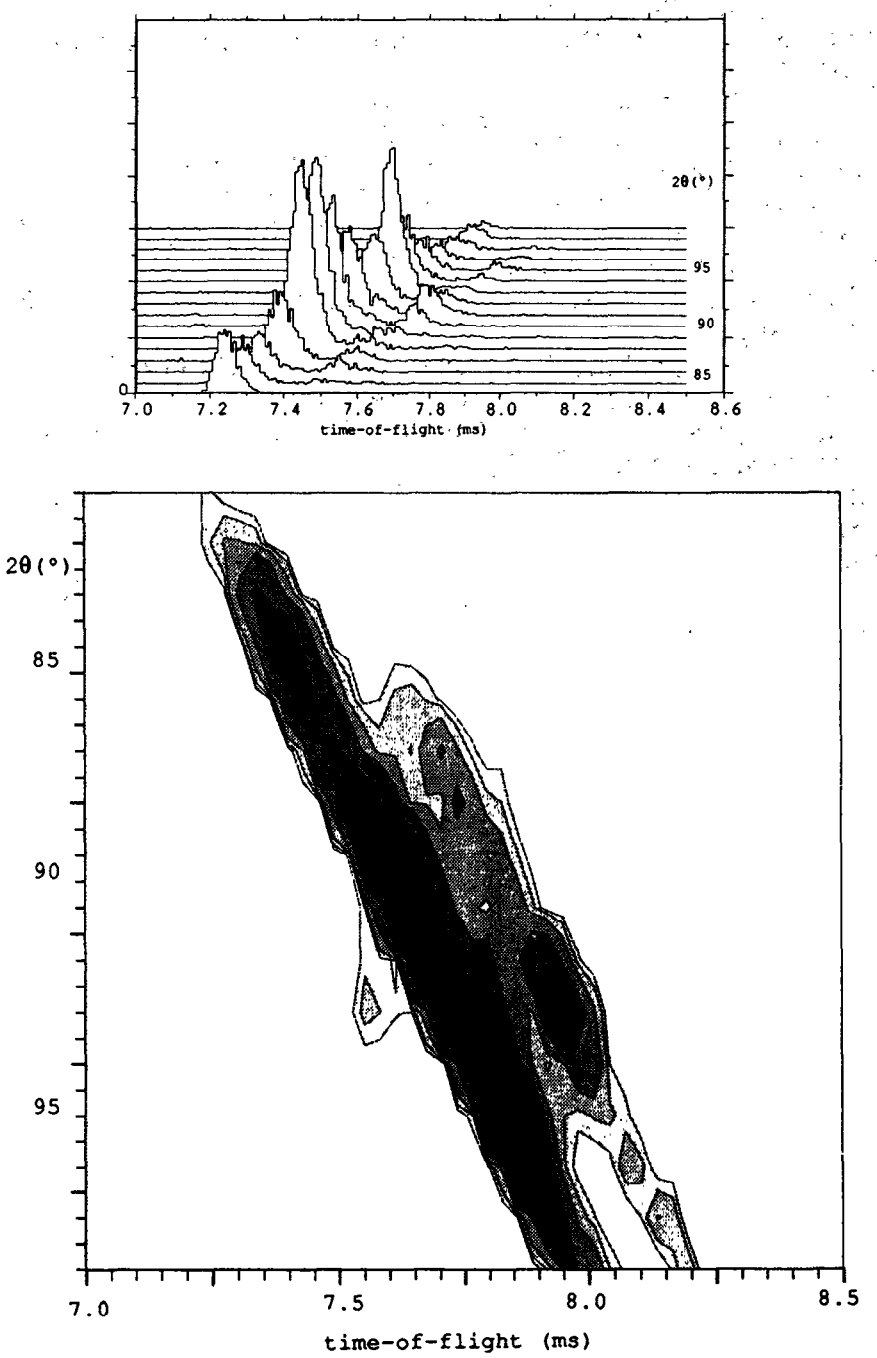

Figure 10 – The profile of the $(1\bar{2}0)$ reflection of $LiKSO_4$ at 60K, displayed as a multiplot of spectra and a contour plot in $(2\theta,t)$ space. The broadening and splitting of this peak, which is narrow and single above 190K, gives information on the ferroelastic domain symmetry.

VI. CONCLUDING REMARKS

It is clear from the results presented in these later sections that the first year or so of science performed on SXD have been rather successful and show great promise for the future, especially in the fields of diffuse scattering and reciprocal space probing. Developments of the detection system are continuing in parallel with the scientific programme, with the next aim to provide a larger version of the fibre-optic encoded ZnS module, the best and most reliable detection system available on SXD to date.

References

Anger H O, Rev. Sci. Insts. 29, 27 (1958)
Brown P J and Matthewman J C, Rutherford Appleton Laboratory Report, RAL-87-010 (1987)
Busing W R and Levy H A, Acta Cryst. 22, 457 (1967)
Cooper M J and Rouse K D, Acta Cryst. A27, 622 (1971)
Davidson P L, Mott E M, Rhodes N J and Johnson M W, in Advanced Neutron Sources 1988, ed D K Hyer, IOP Conference Series 97, 523 (1989)
Forsyth J B, Lawrence R T and Wilson C C, Nucl. Inst. Meth. A273, 741 (1988)
Forsyth J B and Wilson C C, to be published (1990)
Forsyth J B, Wilson C C, Stringer A M, Howard J A K and Johnson O, J. de Phys. Colloque C5-47, 143 (1986)
Forsyth J B, Wilson C C and Sabine T M, Acta Cryst. A45, 244 (1989)
Hull S, Goff J, Hutchings M T and Hayes W, to be published (1990)
Stirling W G, Tang C C, Haycock P W and Wilson C C, to be published (1990)
Wilkinson C, J. de Phys. Colloque C5-47, 35 (1986)
Wilkinson C, Khamis H W, Stansfield R F D and McIntyre G J, J. Appl. Cryst. 21, 471 (1988)
Wilson C C, Rutherford Appleton Laboratory Report RAL-89-014 (1989)
Wilson C C and Forsyth J B, Rutherford Appleton Laboratory Report RAL-89-005 (1989)
Wilson C C and Zaleski T, to be published (1990)

ICANS-XI International Collaboration on Advanced Neutron Sources
KEK, Tsukuba, October 22-26, 1990

Future ISIS single crystal instruments

C C Wilson and W I F David
ISIS Facility, Rutherford Appleton Laboratory, Chilton, Didcot, Oxon OX11 0QX, UK.

ABSTRACT
The designs of two proposed new single crystal instruments for ISIS are described. The biological structures instrument DIBS will allow the study of large unit cell materials in reasonable counting times. HRED, the high resolution elastic diffractometer, will provide a single crystal instrument of resolution $\Delta Q/Q \sim 10^{-3}$, increasing the available resolution for reciprocal space surveying by some 10-fold over that currently obtainable on SXD.

I. INTRODUCTION

The single crystal programme established at ISIS has now begun to illustrate the potential of the time-of-flight Laue technique at a pulsed neutron source. It is clear that the existing SXD is limited in its exploitation of the wide range of crystallographic science available at ISIS. For reasons both of limited unit cell size and limited resolution, there are parts of the programme which are effectively precluded from study by SXD.

To extend the size of structure amenable to study into the large molecule biological and organic chemical regime, the instrument DIBS (Diffraction Instrument for Biological Structures) is proposed. The development of neutron diffractometers for biological applications is hampered by the fact that biology is difficult for neutron crystallography, involving as it does very large unit cells and small crystals. However, there are many biological problems requiring neutron diffraction input, and with the expansion of the biological sciences it is becoming increasingly important that the potential exploitation of neutrons in biology is exploited. The main thrust of DIBS is towards maximising both useful flux on the sample and data accumulation rate, and it is hoped that this would allow such structures to be studied in a reasonable counting time. It is clear that for such an instrument, significant improvements in both hardware and software are required to give optimal performance. The somewhat mutually incompatible required mix of obtaining high flux on the sample, implying a short beamline, while retaining sufficient resolution for the separation of reflections from a large unit cell material, is tackled in the DIBS design.

One of the most successful ISIS instruments to date has been the high resolution powder diffractometer (HRPD). By exploiting the excellent resolution ($\Delta d/d \sim 5\ 10^{-4}$) available on a long flight path instrument at a pulsed neutron source, HRPD has opened new areas of science within the field of powder diffraction and has allowed a much deeper understanding of the detailed physics accessible by the technique. Experience on HRPD has shown that not only can an order of magnitude improvement in resolution lead to a greater understanding of effects previously suspected and partially measured, but can also yield hitherto unsuspected details. The development of single crystal diffraction at ISIS, on the other hand, has concentrated more on rapid reciprocal space surveying at modest resolution. The results obtained to date on SXD have shown the wealth of information available by this technique and have yielded promising results in both near and off Bragg peak diffuse scattering among others. However, the data obtained on SXD are at times tantalising - there is obviously a great deal of information available, much of which is masked by the low instrument resolution. Time-of-flight reciprocal space surveying has reached in some senses the stage reached by neutron powder diffraction before the advent of HRPD. A similar ten-fold improvement in resolution should have the same impact in this aspect of the single crystal field, allowing a greater understanding of that information at present only partially available and also yielding new information at present beyond the limits of SXD. The design of HRED, the High Resolution Elastic Diffractometer, should allow the opening of these new areas.

II. DIBS - SCIENTIFIC CASE AND GENERAL PRINCIPLES

Crystallography underpins all of the solid state sciences and has made a major impact in areas as diverse as high T_c superconductors and in the determination of the structure of DNA. Neutron diffraction, on the other hand, has made a major impact in physics and chemistry but much less in the biological sciences field. The impact of neutron diffraction methods in the latter has been modest to say the least, when compared with the impressive list of discoveries achieved using X-rays.

Neutrons do, however, have an extremely important role to play in the study of biological structures. Many of the mechanisms for biological activity in proteins, nucleic acids and other large scale biological systems, are associated with hydrogen bonding, solvent water structure and other forces depending crucially on a knowledge of the locations of hydrogen atoms within the structure. In the location of these vital hydrogen atoms, neutron diffraction has a significant advantage over all other techniques. In particular, these hydrogen atoms are virtually unlocatable by X-ray methods. In addition, the ability to perform isotopic substitution - exchanging deuterium for hydrogen - further enhances the potential of the neutron as a biological probe.

There are two principal problems with neutron diffraction from large unit cell samples: low neutron flux and small crystal size lead to prohibitively long counting times; the very large incoherent scattering of hydrogen gives a high background, prejudicing the peak/background ratio attained and thus leading to reduced precision. Designed to overcome these problems, DIBS was conceived in part as a result of ideas put forward by Lehmann and Wilkinson (1989) for a quasi-Laue diffractometer (LADI) at the ILL, and by extrapolation (Wilson, 1988) of earlier calculations of requirements for biological crystallography at a pulsed source presented by Jauch and Dachs (1984).

The current single crystal diffractometer (SXD) at ISIS is a time-of-flight Laue instrument, but is designed and optimised for the study of fairly small molecule structures, and is thus primarily a physics/chemistry instrument. With a largest cell edge amenable to study on SXD of some 30-35 Å with current hardware and software, and a largest unit cell volume of some 3000-5000 $Å^3$, much of organic, organometallic and biological crystallography is inaccessible. In addition, SXD is situated on a hot (ambient water) moderator, and the flux distribution peaks at a much shorter wavelength than would be ideal for large structural work. A cold moderator is much more suitable (see below). The aim in designing an instrument such as DIBS is to reach the specifications required in much of contemporary biological crystallography:

(i) Unit cell edges of up to 100 Å;

(ii) Cell volumes > 10^5 $Å^3$;

(iii) d_{min} in the range 1.2-1.5 Å dependent on crystal diffraction characteristics;

(iv) Reasonable data collection times (days/weeks rather than months);

(v) Crystals usually limited to V ~ 1 mm^3 even in favourable cases;

The Laue method, the most obvious data collection technique on a pulsed source, permits the simultaneous measurement of many Bragg peaks and is thus efficient for the rapid collection of many data (> 10^5 reflections for a moderately large protein). A single crystal instrument on a pulsed source has very significant advantages in using the Laue method, related to the fact that time-of-flight allows the separation of different reflection orders, but more importantly "stretches" the incoherent background from hydrogen. This latter scattering is of necessity integrated into the detector on a steady state Laue diffractometer. This factor has a significant effect on the peak/background ratios achieved. With such data, collected on position-sensitive detectors, excellent spatial resolution is necessary to resolve the many Bragg peaks, whose centres are typically closer than 1% in $\Delta Q/Q$.

II.1 Calculations and Assumptions.

Wilson (1988) proposed the following modifications to improve the prospects for biological structural studies on SXD:

(i) Profile fitting for the extraction of integrated intensities (see below) – the limiting resolution (in time) is given by $\Delta Q/Q \sim 0.017$ (assuming peaks separated by $\pm 2.5\sigma$) for SXD at 8 m, ~0.006 at 20 m. The required resolution for 1.2 Å d_{min} along a 100Å cell edge is ~0.006. Profile fitting can reduce peak separation to $< \pm 1\sigma$, reducing the required $\Delta Q/Q$ to some 0.015 or more. An ~8 m instrument would then become tractable in terms of time resolution;

(ii) Angular resolution requirements can also be reduced by using profile extraction of intensities. The assumption of 3 mm resolution detectors at L_2 = 1 m used in one of the earlier extrapolations (see below) is then unnecessarily strict. Placing 3 mm resolution detectors (current technology) at L_2 = 0.3 m is sufficient, if the anticipated resolution in the profile fit is obtained;

(iii) Flux improvements can be gained by using a large wavelength range ($\Delta\lambda$ of > 4 Å for short instrument, ~2–3 Å for a 20 m instrument) and a colder moderator to increase the useful flux of colder neutrons (where the λ^4 reflectivity term in the intensity equation becomes very favourable). A tight pulse is still required, however, for a short instrument to be viable and it may be necessary to sacrifice some flux to poisoning. It should be noted again that to first order the inclusion of a larger λ window does not prejudice the accuracy of the reflections which would be accessible in the short window, due to the favourable aspects of the time-of-flight technique. This is because in time-of-flight the background is time-sorted in a way unique to pulsed sources, allowing one to increase the range of data collection without penalty;

(iv) The detector array can be increased (see below), in light of recent advances in easy to construct ZnS scintillator PSD technology. Pursuing fibre-optic encoding designs for large area PSDs, better than 3 mm resolution is achievable over large (>300×300 mm^2) areas. We can assume a variety of detector arrays, depending on cost and availability of profile fitting for intensity extraction;

(v) The use of a focusing guide extending into the insert shielding can further increase the flux on the sample;

(vi) Data processing would involve the extensive use of front-end transputer-based number crunching, to automate the bulk of the work of integrated intensity extraction. Coupled with the provision of a fast modern-day minicomputer such as VAXstation-3200, this set-up should be able to cope with the rapid data rates expected.

Under various scenarios, the following very approximate extrapolations can be made. These are based on the original estimates (Jauch and Dachs, 1984) of some 10 weeks data collection time for a 20 m instrument with a guide. The assumptions used are of a factor two increase in flux from both pulse exploitation and provision of more cold neutrons, a factor of three in detector coverage in designs (ii) and (iii) below and a factor of some five from the use of a focusing guide on the short beamline. In addition in all these calculations 100% detector efficiency has been assumed (this is not yet realised).

(i) High resolution, SXD-20, guide, 10 PSDs at L_2 = 1 m :
t_{est} ~ 20/2 = 10 weeks for 1.25×10^5 Å^3 cell (10w/25 = 3 days for lysozyme).

(ii) Moderate resolution, SXD-20, guide, 10 PSDs at 0.3 m :
t_{est} ~ 20/2/3 = 3 weeks for 1.25×10^5 Å^3 cell (3w/25 = 1 day for lysozyme).

(iii) Low resolution, SXD-8, focusing guide, 10 PSDs at 0.3 m :
t_{est} ~ 20/2/3/5 = 5 days for 1.25×10^5 Å^3 cell (5d/25 = 5 hours for lysozyme).

Given that software advances allow the 3D profile fitting intensity extraction method to be successfully exploited (and there is already evidence that this is the case), then obviously the most rapid data collection design should be chosen for biological studies. *DIBS would then resemble the ~8m instrument described above.*

The latter design begins to appear very similar to that proposed by Lehmann and Wilkinson (1989) for a protein Laue instrument at the ILL, where they assumed $L_1 = 7$ m, $L_2 = 0.1$ m, angular coverage of PSDs equivalent to 10 modules at 0.3 m, $\Delta\lambda = 2$ Å (achieved through velocity selectors), in which they estimated some three hours for the study of lysozyme, very similar to the data collection time given for DIBS above. Given the approximate nature of some of these estimates, the difference in these numbers (three versus five hours) is probably not significant. The reasons for this favourable comparison of count rate between LADI and DIBS, in spite of the probable order of magnitude greater flux on sample of the former, are two-fold: LADI requires 2–3 wavelength bands in its "quasi"-Laue approach, whereas DIBS time sorts the whole range in a single data set; poor peak/background (1:10) on LADI resulting from the integration of the hydrogen incoherent scattering compares unfavourably with that predicted for DIBS (1:1), giving a further factor of three in required counting time. Thus, in the present very rough approximation, the counting times on the two instruments appear roughly equivalent.

II.2 Software Improvements

In the context of DIBS, these are essentially geared towards the d_{min} for which reliable intensity information may be extracted for a large structure. The resolution limits quoted above are based on the assumption that reliable intensity extraction is only possible for peaks whose centroids are $> 5\sigma$ apart (σ being the FWHM of the peak profile). However, by adopting a strategy analagous to the Pawley (1981) peak fitting method (itself an adaptation of the Rietveld method) one can fit an overall "envelope" or profile to the entire observed pattern. Use of the Pawley method (in one dimension) has been shown to vastly improve the apparent resolution of peaks, i.e. to allow extraction of useful intensity information for peaks separated by considerably less than 5σ . By adopting a three-dimensional extension of this profile fitting technique it should be possible to resolve reflections separated by, say, 1σ ($\pm 0.5\sigma$), improving the apparent resolution by a factor of some five.

Initial work on this profile intensity extraction technique has begun, using data sets collected on the existing SXD. As an example, intensities were extracted from the (00l) row of reflections (Figure 1) from a W-hexaferrite sample with $c = 32.9$ Å. It was found possible in this case to extract intensities for reflections up to (0,0,80), $d = 0.4$ Å, in a region well beyond the normal "resolution" limit (in terms of overlapped peaks) of the instrument. This test bodes well for the implementation of the full 3D profile software.

II.3 Hardware Improvements

As mentioned above, in order to maximise count rate, it is necessary to have a very large array of position-sensitive detectors around the sample, subtending as large an angle as possible. The ILL proposal for LADI uses 100% efficient PSDs with 1 mm resolution situated at 0.1 m from the sample – technology as yet unproven in either aspect but which obviously reduces the area coverage requirements and hence the diffractometer costing. The area detectors proposed for DIBS are envisaged to be based on the fibre-optic encoded ZnS scintillator PSDs recently successfully installed and tested on SXD (Davidson, Mott, Rhodes and Johnson, 1989). The prototype module for this type of area detector has performed very satisfactorily and the extrapolation to the desired properties is being pursued at present. The specified properties for DIBS modules are:

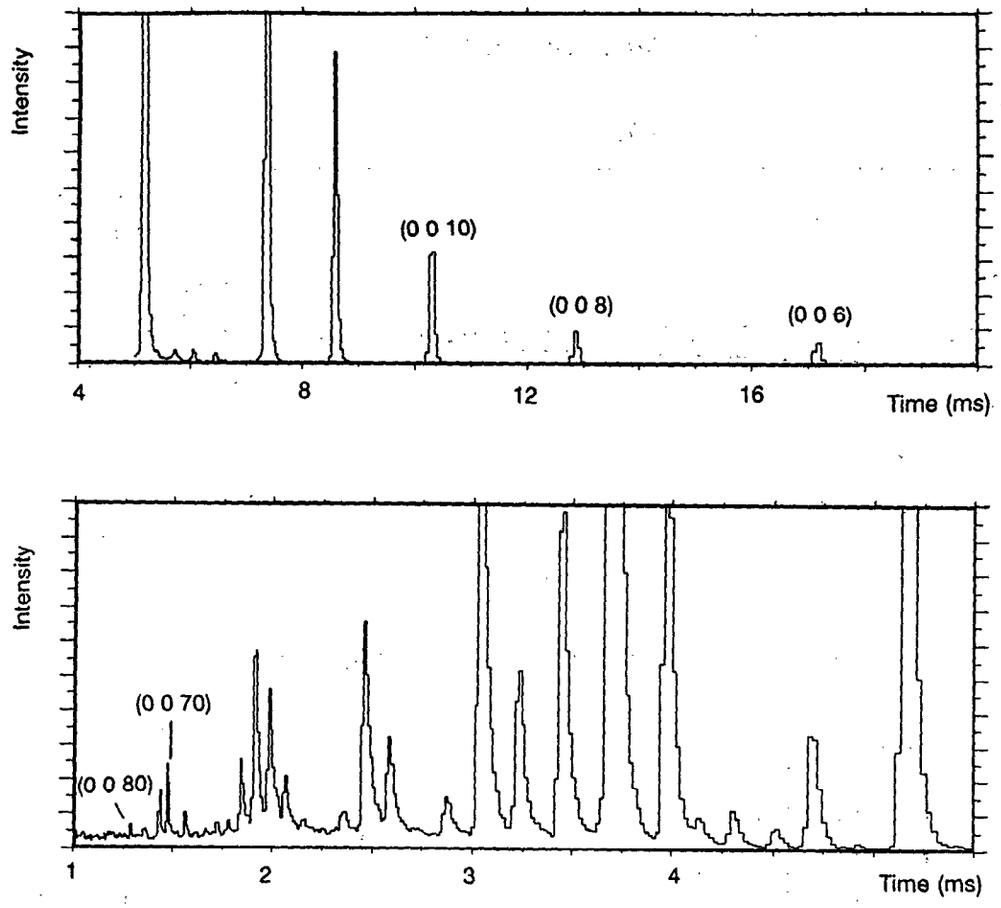

Figure 1 – Time-of-flight spectrum of the (00l) row of the W-hexaferrite, measured on SXD.

(i) 3 mm pixel resolution, possibly reducing to 1.5 mm by interpolation;

(ii) 2–3 μs dead time per module will be adequate for DIBS data collection rates;

(iii) Efficiency > 50% for 1 Å neutrons, approaching 100% for longer λ – significant development is required to realise this for ZnS scintillator modules;

(iv) Ease and speed of construction – 300 × 300 mm^2 modules should be built on a timescale of 1–2 months when this becomes routine. The economical nature of the construction also allows large spatial coverage to be achieved without enormous expense;

(v) The modules could be constructed in a curved array, forming part of a spherical surface surrounding the sample;

(vi) Around 10 of these modules would form the basic DIBS array, situated at L_2 ~ 0.3 m.

The data acquisition and processing capability required for such an extensive data processing array and the data rates anticipated for DIBS would be substantial. The data collection is envisaged to use the proposed ISIS DAE–II and would rely on extensive use of transputers to push many of the number–crunching aspects of data collection and reduction into the hardware at the front–end, including the extraction of integrated intensities from the raw data. The removal of this taxing task from the computing system would allow the use of the extensive CPU for further processing.

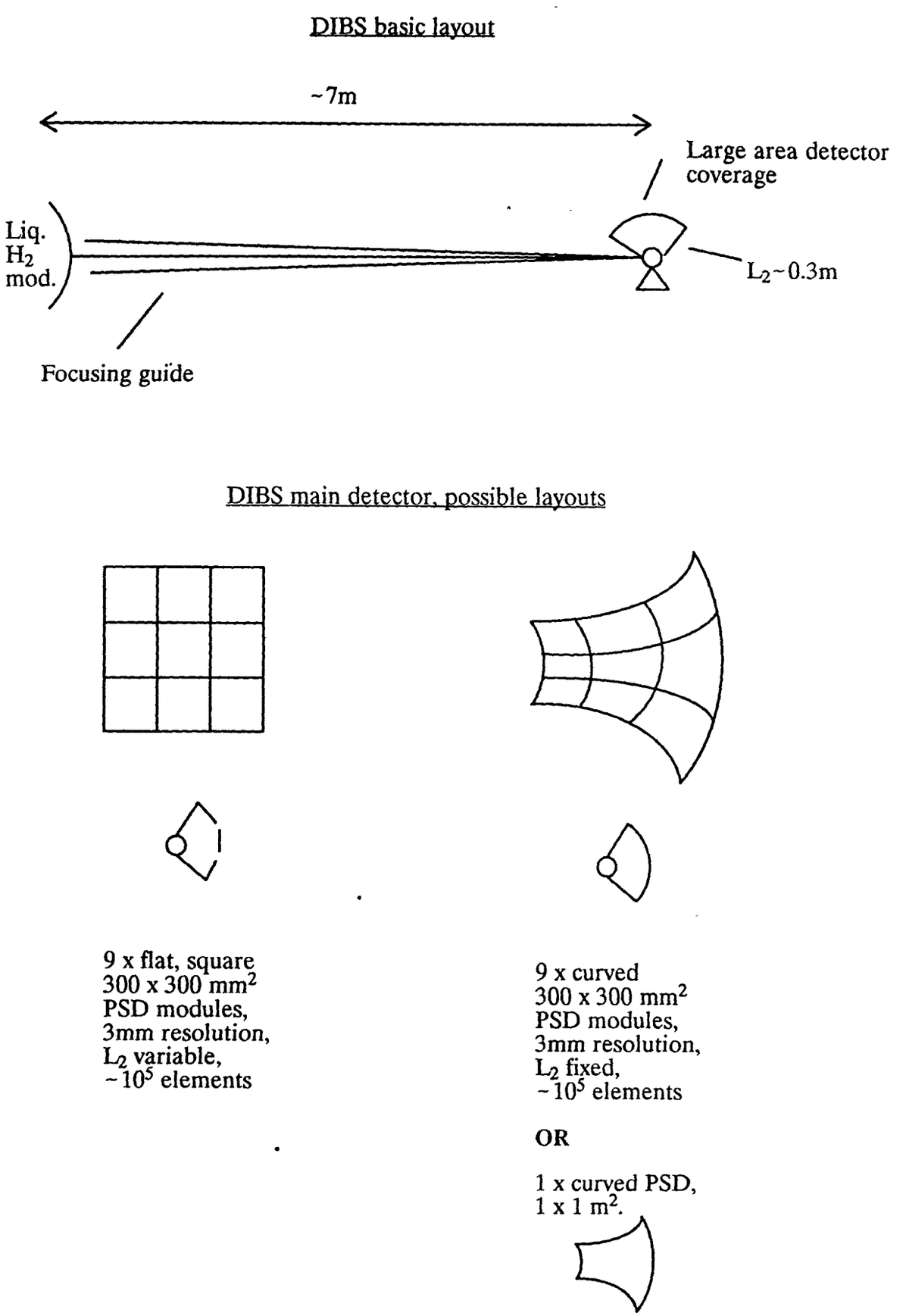

Figure 2 – Schematic DIBS design and detector layout (not to scale).

II.4 DIBS – a provisional design

The essentials of the DIBS instrument design (Figure 2) are therefore :

L_1 ~ 7–8 m;
L_2 ~ 0.1–0.3 m, depending on detector technology;
Cold moderator (liquid CH_4 or liquid H_2) – possibly on S4 or S5 at ISIS (see Figure 6);
Focusing guide;
Large area detector coverage (10 modules of 300 × 300 mm^2 active area, 3 mm resolution at 0.3 m L_2);
Restricted 4–circle geometry as for SXD;
Profile fitting intensity extraction in three dimensions;
Transputer based data treatment.

II.5 Prospects

It is hoped that testing of the DIBS principle can begin shortly on ISIS, with tests on a cold beam using the present ZnS fibre–optic encoded PSD with a moderately large unit cell material such as lysosyme or a large organic material. A larger version of the ZnS module is in construction and is intended to be installed on SXD early in 1991. This module will have most of the desired detector characteristics outlined above for DIBS and will represent a proving of the detector technology required. Further developments of the profile software are in hand, with extension to full 3D processing expected shortly. Given that these developments can proceed with some alacrity, it is hoped that a fully detailed and costed proposal for DIBS will be made in the near future. A working panel has been set up at RAL to further facilitate both this and more general developments in biological crystallography at ISIS.

III. HRED – SCIENTIFIC CASE AND GENERAL PRINCIPLES

The intrinsically high resolution available at pulsed neutron sources offers significant advantages in the study of crystal structures, with resolutions of $\Delta d/d \sim 10^{-3}$ easily achieved using primary flight paths of > 50 m. In addition, the constancy of this resolution function on a time–of–flight instrument implies that multiple orders of a Bragg reflection can be studied simultaneously with equal reciprocal space precision. This can be a great advantage, particularly if there is significant structural detail, such as twinning, satellite reflections and diffuse scattering, in the vicinity of Bragg peaks.

There are several fields in which an ultra–high resolution single crystal instrument such as HRED would obviously make a significant impact, although as stated above, it would be expected that still newer fields would open up in practice as a fully operational instrument of this type to some extent sets its own agenda. Those fields which HRED would obviously benefit are:

(i) High resolution near–Bragg peak scanning in all three reciprocal space dimensions
Twinning topology, incommensurate satellite reflections (intensities, q values, broadening), phase transitions, diffuse and quasielastic scattering, one phonon and magnon scattering;

(ii) Measurement of equivalent Q positions at different 2θ
Thermal diffuse scattering (TDS) and soft phonon studies, critical scattering and central peak measurements, magnetic diffuse scattering (2D and 3D spin correlation studies), extinction and absorption models;

(iii) Reciprocal space topology of diffuse scattering
Defect structures, orientational disorder;

(iv) Quasicrystals

III.1 Resolution considerations in the design of HRED

The resolution of a single crystal diffractometer can be highly anisotropic, with contributions from both time and angular uncertainties. In order to match the time-of-flight resolution, $\Delta t/t \sim 5.10^{-4}$, small detector pixels and long secondary flight paths are required in all but high backscattering angle positions. The proposed main detector for HRED is a quasi-one dimensional 'ribbon' array, using ZnS scintillator and fibre-optic encoding, with 2 mm x 2 mm pixels in an array 10 cm high, subtending angles in the range 60 to 175° at an average L_2 of 2 m. This will result in a FWHM reciprocal space resolution of some 10^{-3} in all reciprocal space directions. Additional 10 cm high ribbon detectors at ±(20–60°) with L_2 of 1.5 m (for long d-spacing information) and a 300 x 300 mm^2 moderate resolution 2D PSD at 90° (primarily for orientation information) would complete the detector array. The overall detector array would thus consist of > 10^5 pixels, which with the large number of time channels required to match the resolution, would preclude the decoupled use of all pixels and all time channels. Selective sampling of reciprocal space would be software controlled and tailored to the experiment.

III.2 The scientific scope of HRED

One phonon TDS

One phonon thermal diffuse scattering (TDS) can already be examined in some detail using SXD, with early measurements (Wilson, 1990; Willis, Carlile, Keen and Wilson, 1990) showing considerable changes in the phonon spectrum as the scattering geometry changes. However, to date the quantification of these effects (Figure 3) has been made difficult by the relatively poor instrumental resolution and by the limited angular range accessible in a single measurement. A full understanding of the TDS close to Bragg peaks is essential in highly precise structural analysis, and the provision of ultra-high resolution and large angular coverage on HRED will make the instrument ideally suited for investigations of the effect.

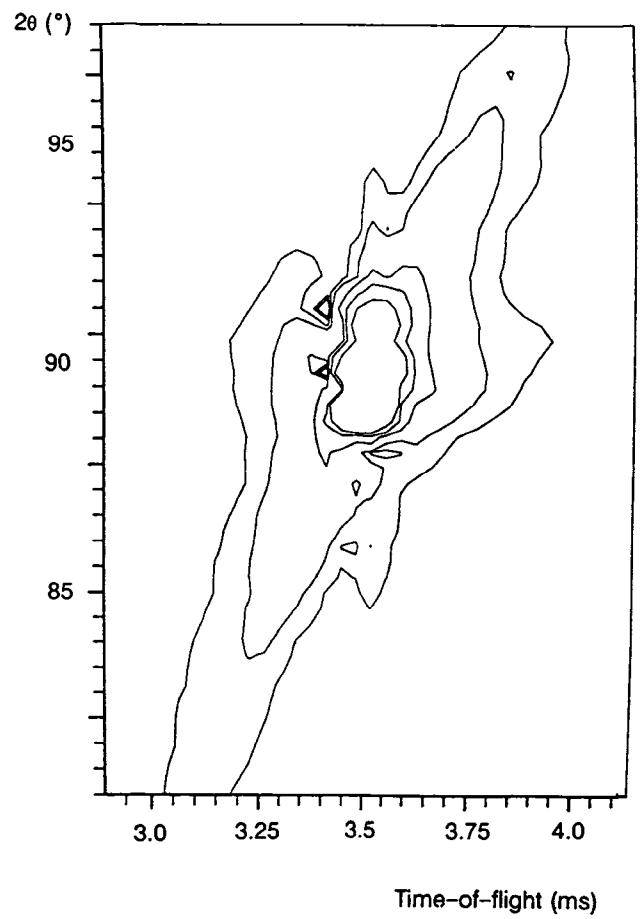

Figure 3 – Thermal diffuse scattering around the (224) reflection of SrF_2, measured on SXD. The features on this plot are seriously instrument resolution limited. The full study of scattering effects of this complexity requires the resolution offered by HRED.

Twinning in $LaNbO_4$

To investigate the potential of the HRED technique, single crystal pilot studies have been performed on HRPD (David, Kamiyama and Ibberson, 1990). By locating an Anger camera area detector at $2\theta \sim 90°$ on HRPD, with its 96 m flight path, fractional resolutions of 0.1% can be achieved, matching the projected performance of HRED. A test experiment was carried out on a single crystal of $LaNbO_4$, which undergoes a monoclinic–tetragonal ferroelastic phase transition at 495°C. This material is often twinned in the low temperature monoclinic phase and previous powder diffraction measurements had indicated unusual peak broadening in the vicinity of the phase transition.

Data were collected in four runs at 360, 430, 470 and 500°C, with the variation of the diffraction pattern close to the (220) reflection illustrated in Figure 4 The twinned nature of the crystal is clearly indicated at 360°C, in which the (220) and $(\bar{2}20)$ reflections can clearly be seen. The separation of these two peaks, some 1%, is clearly resolved and can be seen to reduce as the temperature is increased towards the phase transition and the tetragonal phase. At 470°C, however, an additional reflection is seen, corresponding to the formation of a new type of twin which is only possible with small distortions and involves pinning to crystal imperfections such as dislocations. Above the phase transition at 500°C, the distortion has clearly collapsed and a single (220) Bragg peak is observed. At this temperature, however, the presence of diffuse scattering resulting from very soft acoustic modes can also be observed, further illustrating the wealth of information available at high resolution from single crystal neutron diffraction.

Figure 4 – The evolution of twinning in a single crystal of $LaNbO_4$. These data, measured on HRPD using an Anger camera area detector, are representative of the data available in a single crystal experiment at the resolution of the proposed HRED.

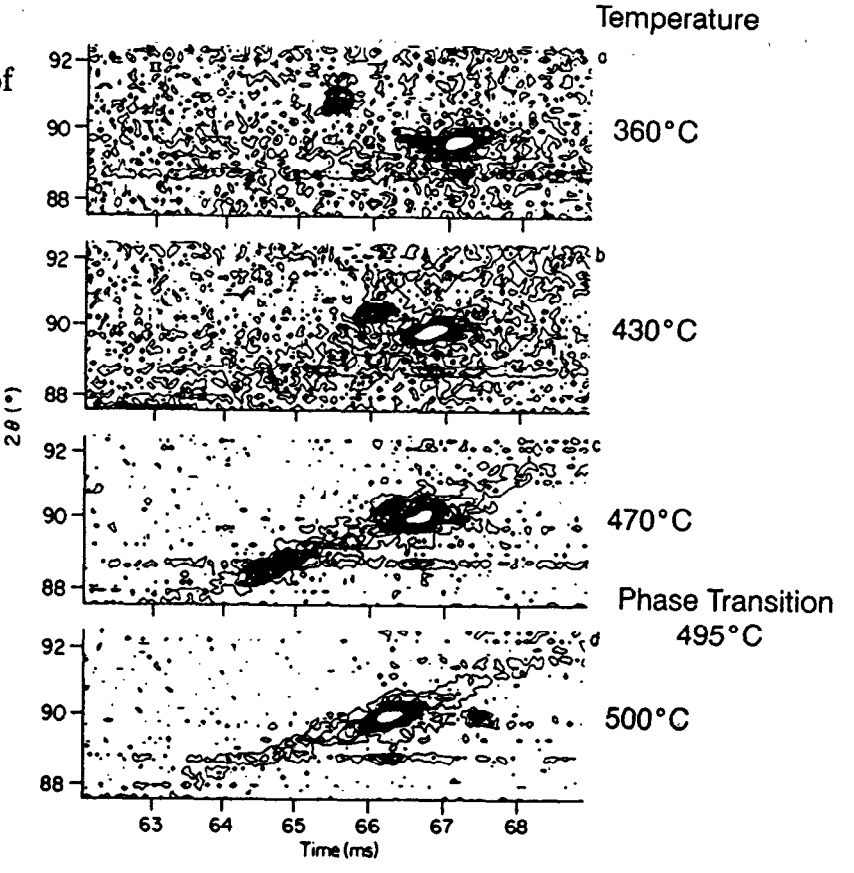

III.3 HRED – a provisional design

The instrument (Figure 5) has essentially the following features:

L_1 ~ 60 m;

Beamline S8, straight guide, CH_4 moderator (see Figure 6);

L_2 ~ 2 m (high angle), 1.5 m (low angle);

2D 'ribbon' PSD, $60° < 2\theta < 175°$, 10 cm high, 2 mm square pixels;

and 2D 'ribbon' PSD, $2\theta = \pm 20\text{–}60°$, as above;

and 2D PSD, $2\theta = 90°$, 300×300 mm^2, 3–5 mm pixel resolution, L_2 = 300 mm;

Resolution $\Delta Q/Q \sim 10^{-3}$;

Selective sampling of reciprocal space volumes.

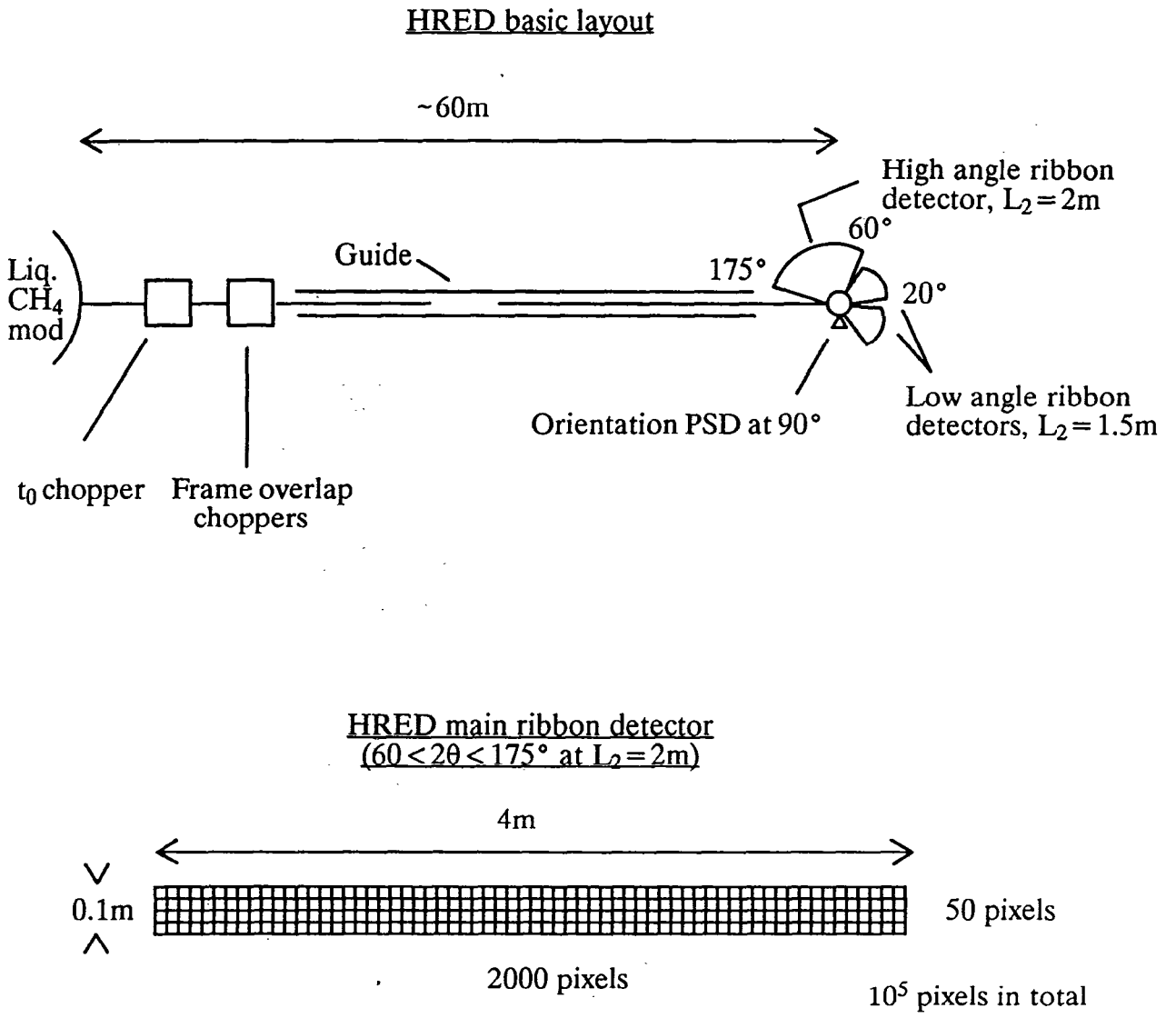

Figure 5 – HRED, basic schematic layout and detector design (not to scale).

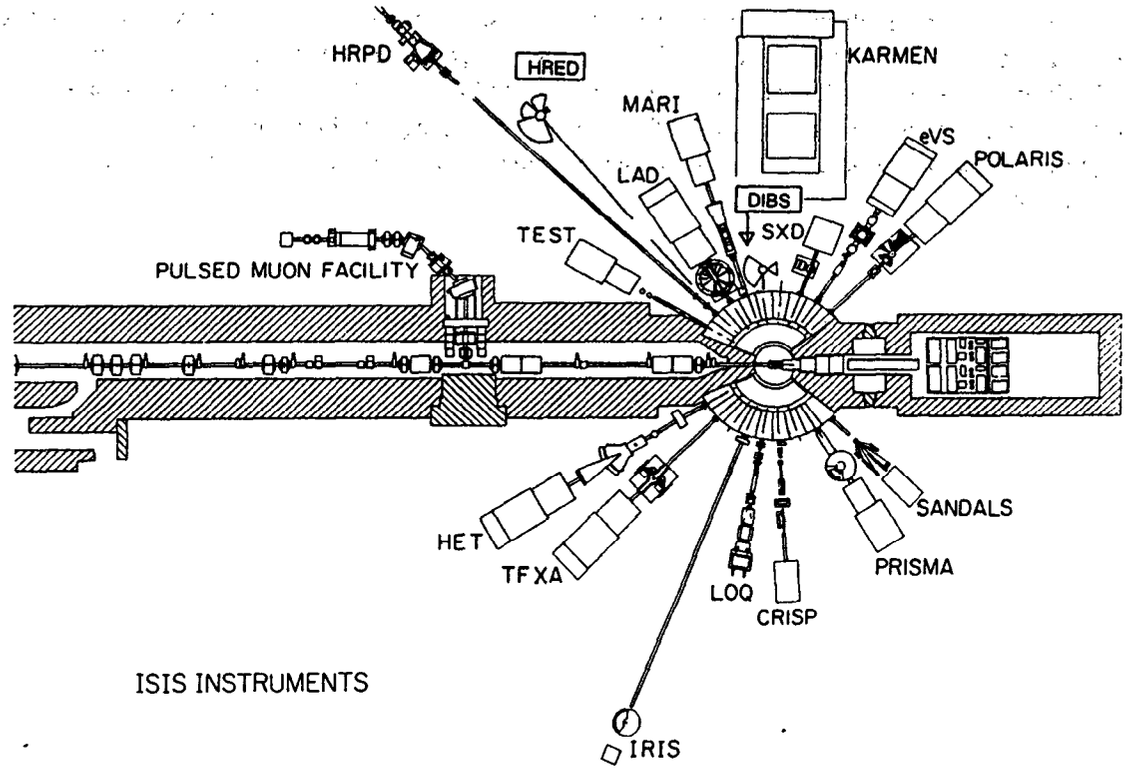

Figure 6 – Layout of the ISIS Experimental Hall, showing the possible locations of the two planned new instruments DIBS and HRED.

III.4 Prospects

Testing of the HRED concept will continue from both the high resolution (HRPD) and low resolution (SXD) limits, as part of the single crystal programme at ISIS. Results obtained from these will further indicate the scope of HRED for exploring new science and will enable, for example, detailed data collection and processing strategies to be examined. In addition, a small prototype fibre-optic encoded ZnS detector is planned, at the 2 mm resolution required for the instrument. In the light of these tests, a fully detailed and costed HRED instrument will be designed in the near future.

References

David W I F, Kamiyama T and Ibberson R M, unpublished (1990)
Davidson P L, Mott E M, Rhodes N J and Johnson M W, in Advanced Neutron Sources 1988, ed D K Hyer, IOP Conference Series 97, 523 (1989)
Jauch W and Dachs H, in Proceedings of a Workshop on SNQ, pp 31–52, Jülich (1984)
Lehmann M S and Wilkinson C, 'Troisieme souffle' proposal, ILL, Grenoble (1989)
Willis B T M, Carlile C J, Keen D A and Wilson C C, to be published (1990)
Wilson C C, Rutherford Appleton Laboratory Report, RAL-88-105 (1988)
Wilson C C, to be published (1990)

C(N.Niimura): In single crystal diffractometer of TOF type, large area detector is essential. But if we want to measure several Bragg reflections with the $\lambda \approx 1$ Å neutrons, the observed number of reflections is limited. We must think about it. The larger detector is the better, but it depends on the kind of an experiment.

A(C.C.Wilson): TOF is ideal for measuring reflections at different λ - allowing for correction of λ dependent terms. We must also, of course, retain diffractometer flexibility to allow the measurement of what you suggest, but the advantages of the pulsed source / time-of-flight technique is not so apparent in such an experiment.

ICANS-XI International Collaboration on Advanced Neutron Sources
KEK, Tsukuba, October 22-26, 1990

Analysis of a Drum Chopper for Use on a New Small Angle Diffractometer at IPNS*

R. K. Crawford, J. E. Epperson, P. Thiyagarajan, and J. M. Carpenter
Argonne National Laboratory, Argonne, IL 60439.

ABSTRACT

Light-weight drum choppers rotating at 15 Hz have been in use on the IPNS powder diffractometers for several years, where they serve to eliminate the delayed-neutron background from much of the spectral region of interest. Monte Carlo simulations indicate that a similar chopper operated at 15 Hz should do an excellent job of delayed-neutron removal in the new small-angle diffractometer being designed at IPNS. The simulations also show that when the same chopper is operated at 7.5 Hz it performs quite successfully as a frame-elimination chopper, effectively eliminating neutrons from alternate pulses and allowing extension of the useful wavelength range of the instrument to ~28 Å. Thus the incorporation of such a chopper should add considerably to the range and flexibility of the new instrument.

I. INTRODUCTION

A major goal in the design of a new small-angle diffractometer at IPNS is the achievement of a much lower Q_{min} than is currently available on the IPNS small-angle diffractometer SAD (current Q_{min} for SAD is ~0.005 $Å^{-1}$). Since

$$Q = (4\pi \sin\theta)/\lambda , \tag{1}$$

reaching smaller values of Q means measuring either to smaller values of the scattering angle $\phi=2\theta$ or to larger values of the wavelength λ, or both. Practical considerations require that the total source-detector distance be at least ~9 m, so that wavelengths beyond ~14 Å are overtaken by neutrons from the next frame of the 30 Hz source. Thus access to wavelengths longer than 14 Å on the new instrument will require the use of some means of either a) eliminating all wavelengths shorter than 14 Å or b) eliminating alternate source pulses. This paper addresses the feasibility of the latter approach.

*Work supported by U.S. Department of Energy, BES, contract No. W-31-109-ENG-38.

A significant problem at pulsed spallation neutron sources using fissionable material in their targets is the "delayed" neutrons which are emitted from short-lived excited states of the target nuclei.[1,2] Because the lifetimes of these excited states range up to tens of seconds, these delayed neutrons leave the target at times which are uncorrelated with the prompt pulses, and so cannot be energy-analyzed by the usual time-of-flight (TOF) methods. Instead they contribute to the sample-dependent background in the neutron scattering instruments. Broad-bandpass neutron choppers have been used to reduce the delayed-neutron background on the IPNS powder diffractometers SEPD and GPPD for the past two years.[3] They have been very successful in reducing this background in the long-wavelength regions of the TOF spectrum, where the scattering signal is usually the weakest and hence background is most troublesome. A similar chopper should likewise be effective in reducing the delayed-neutron background in small-angle diffractometers at pulsed neutron sources.

A simulation program has been written to assess the use of a chopper similar to those used for delayed-neutron removal at SEPD and GPPD to eliminate alternate source pulses, and to study the quality of the small-angle scattering data which results under these conditions. This simulation allows the treatment of delayed neutrons, so the ability of such a chopper to reduce the delayed-neutron background can also be assessed. The simulation program and the results obtained are discussed below. A semi-quantitative comparison between this use of a frame-elimination chopper to access larger values of λ to reach small Q and the alternative of using tighter collimation to allow measurements to smaller values of ϕ to reach the same small Q is also included so that the relative data rates available under the two different approaches might be estimated.

Although the simulation results reported here are specific to the geometries of the IPNS small-angle diffractometers and to the 30 Hz IPNS source repetition rate, the resulting conclusions should be qualitatively applicable to any other pulsed-source small-angle diffractometer where the source pulsing frequency is higher than optimum. Calculations of this type could be readily adapted to other instrument geometries and source frequencies if quantitative information is desired in those cases.

II. THE SIMULATION

The program FECHOPS is a Monte Carlo simulation of a small-angle scattering instrument which was designed to provide a detailed understanding of the effects which would occur if a drum chopper, similar to those used for delayed neutron removal on the powder diffractometers SEPD and GPPD at IPNS, were used to remove the delayed neutrons or to "eliminate" alternate prompt pulses to permit the utilization of long-wavelength neutrons. FECHOPS was modeled after the earlier program DNCHOP[4] which was developed to analyze the use of delayed-neutron choppers on SEPD and GPPD. The geometry for this simulation is shown in Fig. 1, and Appendix 1 develops the equations governing such a drum chopper.

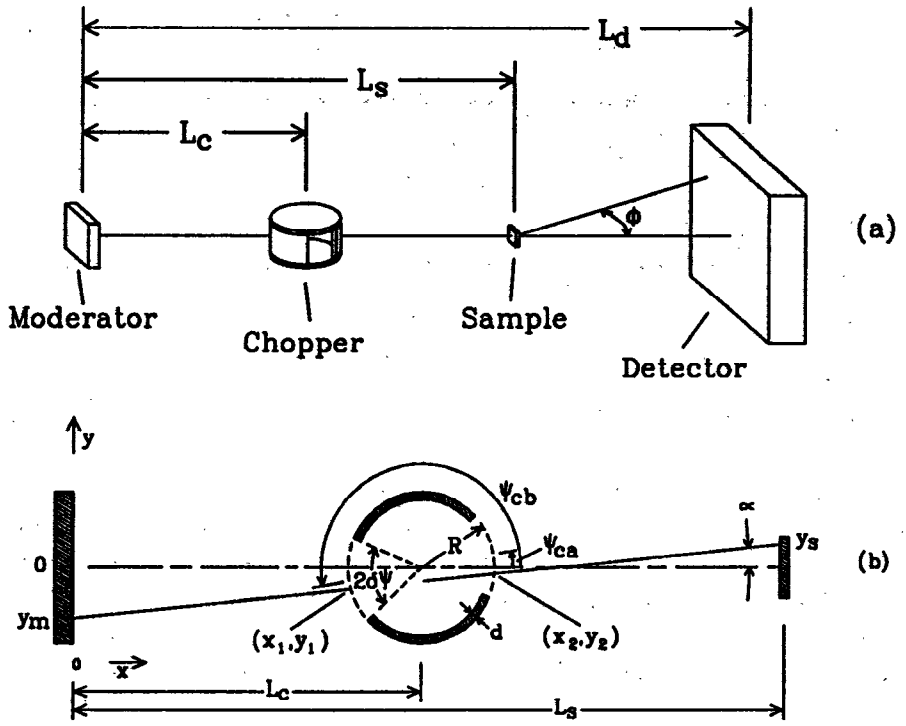

Figure 1. a) Schematic layout of moderator, chopper, sample, and detector used for this simulation. b) Details of chopper geometry.

Neutron Trajectories

The simulation considered neutrons arriving at the detector over two "frames" of the 30 Hz source, or 66667 μs, with the frame-1 prompt pulse occurring at the beginning of this period. FECHOPS generated a set of neutron trajectories from moderator to detector. Each trajectory was analyzed according to whether it was intercepted and/or absorbed by the chopper and according to whether it represented a neutron which would be detected by a real detector. It was also analyzed according to whether it originated from the prompt pulse of frame-1, the prompt pulse of frame-2, or as a delayed neutron. (Delayed neutrons were assumed to be uniformly distributed in time, and to have the same energy spectrum as the prompt neutrons.) Each trajectory was along a line in the x,y plane from a random point on the moderator through a random point on the sample (see Fig. 1), so that the full ranges of relevant angles and positions at the chopper were sampled. For most of the simulations the chopper was operated to pass a broad band of the neutrons originating in the frame-1 prompt pulse, while eliminating most neutrons originating in the frame-2 prompt pulse which occurred 33333 μs after the frame-1 pulse. Figure 2 shows a distance *vs* time diagram for the chopper and pulsed source operating under these conditions. Figure 3 shows the operation of the chopper at twice this frequency in a purely delayed-neutron-removal mode where it is set to pass a broad band of wavelengths from each prompt pulse of the source. Both drawings also show sources of "frame-overlap" neutrons, which are those arriving at a given time but originating from a different pulse and having a different wavelength than intended. For clarity the figures show these

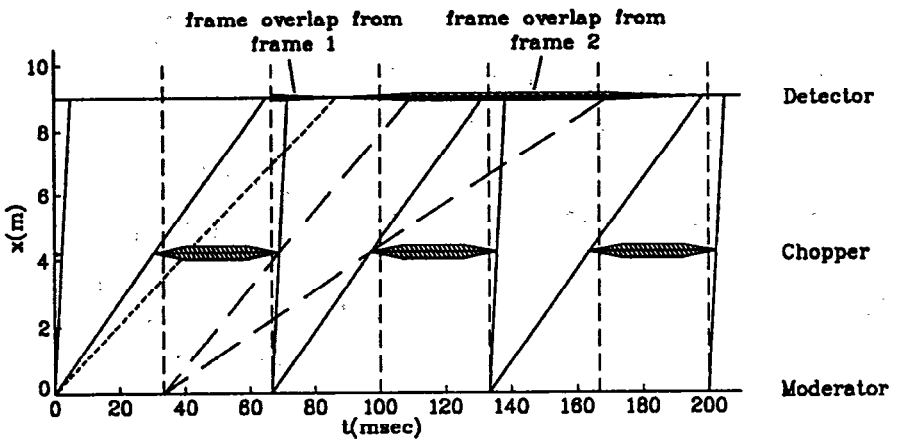

Figure 2. Time-distance diagram for a 20 cm dia drum chopper at 4.2 m from the source when the chopper is operating at 7.5 Hz and the source at 30 Hz. The broad hatched band at x=4.2 m indicates times when the chopper is fully-closed, and the regions where this band tapers to a point indicate times when the chopper is opening or closing, with the width of the band indicating the fraction of the beam blocked by the chopper. The chopper phasing and open-angle have been chosen to provide no interference for prompt frame-1 neutrons arriving at the detector between 5000 and 65000 μs when the chopper is operated at this frequency.

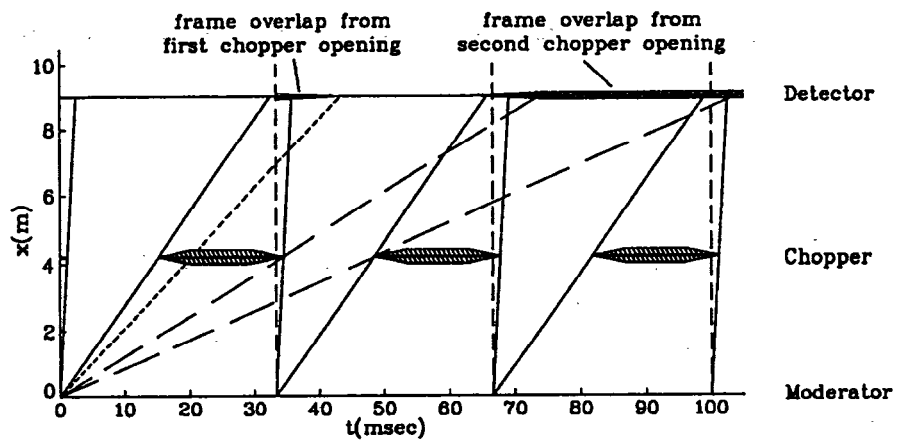

Figure 3. Time-distance diagram for the chopper of Fig. 2 operating at 15 Hz when the source operates at 30 Hz. Chopper open-angle is the same as for Fig. 3, but the chopper phasing has been changed to provide no interference for prompt neutrons arriving at the detector between 2500 and 32500 μs when the chopper is operated at this frequency.

frame-overlap neutrons as originating from only one or two of the prompt pulses, and arriving at the detector at times greater than 66667 μs or 33333 μs for Figs. 2 and 3 respectively. However, it should be remembered that the actual patterns repeat with periods of 66667 μs or 33333 μs (Figs. 2 or 3 respectively) so these "frame-overlap" regions can all be considered to collapse back onto the first 66667 μs for Fig. 2 or the first 33333 μs for Fig. 3.

Neutron trajectories could be selected from an energy distribution in one of two different modes. In the first mode, each neutron was given a random energy E according to the probability distribution

$$I(E) = AEe^{-E/E_0} + B/E[1 + (E/5E_0)^7] \qquad E < E_{max}$$
$$I(E) = 0 \qquad E > E_{max} \tag{2}$$

which is a Maxwellian joined to a 1/E epithermal spectrum with a Westcott joining function, and terminated at some maximum energy E_{max}. Each neutron was then randomly assigned to be "delayed" or "prompt" with relative probability given by the delayed-neutron fraction selected for that particular simulation. Prompt neutrons were randomly chosen to originate in frame-1 or frame-2 (with equal probabilities for 30 Hz source operation, or probability of 1 for frame-1 and 0 for frame-2 for 15 Hz source operation), and left the moderator at t=0 for frame-1 or at t=33333 μs for frame-2. Delayed neutrons left the moderator at a random time between t=0 and t=66667 μs. Each trajectory was inspected to see whether or not it was intercepted by the chopper. If intercepted, the neutrons were randomly "absorbed" or "transmitted" according to the absorption probability for the specified thickness of the absorbing material based on its linear absorption for neutrons of this energy. Each trajectory was also randomly detected or not detected by the detector, according to the assumed detector efficiency at this energy. Because of the form of the spectrum of Eq. (2), this mode resulted in the generation of a large number of trajectories for neutrons of high energies, but very few trajectories in the low-energy tail of the Maxwellian.

In the second mode, the neutron trajectories were chosen randomly from a uniform distribution of wavelengths extending over the range of 0-84 Å, which is three times the nominal range of the instrument. This wide range was chosen to reflect accurately the effects of frame-overlap neutrons on the simulated scattering spectra. Each trajectory was then weighted according to the probability of the occurrence of this wavelength in the original spectrum (Eq. 2) and assigned as above to frame-1, frame-2, or delayed. In this mode also, each trajectory was inspected to see whether or not it was intercepted by the chopper. If intercepted, the trajectory was weighted by the transmission probability for the specified thickness of the absorbing material based on its linear absorption for neutrons of this energy. Each trajectory was also weighted according to the detection probability for neutrons of this energy. This mode of trajectory generation, although requiring more computation time per trajectory than did the first mode, was much more efficient in sampling the long-wavelength behavior of the system. Thus this mode was used almost exclusively for the study reported here.

In either mode, each trajectory was binned according to the arrival time of the neutron at the detector. Arrival times greater than t=66667 μs were "wrapped-around" (had a multiple of 66667 μs subtracted from them to leave an arrival time between 0 and 66667) to provide a realistic treatment of frame-overlap. Each trajectory was actually accumulated into several different histograms, representing various combinations of the probabilities of transmission through the chopper and of detection.

Scattering by the Sample

The various spectra generated from the neutron trajectories as discussed above correspond to what would be called the incident beam "spectrum" in a small-angle diffraction measurement under the corresponding types of measurement conditions. In addition to these, a second set of spectra were accumulated in which the trajectories were weighted according to the probability of scattering from a sample and were binned according to arrival time (as above) and scattering angle. Scattering was assumed to be isotropic, and equal-width angular bins were chosen ranging between a specified minimum and maximum scattering angle. For each trajectory, the Q for scattering to the center of each angular bin was calculated, and the weight assigned to this bin was the scattering probability for each such Q multiplied by the solid angle of this bin ($2\pi\phi\Delta\phi$). Thus each trajectory contributed to scattering at every angle, but with a different probability for each angle. Use of such a fixed set of scattering angles rather than randomly selected scattering angles was dictated by the desire to generate a good statistical sampling of angles in a reasonable amount of computing time. This may have introduced some distortion into the data, but the results shown below indicate that any such distortion is small. The scattering probability assumed for all calculations reported here was that appropriate to the "Bates poly" sample used as a standard on SAD, namely

$$I(Q) = 0.0247\, Q^{-2}. \qquad (3)$$

Sample transmission was assumed equal to unity in generating these scattering spectra. All such scattering spectra were also weighted according to the probability of detection of each neutron, and two separate spectra were collected, one weighted according to the probability of transmission through the chopper and one corresponding to the no-chopper case.

The program REDUCE used for reduction of data from the SAD instrument was modified to give the program FEREDUCE to provide similar reduction of the scattering and spectral data output by FECHOPS. This program allowed a choice of which time-slices and angular bins were to be included in the data reduction, and then produced a "measured" I(Q) vs Q output file resulting from only this subset of the "raw" scattering data generated by FECHOPS.

III. SIMULATION RESULTS

The simulation program was run with a variety of parameters to investigate how such choppers might perform on the IPNS small-angle diffractometers. Parameters chosen were roughly those which would be appropriate to SAD or to the new small-angle diffractometer, and are summarized in Table I. For all calculations described here, the chopper was located in the beam gate cavity at 4.2 m from the moderator, and the detector was assumed to be 9.0 m from the moderator.

TABLE I - Parameters for the Simulations in Figures 4-9

Parameters varied	Figs. 4-5	Figs. 6-7	Figs. 8-9
Source frequency (Hz)	30	30	30
Chopper rotation freq (Hz)	7.5	7.5	15
Fully-open times at det (μs)			
t_{min}	5000	5000	2500
t_{max}	65000	65000	32500
Open-angle $2\delta\psi$ (rad)	1.7754	1.7754	1.7754
Delayed-neutron fraction	0.0	0.028	0.028

Parameters held fixed in all simulations

Moderator-chopper dist L_c (m)	4.2	Sample width (cm)	1.0
Moderator-sample dist L_s (m)	7.5	Minimum scattering angle (rad)	0.0
Moderator-detector dist L_d (m)	9.0	Maximum scattering angle (rad)	0.1
Moderator width (cm)	9.0	Number of scattering angle bins	50
Chopper radius R (cm)	10.0	Moderator spectral energy E_0 (meV)	3.0
Absorber material	B_4C	Thermal/epithermal ratio for moderator	3.0
Absorber thickness d (cm)	1.0	Maximum neutron energy (meV)	10^9
Detector thickness (cm)	2.5	Number of arrival time bins	200
^{3}He fill pressure (atm)	1.5	Number of trajectories	3×10^6

Frame-Elimination - Chopper at 7.5 Hz

Figure 4 shows the scattering detected from "Bates poly", calculated with the source running at 30 Hz and with no delayed neutrons, and Fig. 5 shows the "measured" incident beam spectrum (transmitted by chopper and detected) calculated under these conditions. The chopper was run at 7.5 Hz (15 Hz opening frequency) for these calculations. The chopper opening and phasing were chosen as in Fig. 2, so that frame-1 neutrons arriving at the detector between 5000 and 65000 μs had no chopper interference (the chopper was fully open, meaning that no portion of the chopper absorbing material was in the beam, when these neutrons passed the chopper position). Also shown for comparison in Fig. 4 is the "Bates poly" scattering function which was assumed in generating the simulated scattering data. In order to show more clearly the "instrumentally" introduced errors in the simulated scattering data, a plot of relative differences between the simulated results and the original "Bates poly" data is also included.

The most obvious deviation in Fig. 4 between the "measured" scattering function resulting from reducing the simulated scattering data and the original assumed scattering function ("Bates poly") is the "dip" in I(Q) between Q ~ 0.025 $Å^{-1}$ and Q ~ 0.04 $Å^{-1}$, which results from the relatively high-energy frame-2 prompt neutrons which were not rejected by the chopper. Figure 5 and the data printout from the simulation show clearly that only time-slices 101-112 (33331-37331 μs) were affected by such neutrons, and when these time-slices were eliminated from the analysis

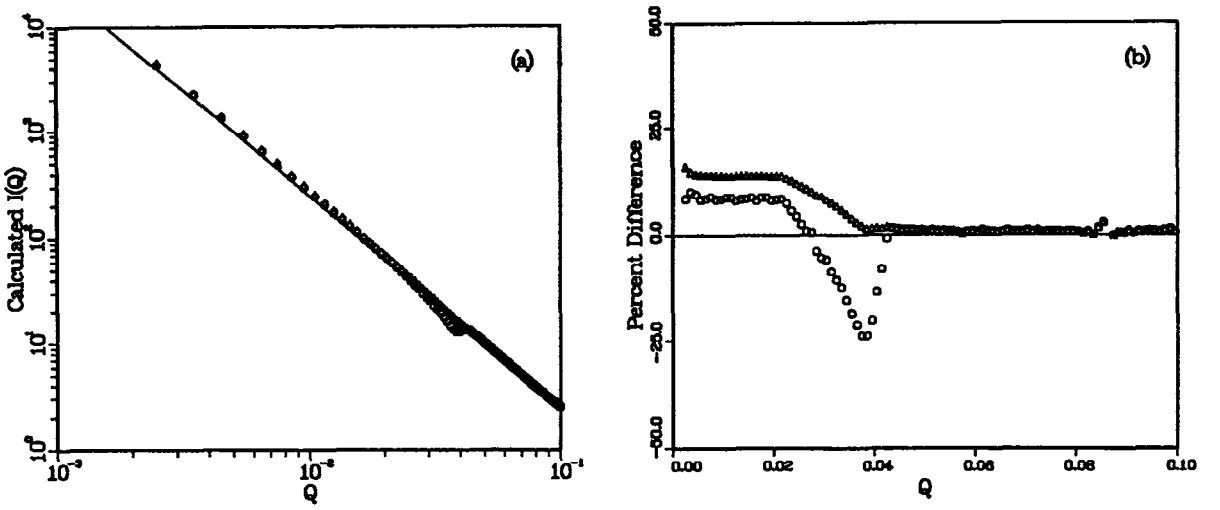

Figure 4. Reduction of simulated scattering data for Bates poly for 7.5 Hz chopper and 30 Hz source with no delayed neutrons. Chopper phasing and open-angle are as in Fig. 2. Other parameters of the simulation are given in Table I. (a) Full I(Q) calculated from the simulated data; (b) percent difference of the simulated I(Q) from the original scattering function. Angular bins between 0.004 and 0.1 rad and all time channels between 0 and 66667 μs were included in the analysis producing the circles, while time-channels between 33331 and 37331 μs were excluded from the analysis producing the triangles.

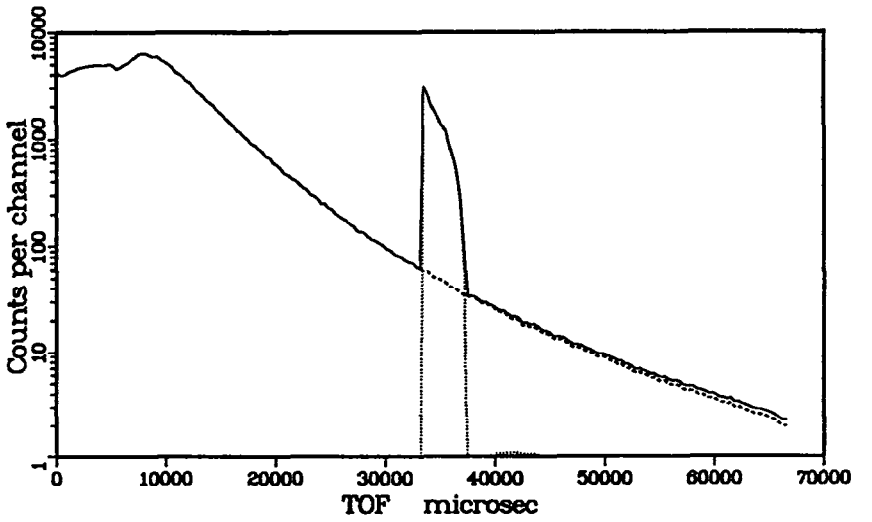

Figure 5. "Measured" spectra transmitted by the chopper and detected for the simulation of Fig. 4. The solid curve is the total spectrum, the dashed curve is the contribution from frame-1, and the dotted curve is the contribution from frame-2.

this deviation was gone from the resulting I(Q) vs Q curves (triangles in Fig. 4). However a more subtle deviation of the "measured" I(Q) from the assumed function still persisted over most of the small-Q portion of the data. This deviation was due to frame-overlap effects from frame-2 long-wavelength neutrons being transmitted through the chopper opening, as can be seen clearly in Fig. 2. Inspection of Fig. 2 suggested that this effect could be mostly eliminated if the chopper opening were designed to pass only the long-wavelength neutrons from frame-1 (say those arriving at the detector between 35000 and 65000 μs), and simulations under these conditions showed that this

was indeed the case, with quite good agreement between the resulting reduced data and the assumed scattering function. However, such a choice for chopper parameters means that several different chopper phasings would be required to cover the entire Q range, thus considerably reducing the effective data rate of the instrument. Alternatively, a suitable set of mirrors in the incident beam might be used to reflect out all wavelengths longer than ~28 Å and hence also eliminate such frame-overlap effects. Since such mirrors should provide only a small perturbation for wavelengths below 28 Å and would permit the full 28 Å range to be sampled with a single chopper setting, this would be the preferable alternative.

Figures 6-7 show data equivalent to that of Figs. 4-5, but this time with delayed neutrons included in the simulation. A delayed-neutron fraction of 0.028, appropriate to present IPNS operation as measured recently on SAD,[5] was assumed. Inspection of Fig. 7 shows that the chopper effectively eliminated those delayed neutrons which would have arrived at the longer times (above ~50000 μs) but did little to those which arrived at shorter times. This is evident in Fig. 6, where even after exclusion of the time-slices containing frame-2 prompt neutrons there is a large discrepancy between the measured and assumed scattering functions at intermediate Q values, while this discrepancy mostly disappears at low Q values. As shown in Fig. 6, these delayed-neutron effects can be largely eliminated by excluding time-slices 71-150 (roughly those where the delayed-neutrons contributed more than 10% of the incident spectrum) from the data reduction. Even with this large range of wavelengths (~10-21 Å) excluded, there is still sufficient redundancy in the data set to provide reduced data which completely cover the entire Q-range, although with somewhat poorer statistics. The resulting low-Q data are then in reasonable agreement with those of Fig. 4, indicating that most of the remaining low-Q discrepancies are due to frame-overlap effects. There are still some remaining delayed-neutron effects at intermediate Q values in the

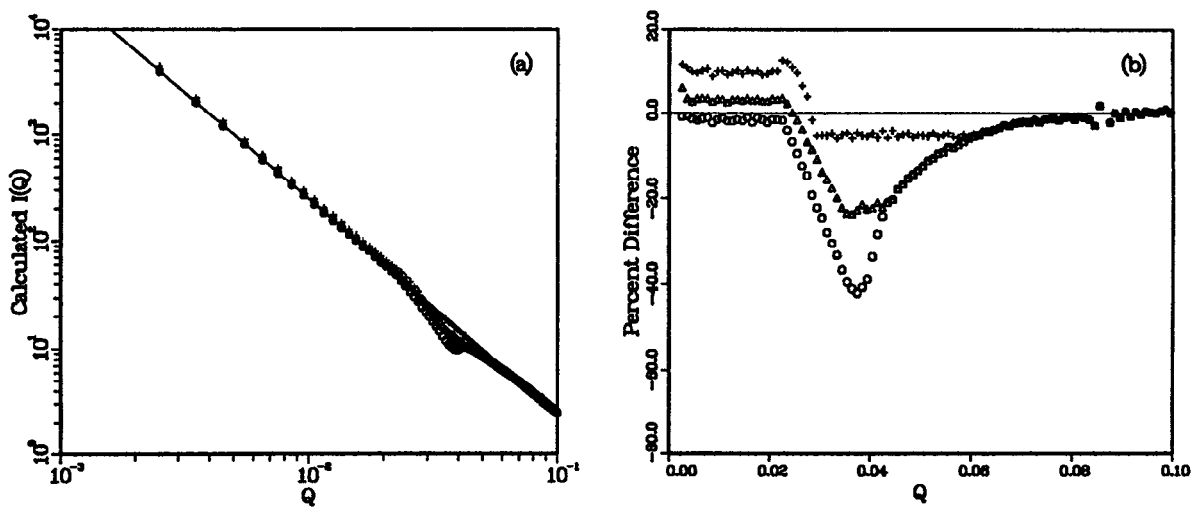

Figure 6. Reduction of simulated scattering data for Bates poly for 7.5 Hz chopper and 30 Hz source with a delayed-neutron fraction of 0.028. Chopper phasing and open-angle are as in Fig. 2. Other parameters of the simulation are given in Table I. (a) Full I(Q) calculated from the simulated data; (b) percent difference of the simulated I(Q) from the original scattering function. Angular bins between 0.004 and 0.1 rad and all time-channels between 0 and 66667 μs were included in the analysis producing the circles, while time-channels between 33331 and 37331 μs were excluded from the analysis producing the triangles and time-channels between 23331 and 50000 μs were excluded from the analysis producing the pluses.

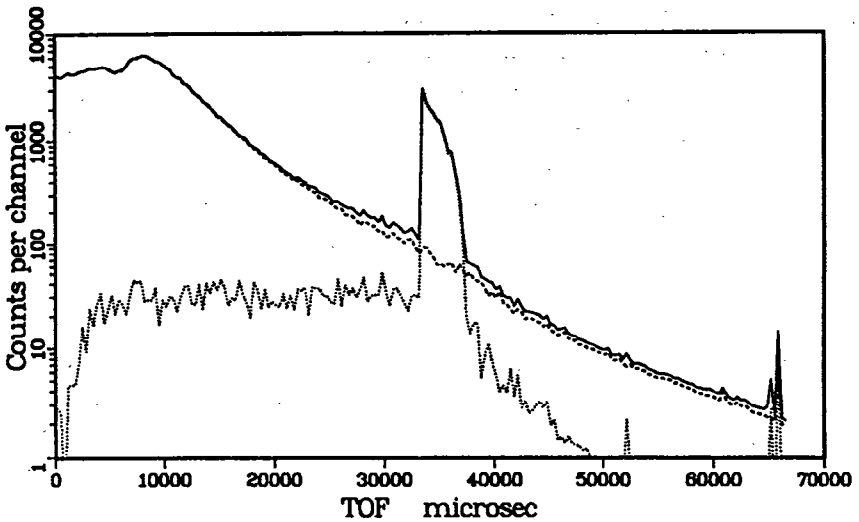

Figure 7. "Measured" spectra transmitted by the chopper and detected for the simulation of Fig. 6. The solid curve is the total spectrum, the dashed curve is the contribution from frame-1, and the dotted curve is the contribution from frame-2.

reduced data, but these result in less than 10% errors (consistent with the choice of time-slices for exclusion) which can be readily handled with analytical correction techniques.[5,6]

Delayed-Neutron-Elimination - Chopper at 15 Hz

Instead of operating the chopper at 7.5 Hz to eliminate alternate prompt pulses, the same chopper can be operated at 15 Hz while utilizing every pulse of the 30 Hz source. In this case the maximum wavelength is restricted to ~14 Å. Figure 3 shows the distance-time diagram which results when the chopper of Fig. 2 is operated at 15 Hz (thus opening and closing at 30 Hz) and phased to provide clear transmission for neutrons arriving at the detector between 2500 and 32500 μs. Figures 8-9 show simulated results with this chopper system when the delayed-neutron fraction was set to 0.028. In Fig. 8, the data are in good agreement with the assumed function except at the lowest Q values where the data lie somewhat above the assumed function. Inspection of Fig. 3 indicates that this is most likely due to frame-overlap. Additional simulations with no delayed neutrons showed data essentially identical to those of Fig. 8, confirming that the chopper had eliminated all significant delayed-neutron effects from the reduced data. This is supported by Fig. 9, which shows that the chopper had indeed eliminated essentially all the delayed neutrons in the incident spectrum which would have arrived at the longer times where the scattering signal and the prompt incident spectrum were small. The chopper passed the delayed neutrons at shorter times, but there the scattering signal and the spectrum were sufficiently large that the delayed neutrons had relatively little effect on the resulting reduced scattering data.

By changing the phase of this same chopper while still operating at 15 Hz, it can be used in a "band-selecting" mode where it is set to pass neutrons arriving at the detector between 35000 and 65000 μs after each pulse, thus covering the long-wavelength part of the range considered in Figs.

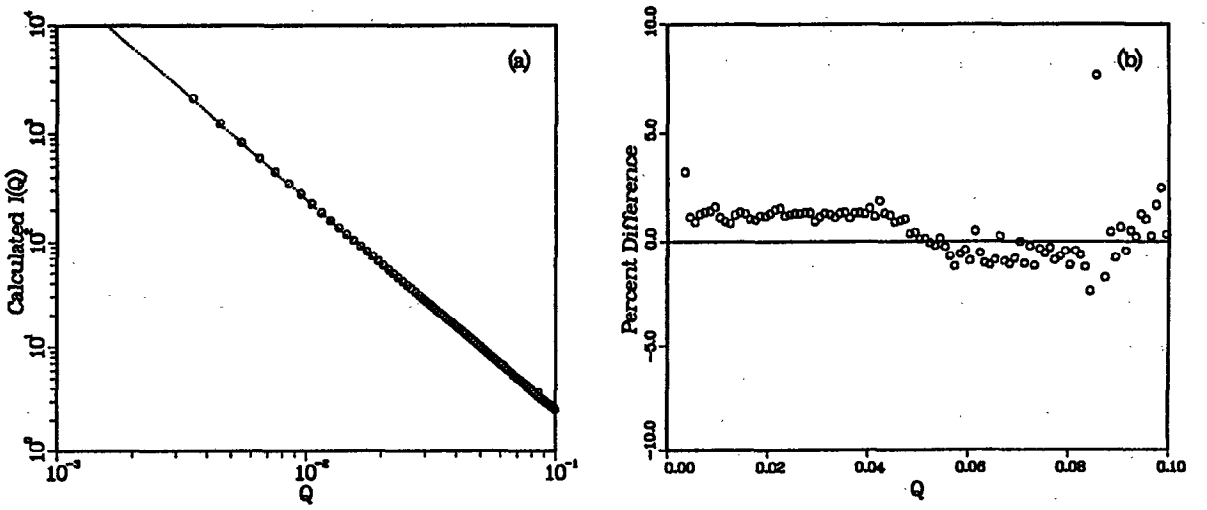

Figure 8. Reduction of simulated scattering data for Bates poly for 15 Hz chopper and 30 Hz source with a delayed-neutron fraction of 0.028. Chopper phasing and open-angle are as in Fig. 3. Other parameters of the simulation are given in Table I. (a) Full I(Q) calculated from the simulated data; (b) percent difference of the simulated I(Q) from the original scattering function. Angular bins between 0.004 and 0.1 rad and all time-channels between 0 and 33331 μs were included in the analysis.

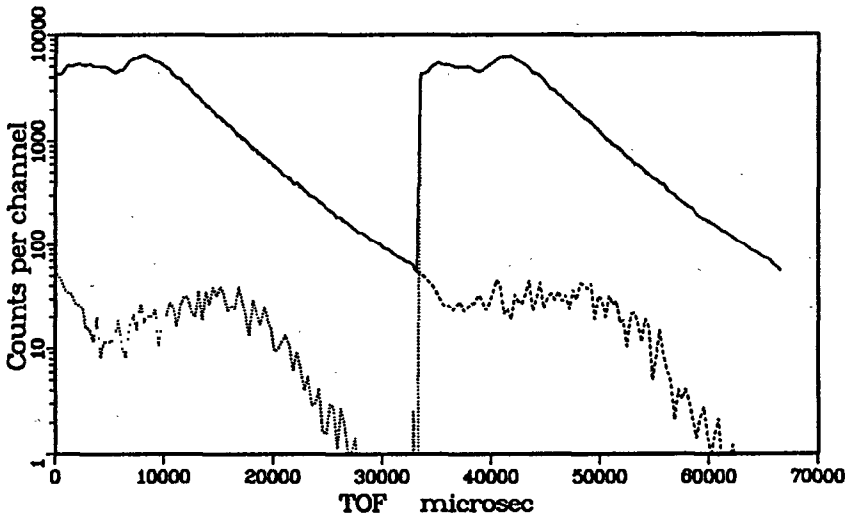

Figure 9. "Measured" spectra transmitted by the chopper and detected for the simulation of Fig. 8. The solid curve is the total spectrum, the dashed curve is the contribution from frame-1, and the dotted curve is the contribution from frame-2.

4-7 but using every pulse. However, inspection of Fig. 3 shows that this is likely to lead to problems. Any choice of chopper phasing other than that shown in Fig. 3 leaves the chopper open at the times these long-wavelength neutrons reach the detector, and thus allows faster delayed neutrons to reach the detector at these same times. Further simulations with such chopper phasing showed that, as expected, virtually all the long-wavelength portion of this spectrum was overwhelmed either by frame-2 prompt neutrons (shorter-wavelength portion of this band) or by delayed neutrons (longer-wavelength portion of the band). Thus it does not appear likely that

different choices of chopper phase (other than those near that shown in Fig. 3) will yield significant amounts of useful long-wavelength data.

Operation at Short Wavelengths - Chopper at 60 Hz

The time required for the chopper to go from fully open to fully closed is the time required for one edge of the chopper opening to sweep through half the beam width, since the exit side of the chopper will be sweeping through the other half of the beam at the same time. For a 20 cm diameter chopper operating at 15 Hz and chopping a 4.52 cm wide beam (this is the beam width at the 4.2 m chopper location in these simulations), this time required to go from fully open to fully closed or *vice versa* is 2419 μs. This translates to a 5183 μs range of times at the detector associated with neutrons which have passed through the partially open chopper (tapered portion of the shaded chopper band in Fig. 3). If this chopper is phased to begin opening at time t=0, then the first neutrons for which it is fully open are those arriving at the detector at t=5183 μs, which have λ=2.28 Å. In order to have the chopper be fully closed at t=0 and fully open for shorter-wavelength neutrons, it must be operated at a higher speed. This in turn will reduce the maximum wavelength which it will transmit.

Simulations were carried out for the case when the chopper was operating at 60 Hz (opening and closing at 120 Hz) and was phased to be fully open for neutrons detected at 1200 μs (starting to open at -96 μs). With this phasing the chopper was fully open for neutrons detected between 1200 and 8700 μs (0.53-3.82 Å) and after one-half revolution was again fully open for neutrons detected between 19057 and 26557 μs (8.38-11.67 Å). Analyzing only the data from time-frames corresponding to these two full-transmission regions lead to excellent agreement with the original scattering law, so it may be useful sometimes to operate the chopper at these higher frequencies when short-wavelength neutrons are desired. However, even with 60 Hz operation it does not appear feasible to utilize neutrons much below 0.5 Å without rephasing to let some of the initial fast burst through the chopper, and this may lead to background and detector-recovery problems. Also, with 60 Hz operation, roughly half of the potentially useful wavelengths are discarded by the chopper, so this mode is not very efficient.

IV. SEMI-QUANTITATIVE COMPARISON OF INTENSITIES

The intensity I measured in a solid angle $d\Omega$ and wavelength interval $d\lambda$ from a sample with cross-section $d\Sigma/d\Omega$ is

$$I = I_0 A_s t_s T_s \epsilon (d\Sigma/d\Omega)\, d\Omega d\lambda \tag{4}$$

where I_0 is the total intensity per unit wavelength on the sample of area A_s and thickness t_s, T_s is the sample transmission, and ϵ is the detection efficiency. If converging multiple-aperture collimators are used and the distances from source-to-sample and sample-to-detector are kept fixed, then the intensity on the sample will vary at least as fast as $\Delta\alpha^2$, where $\Delta\alpha$ is the incident beam divergence permitted by a single channel of the collimators, assuming the collimators are ideal

(zero blade thickness).[7] If a chopper is used to remove n-1 pulses out of every n pulses, then the incident beam intensity at a given wavelength will be proportional to 1/n. With these assumptions, and considering only the long-wavelength λ^{-5} portion of the incident beam spectrum

$$I_o \propto n^{-1} \lambda^{-5} \Delta\alpha^2 . \tag{5}$$

The size of the penumbra of the direct beam at the detector determines the minimum useful scattering angle $2\theta_{min}$, and this penumbra size is nearly linearly related to $\Delta\alpha$, so to a reasonable approximation

$$\Delta\alpha \propto \theta_{min} . \tag{6}$$

When the instrument is configured for a specific Q_{min}, and Q is measured for a specific combination of θ, λ, $\Delta\theta$ and $\Delta\lambda$, the measured intensity is thus

$$I(Q \geq Q_{min}) \propto (d\Sigma/d\Omega)\, n^{-1} \lambda^{-5} \theta_{min}^2 \, d\Omega d\lambda . \tag{7}$$

At some small $Q = Q_{min}$ we must have $\theta = \theta_{min}$ and $\lambda = \lambda_{max}$, since

$$Q_{min} \propto \theta_{min}/\lambda_{max} , \tag{8}$$

and to provide appropriate resolution

$$\Delta\theta \propto \theta_{min} \tag{9}$$

$$\Delta\lambda \propto \lambda_{max} . \tag{10}$$

Furthermore, for isotropic scattering

$$d\Omega \propto \theta \Delta\theta \propto \theta_{min}^2 . \tag{11}$$

Combining these results in the relationship

$$I(Q=Q_{min}) \propto (d\Sigma/d\Omega)\, n^{-1} Q_{min}^4 . \tag{12}$$

Thus with the approximations made here, the measured intensity at Q_{min} for a given Q_{min} depends only on n, and is highest (n=1) when Q_{min} is achieved by tightening the collimation rather than by eliminating pulses. However this dependence is only first order, and when the realities of practical converging multiple-aperture collimator construction (such as blade thicknesses on soller collimators) are taken into account it is likely that the two approaches would yield intensities of comparable magnitude at a Q_{min} of ~0.002 $Å^{-1}$, which is the goal for the new IPNS small-angle diffractometer.

V. DISCUSSION

These simulation results showed that a drum chopper of the type described in Fig. 1 and Table I operating at 7.5 Hz could be effective in the elimination of most of the prompt neutrons from the second frame, permitting collection of data with neutrons out to ~28 Å on the IPNS small-angle diffractometers. The same chopper operating at 15 Hz could eliminate most delayed-neutron effects from the data obtained with normal 30 Hz source operation which utilizes neutrons out to ~14 Å, thus resulting in much better signal-to-noise than is currently available on SAD for the long-wavelength data. However, when the chopper was operated at 7.5 Hz in the simulation both delayed-neutron and frame-overlap problems were evident in the data. The delayed neutron effects were mostly eliminated in this case by rejection of time-slices arriving at times between ~24000 and ~50000 μs. The frame-overlap effects could be mostly eliminated by use of a chopper with a narrower opening (which would then restrict the Q-range which could be covered with one setting), or possibly by other means such as critical reflection from suitably-arranged mirrors.

The geometries of SAD and and the new IPNS small-angle diffractometer are somewhat restrictive with regard to use of such a chopper. All the simulations reported here have been for a chopper at 4.2 m from the source, which corresponds to the gate cavity location for these instruments. The chopper diameter was therefore set at 20 cm, which is roughly what would fit in this cavity. Some simulations were also carried out with the chopper located just outside the biological shield (5.65 m from the source). As would be expected from Fig. 2, this mode of operation was much less satisfactory, with much more of the frame-2 prompt pulse being transmitted, and agreement between reduced data and the assumed scattering function was not achieved for the limited number of situations simulated with this chopper distance. (Agreement could probably be achieved if the chopper opening were made sufficiently narrow, but this would lead to other operational problems.)

Semi-quantitative arguments comparing the options of tightening collimation or using longer wavelengths to reach smaller Q values, indicate that tightening collimation appears to give a higher intensity near Q_{min}. Many details such as the minimum resolution achievable on the detector, the non-zero thickness of the collimator blades, *etc.*, have been ignored in obtaining this rough estimate. As the collimation is pushed to smaller values of $\Delta\alpha$, collimator blade thickness will start to become important, and detector resolution will become important when θ_{min} or the $\Delta\theta$ necessary at θ_{min} are reduced to values comparable to the detector resolution divided by the sample-detector distance. For the small-angle diffractometers at the 30 Hz IPNS source, both of these effects become important below Q_{min} ~0.003 $Å^{-1}$. Thus the approximate intensity relationship derived above should be considered to be merely a rough guide, but the conclusions should still be valid; namely that the use of a frame-eliminating chopper of the type considered appears to be feasible, at least in terms of intensities, and that the use of such a chopper probably would result in data rates comparable to those which would be obtained if tighter collimation alone were used to achieve the same small values of Q_{min}.

If a frame-elimination chopper were used, it would be relatively simple to stop it in the open position or to have it open at the 30 Hz rate (rotation at 15 Hz), thus setting n=1 and giving one particular value of Q_{min}. It would then be quite easy to change the chopper opening rate to 15 Hz

(rotation at 7.5 Hz) to give n=2 and a factor of 2 reduction in Q_{min} with the same collimators. Changing between Q_{min} values in this fashion should be much simpler than the elaborate automated collimator and beamstop insertion mechanisms which would be required to vary $\Delta\alpha$ to change Q_{min}.

In conclusion, the simulations have shown that a chopper of the type considered would make a significant improvement in the signal/background at the IPNS small-angle scattering instruments. It would also provide much greater flexibility and the option of using, when the need arises, longer-wavelength neutrons than would otherwise be possible. Thus the IPNS small-angle-scattering instruments will be equipped with such choppers as soon as is practical. Similar choppers would likely be beneficial on other pulsed-source small-angle-scatering instruments as well.

APPENDIX 1 - Drum Chopper Description

Chopper Phase and Opening Angle

The chopper is designed to be completely open for prompt neutrons arriving at the detector at times between t_{min} and t_{max}. If the total flight path to the detector is L_d, then the chopper must be completely open between t_{cmin} and t_{cmax} given by

$$t_{cmin} = (L_c/L_d)t_{min} \tag{A1}$$

$$t_{cmax} = (L_c/L_d)t_{max} \,. \tag{A2}$$

If the beam is designed to have a width W_m at the moderator and W_s at the sample, then its width W_c at the chopper is

$$W_c = [W_s L_c + W_m(L_s - L_c)]/L_s \,, \tag{A3}$$

where L_c and L_s are defined in Fig. 1. This width translates into an angular chopper opening of

$$\delta\psi_w = 2\sin^{-1}(W_c/2R) \tag{A4}$$

where R is the chopper radius (Fig. 1). Between the times t_{cmin} and t_{cmax} the chopper rotates through an angle

$$\delta\psi_r = \omega(t_{cmax} - t_{cmin}) \tag{A5}$$

where ω is the angular rotational frequency of the chopper. The total chopper opening angle (Fig. 1b) is then

$$2\delta\psi = \delta\psi_w + \delta\psi_r \,. \tag{A6}$$

The center of the chopper opening must be lined up with the beam axis at the time t_c given by

$$t_c = (t_{cmax} + t_{cmin})/2 \,. \tag{A7}$$

Interception of Neutrons

The neutron is emitted at time t_e from the position y_m on the moderator. It then travels with velocity v at an angle α to the beam centerline (Fig 1b). The chopper is a hollow cylindrical drum, which can be treated as a thin shell of radius R rotating with angular frequency ω if the thickness of the absorbing material is small compared to R. The chopper has openings on opposite sides, each of which subtends an angular range, at the chopper center, of $\pm\delta\psi$ about a line through the centers of these two openings. The chopper axis is located at $x=L_c$, $y=0$, and the chopper phase is such that the center of the chopper openings lines up with the beam centerline at time t_c.

The neutron trajectory makes two intersections with the chopper shell or its openings. These are at positions (x_1,y_1) and (x_2,y_2), shown in Fig. 1b. If α is assumed to be small, it can be shown that for i=1 or i=2

$$x_i = L_c - [B - (-1)^i D]/A \tag{A8}$$

$$y_i = y_m + \alpha x_i \,, \tag{A9}$$

where

$$A = 1 + \alpha^2 \tag{A10}$$

$$B = \alpha(y_m + \alpha L_c) \tag{A11}$$

$$D = \{\alpha^2(y_m + \alpha L_c)^2 - (1 + \alpha^2)[(y_m + \alpha L_c)^2 - R^2]\}^{1/2} \,. \tag{A12}$$

These two intersections occur at the times t_1 and t_2 given by

$$t_i = t_e + [x_i^2 + (y_i - y_m)^2]^{1/2}/v \,. \tag{A13}$$

The points (x_1,y_1) and (x_2,y_2) can be represented as the points (R,ψ_1) and (R,ψ_2) in a polar coordinate system centered on the chopper axis.

$$\psi_i = \tan^{-1}[y_i/(x_i - L_c)] + (i-2)\pi \,. \tag{A14}$$

In this same coordinate system at time t_i the two chopper openings are centered at (see Fig. 1b)

$$\psi_{cai} = \omega(t_i - t_c) - \pi \tag{A15}$$

$$\psi_{cbi} = \omega(t_i - t_c) \,. \tag{A16}$$

For a "black" chopper, the neutron will be transmitted at its ith intersection with the chopper periphery if it lines up with either opening, or hence if for some integer n

$$\psi_{cai} - \delta\psi \pm 2n\pi < \psi_i < \psi_{cai} + \delta\psi \pm 2n\pi \tag{A17}$$

or if

$$\psi_{cbi} - \delta\psi \pm 2n\pi < \psi_i < \psi_{cbi} + \delta\psi \pm 2n\pi . \tag{A18}$$

In order for the neutron to reach the sample, it must be transmitted for both i=1 and i=2.

If the chopper is not "black", there is some probability of transmission even if the neutron is intercepted by the chopper. This can be easily computed from the linear absorption coefficient of the absorbing material and its thickness, and on whether the trajectory of the neutron traverses this thickness once or twice.

References

1. J. M. Carpenter. Nucl. Instr. and Meth. 145, 91-113 (1977).
2. J. M. Carpenter. Nucl. Instr. and Meth. 175, 287-292 (1980).
3. B. S. Brown, J. M. Carpenter, R. K. Crawford, A. V. Rauchas, A. W. Schulke, and T. G. Worlton. Advanced Neutron Sources 1988, Proceedings of the 10th Meeting of the International Collaboration on Advanced Neutron Sources (ICANS X), held at the Los Alamos National Laboratory, Oct. 3-7, 1988. Institute of Physics Conference Series Number 97, IOP Publishing Ltd, New York. pp 27-45 (1989).
4. R. K. Crawford. Unpublished notes (1986).
5. J. E. Epperson, J. M. Carpenter, P. Thiyagarajan, and B. Heuser. Nucl. Instr. and Meth. A289, 30-34 (1990).
6. J. M. Carpenter, D. F. R. Mildner, J. W. Richardson, Jr., and W. Dimm. "Correcting Beam Monitor and Diffraction Data for Chopped Delayed Neutron Backgrounds", these proceedings.
7. R. K. Crawford and J. M. Carpenter. J. Appl. Cryst. 21, 589-601 (1988).

ICANS-XI International Collaboration on Advanced Neutron Sources
KEK, Tsukuba, October 22-26, 1990

OPTICAL NEUTRON POLARIZERS

John B. Hayter
Oak Ridge National Laboratory
FEDC/MS-8218
P.O. Box 2009
Oak Ridge, TN 37831-8218, U.S.A.

ABSTRACT
A neutron wave will be refracted by an appropriately varying potential. Optical neutron polarizers use spatially varying, *spin-dependent* potentials to refract neutrons of opposite spin states into different directions, so that an unpolarized beam will be split into two beams of complementary polarization by such a device. This paper will concentrate on two methods of producing spin-dependent potentials which are particularly well-suited to polarizing cold neutron beams, namely thin-film structures and field-gradient techniques. Thin-film optical devices, such as *supermirror* multilayer structures, are usually designed to deviate only one spin-state, so that they offer the possibility of making insertion (transmission) polarizers. Very good supermirrors may now be designed and fabricated, but it is not always straightforward to design mirror-based devices which are useful in real (divergent beam) applications, and some practical configurations will be discussed. Field-gradient devices, which are usually based on multipolar magnets, have tended to be too expensive for general use, but this may change with new developments in superconductivity. Dipolar and hexapolar configurations will be considered, with emphasis on the focussing characteristics of the latter.

I. INTRODUCTION

The momentum of a neutron will vary with changes in local potential, so that a neutron beam which passes through an inhomogeneous potential will experience refraction effects analogous to light waves. If the potential has a magnetic component, the interaction between the neutron and the field will depend on the orientation of the neutron moment, μ, relative to the field, and the refraction effects will thus be polarization dependent. This effect has been applied in a variety of techniques which produce spatial separation of the two spin states of the beam, allowing production of fully polarized beams [1]. In this article, I shall describe two basic classes of polarizing device which use such refractive effects to polarize (or analyze) neutron beams in the thermal to cold range; such devices are known as optical neutron polarizers. Attention here will be directed to the production of linear polarization; that is, beams with the neutron parallel (-) or anti-parallel (+) to the magnetic guide field direction.

The methods may be extended to produce circular (or precessing) polarization by using appropriate spin-turn devices, which are described in detail elsewhere [2]. A thorough review of neutron optics in general has been given by Klein and Werner [3].

II. THIN-FILM OPTICS

Total external (or mirror) reflection from a magnetic material has long been used to polarize neutrons. Bulk magnetic mirrors are difficult to saturate, however, and the associated magnetic circuits made such devices large and heavy. Use of easily saturated thin films of magnetic material, deposited on a substrate by sputtering or evaporation, removed this difficulty and allowed production of compact devices which could be considered routine spectrometer components. A neutron of wavelength λ which enters a material with number density N of scatterers with mean nuclear scattering amplitude b, and magnetic induction B, experiences a refractive index which is double-valued (corresponding to $2s+1$ states, $s=1/2$):

$$n_{\pm} = 1 - \lambda^2(Nb/2\pi \mp m_n(B\text{-}H)\mu/h^2) \tag{1}$$

where m_n is the neutron mass, H is the magnetic field strength, and h is Plank's constant; the signs correspond to the two possible polarization states of the neutron. The refractive index differs only slightly from unity (typically, $|n\text{-}1| \approx 10^{-5}$). An elementary application of Snell's law shows that there will be a wavelength-dependent critical angle for total reflection which is also spin-dependent:

$$(\theta_c/\lambda)_{\pm} = [Nb/\pi \mp 2m_n(B\text{-}H)\mu/h^2]^{1/2} \tag{2}$$

Inspection of eqn (2) shows that for a suitable choice of material, the critical angle will be null when $Nb = 2\pi m_n(B\text{-}H)\mu/h^2$, so that only one spin-state will be reflected. This is the basis for all thin-film optical polarizers. For commonly used materials, such as FeCo alloys, the critical angle is less than $1° \cdot nm^{-1}$. The essential features of the effect are shown in Fig. 1.

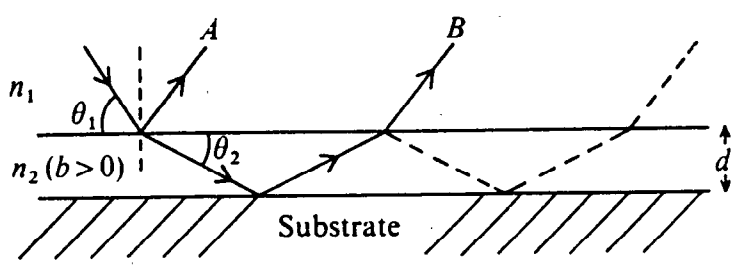

Figure 1. Reflection of neutrons from a plane parallel plate. The refractive indices in air and in the thin film are n_1 and n_2, respectively. All angles are greatly exaggerated for clarity.

The reality of the optical effects involved was shown clearly in early measurements of the reflectivity of thin-film polarizing mirrors. Constructive interference would be expected betweens the rays A and B of Fig. 1 whenever the path difference is a multiple of the wavelength. If the glancing angle θ_1 is held fixed, this leads to the expectation that interference fringes will be observed when

$$\lambda = 2(d/k)\,(\theta_1^2 - \theta_c^2)^{1/2} \qquad (k=1,2,\ldots) \tag{3}$$

and these fringes were indeed observed [4] (Fig. 2). The system of Fig. 1 is essentially a Lummer-Gehrke multiple-beam interferometer [5] which allows the refractive index profile of the surface to be measured, and it was recognized that this would be a valuable tool for surface studies [6]. A recent review shows that this type of measurement is now a growth industry [7].

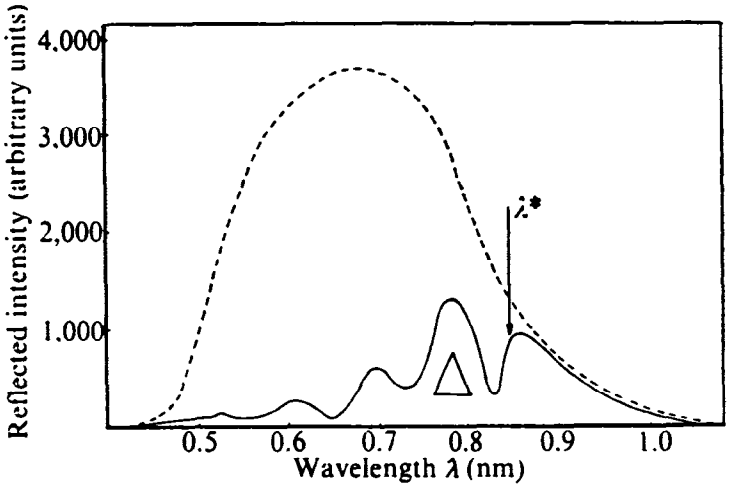

Figure 2. Neutron intensity as a function of wavelength reflected at a glancing angle θ=0.015 radian from a magnetized thin film (150 nm of FeCo on glass), showing interference fringes [4]. The wavelength spectrum of the incident beam is shown dashed (not to scale) for comparison. λ^* is the critical wavelength for this material and angle. Δ represents the wavelength resolution.

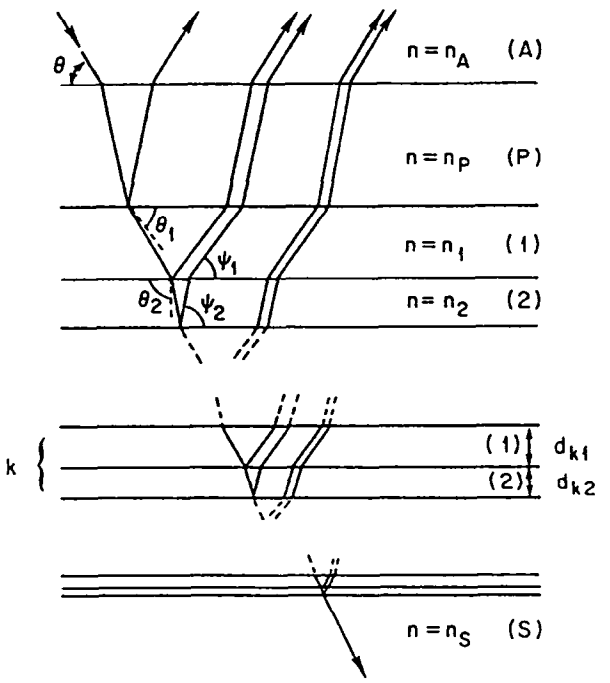

Figure 3. Geometry of a general multi-bilayer structure composed of $2N$ alternating thin films of generic materials 1 and 2, having respective refractive indices n_1 and n_2, and thicknesses d_{k1} and d_{k2} in the k'th bilayer (k=1,...,N). The structure is assumed to lie on a substrate S and to be protected from an atmosphere A by a protective coating P. All angles have been greatly exaggerated for clarity.

The small values of θ_c have been a source of great difficulty in making use of these effects in practical spectrometers, since beam divergences often exceed the angular range of mirror reflection. Two different approaches have been taken to overcome this problem, both based on fabricating mirrors with multilayered structures. The first approach is to construct a synthetic crystal, by depositing alternating layers of magnetic and non-magnetic materials, chosen such that the matching condition derived from eqn (2) now also applies between layers for one spin state. The structure will thus act as a diffracting crystal only for the unmatched spin state, and the diffracted beam will be polarized, as well as monochromatic [8]. The second approach [9,10] is a generalization of the multilayer monochromator structure to a graded series of multilayers, as shown in Fig. 3.

The basic physical idea behind the structure of Fig. 3, which is called a supermirror structure [9,10], is to superimpose a series of multilayer monochromator crystal structures, each of which has a slightly different d-spacing, so that the complete structure responds like a mirror, but to larger angles than would be achieved with a single layer. Apart from the obvious physical constraint that the spacing should change slowly over an extinction length, so that each "crystallite" can reflect fully, the optical problem of designing such a structure is ill-conditioned, and various designs have been proposed [9-13]; a review of the properties of such thin-film structures has been given by Majkrzak [14].

For simplicity, I shall only consider non-absorbing materials, in which case the angles ψ in Fig. 3 will coincide with the angles θ corresponding to Snell's law; in general, however, the angles θ will be complex, while the ψ are real [13]. In the absence of absorption, the angle ψ in a layer of material of type μ is related to the exterior glancing angle θ and the critical angle θ_c by

$$\psi_\mu = (\theta^2 - \theta_c^2)^{1/2} \tag{4}$$

Optimal reflectivity from any bilayer k will occur when the bilayer acts as a $\lambda/2$ plate, with each component sublayer having $\lambda/4$ optical thickness of material μ; the equivalent physical thickness is given by

$$d_\mu = \lambda_0 / 4\psi_\mu \tag{5}$$

Applying eqns (4) and (5) to each half of the bilayer gives the refraction-corrected expression of Bragg's law for the bilayer. It is important to note that, at low angles, Bragg peaks may shift by 20% from the positions computed without allowance for refraction, and the full expressions must be used when designing multilayer monochromator structures as well as supermirrors.

Significant improvement in the angular range of reflectivity of a mirror may be obtained by using a supermirror structure just a few bilayers thick. Figure 4(a) shows a 50% gain (FWHM) over a simple mirror, using 8 bilayers. For more ambitious mirrors, the number of layers increases rapidly, since, in the asymptotic limit of very thin layers, the thickness of the k'th layer varies as

$$d_{k\mu} \propto (\lambda_0/4\psi_\mu)\, k^{-1/4} \tag{6}$$

and many layers must be added for a small change in angular reflectivity. Most designs have been based on continuum arguments; the best optimized is probably that of Schelten and Mika [11], an example of which is given in Fig. 4(c). More recently, a discrete thin-film multilayer (DTFM) design has been proposed [13] which provides the same response with fewer layers, and overcomes the problems of sustaining reflectivity in the vicinity of the critical edge, as shown in Fig. 4(b). Recently, experimental neutron reflectivity

data on mirrors constructed to different designs have confirmed the superiority of the DTFM structure [15].

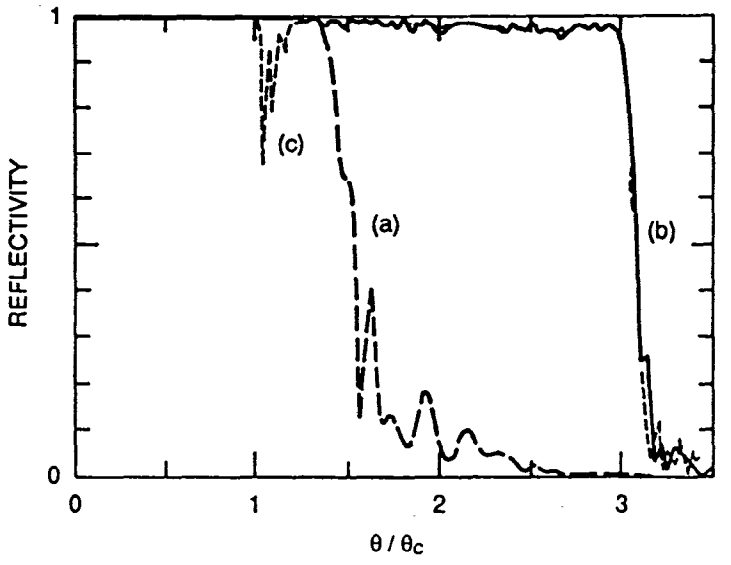

Figure 4. Calculated neutron reflectivities for different Ni-Mn multilayer mirrors, shown as a function of glancing angle θ scaled to the critical angle for total mirror reflection, θ_c. (*a*) DTFM design with 16 layers total; (*b*) DTFM with 350 layers total; (*c*) continuum design of Schelten and Mika with 404 layers total. (Note the dip near the critical angle in the latter design.)

III. PRACTICAL THIN-FILM DEVICES

Successful fabrication of a polarizing supermirror structure provides only a partial answer to the problem of producing an efficient polarizing insertion device using a supermirror stack. This is because the topology of a stack is not equivalent to that of a long, flat mirror, but rather to that of a *channel*, which has quite different characteristics. A channel can only be designed for perfect reflection of an exactly parallel beam; any divergence allows some rays in the beam to be doubly reflected (Fig. 5, ray *B*), while other rays may not be reflected at all. Simulation studies of the problem (Fig. 6) show that, in general, only about 40% efficiency can be achieved for realistic systems.

One approach is to curve the channels, so that the Soller-like structure acts as a set of parallel polarizing neutron guides. If the spacing between reflecting layers is a and the radius of curvature is R, the length which corresponds to avoiding direct line-of-sight is

$$L_d = (8aR)^{1/2} \tag{7}$$

corresponding to a characteristic angle

$$\gamma^* = (2a/R)^{1/2} = L_d / 2R \tag{8}$$

Such a guide structure only transports wavelengths longer than that at which $\gamma^*=\theta_c$, which restricts the utility of such polarizing Sollers. A further disadvantage is that the exit divergence is determined by θ_c, rather than the entry divergence, so that they cannot be used as insertion devices on a triple-axis spectrometer, for example, without an undesirable effect on the resolution. These devices nevertheless provided the first practical solution to

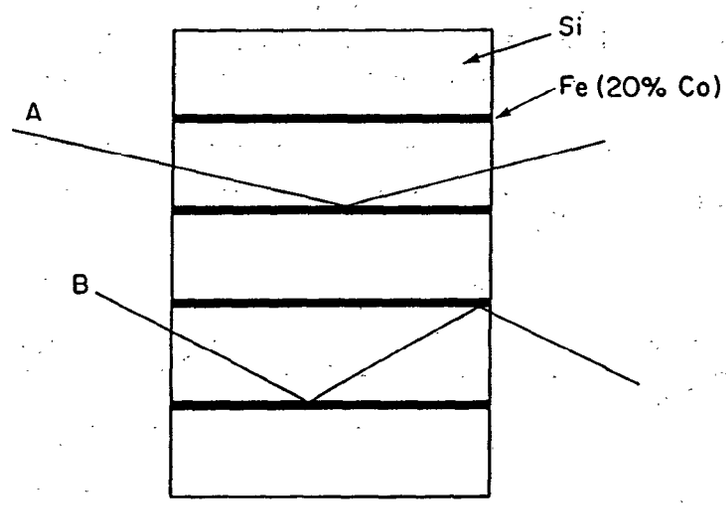

Figure 5. Schematic diagram of a mirror assembly using Si wafers. The beam enters nearly perpendicular to the Si substrate, so that glancing reflection at the air-Si interface is not possible. The mirror layers between wafers need not necessarily be the same. There is very little attenuation in the material, so that either the reflected or transmitted beams (which have opposite polarization) may be used.

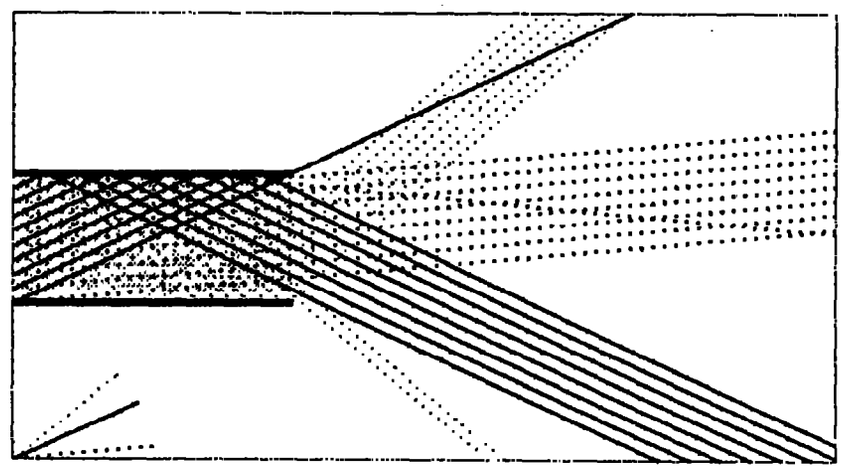

Figure 6. Transmission of a beam with 20' divergence through a supermirror stack, calculated by simulation with periodic boundary conditions at the top and bottom of the channel. The solid lines represent neutrons parallel to the mean beam direction; dotted lines are at the half-width limits of beam divergence; the relevant angles are shown at bottom left in the scaled units of the figure. If the incident angle is matched to θ_c, only about 40% of the beam is reflected correctly. Increasing the incident angle allows recovery of some of the divergent neutrons, but the mean beam direction then becomes doubly reflected; efficiency remains around 40%.

the problem of producing a compact, lightweight long-wavelength polarizer [16], and were used, for example, on the first full-scale spin-echo spectrometer [17]. Many other variations on stacked practical designs have been proposed [18-20]. There is considerable incentive to improve the response of a plane, polarizing mirror stack, since such devices have many desirable properties; when used in transmission, for example, they become true insertion devices which do adversely effect spectrometer resolution. One solution is to make use

of the bandpass filter capabilities of the DTFM design [13] to place mirrors of different bandwidth strategically through a stack structure, rather than duplicating the same mirror throughout. Such structures show greatly improved handling of divergent beams (Fig. 7).

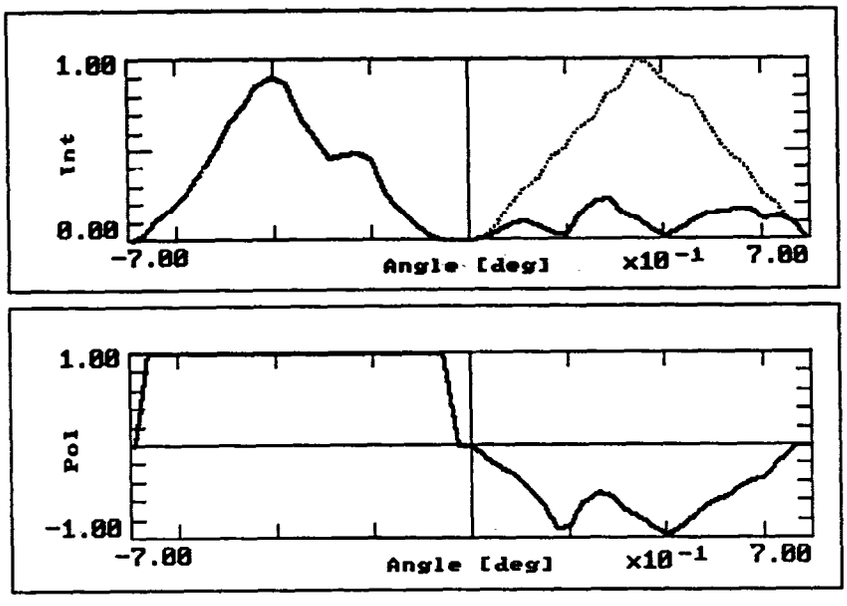

Figure 7. Intensity and polarization in a beam after transmission through a supermirror stack made of alternating mirror types with bandpass reflection characteristics. The incident beam (dashed line) is mostly reflected (solid line) into a cleanly separated beam with about 79% efficiency and complete polarization. Results were computed by recursive simulation using $2x10^4$ neutrons.

IV. FIELD-GRADIENT OPTICS

Multipolar magnetic fields provide a different means of providing a suitable optical potential gradient to separate the spin states in a beam. If the induction **B** has a gradient in the r-direction, the neutron will experience a force

$$F_r = -\partial(\mu \cdot \mathbf{B})/\partial r \tag{9}$$

This is the well-known Stern-Gerlach effect, and it provides a useful method of measuring the absolute polarization of a linearly polarized beam, by physically separating the two polarization states into two detectors of calibrated efficiency. It is not a generally useful way of polarizing a spectrometer beam, however, since the separated beams have asymmetric divergence characteristics. The latter problem may be overcome by using a hexapolar magnet geometry [21]. For a cylindrical hexapole magnet with current distribution

$$J = J_0 \cos 3\varphi \tag{10}$$

where φ is the azimuthal angle, the radial and angular field components are

$$\begin{aligned} B_r &= -B_0 (r/R)^2 \sin 3\varphi \\ B_\varphi &= -B_0 (r/R)^2 \cos 3\varphi \end{aligned} \tag{11}$$

where B_0 is the field at R, the inner radius of the conductor. The absolute value of the field is then independent of φ, depending only on the radius r from the central axis:

$$|B| = B_0 (r/R)^2 \tag{12}$$

The force on a neutron in such a field is therefore proportional to r and is directed radially inwards or outwards, depending on the neutron spin direction in the field:

$$F = \pm 2\mu B_0 \, r/R^2 \tag{13}$$

This radial force leads to equations of motion of the neutron having the form

$$\begin{aligned} \partial^2 x_i \,/\, \partial t^2 &= \pm \omega^2 x_i \\ \omega^2 &= 2\mu B_0 / m_n R^2 \end{aligned} \tag{14}$$

where $r^2 = x_1^2 + x_2^2$, and the time variable is $t = z/v$, where z is the axial direction and v is the neutron velocity. Solutions to eqns (14) are of the form cos ωt for (-) neutrons, and cosh ωt for (+) neutrons. The latter thus diverge away from the axis, while the former oscillate about it on a path which has the interesting property that all neutrons entering parallel to the axis focus to an axial point after exit from the hexapole, at a focal length given by

$$f = |L \cot(\omega L/v)/(\omega L/v)| \tag{15}$$

independent of their radial position at entry. The calculation for a divergent beam, which is best undertaken by simulation, gives essentially the same result for typical divergences: it is possible to focus one spin state in the beam onto a focal plane with 100% polarization. (A truly axial neutron of either spin state experiences no force, so that a small beam stop needs to be placed on the axis.)

To date, hexapoles have not seen widespread use as polarizers, because the magnets required for beams typically encountered (say, 30 mm diameter) require specifications close to the limits of commercial superconducting technology. However, with recent developments likely to bring down the cost of operating superconducting magnets, they may see a renewed role in the future.

Oak Ridge National Laboratory is operated by Martin Marietta Energy Systems, Inc., under Contract No. DE-AC05-84OR21400 with the United States Department of Energy.

REFERENCES

1. J. B. Hayter, in *Neutron Diffraction*, ed. H. Dachs (Springer-Verlag, Berlin, 1978) p. 41.
2. J. B. Hayter, *Z. Physik*, **B31**, 117 (1978).
3. A. G. Klein and S. A. Werner, *Rep. Prog. Phys.*, **46**, 259 (1983).
4. J. B. Hayter, J. Penfold and W. G. Williams, *Nature*, **262**, 569 (1976).
5. M. Born and E. Wolf, in *Principles of Optics*, chap. VII (Pergamon Press, Oxford, 1970).
6. J. B. Hayter, R. R. Highfield, B. J. Pullman, R. K. Thomas, A. I. McMullen and J. Penfold, *J. Chem. Soc., Faraday Trans. I*, 77, 1437 (1981).
7. J. Penfold and R. K. Thomas, *J. Phys: Cond. Matter* (in press).

8. A. M. Saxena and B. P. Schoenborn, *Acta Cryst.*, **A33**, 805 (1977).
9. F. Mezei and P. A. Dagleish, *Commun. Phys.*, **2**, 41 (1977).
10. A. G. Gukasov, V. A. Ruban and M. N. Bedrizova, *Sov. Tech. Phys. Lett.*, **3**, 52 (1977).
11. J. Schelten and K. Mika, *Nucl. Instrum. Methods*, **160**, 287 (1979).
12. O. Schaerpf, *A.I.P. Conf. Proc.*, **89**, 182 (1982).
13. J. B. Hayter and H. A. Mook, *J. Appl. Cryst.*, **22**, 35 (1989).
14. C. F. Majkrzak, *Physica*, **136B**, 69 (1986).
15. C. F. Majkrzak, D. A. Neumann, J. R. D. Copley and D. F. R. Mildner, *NIST Reactor: Summary of Activities, July 1989 through June 1990* (in press).
16. J. B. Hayter, J. Penfold and W. G. Williams, *J. Phys. E: Sci. Instr.*, **11**, 454 (1978).
17. P. A. Dagleish, J. B. Hayter and F. Mezei, in *Neutron Spin Echo*, ed. F. Mezei (Springer-Verlag, Heidelberg, 1980) p. 66.
18. F. Mezei, *Kerntechnik*, **44**, 735 (1984).
19. L. A. de Graaf and M. Th. Rekveldt, *Kerntechnik*, **44**, 776 (1984).
20. H. A. Mook and J. B. Hayter, *Appl. Phys. Lett.*, **53**, 648 (1988).
21. B. Hamelin, N. Xiromeritis and P. Liaud, *Nucl. Instrum. Methods*, **125**, 79 (1975).

Q(W.G.Williams): Use of supermirror guides for epithermal neutrons. Any possibilities?

A(J.B.Hayter): It looks as if $4\theta_c$ may be a realistic goal for supermirrors, which means a guide divergence (full-width) of about 8°/nm. For a beam at, say, 1eV, this would restrict the divergence to less than 1/4°.

Q(R.Pynn): How long was your polarizer and was it a reflection or a transmission device? As a follow up question, do you need to use your band-pass ideas for the design of a transmission polarizes?

A(J.B.Hayter): The polarizer was about 5cm long, with a beam cross-section of 35 x 60mm^2. It was used in reflection. For transmission use, it is possible to use two simple supermirror stacks, one behind the other, each handling 1/2 of the beam divergence.

ICANS-XI International Collaboration on Advanced Neutron Sources
KEK, Tsukuba, October 22-26, 1990

A DOUBLE REFLECTION MULTILAYER MONOCHROMATOR FOR COLD NEUTRON POLARIZING AND SMALL ANGLE SCATTERING EXPERIMENTS.

T. Ebisawa, S. Tasaki, and T. Akiyoshi
Research Reactor Institute, Kyoto Univ., Kumatori, Osaka, 590-04, Japan

N. Achiwa
Department of Physics, Kyushu Univ., Higashi-ku, Fukuoka, 812, Japan

ABSTRACT
A multilayer monochromator using double reflection has been developed for cold neutron polarizing and small angle scattering experiments. It utilizes a successive double reflection by a pair of two identical multilayer mirrors arranged at a designed angle, which have a layer spacing distribution of $d \pm \Delta d$. A number of the pairs are assembled in a Soller type to cover the width of the neutron beam. The double reflection multilayer monochromator functions as a monochromator, polarizer, beam bender and collimator of the beam at the same time. The performance tests gives a promising characteristics of the double reflection monochromator.

I. INTRODUCTION

Multilayer neutron mirror was first reported by Schoenborn et al. for monochromator and by Mesei for supermirror[1),2)]. We have developed a various kind of devices for cold neutrons using multilayer mirror during over ten years[3),4)]. In the devices are included supermirrors for guide tubes and experimental devices[5),6),7)], polarizers and analyzers for polarizing experiments[8)] and monochromators for cold, very cold and ultra cold neutron experiments[9),10),11),12)].

We present a double reflection multilayer monochromator for a cold neutron polarizing experiment and a small angle scattering experiment.

The device is something that two identical multilayer mirrors connected at a designed angle 2θ are assembled in a Soller type as shown in Fig.1. The successive double Bragg reflection

by the two mirrors determines the characteristics of the device. The multilayer mirror is a monochromator with a spacing distribution $d \pm \Delta d$. We present here only a brief description of it's principle and structure. More detailed discussions are given elsewhere[9),10)].

II. PROPERTIES OF DOUBLE REFLECTION MONOCHROMATOR

We consider Bragg reflection of neutron by a multilayer monochromator. Neutron wavelength λ satisfying Bragg condition is given by the following equation under the assumption of $\theta \ll 1$ and $\Delta\theta \ll 1$,

$$2(d-\Delta d)(\theta - \Delta\theta) < \lambda < 2(d+\Delta d)(\theta + \Delta\theta) \qquad (1)$$

where θ is the neutron incident angle and $\Delta\theta$ is the beam divergence angle. Expressing the permissible neutron wavelength as $\lambda_0 \pm \Delta\lambda$. Then, λ_0 and $\Delta\lambda$ are given by Eq. (2) neglecting $\Delta d\ \Delta\theta$

$$\lambda_0 = 2d\,\theta, \qquad \Delta\lambda = 2(d\,\Delta\theta + \theta\,\Delta d) \qquad (2)$$

Neutrons with longer wavelength are reflected at larger angle and neutrons with shorter wavelength are reflected at smaller angle.

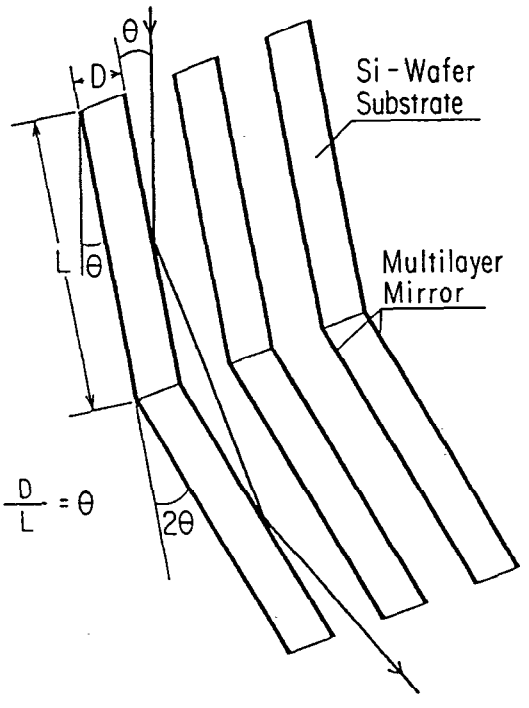

Fig. 1 Structure of a double reflection multilayer monochromator of a Soller type.

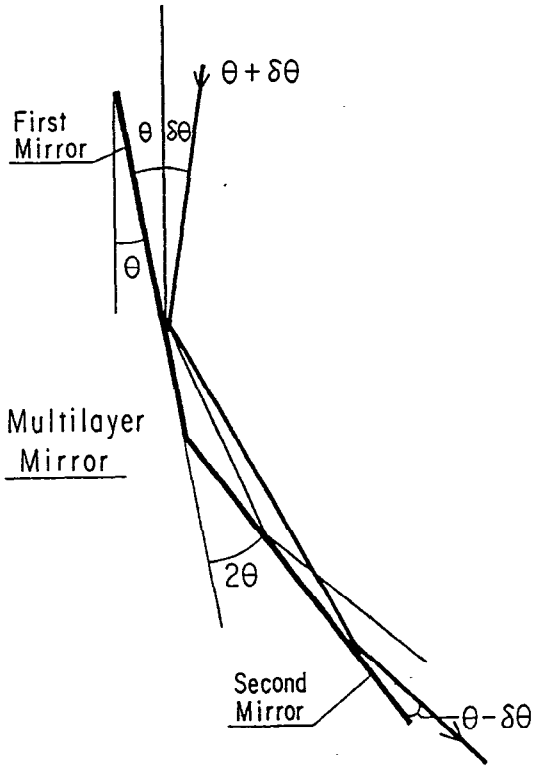

Fig. 2 A neutron trajectory taking a successive double reflection by two identical multilayer mirrors connected at a designed angle.

Next, we consider characteristics of neutrons reflected successively doubly as shown in Fig.2. Two identical mirrors connected at a designed angle 2θ. Angle θ and $\delta\theta$ correspond to the glancing angle and divergent angle of the incident neutron, respectively. Neutrons incident on the first mirror at the angle of $\theta + \delta\theta$ are incident on the second mirror at $\theta - \delta\theta$. Neutron wavelength reflected by the first and the second mirror should satisfy the Eqs. (3) and (4) simultaneously,

$$2(d-\Delta d)(\theta + \delta\theta) < \lambda < 2(d+\Delta d)(\theta + \delta\theta) \quad (3)$$

$$2(d-\Delta d)(\theta - \delta\theta) < \lambda < 2(d+\Delta d)(\theta - \delta\theta) \quad (4)$$

Denoting the allowable wavelength region of neutrons reflected doubly as $\lambda_0 \pm \Delta\lambda$ and it's permissible divergent angle as $\theta \pm \Delta\theta$, respectively, the resolutions of wavelength in FWHM and the allowable divergent angle are given by Eqs. (5) and (6), respectively[10]

$$\Delta\lambda / \lambda_0 = \Delta d/d \quad (5)$$

$$\Delta\theta = \pm \Delta d\, \theta /d \quad (6)$$

These resolutions depend on only Δd and not $\Delta\theta$, different from the single reflection case. Equation (6) indicates the effect of beam collimation by the device.

The properties of the neutron beam reflected successively doubly are summarized as the following.

(1) the neutron wavelength : $\lambda_0 = 2d\,\theta$
(2) the wavelength resolution in FWHM : $\Delta d/d$
(3) the beam bent angle : $4\,\theta = 2\,\lambda_0/d$
(4) the allowable divergent angle : $\Delta\theta = \pm \Delta d\,\theta /d$
(5) the effective reduction of undesirable neutrons with low reflectivity.

In order to shorten the device length of double reflection multilayer monochromator available for a wide neutron beam, pairs of multilayer mirrors connected at a designed angle should be assembled in a Soller type as shown in Fig.1. In this case, two identical mirrors are deposited on both surfaces of a Si-substrate.

Double reflection multilayer monochromators as bender enable a guide tube to install multiple spectrometers for cold neutrons. Larger bent angle could be realized by a multiple reflection more than twice at the small cost of neutron yield by using mirrors with high reflectivity.

The above monochromator device would be useful for small angle scattering, polarizing experiments and various kinds of cold neutron experiments.

III. PERFORMANCE TESTS OF DOUBLE REFLECTION MONOCHROMATOR

Performance tests of a typical double reflection multilayer monochromator are made for cold neutron polarizing experiments. Arrangement for the tests are shown in Fig.3. Parameters of the

double reflection multilayer monochromator are given in Table 1. It should be noted that the size of the device is very small (the total length is only 6.2 cm). The analyser mirror with Soller type made of $Fe_{50}Co_{50}$-V multilayer have 2d=360 A, $\Delta d/d$=0.9 and L=10 cm.

Table 1 Design parameters of double reflection monochromator with Fe50Co50-V multilayer.

2d(A)	$\Delta d/d$	θ (rad)	4θ (rad)	$\Delta\theta$ (rad)	λ_0(A)	$\Delta\lambda/\lambda_0$	L(mm)	D(mm)	R[1]	Y[2]
280	0.075	1/51.7	1/12.9	1/690	5.4	0.075	31	0.60	0.9	0.69

1) : Reflectivity of mirror
2) : Neutron yield at the peak by double reflection multilayer monochromator estimated numerically[10].

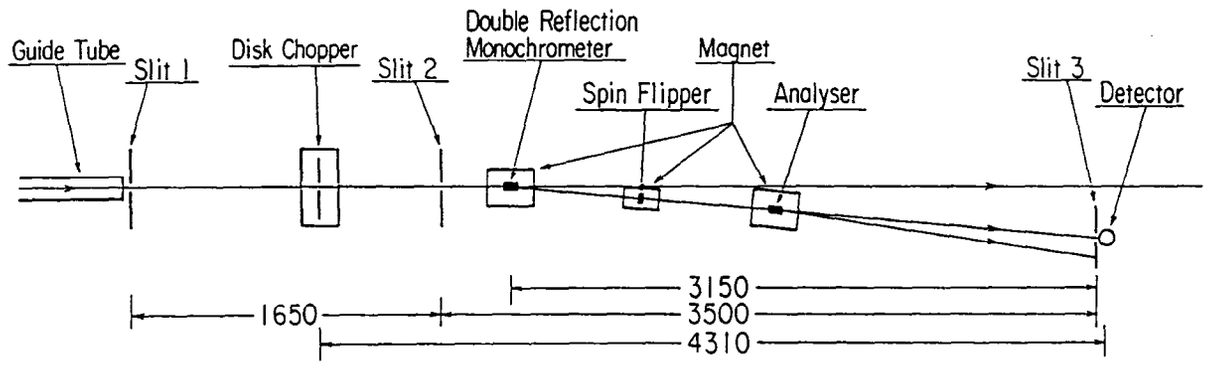

Fig. 3 Arrangement for the performance test of double reflection multilayer monochromator.

The neutron yield, wavelength and resolution are evaluated from TOF data. The results for the single and double reflection are shown in Fig.4 for the incident beam with the divergence of ± 1/400. The neutron yields are normalized by the direct spectrum. The results of the double reflection reproduce the properties listed in Table 1 except the neutron yield. The small reduction in the neutron yield may result from the under reflectivity (about 0.85) of the mirrors indicated by the single reflection data.

Measured divergent angles by the double reflection and the single reflection are given in Fig.5 for the incident beam with the divergence of 1/235. Comparison of the double reflection with the single reflection proves the characteristics of the double reflection multilayer monochromator as collimator for the incident beam as expected in Table 1. Bent angle is given easely from the center position of the beam profile.

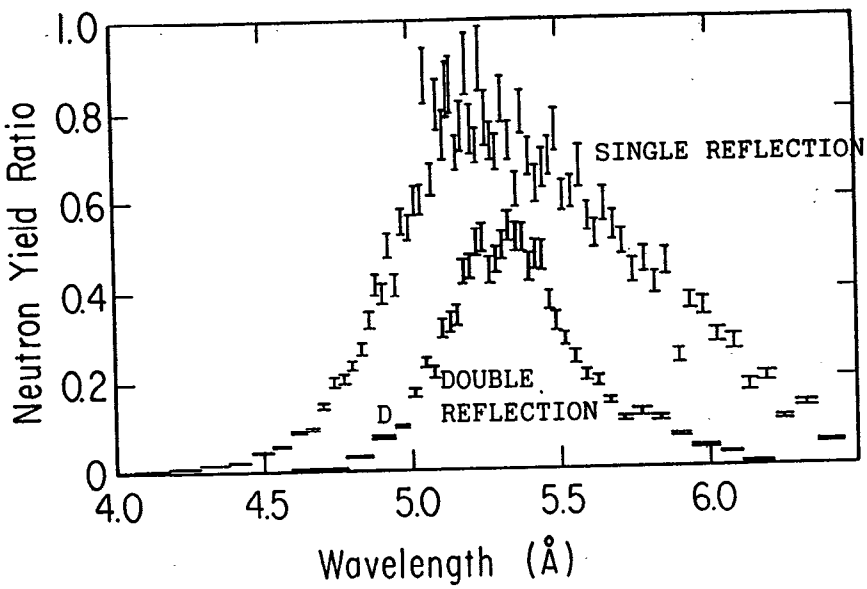

Fig. 4 Neutron yield by TOF methods for single and double reflection.

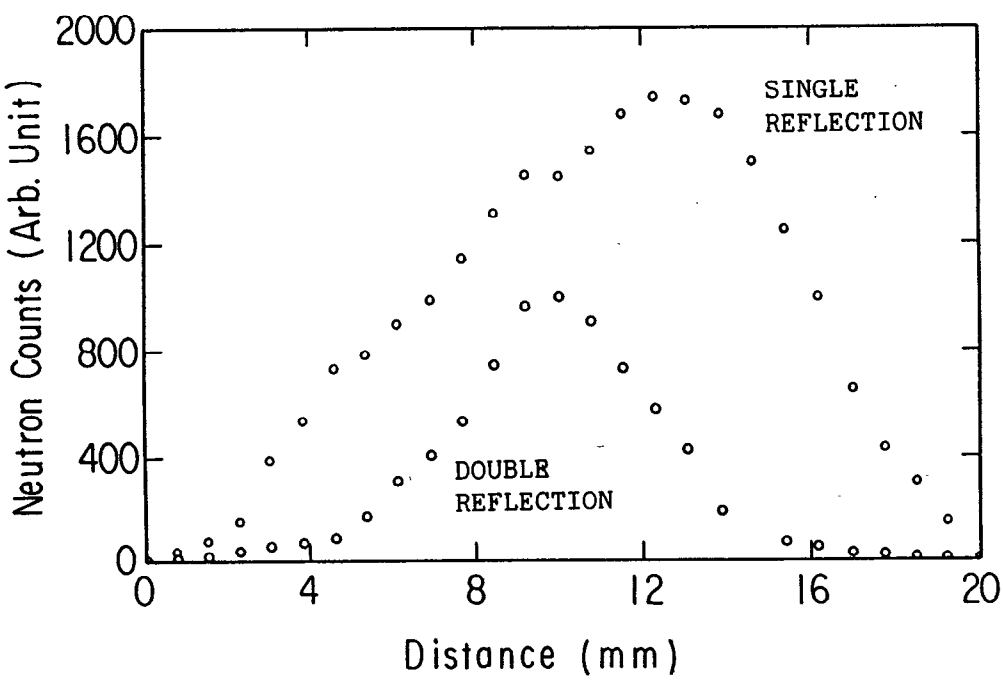

Fig. 5 Spread of the output beam by the single and double reflection for the incident beam divergence of 1/235.

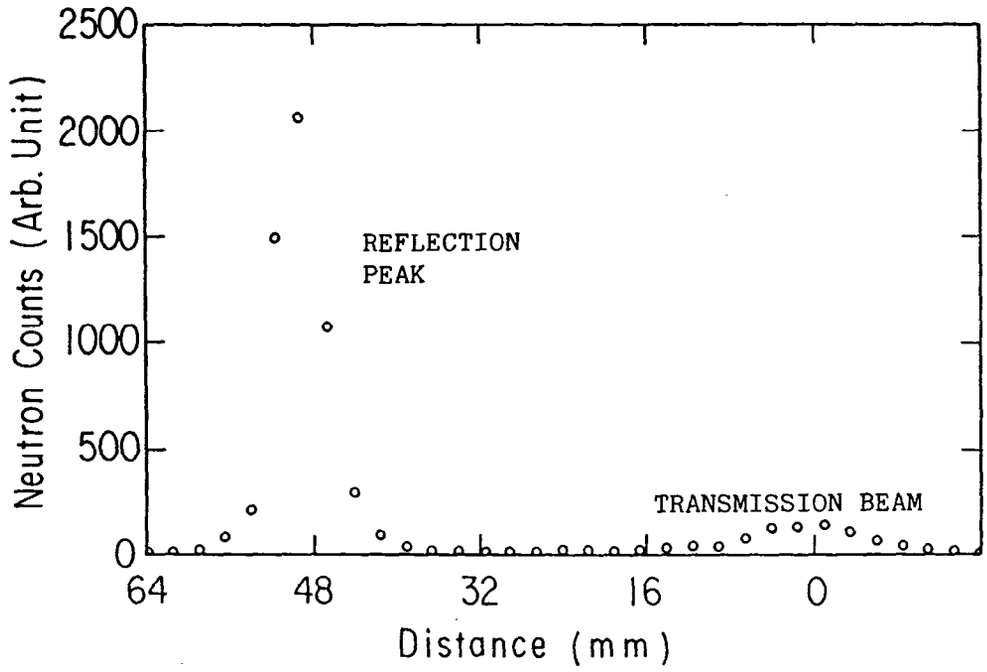

Fig. 6 Beam profile of the reflection and transmission by the analyser mirror.

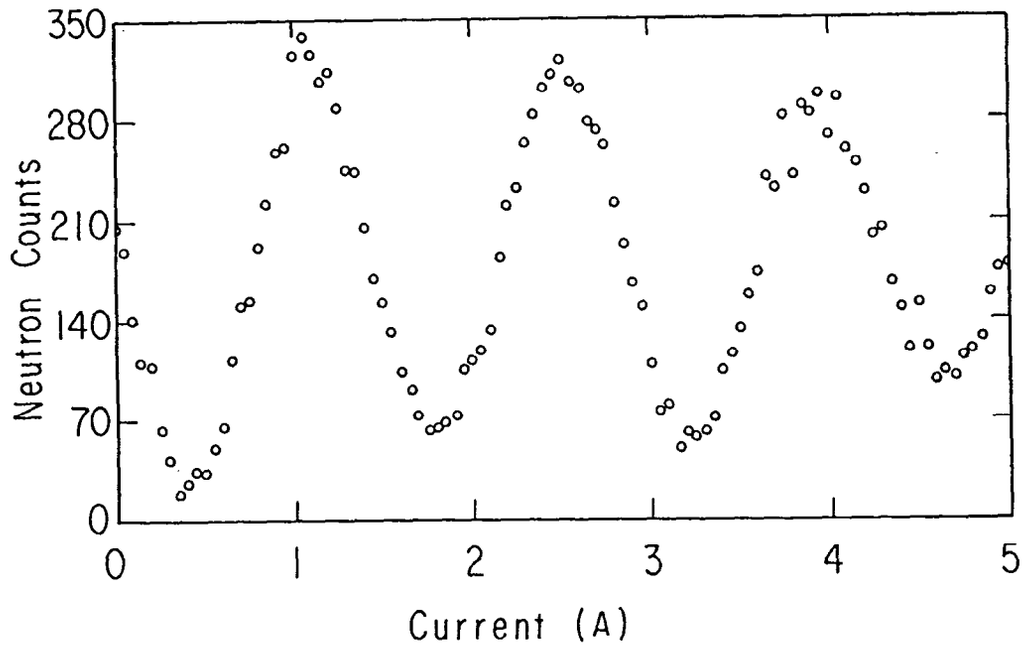

Fig. 7 Spin flipping data. The abcsissa indicates spin precession current of Mesei spin flipper.

When analyser mirror is set, the beam is reflected nearly perfectly (Fig.6). and the system gives the flipping ratio of about 1/20 (Fig.7).

A double reflection multilayer monochromator, with magnetic multilayer functions as a monochromator, polarizer, beam bender and beam collimator simultaneously.

For unpolarizing experiment, double reflection multilayer monochromators with Ni-Ti multilayer mirrors are adequate.

IV CONCLUSION

The double reflection multilayer monochromator with very small size functions as monochromator, polarizer (using magnetic mirror), beam bender and collimator simultaneously. Multiple reflections more than twice would be bring us larger bent angle at the cost of neutron intensity. The device would be useful for small angle scattering, polarizing experiments and various kinds of cold neutron experiments.

References

1. B. P. Schoenborn, D. L. D. Caspar and F. Kammerer, J. Appl. Cryst. 7, 508 (1974).
2. F. Mesei, Commun. Phys. 1, 81 (1976).
3. S. Yamada, T. Ebisawa, N. Achiwa, T. Akiyoshi, S. Okamoto, Annu. Rep. Res. Reactor Inst. Kyoto Univ., 11, 8 (1978).
4. T. Ebisawa, N. Achiwa, S. Yamada, T. Akiyoshi, S Okamoto, J. Nucl. Sci. Technol. 16, 647 (1979).
5. T. Ebisawa, T. Akiyoshi, S. Tasaki, T. Kawai, N. Achiwa, M. Utsuro, S. Okamoto, Proceedings of SPIE-The International Society for Optical Engineering, 983, 54 (1988).
6. T. Ebisawa, T. Kawai, T. Akiyoshi, M. Utsuro, Y. Maeda, K. Yoneda, S. Kawano, S. Tasaki, H. Yamaoka, S. Okamoto, Annu. Rep. Res. Reactor Inst. Kyoto Univ., 21, 1 (1988).
7. M. Utsuro, T. Ebisawa, K. Okumura, S. Shirahama and Y. Kawabata, Nucl. Instr. & Methods, A270, 456 (1988).
8. S. Komura, T. Takeda, T. Miyazaki, M. Saga and S. Ueno, Nucl. Instr. & Methods, A267, 425 (1988).
9. S. Tasaki, T. Ebisawa, N. Achiwa, T. Akiyoshi, S. Okamoto, Proceedings of SPIE-The International Society for Optical Engineeing.
10. T. Ebisawa, S.Tasaki, T. Akiyoshi, N. Achiwa, S. okamoto, Annu. Rep. Res. Reactor Inst. Kyoto Univ., 23, (1990).
11. T. Ebisawa, et al., to be published.
12. M. Utsuro, et al., private communication.

Q(J.B.Hayter): I was interested to see that you used time-of-flight at your reactor to measure reflectivity performance. Since we are at a pulsed source conference, I can admit that G.Williams, J.Penfold and I found time-of-flight the method of choice for our thin-film interferometry work at ILL many years ago. Working at a fixed angle offer significant advantages.

A(T.Ebisawa): I like TOF method for a continuous source, if we have neutron intensity enough for measuring.

ICANS-XI International Collaboration on Advanced Neutron Sources
KEK, Tsukuba, October 22-26, 1990

POLARISING FILTER TESTS AT ISIS

R Heap[(a)], P W Mitchell[(a)], J Mayers[(b)] and A D Taylor[(b)]

[(a)] Schuster Laboratory, Manchester University, Manchester, M13 9PL
[(b)] ISIS Facility, Rutherford Appleton Laboratory, Oxfordshire, OX11 0QX

1. INTRODUCTION

For the efficient use of polarised neutrons on a pulsed source such as ISIS, a neutron polariser capable of polarising over a broad band of neutron energies is required, so that time of flight techniques can be used. For this reason monocromating polarisers such as Heusler crystals, which are used at reactor sources, are not suitable. Furthermore, although supermirrors do provide white beam polarisation, they are inefficient at energies greater than $\simeq$ 30 meV. In principle neutron polarising filters, based on preferential absorption of one of the two neutron spin states by aligned Sm^{149} nuclei, give a good performance at all neutron energies below 200 meV [1,2]. However, in order for adequate nuclear alignment to be obtained, the filter must be maintained at $\simeq$0.02K in a dilution refrigerator. Previous measurements[2] have shown that heating of the filter is too great for efficient operation of the filter in a white beam on ISIS, given the limited cooling power of the currently available dilution refrigerator.

The primary purpose of the measurements presented here was to determine whether the filter is suitable for polarising an incident beam which is monochromated by a Fermi chopper. It was anticipated that the large reduction of neutron intensity by the chopper would largely eliminate any beam heating problems. In section 2 we outline the principle of neutron polarisation by Sm filters, in section 3 we describe the measurements and in section 4 we discuss the interpretation of these measurements and their implications for future progress.

2. PRINCIPLE OF FILTER OPERATION

The nuclear absorption cross-section for the two neutron spin states is[1]

$$\sigma\pm = \sigma(1\pm\rho)PN \tag{1}$$

where $\sigma+$ and $\sigma-$ are the absorption cross-sections for the + and - spin states, ρ is a statistical spin weighting factor (ρ = 7/9 for Sm^{149}) and PN is the nuclear polarisation. Thus the filter transmission for the two spin states is

$$T\pm = \exp[-Nt\sigma(1\pm\rho)PN] \tag{2}$$

where Nt is the number of Sm^{149} atoms/unit area of filter.

The polarising efficiency of the filter is defined as the beam polarisation of an initial unpolarised beam after it has passed through the filter.

$$P = (T+ - T-)/(T+ + T-) = -\tanh(\rho PN\sigma) \tag{3}$$

The fraction of incident neutrons transmitted by the filter is

$$T = (T+ + T-)/2 = \exp(-\sigma Nt)\cosh(\rho PN\sigma Nt) \tag{4}$$

These equations are complicated by the presence of any depolarisation effects due to domain misalignment within the filter. However previous measurements [1,2] have shown that these effects are small and they can be neglected.

The filter operates efficiently within the region of energy where the Sm^{149} absorption cross-section is the dominant source of neutron attenuation. For Sm^{149} the 96 meV resonance absorption peak provides a sufficiently large cross-section for incident neutron energies between 0 and 200 meV.

3. MEASUREMENTS

The preparation and characterisation of the filter has been described in a previous report[2]. A schematic diagram of the experimental apparatus is shown in figure 1. The choppper was phased to give an incident energy of 88±1 meV. In figure 2 we show a superposition of spectra from the four detectors indicated in figure 1 in the absence of the filter. In figure 3 is shown the transmission of the filter as a function of time, after the circulation was started on the dilution refrigerator. As the filter cooled, the transmission of the filter increased according to equation 4. The ratio of the transmission with the filter cold to that 'warm' (ie > 1K where PN = 0) is

$$R = \cosh(\rho PN\sigma Nt) \qquad (5)$$

It can be seen from figure 3 that $R \simeq 0.0062/0.0024 = 2.6$, so that from equation (5), $\rho PN\sigma Nt = 1.6$. The value of σNt can be obtained from the 'warm' transmission; $\sigma Nt = -\ln(0.0024) = 6.03$. Thus using $\rho = 7/9$, we obtain $PN = 0.34$. The observed nuclear polarisation is given by the product of the nuclear polarisation within a single domain and the average alignment of the domains within the sample. Previous measurements have shown that the latter quantity is $\simeq 0.9$, so that the nuclear polarisation within a single domain is $\simeq 0.34/0.9 = 0.38$. From this value for the nuclear polarisation the temperature of the filter can be determined from the Brillouin function, given the known hyperfine interaction between the Sm nuclei and the Sm f electrons [3].

A nuclear polarisation of 0.38 corresponds to a filter temperature of $\simeq$0.07K.

We note that the neglect of depolarisation effects within the filter leads to a worst case estimate for the filter temperature. If depolarisation is taken into account the calculated operating temperature is reduced. However the estimate of 0.07K should be accurate to within 10%.

A measurement of R at 88 meV with the chopper removed from the beam gave a value of $R \simeq 1.2$, which corresponds to a temperature of 0.2K. Thus since the cooling power of an ideal dilution refrigerator [4] is proportional to T^2, it follows that the presence of the chopper reduced the beam heating by a factor $(0.2/0/07)^2 \simeq 8$.

Previous white beam measurements[2] on the filter in a beam current of 1μA (compared with 100μA during the measurements reported here) gave a transmission ratio of 10, which corresponds to a temperature of 0.03K. Assuming, as previously mentioned, that the cooling power of the refrigerator is proportional to T^2, the heating was less by a factor of $(0.2/0.03)^2 \simeq 50$ at 1μA than at 100μA. The discrepancy of a factor 2 between this estimate of the beam heating and the reduction expected from the reduced beam current gives an indication of the accuracy of the estimation of beam heating.

4. DISCUSSION

The reduction of beam heating by a factor of only $\simeq$8 in the presence of the chopper suggests that significant beam heating is produced by high energy neutrons and also possibly by the t = 0 gamma ray flash from the incident beam. The measurements suggest

that in order to reduce the filter operating temperature to below 0.02K, we require a further reduction in beam heating by a factor $\simeq 10$. In figure 4 we show the neutron transmission of the Fermi chopper as a function of time of flight. Many more neutrons are transmitted at short times, where the incident neutron intensity is high, than in the chopper pulse.

The high energy neutrons and the γ flash can be eliminated by the installation of a Nimonic chopper, such as those used on HET and MARI to reduce fast neutron background. This should result in a further reduction in beam heating and allow for efficient operation of the polarising filter.

REFERENCES

1. J Mayers, R Cywinski,T J L Jones and W G Williams. 'Neutron Tests on Samarium Polarising Filters' Rutherford Appleton Laboratory Report RAL-84-118 (1984).

2. J Mayers A C Hannon and W G Williams. ' Samarium Polarising Filters at ISIS' Rutherford Appleton Laboratory Report RAL-89-122 (1989)

3. F F Freeman and W G Williams J Phys E *11* 459 (1978)

4. O V Lousanama ' Experimental Principles and Methods Below 1K' Academic Press, London (1972).

ACKNOWLEDGEMENTS

We gratefully acknowledge the contributions of ISIS staff who made these measurements possible. In particular; Jim Chauhan for preparation and operation of the dilution refrigerator, Terry Jones for provision of the chopper and Zoë Bowden for organisation of installation and setting up of detectors.

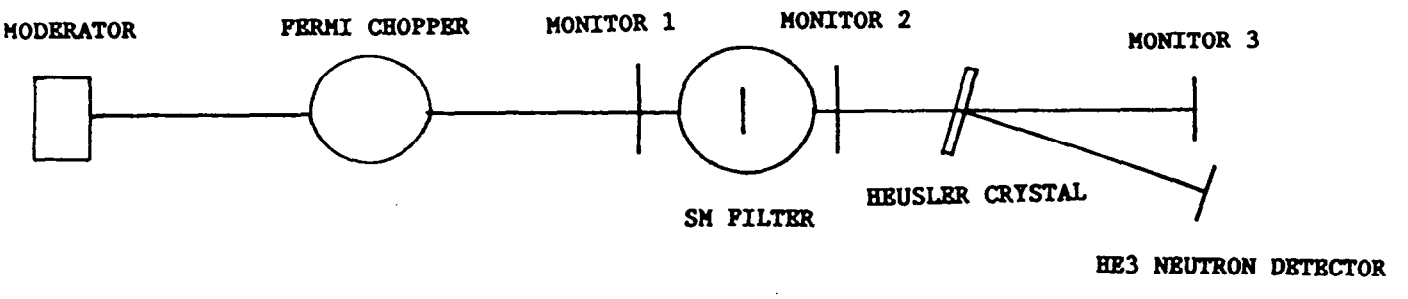

FIGURE 1. SCHEMATIC DIAGRAM OF APPARATUS

Q(J.B.Hayter): What is the cost of a polarizing filter with current technology?
A(W.G.Williams): The best high power dilution refrigerators cost about £120K.

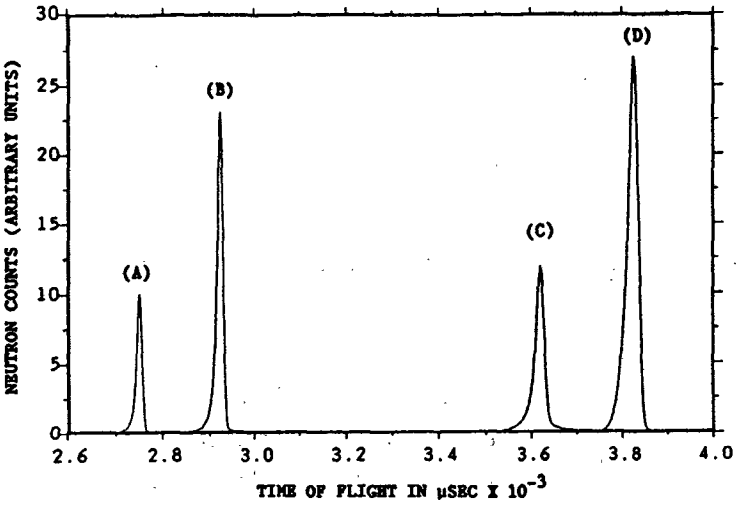

FIGURE 2. DETECTED INTENSITY WITH CHOPPER PHASED TO GIVE INCIDENT ENERGY OF 88.7 MEV. POLARISING FILTER OUT OF BEAM. (A) MONITOR 1, (B) MONITOR 2, (C) MONITOR 3, (D) INTENSITY IN HE3 COUNTER AFTER REFLECTION FROM HEUSLER.

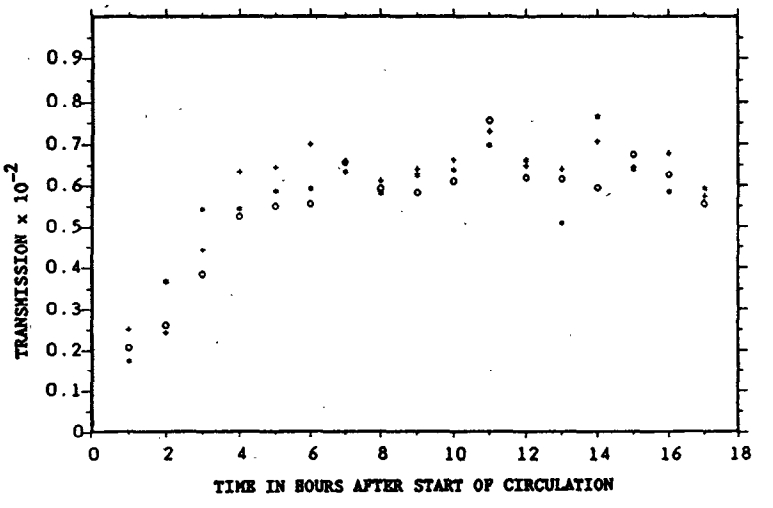

FIGURE 3. TRANSMISSION OF POLARISING FILTER AS A FUNCTION OF TIME. THE CIRCULATION ON THE DILUTION REFRIGERATOR WAS STARTED AT TIME ZERO. THE TRANSMISSION WAS MEASURED INDEPENDENTLY USING MONITOR 2 (+), MONITOR 3 (*), AND THE HE3 COUNTER (o).

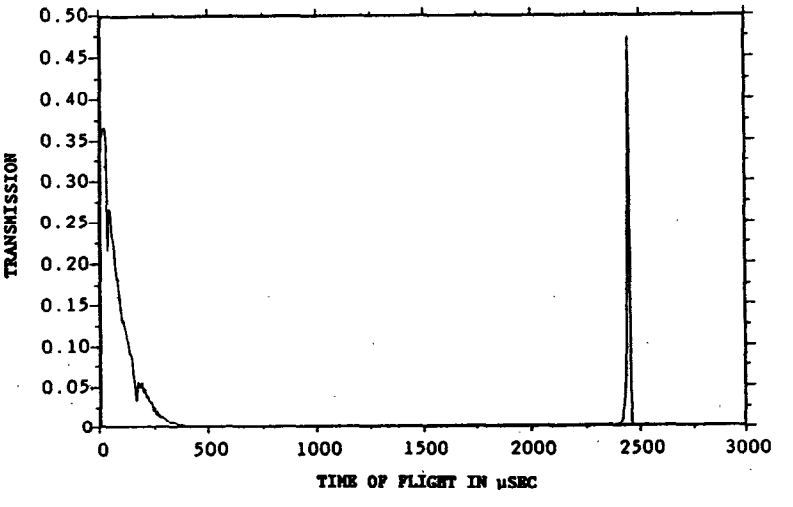

FIGURE 4. TRANSMISSION OF CHOPPER

ICANS-XI International Collaboration on Advanced Neutron Sources
KEK, Tsukuba, October 22-26, 1990

INVESTIGATION AND GROWTH OF MULTILAYERS

P. Böni and I. S. Anderson
Paul Scherrer Institut
CH-5232 Villigen PSI, Switzerland

R. Hauert
EMPA
CH-8600 Dübendorf, Switzerland

P. Ruterana
EPFL
CH-1015 Lausanne, Switzerland

K. Solt
Landys & Gyr
CH-6301 Zug, Switzerland

B. Farnoux
Laboratoire Léon Brillouin
CEN-Saclay
F-91191 Gif-sur-Yvette Cédex, France

G. J. Herdman and J. Penfold
Rutherford Appleton Laboratory
Chilton, Didcot, Oxon OX11 0QX, United Kingdom

O. Schärpf
Institut Laue Langevin
F-38042 Grenoble, Cedex, France

ABSTRACT

Following the pioneering work on multilayers for neutron mirrors and polarisers performed at ILL, there has been a recent upsurge in the efforts to produce high quality mirrors on a large scale. Modern analytical techniques allow the detailed structure of thin metallic films and their interfaces to be investigated and related to the deposition parameters. By combining such studies with neutron reflection measurements, it is possible to determine the effect of structural properties and defects on the neutron reflectivity and thus eventually refine the deposition technique and parameters. Results will be presented on multilayers

produced by various methods and studied by neutron spectroscopy, Auger depth profiling, and transmission electron microscopy.

I. INTRODUCTION

Neutron guide tubes provide an efficient transport of neutrons to a wide variety of instruments in areas with low backgrounds.[1] Up to now most of the guides have been coated with natural Ni (Ref. 2) having a critical angle of reflection $\theta_c/\lambda = 1.7$ mrad/Å (6 min/Å). Recently ^{58}Ni has replaced natural Ni as a guide coating [3] with the advantage that the critical angle is increased by a factor $m = 1.2$ resulting in flux gains up to m^2 (Ref. 4). More recent progress in this area suggests that it may become possible to produce supermirrors with an excellent reflectivity ($R > 0.98$) and with even larger θ_c, namely $m \geq 1.5$. Guides coated with such supermirrors, in addition to the overall flux gains that may be achieved, allow increased transmission at short wavelengths, suggesting the feasibility of their use in normal beam tubes.

These properties are particularly important at a continuous spallation source like SINQ at PSI, where the production of high energy neutrons necessitates rather bulky target shielding. Supermirror coated guides and beam tubes may efficiently transmit even short wavelength neutrons over the large distances required. More effective use of the available neutrons at the instruments may be achieved by the use of additional optical elements such as polarizers, focussing devices, monochromators, band pass filters etc., which also depend on the development of artificial multilayers. For this reason we have an ongoing project to study the production and the properties of thin films for neutron optics.

The results we present here review some aspects of our work on Ni/Ti multilayers produced by various deposition techniques and characterised using a number of analytical techniques such as neutron reflection, transmission electron microscopy (TEM), and Auger depth profiling.

II. EXPERIMENTAL

Our investigations have been based on the study of Ni/Ti multilayers of constant bilayer spacing (usually between 100 and 140 Å) deposited onto polished silicon wafers with the aim of determining the effect of the deposition parameters on the structure and reflectivity of the multilayer stack. Some characteristics of the deposition techniques that we have used may be summarised as follows:

Evaporation: The target is heated in a high vacuum chamber ($10^{-5} < p_i < 10^{-6}$ mbar) to produce a vapour pressure of the order of 10^{-2} mbar. The evaporated particles have thermal energies (0.05 to 0.5 eV) and follow an almost collisionless path to the substrate. Due to the very non linear dependence between vapour pressure (hence deposition rate), and temperature the process is difficult to control and thickness monitors must be used. Moreover the rather low energies of the incident particles at the growing film leads to underdense structures usually under tensile stress.

Magnetron sputtering: In this case the atoms are sputtered from the surface of a target due to bombardment by energetic inert gas ions produced in a glow discharge plasma which is confined to the target surface by a magnetic field. The sputtered atoms are ejected with considerable kinetic energy, 50 - 100 times higher than in vacuum evaporation, with an average energy of the order of 10 - 40 eV. Additionally, reflected working gas atoms, which have been neutralised at the target by emitted electrons, may reach the substrate with a considerable fraction of their initial energy so that the growing film may be significantly modified by the bombardment by energetic particles. The final energies of both the sputtered species and the

reflected working gas atoms at the substrate will depend on the product of the working gas pressure (usually in the range 1 - 5 mbars) and the distance from target to substrate so that these parameters may be used to control film growth properties.

Ion Beam Sputtering: The glow discharge sputtering described above is limited in the sense that target current density and the particle energy cannot be independently controlled except by varying the working gas pressure. Ion beam sputtering permits independent control over the energy and current density of the bombarding ions. The sputtering target is arranged to obliquely intercept an ion beam of given energy and flux density that is created by an independent ion source. Ion beam sources permit sputtered coatings to be deposited at very low working gas pressures ($\simeq$ 0.1 mbar) onto substrates which are not in contact with the plasma so that uncontrolled particle bombardment and therfore heating rates may be minimised. In addition secondary ion sources may be used (Ion beam assist) to provide direct, controlled bombardment of the growing film during deposition in order to modify its properties.

The reflection profiles of the samples were measured on neutron reflectometers installed at the pulsed spallation source ISIS and at the Orphée reactor in Saclay. Such instruments have the particular advantage of using fixed sample geometry and therefore constant illumination, the profile being determined by a wavelength scan. Additional measurements of the reflectivity of the Bragg peak have been performed on the S3 double axis spectrometer at the Institut Laue Langevin[2] using a fixed wavelength $\lambda = 7.2$ Å. In this case special precautions were taken to confirm that the illumination remained constant by using extra large samples.

In the present work we have characterized the samples using TEM results obtained on a Philips EM430ST microscope which provides a point resolution better than 0.2 nm. The cross-section sample preparation was carried out by ion-milling at liquid-nitrogen temperature ensuring minimal damage to the layer structure.[5] Both dark field and bright field images were obtained in addition to electron diffraction patterns, yielding detailed information on the crystalline structure and morphology of the layers.

The Auger depth profile was performed at EMPA. A Perkin Elmer PHI-4300 high resolution scanning Auger system was used. The analysis was performed on a 5×15 μm^2 area, at a primary electron beam voltage of 5.0 kV and at a beam current of 500 nA. The CMA (Cylinder Mirror Analyzser) was operated at 0.6% resolution. Profiling was done by sputtering for 15 s inbetween Auger spectra by Ar-sputtering at 4.5 kV over a 5×5 mm^2 rectangular area. The sputter rate was calibrated to 8 nm/min on a SiO_2 standard reference. The base pressure in the analysis chamber was $5 \cdot 10^{-10}$ mbar. The depth resolution of 20 Å could not be reached due to ion-mixing caused by the Ar-sputtering while depth profiling. By the same reason some of the Ti and Ni was driven into the Si substrate during Auger depth profiling (Knock-on effect). For details see Ref. 6.

III. RESULTS

We have made Ni/Ti multilayers using all the deposition methods mentioned in the previous paragraph and have analyzed their structure and reflectivity. As a first comparative step the Bragg peak reflectivities of various specimens were measured using the S3 spectrometer at the ILL. We show the results of these measurements in Table 1. and compare them with theoretical estimates based on the measured bilayer thickness. Also listed in the tables are the main deposition parameters used for each sample.

The comparison between the experimental and theoretical reflectivities clearly shows that the evaporated samples were inferior to the sputtered ones. The Bragg peak of sample

E1 has large wings, indicating that the layer thicknesses d_i (i = Ni, Ti) are not uniform a result confirmed by TEM (see later). Moreover, d_i depends even on the position of the samples inside the apparatus therefore the evaporation process is not homogenous.

The high rate sputtered samples have generally a significantly better reflectivity than the low rate sputtered samples. Decreasing the pressure during sputtering at high rate increases the reflectivity of the multilayers, whereas etching turns out to be a less important parameter. The reflectivity of the ion beam sputtered samples is rather low. Neutron reflectometer and TEM results show that this is primarily due to poor thickness control during deposition.

Table 1: Characteristic properties of the evaporated and sputtered samples. p_i is the pressure, v the deposition rate, R is the measured reflectivity, and R_{th} is the calculated reflectivity, based on the measured bilayer thickness $2D$.

Evaporation (20 bilayers Ni/Ti 50 Å)

sample	etch	p_i (mbar)	v (Å/s)	D (Å)	R (%)	R_{th} (%)
E1	no	$\simeq 10^{-5}$	10	51.2	40	82

Low rate sputtering (20 bilayers Ni/Ti 50 Å)

ML1	no	$4 \cdot 10^{-3}$	Ni 1.42, Ti 3.3	51.1	67	82
ML2	no	$4 \cdot 10^{-3}$	Ni 1.42, Ti 3.3	52.5	63	85

High rate sputtering (15 bilayers Ni/Ti 50 Å)

MH1	yes	$6 \cdot 10^{-3}$	17.5	46	46	53
MH2	yes	$6 \cdot 10^{-3}$	17.5	46	41	53
MH3	yes	$3 \cdot 10^{-3}$	18.7	48.5	60	60
MH4	yes	$3 \cdot 10^{-3}$	18.7	48	57	59
MH5	no	$3 \cdot 10^{-3}$	18.7	49	57	61.5
MH6	no	$3 \cdot 10^{-3}$	18.7	48	56	59

Ion beam sputtering (15 bilayers Ni/Ti 50 Å)

sample	ion ass.	p_i (mbar)	v(Å/s)	D (Å)	R (%)	R_{th} (%)
I1	no	$1.5 \cdot 10^{-4}$	Ni 1.8, Ti 1.4	53	44	71
I2	no	$1.5 \cdot 10^{-4}$	Ni 1.8, Ti 1.4	51	43	67
I3	yes	$1.5 \cdot 10^{-4}$	Ni 0.95, Ti 0.72	56	49	77
I4	yes	$1.5 \cdot 10^{-4}$	Ni 0.95, Ti 0.72	55	51	75
Ion beam parameters:			sputtering	150 mA	1000 eV	
			assist	75 mA	250 eV	

In order to understand the origin of the widely differing reflectivities of our samples we have studied the structure of the layers by means of high resolution TEM. The results for

the evaporated samples show that only the first few layers are of good quality. The following layers become increasingly wavy due to the growth of large crystal grains within the layers, and even island formation starts. This explains the low reflectivity of the evaporated samples. Similar TEM observations have been made on the low rate sputtered samples: The Ni and Ti layers are crystalline with a preferred orientation in the [111] direction and the [002] direction, respectively. The build up of roughness caused by large crystallites eventually leads to the breakdown of the regular layer structure.

The TEM results on the high rate magnetron sputtered samples are particularly interesting. Fig. 1a shows as an example the excellent morphology of the layers of a sample that was made under low pressure conditions. A close inspection of the TEM-pictures shows that the Ni layers are crystalline with a preferred orientation [111] as before. The Ti layers, however are crystalline for high pressure conditions and amorphous for low pressure conditions. This observation correlates with the neutron reflectivities, namely the amorphous Ti layers seem to smooth out irregularities in the layer stack and yield samples with a higher reflectivity.

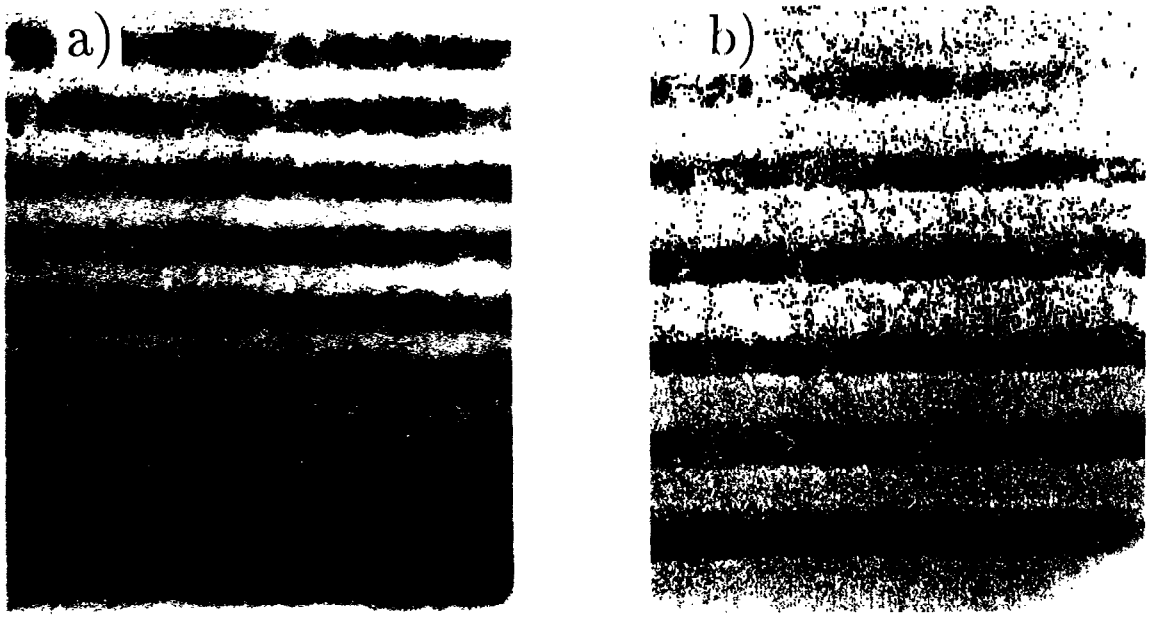

Fig. 1. *a) TEM photograph of the high rate sputtered multilayer MF5. The bright layers are composed of amorphous Ti ($\simeq$ 55 Å), the dark layers ($\simeq$ 44 Å) are composed of small grained Ni crystals. b) TEM photograph of an ion beam sputtered sample (15 bilayers Ni/Ti, $d_i \simeq$ 50 Å) which was concurrently bombarded by a second ion beam. Note the well defined interfaces.*

In Fig. 1b we show a TEM for an ion beam sputtered sample. The appearance of the layers is impressive. Again the Ni layers are crystalline ([111] in the layer) and the Ti layers are mostly amorphous with some evidence of crystallinity in the center. The samples deposited with ion beam assist seem to have Ti layers that are completely amorphous and the Ni layers have a reduced grain size. However, because of the poor thickness control it is not possible to judge unambiguously the effects on the reflectivity.

In addition we also studied the atomic composition of the high rate sputtered multilayers by means of Auger depth profiling. In Fig. 2 we show a typical scan. The resolution of the instrument is only approximately 50 Å due to ion mixing during Ar sputtering. The dominant substances are clearly Ni and Ti, namely $c_{Ni} \simeq$ 54 at.% and $c_{Ti} \simeq$ 42 at.%. These numbers

correlate nicely with the fitted thicknesses from the reflectivity measurements to be discussed below, namely $d_{Ni} = 54.8 \pm 0.2$ Å and $d_{Ti} = 44.2 \pm 0.1$ Å. Since Argon gas was used for sputter etching, its concentration could not be directly determined, however an upper limit of the analysis yields $c_{Ar} < 2.2$ at.%. Furthermore, concentration limits for carbon and nitrogen impurities can be given from ESCA spectra: $c_C < 1.3$ at.%, and $c_N < 0.4$ at.%.

An interesting behaviour is observed for the concentration of oxygen. The mean concentration is $c_O \simeq 2.4$ at.%. It shows a periodic oscillation in time (depth), similar as Ni and Ti. A closer inspection of Fig. 2 shows that the oxygen content rises at the beginning of the Ti layers. Obviously, Ti acts as a getter material and absorbes O_2 from the environment, in contrast to Ni. This observation is particularly interesting because this effect offers the possibility to create a diffusion barrier TiO_2 between the Ni and Ti layers by controlled implementation of O_2.[7] Indeed, reflectivity and TEM measurements indicate that the interface of Ti on Ni (10 Å) is sharper than the interface of Ni on Ti (14 Å).

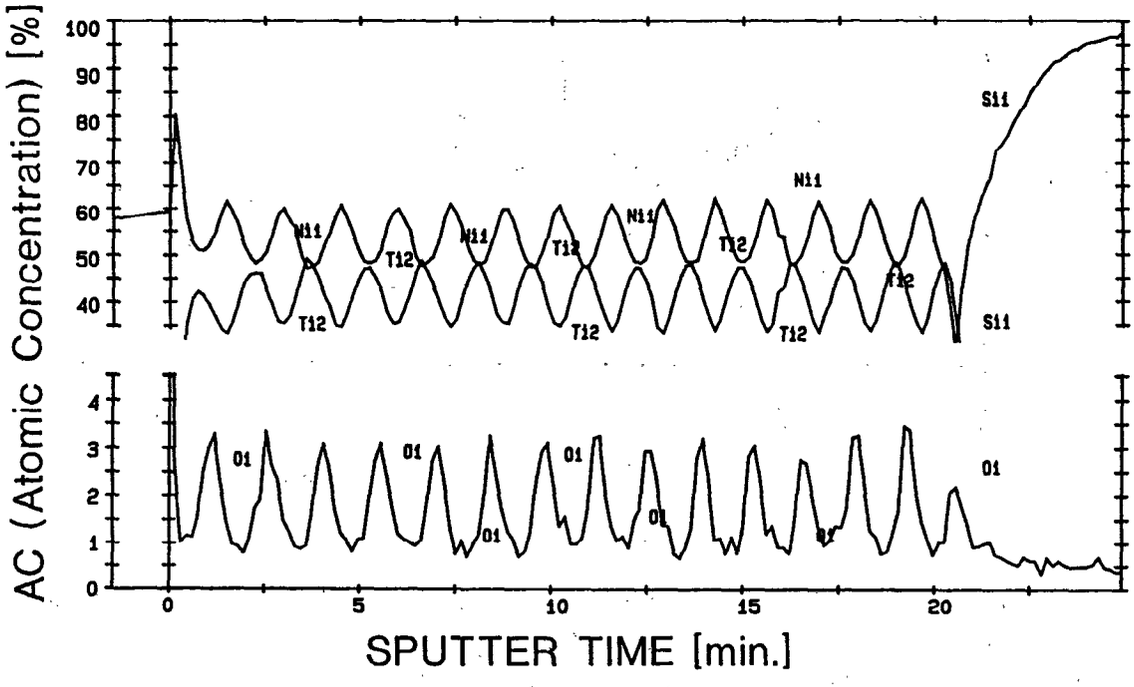

Fig. 2. *Auger depth profile of a high rate sputtered sample containing 15 bilayers Ni/Ti. The signals for Ni and Ti are exactly out of phase, whereas the O_2 signal appears only at the beginning of each Ti layer.*

Finally we investigated in a preliminary study the temperature dependence of some high rate sputtered samples. In Fig. 3 we show typical reflection profiles measured at temperatures of 30° and 149°C and an angle of incidence $\theta = 1.05°$. The peak at 3.57 Å is the principal Bragg peak corresponding to a d-spacing of 99.0 Å of the multilayer. The solid line is a fit to the data taking into account only the data points between 3 Å and 11 Å. The data at longer wavelength is possibly strongly influenced by the detailed structure of the substrate interface what we have so far been unable to model satisfactorily. The fitting function is based on conventional optics[8], including refraction and diffraction. The fitted parameters are a normalisation constant for the neutron intensity, the angular resolution of the instrument $\delta\theta$ and the thicknesses d_i, i = Ni, Ti (4 parameters). For the scattering densities g_i we used the bulk values of Ni ($9.4 \cdot 10^{-6}$ Å^{-2}) and Ti ($-1.95 \cdot 10^{-6}$ Å^{-2}). Fitting g_i did not significantly

improve the fits because g_i and d_i are strongly correlated. The fits yielded $d_{Ni} = 54.8 \pm 0.2$ Å and $d_{Ti} = 44.2 \pm 0.1$ Å. The agreement between the fits and the data is excellent within the restricted range of λ. An increased angular resolution $\delta\theta$ which varies between 0.045^0 and 0.072^0 for various high rate sputtered samples may be attributed to bending of the samples.

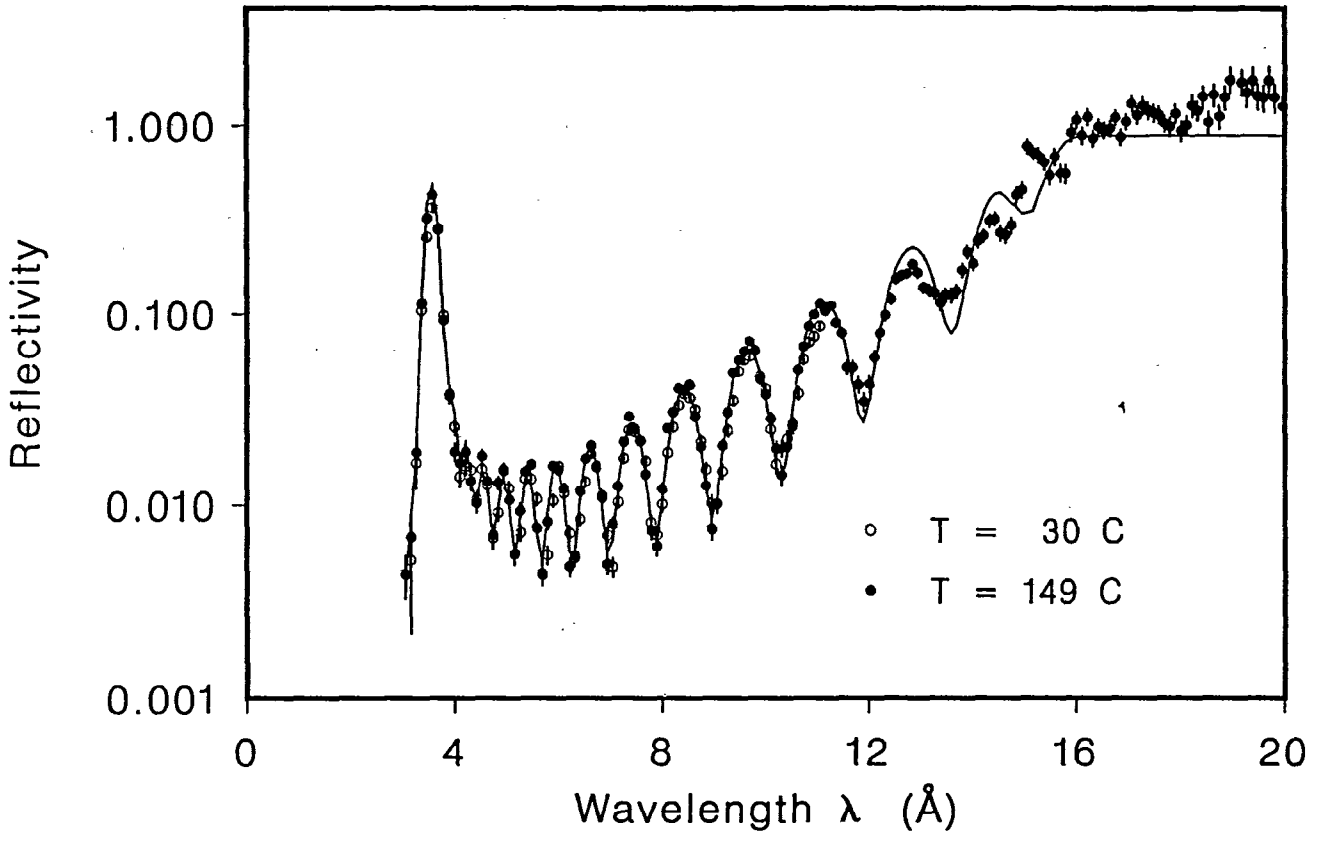

Fig. 3. *Measured reflectivities of the high rate sputtered multilayer MF5, containing 15 bilayers of Ni/Ti (50 Å), versus wavelength. The angle of incidence is $\theta = 1.02°$. The solid line is a fit to the 149° C data, using data within the range $3 < \lambda < 11$ Å.*

The reflectivity increases slightly when the samples were heated from room temperature to 149 C. The fits indicate that the d-spacings decreased by roughly 0.5 % and $\delta\theta$ decreased. The former effect is equivalent to an increase of the density of the multilayer stack whereas the latter effect may be related to a reduced bending of the Si wavers. We have initiated further measurements to address the dependence of a heat treatment on the layer properties in more detail by means of both neutron reflection and TEM with micro-analysis.

IV. DISCUSSION

In the previous sections we have demonstrated that the morphology and the reflectivity of the artificial multilayers depend strongly on the physical conditions near the substrate during the deposition process. Let us summarize the previous results as follows. All samples with amorphous Ti layers and small Ni grain sizes show a nominally better reflectivity. Large grains favour buckling of the layers and island formation. We speculate that the ideal multilayer would consist of amorphous layers only. The amorphicity of Ti is linked to the energy of the

incident sputtered atoms, the energy of the reflected neutral working gas atoms, and the rate at which the sputtered species arrive at the growing film.

High rate sputtering favours small grain sizes possibly because the crystallites do not find time to grow under the intense bombardment of the energetic sputtered particles. Ion beam sputtering, on the other hand, yields well defined layers, although the growth process is slow. However, because the pressure is very low, $p_i = 1.5 \cdot 10^{-4}$ mbar, the sputtered particles have a higher energy (although a lower flux) and reduce the grain size. This effect can be independently enhanced by means of ion assisted sputtering. We conclude that high rate, low pressure, and high energy of the sputtered particles favour the growth of high quality Ni/Ti multilayers.

Presumably the ion beam technique is the most promising for future multilayer production due to its flexibility in optimizing independently the various deposition conditions. However, systems which are capable of coating the large surface areas necessary for a neutron guide system, exist only as prototypes and may require some years of development before full optimization is achieved.

Rather, based on the surface area required for the SINQ quide system, taking into account the planned commissioning schedule and following the philosophy of acquiring only fully tested equipment we have opted to buy a commercially available magnetron sputtering system, which is due for delivery in Spring 1991. The machine comprises a load lock module and a deposition chamber in which the substrates are translated below three high power DC magnetron targets to produce coatings with a design uniformity of 3% over an area of 500×360 mm^2.

On our present schedule we will benefit from approximately 15 months of time to optimize the deposition characteristics before guide production must begin. Besides we will proceed with various other lines of investigations such as smoothing layers, alternative high contrast materials, substrate effects and of course long term stability with respect to thermal and radiation cycling.

OBITUARY

During the preparation of this manuscript we (ISA and PB) were deeply saddened to hear of the untimely decease of our colleague John Herdman, following an intermittent period of illness. We are greatly indebted to him for his very thorough work on describing the neutron reflection profiles from which we learned a great deal. We wish to express our sincere respect for him as a scientist and colleague.

REFERENCES

1. H. Maier-Leibnitz and T. Springer, Reactor Sci. & Techn. **17**, 217 (1963).
2. Guide to Neutron Research Facilities at the ILL, ed. by H. Blank and B. Maier, December 1988.
3. K. Werner, T. Springer, and J. Duppich, IAEA-CN-46/54P, 393 (1985).
4. I. S. Anderson, SPIE Vol. **983**, 84 (1989).
5. P. Ruterana, J.-P. Chevalier, and P. Houdy, J. Appl. Phys. **65**,3907 (1989).
6. Practical Surface Analysis, Eds. D. Briggs, M. P. Seah, John Wiley & Sons (1983).
7. O. Schärpf, Physica B **156 & 157**, 631 (1989).
8. S. Yamada, T. Ebisawa, N. Achiwa, T. Akiyoshi, and S. Okamoto, Annu. Rep. Res. Reactor Inst. Kyoto Univ. Vol. **11**, 8 (1978).

Q(T.Ebisawa): In the case of evaporation technique, vacuum pressure control is important. How many pressure do you have. The pressure used is the optimum condition?

A(P.Boni): The pressure p_i in the deposition chamber was chosen in between $10^{-5} \sim 10^{-6}$mbar. p_i may not have been at the optimum value.

ICANS-XI International Collaboration on Advanced Neutron Sources
KEK, Tsukuba, October 22-26, 1990

OPTIMIZATION of the Transmission of a Double-Trumpet Neutron Beam Compressor

R. E. Lechner and F. Mezei
Hahn-Meitner-Institut, Postf.390128,D-1000 Berlin 39

ABSTRACT
With the aid of the Monte-Carlo method the transmission of a super-mirror coated double-trumpet beam compressor and its intensity distribution over the beam cross-section are studied numerically. The purpose of these calculations is the optimization of the geometrical dimensions of the neutron guide section before the sample,in order to obtain maximum neutron flux at the sample position. The transmission and the optimized parameter values are found to be wavelength-dependent. As a consequence we propose a variable compressor geometry.

I. INTRODUCTION

In a contribution to the ICANS-X conference, concerning neutron beam compressors for pulse widthreduction in a time-of-flight spectrometer, the use of a "double-trumpet" neutron guide arrangement was proposed as a useful component relevant for intensity and resolution optimization /1/. Such a "bottleneck" arrangement is a sequence of neutron guide sections, consisting of a conventional straight guide (with parallel walls) followed by a converging guide section (CGS) just before the last chopper of the spectrometer and a diverging guide section (DGS) just after this chopper. The latter two sections are supermirror (SM) coated, in order to compensate for the inclination of the double-trumpet side-walls.
The total transmission T of the double-trumpet (DT) is defined by the number of neutrons transmitted through its exit, divided by the number of neutrons entering into the DT. Even more important than T for practical purposes is the transmission T_s through a hypothetical window with dimensions corresponding to the sample size, located in a plane perpendicular to the incident neutron beam at the sample position. Both quantities depend on a number of parameters, such as mechanical dimensions of the double-trumpet, reflectivities, critical angle γ_c of the conventional guide section, maximum reflection angle γ_{cc} of the SM coated sections and neutron wavelength λ. The quantity T_s refers to a position in the neutron beam located after the double-trumpet exit at some finite distance from the latter. Therefore in addition to transmission it is also a measure of the DT's focusing properties and depends on the window (i.e.sample) size. The optimization of the double-trumpet leads to a certain choice of mechanical dimensions. This is necessarily a compromise, since beyond intensity and resolution considerations a number of

boundary conditions imposed by space and budget limitations have to be taken into account.
In the present paper we report on Monte-Carlo calculations of the transmission and focusing properties of double-trumpets. They were carried out, in order to optimize this component as a neutron beam compressor to be used in the multi-chopper time-of-flight spectrometer "NEAT" at the Hahn-Meitner-Institut in Berlin. The calculations are limited to the horizontal plane, since only a horizontal but no vertical beam compression is intended.

II. COMPARISON of CGS and DT Transmissions

An analytical result for the flux gain at the exit of a SM coated CGS, following a straight guide (see schematic drawing of Fig. 1a) was given by another author /2/. For our purpose this result is most conveniently discussed in terms of the total transmission T of the CGS, since we wish to obtain information on the intensity loss due to the use of this type of bottleneck in the neutron beam. Let us define the real-space reduction factor $\beta = B/b$ (see Fig. 1a) and the divergence quotient $m = \gamma_{cc}/\gamma_c$ (ratio of the SM limiting reflection angle γ_{cc} to the straight guide critical reflection angle γ_c).The transmission curve as a function of the neutron wavelength - according to ref. /2/ - displays oscillations which are periodic for $\beta = m$. Our Monte-Carlo calculations of the total transmission T of a CGS confirm this result: This is shown in Fig.2 where the open circles indicate calculated values; the full line is drawn to guide the eye. Here the realistic values $\beta = m = 2$ have been chosen. In order to make the results more transparent, the reflectivities have been set equal to 1 for reflection angles $\alpha \leq \gamma_c$ in the straight guide and for $\alpha \leq \gamma_{cc}$ in the CGS. Under these circumstances the transmission of the CGS shows periodic oscillations with maxima equal to 1 (i.e. <u>all</u> neutrons are transmitted) for values of $k = \psi/\gamma_c = 1, 1/3, 1/5, 1/7$, etc., where ψ is the CGS inclination angle (see Fig. 1a). This angle was chosen equal to γ_c (at $\lambda = 2$Å) for the natural isotope mixture of Ni in this particular calculation. As a consequence the transmission maxima are obtained at wavelength values of $\lambda = 2(2N-1)$Å, $N = 1,2,3,\ldots$ .The maxima are necessarily separated by dips in T, but T is nowhere smaller than 0.92, except for $\lambda < 2$Å. There, due to the particular choice of the inclination angle ψ, the contribution to T of neutrons reflected within the CGS rapidly vanishes, so that T approaches its limiting value, which is 0.5 at $\lambda = 0$.
Although this result is encouraging, the simple CGS arrangement is not the best choice of a beam compressor for the present purpose. It has been suggested, that a CGS-DGS double-trumpet arrangement should be used instead because of its better focusing properties. This type of beam compressor has the same total transmission as the CGS alone, whether the DGS is truncated (Fig. 1c) or fully symmetrical (Fig. 1d), if both guide sections have the same inclination angle and the reflectivities are equal to 1 /1/. Therefore the calculated T values of Fig. 2 (circles) are valid for all four cases (a to d) of Fig. 1. This is quite evident. What we really are interested in, however, is the transmission through a window (representing the sample) at a certain distance from the exit of the neutron beam compressor. This is where the advantageous focusing properties of a double-trumpet become important. Infact the four cases of Fig. 1 are quite different from each-other in this respect. The Monte-Carlo calculation of T_s, carried out for a guide width of 2B = 30mm

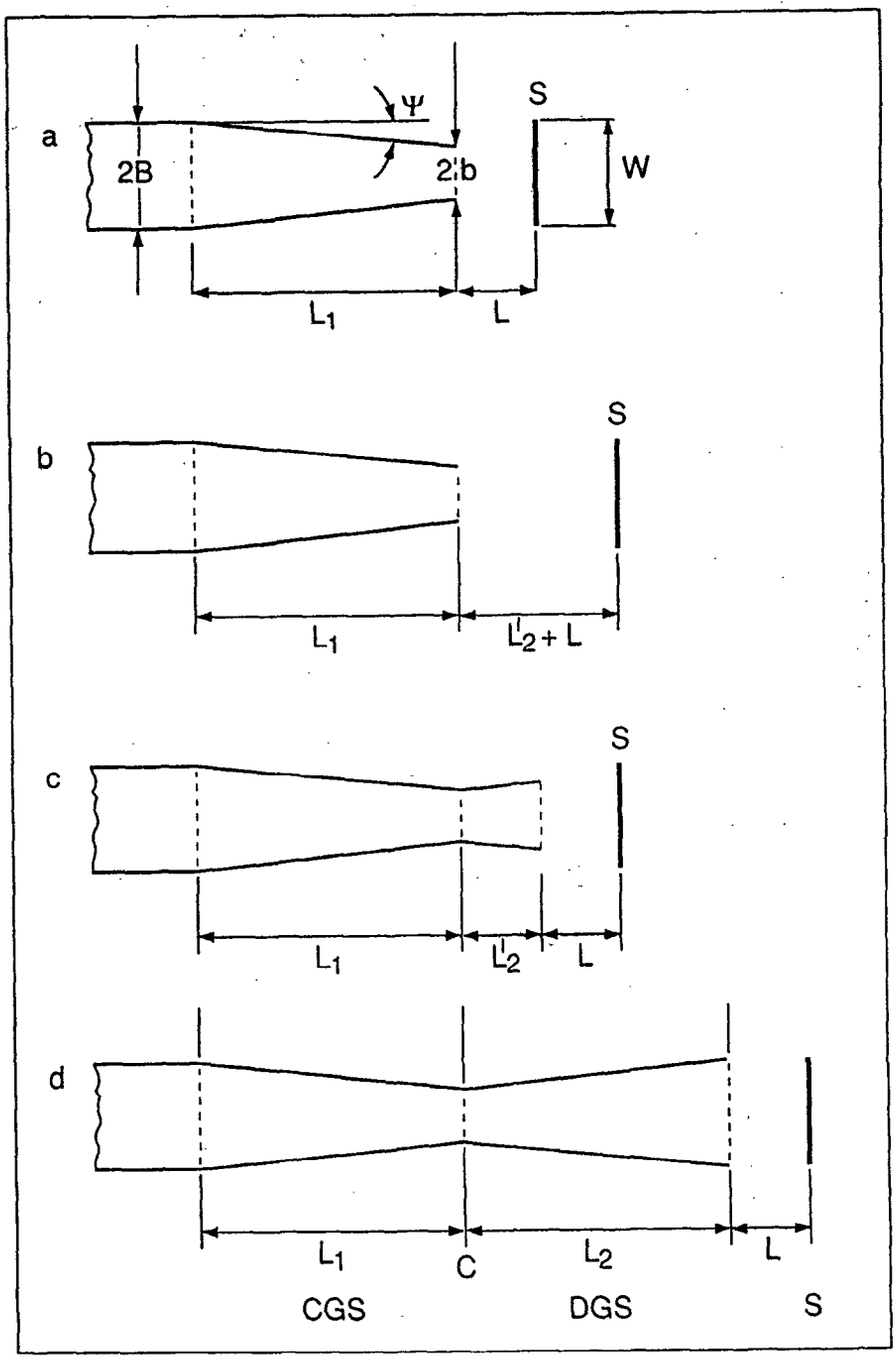

Fig. 1

Neutron beam compressor arrangements (shown schematically) in the neighbourhood of the chopper (chopper location indicated by C), following a straight neutron guide (G): G is followed by an "anti-trumpet" type converging guide section (CGS) of length L_1, width 2B at its entrance, width 2b at its exit.

a) sample S is placed at distance L from CGS exit.
b) sample at distance (L_2'+L) from CGS exit.
c) a "trumpet" type diverging guide section (DGS) of length L_2' is added after the CGS, thus forming an asymmetric double-trumpet; sample is at same location as in b), i.e. at distance L from exit.
d) symmetric double-trumpet arrangement, S at distance L from exit.

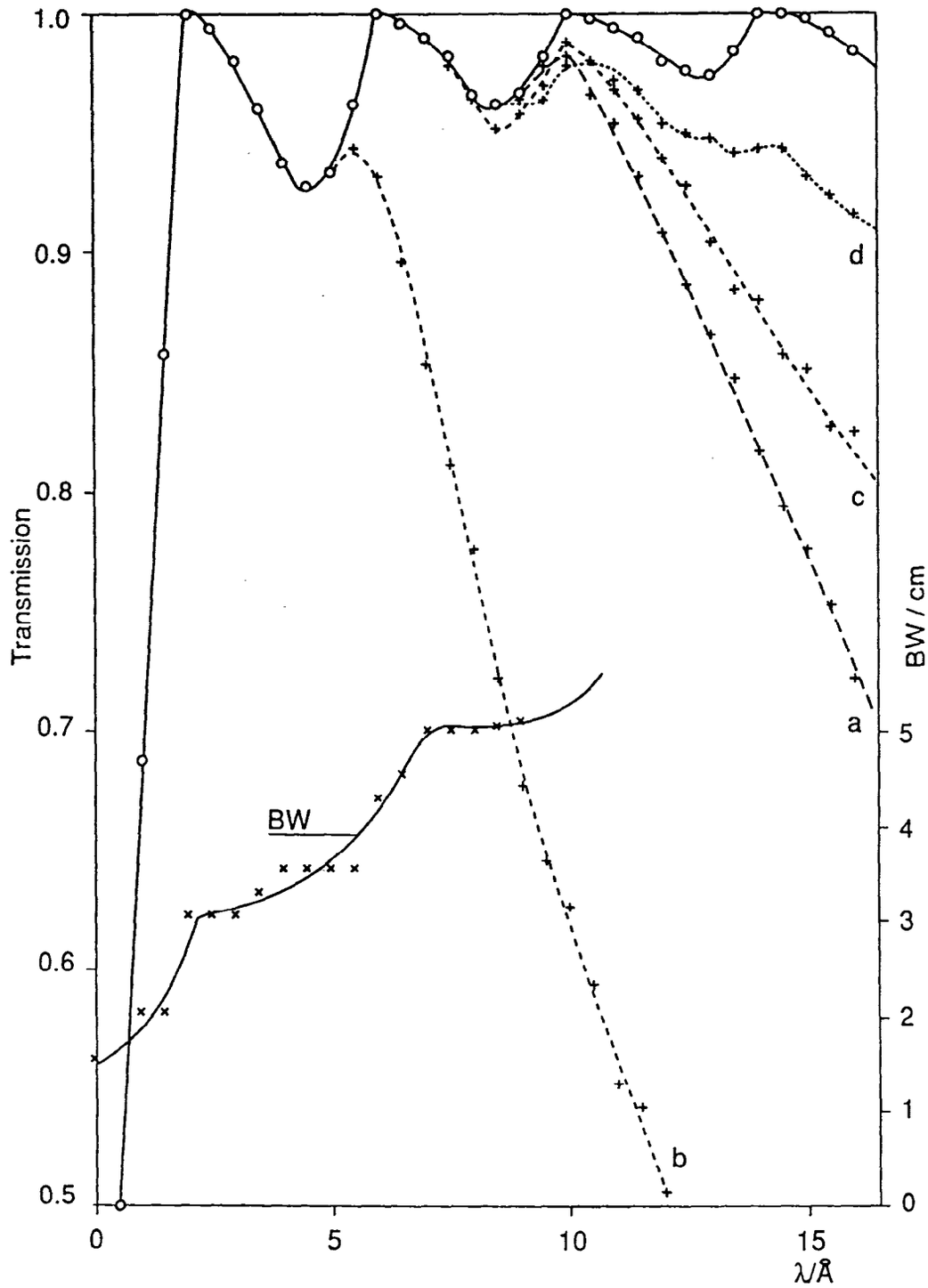

Fig. 2

Neutron beam compressor transmissions from Monte-Carlo calculations as a function of the neutron wavelength λ for the four different arrangements, a to d, of Fig. 1. Circles: total transmission (same for all four arrangements). Crosses (+): transmission through a window (width w = 50mm) at the sample location. Also shown is the calculated "focal" beam width (BW) at the sample position for case a); lines are drawn to guide the eye. Total reflection and supermirror reflectivities have been set equal to 1. Parameter values: $L_1=L_2=2143$, $L_2'=550$, L=615, 2B=30, 2b=15 (units: mm). The parallel-walled neutron guide is coated with the natural Ni isotope mixture (critical angle of total reflection γ_c), the CGS-DGS element is supermirror coated (cut-off reflection angle $\gamma_{cc} = 2\gamma_c$).

and a sample width of w = 50mm, confirms this. It shows that the symmetrical double-trumpet clearly has the best focusing properties: T_s only starts to deviate slightly from the total transmission curve above $\lambda \sim 9$Å; but even at $\lambda = 16$Å the loss in transmission is only about 7% (Fig.2, curve d; crosses indicate calculated values, dashed lines are drawn to guide the eye). If the DGS is truncated, T_s decreases somewhat faster with increasing λ. But even for an appreciable truncation, e.g. reducing the DGS to about 25% of its original length, the loss in transmission does not rise to more than about 17% at $\lambda = 16$Å (Fig.2, curve c). This is certainly much better than the case, where the DGS is completely omitted, while the sample is kept at the same position. In this case T_s starts to deviate from T appreciably already at $\lambda \sim 6$Å and decreases very rapidly with increasing wavelength (Fig.2, curve b). In summary the curves of Fig. 2 suggest, that the distance from the guide exit to the sample roughly determines the λ- limit where T_s starts to deviate from T, while the slope of the decreasing T_s curve is governed by the length of the DGS.
At this point we should like to mention, that the final geometrical parameter values (lengths, widths, angles) which we have actually chosen for the construction of the double-trumpet to be used in the spectrometer NEAT, were not only influenced by the results of the Monte-Carlo calculations but to a large extent also by instrument "boundary conditions". These final values are very close to the following numbers used in the calculations which resulted in curve c of Fig.2 :

L_1 = 2143mm; length of CGS.
L_2' = 550mm; maximum possible DGS length (it has to end before the wall of the sample chamber).
L = 615mm; remaining distance to the sample position.
$L_2' + L$ = 1165mm; distance from the CGS exit (location of the chopper) to the sample.

It should be noted, that the cases a) and d) of Fig.1 (corresponding to curves a) and d) of Fig.2) can not be realized in the spectrometer NEAT because of the boundary conditions (due to resolution considerations and space requirements) which essentially determine the distance from the CGS exit to the sample. The curves a) and d) were merely calculated for the purpose of comparison.
Another result is seen in Fig.2. As an example the numbers calculated for case a) of Fig.1 were used here. This concerns the reason for the decrease of the transmission T_s, as the wavelength increases beyond $\lambda \sim 9$Å. This is elucidated by the calculation of the width of the "illuminated" surface on the plane perpendicular to the neutron beam at the sample position. This width starts to be larger than the selected sample "window" near $\lambda \sim 9$Å (curve BW in Fig.2).

III. DEPENDENCE of the Transmissions on the Length of the CGS and on the Reflectivities

While the instrument boundary conditions are rather stringent regarding the choice of the values of B, b, L and L'_2, the range of possible values of the length L_1 of the CGS is fairly large in the case of NEAT. Therefore the transmissions of a double-trumpet were studied numerically as a function of L_1. In these calculations all other parameters, including the reflectivities and guide coatings were the same as in the case of curve c in Fig.2 (see Section II). The results are shown in Fig.3a, b and c for L_1 = 4286mm, 2143mm

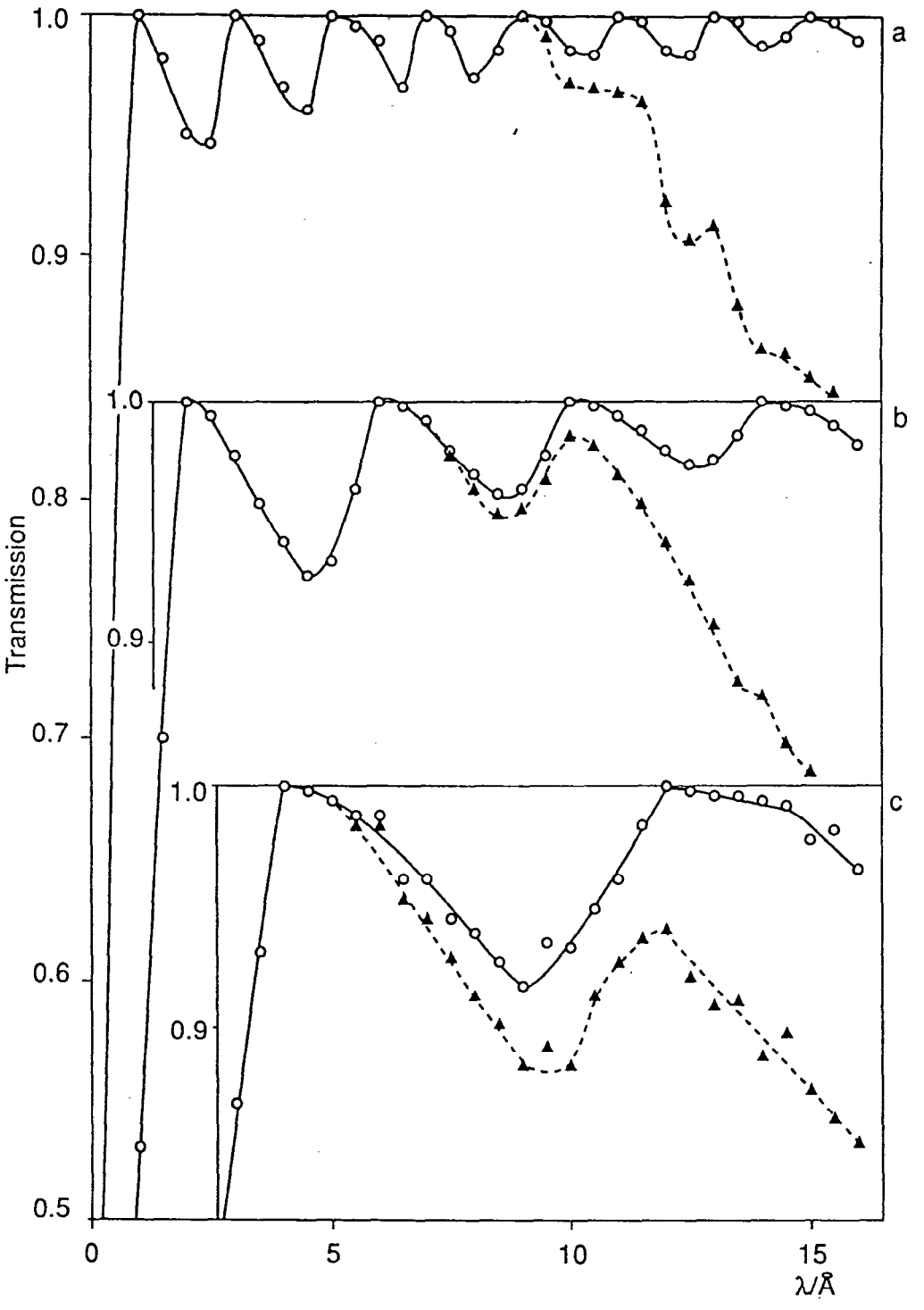

Fig. 3

Total transmissions (circles) and transmissions through a window at the sample position (triangles) for three double-trumpet arrangements differring in the length L_1 of the CGS: a) L_1 = 4286mm, b) L_1 = 2143mm, c) L_1 = 1071.5mm. All other parameters are the same in the three cases: L'_2 = 550mm, L = 615mm, 2B = 30mm, 2b = 15mm, w = 50mm; reflectivities and guide coatings are the same as in Fig.2.

and 1071.5mm, respectively. The values of T are indicated by circles, those of T_s by triangles. The following observations are made: i) the period of oscillation of T as a function of the neutron wavelength λ is inversely proportional to the length L_1 of the CGS.

The transmission maxima are obtained at wavelength values of λ = (2N-1)Å, 2(2N-1)Å and 4(2N-1)Å in Fig.3a, b and c, respectively. This is, because the CGS (and DGS) inclination angles ψ were chosen such, that $\psi = \gamma_c$ (at λ = 1Å, 2Å and 4Å, respectively).
ii) the amplitude of the oscillation increases with decreasing L_1.
iii) the λ-limit, where T_s starts to deviate from T, decreases with L_1.
iv) the transmission "gap" at low wavelengths increases, as L_1 decreases.
All these features would favour a maximization of the length L_1. A conclusion can however only be drawn, when the ideal reflectivity values (so far set equal to 1) are replaced by realistic ones. Therefore the next step in this study was a calculation of the transmissions for various combinations of reflectivity values in the straight neutron guide and in the SM coated double-trumpet. The following assumptions concerning the reflectivities were made in these calculations: Firstly, the reflectivity in the total reflection region (RTR) was assumed to be constant in the whole region. Secondly, in the supermirror region, $\gamma_c \leq \alpha \leq \gamma_{cc}$, the reflectivity was assumed to be linearly decreasing towards a minimum value at γ_{cc}, the "reflectivity at maximum angle" (RMA). Finally, for $\alpha > \gamma_{cc}$ the reflectivity was set equal to zero.
In Fig.4 we compare as an example the calculated total transmission values (curve a) for a double-trumpet with the same specifications as used in Fig.3a (L_1 = 4286mm, L'_2 = 550mm, 2B = 30mm, 2b = 15mm, RTR = 1, RMA = 1) to three curves corresponding to different combinations of the RTR and the RMA. In the case of the curves b and d a realistic value of 0.98 was chosen for the RTR, whereas for the curve c this was set equal to 1. The RMA was set equal to 0.98 in the case of curve b, whereas for the curves c and d somewhat pessimistic values (0.75 and 0.735, respectively) were used. As expected the total transmission decreases with increasing wavelength, when the reflectivities are smaller than 1. This is due to the fact, that the number of reflections increases with λ. In addition it is observed, that the oscillations of T with λ appear to be damped in the cases, where the RMA is appreciably smaller than 1 (curves c and d).
We wish to conclude this discussion by comparing the transmissions, T and T_s, of the double-trumpet with those of a "normal" parallel-walled neutron guide. So far in all our calculations a natural Ni isotope mixture coating was assumed for the parallel guide section. For the SM coated DT-part of the arrangement $\gamma_{cc} = 2\gamma_c$(Ni-nat.) was used. In the actual case of the NEAT spectrometer it was however decided, that neutrons will be supplied by a parallel-walled guide coated with the isotope Ni-58, which has a γ_c-value larger by 20% than that of Ni-nat. The CGS-DGS sections will be coated such, that the γ_{cc}-value is the same as mentioned above (i.e. twice the γ_c-value of Ni-nat.). Thus $\gamma_c > \gamma_{cc}/2$ and the divergence quotient m is then smaller than 2. As a consequence the transmissions T and T_s are expected to be generally somewhat lower, than they would be for m = 2, if otherwise identical parameter values are used. In Fig.5 we show the T (open circles) and T_s (full circles) values calculated under such conditions for a double-trumpet with L_1 = 2143mm and L'_2 = 550mm. The values of B,b,w and L are the same as the ones used for the calculations of Fig.2. Realistic numbers were chosen for the reflectivities: RTR = 0.98 and RMA = 0.833. For comparison T and T_s were also calculated for a straight parallel-walled guide of the same total length (L_1+L'_2 = 2693mm) and with the same coating as

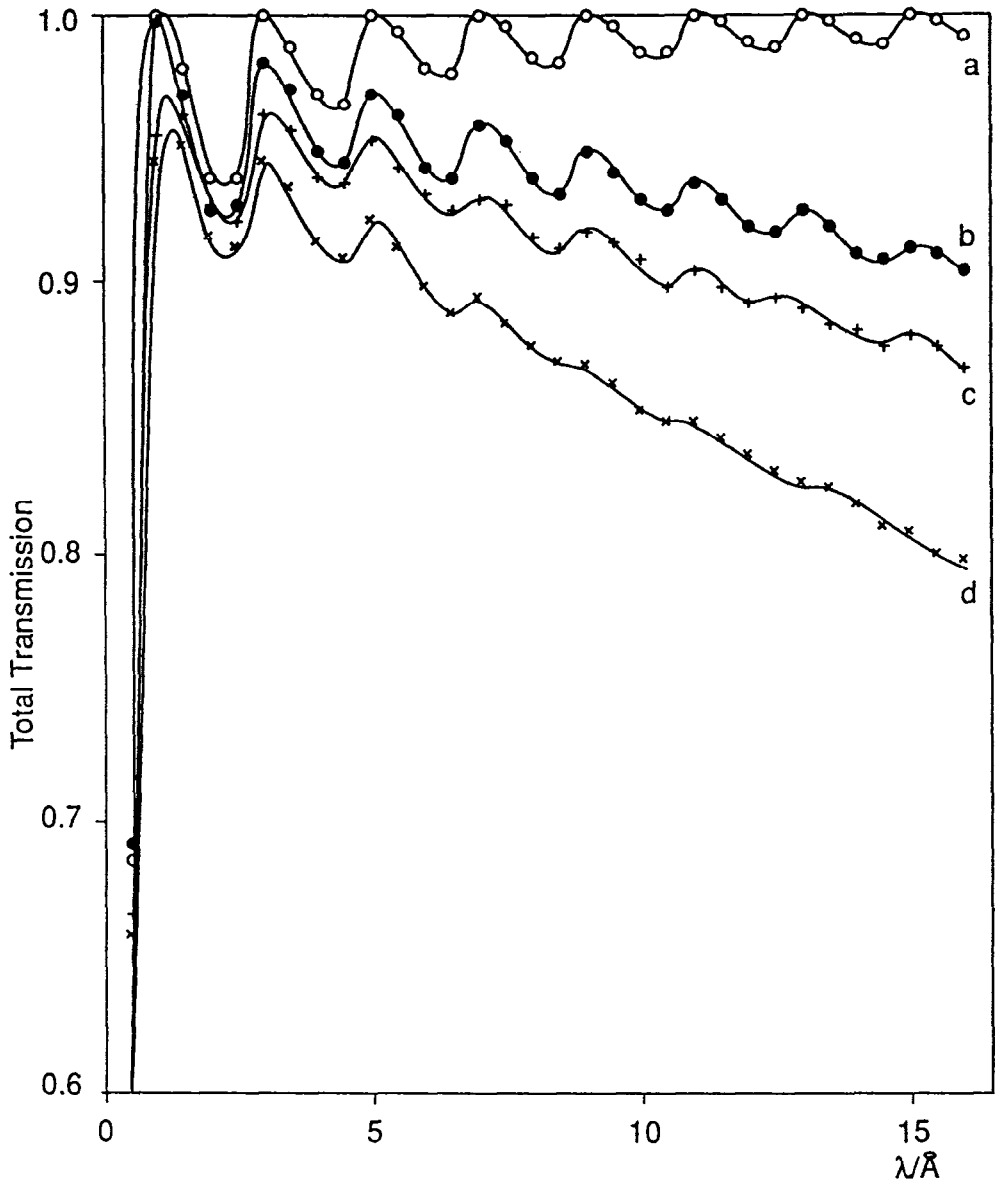

Fig. 4

Total transmission for various combinations of reflectivity values in a double-trumpet arrangement with the following dimensions: L_1 = 4286mm, L'_2 = 550mm, 2B = 30mm, 2b = 15mm. The reflectivity is assumed to be constant for reflection angles $\alpha \leq \gamma_c$, but to decrease linearly in the region $\gamma_c < \alpha \leq \gamma_{cc}$ down to a minimum value at γ_{cc}. The definitions of γ_c and γ_{cc} and the guide coatings are the same as in the calculations for Fig.2.

a) Reflectivity in the total reflection region (RTR) = 1.
   Reflectivity at the maximum angle γ_{cc} (RMA) = 1.
b) RTR = 0.98, RMA = 0.98
c) RTR = 1, RMA = 0.75
d) RTR = 0.98, RMA = 0.735

the DT: curves a and b, respectively, in Fig.5. It is seen that the transmissions of the DT are generally lower by roughly 10 to 20%, in the λ-range from 2.5 to 16Å, than the corresponding transmissions of the parallel-walled guide. Nevertheless - because of the beam compressor action - the flux gain factor of the double-trumpet

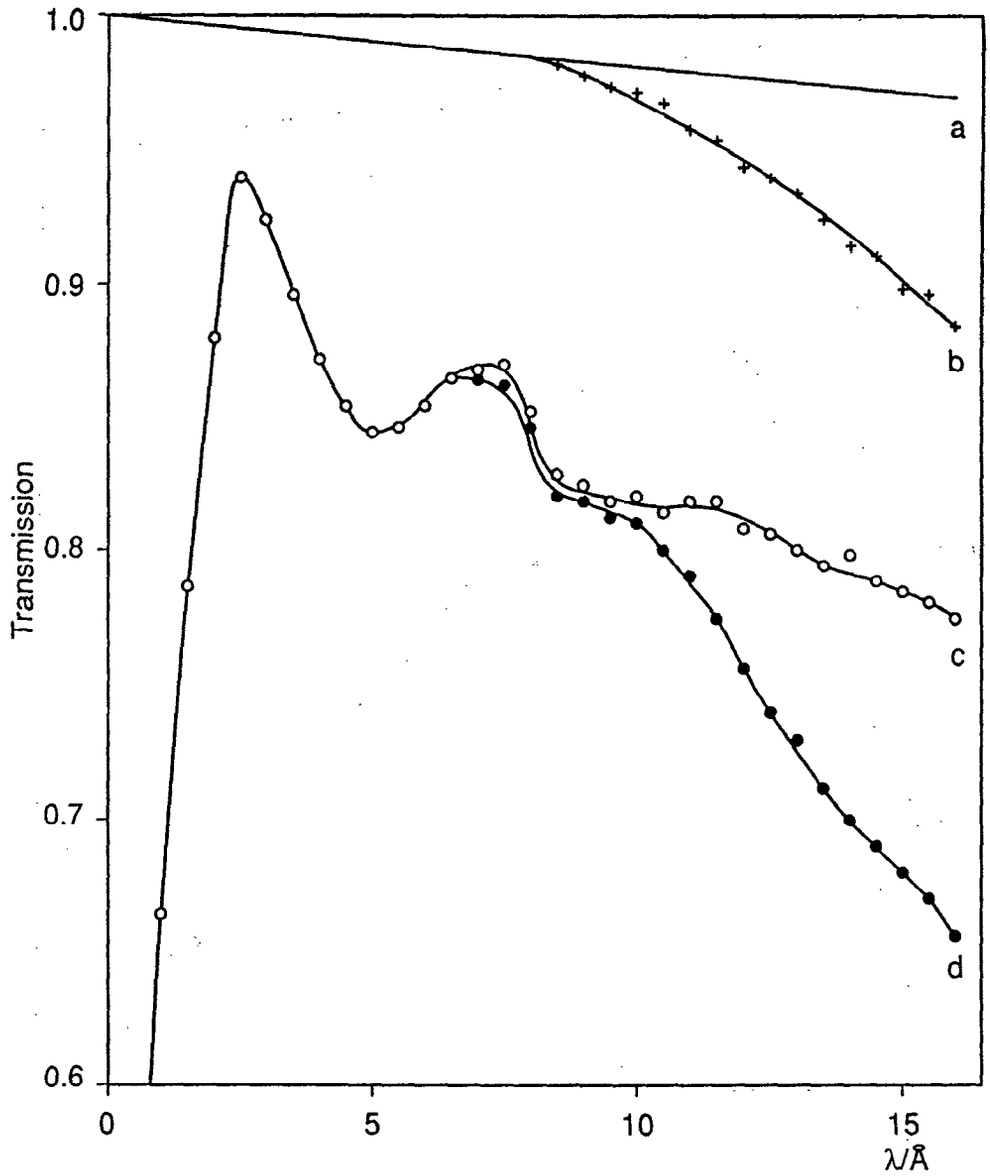

Fig. 5

Comparison of transmission properties of a straight guide (upper 2 curves) with those of a double-trumpet (lower 2 curves) of the same total length, $(L_1+L'_2)$ = (2143 + 550)mm; the parameter values B, b, w and L are the same as in Fig.2. The arrangement is supermirror coated with γ_{cc} = $2\gamma_c$(Ni-nat.) in both cases, whereas the incoming straight guide is coated with Ni-58. Note that γ_c(Ni-58)~ $1.2\gamma_c$(Ni-nat.). The curves a and c correspond to total transmission; the curves b and d show the transmissions through a window of width w at a distance L from the exit of the guide arrangement (sample position). Realistic values of the reflectivities were used: RTR = 0.98, RMA = 0.833 .

over the parallel guide (which is twice the transmission for ß= 2) lies between 1.8 and 1.6 in the whole λ-range mentioned above, at the exit of the CGS.
The effect of changing the length of the CGS can be judged from Fig.6, where results of calculations analogous to those of Fig.5 are shown. Here L_1= 4286mm was chosen; all other parameter values were the same as in Fig.5. It is quite evident from these figures,

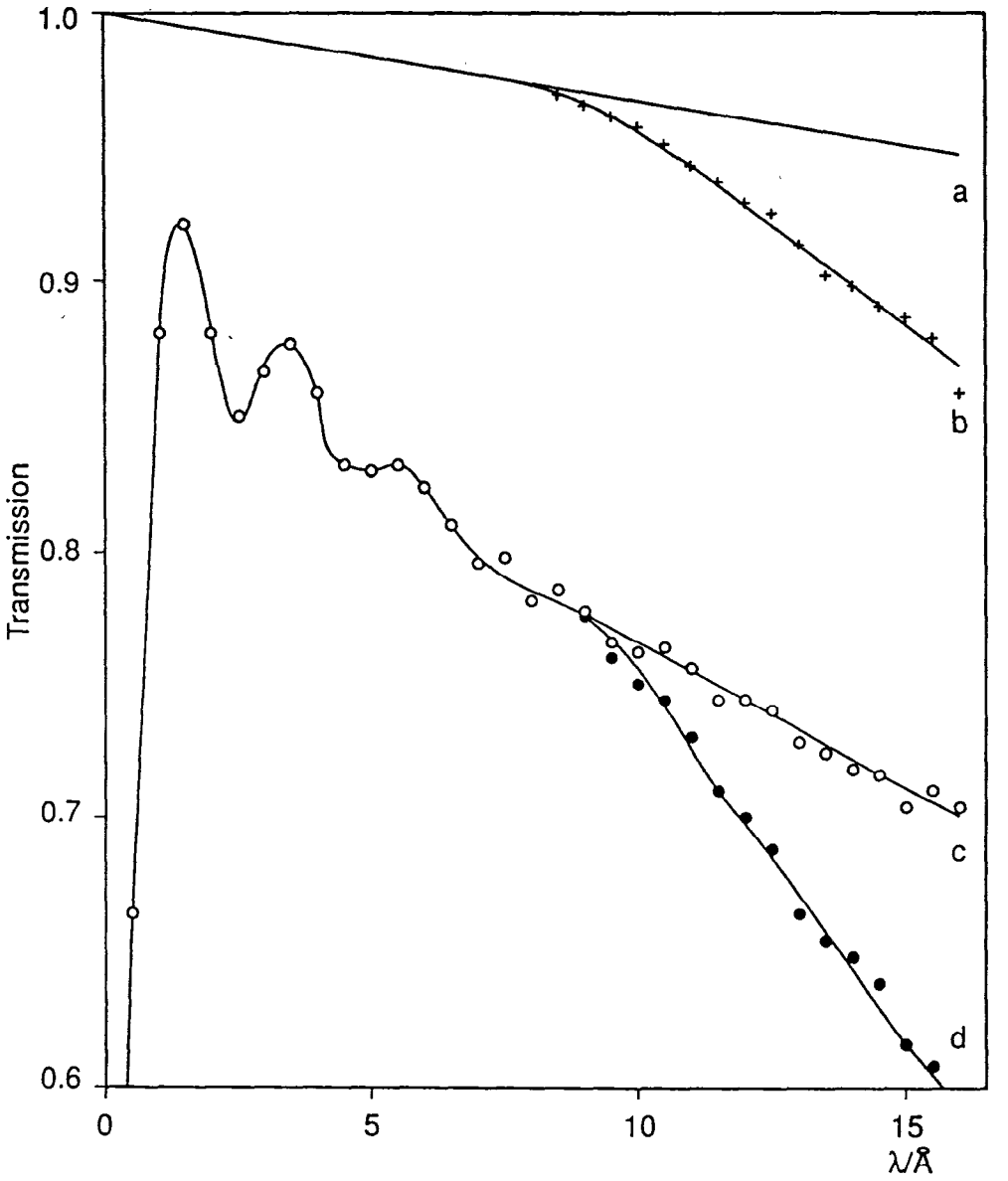

Fig. 6

Comparison of straight guide and double-trumpet as in Fig.5, except that L_1 was doubled: L_1= 4286mm.

that the transmission values of the longer DT are generally lower than those of the shorter one. It seems obvious, that this must be due to a larger number of reflections occurring within the longer flight path. In order to make this comparison completely fair, the attenuating effect of a parallel guide section before the shorter DT, which would compensate for the difference in length of the two DTs, should be added. Although this was not taken into account in Fig.5, it is easy to see by inspection of curves a and b, that the inclusion of this effect would not change the qualitative result of this comparison. Therefore we have chosen the shorter one of the two double-trumpets as a beam compressor to be built for the time-of-flight spectrometer NEAT.
Finally we would like to point out, that it is also possible - in principle - to optimize the construction of a double-trumpet with respect to the positions of oscillation maxima of the transmission

as a function of λ. If the inclination angle ψ of the double-trumpet side-walls is made variable, in general one of the maxima of T (or T_s) may be shifted into the λ-value selected for the experiment, in order to maximize the intensity. A double-trumpet constructed in this way may also be transformed without difficulty into a parallel-walled guide for experiments, where this is an advantage.

References

/1/ R. E. Lechner, in "Advanced Neutron Sources 1988", ed. D. K. Hyer (Institute of Physics Conf. Series No.97, Institute of Physics, Bristol and New York), page 843(1989).

/2/ I. S. Anderson, in "Thin Film Neutron Optical Devices", Proc. SPIE 983 (1988).

Q(H.Tietze): What is the cross-section shape of the double trumpet used and what about an influence of a non-circular cross-section shape on the transmission and performance of the device with respect to an isotopic circular cross-section?

A(R.E.Lechner): The cross-section is rectangular. Because of the purpose of the double-trumpet (pulse-width reduction of a disk-chopper) it has to be rectangular. For other purposes (e.g. purely spatial focusing) a circular cross-section could be useful. The transmission could be calculated in an analogous way; the problem is two-dimensional, whereas my calculation is in one dimension only: the flux is calculated in a horizontal axis perpendicular to the beam.

ICANS-XI International Collaboration on Advanced Neutron Sources
KEK, Tsukuba, October 22-26, 1990

Summary of Instrument Workshop on Polarizers and Thin Film Multilayer Devices

W G Williams
ISIS Science Division
Rutherford Appleton Laboratory
Chilton, Didcot, OX11 OQX
United Kingdom

The topics discussed in this session were: the calculation and optimisation of the performance of multilayer polarizers (J B Hayter), the design and performance of a double reflection multilayer polarising monochromator for cold neutrons (T. Ebisawa et al), an experimental investigation of the growth of multilayers (P B Böni et al), the optimisation of the transmission of a double-trumpet neutron beam compressor (R E Lechner and F Mezei), and plans for polarisation work at ISIS (A D Taylor).

The paper by J B Hayter stressed that it is now straightforward to calculate the response or reflectivity of any multilayer structure such as a supermirror. A discrete thin-film multilayer (DTFM) design has been proposed (Hayter and Mook) which uses fewer layers to provide the same response as earlier designs based on continuum arguments. The DTFM also overcomes the reflectivity loss near the critical edge which was a characteristic of earlier supermirror designs. Although excellent supermirrors, with reflectivities extending to $\theta/\theta c(Ni) > 3$ can now be designed and fabricated, it is less straightforward to design mirror-based devices in real (divergent beam) applications. A stacked device, using mirrors with different bandwidths at strategic positions in the structure, has been shown to give a much improved handling of divergent beams compared with a stacked structure containing one type of supermirror.

T. Ebisawa et al presented results on a compact double-reflection polarizing monochromator for cold neutrons. The device contains two stacks of constant layer-spacing $(Fe_{50}Co_{50})$:V bilayers deposited on Si-wafer substrates, and these stacks are inclined to each other at an angle 2θ where θ is the mean reflection angle of the two reflections. The length of the device is only 62mm, and it gives an excellent performance at a neutron wavelength $\lambda = 5.4$ Å : neutron polarization ~98%, neutron yield ~69%.

Although thin film multilayer structures have been fabricated for neutron applications for the past 15 years, there have been few systematic studies of the processes involved in the growth of these structures. Böni et al have now applied the techniques of neutron reflectometry, Auger depth profiling and transmission electron microscopy to investigate the parameters important to the fabrication of constant-spacing Ni/Ti bilayers. They were able to make several important

conclusions: high rate sputtered samples were superior to both low rate sputtered samples and evaporated samples, and also the best samples were prepared at low pressure. Their highest reflectivity samples contained amorphous Ti layers and small Ni grain sizes, and they speculated that the ideal multilayer should consist only of amorphous layers.

In the final paper on multilayer devices, Lechner and Mezei showed how a combination of converging and diverging neutron guides fabricated from supermirrors could be used to optimise the flux at the sample position is a double chopper neutron spectrometer. The arrangement is called a double-trumpet beam compressor, and the geometrical dimensions (ie lengths and inclination angles) were optimised using a Monte Carlo procedure for a supermirror with $\theta/\theta c(Ni) = 2$. The transmission and optimised parameters were found to be wavelength dependent over the wavelength range of interest (~2-15 Å), therefore these authors proposed to construct a variable compressor geometry.

The angular range of the reflectivity of supermirrors has meant that most applications up to now have been in the cold and thermal neutron ranges, where these angles are well-matched to the beam divergences normally required in the scattering instruments. Improved supermirror performance has meant however that the concomitant larger beam divergence cannot always be used, particular when one considers the design of real devices (see Hayter). It is perhaps now opportune to exploit the improved supermirror performance in hot and epithermal neutron instruments, where the angular ranges of the reflections are correspondingly smaller.

The paper by A D Taylor on plans for polarization work at ISIS was an exception for the session in that it did not involve an optical device. This concerned the use of a polarised $SmCo_5$ filter in a test experiment to polarize the monochromatic beam in a chopper spectrometer. Previous measurements at ISIS have demonstrated that the selective spin absorption principle of the $SmCo_5$ filter works well in low-flux white beams (POLARIS measurements with ISIS operating at ~3μA), but that the beam heating was prohibitively large at full ISIS current. With the filter placed behind a monochromating chopper, the beam flux is reduced by some 3 orders of magnitude, and this polarizing method should easily be viable. Tests are scheduled for November 1990.

ICANS-XI International Collaboration on Advanced Neutron Sources
KEK, Tsukuba, October 22-26, 1990

Area detector for small angle neutron scattering at KUR

Y. Maeda, M. Sugiyama and S. Uehara
Research Reactor Institute, Kyoto University,
Kumatori-cho, Sennan-gun, Osaka, 590-04, Japan

ABSTRACT

The two-dimensional position-sensitive neutron detector has been developed for the small angle neutron scattering experiments at KURRI. The construction and the performance of the detector are described.

I. INTRODUCTION

Position-sensitive detectors (PSDs) are being widely used in neutron beam experiments. Especially, a large area PSD is essential for small angle neutron scattering (SANS) experiments. Research Reactor Institute, Kyoto University is engaged in the development of PSDs for use at SANS which will be situated at a cold neutron guide of Kyoto University Reactor (KUR). A variety of neutron PSDs have been developed and well used in neutron research centers, such as ILL, BNL, ORNL and Risø.[1,2] Most of them are ^{3}He-filled multi-wire proportional chambers (MWPCs) for the use at steady neutron sources. The important points in our design of the PSD are the best compromise of accumulated knowledge on the performance of detectors and the easiness of manufacture and maintenance of PSDs.

II. CONSTRUCTION

A 51x51 cm^2 detector (Type D) was designed for the use at SANS. In order to check the performance of the MWPC, we made a small prototype PSD (Type A), in which the electrode construction of the MWPC is the same as the large detector. The characteristics of two PSDs are given in Table, and their electrode configurations are shown in Fig.1. The MWPC electrodes of Au-coated tungsten wires and an aluminized Mylar sheet are kept under tension by being fixed to frames of glass epoxy resin (G10). Each MWPC is installed in an aluminium high pressure vessel. In Type A PSD a flat entrance window is used. In Type D PSD, however, an additional spherical dome filled with ^{4}He at the same pressure with the counter gas, is attached on the flat window, preventing deformations of the vessel and

Characteristics of Two Neutron Detectors

	Type A	Type D
Active Area [cm²]	21x21	51x51
Resolution [pixels]	56x56	64x64
Pixel Size [mmxmm]	3.75x3.75	8x8
Case Material	Aluminium	Aluminium
Window	10mm Al.	14mm Al. (4mm dome plus 10mm diaphram)
Active Depth [cm]	2.6	2.6
Anode	20μ Au-coated W wires spacing 2.5mm	20μ Au-coated W wires spacing 4.0mm
Readouts	50μ Au-coated W wires spacing 1.25mm	50μ Au-coated W wires spacing 2.0mm
Cathodes	Alminized Mylar plus 50μ Au-coated W wires	50μ Au-coated W wires
Wire Plane Spacing [mm]	6.5	6.5
Fill Gas	$^3He-Ar-CO_2$	$^3He-Ar-CO_2$
Gas Pressure [Pa]	max. $4.3x10^5$	max. $7x10^5$
Gas Purifier	540 ℃ heated Ca-shot	540 ℃ heated Ca-shot

reducing the thickness of windows which cause neutron scattering. There are two ports for gas inlet and circulation and electrical feed-throughs on the backside of PSDs. The preamplifiers and the gas purifier are connected with them.

As shown in Fig.1, the electrode arrangement of the MWPCs is symmetrical and two orthogonal readout grids are used for X- and Y-position readout by measuring induced charges, respectively. The readout grids are kept on the ground potential. The regions between the grid and the cathode plane are regarded as drift gaps, increasing the neutron detection efficiency with rather low anode voltage. The readout electrodes are strips, connected in groups of two or three wires in Type A and four wires in Type D. The various position readout techniques are proposed for two-dimensional PSDs. Among them, we intended to use the "strip-per-strip" encoding method and compared it with the delay-line method.

III. PERFORMANCE

1)Choice of counter gas

From the easiness of handling, the mixture of ^3He and Ar was used as the main component of the counter gas. The selection of the quenching gas was performed by using a cylindrical proportional counter, and the mixture of ^3He50%-Ar47.5%-$CO_2$2.5% was determined to be the best for our

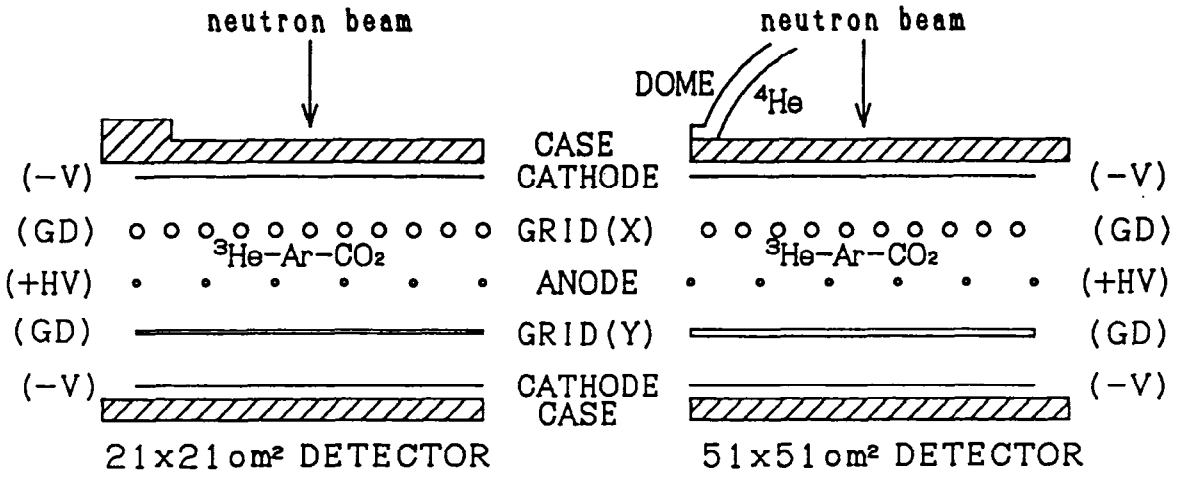

Fig.1. Electrode configurations of two position-sensitive detectors (Type A and Type D).

PSD. The filling of 4.5×10^5 Pa counter gas into our MWPC gives an efficiency of 96% for 4 Å neutron.

2)Gas purification

As a large quantity of glass epoxy resin is used in the electrode fixing frame of our MWPCs, it is inevitable to remove water and oxygen from the counter gas. The purification system containing Ca metal shots is heated to 540°C and the counter gas is circulated by convection and purified. Enough purification is achieved with 24 hrs operation.

3)Characteristics of MWPC

With the PSD (Type A) filled 3.5×10^5 Pa ^{3}He50%-Ar47.5%-CO_2 2.5% the characteristics of the MWPC was checked in the thermal neutron beams from an Ni guide tube. Figure 2 a) shows the pulse height spectrum obtained on the anode of the MWPC. The best performance was obtained by applying +2500 V on the anode and -500 V on the cathodes. The resolution of the sum peak is 13%, and the neutron signal

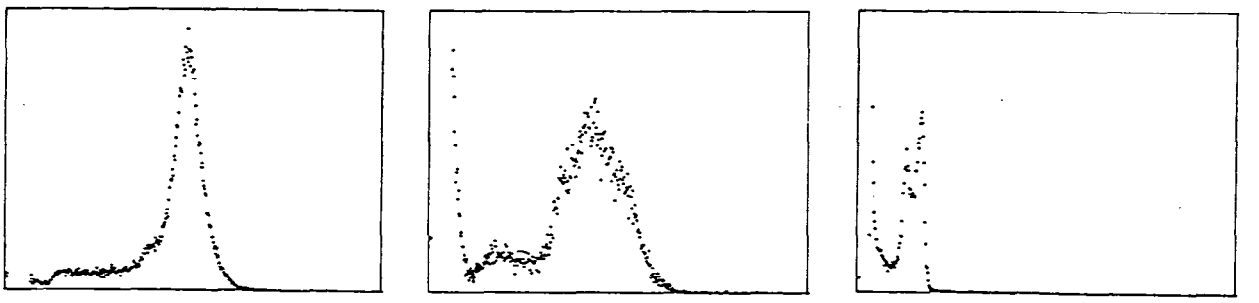

a) b) c)

Fig.2. Pulse height spectra for neutrons. a) Total anode signal, b) signal induced on the grid strip just in the beam line, and c) signal induced on the grid strip separated by five strips from the beam line.

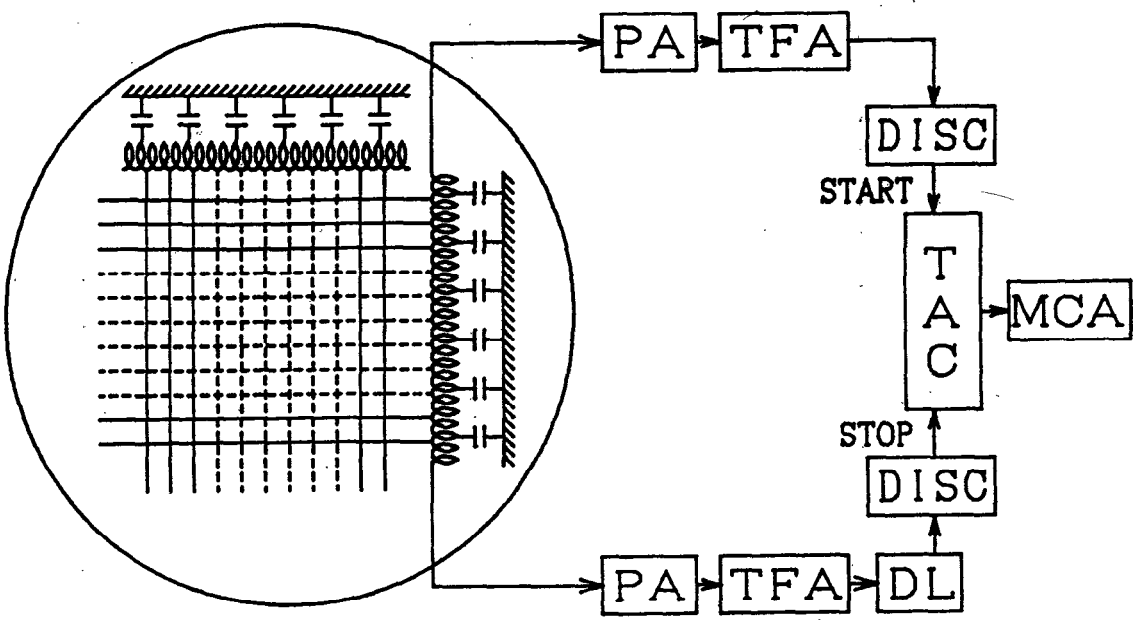

Fig.3. A block diagram of the position decoding using the delay-line.

is easily discriminated from the background noise. On the readout grids the signals are distributed over fifteen strips, and the pulse height spectra are well separated from noise level, as shown in Fig.2 b) and c). Therefore, the position determination is easily made by using "stripper-strip" encoding method. Under the this condition the MWPC is operated with an avalanche charge of $\sim 5 \times 10^6$ electrons corresponding to a gas gain of ~ 150.

4)Position resolution for neutrons

Neglecting count rate capability, the delay-line encoding is more attractive in the sense of its simple construction and long term stability than the "stripper-strip" encoding method. The delay-line readout was applied in the PSD Type A. As shown in Fig.3, the signal induced in the readout strips propagates towards both sides of the delay-line, and the difference in time of arrival at both ends gives a measure for the position of the avalanche. The delay-lines have 83 taps, each of which is connected to a readout strip being made up of two grid wires. The total delay time is 1328 nsec. The position resolution for neutrons is measured by using a pinhole of a cadmium mask on the face of the PSD. As shown in Fig.4, the detector response is linear, and the position resolution is determined to be 5 mm FWHM.

IV. CONCLUDING REMARKS

The basic tests with the 21x21 cm^2 PSD promissed an excellent performance of the large area detector. The 51x51 cm^2 PSD will be used for the SANS experiments at KUR, after checking the total performance such as uniformity, count rate capability, and long term stability.

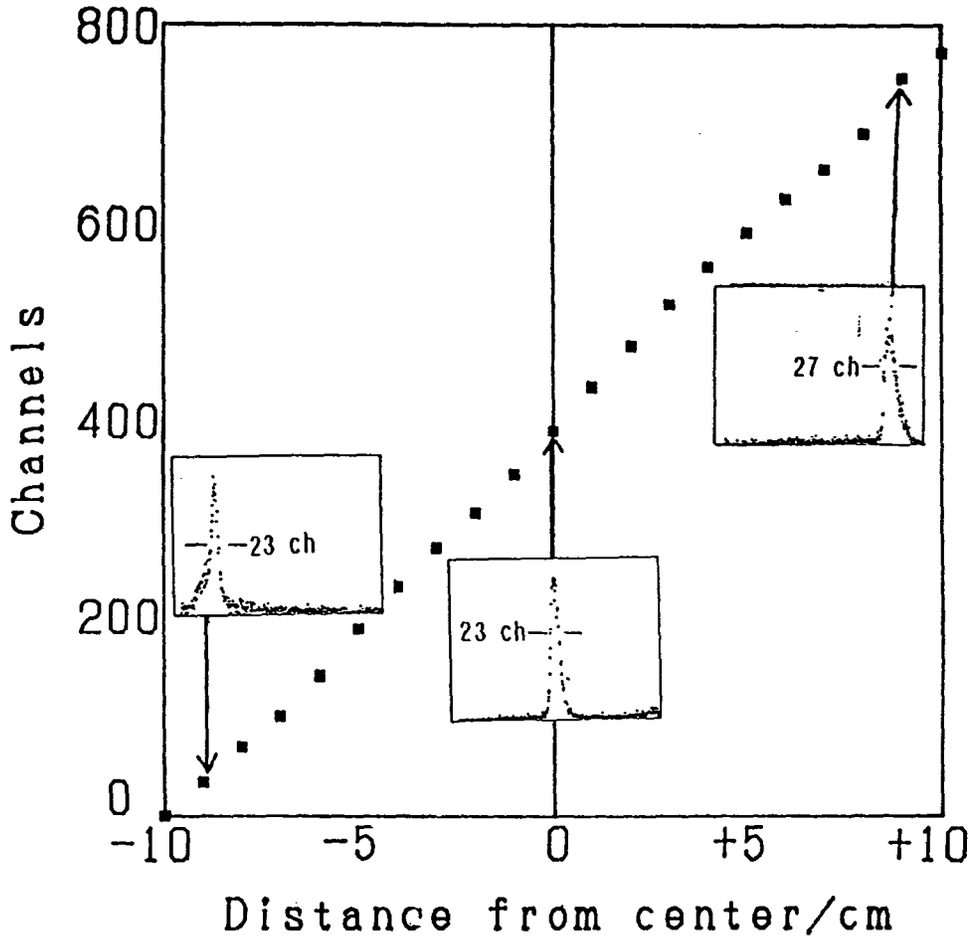

Fig.4. Relation between impact position (X) and channel assignment. 1 channel = 3.6 nsec = 0.25 mm. The inserts show the response to a pinhole beam giving the position resolution.

References

1. P. Convert and J. B. Forsyth (eds), Position-Sensitive Detection of Thermal Neutrons, Academic Press, London (1983).
2. J. K. Kjems, R. Bauer, B. Breiting, and A. Thuesen, Neutron Scattering in the 'Nineties, p.489 (1985).

Q(I.Kanno): What is the material of the dome and also the chamber itself? Is the pressure of ^{4}He in the dome almost the same with the one of active gas?

A(Y.Maeda): Both the dome and chamber are made of Al. The pressure of ^{4}He and active gas are almost the same. It is important to make the window thin and avoid deformations of the vessel. The pressure difference is kept to be less than 0.1Kg/cm^2 and the maximum displacement of the diaphragm is 1mm.

Q(H.Tietze): What is the decay time of the counting pulses obtained?

A(Y.Maeda): About 50μsec. But it depends on the position. The signal induced on read-wire just in the beam line has an additional signal due to Ar ion arriving directly at the wire. The delay of this signal from the signal induced by avalanche is ~200μsec.

Q(R.K.Crawford): Have the various encoding methods possible with this detector been compared?

A(Y.Maeda): Neglecting counting rate capability, the delay-line encoding is the most attractive in the sense of its simple construction and long term stability. After checking the total performance such as uniformity and counting rate capability, we want to decide whether "strip per strip" encoding is necessary or not.

ICANS-XI International Collaboration on Advanced Neutron Sources
KEK, Tsukuba, October 22-26, 1990

Scintillation Detector System in Neutron-Nucleus Experiments

H.M.Shimizu* , T.Adachi** and Y.Masuda**

* Department of Physics, Kyoto University
Kyoto 606, Japan
** National Laboratory for High Energy Physics
1-1 Oho Tsukuba 305, Japan

I. Introduction

Very large enhancement of parity-nonconservation (PNC) effect in the neutron-nucleus reaction has been studied for a decade.[1,2,3,4] The enhancement of the PNC effect is interesting phenomena itself. And furthermore, it has another interesting point, namely, the mechanism of enhancement is expected also for time reversal symmetry breaking terms[5,6,7,8]. We have been studying longitudinal asymmetries in (n,γ) reaction cross sections denoted by $A_{L,\gamma}$ for several nuclei[3]. Very large enhancement up to 10^6 of magnitude has been observed in the radiative capture p-wave resonance of ^{139}La at the incident neutron energy of 0.734 eV. In the experiment, capture γ rays and transmitted neutrons were counted as a function of the neutron energy by using the time-of-flight (TOF) method. The γ-ray detection takes an advantage to identify the radiative capture reaction, while the neutron transmission includes large contribution of the neutron scattering. In this report, we will describe our current experimental arrangement and recent results.

II. Experimental Arrangement

The experiment was carried out in a polarized neutron beamline at KENS. The schematic view of our experimental arrangement is shown in Fig. 1. Neutrons were transversely polarized upon transmission through a dynamically polarized proton filter which was placed at 5.2 m from the neutron source. A typical neutron polarization around E_n = 1 eV was about 70%. A typical instantaneous incident neutron intensity was 3×10^7 polarized neutrons/sec/cm^2/eV (E_n=1 eV) at 6.6 m from the neutron source. A target was placed at 6.6 m from the neutron source. The neutron spin was rotated from the transverse to longitudinal direction following an adiabatic passage. The neutron helicity was reversed every 2.5 seconds.

A plastic scintillator for a beam monitor was placed at 4.5 m from the neutron source. Three sets of BaF_2 crystals were placed cylindrically surrounding the target for capture γ-ray detection at three polar angles with respect to the incident neutron momentum. The capture γ rays were detected inclusively with energy threshold of 1 MeV. Transmitted neutrons were detected by a ^{10}B loaded liquid scintillation counter located at 9.4 m from the neutron source.

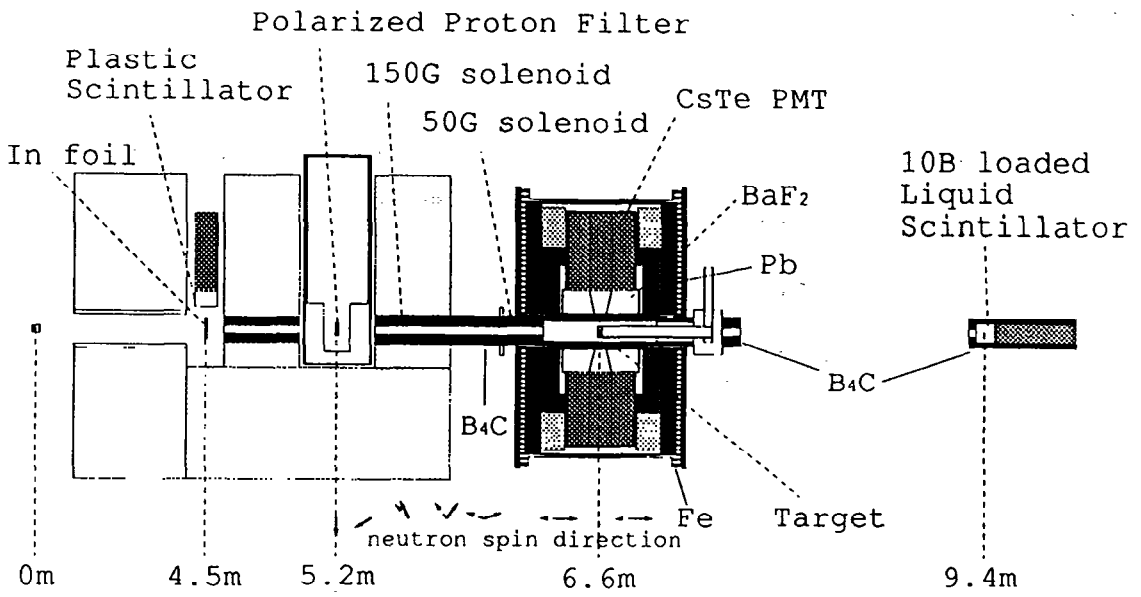

Figure 1.
Schematic view of our experimental arrangement

III. Counters

(a) Plastic Scintillator for Beam Monitor

An annular 0.02-mm thick indium foil was placed most upstream of our system for monitoring the number of incident neutrons by detecting capture γ rays from indium nuclei. A plastic scintillation counter was used for the detection of the capture γ rays, since it has a good timing characteristics. The scintillator size was 5 cm in thickness and 5 cm in diameter. A photomultiplier (Hamamatsu H1161) with bialkali photocathode and borosilicate window was used to detect the scintillation light from the plastic scintillator. The pulse width was about 10 ns in FWHM. Since plastic scintillator contains only low Z atoms, the contribution of the compton scattering is much larger than that of full energy absorption. The full energy absorption, however, is not necessary for the beam monitoring.

(b) ^{10}B Loaded Liquid Scintillator[9] for Transmission Measurement

An NE311A ^{10}B loaded liquid scintillator was used for the transmission measurement. ^{10}B nuclei are contained 2.4×10^{21} cm^{-3} in the liquid scintillator. Neutrons are detected by the following reactions.

$n + {}^{10}B \rightarrow {}^{7}Li + {}^{4}He + 2.792MeV$

$n + {}^{10}B \rightarrow {}^{7}Li^{*} + {}^{4}He + 2.310MeV$

The cross section of these reactions is about 600 barns at $E_n = 1$ eV. The scintillator size was 3.5 cm in thickness and 3.5 cm in diameter. Therefore, the detection efficiency is 99.4% for 1-eV neutrons. The kinetic energy of charged particle is converted to scintillation photons in organic liquid. The photomultiplier (Hamamatsu H1161) was used for scintillation light detection. Since the deposit energy is determined by the Q-value of these reactions, pulse height spectrum of neutron signal has a definite peak. Typical raw pulses obtained with neutron beam are shown in Fig. 2. The pulse width was about 15 ns. The separation of neutron pulse

was remarkably good. Neutron pulses was extracted by using window type discrimination.

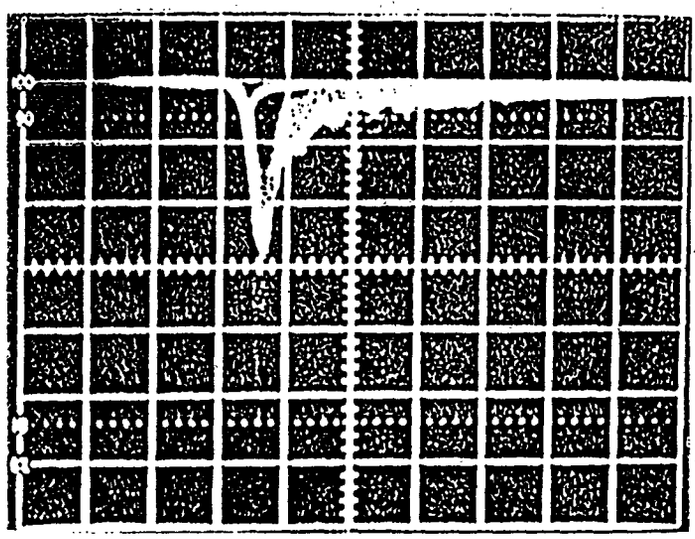

Fig. 2. Typical neutron signal of ^{10}B loaded liquid scintillator. The neutron signals form a clear band corresponding to reaction Q-value. The scale of x-axis is 20ns/div, y-axis 50mV/div.

(c) BaF_2 Crystal for Capture γ-Ray Measurement from the Target

BaF_2 crystals were used for the detection of capture γ rays from target nuclei. A solid angle of ϑ=30-150° and ϕ=0-360° was covered by the whole BaF_2 γ-ray counter. The thickness in the γ-ray emission direction was more than 6 cm. Since the radiation length of BaF_2 crystal (2.1 cm) is shorter than that of NaI(Tl) crystal (2.6 cm) which is commonly used for γ-ray detection, the full energy absorption efficiency of BaF_2 is better than that of NaI for the same dimension. BaF_2 crystal has two light emission peaks at 220 and 310 nm in wave length. The decay constants for the two components are 0.6 and 620 ns, respectively. Hamamatsu R329QTE photomultiplier with a CsTe photocathode was used to detect only the fast component of scintillation light which has a good timing characteristics. A quartz plate is used as a window for R329QTE so as to transmit the fast component light in the ultra violet region. Typical raw pulses of the fast component of BaF_2 scintillation light are shown in Fig. 3. The pulse width was about 10 ns in FWHM.

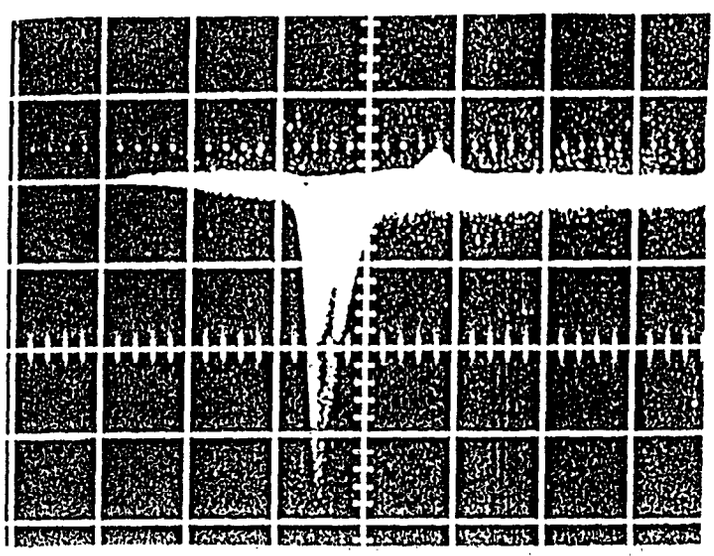

Fig. 3. Typical fast component signal of BaF_2 scintillator. UV (ultra violet) sensitive photomultiplier with CsTe photocathode and quartz window is used. The scale of x-axis is 20ns/div, y-axis 100mV/div.

IV. Results of $A_{L,\gamma}$ Measurement

Typical TOF spectra obtained by the beam-monitor counter, BaF_2 γ-ray counter and transmission counter as a function of incident neutron energy are shown in Fig. 4. In the TOF spectrum of the beam-monitor counter, a resonance is found at E_n = 1.457 eV for ^{115}In. The count around the resonance peak was used to normalize the counts of the BaF_2 γ ray and the transmission counters. In the TOF spectra of the BaF_2 γ-ray counter and the transmission counter, a p-wave resonance of ^{139}La is found at E_n = 0.734 eV, and an s-wave resonance of ^{138}La at E_n = 2.99 eV. Small resonances were observed with a good signal to background ratio in the capture γ-ray measurement in comparison with the transmission measurement.

The preliminary results of $A_{L,\gamma}$ for several nuclei are listed in table 1. The longitudinal asymmetry corresponds to $\sigma_n \cdot \mathbf{k}_n$ correlation, which contains only the entrance channel quantities. The enhancement of the longitudinal asymmetry is explained by many theoretists.[7,10,11] The present results are consistent with the parity mixing in the entrance channel into the compound nucleus.

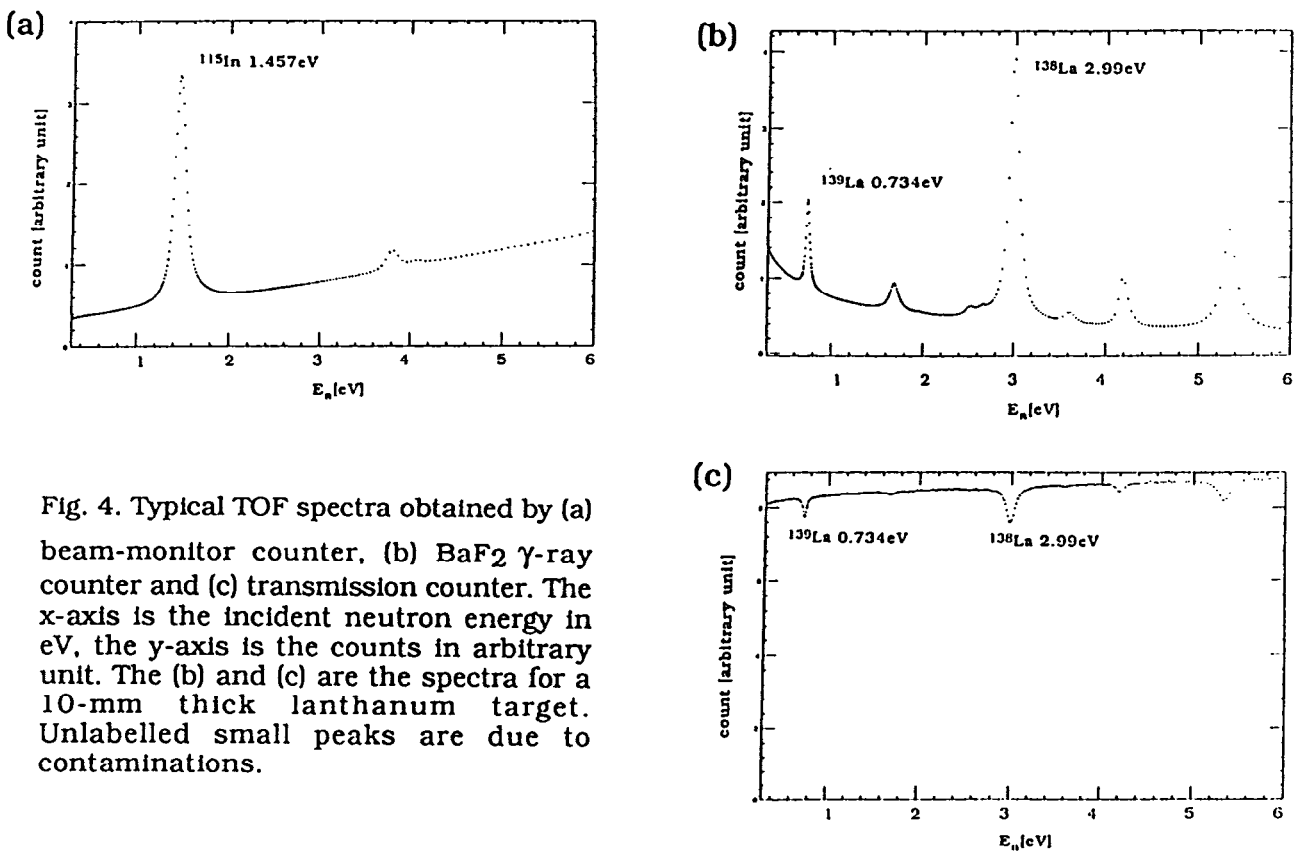

Fig. 4. Typical TOF spectra obtained by (a) beam-monitor counter, (b) BaF_2 γ-ray counter and (c) transmission counter. The x-axis is the incident neutron energy in eV, the y-axis is the counts in arbitrary unit. The (b) and (c) are the spectra for a 10-mm thick lanthanum target. Unlabelled small peaks are due to contaminations.

	^{139}La	^{81}Br	^{111}Cd
E_n[eV]	0.734	0.88	4.53
$A_{L,\gamma}$	(9.9±0.5)%	(2.4±0.5)%	-(1.0±0.5)%

Table 1. The preliminary results of $A_{L,\gamma}$ measurement using the present BaF_2 counter. The $A_{L,\gamma}$ for ^{139}La is consistent with our previous measurements.[3]

V. Development for Exclusive γ-ray Detection

In capture γ-ray measurement, many other PNC correlation terms can be observed. These correlation terms contain the quantities in the exit channel from the compound nucleus (k_γ or γ helicity). The similar enhancements are expected also for such correlations, for example, $\sigma_n \cdot \mathbf{k}_\gamma$ correlation term[12]. The inclusive detection of capture γ-rays is not sufficient to measure such correlation terms because of the following reason. Many γ-ray transitions are induced in deexcitation of the compound nucleus. The spectroscopic factor of each γ-ray transition is different in magnitude and sign. As the result, the PNC effect may be smeared after integrating the contributions of these γ-ray transitions. Therefore, the detection of specific transition is required.

Bismuth germanate (BGO) crystal is a hopeful candidate for this purpose. Better efficiency of full energy absorption can be obtained with smaller crystal size because of its short radiation length (1.1 cm). The compactness is an important point in actual measurement, since very large shields for background γ-rays and neutrons is required for a large detector. We studied the pulse height spectrum of 2"ϕx2" BGO by using several γ-ray sources. Hamamatsu H1161 photomultiplier was used for scintillation light detection. As the result, fill energy peak was observed clearly with energy resolution 8% in FWHM for 4.43-MeV γ rays as shown in Fig. 5. The decay constant of light emission of BGO is 300 ns, which is rather slow. But it is not problem because a typical counting rate of capture γ rays from the target is less than 100 kHz. We have built a BGO counter set (shown in Fig. 6) for the measurements of some correlations which contain exit channel quantities mentioned above.

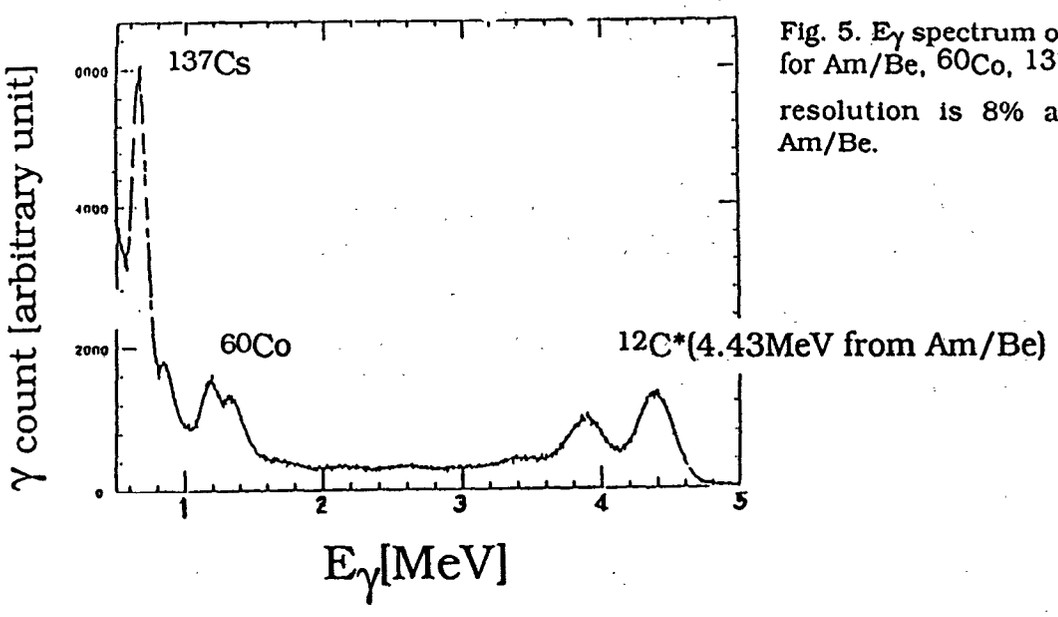

Fig. 5. E_γ spectrum of 2"ϕx2" BGO crystal for Am/Be, ^{60}Co, ^{137}Cs sources. Energy resolution is 8% at 4.43MeV γ from Am/Be.

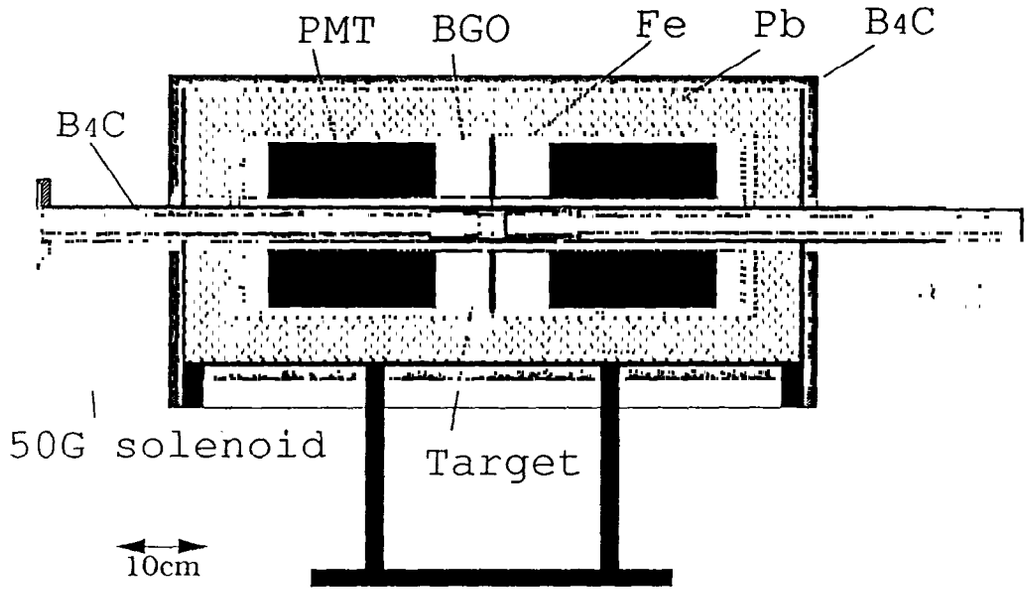

Fig. 6. Counter arrangement of BGO detector system.

The authors would like to thank Prof. A. Masaike, Prof. K. Morimoto for their helpful and valuable discussion. We also thank Prof. H. Sugawara, Prof. N. Watanabe and Prof. K. Nakai for their kind encouragements.

References

1. M.Forte, et.al., Phys.Rev.Lett. **45** (1980) 2088
2. V.P. Alfimenkov, Nucl.Phys. **A398** (1983) 93
3. Y. Masuda, et.al., Hyperfine Interactions **34** (1987) 143
   Y. Masuda, et.al., Nucl.Phys. **A478** (1988) 737c
   Y. Masuda, et.al., Nucl.Phys. **A504** (1989) 269
4. J.D. Bowman, et.al., Phys.Rev.Lett. **65** (1990) 1192
5. L.Stodolsky, Nucl.Phys. **B197** (1982) 213
   L. Stodolsky, Phys.Lett. **172B** (1986) 5
6. P.K.Kabir, Phys.Rev. **D25** (1982) 2013
   P.K. Kabir, Phys.Rev.Lett. **60** (1988) 686
7. V.E.Bunakov and V.P.Gudkov, Nucl.Phys. **A401** (1983) 93
8. Y.Yamaguchi, J. Phys. Soc. Jpn. **57**(1988)1525(L); ibid 2331
9. L.W.Bollinger and G.E.Thomas, Rev.Sci.Instr. **28** (1957) 489
10. O.P.Sushkov and V.V.Flambaum, Sov.Phys.Usp. **25** (1982) 1
11. Y.Yamaguchi, J. Phys. Soc.Jpn. **57**(1988)1518(L);ibid1522(L);ibid 3344.
12. V.V.Flambaum and O.P.Sushkov, Nucl.Phys. **A435** (1985) 352

Q(Y.Maeda): Would you tell me what kind of grease are used between the BaF_2 scintillator and the photomultiplier?

A(H.M.Shimizu): Air Contact!

ICANS-XI International Collaboration on Advanced Neutron Sources
KEK, Tsukuba, October 22-26, 1990

Neutron Detectors at IPNS*

R. K. Crawford, J. R. Haumann, and G. E. Ostrowski
Argonne National Laboratory, Argonne, IL 60439.

ABSTRACT

The heart of each time-of-flight neutron scattering instrument is its complement of detectors and the associated encoding and counting electronics. Currently there are ten fully-scheduled neutron scattering instruments in operation at IPNS, with three more instruments under development. Six of these instruments use position-sensitive neutron detectors (PSDs) of various types. These PSDs include a 30 cm x 30 cm, ~3 mm resolution, neutron Anger camera area PSD with ^{6}Li-glass scintillator; a 2.5 cm dia, ~0.7 mm resolution, microchannel-plate area PSD with ^{6}Li-glass scintillator; a 20 cm x 20 cm, ~5 mm resolution, ^{3}He proportional counter area PSD; a 40 cm x 40 cm, ~4 mm resolution, ^{3}He proportional counter area PSD; a flat 25 cm long, ~1.6 mm resolution, ^{3}He proportional counter linear PSD; and 160 cylindrical ^{3}He proportional counter linear PSDs, each of which is 1.27 cm in dia and 60 cm long and has ~14 mm resolution. In addition to these PSDs, ~750 standard cylindrical ^{3}He proportional counters of various sizes are utilized on IPNS instruments, and ~20 BF_3 pulsed ion chambers are in use as beam monitors. This paper discusses these various detectors and associated electronics, with emphasis on the instrumental specifications and the reasons for the selection of the different types of detectors. Observed performance of these detectors is also discussed.

I. INTRODUCTION

A large number of standard detectors and position-sensitive neutron detectors (PSDs) are in use on the thirteen IPNS neutron scattering instruments. (Three of these instruments are still under development.) IPNS instruments now utilize nearly 800 standard neutron detectors (^{3}He proportional counters or BF_3 pulsed ion chambers) of various sizes. In addition, six of these instruments are based primarily on the use of PSDs. All IPNS instruments operate using the time-of-flight (TOF) principle, so they must all have their resulting raw data binned into histograms with both time (neutron TOF) and spatial (angular) dimensions. The data acquisition electronics and

*Work supported by U.S. Department of Energy, BES, contract No. W-31-109-ENG-38.

software for the IPNS instruments have been described elsewhere,[1-4] so this paper will focus on details of the detectors used on the different instruments, the reasons for these particular choices of detectors, and the performances which have been achieved with these detectors at IPNS. Some aspects of the IPNS PSDs have recently been discussed elsewhere,[5] but are summarized here for completeness.

II. BEAM MONITORS AT IPNS

Incident Beam

The incident-beam monitor is a low-efficiency detector located upstream from the neutron-scattering sample. This detector samples the entire incident beam and provides continuous monitoring of the intensity and wavelength distribution of the neutrons in this beam. Because the beam always passes through this monitor, the monitor must be designed to produce only a minor perturbation on the incident beam. Thus the detection efficiency of this monitor must be kept quite low and the monitor must be designed so it scatters very few neutrons. Most IPNS instruments use flat ionization chambers operating in the pulse mode, which span the entire beam to monitor the incident beam intensity as a function of TOF. Although similar detectors are used in the chopper instruments, the functions in this case are to monitor the total incident intensity and to measure the shape and position (in TOF) of the pulse transmitted by the chopper.

These ion chambers are commercially available detectors (Reuter-Stokes, Twinsburg, OH, USA; models RS-P1-3402-101(or -103) or RS-P1-6802-101(or -103)) with an active volume which is ~2.5 cm thick and either 7.6 or 15.3 cm in dia. These monitor detectors have Al bodies and windows and are filled to ~1 atm with a fill gas which is a mixture of Ar, CH_4, and CO_2, with sufficient BF_3 added to achieve the desired detection efficiency, usually in the range 10^{-3} - 10^{-5} for thermal neutrons. Measurements indicate that the sensitivity of these detectors is quite uniform over the active volume, so they provide an accurate sampling of the entire beam. Neutron detection efficiencies have been found to be proportional to neutron wavelength, as expected, over the full wavelength range of interest to the IPNS instruments. This type of detector was chosen because of their commercial availability, uniform sampling of the entire beam, well known variation of efficiency with wavelength, resistance to radiation damage, and relative insensitivity to both gamma rays and fast neutrons.

Early experience using a variety of both commercial and Argonne-built charge-sensitive preamplifiers with these detectors was not entirely satisfactory. Because of the hydrogen atoms in the CH_4 component of the fill gas, the detectors have some sensitivity to high-energy neutrons. At the TOF values at which most measurements are made, pulses from these high-energy neutrons are easily eliminated by pulse-height discrimination. However immediately following the proton pulse on the target, these detectors are bombarded with a very high instantaneous flux of high-energy neutrons, and this led to severe overload of the preamplifiers. On most beamlines this overload was sufficient to completely "black out" the detector so that it was unable to count for the first few hundred microseconds after the proton pulse. Even after the detector system had resumed counting, the TOF spectrum it measured was distorted for additional hundreds of microseconds as the

baseline recovery from the overload shifted the detector pulse-height spectrum relative to the discriminator window. For most instruments this overload recovery occurred before the TOF range of interest, so it was no problem. On other instruments, the intensity of such fast neutrons was significantly reduced by a filter or a chopper, so such overload did not occur and recovery was never a problem.

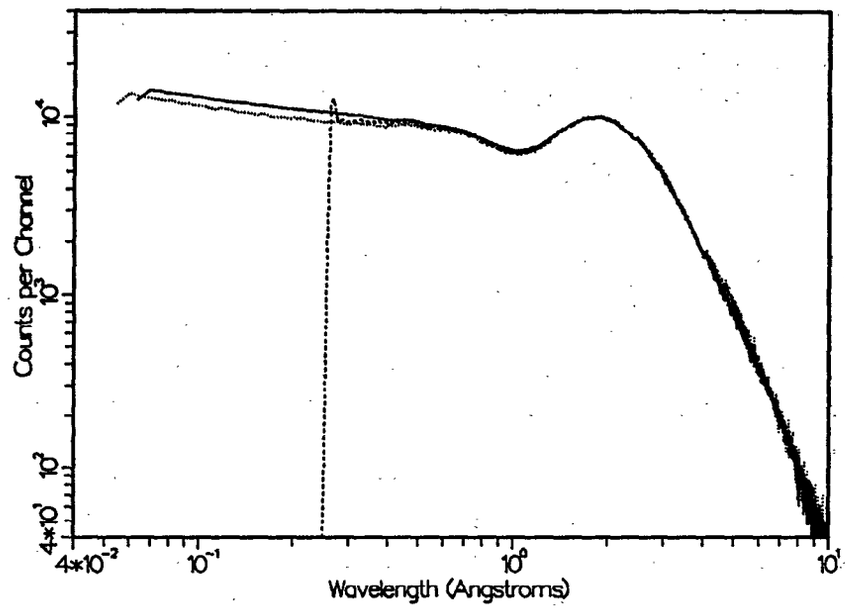

Figure 1. Beam monitor raw data (not corrected for efficiency) measured on the H1 beamline at IPNS using a BF_3 ionization chamber. Dashed line - original preamplifier/amplifier; Solid line - new bipolar preamplifier/amplifier; Dotted line - same new preamplifier and same detector, but in a location further downstream where the incident intensity was attenuated by a factor of 6. All were arbitrarily scaled to match at the Maxwellian peak. Note that with the old preamplifier the detector was effectively "dead" for wavelengths below ~0.25 Å and the spectrum was somewhat distorted for wavelengths just above this. The small discrepancies at short wavelengths between the two measurements with the new preamplifier/amplifier are not yet fully understood and may represent real spectral differences at the two beam locations. Small differences at the longer wavelengths are due to differing numbers of Al windows upstream from the detector.

However, there was still interest in pressing the capabilities on some instruments to shorter and shorter wavelengths, so it became important to minimize or eliminate such overload effects. This has been accomplished by the development of a preamplifier/amplifier combination which produces a short bipolar pulse tailored to result in no baseline shift. Figure 1 shows a comparison of the spectra measured on one of the IPNS beamlines with this new preamplifier/amplifier and one of our older versions, both with the same detector in the same location. The improvement achieved with the new preamplifier is evident in the figure. This figure also includes the spectrum measured in another location on the same beam where the incident intensity has been attenuated by a factor of ~6, showing that the spectra as measured with these beam monitors are not data rate dependent at any of the rates encountered at IPNS.

Several other types of beam monitors have been tried at IPNS. One of these was a gas proportional counter with a planar geometry, having CF_4 with a small amount of ^3He as the fill gas. This detector worked quite well for short periods of time, but its efficiency was found to

degrade by a factor of ~2 per month of operation. Inspection of this detector after disassembly indicated that the degradation was due to a film of unknown composition which had been plated on the anode, presumably because of the chemical reactions occurring in the highly-ionized fill gas near the anode.

Another unsuccessful beam monitor attempt was the use of Si surface barrier detectors with a ^{6}Li coating. These were commercial charged-particle detectors (EG&G Ortec, Oak Ridge, TN, USA; Series A silicon surface-barrier detector) which had ^{6}Li evaporated onto their front surfaces so that either the alpha particle or the triton from the reaction

$$^6\mathrm{Li} + \mathrm{n} \rightarrow {}^3\mathrm{He} + {}^4\mathrm{He} + 4.79\ \mathrm{MeV} \qquad (1)$$

was detected in the surface-barrier detector. Detection efficiency was determined by the deposition density of the ^{6}Li layer, which was chosen to be 9.5 μgm/cm^2 to give an efficiency of ~5x10^{-4} for 1 Å neutrons, increasing linearly with wavelength. The thin single-crystal of high-purity Si (resistivity 6.0 KΩ-cm) which formed the bulk of the detector produced little neutron absorption or scattering in the relatively long-wavelength range of interest to the Small-Angle Diffractometer (SAD), and so transmitted the neutrons not absorbed in the ^{6}Li with little or no perturbation. This detector worked quite well initially, but over the period of roughly one year its performance degraded to the point where it was no longer usable. This degradation was attributed to radiation damage. Subsequent tests with other similar detectors showed that detectors made with higher purity Si (resistivity 8.4 KΩ-cm) degraded much faster, as would be expected from this mechanism, and no detector of this type was found to provide satisfactory long-term stability.

Transmitted Beam

The transmitted beam monitor is located downstream from the neutron-scattering sample, and is used to measure the intensity and wavelength distribution of the neutrons transmitted through the sample. On the chopper instruments, the transmitted beam monitor data are also used in conjunction with the incident beam monitor data to determine precisely the energy of the chopped pulse of neutrons and the arrival time of this pulse at the sample position. Many of the IPNS instruments also use flat pulsed ionization chambers of the type described above as transmitted beam monitors.

Several IPNS instruments instead use a pinhole mask in front of a high-efficiency ^{3}He gas proportional counter to monitor the beam transmitted through the samples. In this case, the detector is frequently of the same type as that used to detect the scattered neutrons, so that detector efficiencies do not enter the data reduction. One such monitor is described elsewhere in these proceedings.[6] On SAD, a proportional counter detector and associated mask are mounted on a computer-interfaced translation stage so they can automatically be inserted into the beam whenever transmission measurements are to be made, and can otherwise be completely withdrawn from the path of the scattered neutrons.

III. STANDARD DETECTORS AT IPNS

Cylindrical ^{3}He-filled gas proportional counters are used as detectors on many of the IPNS instruments. These detectors were chosen because of their low intrinsic backgrounds, high reliability, and commercial availability (Reuter Stokes, Twinsburg, OH, USA; most IPNS detectors are models RS-P4-0415-101, RS-P4-0818-150, or RS-P4-0205-201, but small numbers of several other models are in use). Table I indicates the variety of sizes and fill pressures and the numbers of such detectors in use at the present time on the various IPNS instruments. Nearly all of these detectors have Al walls coated on the inside with Ni. When sufficient attention is paid to shielding against the cosmic ray and other natural backgrounds, intrinsic background count rates below 0.1 count/minute are routinely achieved for such detectors.

Table I - Standard ^{3}He Proportional Counters at IPNS

Instrument[a]	Standard ^{3}He Detectors	Diameter	Active Length	^{3}He Fill Pressure
EVS	16	1.59 cm	20.3 cm	6 atm
GPPD	142	1.27	38.1	10
HRMECS	~240	2.54	45.7	6
LRMECS	116	2.54	45.7	6
	40	2.54	22.9	6
	4	2.54	11.4	6
PHOENIX	32	2.54	45.7	6
POSY	1 [b]	0.64	2.5	20
POSY-II	1 [b]	0.64	2.5	10
QENS	34	0.64	12.5	10
SEPD	120	1.27	38.1	10
	~ 746			

a EVS → eV spectrometer/low-resolution diffractometer
GPPD and SEPD → powder diffractometers
HRMECS, LRMECS, and PHOENIX → chopper spectrometers
POSY and POSY-II → neutron reflectometers
QENS → quasielastic spectrometer

b Masked and used as beam monitors.

Because of the large numbers of such detectors involved, relatively inexpensive preamplifier/amplifiers and discriminator/time-encoders were developed for these detectors, with identical electronics being used on all instruments utilizing such standard detectors. Most of these electronics have been described previously.[1,2] Many of the detectors on HRMECS and all of the detectors on LRMECS (Table I) are operated in the vacuum of the scattering flight path, but all external high-voltage connections, preamplifiers, etc. are located outside this vacuum. For all instruments, the high-voltage connections and preamplifiers are contained in a controlled environment of dry nitrogen gas. Careful control of this environment was found to be necessary in order to prevent the high background counting rates which would otherwise result from high-voltage breakdown due to the humidity in the air in the IPNS experimental hall. In all cases,

careful attention has been paid to detector grounding and other sources of ground loops, and to electromagnetic shielding of all components in the signal train. These precautions have, in most cases, prevented contamination of the collected data by the high levels of electromagnetic noise from the accelerator system and other sources which are always present in the experimental hall during operation.

IV. PSDs AT IPNS

Six of the IPNS instruments use PSDs in order to provide the necessary angular resolution and coverage. Table II lists these six instruments and provides some of the specifications for the associated PSDs, which are discussed individually in the sections below.

Table II - PSDs at IPNS

	SCD	SAD	new[a]	POSY	POSY-II	GLAD
Number of PSDs	1	1	1	1	1	160
PSD type	Anger	Prop.	Prop.	Micro.	Prop.	Prop.
Encoding method[b]	Anger	RT	RT	CD	RT	CD
Encoded dimensions	2	2	2	2	1	1
Encoded channels (x,y)	128x128	256x256	256x256	256x256	256	64
Histogram channels (x,y)	85x85	64x64	128x128	128x1	256	64
Active mat'l/pressure (atm)	^{6}Li glass	^{3}He/1.3	^{3}He/2.6	^{6}Li glass	^{3}He/2.6	^{3}He/10
Stopping gas/pressure (atm)	--	CF_4/0.7	CF_4/1.4	--	CF_4/1.4	Ar/2
Active area (cm)	30x30	20x20	40x40	2.5 dia	5x20	1.1x60[c]
Active depth (mm)	2	32	25	0.5	25	11[b]
Resolution (mm fwhm)	3.5	3-9[d]	4-6[d]	0.7	1.6[d]	14
Dead-time (μs)	~3	~10	~5	~8	~10	8
Efficiency at 1.8 Å	0.98	0.55	0.61	0.63	0.61	0.77[e]
Efficiency at 0.6 Å	0.73	0.23	0.27	0.28	0.27	0.39[e]

a New small-angle diffractometer.
b RT stands for rise-time encoding, CD for charge-division encoding.
c GLAD detectors are cylindrical, 1.27 cm outside dia x 60 cm long.
d Depends on electronics. There is a tradeoff with linearity and dead-time.
e Efficiency averaged over cylinder.

Anger Camera

A neutron Anger camera with ^{6}Li-glass scintillator, which was developed and built at Argonne, is used as an area PSD on the Single Crystal Diffractometer (SCD).[7] This instrument uses the time-of-flight Laue technique to obtain diffraction data from single crystals. Figure 2 provides a schematic representation of the Anger camera detector, indicating its use on SCD. This

detector, which has been described in detail elsewhere,[8] has an active area of 30 x 30 cm^2, with a resolution of ~3.5 mm fwhm and a dead-time of ~3 μs per event. The 2 mm thick ^{6}Li-glass scintillator which is the active material on this detector provides a detection efficiency of ~66% for 0.5 Å neutrons. If the detection volume were thicker, parallax would result in a serious degradation of the resolution because the detector is normally operated only ~30 cm from the scattering sample. This good spatial resolution, negligible parallax, high efficiency at short wavelengths, and the short dead-time were the primary reasons a detector of this type was developed for this instrument. The electronics encode the 30 x 30 cm^2 active area as 128 x 128 pixels, and also provide sufficient additional information so that accurate dead-time corrections can be made on the data as a function of TOF. The ^{6}Li-glass scintillator material has appreciable gamma-ray sensitivity, so lithium carbonate enriched with ^{6}Li, which produces no gammas upon absorption of neutrons, was used as the shielding material close to the detector. This, combined with pulse-height discrimination and the careful use of other shielding materials, has reduced the detected gamma and fast-neutron backgrounds to acceptable levels.

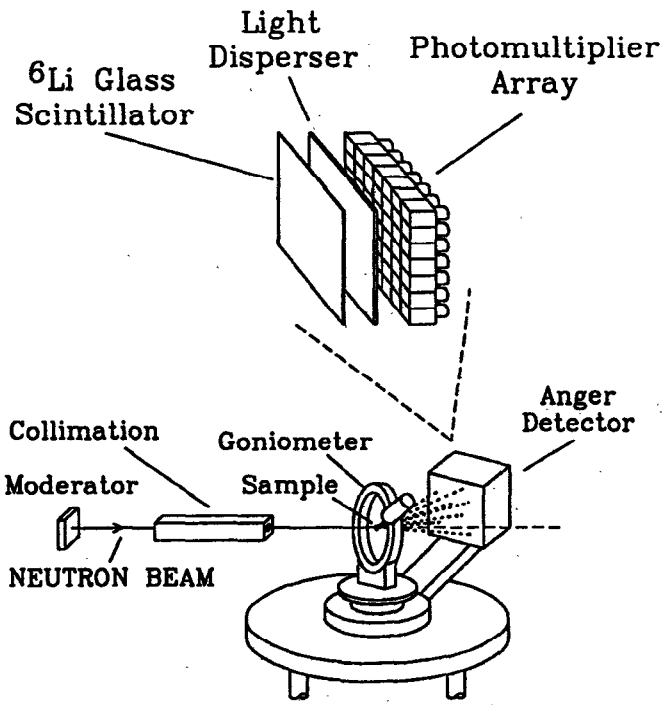

Figure 2. Schematic exploded view of the Anger camera area PSD and a representation of its use on SCD. In normal use, the light disperser plate of the Anger camera is in direct contact with the face of the photomultiplier array, and the 2 mm thick glass scintillator plate is separated from the disperser plate by a thin air gap which serves to truncate the scintillation light cone. The output of each 5.1 cm square photomultiplier is resistor-weighted according to its x and y coordinates, and the normalized sums of the weighted signals are used to determine the centroid of the cone of scintillation light from the neutron absorption event.

Area Proportional Counters

The small-angle diffractometer SAD has been in operation for a number of years,[9] and a second small-angle diffractometer[10] is currently being developed. Both of these instruments utilize

rise-time-encoded ^{3}He proportional counter area PSDs located in line with the direct beam to make measurements at small scattering angles. Figure 3 shows one of these PSDs schematically, and also indicates its use on the instrument. These instruments utilize a large wavelength range in order to span a large dynamic Q-range. The scattering signal is usually quite weak over some parts of this range, so the low intrinsic background counting rate and relative insensitivity to gamma rays and high-energy neutrons of a proportional counter are distinct advantages. Because of the relatively large sample-detector distances on these instruments (1.5-2.0 m), the parallax associated with the thick active volume of these detectors is not a significant problem.

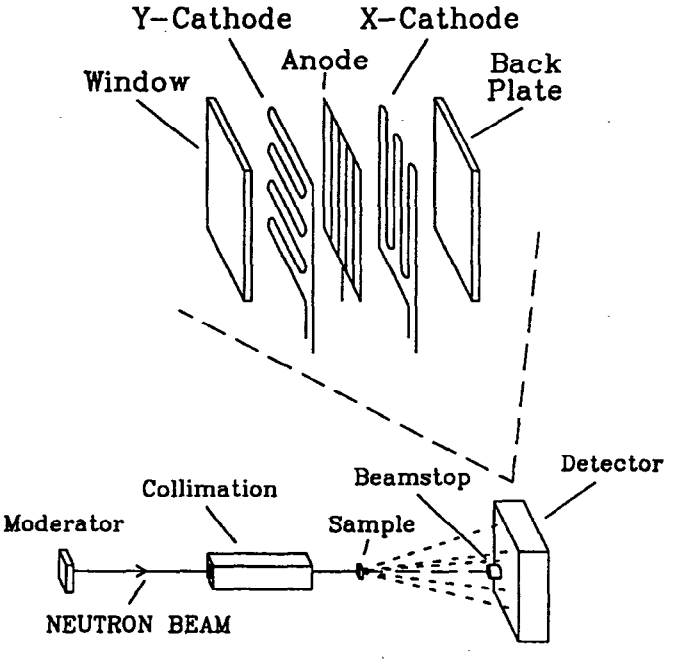

Figure 3. Schematic representation of the arrangement of the electrodes in the proportional-counter area PSDs. Use of one of these PSDs on a small-angle diffractometer is also shown schematically. Wire spacing is 2 mm in the SAD detector and 4 mm in the detector for the new small-angle diffractometer, requiring ~100 loops for each of the actual cathodes in both cases.

The area PSD used on SAD was built as a joint effort by Argonne National Laboratory and Oak Ridge National Laboratory personnel.[9] It has an active volume 20 x 20 cm^2, 3.2 cm thick, which was originally filled with a mixture of ^{3}He, Xe, and CO_2 to a pressure of ~5 atm. However, in order to reduce the gamma sensitivity still further, it was later refilled with a mixture of 65% ^{3}He and 35% CF_4 to a total pressure of 2 atm. This detector has been in continuous operation for more than 10 years with only this one change of fill-gas, and has shown no sign of degradation over this period. The detector is of the Borkowski-Kopp[11] type, in which an anode plane in the center is sandwiched between two single-wire cathode planes as indicated schematically in Fig. 3. The wires in the two cathode planes are strung in zig-zag patterns with 2 mm spacing. The wire directions in the front plane are orthogonal to those in the rear (Fig. 3) so the x-position can be derived from the signals from one of these cathode planes and the y-position can be derived from the other plane. The intrinsic RC time-constant for each cathode is ~0.8 μs. The 8-bit-each digital x and y positions are produced using rise-time encoding[11] with a direct-time-digitizer[12] operating on the signals from each cathode. Most events due to gammas or to fast neutrons are eliminated by pulse-height

discrimination. The best resolution so far determined from actual neutron measurements is ~5 mm fwhm. This value is very sensitive to the quality of the preamplifiers and encoding electronics, and to the time constants used for shaping the signals prior to encoding. Since the nominal resolution of ~3 mm has not yet been achieved, some current developments are aimed at further improvements in resolution. The position encoding exhibits some nonlinearity over the entire detector, and this becomes much worse near the detector edges. The extent of these nonlinearities can be modified by the choice of shaping time-constants as well as by the type of termination impedance used at the ends of the detector cathodes. However, even the best results that have been achieved so far have left nonlinearities around the detector edges, and these were still so bad that an appreciable amount of data from regions around the detector edges had to be discarded (using software masks), leading to a useful active area of ~17 x 17 cm^2. Detailed simulations of the detector and associated circuitry, coupled with an active electronics development program, are underway in an attempt to eliminate the encoding nonlinearity and to improve the spatial resolution.

The PSD to be used on the new small-angle diffractometer is a commercial unit (Ordela, Inc, Oak Ridge, TN, USA; model 2400N) with construction, fill gas, and encoding electronics similar to those of the SAD detector. The active volume in this PSD is 40 x 40 cm^2, 2.5 cm thick, filled to 4 atm with the same ^3He-CF_4 mixture as above. The best resolution so far achieved in actual neutron measurements on this detector is ~6 mm fwhm, while the nominal resolution is ~4 mm fwhm, so efforts to modify the encoding electronics to improve the resolution are continuing. Linearity problems similar to those found for the SAD detector have also been found for this detector, and in fact the simulations so far indicate that such linearity problems are inherent to the rise-time encoding method.

On both of these instruments the area PSDs are operated with part of the active area in line with the direct beam (Fig. 3), in order to achieve the required small scattering angles. A small beamstop immediately in front of the detectors is used to eliminate as much of the direct beam as possible, but the high-energy neutrons which arrive within a very short time at the beginning of the time-frame are not sufficiently well collimated to be completely removed by this beamstop. The pile-up of pulses from this high instantaneous intensity of fast neutrons led to a significant overload of the detector and electronics at the start of each time-frame, and this was followed by a long (~10 ms) recovery period during which the detector response was subtly distorted. A single-crystal MgO filter was therefore placed in the incident beam of SAD. This removes most of the fast neutrons and eliminates the overload problem, and has had the additional advantage of reducing the background due to delayed fast neutrons. However electronic solutions to the overload problem are also being explored, as there are some types of measurements for which the MgO filter is not desirable.

Microchannel-Plate

The Polarized Neutron Reflectometer (POSY)[13] measures the reflection of polarized neutrons to obtain magnetization density information in thin films or near the surfaces of bulk materials. The detector for this instrument is an area PSD utilizing a microchannel-plate. This detector and its location in the POSY instrument are shown schematically in Fig. 4. Since the detector is located

fairly close to the sample, good spatial resolution at the detector is required to provide the necessary angular resolution. This resolution was the primary reason for this particular choice of detector.

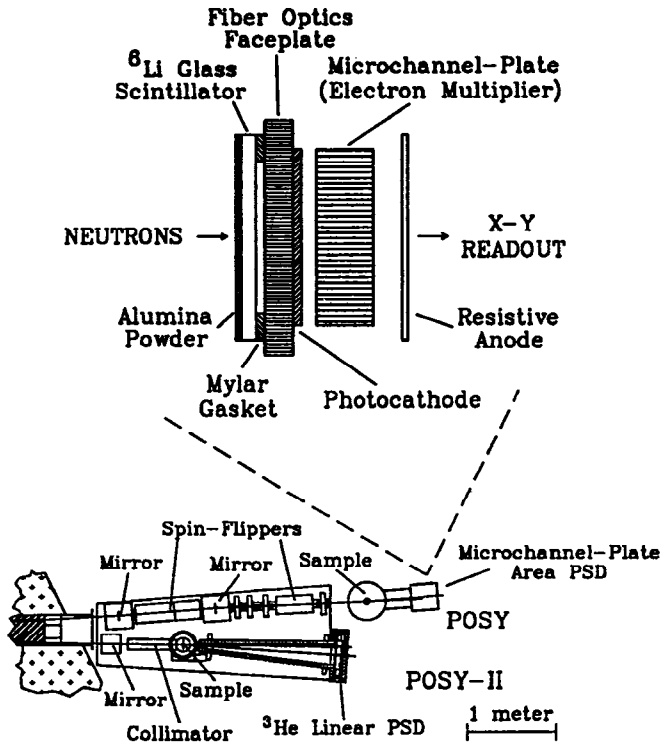

Figure 4. Schematic representation of the microchannel-plate area PSD. A layout of the two neutron reflectometers POSY and POSY-II is also included to show the use of this PSD on POSY. The scintillator glass is 0.5 mm thick and has its front surface is covered with alumina powder which diffusely reflects back some of the scintillation light to enhance the signal. The 0.025 mm thick mylar gasket produces an air gap between the scintillator and optical coupler to truncate the scintillation light cone.

A commercial microchannel-plate photon detector with integral photocathode and resistive anode readout (Surface Science Laboratories, Inc., Mountain View, CA; model 3006-SG) serves as the basis for this area PSD.[13] The addition of a ^{6}Li-glass scintillator, 25 mm dia x 0.5 mm thick, optically coupled to the photocathode of the microchannel-plate assembly (see Fig. 4) provides the necessary sensitivity to neutrons. Schrack[14] has described the operation of a similar neutron detector for a somewhat different purpose. The IPNS detector was supplied with charge-division position encoding electronics to produce a digitized 8-bit-each x,y output from the resistive anode signal. However, the y-encoding was modified at IPNS to give 7 bits of position with the 8th bit optionally used to signal the polarization state of the neutrons. Resolution has been measured with neutrons to be ~0.7 mm fwhm. As for the SCD detector, ^{6}Li-enriched lithium carbonate was used as the shielding material around the detector, with quite low gamma backgrounds as a result.

Linear Proportional Counters

As shown in Fig. 4, a second reflectometer (POSY-II)[10] has been constructed on the same beamline as POSY. The POSY-II instrument uses unpolarized neutrons. A commercial (Ordela,

Inc., Oak Ridge, TN, USA; model 1204N) ^{3}He-proportional-counter linear PSD serves as the detector for this instrument. This detector is planar, with an active volume of 20 x 5 cm^2, 2.5 cm thick. Position encoding is along the long dimension of the detector via rise-time encoding on the signals from the anode. This anode is made of a single carbon-coated quartz fiber which provides a high anode resistance so that good position resolution can be achieved. Measured resolution for this detector is ~1.6 mm fwhm. This spatial resolution yields adequate angular resolution for POSY-II since the sample-detector distance is much longer than on POSY. The much larger angular range covered by the 20 cm active length provides additional versatility for this instrument.

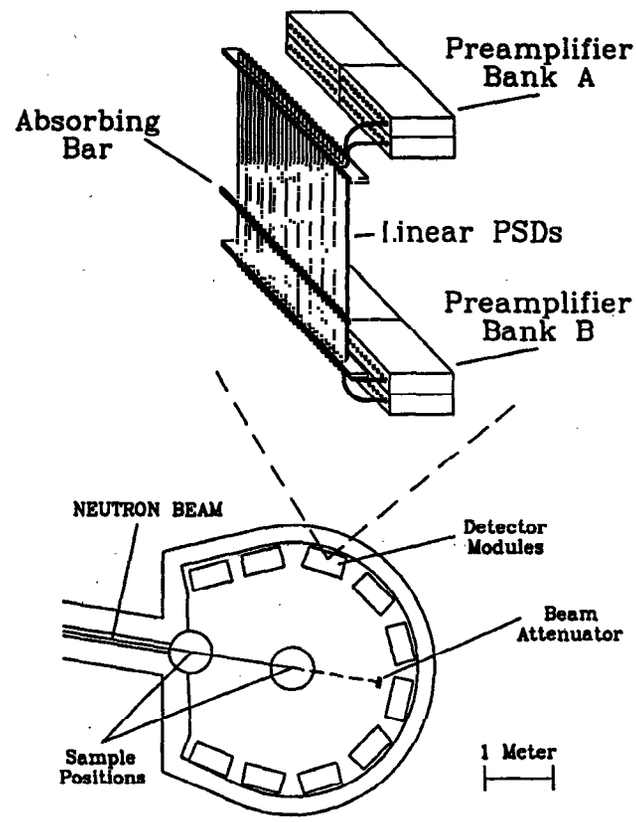

Figure 5. One of the detector modules for GLAD, showing the relative placement of the linear PSDs, preamplifiers, and motor-driven absorbing bar used for calibration. A layout of the GLAD instrument is also shown to indicate the locations of the 10 detector modules.

The Glass, Liquids, and Amorphous Materials Diffractometer (GLAD)[15,16] is optimized to obtain structural information from glasses and liquids. GLAD was designed to use multiple banks (detector modules) of linear PSDs, which permit it to handle high data rates and to cover low scattering angles. One such bank of PSDs is shown schematically in Fig. 5, which also indicates where all the detector modules are located in the instrument. GLAD is just being commissioned, but a prototype flightpath was in operation for two years prior to the installation of GLAD. This prototype enabled the making of extensive preliminary measurements to test the new detector and data acquisition systems and some of the calibration and data analysis procedures.

GLAD contains 160 commercial (Reuter-Stokes, Twinsburg, OH, USA; model RS-P4-0424-104) linear ^{3}He-proportional-counter PSDs at the present time, and this will eventually be

expanded to a total of 408. These detectors are mounted in modules with each module containing from 38 to 53 PSDs, depending on the location of the module in the instrument (Fig. 5). Each PSD is cylindrical with a diameter of 1.27 cm and an active length of 60 cm, and contains 10 atm of ^{3}He plus appropriate stopping gases (mostly Ar). Charge-division encoding is used to encode each of these detectors into 64 segments, and the resulting position resolution is currently measured to be ~14 mm fwhm. (These detectors and the mounting arrangements are similar to those used earlier on a steady-state instrument at the University of Missouri reactor[17] and on the SAN instrument at the KENS pulsed neutron source.[18] The encoding and data acquisition electronics for GLAD, which are quite different from those used in either of these other two instruments, have been discussed in detail elsewhere.[4]) The large integral nonlinearity near the PSD ends produced with the initial charge-division encoding electronics has now been fully understood and cured,[19] so that the entire active length of the detectors can be routinely used. Segments of these PSDs located in line with the direct beam have been successfully used to monitor sample transmissions[6] concurrently with the scattered neutron measurements which utilize the remainder of the segments of these same PSDs.

The GLAD detector mounting assemblies, preamplifiers, encoding modules, and operating software have been designed to facilitate initial tuning of the position encoding, absolute calibration of the encoded positions, and automatic testing for drifts in calibration. These calibration-related features have been described in detail elsewhere.[4,15,16] When the full GLAD detector complement is installed, data rates are expected to be relatively high (in extreme cases up to ~20,000,000 events/sec instantaneous and up to ~300,000 events/sec time-averaged). PSDs were required to provide the necessary angular resolution, particularly at small scattering angles. Since area PSDs typically have severe overall instantaneous data rate limitations and are difficult to fabricate with high efficiency for short-wavelength neutrons, arrays of linear PSDs were used instead. Gas proportional counters were chosen because of their commercial availability, reliability, and low intrinsic background counting rates.

V. SUMMARY

Beam monitors at IPNS are primarily ionization chambers, operated in the pulsed mode. These have been quite satisfactory. They are rugged, have a high degree of reliability, sample the entire beam uniformly, and have a well-defined efficiency variation with wavelength. Recent improvements in the preamplifiers used with these detectors have extended their range of usefulness to very short TOF values.

Most of the standard detectors at IPNS are cylindrical ^{3}He gas proportional counters. These are very reliable and have a very low intrinsic background counting rate. Nearly 750 such detectors are in use on the IPNS instruments at the present time.

Six different instruments at IPNS use neutron PSDs, and several different detector types have been adapted to meet the problems peculiar to these instruments and to their use at a pulsed neutron source. For all of these types of detectors the position encoding has been found to be quite stable and has shown little drift with time. Both the Anger camera and the microchannel-plate area PSDs

have operated satisfactorily for a number of years in their respective applications. The large number of linear PSDs in the GLAD instrument have been in operation for a much shorter period of time. During that time their performance was satisfactory for the requirements of that instrument, but some improvements in the encoding electronics are still being explored. The POSY-II linear PSD and the two small-angle diffractometer area PSDs are rise-time encoded proportional counters. These perform adequately for their present requirements, but have significant encoding nonlinearities near the detector edges. For the area PSDs these nonlinearities are sufficiently severe that portions of the active areas of these detectors are effectively unusable. Improvements in the linearity, spatial resolution, and overload response of these rise-time-encoded detectors and their respective encoding systems are under study.

Acknowledgements

The authors would like to thank numerous persons at Argonne and elsewhere who have contributed to the development of the detectors and electronics at IPNS. Particular thanks are extended to Mike Strauss, Raul Brenner, and Frank Lynch of the Argonne detector development group who were responsible for the Anger camera and the early gas area PSD. The authors would also like to acknowledge many helpful interactions Joe Skarupa and others at Reuter-Stokes, and with Manfred Kopp at Ordela.

References

1. R. K. Crawford, R. T. Daly, J. R. Haumann, R. L. Hitterman, C. B. Morgan, G. E. Ostrowski, and T. G. Worlton. IEEE Trans. Nucl. Sci. NS-28, 3692-3700 (1981).
2. J. R. Haumann, R. T. Daly, T. G. Worlton, and R. K. Crawford. IEEE Trans. Nucl. Sci. NS-29, 62-66 (1982).
3. J. R. Haumann and R. K. Crawford. IEEE Trans. Nucl. Sci. NS-34, 948-953 (1987).
4. R. K. Crawford and J. R. Haumann. IEEE Trans. Nucl. Sci., NS-37, 72-81 (1990).
5. R. K. Crawford, J. R. Haumann, A. J. Schultz, G. P. Felcher, J. E. Epperson, P. Thiyagarajan, D. G. Montague, and R. J. Dejus. Nucl. Instr. and Meth, in press.
6. D. G. Montague, J. M. Carpenter, R. K. Crawford, R. Dejus, D. L. Price, and S. Susman. "Use of a Semi-Opaque Beamstop for Monitoring Sample Transmissions at GLAD", these proceedings.
7. A. J. Schultz and P. C. W. Leung, Jr.. J. Phys. (Paris) Colloq. C5, 137-142 (1986).
8. M. G. Strauss, R. Brenner, H. P. Chou, A. J. Schultz, and C. T. Roche. Position-Sensitive Detection of Thermal Neutrons, ed. P. Convert and J. B. Forsyth, Academic Press, London. pp 175-187 (1983).
9. C. S. Borso, J. M. Carpenter, F. S. Williamson, G. L. Holmblad, M. H. Mueller, J. Faber, Jr., J. E. Epperson, and S. S. Danyluk. J. Appl. Cryst. 15, 443-448 (1982); J. E. Epperson, J. M. Carpenter, R. K. Crawford, P. Thiyagarajan, and T. E. Klippert, unpublished (1990).
10. R. K. Crawford, G. P. Felcher, R. Kleb, J. E. Epperson, and P. Thiyagarajan. Advanced Neutron Sources 1988, Proceedings of the 10th Meeting of the International Collaboration on

Advanced Neutron Sources (ICANS X). Institute of Physics Conference Series Number 97, IOP Publishing Ltd, New York. pp 257-262 (1989).
11. C. J. Borkowski and M. K. Kopp. Rev. Sci. Instrum. 46, 951-962 (1975).
12. F. J. Lynch. IEEE Trans. Nucl. Sci. NS-27, 327-328 (1980).
13. G. P. Felcher, R. O. Hilleke, R. K. Crawford, J. Haumann, R. Kleb, and G. Ostrowski. Rev. Sci. Instrum. 58, 609-619 (1987).
14. R. A. Schrack. Nucl. Instr. and Meth. 222, 499-506 (1984).
15. R. K. Crawford, D. L. Price, J. R. Haumann, R. Kleb, D. G. Montague, J. M. Carpenter, S. Susman, S., and R. J. Dejus. Advanced Neutron Sources 1988, Proceedings of the 10th Meeting of the International Collaboration on Advanced Neutron Sources (ICANS X). Institute of Physics Conference Series Number 97, IOP Publishing Ltd, New York. pp 427-450 (1989).
16. R. K. Crawford, J. M. Carpenter, R. Dejus, J. R. Haumann, R. Kleb, D. G. Montague, D. L. Price, and S. Susman. "Status of the New GLAD Instrument at IPNS", these proceedings.
17. R. Berliner, D. F. R. Mildner, O. A. Pringle, and J. S. King. Nucl. Instr. and Meth. 185, 481-495 (1981).
18. Y. Ishikawa, M. Furusaka, N. Niimura, M. Arai, and K. Hasegawa. J. Appl. Cryst. 19, 229-242 (1986).
19. R. K. Crawford and J. R. Haumann. Nucl. Instr. and Meth. A292, 657-670 (1990).

Q(M.W.Johnson): Variation in BF_3 monitor efficiency! What is possible?

A(R.K.Crawford): Beam monitor efficiency for ion chamber is quite stable. There is no gas gain, so temperature stability is unimportant for detector high-voltage. Only the stability of the amplifier system is important, and this is not too critical. (Don't have quantitative info, however.)

ICANS-XI International Collaboration on Advanced Neutron Sources
KEK, Tsukuba, October 22-26, 1990

AN UPDATE ON ISIS DETECTORS

P L Davidson, M W Johnson and N J Rhodes
ISIS Instrumentation Division
Rutherford Appleton Laboratory, Chilton, Didcot, Oxon, OX11 0QX, UK

At the last ICANS meeting we reported the successful trial of a lithium loaded ZnS scintillator material and predicted that this would be the basis of new ISIS detectors of the next few years. This has in fact been the case, and in this paper we report on the construction and performance of three detector types that have been put into successful operation. A fourth, PSD design, is at the prototype stage.

IRIS DETECTOR

The simplest of the designs is that for the IRIS backscattering spectrometer at ISIS shown in Figure 1. The detector consists of 51 elements each with an active area of 52 x 12 mm situated 610 mm from the graphite or mica analyser. The detector must be capable of running in the IRIS vacuum tank, and Figure 2 shows a close-up of both the PM manifold (enabling the PMs to run at ambient pressure) and the reflectors dividing the detector elements.

The light collection on this directly-viewed geometry is very good (Figure 3) and as a result the gamma discrimination ($ef_\gamma = 10^{-8}$) is the best of the detector types so far constructed.

The intrinsic background is also low, at 2 cts/element hour and as a consequence some excellent science has been performed on IRIS since the modifications. As an example, Figure 4 shows the rotor minimum in the ^{4}He at 1.2K. The signal is a weak one which could well have been swamped if the detector was at all noisy. In fact, the majority of background counts in this pattern are either 1 or 0, enabling the signal to be clearly seen.

HRPD 90° DETECTOR

The HRPD module was constructed, both to provide the excellent noise characteristics available for the ZnS detector, but also to provide the large solid angle/high θ resolution necessary at the HRPD 90° position. The detector consists of six modules stacked vertically on top of each other, each module consisting of 66 vertical strips 3 mm wide by 200 mm high. These are placed 1300 mm from the sample position and hence the completed detector will subtend a solid angle of 0.141 sr with a θ resolution of $\Delta\theta = 0.001$ rad.

The geometry of the scintllator and light coupling to the optical fibres is shown in Figure 5 and a picture of a completed module is shown in Figure 6. The use of optical fibres enables more efficient use of PMs, but results in a less efficient light collection. As a result, the γ rejection is slightly worse (at $ef_\gamma = 10^{-6}$) than that for the directly viewed IRIS detector, but is still close to that of a ^{3}He detector. The lowering of the background from this detector is illustrated (Figure 6a) by the patterns recorded for mythyl pyridine both in back scatter (using Li glass scintillator) and at 90° (using ZnS).

SANDALS 10°-20° DETECTOR

The SANDALS detectors for this angular range have been constructed in modules of 20 detectors, each detector having an active area of 10 x 200 mm. The modules use 21 PMs in a 'walking coincidence' arrangement to directly view the ZnS scintillator packs on edge (Figure 7). By adopting this geometry, a large number of scintillator elements may be placed in the path of the scattered neutron, and efficiencies of roughly 1.8 times that of a ^{3}He (10 bar) gas detector achieved at high neutron energies (10 eV). A photograph of the completed module together with the scintillator packs is shown in Figure 8.

Glass spacers are used to separate the individual ZnS elements in the scintillator pack, and it is believed that this relatively high mass of viewed material is contributing to the high intrinsic background of around 6 cts/element minute. The cause is thought to be Cerenkov radiation from cosmic ray events stopped in the scintillator path. While this background rate is not a serious problem on SANDALS, efforts to reduce it are being investigated by using 'air gaps' in the scintillator assembly.

PSD MODULE

Because of the intrinsically high light output from the ZnS scintillator, it has become clear that an x-y coded fibre-coupled PSD is a real possibility.

An outline for such a geometry is shown in Figure 9, illustrating how a bundle of four 1 mm optic fibres will be used to view each 3 x 3 mm active area of the detector. The fibres will then be used (2x, 2y) in a block coding system requiring only 32 PMs to code a 64 x 64 area PSD. An example of the quality of the data that can be recorded from such a system is shown in Figure 10, a prototype 16 x 16 module in use on the SXD machine at ISIS.

To summarise, we believe the use of ZnS scintillation in place of the Li-loaded glass of earlier designs is a great success, and has enabled new science and better results to be recorded on ISIS instruments. To give others some idea of the performance of these devices the results of the detectors is summarised in Table 1.

TABLE 1

Detector	$effic_n$	$effic_\gamma$	Intrinsic background cts/element hour
IRIS	36% @ 1Å 90% @ 6Å	10^{-8}	< 2
HRPD	36% @ 1Å	10^{-6}	3
SANDALS	9% at 10 eV	10^{-4}	360

Fig.1

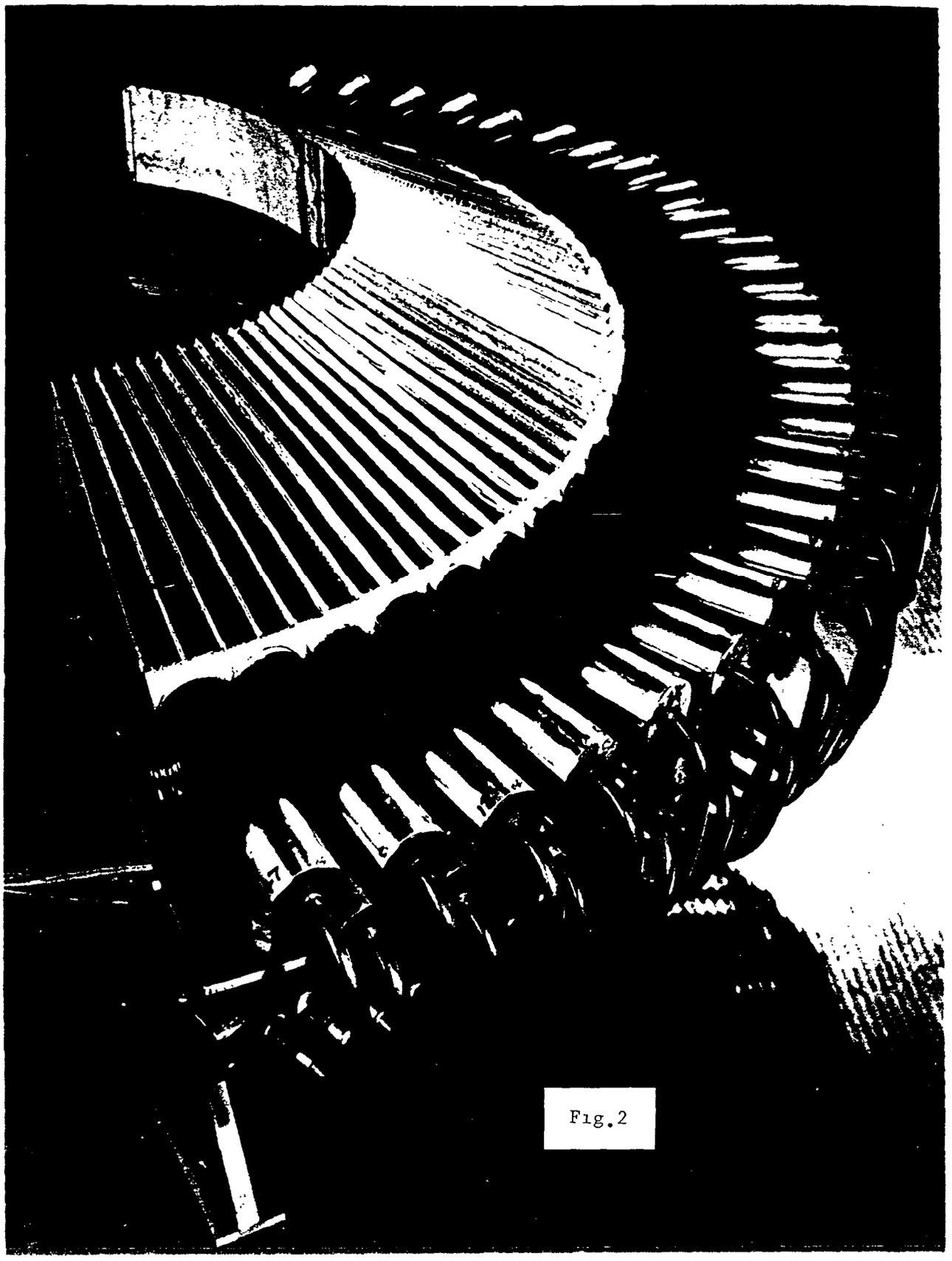

Fig.2

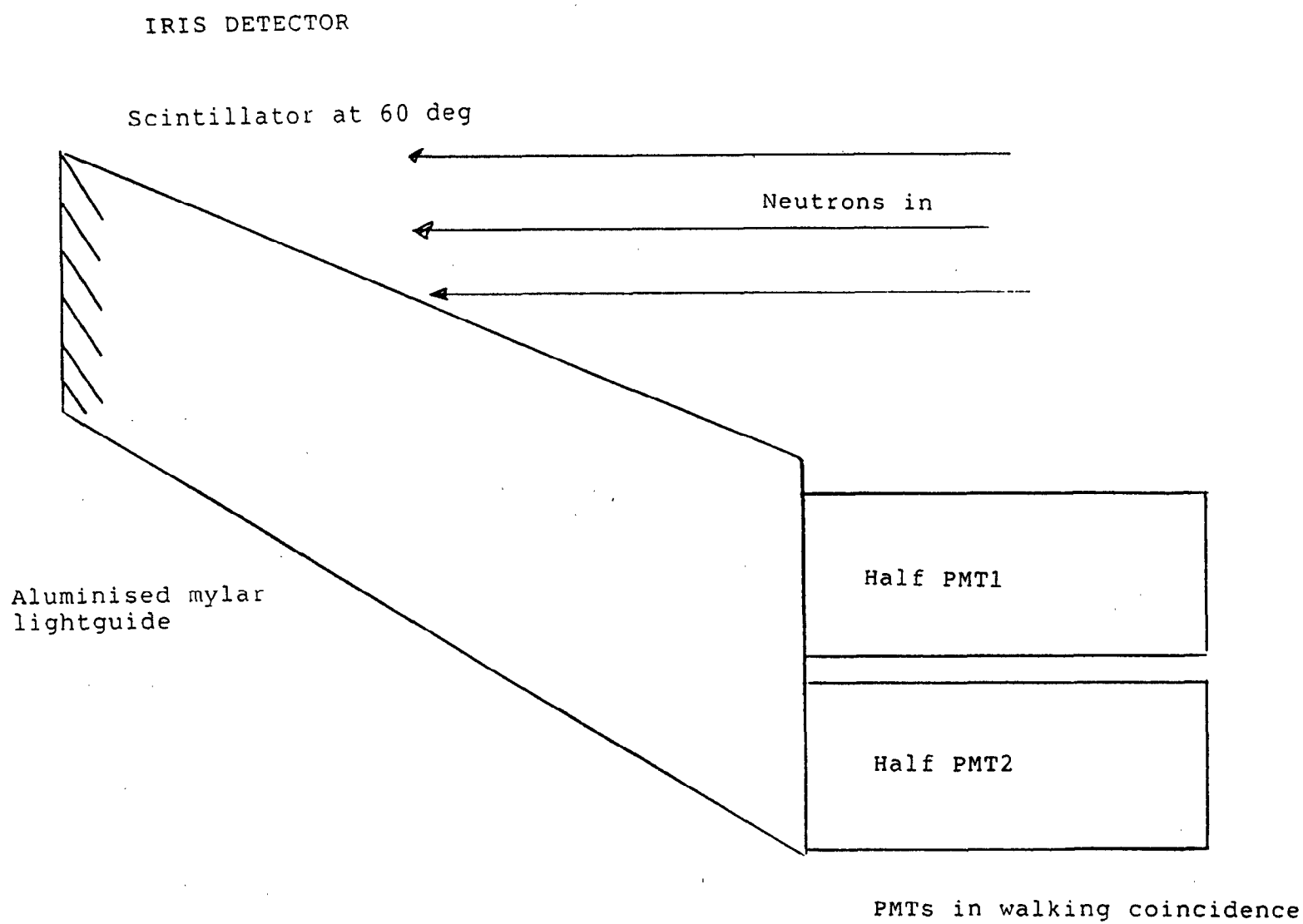
IRIS DETECTOR
Scintillator at 60 deg
Neutrons in
Aluminised mylar
lightguide
Half PMT1
Half PMT2
PMTs in walking coincidence

Fig.3

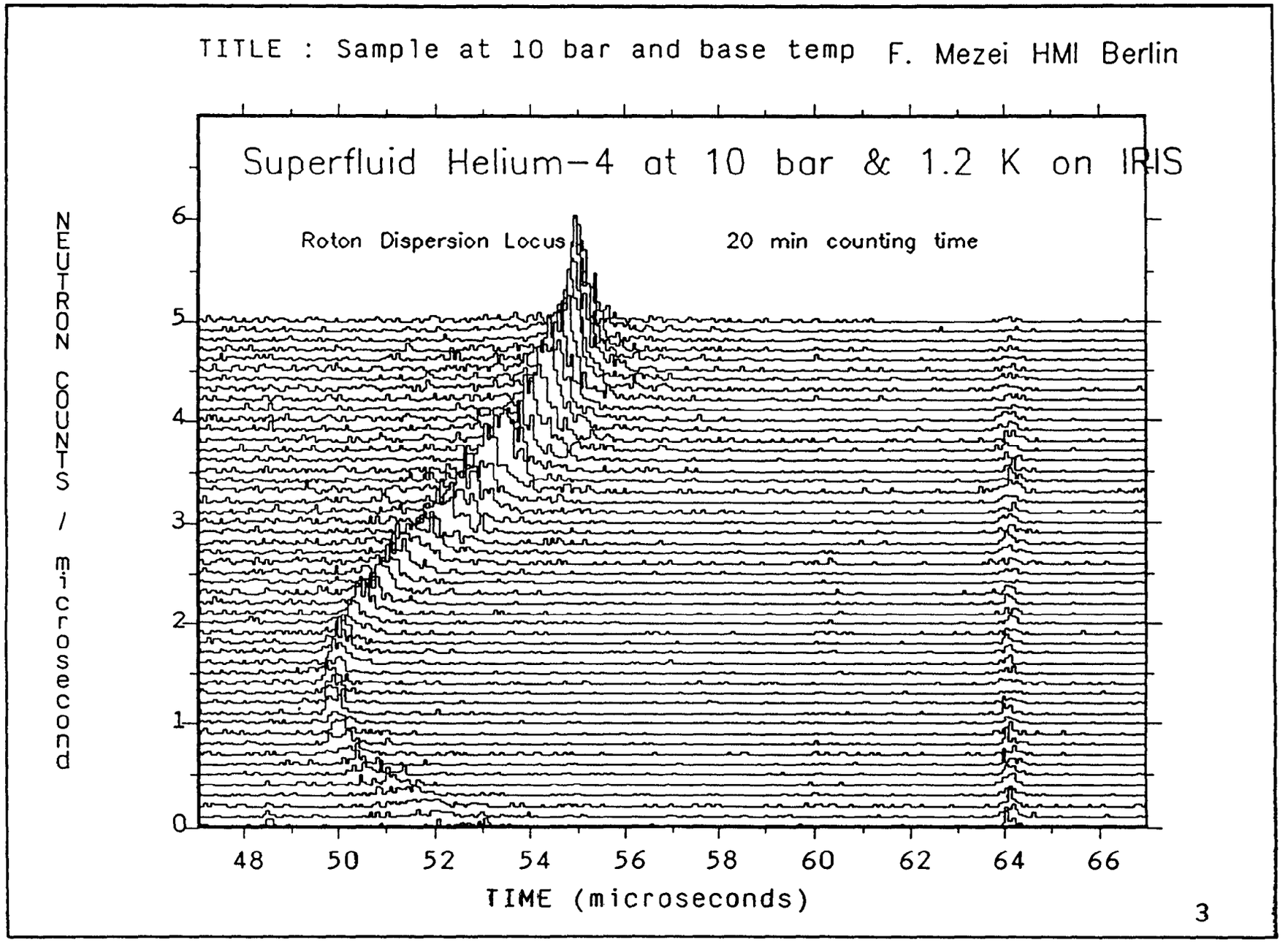
TITLE : Sample at 10 bar and base temp
F. Mezei HMI Berlin
Superfluid Helium-4 at 10 bar & 1.2 K on IRIS
Roton Dispersion Locus
20 min counting time
NEUTRON COUNTS / microsecond
0
1
2
3
4
5
6
48
50
52
54
56
58
60
62
64
66
TIME (microseconds)
3

Fig.4

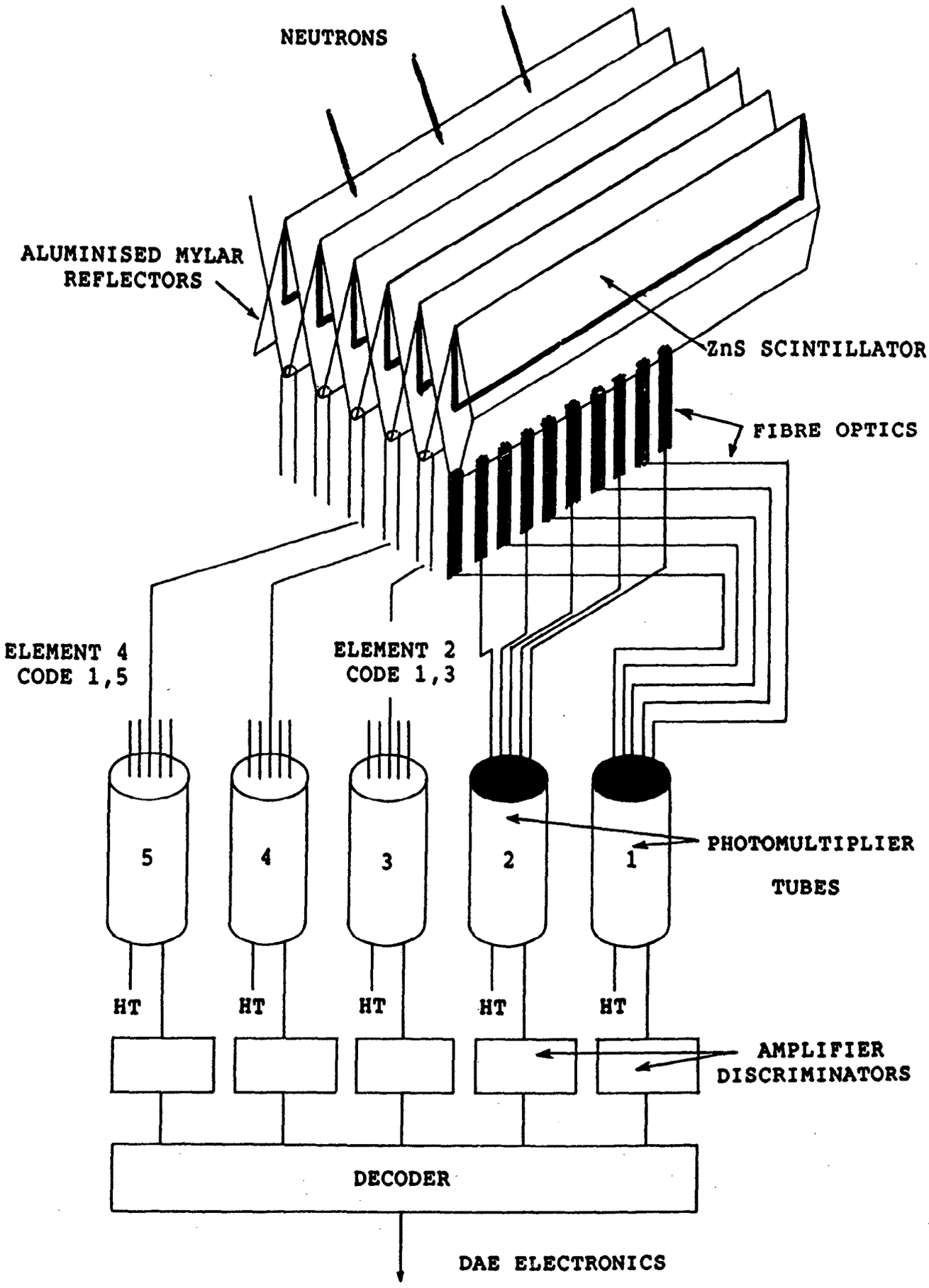
NEUTRONS
ALUMINISED MYLAR
REFLECTORS
ZnS SCINTILLATOR
FIBRE OPTICS
ELEMENT 4
CODE 1,5
ELEMENT 2
CODE 1,3
5
4
3
2
1
PHOTOMULTIPLIER
TUBES
HT
HT
HT
HT
HT
AMPLIFIER
DISCRIMINATORS
DECODER
DAE ELECTRONICS

Fig.5

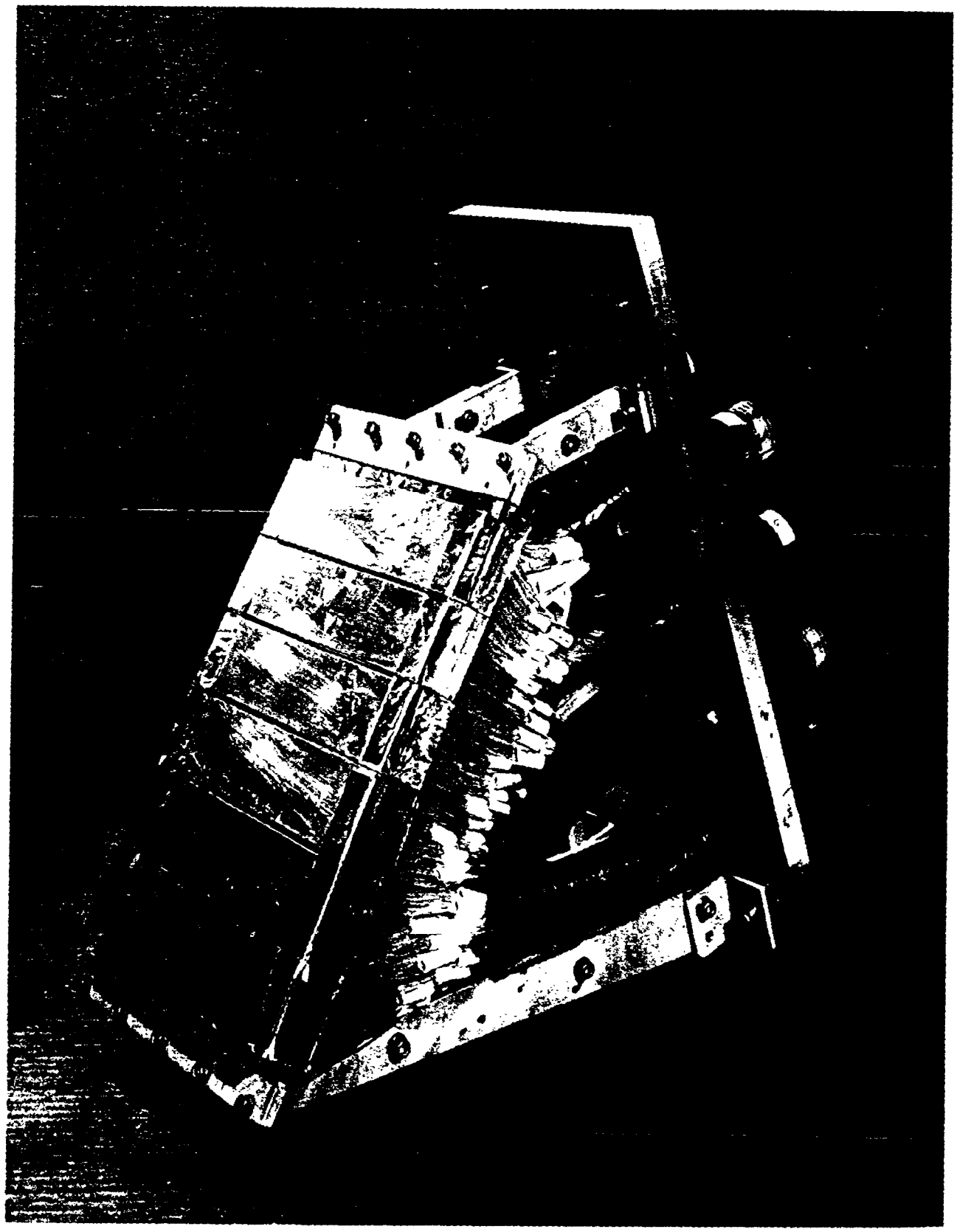

Fig.6

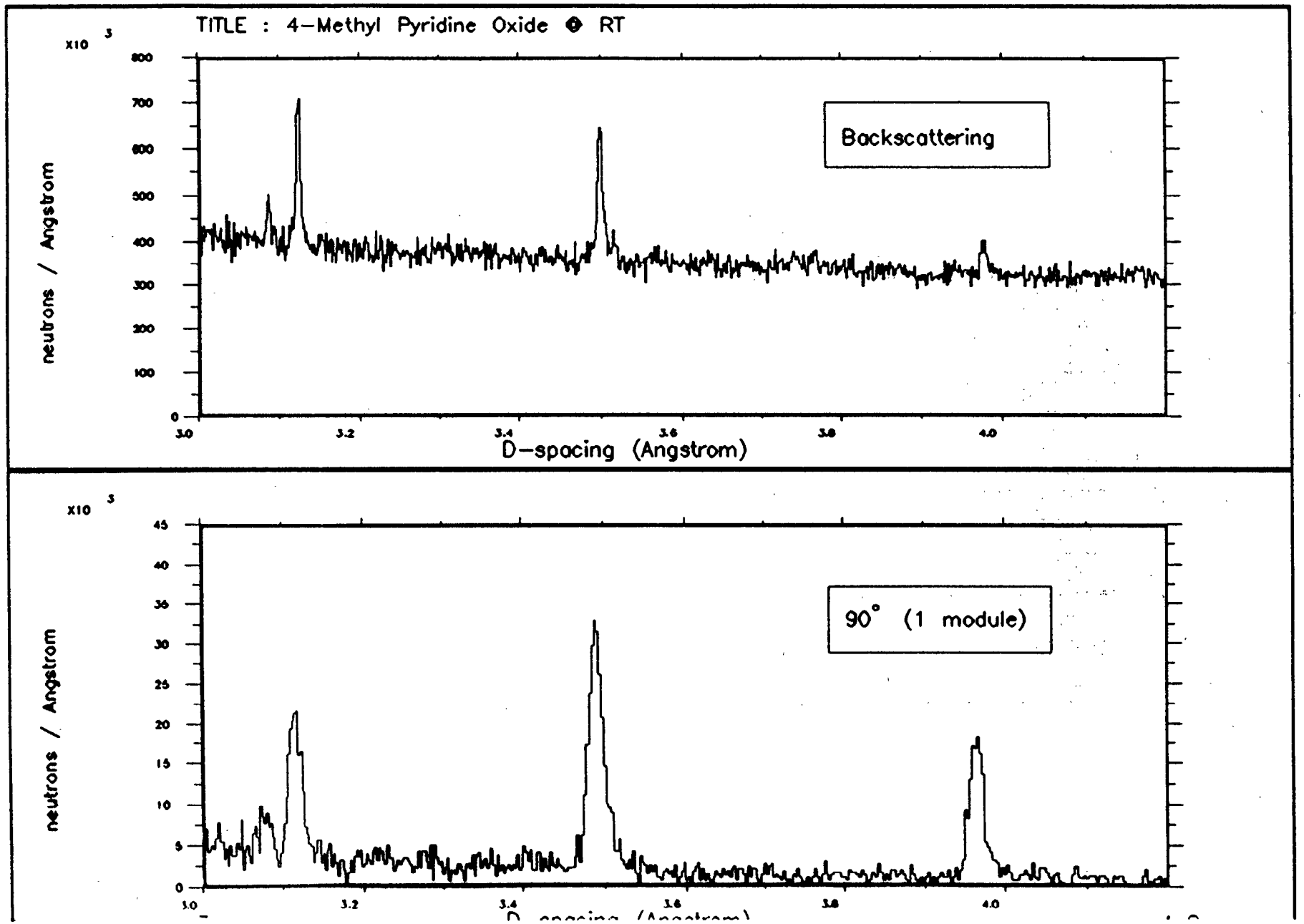
TITLE : 4-Methyl Pyridine Oxide @ RT
x10 3
neutrons / Angstrom
Backscattering
D-spacing (Angstrom)
90° (1 module)

Fig.6a

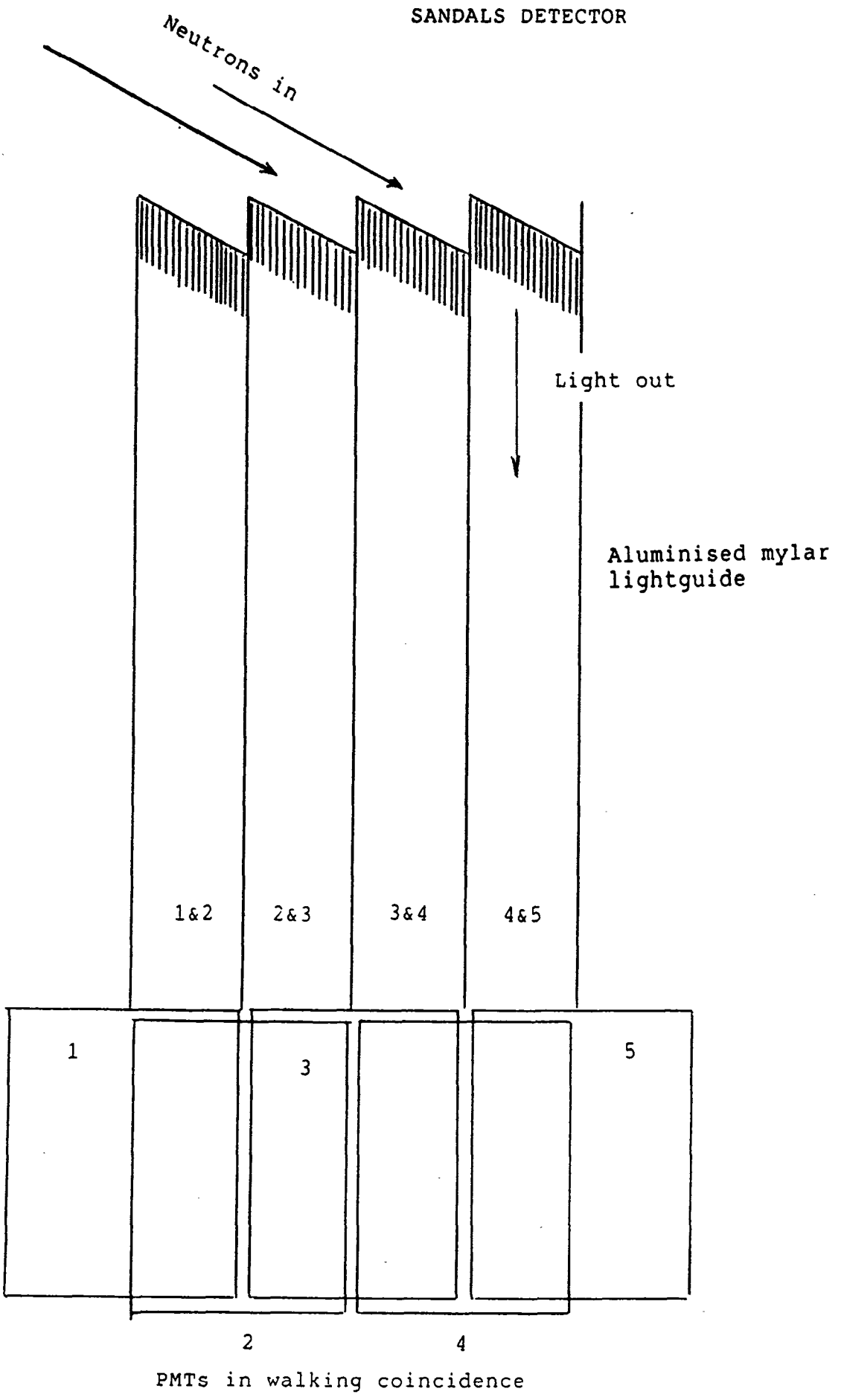
SANDALS DETECTOR
Neutrons in
Light out
Aluminised mylar lightguide
1&2
2&3
3&4
4&5
1
3
5
2
4
PMTs in walking coincidence

Fig.7

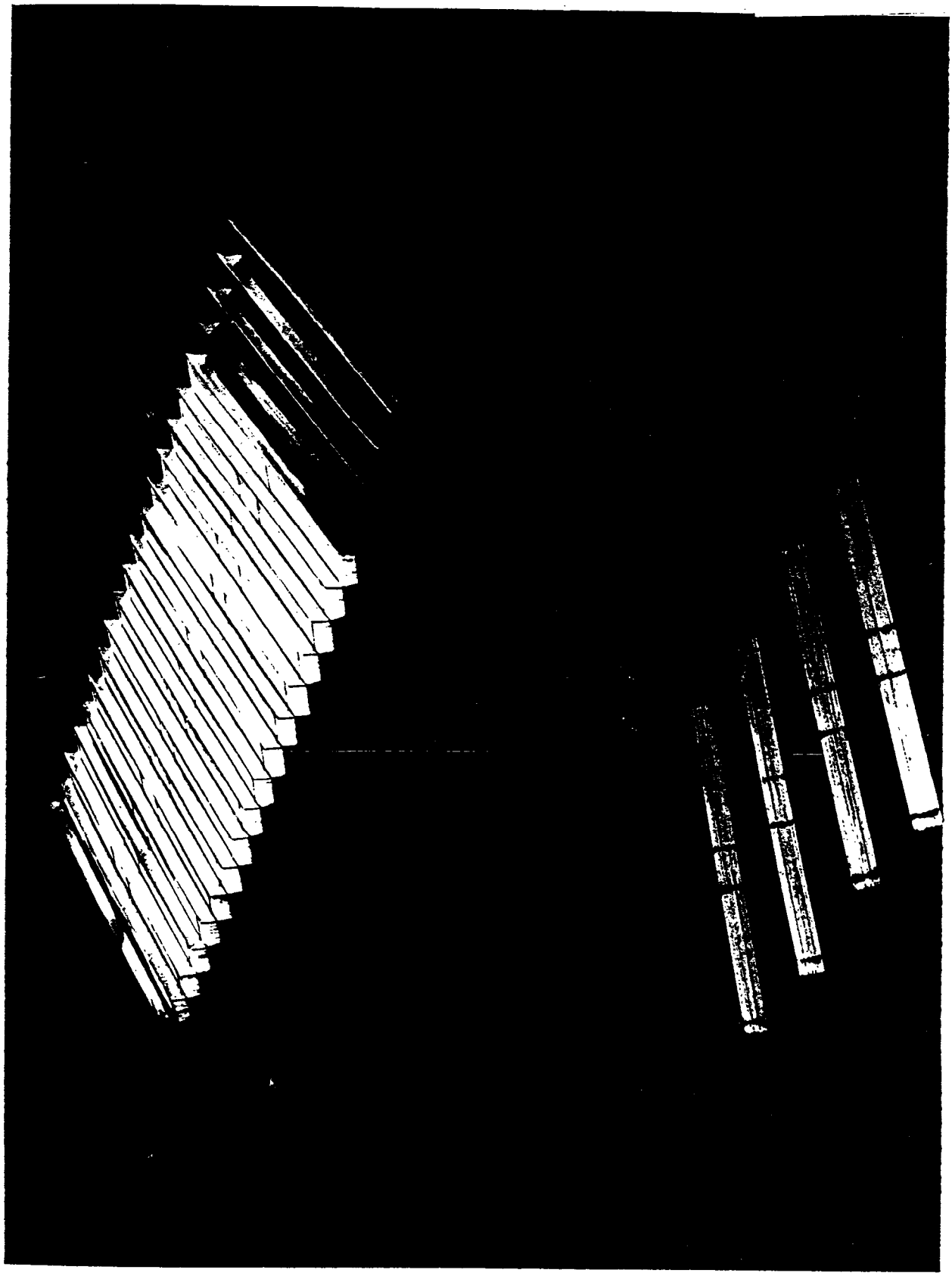

Fig.8

Fig.9

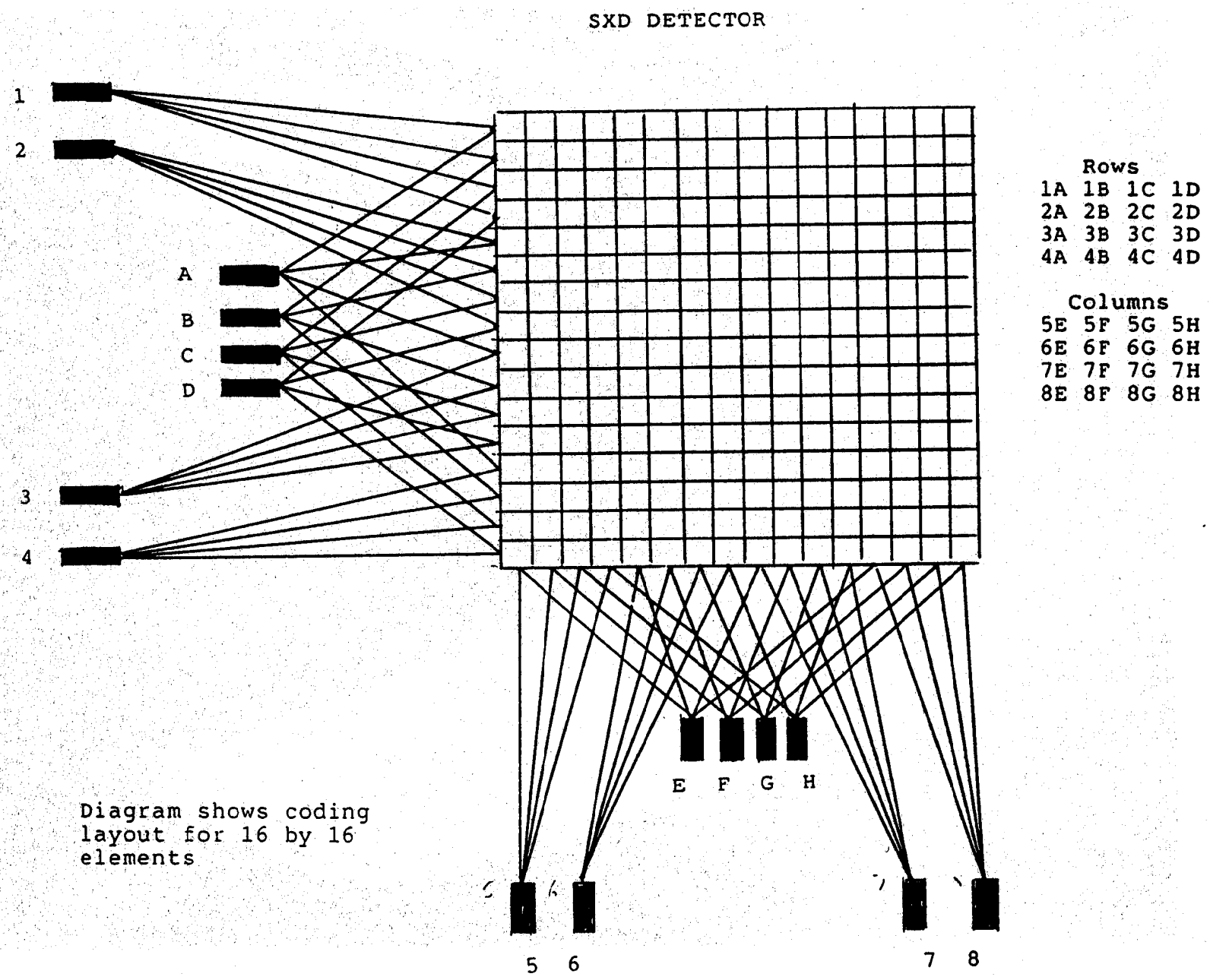

Diagram shows coding layout for 16 by 16 elements

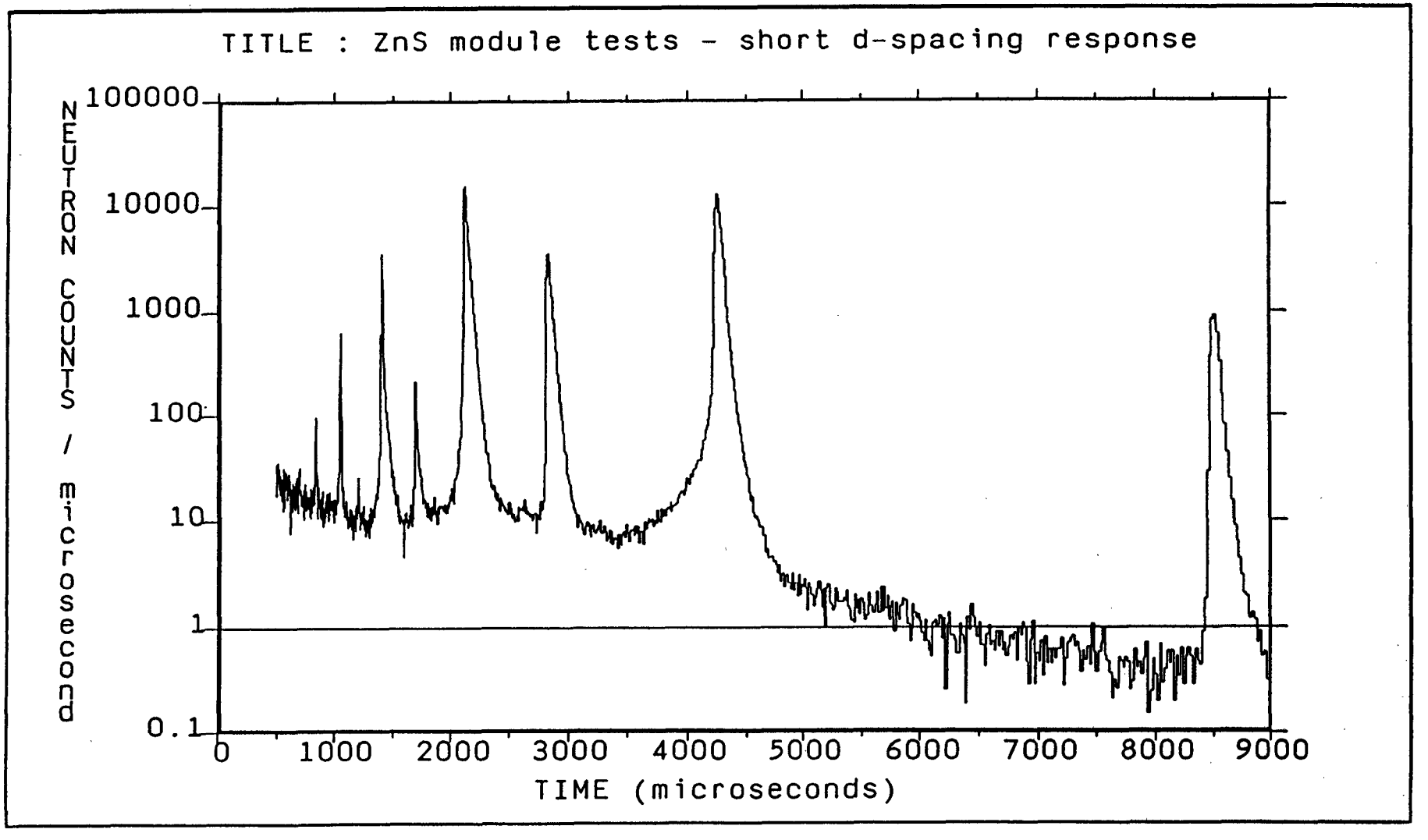
TITLE : ZnS module tests - short d-spacing response
NEUTRON COUNTS / microsecond
100000
10000
1000
100
10
1
0.1
0
1000
2000
3000
4000
5000
6000
7000
8000
9000
TIME (microseconds)

Fig.10

Q(Y.Masuda): Why did you use two phototubes for one detector?

A(M.W.Johnson): By using a coincidence technique, it gives a lower quiet count rate by eliminating much of the inherent noise from a single photomultiplier tube.

Q(J.B.Hayter): What count-rate can be handled by your 2-D detectors?

A(M.W.Johnson): The dead time for ZnS is about 2 μs, with some possibility to reduce it to about 1 μs. The 2-D detector can therefore easily run at 50-100kHz without major dead-time corrections.

Q(N.Niimura): Why do you think the S/N ratio of ZnS is so good, if we compare it with Li-glass scintillator? Is it the difference of the photon production?

A(M.W.Johnson): Yes, It is simply that the light output for ZnS is approximately ten times that of Li loaded glass.

Q(C.C.Wilson): Can the efficiency of ^{6}Li-loaded ZnS scintillator be increased by using thicker scintillator than the 0.4 mm used commonly?

A(M.W.Johnson): Not at present. The binder used with ZnS is not fully transparent and increasing the thickness will simply reduce the light output. What we need is a high refractive index transparent binder to hold the ZnS scintillator crystals.

ICANS-XI International Collaboration on Advanced Neutron Sources
KEK, Tsukuba, October 22-26, 1990

Several experiences of using Li-glass scintillators

N.Niimura, H.Hirai*1, K.Aizawa*2, K.Yamada*3 and F.Okamura*4

Laboratory of Nuclear Science, Tohoku University, Mikamine 1-2, 982 Sendai, Japan
*1 Kanagawa Institute of Technology, Atsugi 234-02, Japan
*2Institute for Materials Research, Tohoku University, Sendai, Japan
*3 Faculty of Science, Tohoku University, Sendai,Japan
*4 National Institute for Research in Inorganic Materials, Tsukuba, Japan

ABSTRACT

This paper describes several experiences using Li-glass scintillators as neutron detectors in KENS. Detectors reported in this paper are an epithermal and thermal neutron beamline monitor, a semicircle one-dimensional position sensitive detector and an annular detector. These are specially designed , constructed and equipped in the real spectrometers in KENS.

I. INTRODUCTION

^{6}Li glass scintillators have several advantages as well as disadvantages. The advatages are as follows: 1) The dead time is less than 100 nsec, and 2) It is easy to modify the shape artificially, and the disadvatages are as follows: 1) It is sensitive for γ- ray, and 2) It produces small amounts of photons.With the use of the advatages of the scintillators we have specially designed three kinds of detectors, those are,an epithermal and thermal neutron beamline monitor[1], a semicircle one-dimensional position sensitive detector[2] and an annular detector[3].

II. NEUTRON BEAMLINE MONITOR

Conventionally, fision detectors made of thin layers of $^{235}U_3O_8$ powder are equipped to monitor the intensity of the neutron beam. In spite of good signal to noise ratio, they have some disadvantages such as slow response and complex efficiency vs energy relationship at epithermal energies. On the contrary, our detectors using ^{6}Li glass scintillator (GS) have the advantageous to overcome such problems, i,e., they are prompt and have a simple efficiency vs energy relationship over the cold and epithermal range of neutron energy. To cover the whole area of neutron beam cross section homogeneously and to realize minimum attenuation of the incident beam, we have decided to use GS in powder form.

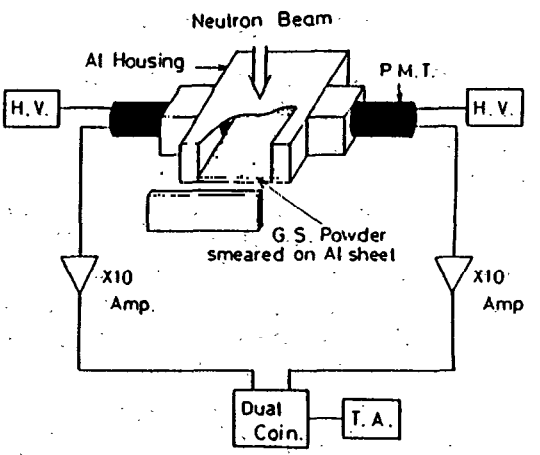

Fig. 1. The layout of the neutron beamline monitor.

Fig.1 shows the layout of the new type of monitor system using GS powder. 0.8 mg/cm^2 GS powder of 95 μm diameter in average is coated on a thin aluminium square sheet 6x6 cm^2 in area, 0.2 mm in thickness. A pair of photomultipliers (PMTs) is attached to the side of the housing. The output signals of these PMTs are fed to a 2-input coincidence circuit to remove electric noise.

The neutron counting efficiency ic controlled by changing the quantity of GS powder coating. As a matter of fact, the same type of GS monitor is put to practical use for transmission measurements by increasing the counting efficiency with the use of the thick GS powder coating.

These detectors have been equipped in KENS's thermal neutron small angle scattering instrument (WIT).

III. ANNULAR DETECTORS

Annular ^{6}Li glass scintillators are designed and constructed for the detector system of WIT since the small-angle neutron scattering (SANS) pattern on the area detector is annular about the beam center for the case of the isotropic scattering sample. If an annular detector is provided in SANS, the data handling system including electronics becomes extremely simple. Since a large and continuous Q range is required, annular detectors with different radii are preferable.

Pieces of Li glass scintillators (2 mm in thickness) were stuck on the surface of the annular transparent acrylic resin with optical cement. The ring was wrapped with aluminum foil to reflect scintillation photons escaping out of the acrylic resin. As shown in Fig. 2., eight PMTs were coupled to the rear side of the annular acrylic resin. Thickness of the acrylic resin has been determined to be 5 cm so that any position where a scintillation event occurs can be subtended directly by more than two PMTs, to allow detection of scintillation photons in coincidence.

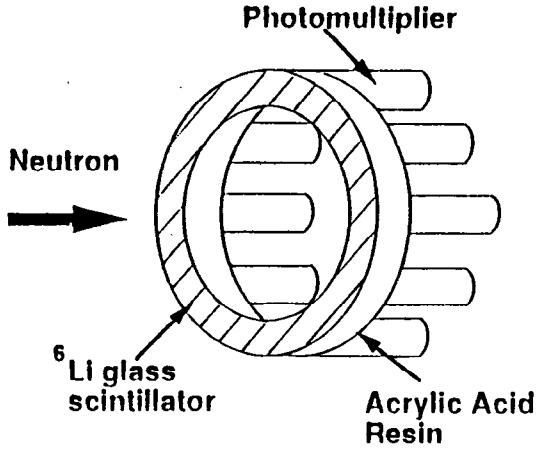

Fig. 2. The couplig of the photomultiplier tubes and the annular acrylic resin.

The width of the ring defines the spatial resolution. The resolution of the momentum transfer Q for small angle ($=2\pi\phi/\lambda$, where ϕ is a scattering and λ is a wavelength) is written as follows:

$$\Delta Q/Q=\Delta\phi/\phi,$$

$$\Delta\phi^2=\Delta\phi^2_{col}+\Delta\phi^2_{det},$$

where $\Delta\phi^2_{col}$ and $\Delta\phi^2_{det}$ are the fluctuations of the scattering angle which come from the collimator divergence and the width of the ring detector, respectively.

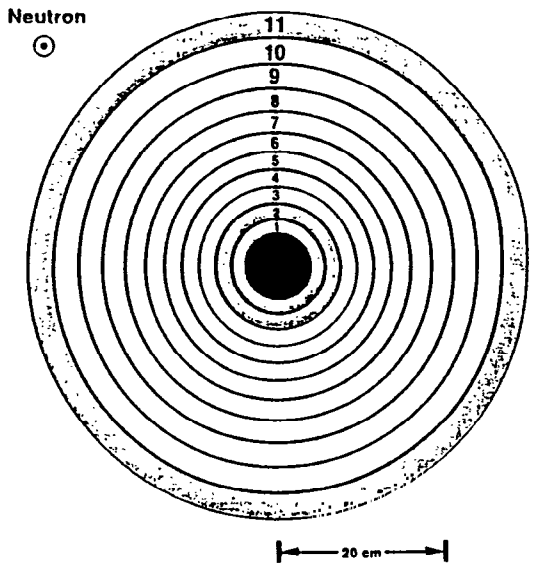

Fig. 3. The whole assembly of the annular detectors equipped in WIT.

The whole assembly of the annular detectors is given in Fig. 3, where #1 and #2 are not used for measurement any more because the foot of the incident beam profile touches them, and #11 is neither used because PMTs are not yet installed there. The radius and the widths of 12 annular detectors are tabulated with Q range covered using neutrons of wavelength between 0.4 A and 6 A in Table I.

The Q-range covered by the detector assembly is from 0.027 A^{-1} to 0.967 A^{-1} when neutron wavelengths from 0.5 A to 6 A are used.

IV. SEMICIRCLE ONE-DIMENSIONAL POSITION SENSITIVE DETECTORS

When a one-dimensional position sensitive detector (PSD) is used on a time-of-flight(TOF) single crystal diffractometry, a two-dimensional area of reciprocal space can be accessed, because white neutrons of continuous wavelength are used in TOF diffractometry.

To test the feasibility of the method, we have used the linear gas proportional PSD and found the several problems. First,the range of scattering angle is very limited, and the positional resolution at the end part of the detector becomes extremely poor since the detector is linear and the diffractd neutron injects obliquely there. Secondly, the detector has a long dead time (*i.e.* several μsec). Especially,in TOF measurements the dead time of detectors is a big problem, since the peak flux of neutrons is more important than the time-averaged flux,and all the neutrons reaching the detectors in one burst must be separately detected.

Ring NO.	Mean R mm	Delta R mm	scattering angle 2θ	q min A^{-1}	q max A^{-1}
1	49	16	14.1mrad	0.015	0.178
2	68	18	19.7	0.021	0.248
3	88	18	25.5	0.027	0.320
4	109	20	31.6	0.033	0.397
5	131	20	37.8	0.040	0.476
6	154	22	44.7	0.047	0.562
7	179	24	51.8	0.054	0.651
8	206	26	60.0	0.063	0.750
9	235	28	68.1	0.071	0.855
10	266	30	77.0	0.081	0.967
11	299	32	86.2	0.090	1.083

Table I

To solve the above problems, a semicircle one dimensional PSD using ^{6}Li-glass scintillators (GSs) has been constructed. The GSs respond to the neutron detection very quickly (70 ns), and have the advantage of allowing the possibility of a semicircle detectors since it is easy to modify the shape artificially . A fibre optic encoding method is applied for position definition of the one-dimensional PSD for the TOF single crystal diffractometry, since in this method the over all dead time of the PSD can be guaranteed to be less than 1 μsec.

We have constructed a new semicircle one dimensional PSD. The PSD is now installed at the four circle single crystal diffractometer (FOX) .

The layout of the PSD is shown in Fig. 4. A scintillation element is cylindrical, 3mm in diameter and 30 mm in height. A total of 384 scintillator elements sits side by side and forms a semicircle 45cm in radius. Flexible plastic optical fibres (3mm in diameter) are connected to both ends of the scitillator element. One detector element consists of 3 scintillator elements, so the size of the detector element is 9mm x 30mm. This size is adopted by considering the divergence of the incident beam and the normal degree of mosaicity in a single crystal specimen. The lowest and the highest scattering angle are 10.6 degree and 167.8 degree, respectively. An azimuthal angle of one scintillator element subtended by a sample is 3.82 degee.

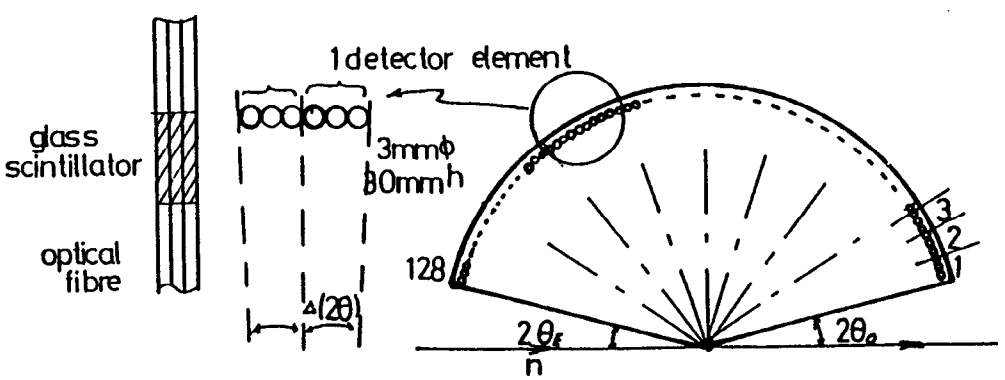

Fig. 4. The layout of the semicircle one-dimensional position sensitive detectors equipped in FOX.

References

1) M.Hirai, N.Niimura and A.Ishida, Nucl. Instr. Meth.,A259 (1987) 497
2) N.Niimura, K.Aizawa, A.Ishida, M.Ueno, M.Hirai, U.Sangawa and K.Yamada, to be submitted in J. Appl. Cryst.
3) N.Niimura, I.Kawada, M.Isobe, F.Okamura and K.Yamada, to be submitted in J. Appl. Cryst.

Q(C.C.Wilson): What is the angular resolution of the linear PSD on the 4-circle diffractometer i.e. What is L_2, the secondary flight path.

A(N.Niimura): Angular resolution is determined just by the size of one pixel, that is, 9 mm x 30 mm. L_2 is fixed to 45 cm.

Q(I.Kanno): In the neutron beam monitor with glass scintillator powder, how do you transport the photons to the photomultiplier? Do you use any reflector in the box? Are several sheets used?

A(N.Niimura): The photons are transported though the air. No reflector. Aluminum sheet itself is a reflector. One sheet.

Q(H.M.Shimizu): What is photon collection efficiency of your powder Li glass scintillator?

A(N.Niimura): I did not calculate it, but it is just the solid angle subtended by the photomultiplier, if we neglect the absorption loss of photons in the air.

ICANS-XI International Collaboration on Advanced Neutron Sources
KEK, Tsukuba, October 22-26, 1990

Instrument Workshop Summary on New Components - Detectors

R. K. Crawford
Argonne National Laboratory, Argonne, IL 60439, USA
and
N. Niimura
Laboratory of Nuclear Science, Faculty of Science, Tohoku University
1-2-1 Mikamine, Taihaku-ku, Sendai-shi 982, Japan.

The number of formal presentations in this workshop session was deliberately limited in order to allow some time for general discussion of detector-related topics of interest. The five formal presentations corresponding to papers submitted for the proceedings and the discussions specific to them are summarized first. Since the full papers are available in the proceedings, these summaries are very brief. The detection system which was to have been presented by Charlie Bowman is summarized in somewhat greater detail, since there is no other paper on that system in the proceedings. Finally, the topics raised in the general discussion period and the discussions which they gave rise to are presented in summary form.

Dr. Maeda described the development of and initial results obtained with two-dimensional multi-wire gas proportional counters using a ^{3}He-Ar-CO_2 fill gas. Both a 21x21 cm^2 prototype and a 51x51 cm^2 detector were constructed. This latter detector was developed for use on a small-angle scattering instrument at the KUR reactor at Kyoto. These detectors could be encoded by charge-division encoding, delay-line encoding, or by wire-by-wire readout, offering an useful intercomparison of the various encoding techniques. Delay-line encoding resulted in a resolution of ~5 mm fwhm. Details of these detectors are provided in the paper "Area detector for small-angle neutron scattering at KUR" by Y. Maeda, M. Sugiyama, and S. Uehara in these proceedings.

Dr. Shimizu discussed several different scintillation counters which were used in a nuclear-physics experiment on parity non-conservation in neutron-nuclear interactions, being done on one of the neutron beams at KENS. The neutron detectors in this experiment were a 10-micron thick indium foil coupled with a plastic scintillator and used as a beam monitor, and a ^{10}B liquid scintillator used to detect the main neutron beam after its passage through the sample target. The gamma rays produced by interactions in the sample were detected using BaF_2 scintillators. The liquid scintillator has high-data-rate capabilities which may be of interest for some neutron scattering experiments, as it can operate at 10 MHz data rates with no apparent problems. Details of these detectors are included in the paper "Scintillation detector system in neutron-nuclear experiments" by Y. Masuda, H. M. Shimizu, and T. Adachi in these proceedings.

Kent Crawford gave a general overview of the neutron detectors in use at IPNS, with emphasis on the beam monitors and the various types of position-sensitive detectors used there. This detector summary is contained in the paper "Neutron detectors at IPNS" by R. K. Crawford, J. R. Haumann, and G. E. Ostrowski in these proceedings.

Mike Johnson presented Peter Davidson's paper, which brought us up to date on the current status of the ^{6}Li-containing ZnS scintillation detectors being developed and used at ISIS. Three instruments, IRIS, HRPD, and SANDALS now rely heavily on these detectors, and a large position-sensitive detector of this material is currently being fabricated for use on SXD (see "Single crystal diffraction at ISIS" by C. C. Wilson in these proceedings). In all cases coincidence between two or more photomultipliers (PMTs) is required to produce a countable event, and this essentially eliminates problems from intrinsic PMT noise. For the 51-element IRIS detector, the gamma/neutron discrimination is ~10^{-8} and the intrinsic background is ~2 counts/element/hour. For the HRPD detectors the corresponding numbers are ~10^{-6} gamma/neutron discrimination and ~3 counts/element/hour intrinsic background. The ZnS scintillator is nearly opaque, so the individual scintillator pieces are made thin to allow the light to escape. In most of these detector systems neutrons are incident at an angle to the plane of the ZnS scintillator in order to increase the detection efficiency. In the SANDALS detectors where high efficiency is required down to quite short wavelengths, a number of layers of the scintillator are stacked with space between them for the light to escape. Details of these detectors can be found in the paper "Developments on neutron detectors" by P. L. Davidson in these proceedings.

Nobuo Niimura discussed some of the detectors made with ^{6}Li-glass scintillator material at KENS. These have been made in a variety of geometries with several different types of encoding, using glass from Japanese manufacturers. Particularly heavy use is on the WIT thermal-neutron small-angle diffractometer, which has an area detector with concentric annular segments made of this scintillator, and also has an incident beam monitor utilizing powdered glass scintillator. The annular detector uses pattern discrimination applied to the signals from the various PMTs in order to reduce background noise. A wide-angle detector array of this scintillator is used on the FOX single-crystal diffractometer at KENS as well. More details are available in the paper "Several experiences of using Li-glass scintillators" by N. Niimura, H. Hirai, K. Aizawa, K. Yamada, F. Okamura, and M. Isobe in these proceedings.

Although Charlie Bowman was unable to attend the ICANS meeting and hence could not give his talk scheduled for this session (C. D. Bowman and H. G. Priesmeyer, "Current-mode neutron detection for stroboscopic diffraction studies"), he was kind enough to send some materials describing the Bowman-Priesmeyer detection system used for very-high-instantaneous intensity (up to ~10^{11} neutrons/sec) in-beam transmission measurements. This is the detection system used for the single-pulse test experiment reported by Peter Egelstaff above ("Experiments using single neutron pulses" by C. D. Bowman, P. A. Egelstaff, and H. G. Priesmeyer in these proceedings). The material Charlie sent has been presented for publication elsewhere (J. D. Bowmam, J. J. Szymanski, V. W. Yuan, C. D. Bowman, A. Silverman, and X. Zhu. "Current-Mode Detector for Neutron Time-of-Flight Studies"), and so is only summarized briefly here.

This detection system involves current-mode operation of a photomultiplier tube coupled to a thick ^{6}Li-glass scintillator. The detector and data collection system are shown schematically in Fig. 1. Since the system was designed to have high efficiencies at rather high neutron energies, a 1 cm thick NE905 ^{6}Li-glass scintillator was used. This scintillator was 13.3 cm in diameter and optically coupled to a Hamamatsu R1513 12.5 cm photomultiplier. The S20 type photocathode was used to provide the large photocathode currents (up to 1.6 μA) required at the highest instantaneous detection rates (~10^{11}/sec). Each of the last 4 dynodes of the 10-dynode chain in the PMT was connected to its individual high-voltage/high-current power supply in order to keep the last 4 dynode voltages fixed for all photocathode voltages. With this design the maximum allowed instantaneous anode current was 32 mA. A transient digitizer (DSP model 2012S) was used to read out the resulting time-of-flight spectrum from a single pulse (see the Egelstaff presentation cited above). The sampling time interval of this digitizer can be varied between 50 ns and 10 μs. A multipole filter was used to shape the incoming signal with a time constant matched to this sampling time interval. The digital output of the transient digitizer was transferred to the signal-averaging memory (DSP model 4101) after each pulse. Results from a single pulse or a number of pulses could be accumulated there, and this memory could also be used to subtract out spurious signals which were in phase with the 60 Hz line frequency.

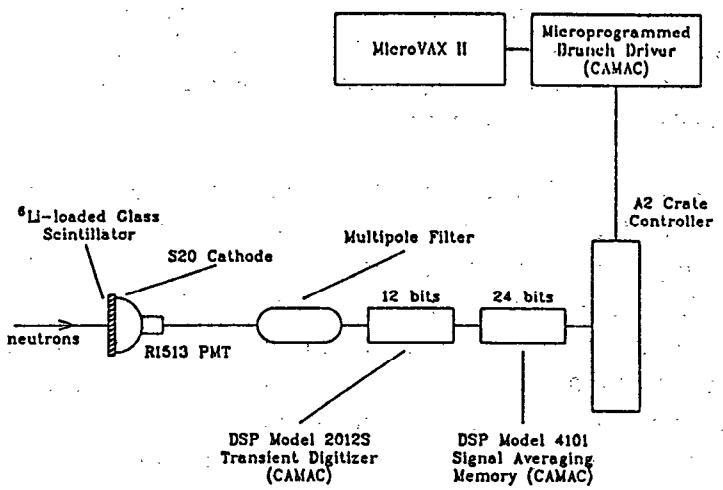

Figure 1. Schematic diagram of the Bowman-Priesmeyer current-mode neutron detection system.

Figure 2 shows the transmission of a ^{238}U sample measured with this detection system. A number of resonance absorption lines can be clearly seen. Also shown in the figure are similar measurements at much lower counting rates made using traditional pulse-counting techniques. The current-mode measurements did not permit discrimination against gamma rays (as is done with pulse-height discrimination in the usual pulse-counting measurements), so there is a significant gamma background in the current-mode measurements. This is seen most clearly for the resonance at 66 eV (near 500 μs) where the transmission goes nearly to zero as measured in the pulse-counting mode but is significantly above zero as measured in the current mode. Such gamma problems would likely be significantly reduced if a 1-2 mm thick ^{6}Li-glass scintillator, which is adequate for neutrons below ~1 eV, were used. Despite these gamma-ray problems, this current-mode measuring technique does offer the capability for collecting neutron time-of-flight data at the

extremely high instantaneous rates required to obtain adequate data from a single pulse. As the intensity of pulsed neutron sources continues to increase it is likely that this technique will find more and more uses among the neutron-scattering community.

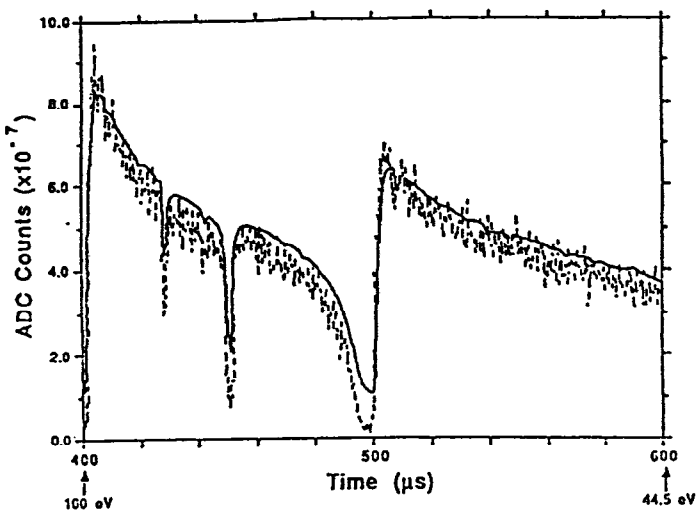

Figure 2. Neutron transmission through a ^{238}U sample. The solid curve is the time-of-flight spectrum collected using the current-mode detection system discussed here. The dashed curve shows transmission through the same sample, measured with traditional pulse-counting techniques. The axis-labels refer to the solid curve, and the dashed curve has been scaled to provide rough correspondence.

In the discussion it was noted that the session co-chairmen were developing a survey of neutron detectors in use or under development at the various steady-state and pulsed neutron sources in the world, and input into this survey was solicited from the workshop participants. Considerable discussion also centered on the need for very small detectors (2-3 mm) for use as transmission beam monitors for small-angle scattering experiments. It was noted, however, by John Hayter and Peter Egelstaff that any direct measurement of transmission in a small-angle-scattering experiment will be contaminated by the sample small-angle-scattering, so care should be exercised when using this means of measuring the sample transmissions. There was some discussion concerning the lack of uniformity in efficiency of the ^{6}Li-glass scintillators. Glass obtained in Europe seems to have varied in efficiency from batch to batch, complicating the fabrication of detectors from this material. Nobuo Niimura stated that no such problems had been detected with ^{6}Li-glass from their Japanese source. General concerns were expressed about the time and temperature stability of detectors and detection electronics, and the effect this might have on absolute intensity measurements. No one had any hard numbers on this for any of the different types of detection system discussed, but there was some feeling that photomultiplier-based systems might suffer the most from such problems.

In conclusion, it was very encouraging to see the large numbers of different types of detectors which were being operated successfully in the various laboratories, and the considerable amount of detector and electronics development which is ongoing. The excellent results obtained with the ZnS scintillator detectors at ISIS are particularly encouraging, and it is likely that the use of such detectors will spread rapidly to other neutron-scattering laboratories.

ICANS-XI International Collaboration on Advanced Neutron Sources
KEK, Tsukuba, October 22-26, 1990

Neutron diffraction study in pulsed high magnetic field

M.MOTOKAWA, H.NOJIRI, M.UCHI and S.WATAMURA
Department of Physics, Faculty of Science, Kobe University, Rokkodai Kobe 657

H.KAWAI and Y.ENDOH
Department of Physics, Faculty of Science, Tohoku Universi ty, Sendai 980

ABSTRACT

We have developed a technique for neutron diffraction experiments in pulsed high magnetic fields to determine magnetic structures in high field. Our system is capable to produce pulsed fields up to 20 T every 2 sec. The experiment was done using MRP diffractmeter at KENS. The magnet was the so-called Bitter type water cooling solenoid with 40 mm inner diameter, 240 mm outer diameter and 220 mm length. It was horizontally installed on the goniometer. The flow type FRP cryostat was set in the magnet and the temperature was down to almost 4.2 K but there was a heating problem for metal sample when a pulsed magnetic field was applied. The first application has been done for a determination of high field magnetic structure of metamagnetic $PrCo_2Si_2$.

I. INTRODUCTION

As is well known, many magnetic materials show magnetic phase transitions in high magnetic field and it is important to investigate magnetic structures in such high field phases by neutron diffraction. However, the magnetic field available in neutron diffraction experiments has been limited below 10 T so far even a superconducting magnet is used. The discussion in this paper is on the method to do neutron diffraction experiments in magnetic fields above 10 T.

There are several ways to produce high magnetic field, and they are classified usually to two categories. One is DC field

and another is pulsed field. DC field can be produced by using conventional electromagnet, superconducting magnet, water cooling Bitter type magnet and hybrid magnet. The electromagnet which produces only 2 or 3 T is out of question for our purpose. The available field by using superconducting magnet is now up to 20 T but when used for neutron diffraction experiment, it may be limited to 10 T due to complicated configuration of equipments. The water cooling Bitter type magnet can provide 20 T and the hybrid magnet which is the combination of Bitter type magnet and large superconducting magnet is capable to generate 30 T[1]. The electric power necessary for Bitter type magnet[2] is calculated by

$$H = G\sqrt{\frac{W_{DC}}{\rho}}, \qquad (1)$$

where H is the produced field, G geometrical factor of the magnet, W_{DC} electric power, ρ resistivity of the coil material. W_{DC} is roughly estimated to be a few MW for 20 T in a space of about 100 cm^3. This power is converted to heat and then cooling system for the magnet is also huge. Then we consider it is almost impossible to use them for neutron diffraction experiments.

On the other hand, techniques for producing pulsed high magnetic field and its application to physics have been well developed in this decade. We do not discuss the destructive methods which can produce fields above 100 T[3] because it is considered to be impossible to combine with neutron diffraction experiments. In the non-destructive way, it is possible to obtain 80 T[4] by a method developed in Osaka University. But it is not so

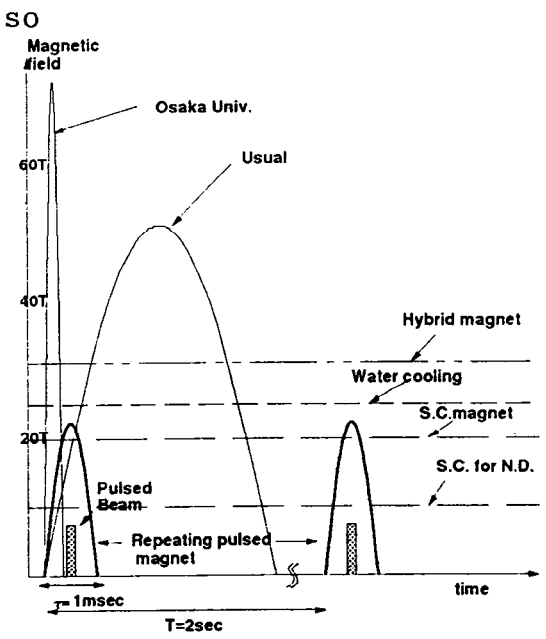

Fig.1 Methos to produce high magnetic and time duration

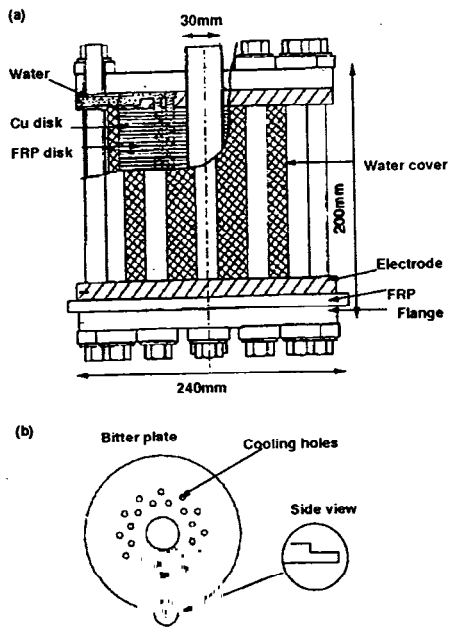

Fg.2 (a) Cut view of the magnet and (b) top view of a disk

compact to be installed in neutron facility. The most conventional and popular way is to use a magnet wound by copper wire and cooled by liquid nitrogen. This method is capable to produce fields up to 40 T and is widely used. The maximum fields obtained by these methods are summarized in Fig.1 with time duration of pulsed field. Grössinger *et al*[5] have tried to use single shot pulsed field with a reactor operated in a flushed manner, but the beam intensity was not strong enough to detect the diffraction.

We have considered that repeating pulsed fields synchronized with the neutron beam pulses will be useful for high field neutron diffraction experiments and have developed the technique for it[6].

II. REPEATING PULSED FIELD

The repeating pulsed field is defined as a pulsed field which is produced cyclically with an interval T as is shown in Fig.1. What we have to consider to design the repeating pulsed field are the followings:

1) Type of magnet.
2) Field shape as a function of time
3) Pulse width
4) Interval of pulsed field
5) Available maximum field
6) Configuration of installation

1) Type of magnet

Repeating pulsed field is the intermediate between a DC field and a single shot pulsed field. The heat is integrated by every shot and then the magnet must be cooled. The easiest way for cooling is to use a Bitter type magnet. We made disks with thickness of 1 mm and a shape shown in Fig.2(b) and stacked around 100 disks with insulator disks. The cut view of the magnet is shown in Fig.2(a).

2) Field shape

We use capacitor discharge method as is discussed in reference 6, then the field shape is inevitably half-sin curve. For neutron diffraction experiments, however, rectangular shape is favorable. It is possible using a complicated circuit if a budget is enough but difficult by using a simple circuit like ours. We are planning to make a flat-top field as is shown in Fig.3 in an economical way.

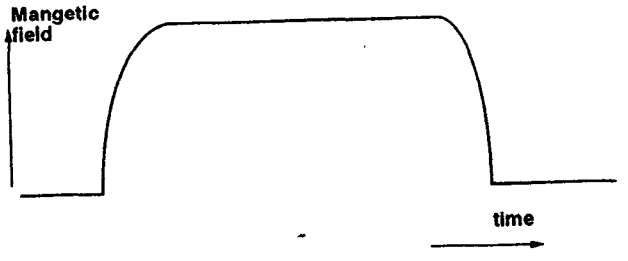

Fig.3 Shape of flat-top field

3) Pulse width

This is determined by the inductance L of the magnet and the capacitance C of the capacitor bank as $\tau = \sqrt{LC}$. When we use Bitter type magnet, L is determined by the volume of the field space and is of the order of 100 μH. From the field intensity and the volume of the field space, the energy of the capacitor bank is given and from the limitation of available charging voltage, C is estimated to be of the order of mF. Then τ is of the order of msec. In our case, the energy of capacitor bank is 60 kJ with C=1.2 mF and τ is 1 msec.

4) Interval of pulsed field

This is determined by charging ability of the power supply and ability of the cooling system. The cooling rate is reduced by the relation

$$W_{RP} = (\tau/2T)\cdot W_{DC}, \qquad (2)$$

for half-sin shape, where W_{RP} is the electric power consumed by repeating pulsed field system. Both charging ability and cooling ability partly depend on budget but T~0.1 sec may be a limit bcause the system must be compact and easy for treatment. In our case T=2 sec as is discussed in reference 6.

5) Available maximum field

This is limited by the strength of the magnet material. By normal copper, we obtained fields up to 20 T. If we use reinforced copper, 30 T may be available. For one shot pulsed field, maraging steel is used in Osaka University[4]. It has a strength capable to produce fields up to 40 T. When it is used for repeating pulsed field, W_{DC} is estimated from Eq.(1) to be about 40 times larger than that of copper case due to almost 10 times larger resistivity. At present time, we can produce 20 T field by using copper disk magnet.

6) Configuration of installation

As will be discussed later, we now use a magnet whose field direction is almost parallel to the neutron beam direction. Sample is set at the center of the magnet and liquid He flow type cryostat is used. In this configuration, however, we consume too much liquid He and also the available scattering angle is small due to small diameter of the magnet. We are now planning to build a split type magnet with vertical field. This will enable us to use vertical cryostat and to have large scattering angle. But the maximum field in the gap will be reduced to about 75 % of that of solenoid.

III. HIGH FIELD NEUTRON DIFFRACTION OF $PrCo_2Si_2$

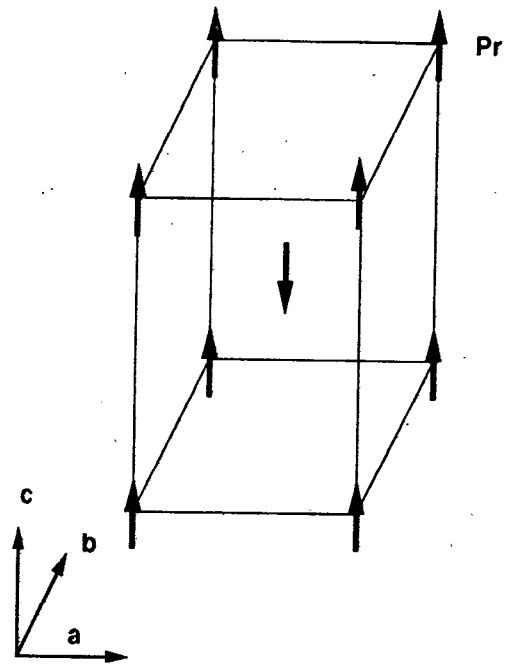

Fig.4 Magnetic structure of $PrCo_2Si_2$

Only Pr has magnetic moment in this crystal and it aligns ferromagnetically in the c-plane while antiferromagnetic coupling with the adjacent layer below T_1=9 K as is shown in Fig.4. Between T_1 and T_2=17 K, it turns to a long pitch incommensurate structure with a propagation vector k=0.926 and has another structure with k=0.777 between T_2 and T_N=30 K, as are shown in Figs.5 and 6[7]. On the other hand, when an external field is applied along the c-axis at 4.2 K, it shows metamagnetic transitions at 1.2, 3.8 and 12.2 T[8] due to Ising like strong anisotropy. From the field induced

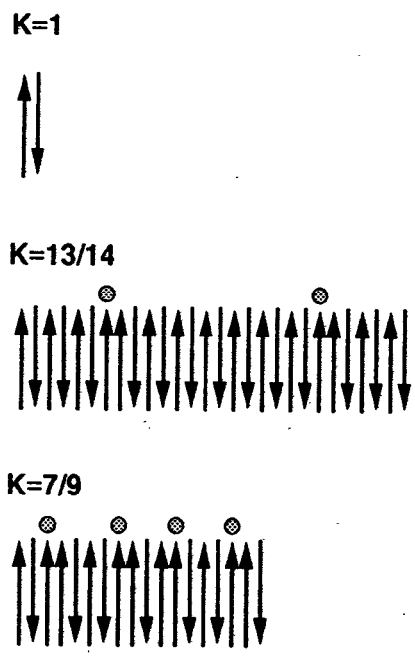

Fig.5 Magnetic alignments of antiferromagnetic and incommensurate states

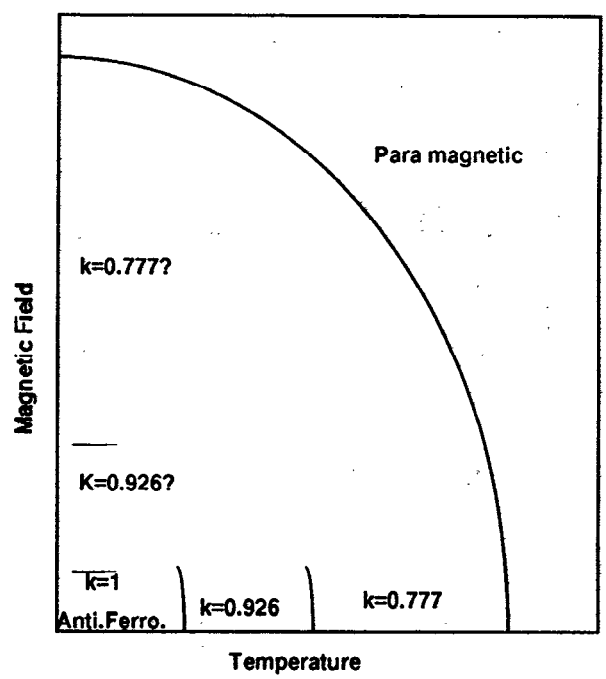

Fig.6 Inferred phase diagram

moment, the magnetic structures in these states are inferred to be same as those appears in the intermediate temperatures. The results are schematically summarized in Fig.6. Our present purpose is to confirm these structures by neutron diffraction.

The sample size was 6mm in diameter and 7 mm thickness and the magnetic field was parallel to the c-axis. The beam size was about 15 × 10 mm^2. The diffraction angle was kept at $2\theta=10^\circ$ and the horizontal rotation of the sample was limited within a few

degrees because of small aperture of the magnet. This configuration was enough to scan the area of reciprocal space concerning the expected propagation vectors. The wave length of used neutron was about 1 Å. Since the metallic materials cannot be used for both cryostat and sample holder due to eddy current heating, we used a FRP cryostat and a BN ceramics sample holder. The magnet and cryostat was set up on a goniometer which adjusted the angle between the incident neutron beam and the c-axis of the sample. The experimental set up is shown in Fig.7.

First we observed diffraction changing temperature at zero field to adjust the configuration of equipment and to check the sensitivity and accuracy of the system. Next we applied external fields up to 16 T at 4.2 K and obtained the expected Bragg reflection corresponding to the complicated magnetic structures. The experiment was done by time of flight method. The wave length λ of neutron beam is proportional to time after spallation. Fig.8

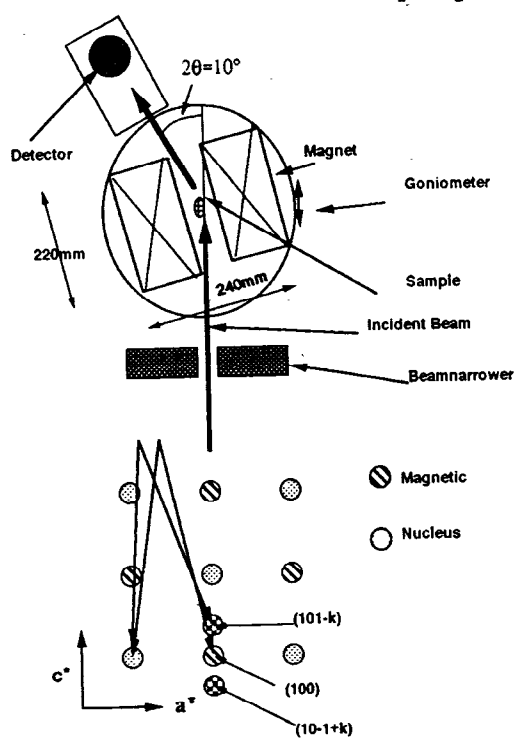

Fig.7 Experimental set up for high field neutron diffraction experiment

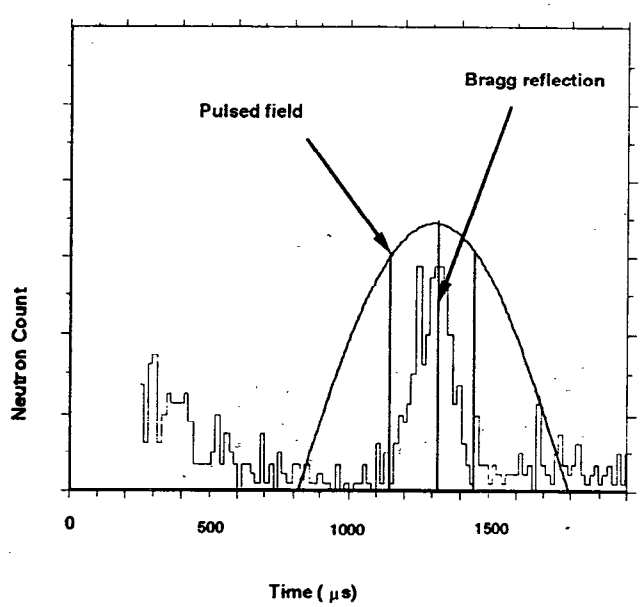

Fig.8 Synchronized pulsed field to neutron beam of relevant wave length

shows the time relation between the neutron beam with relevant λ and the generated pulsed field. To observe a Bragg reflection at high field, the field pulse was synchronized so as to coincide with the neutron beam of desired λ at the field peak. The observed Bragg reflection had a width due to resolution of detector and mosaic structure of the specimen and the resultant width was about 200 msec in time spectrum. Because of half-sin shape of the field, field change during this time was about 10%. But this was not a serious problem in this case because the structure was supposed to be same in a phase when an applied field was adjusted

at the intermediate of the transition fields. The interval of the pulsed field was 2.5 sec because of the accelerator operation program and then it took 40 times longer time than the ordinary experiment. However the intensity of the Bragg reflection strong enough to take data in an hour or two. We scanned mainly around (1,0,0) magnetic peak and observed (1,0,1-k) satellite peak arising from the incommensurate structure with propagation vector k. The scanning was done by changing an angle of the incident neutron beam to the c-axis of the sample. The value of k was determined by the change of incidence angle of neutron beam. Heating of sample by eddy current occurred during field generation, then the temperature was higher than 4.2 K when the Bragg reflection observed in high field. The real temperature of the specimen in a pulsed field was estimated by the following way. We applied a pulsed field just before the time corresponding to the Bragg reflection of antiferromagnetic state, and measured the reflection intensity at zero field, which reflected the temperature just after the field application. As the relation between temperature and intensity of Bragg reflection had been obtained by Shigeoka *et al.*[7], we calibrated temperature using it.

An example of the obtained data is shown in Fig.9, in which the Bragg reflection by (1,0,0.777) corresponding to the incommensurate state is seen at 11.5 T but it disappears at 14 T. All the data obtained by our experiments are summarized in Fig.10 as a phase diagram. The phases determined by the present experiment is consistent with the expected ones from the magnetization measurement.

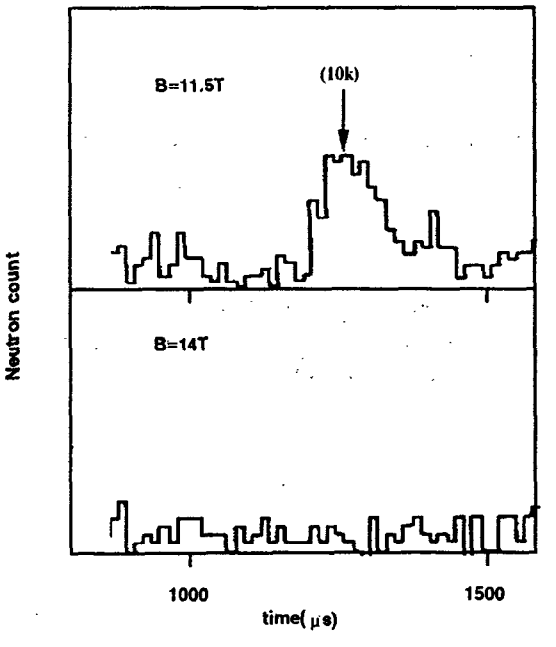

Fig.9 Bragg reflection at 11.5 T which disappears at 14 T.

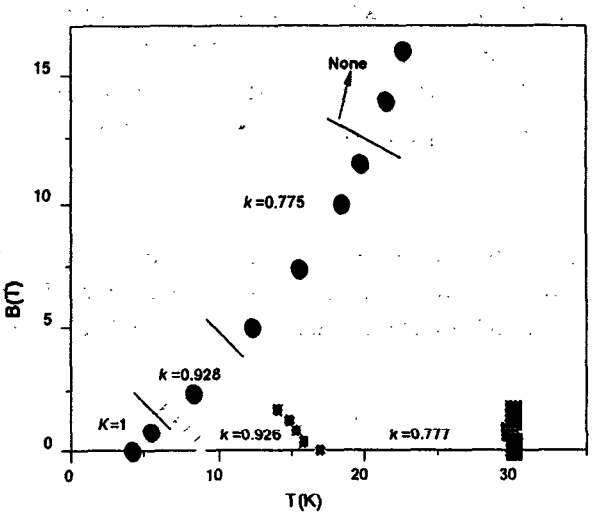

Fig.10 Confirmed phase diagram
● is observed point

IV. CONCLUSION

We have succeeded in neutron diffraction experiments in a high magnetic field up to 16 T and shown the repeating pulsed magnetic field is quite useful for pulse neutron experiments.

ACKNOWLEDGMENT

The authors would like to express sincere thanks to Professor M.Date of Osaka University for his encouragement and to Professor N.Watanabe of National Laboratory for High Energy Physics for his encouragement and collaboration. They are also indebted to the members of KENS for their collaboration and to Dr. T.Shigeoka for supplying single crystals of $PrCo_2Si_2$. This work was supported by a Grant-In-Aid for Science Research from Japanese Ministry of Education, Science and Culture.

References

1. F.Herlach, Strong and Ultrastrong Magnetic Fields and Their Applications (Springer-Verlag, 1985)
2. D.B.Montgomery, Solenoid Magnet Design (Wiley-Interscience, 1969)
3. N.Miura and F.Herlach, Strong and Ultrastrong Magnetic Fields Their Applications (Springer-Verlag, 1985) ed. F.Herlach p.247
4. A.Yamagishi and M.Date, Physica B155, 91 (1989)
5. Grössinger, G.Badurek, Ch.Gigler and Ch.Schotzko, Physica B155, 392 (1989)
6. M.Motokawa, H.Nojiri, J.Ishihara and K.Ohnishi, Physica B155, 39 (1989)
7. T.Shigeoka, N.Iwata, H.Fujii, T.Okamoto and Y.Hashimoto J.Mag.Mag.Mater.70, 239 (1987)
8. T.Shigeoka,H.Fuji,K.Yonenobu,K.sugiyama and M.Date J.Phys. Soc.Jpn. 58, 394 (1989)

Q(R.Pynn): Can one look at time-dependent phenomena after a magnetic pulse has been applied?

A(M.Motokawa): Yes, It is easy to look at time-dependent phenomena after a field pulse. One can see the time dependence of diffraction after an pulsed field applied just before the relevant λ(or k).

ICANS-XI International Collaboration on Advanced Neutron Sources
KEK, Tsukuba, October 22-26, 1990

High pressure diffraction at ISIS

S Hull, W I F David, R M Ibberson and C C Wilson
ISIS Facility, Rutherford Appleton Laboratory, Chilton, Didcot, Oxon OX11 0QX, UK

ABSTRACT
The development of the high pressure diffraction programme at ISIS is reviewed. Along with general accounts of the technique and the pressure cells used, examples of science carried out in this field are given.

I. INTRODUCTION

High pressure diffraction is ideally carried out at a pulsed spallation neutron source such as ISIS. The ability, on such a source, to collect the entire diffraction pattern from a polycrystalline sample at a single, fixed, scattering angle enables the convenient design of sample environment apparatus to minimise scattering from the pressure cell and pressure transmitting components. The elimination of the contaminating diffraction lines from these extraneous components is vital in obtaining reliable structural refinements from samples under high pressure.

The medium resolution powder diffractometer POLARIS at ISIS (Hull and Mayers, 1989), is well configured to perform such science. POLARIS (Figure 1) is relatively close to the moderator (sample to moderator distance L_1 = 12 m), giving high flux on the relatively small samples typical in a pressure experiment. It also has a detector bank situated at a scattering angle of 90°, the most convenient for the examination of samples under high pressure. The POLARIS 90° bank consists of 20 ^{3}He gas detectors at fixed scattering angles in the 2θ range 88–92°, covering an angle of some 25° above and below the horizontal plane of the instrument, and gives a resolution of $\Delta d/d \sim 6 \times 10^{-3}$ that is essentially independent of d spacing.

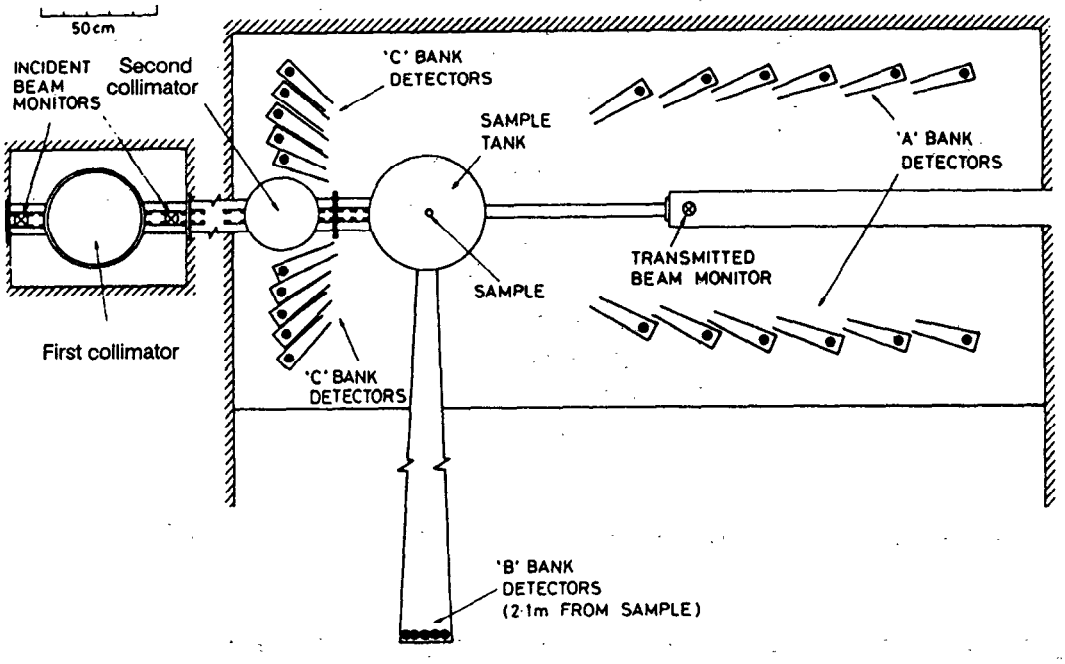

Figure 1 – Layout of the POLARIS medium resolution powder diffractometer at ISIS.

The advantage of the time-of-flight technique is illustrated in Figure 2. The ability to measure the entire diffraction pattern at fixed 2θ allows neutron collimation to be constructed inside the pressure cell, thus precluding the diffraction of neutrons from the cell casing or the Al_2O_3 insert from reching the detectors. In the McWhan cell discussed below, these B_4C collimators have apertures of some 3 mm wide by 8 mm high for the incident and scattered beams. This enables diffraction patterns to be obtained which are unaffected by scattering from the pressure cell itself. From the figure it is clear that 90° scattering maximises sample volume while minimising contamination from sample environment equipment.

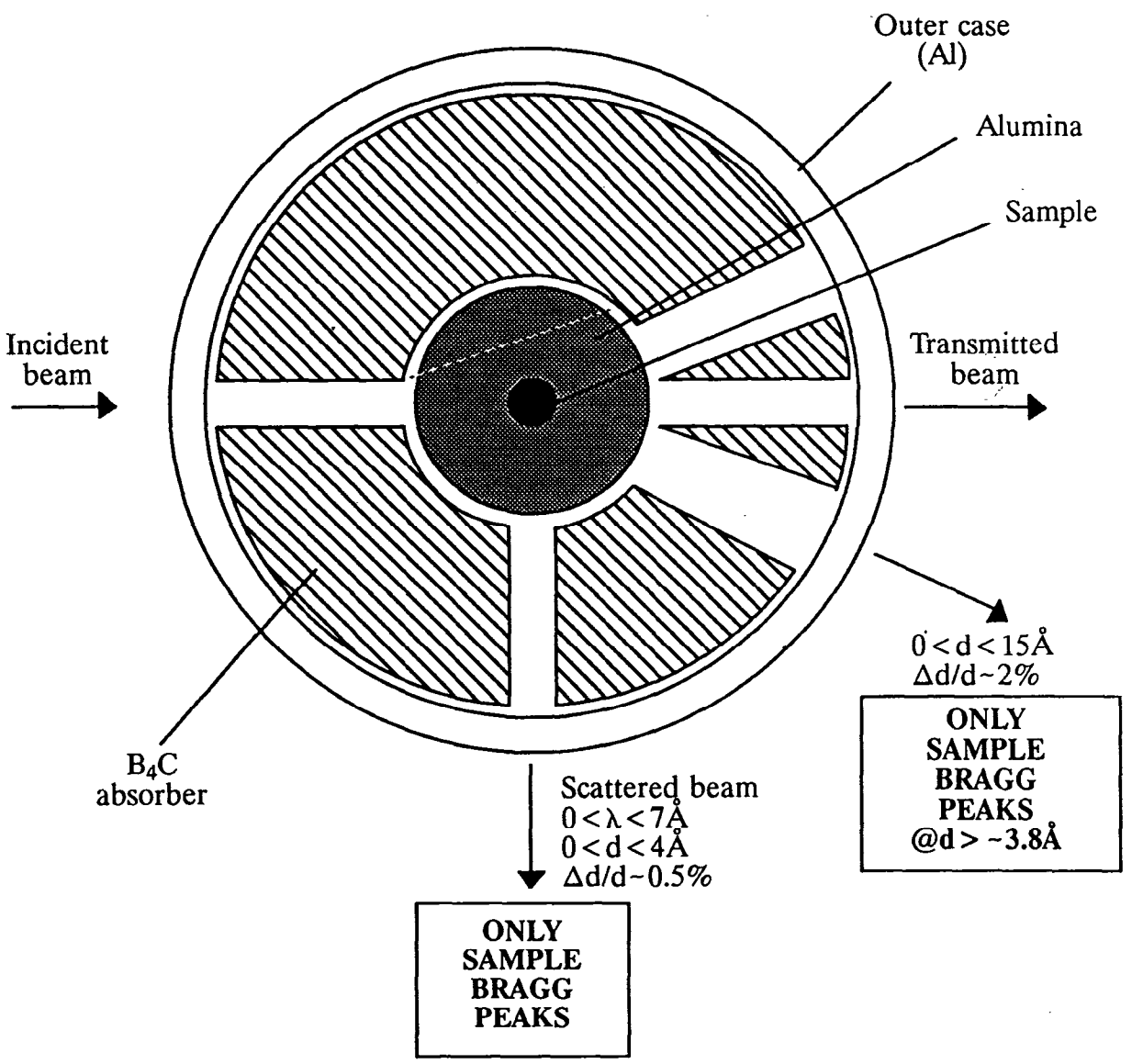

Figure 2 – Schematic view of the pressure cell collimation on POLARIS.

II. MODERATELY HIGH PRESSURES – THE McWHAN CELL ON POLARIS

For pressures up to around 25 kbar, the McWhan pressure cell design (McWhan, Block and Parisot, 1974) is widely used in neutron scattering. In this design (Figure 3; Adams, Hull and

Paranjpe, 1990) the aluminium sample can is sealed with a beryllium-copper plug and is enclosed in a pre-stressed Al_2O_3 insert. Pressure is applied via tungsten carbide pistons above and below the sample can. Approximately hydrostatic conditions are maintained by including a pressure transmitting fluid inside the sample can. Normally, calibration of the pressure value is obtained using an internal calibrant, usually NaCl, mixed with the sample. Refinement of the lattice parameter of the NaCl standard then gives the value of the applied pressure. However, in order to maximise the amount of sample present in the necessarily limited sample volume available, it is sometimes preferable to perform such calibration separately. In this case, the pressures are estimated by comparison with the applied load versus measured pressure calibration determined using separate diffraction measurements on the calibrant material alone. The pressures obtained using this method are expected to be accurate to within 10%, which is quite sufficient for a large proportion of high pressure work.

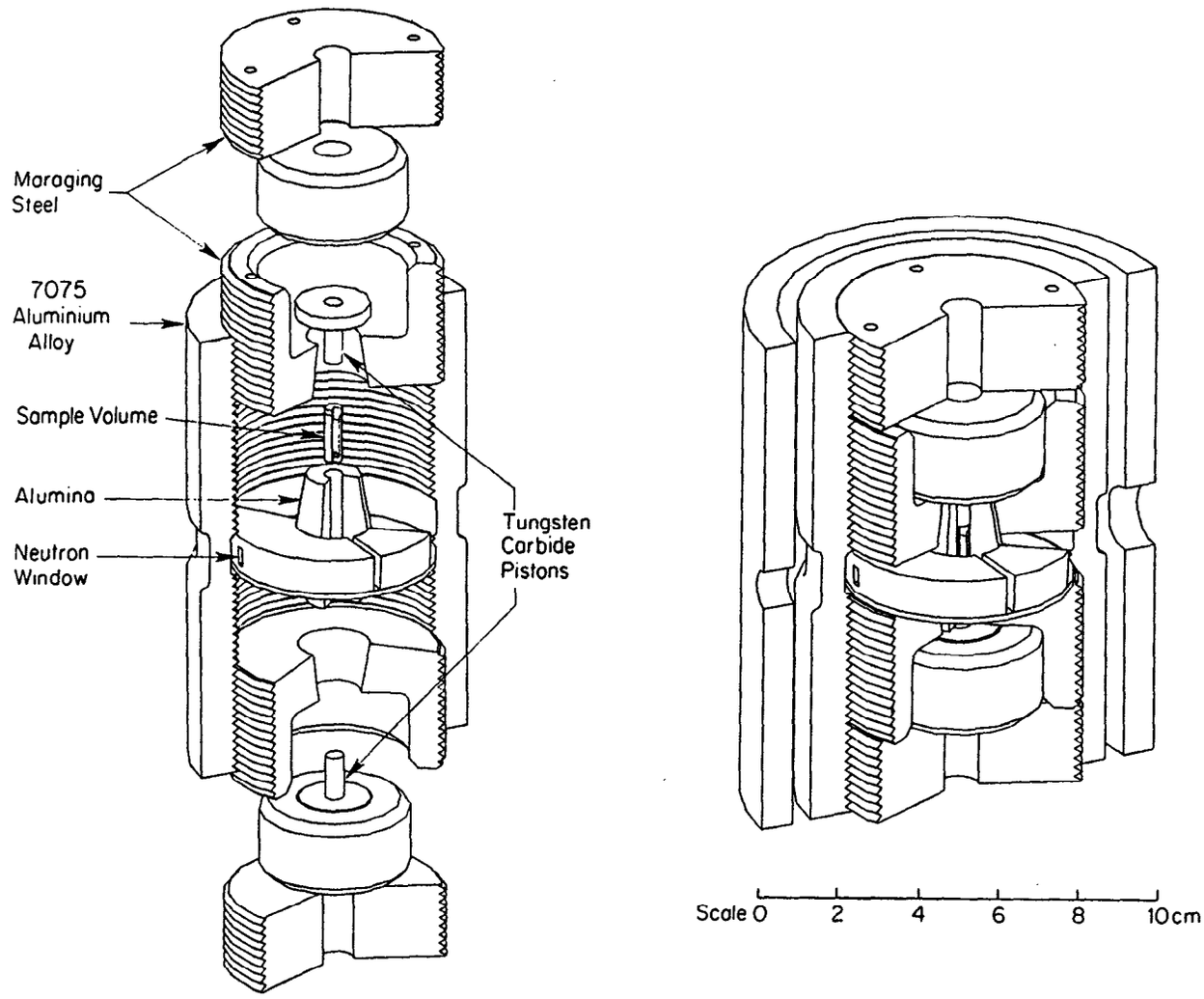

Figure 3 - An exploded and assembled view of the McWhan clamped pressure cell.

With the POLARIS set-up, and an effective sample volume in the McWhan cell of some 100 mm^3, it is necessary to count, at present ISIS current of some 100 μA, for some 10-20 hours for a typical sample, to obtain data for which a reasonable structural refinement can be carried out. This is not a prohibitively long time, and allows a great deal of high pressure structural science to be performed within the constraints of a diverse scientific programme on a user instrument such as POLARIS.

II.1 Science Using the McWhan Cell - High Pressure Studies of Ferroelastic $LaNbO_4$

$LaNbO_4$ undergoes a phase transition at high temperature from the monoclinic fergusonite structure to a ferroelastic phase with the tetragonal scheelite structure. Unlike the closely related material $BiVO_4$, the driving mechanism for this phase transition is not a soft optic mode, but instead is associated with the oxygen coordination around the Nb^{5+} anion. In niobate compounds the Nb^{5+} ion is generally octahedrally co-ordinated by oxygen but its rather small ionic radius (0.64 Å) means that the octahedral co-ordination is often rather distorted, as in the low temperature monoclinic phase of $LaNbO_4$. In the high temperature tetragonal phase of $LaNbO_4$ the Nb^{5+} ion exhibits tetrahedral co-ordination and it is the stereochemical competition between low-temperature distorted octahedral and high temperature tetrahedral co-ordination that is the driving mechanism for the ferroelastic phase transition. The application of hydrostatic pressure has the tendency to increase the number of anions surrounding a given cation. In the case of $LaNbO_4$, therefore, application of pressure will force the Nb^{5+} ion away from tetrahedral and towards octahedral co-ordination. Since the tetrahedral and distorted octahedral co-ordinations are associated with the tetragonal and monoclinic structures respectively, the application of hydrostatic pressure is predicted to increase the ferroelastic transition temperature. At constant temperature it is expected, therefore, that the spontaneous strain, that is, the monoclinic nature of the structure, should increase with increasing pressure.

To confirm this hypothesis, powder diffraction data from $LaNbO_4$ were collected on POLARIS at ambient pressure and at hydrostatic pressures of 10 and 20 kbar (David, Hull and Ibberson, 1990). The diffraction data collected in the POLARIS 90° bank are shown in Figure 4. Rietveld profile refinement was performed on each data set using the program TF14LS based on the Cambridge Crystallographic Subroutine Library (Brown and Matthewman, 1987). A typical fit is shown in Figure 5, with the resulting structural parameters in Tables 1 and 2.

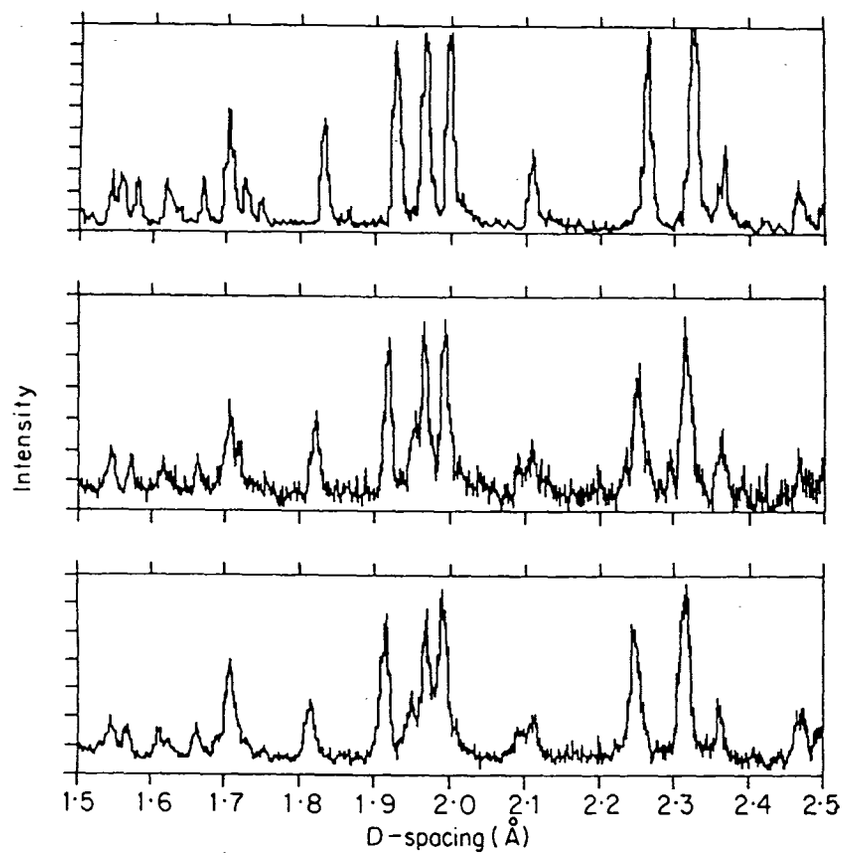

Figure 4 - Diffraction patterns from $LaNbO_4$ collected on POLARIS at ambient pressure (top), 10 kbar (middle) and 20 kbar (bottom).

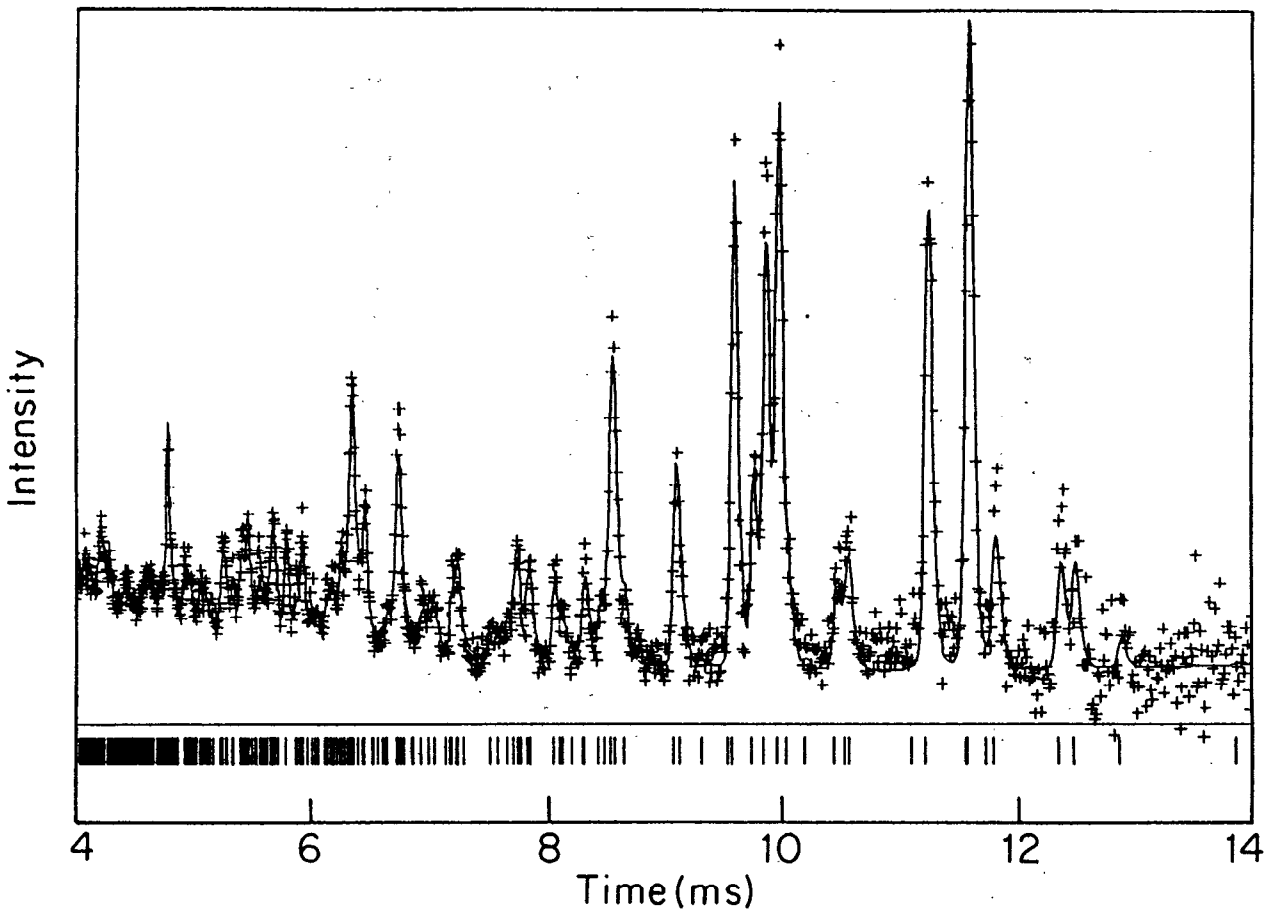

Figure 5 – Rietveld profile refinement of the data collected from $LaNbO_4$ at 20 kbar. The fitted line confirms that no additional peaks are observed from the alumina and other components of the pressure cell.

TABLE 1 – Lattice constants and spontaneous strains of $LaNbO_4$

	0 kbar	10 kbar	20 kbar
a(Å)	5.5600(4)	5.5602(12)	5.5615(8)
b(Å)	5.1963(4)	5.1703(15)	5.1616(10)
c(Å)	11.5067(8)	11.4445(25)	11.4187(20)
γ(°)	85.886(5)	85.505(12)	85.331(9)
V(Å)^3	331.59(5)	327.99(15)	326.70(10)
ϵ_{11}	3.381×10^{-2}	3.634×10^{-2}	3.729×10^{-2}
ϵ_{12}	3.592×10^{-2}	3.925×10^{-2}	4.077×10^{-2}
$\epsilon_{11}/\epsilon_{12}$	0.9413	0.9259	0.9146
ϵ_S	6.976×10^{-2}	7.565×10^{-2}	7.814×10^{-2}

$\epsilon_{11} = (a-b)/(a+b)$, $\epsilon_{12} = \tan(\frac{1}{2}(90-\gamma))$, $\epsilon_S = (2\epsilon^2_{11} + 2\epsilon^2_{12})^{1/2}$

TABLE 2 - Bond lengths (Å) in $LaNbO_4$

	0 kbar	10 kbar	20 kbar
Nb - 01	1.917	1.926	1.931
Nb - 02	1.824	1.795	1.781
Nb -01'	2.540	2.508	2.480
Nb - 02'	3.259	3.255	3.257
La - 01	2.484	2.489	2.472
La - 02'	2.464	2.459	2.457
La - 01'	2.553	2.539	2.561
La - 02'	2.513	2.513	2.522

The lattice parameters clearly indicate a volume reduction as a function of pressure. More importantly, however, it is clear that the expected increase in spontaneous monoclinic distortion with increasing pressure is observed. Of especial note is the fact that the length of the a axis actually **increases** with increasing applied pressure. Although the precision of the structural parameter data is modest, because of the low counting statistics in the high pressure data, significant changes in the derived bond lengths (Table 2) are observed. The most marked reduction in bond length with increasing pressure is the Nb–O(1)′ distance, which corresponds to the longest bonds in the distorted NbO_6 octahedron. This has the effect of polarising the four nearest neighbour O^{2-} ions, leading to the observed **increase** in Nb–O(1) distance with pressure. These trends in the observed distortions support the model of the phase transition in $LaNbO_4$ being driven by stereochemical factors related to the oxygen coordination around the Nb anion.

III. VERY HIGH PRESSURES - THE PARIS CELL

In order to extend the range of pressures accessible beyond the 25 kbar available from the McWhan cell, a collaborative project has been set up between RAL and the Universities of Edinburgh and Pierre et Marie Curie in Paris to develop a cell for very high pressure neutron powder diffraction experiments. The aim of the cell (Figure 6), designed and constructed in Paris, is to reach pressures well in excess of 100 kbar. Performing neutron powder diffraction at such extreme pressures promises to open new, unexplored areas in structural science.

After a considerable amount of development both of the cell itself and regarding its neutronic properties, the first very high pressure experiments have recently been performed on POLARIS.

III.1 Equation of State of ^7LiD to 60 kbar

In this experiment, diffraction patterns were measured on POLARIS from 100 mm^3 of a lithium deuteride sample enriched (to 99%) in ^7Li, at pressures up to 60 kbar (Besson et al, 1990). NaCl was used as an internal calibrant. From data collected in some 3–6 hours per pressure, cell dimensions were obtained to an accuracy of some 0.001 Å. This enables the volume compression versus pressure curve to be obtained to good accuracy (Figure 7). As can be seen from this plot, the POLARIS data, from both the McWhan (below 25 kbar) and Paris (above 25 kbar) cells, are well explained by the most recent theoretical calculations. These data not only extend the pressure range over previous measurements, but also are significantly more precise.

Figure 6 – Schematic view of the Paris pressure cell

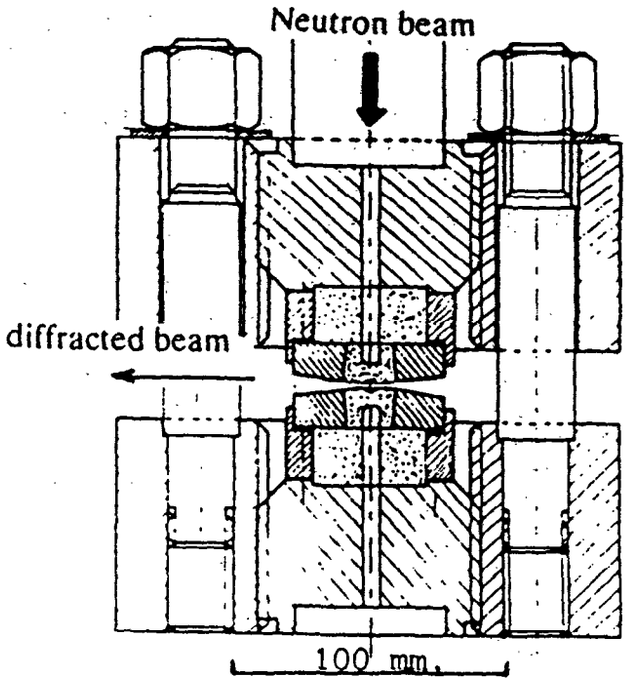

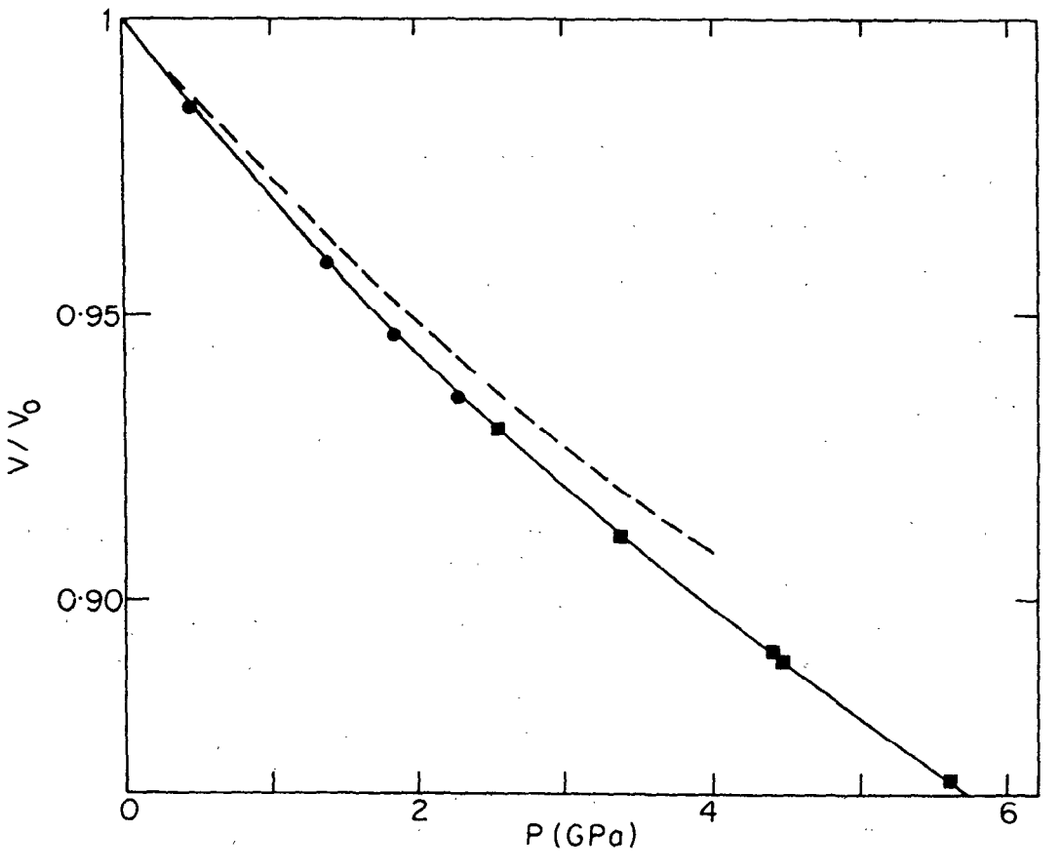

Figure 7 – Equation of state of LiD up to 60 kbar. The circles represent points measured using the McWhan cell on POLARIS, the squares from the Paris cell. The solid line is the best theoretical calculation available to date. The previous available data, represented by the dashed line, are seen not to agree with these recent calculations, whereas the POLARIS data show excellent agreement.

This demonstration of the determination of the equation of state in this fundamental quantum solid illustrates the basic physics one can probe when extremes of sample environment are attained. Pressures of over 100 kbar have already been achieved, and developments on both the Paris pressure cell and on the POLARIS instrument are continuing in an effort to further extend and exploit this new field of study.

IV. CONCLUSIONS AND FUTURE PROSPECTS

Work is expected to continue on both branches of the high pressure powder diffraction work at ISIS, with improvements planned to both the instrument and to the pressure cells. It is hoped to improve the count rate of POLARIS by installing a second 90° detector bank on the opposite side of the sample to that currently used. In addition, the prospect of performing high pressure studies at high resolution should be realised with the installation of a full 90° detector array on HRPD. On the pressure cell side, developments are planned on the McWhan cell to allow pressures up to 35 kbar to be reached, and it is hoped that 150 kbar will be obtained shortly in the Paris cell, with the replacement of the present tungsten carbide anvils by sintered diamond. In conclusion, the first year of high pressure diffraction experiments at ISIS has been rather successful, and has opened up the prospect of increased exploitation of these techniques.

V. ACKNOWLEDGEMENTS

The high pressure programme at ISIS has benefitted substantially from the input of M A Adams and I F Bailey (RAL), S K Paranjpe (BARC), and the groups of R J Nelmes (Edinburgh) and J M Besson (Paris).

References

Adams M A, Hull S and Paranjpe S K, Rutherford Appleton Laboratory Report, in preparation (1990)
Besson J M, Weill G, Nelmes R J, Loveday J S and Hull S, High Pressure Research, submitted (1990)
Brown P J and Matthewman J C, Rutherford Appleton Laboratory Report, RAL-87-010 (1987)
David W I F, Hull S and Ibberson R M, Rutherford Appleton Laboratory Report RAL-90-024 (1990)
Hull S and Mayers J, Rutherford Appleton Laboratory Report RAL-89-118 (1989)
McWhan D B, Block D and Parisot G, Rev. Sci. Inst. 45 643 (1974)

Q(Y.Endoh): The McWhan cell has been readily used for the steady source neutron scattering by opening the window wide. Then what is advantage by using McWhan cell with pulsed sources?

A(C.C.Wilson): Certainly at moderate pressure (~25kbar), the McWhan cell is well-established at steady-state sources. The ability at a pulsed source to use very tight collimation for both incident and scattered beams in a pressure cell experiment should allow the attainment of ultra-high pressures (200kbar), with designs other than the McWhan cell. The Besser/Paris clamped cell is just such a device.

Q(Y.Endoh): If anyone has an experience to use the sapphire anvil technique, I would like to know the pressure value reached.

A(C.C.Wilson): John Finney has used a sapphire anvil cell to about 7kbar.

Q(A.D.Taylor): Do these Besser cells operate at low temperatures other than ambient?

A(C.C.Wilson): Yes, the McWhan cell has operated at low temperature inside an orange cryostat. Also, a cell is in design stage to perform high pressure work at high temperatures at ISIS.

ICANS-XI International Collaboration on Advanced Neutron Sources
KEK, Tsukuba, October 22-26, 1990

Feasibility studies for high pressure neutron powder diffraction experiments

R.B. Von Dreele, LANSCE, MS H805, Los Alamos National Laboratory, Los Alamos, NM 87545, USA and J. Parise, Earth and Space Sciences, SUNY, Stony Brook, NY 11794-2100, USA

ABSTRACT

We recently performed two neutron powder diffraction experiments on very small samples on the High Intensity Powder Diffractometer (HIPD). These were done to determine the feasibility of performing *in situ* high pressure/high temperature neutron diffraction experiments on HIPD at pressures which would exceed the previous limit of ~50kbar achievable in a neutron diffraction experiment. The first experiment consisted of examining the product from a high pressure preparation done at Stony Brook. The sample, which had been prepared at 65kbar and 1000°C, consisted of a small platinum capsule (3x3x3 mm) filled with $CaGeO_3$ perovskite . The weights of the capsule included 225mg of platinum and 49mg of the germanate. A diffraction experiment taking ~8.6hrs at a LANSCE proton beam current of ~53μA gave peaks of good intensity from both Pt and $CaGeO_3$; we could begin to see them after only 20min of beam time. The second experiment was to test the possibility of diffraction from a high pressure apparatus. We placed in the HIPD sample position the central assembly from a 100kbar octahedral press. Four tungsten carbide anvils and a copper block previously pressed to 65kbar were held in an aluminum frame. The sample consisted of a small bit of nickel foil (175mg) placed in a 3mm hole in the copper block. The active sample volume (~1mm^3) is defined by the gap (~0.7mm) between the anvils and the length of the sample (~4mm). A small portion of the copper block is also seen in this arrangement. This is viewed at 90° 2Θ through a similar gap between the anvils by 4 1/2"x12" ^{3}He counter tubes. This arrangement simulates the operating conditions of a high pressure run at 100kbar and takes advantage of the fixed instrument geometry possible in time-of-flight neutron diffraction experiments. We obtained a diffraction pattern in ~7.1hrs and ~57μA beam current which clearly showed peaks from both copper and nickel with no evidence of diffraction from the anvils or any other part of the assembly. These two experiments clearly demonstrate the feasibility of performing high pressure *in situ* diffraction experiments in excess of 100kbar on HIPD at LANSCE.

I. INTRODUCTION

Due to its very short incident flight path (9m), the High Intensity Powder Diffractometer (HIPD) at the Manuel Lujan, Jr. Neutron Scattering Center (LANSCE) provides a very intense incident neutron beam so that typical "little finger" sized samples frequently scatter sufficiently strongly so that data collection times are often much less than one hour. Thus it was possible to consider obtaining diffraction patterns from considerably smaller samples and in the very

restricted geometry of a high pressure apparatus. To explore these possibilities two experiments were envisioned; one on material obtained from a high pressure/temperature synthesis run and one on a dummy sample inside a mockup of a pressure apparatus.

II. EXPERIMENTAL

A high pressure/temperature synthesis of $CaGeO_3$ was performed at the High Pressure Laboratory, SUNY, Stony Brook, NY. A stoichiometric mixture of CaO and GeO_2 was placed in a 3mm Pt capsule which was inserted in a 6x6x6mm Cu block. The Cu block was subjected to 65kb pressure and 1000°C temperature in the Kobe Steel D1A-6 octahedral press to effect the synthesis.

For the first diffraction experiment, the Pt capsule containing the synthesized $CaGeO_3$ was supported in a LANSCE standard 1/4"x1-3/4" vanadium can by a small piece of Ta foil so that the capsule would be centered in the HIPD beam. A diffraction data set was taken over 8.7hrs with the LANSCE source operating at ~53μA. After the diffraction experiment, the $CaGeO_3$ was extracted from the Pt capsule and weighed. There was 49mg of $CaGeO_3$ and 225mg of Pt in the sample. The Ta foil was not weighed. The part of data set with 4.8Å≥d≥0.4Å obtained from the four 1/2"x12" 10atm ^{3}He counter tubes positioned 1.25m from the sample at ~153°2Θ were subjected to a 3 phase ($CaGeO_3$, Pt and Ta) Rietveld refinement using the software GSAS[1] to give the residuals R_{wp}=4.78%, R_p=3.12% and χ^2=1.76. The results of this refinement are given in Table 1.

Table 1. Results of refinement of $CaGeO_3$

CaGeO3 - orthorhombic, Pbnm

a = 5.258(3)Å, b = 5.271(3)Å, c = 7.448(4)Å at 300K

Atom parameters

atom	x	y	z
Ca	0.026(5)	-0.18(7)	1/4
Ge	1/2	0	0
O(1)	0.038(6)	0.426(7)	1/4
O(2)	-0.266(4)	0.282(5)	0.040(2)

U_{iso} = 0.0038(9)Å^2

The fit to the data from the final refinement is displayed in Figure 1 in three ways to emphasize different aspects of its quality. The orthorhombic $CaGeO_3$ structure is that of one of the most common distortions of perovskite[2] and results from a twisting of the GeO_6 octahedra as shown in Figure 2. The lattice parameters for the other two phases present in the sample (Pt, a=3.92261(6)Å and Ta, a=3.3035(4)Å) obtained in the refinement agree quite well with the commonly accepted values[3].

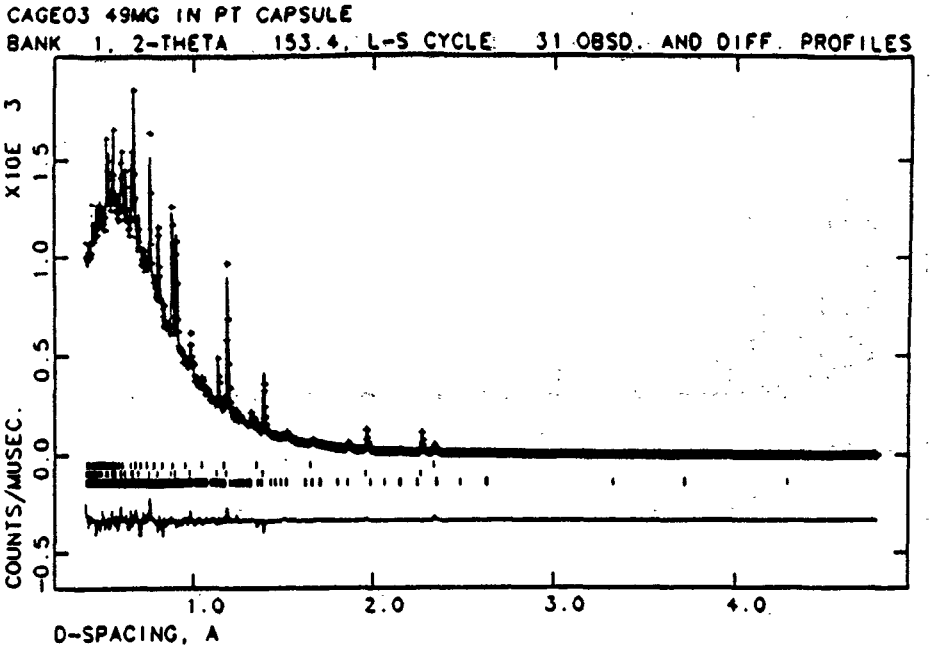

Figure 1a. Observed and calculated profile for the $CaGeO_3$ in Pt capsule for data from 153°2Θ bank on HIPD. The reflection markers are for $CaGeO_3$ at bottom, Pt in middle and Ta at top. The difference (I_{obs}-I_{calc}) curve is also shown. The intensities are shown as counts/μsec.

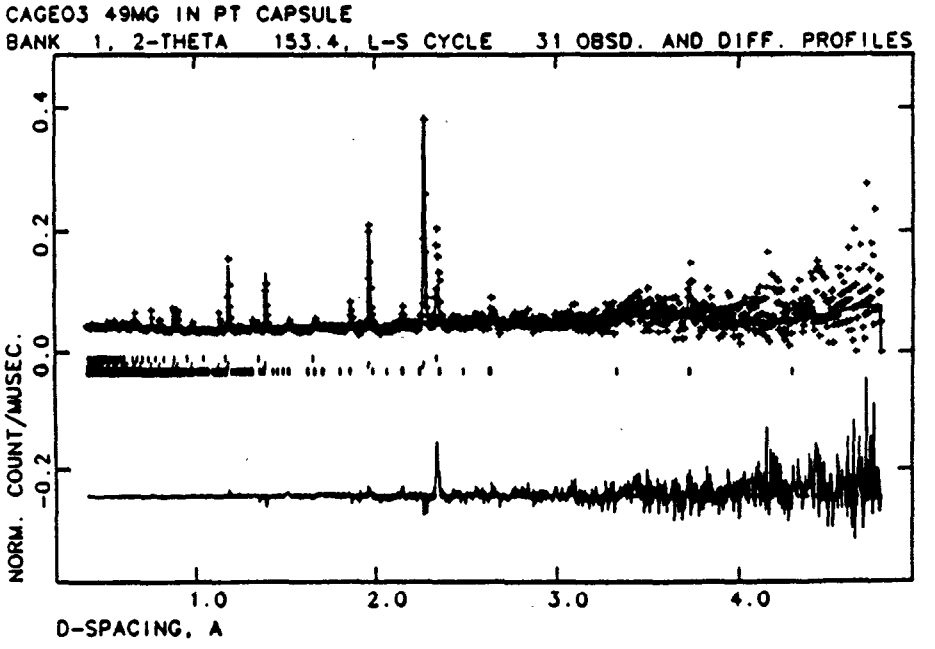

Figure 1b. The same data as shown in Figure 1a except that the intensities are normalized by an incident spectrum measured by the counter bank from a V/Nb alloy rod. The flatness of the background is evident in this figure.

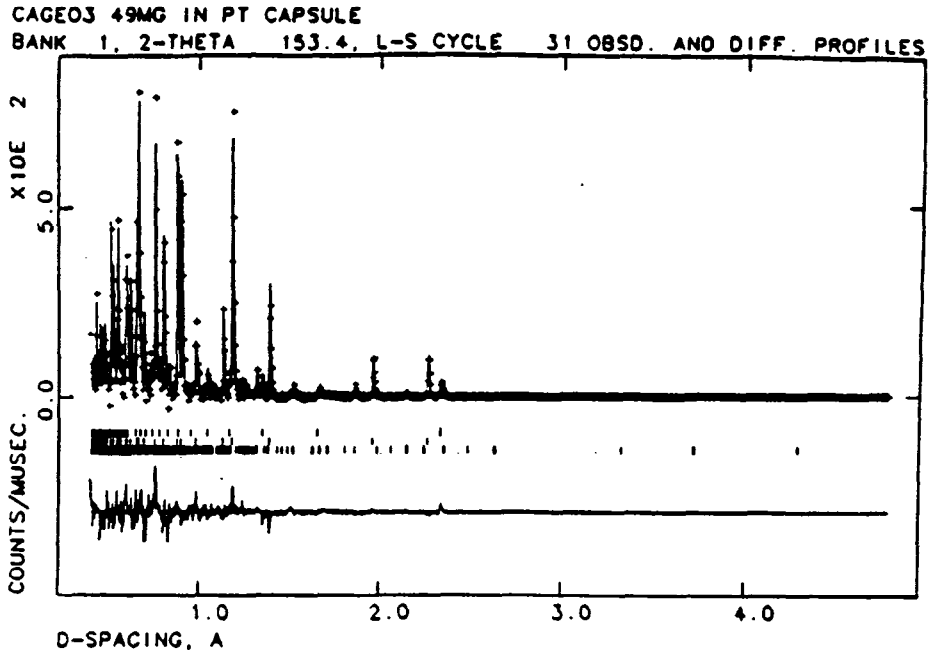

Figure 1c. The same data as shown in Figure 1a except that the calculated background from the Rietveld refinement is subtracted from both the observed intensities and the calculated curve. This shows the fit to the Bragg peaks.

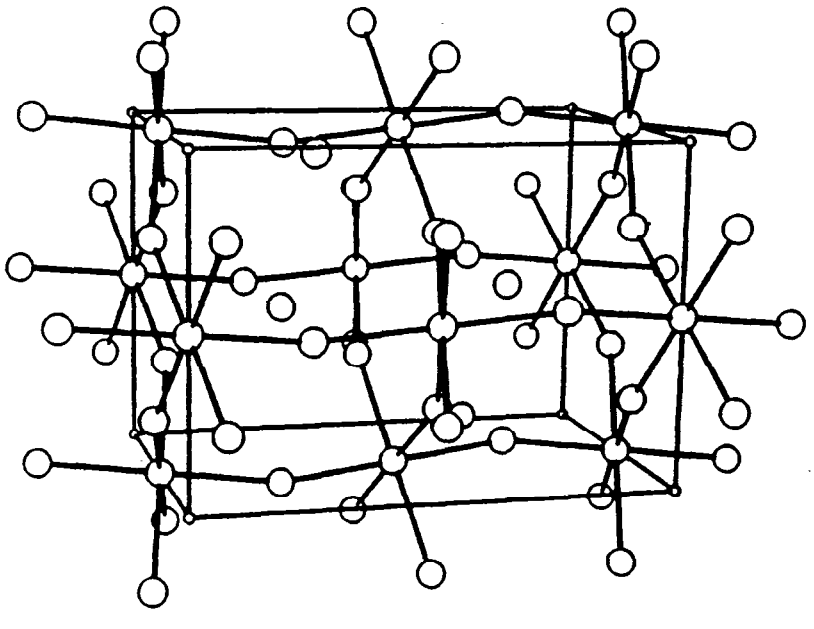

Figure 2. A sketch of the structure of CaGeO3. in this view the a axis is into the paper, the b axis is vertical and the c axis is horizontal. Bonds are shown between the Ge and O atoms.

For the second diffraction experiment, four of the six WC anvils and the previously pressed Cu block from the D1A-6 press were assembled (Figure 3) in a specially constructed Al frame so that the anvils were positioned to simulate the arrangement at 65kb.

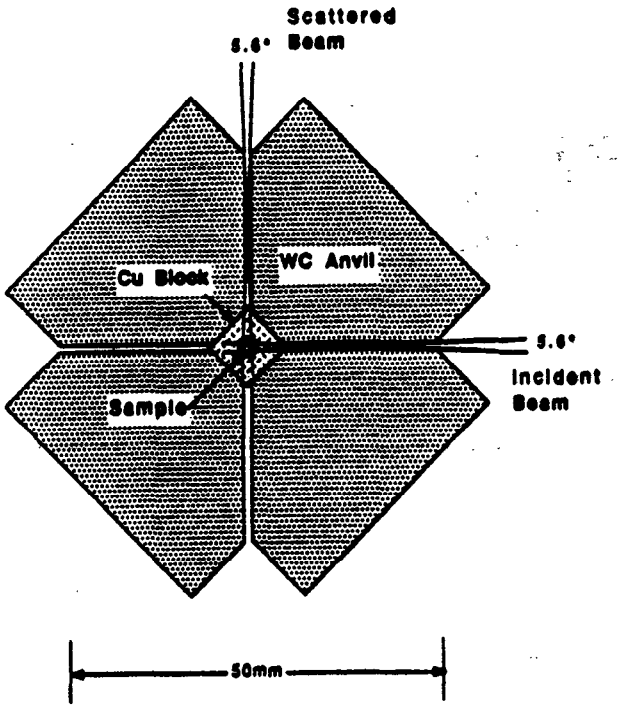

Figure 3. A sketch of the mockup of the arrangement of four WC anvils in an octahedral high pressure apparatus. The incident beam enters between a gap in the anvils and the scattered beam at 90°2Θ exits between a similar gap. The simultaneously illuminated and viewed volume is confined to the sample and does not include any part of an anvil.

The openings between the WC anvils were ~0.7mm giving angular apertures of 5.6°. A small bit of Ni sheet (175mg) was placed in the sample hole in the Cu block. Sheet Cd was affixed to outside of this apparatus to provide crude shielding leaving apertures for the incident and 90°2Θ scattered beams. This assembly was placed in the HIPD and a diffraction data set was taken for 7.1hrs with the LANSCE source operating at ~57μA. The part of data set with 2.75Å≥d≥0.4Å obtained from the four 1/2"x12" 10atm ^{3}He counter tubes positioned 1.0m from the sample at ~90°2Θ were subjected to a 2 phase (Ni and Cu) Rietveld refinement using the software GSAS to give the residuals R_{wp}=5.22%, R_p=3.21% and χ^2=3.10. The fit to the data from the final refinement is displayed in Figure 4 in three ways to emphasize different aspects of its quality. The lattice parameter for Ni (a=3.5235(2)Å) agrees very well with the accepted value[3] but the value obtained for Cu (a=3.6129(3)Å)is 0.057% smaller than expected because of residual stress after relaxation from the 65kb synthesis run. Both phases showed substantial preferred orientation and the unmodeled component was the major error in the least squares fit. In addition, there was an extra background contribution at short d-spacings above the flat background found in the first experiment (compare Figs. 1b and 4b) and in patterns from typical large samples. It probably arose from scattering by the anvils and the Al frame because the incident beam was not collimated to match the extremely small acceptance of the high pressure assembly.

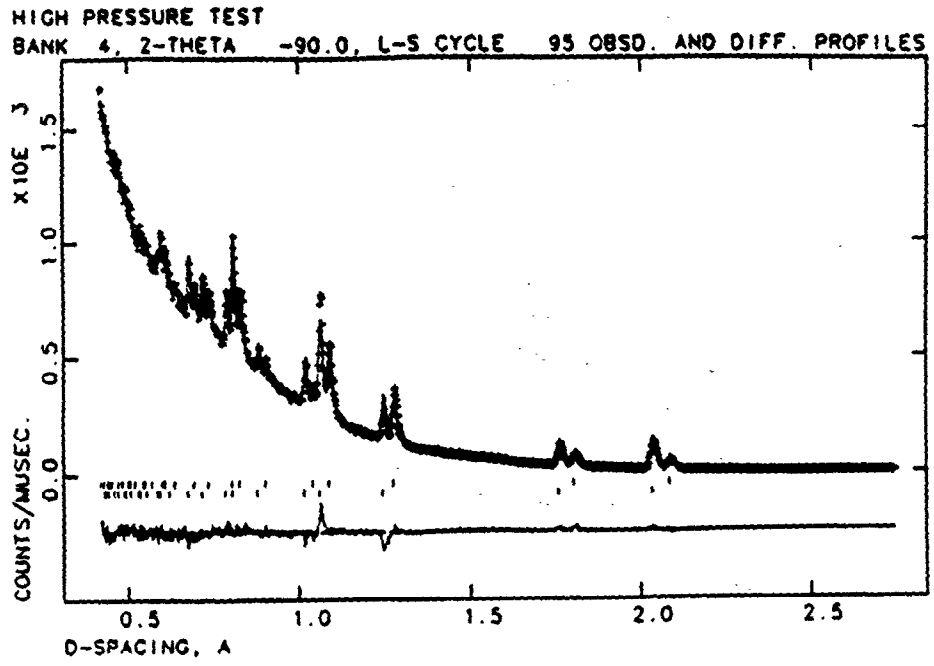

Figure 4a. Observed and calculated profile for the high pressure mockup for data from 90°2Θ bank on HIPD. The reflection markers are for Ni at bottom and Cu at top. The difference (I_{obs}-I_{calc}) curve is also shown. The intensities are shown as counts/μsec.

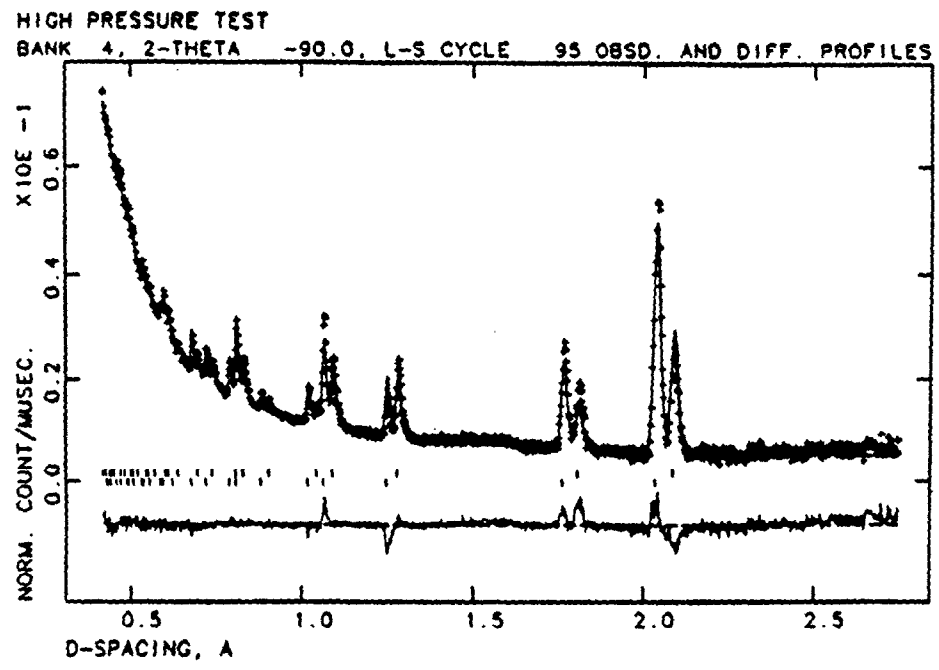

Figure 4b. The same data as shown in Figure 4a except that the intensities are normalized by an incident spectrum measured by the counter bank from a V/Nb alloy rod. The extra background at short d-spacings is evident.

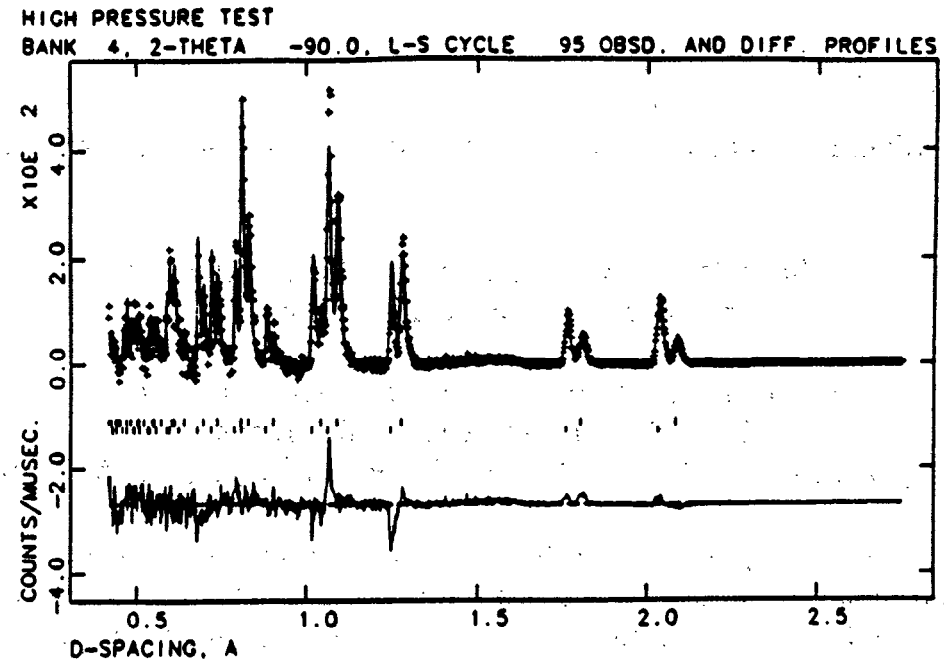

Figure 4c. The same data as shown in Figure 4a except that the calculated background from the Rietveld refinement is subtracted from both the observed intensities and the calculated curve. The error in the fit to the Bragg peaks from preferred orientation is evident.

III. CONCLUSION

Clearly diffraction data can be obtained from small samples on HIPD that when subjected to Rietveld refinement can give useful crystal structure information. This result was sufficiently encouraging that we have performed a number of diffraction experiments on a variety of small (20-300mg) samples with generally good results. In addition, it is feasible to perform diffraction experiments in a high pressure apparatus despite its extremely restrictive aperatures.

References

[1]Larson, A.C. and Von Dreele, R.B., "GSAS - Generalized Crystal Structure Analysis System", Los Alamos National Laboratory Report No. LA-UR-86-748 (1986).

[2]Wycoff, R.W.G., "Crystal Structures, Vol. 1", 2nd ed., Wiley Interscience, New York, pp. 10,16 (1963).

[3]Wycoff, R.W.G., "Crystal Structures, Vol. 2", 2nd ed., Wiley Interscience, New York, pp. 407-410 (1964).

ICANS-XI International Collaboration on Advanced Neutron Sources
KEK, Tsukuba, October 22-26, 1990

Lanthanum nuclear polarization for T-violation experiment

Y. Masuda, T. Adachi, S. Ishimoto, A. Masaike*
K. Morimoto and H.M. Shimizu*

National Laboratory for High Energy Physics
1-1 Oho, Tsukuba-shi, 305 Japan
*Department of Physics, Kyoto University, Kyoto, 606 Japan

Abstract Nuclear polarization for the measurement of a triple correlation between the neutron spin, the neutron momentum and the nuclear spin in the neutron-nucleus interaction is discussed. Productions of polarized neutron and polarized lanthanum target are presented. Also, feasibility of polarized ^{3}He nuclei as a polarized neutron detector is discussed.

Introduction

Nuclear polarization has been used for tests of fundamental symmetry violations, P violation and T violation. In the experiments, psuedoscaler terms under space/time reversal are measured. In the P-violation experiment, a $\sigma \cdot \mathbf{k}$ term is measured, where σ is a particle spin and $\mathbf{k}$ is a particle momentum. In the nucleon-nucleon interaction, P-violation effect is very small. An asymmetry in the cross section with respect to the helicity is about 10^{-7} for the proton-proton scattering. Concerning T violation, only CP violation is observed in the K^0 decay. If we assume the CPT theorem, T invariance is violated in the K^0 decay. No other T-violation process is found yet. In the nucleus, the symmetry violations are occasionally enhanced. For example, P-violating asymmetries in $\mathbf{I} \cdot \mathbf{k}_\gamma$ terms of γ-ray angular distribution from polarized nuclei are enhanced to 10^{-2}_10^{-4}. Circular polarizations of γ-rays from unpolarized nuclei, namely $\sigma_\gamma \cdot \mathbf{k}_\gamma$ terms are enhanced to 10^{-3}_10^{-4}. Here, $\mathbf{I}$ is the nuclear spin, $\mathbf{k}_\gamma$ is the photon momentum and σ_γ is the photon spin. Recently, far more enhancement has been found in the neutron-nucleus interaction. The largest observed effect is for a p-wave resonance of ^{139}La at the neutron energy of E_n = 0.734 eV. An asymmetry in the neutron helicity, namely the $\sigma_n \cdot \mathbf{k}_n$ term is about 10 %[1,2,3,4], where σ_n is the neutron spin and $\mathbf{k}_n$ is the neutron momentum.

Many theoreticians expect such large enhancement also in T-violation effects as in the P-violation effect[5,6,7,8]. It is proposed to measure a triple correlation term, $\mathbf{I} \cdot \sigma_n \times \mathbf{k}_n$ in the neutron transmission for the T-violation test. In the T-violation experiment, transmission of polarized neutrons through a polarized target is measured as it is schematically shown in Fig. 1. The two processes in Fig. 1 transform to each other under time reversal and two rotations around the nuclear polarization axis and the beam axis. The second process is realized by inversion of the neutron polarization in the first process. The T-odd asymmetry which is defined as,

$$A_T = (T(+)-T(-))/(T(+)+T(-)) \qquad (1) ,$$

is considered to be free from final state interactions, since initial and final states as well as motion directions are reversed in the two processes in Fig. 1. Here, T(+) and T(-) are neutron transmission for the first and second processes, respectively. The effect of final state interactions is serious problem in the measurements of T-odd angular correlations in γ-decay and β-decay, since initial and final states can not be interchanged in the decay processes.

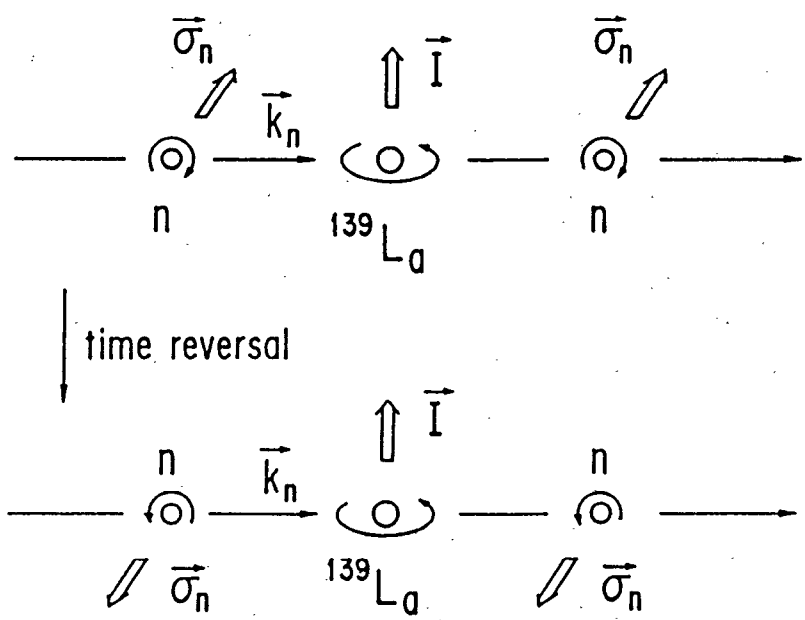

Fig. 1 T-violation test on the polarized neutron transmission through a polarized nuclear target.

Nuclear polarization for T-violation experiment

For the T-violation experiment, we need polarized neutron beam, polarized nuclear target and polarized neutron detector. We have already a neutron polarizer, namely the polarized proton filter[9]. Protons in organic

material in a liquid ^4He container are polarized by means of the dynamic nuclear polarization. The liquid ^4He is cooled by 0.5 K liquid ^3He from outside through a heat exchanger in order to avoid neutron absorption by ^3He nuclei. The proton polarization is 80%. Neutrons from the spallation neutron source are polarized upon passing through the filter. The neutron polarization in eV region is more than 70% for a 1-cm thick filter.

The second problem is to polarize lanthanum nuclei. For this purpose we also used the dynamic nuclear polarization in a LaF_3 single crystal. We replaced about 0.1% of lanthanum atoms with neodymium atoms. The space group of the LaF_3 crystal is P3c1, but the crystal shows hexagonal symmetry by the twinning. Therefore, there are six magnetically inequivalent lanthanum sites into which a paramagnetic ion may substitute[10]. The orbital angular momentum of the paramagnetic electron of the neodymium atom is quenched in the crystal, but the Zeeman energy of the paramagnetic electron is affected by the orbital angular momentum through the spin-orbit interaction. Therefore, the g-factor of the paramagnetic electron changes from the free electron g-factor, $g_e = 2$. The g-factor is generally expressed by a tensor. The g-tensor is same for the six sites, because of the symmetry property of the crystal. The only difference is in orientation of the principal axes of the g-tensor. We measured the paramagnetic resonance of this crystal as a function of crystal orientation. A typical result is shown in Fig. 2. In this figure, the crystal is rotated around the crystal a* axis, which is set to be perpendicular to the magnetic field H_0. The rotation angle θ is defined by the angle between the crystal c axis and the magnetic field H_0. The present result is consistent with the result of Baker and Rubins[11]. The g-factors for the six sites should coincide with each other at $\theta = 0^o$. The experimental results did not coincide, since the a* axis slightly deviated from the vertical axis to the magnetic field. For the dynamic polarization, we set the crystal orientation angle at $\theta = 45^o$. The signal of the electron spin resonance (ESR) is shown in Fig. 3 in this orientation. Here, the temperature of the crystal was 0.5 K and the microwave frequency was 69.5 GHz. In the measurement of the ESR, a carbon resister was used as a bolometer of the microwave radiation in the microwave cavity where the crystal placed. The dynamic polarization was carried out at the magnetic field of 19.6 kG. The microwave frequency was shifted from the center of the ESR. The shift in the frequency corresponded to the nuclear Zeeman energy. The microwave power of about a few tens mW was switched on and a nuclear polarization build-up was observed. The result is shown in Fig. 4. In the figure, nuclear magnetic resonance (NMR) signal amplitude for fluorine nuclei is plotted against time in minute. The polarization of lanthanum nuclei can be estimated from the polarization of fluorine nuclei by means of the spin temperature theory. The present NMR detector is not calibrated for the signal amplitude. We could not obtain the value of the polarization. However, the effect of the dynamic polarization is clear as

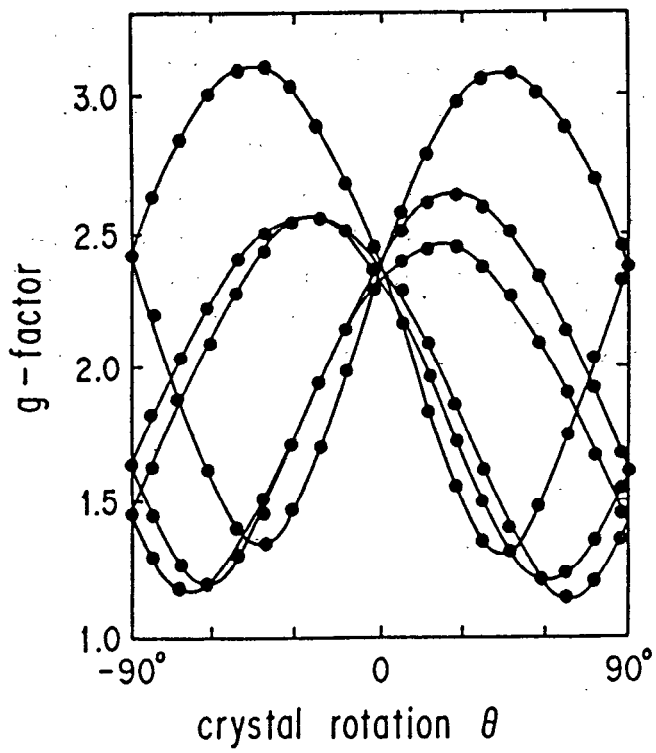

Fig. 2 g-factor of Nd in LaF_3 as a function of the crystal orientation.

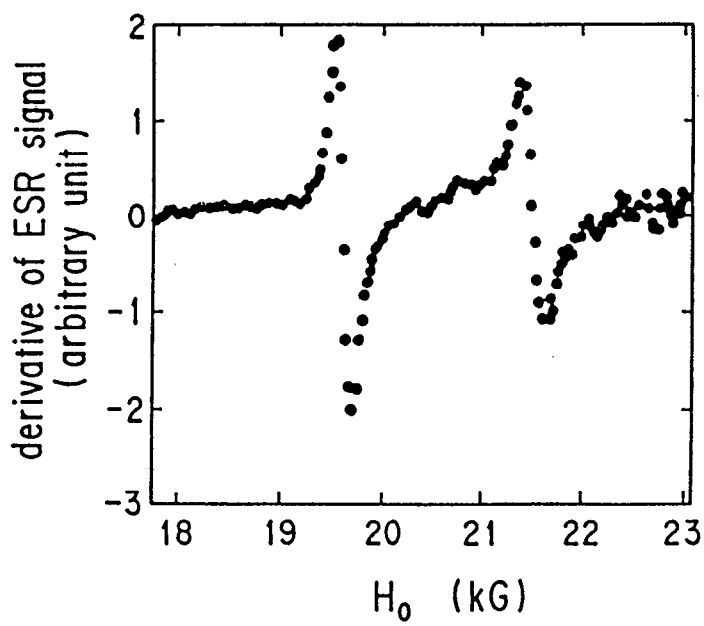

Fig. 3 Paramagnetic resonance of Nd in LaF_3.

shown in Fig. 4. The NMR signal showed small relaxation after the microwave power was switched off. This is also shown in Fig. 4. The nuclear spin relaxation time was more than several days. The present polarization is small, but we can improve it by overlapping the g-factors for the six sites so that all the paramagnetic electrons contribute the dynamic polarization. It is possible by setting the crystal at $\theta = 0^o$ accurately, or by using some paramagnetic centers which show no anisotropy in the g-factor. We can also improve the nuclear polarization by using more strong magnetic field and a lower temperature cryostat, since the nuclear relaxation time become longer in these conditions.

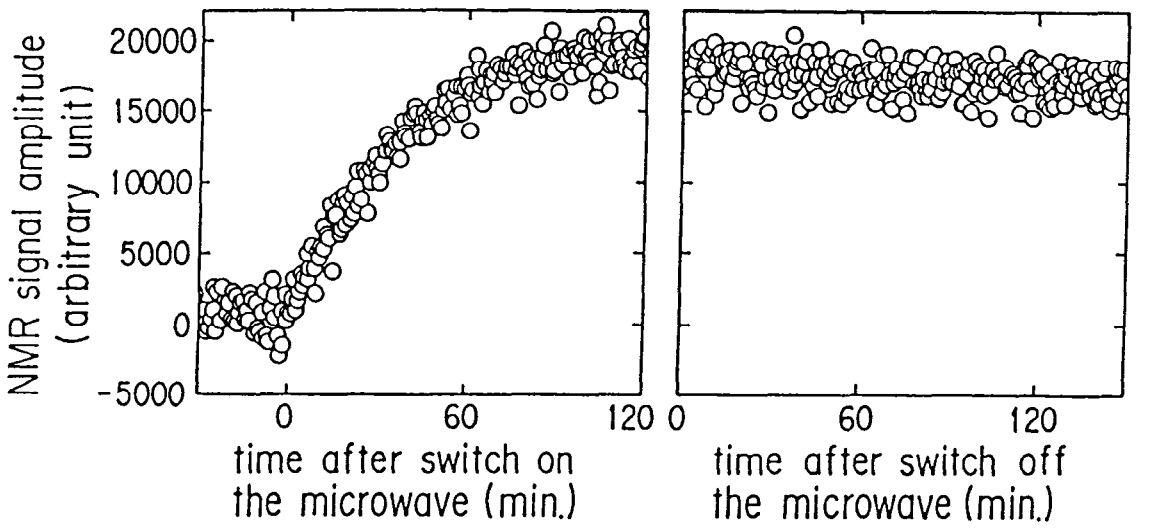

Fig. 4 Dynamic nuclear polarization of La(Nd)F_3.

Lanthanum nuclei in a $La_2Mg_3(NO_3)_{12}\cdot 24H_2O$ (LMN) crystal can be of course polarized[12]. However, other nuclei have the large neutron scattering cross section and the concentration of lanthanum nuclei is very small. In this point of view, LaF_3 is quite suitable for the transmission measurement, since the concentration of lanthanum nuclei is large and the neutron scattering cross section of the fluorine nucleus is very small. In fact, we could observe clear parity violating transmission difference for this crystal. A typical example is shown in Fig. 5. The dip at $E_n = 0.734$ eV is due to the p-wave resonance of ^{139}La. Other small dips are due to the nuclear Bragg scattering.

In the measurement of the T-violating transmission difference, we must control the neutron spin rotation. The neutron spin precesses around the magnetic field which is used for the polarization of the target nucleus spin. For example, the neutron spin precesses 60 turns during the passage through a 1-cm thick target in the magnetic field of 25 kG at $E_n = 0.734$ eV. The neutron spin also rotates around the nuclear polarization because

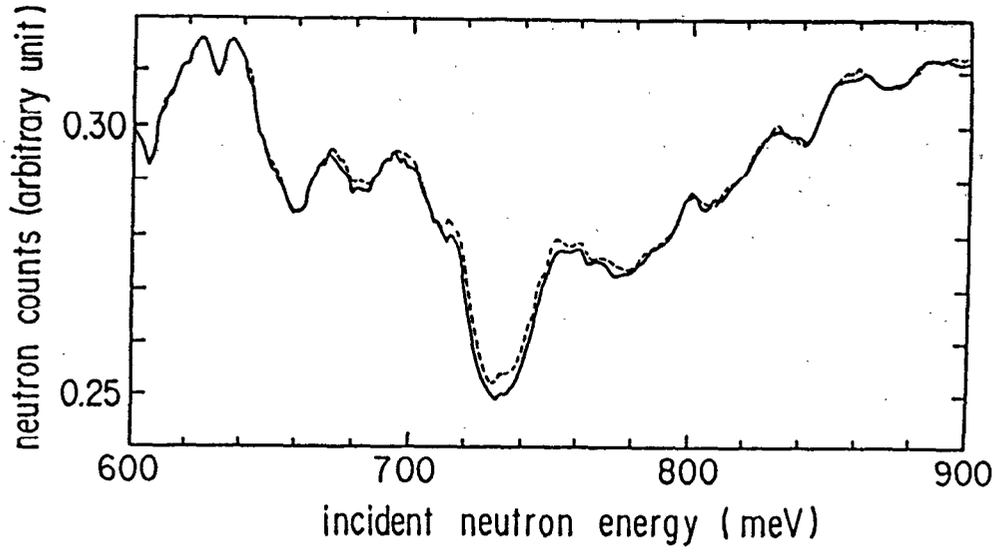

Fig. 5 P-violating transmission difference for a LaF_3 target. The solid and dotted lines are the results for positive and negative helicity states, respectively.

of the spin dependent neutron-nucleus interaction[13]. This rotation is called pseudomagnetic rotation. This phenomena was observed by the Saclay group[14]. The pseudomagnetic rotation is obtained by the following equations,

$$\omega = -\gamma_n H^* \quad (2),$$

$$H^* = 4\pi N_0 \mu_N{}^* P \quad (3),$$

$$\mu_N{}^*/\mu_B = I/\, g_n \cdot ((b_+ - b_-)/(I+1/2))/r_0 \quad (4).$$

Here, γ_n is the gyromagnetic ratio of the neutron, N_0 the number of nuclei in the target, P the nuclear polarization, g_n the neutron magnetic moment expressed in nuclear magneton, r_0 the classical electron radius and μ_B the Bohr magneton. b_+ and b_- are neutron scattering amplitudes for parallel and antiparallel spin states between neutron and nuclear spins. The pseudomagnetic field H^* corresponds to about 2 kG for the 100% polarized LaF_3 crystal. We can cancel out the two rotation in the target crystal, the Larmor precession and the pseudomagnetic rotation by adjusting the magnetic field strength. After the dynamic polarization, we can switch off the microwave power. The microwave heating disappear and the temperature in the crystal decrease. Therefore, we can reduce the magnetic field strength without a loss of the nuclear polarization so that the two rotation are cancelled out.

Finally, we need a polarized neutron detector. ^3He nuclei are quite suitable for the detection of polarized neutrons. The ^3He nucleus has the large resonance capture cross section for neutrons in the eV region. The

resonance energy is E_0 = -518 keV and the width is Γ = 1153 keV. The capture cross section is about 1000 b at E_n = 0.7 eV. In the resonance, the neutron spin is antiparallel to the ^{3}He spin. Therefore, polarized ^{3}He nuclei are quite suitable to detect polarized neutrons. ^{3}He nuclei are polarized by ^{3}He-Rb optical pumping. The Princeton group polarized 3 x 10^{20} ^{3}He nuclei up to 90% in order to polarize the neutron beam[15]. However, the number is short for this purpose. Recently, the TRIUMF group polarized the larger number of ^{3}He nuclei up to 60_70% by using a powerful Ti-sapphire laser[16]. The polarized ^{3}He nucleus number is 1.4 x 10^{21}. The number is sufficient to detect polarized neutrons. The detection efficiency for 100% polarized neutrons is about 40% in the detection area of 4 cm^2.

In conclusion, the T-violation test on the p-wave resonance of ^{139}La is quite promising. The upper limit of the T-violating transmission asymmetry is depend on the neutron counting statistics and the systematic error which comes from an uncertainty of the cancellation of the neutron spin rotation in the target. We estimated we can obtain the upper limit of less than 10^{-3}. Of course, we need to improve the lanthanum nuclear polarization and to develop the ^{3}He polarization for this purpose. We believe this is not out of the present technology.

The authors thank Prof. H. Nagasawa, Dr. Y. Saito and Dr. Y. Uchida for their kind help in the ESR study and Dr. F. Okamura for his kind help in the crystallography. We also thank Prof. H. Sugawara, Prof. N. Watanabe and Prof. K. Nakai for their kind encouragements.

References

1. V.P. Alfimenkov et al., Nucl. Phys. A398(1983)93.
2. Y. Masuda et al., Hyperfine Interactions 34(1987)143.
   Y. Masuda et al., Nucl. Phys. A478(1988)737c.
   Y. Masuda et al., Nucl. Phys. A504(1989)269.
3. S.A. Biryukov et al., Sov. J. Nucl. Phys. 45(1987)937.
4. C.D. Bowman et al., Phys. Rev. C39(1989)1721.
5. Y. Yamaguchi, J. Phys. Soc. Jpn. 57(1988)1518(L); ibid1522(L); ibid 1525(L); ibid 2331; ibid 3339; ibid 3344.
6. V.E. Bunakov and V.P. Gudkov, Z. Phys A308(1982)363.
7. P.K. Kabir, Phys. Rev. D25(1982)2013.
   P.K. Kabir, Phys. Rev. Lett. 60(1988)686.
8. L. Stodolsky, Nucl. Phys. B197(1982)213.
   L. Stodolsky, Phys. Lett. 172B(1986)5.

9. Y. Masuda et al., Nucl. Instr. Meth. A264(1988)169.
10. M.B. Schulz and C.D. Jeffries, Phys. Rev. 149(1966)270.
11. J.M. Baker and R.S. Rubins, Proc. Phys. Soc. (London) 8(1961)1353.
12. A. Abragam and M. Chapellier, Phys. Lett. 11(1964)207.
13. A. Abragam and M. Goldman, "Nuclear magnetism: order and disorder" Clarendon Press, Oxford(1982).
14. H. Glattli et al., Journal de Physique 40(1979)629.
15. K.P. Coulter et al., "Tests of time reversal invariance in neutron physics" ed. N.R. Roberson, C.R. Gould, J.D. Bowman(1987)140.
16. O. Hausser et al., KEK Report 90-15(1990)294.

Q(J.B.Hayter): When you move to a new, 4T magnet? What microwave system do you plan to use? Will you choose a high g-factor sample orientation?

A(Y.Masuda): A new microwave oscillator will be used. Varian's klystron is one of candidates.

ICANS-XI International Collaboration on Advanced Neutron Sources
KEK, Tsukuba, October 22-26, 1990

Neutron Scattering at Ultra-low Temperatures

K. Kakurai
Physics Department, Tohoku University, 980 Sendai, Aoba, Aramaki

Abstract
Two examples of neutron scattering experiments at ultra-low temperatures are described where the spin-dependent part of the nuclear scattering is used.

Introduction

In the very beginning of the application of the thermal neutron scattering, all possible contributions to the scattering cross-section have been calculated theoretically[1]. Despite this fact and although Shull and Ferrier [2] demonstrated experimentally the observability of the spin-dependent part of the cross-section quite early, it has been utilized in only few neutron scattering experiments [3]. The reason for this is straightforward: Because of the smallness of the nuclear spin moment , the nuclear temperature at which the nuclear spin polarization $\langle I \rangle \neq 0$ occurs, is at least three orders of magnitude lower than that needed for the electronic magnetic moment to be polarized. This mK temperature range became first commonly available after the recent development of the commercial dilution units.
By now, starting from this mK temperature range, the nuclear adiabatic demagnetization can be applied to reach even lower μK and nK nuclear temperatures. At these ultra-low temperatures spontaneous nuclear spin ordering can be expected. Remembering the unique role of the magnetic neutron scattering for investigating the electronic magnetic properties of solids, one easily can think of the importance of the spin dependent cross-section term in connection with the nuclear spin ordering and its properties. In this contribution I would like to demonstrate the importance of the neutron scattering at these low temperatures by which new and unique informations of the nuclear spin system can be obtained.

Neutron scattering cross-section

The fundamental quantities for neutron scattering at nucleus with spin I are the spin-independent scattering length

$$b_0 = \frac{b^+(I+1) + b^- I}{(2I+1)}$$

and the spin-dependent scattering length

$$b = 2\frac{b^+ - b^-}{(2I+1)}$$

where b^+ and b^- are respectively the scattering length for neutron spin parallel and antiparallel to nuclear spin. In the case of the unpolarized nuclear spins the spin-dependent scattering length gives the well known spin incoherent cross-section

$$\sigma_{inc} = \frac{1}{4} I(I+1)|b|^2$$

With $\vec{P}_n = \langle \vec{I} \rangle / I$ defined as the nuclear polarization vector, the coherent cross-section for an electronically nonmagnetic sample can be written in the following three contributions:

$$\left(\frac{d\sigma}{d\Omega}\right) = \left|\sum_{\nu} \exp(i\vec{Q}\vec{R}_\nu)\, b_{0_\nu}\right|^2 \qquad (1)$$

$$+ \frac{1}{4}\left|\sum_{\nu} \exp(i\vec{Q}\vec{R}_\nu)\, b_\nu I\, \vec{P}_n\right|^2 \qquad (2)$$

$$+ \mathrm{Re}\left\{\sum_{\nu\neq\mu} \exp\left[i\vec{Q}\left(\vec{R}_\nu - \vec{R}_\mu\right)\right] b^*_{0_\nu} b_\mu I\, \vec{P}_n \vec{P}^N\right\} \qquad (3)$$

where $\vec{P}^N$ represents the neutron polarization. For the simplicity only the special (but most common) case of the nuclear polarization along the external field is considered here for the term including the neutron polarization P^N (Term (3)). The first term is the spin-independent part, the second is the term purely due to the nuclear polarization and the third term is the interference term of the first two contributions. As can be seen the third term can be only observed if $P^N \neq 0$, i.e. only with the use of polarized neutrons.

In the following the observation of the nuclear spin ordering in Cu through the second term and the polarized neutron thermometry using the third term will be described as examples for the use of the spin-dependent scattering length.

Nuclear spin ordering in Cu

(The details of this experiment are given in ref. 4)

The first experimental evidence for spontaneous antiferromagnetic (AF) nuclear spin ordering in Cu was found in studies of the low-frequency ac susceptibility on a polycrystalline sample at temperatures below 60nK[5] and subsequently the AF order in the field was studied in detail on a single crystal[6]. The latter experiment yielded three different regimes in the field and entropy phase diagram. To obtain more insight into the complicated phase diagram, a direct study of the periodicity of the AF order is mandatory, which can be only performed with neutron scattering using the spin-dependent cross-section term (2).

The Hamiltonian of the Cu nuclear spin system consists out of the indirect Ruderman-Kittel and the dipolar interaction. All theoretical calculations for the zero-field case predict an AF structure where the magnetic translation period is equal to the cubic lattice constant. This would lead to the appearence of (100) superlattice peaks in the nuclear spin ordered phase. A two axis neutron diffractometer was specially modified for this ultra-low temperature application, including the vibration damping and the position sensitive detector, and installed at the neutron guide from the cold source in the DR-3 reactor at Risø. A new two-stage nuclear demagnetization cryostat with the split type magnet for the second stage was constructed to allow the neutron beam access to the sample. ^{65}Cu was choosen as the sample material because of the large spin-dependent scattering length for this isotope. The slablike single crystal with the approximate dimensions of 35*7*0.6 mm^3 with the [011] direction along the largest edge. [100] and [011] axes were oriented into the scattering plane and the external field, a vertical field, was applied

along the [01$\bar{1}$] direction. The whole nuclear demagnetization stage is precooled by the dilution unit. Using the first demagnetization stage the sample in the field of 4.5T is cooled to a lattice temperature of about 100mK. The demagnetization of the second stage (the sample) from 4.5T to a field below 0.3mT cooles the nuclear spin system to the final temperatures $T<T_N=60$nK. After the final demagnetization the nuclear spin temperature begins to relax towards the electron temperature. The spin-lattice relaxation time in the experiment with a neutron flux of 10^5 n/cm^2/sec was ~20min. which allowed the observation of the ordered phase for 7~8 min.. Fig.1 shows the time evolution of the (100) peak after the demagnetization to the zero field, as observed in the position sensitive detector. The decay of the AF nuclear spin Bragg peak as the nuclei warm up with time is clearly seen. To obtain more

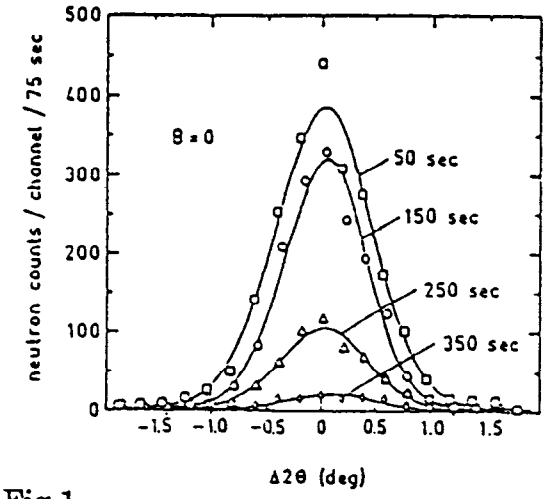

Fig.1

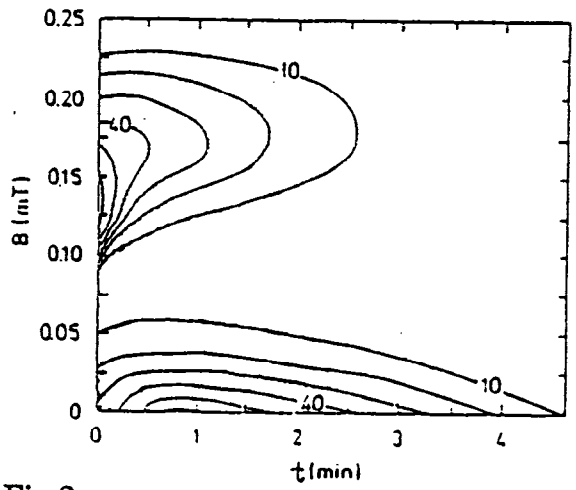

Fig.2

information about the phase diagrm, experiments were also performed at nonzero external fields. In fig.2 the neutron intensity contour diagram of the (100) Bragg peak as a function of time and external magnetic field is shown. It is noteworthy that there is a region around 0.07mT where the (100) intensity is effectively zero, although the susceptibility measurement carried out simultaneously clearly indicates AF ordering. This is a clear indication of another type of the spin ordering in this phase diagram regime. The more recent neutron scattering results indeed show that (0,2/3,2/3) type nuclear spin Bragg peaks are present in this regime[7]. The commensurate ordering vector $\vec{k}=(2\pi/a)(0,2/3,2/3)$ causing this type of Bragg peaks has not been observed in any electronic fcc AF systems sofar. In the fcc nuclear spin system Cu, the comparable size of the Ruderman-Kittel and dipolar interactions and the quantum effects might stabilize this novel ordering vector. This results add a new aspect to the old problem of the frustration in the fcc AF system.

Polarized neutron thermometry

(The details of this method are described in ref. [8].)

In the following measurements we have used polarized neutrons to determine the nuclear temperature of Cu in the range between 100μK and 20mK. Using the cross-section formula above the Bragg intensity for the fcc lattice with four atoms per unit cell can be written as

$$I_{\pm}=16\left(b_0^2 \pm b_0 b I P_n \left|P^N\right| + \left(\frac{I}{4}\right)^2 b^2 P_n^2\right)$$

for an extinction-free case.

The flipping ratio (FR), i.e. the ratio between the intensity of scattered neutrons in the two spin state then is

$$FR(P_n) = \frac{I_+}{I_-}$$

This equation gives the relationship between the nuclear polarization and the FR, a quantity which is less sensitive to experimental errors than the measurement of absolute intensities. In the paramagnetic regime the nuclear polarization P_n is related to the nuclear temperature T_n via the Brillouin function B_I:

$$P_n = B_I\left(\gamma_n \hbar I B / kT_n\right)$$

where γ_n is the gyromagnetic ratio of the nucleus and B is the applied external field.

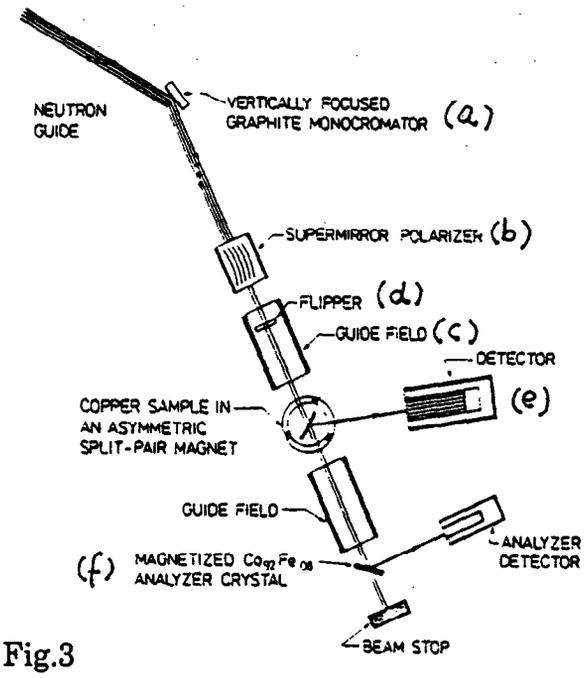

Fig.3

The following neutron diffractometer set up was used (fig.3). Neutrons from the cold neutron guide are monochromatized using a vertically pyrolytic graphite monochromator(a). The beam is then polarized by a supermirror bender (b). Permanent magnets are used to magnetize the vertical guide fields before and after the cryostat(c). A dc-flipper(d), located in the guide field in front of the cryostat , determines the + or - polarization of the beam. The Bragg reflected neutrons at the sample is detected by the main counter (e). The sample enviroment is identical to that of the nuclear spin ordering experiment mentioned above. The beam polarization is monitored by an analyser system in the through going beam behind the sample using a magnetized $Co_{92}Fe_{08}$ analyzer crystal(f).

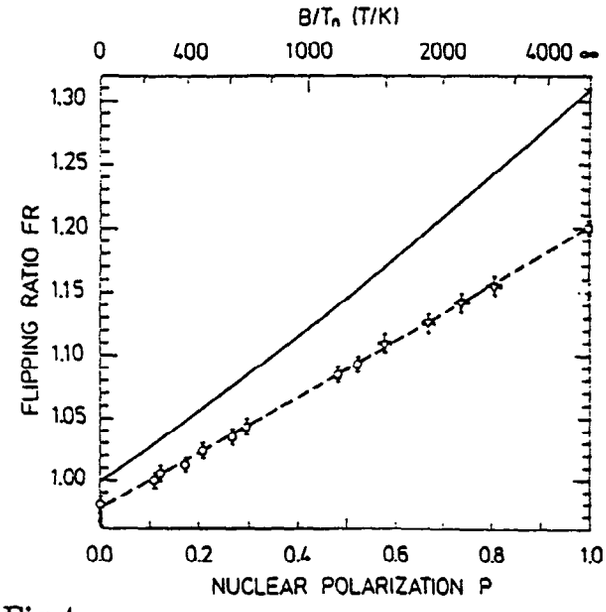

Fig.4

Although this thermometry is in princip calibration free, the extinction effect of the single crystal Bragg intensity does cause the deviation of the relation $I \propto /F/^2$ and hence a calibration over the entire temperature range is required. Because of the limited space available I only show the result of such a calibration (fig.4) without going into detail but mentioning that the Co thermometry was used in the B/T range of B<4T and T>3mK. For even larger B/T-values the temperatures were determined by extrapolating back the warm-up curve to the measurable temperature after having first cooled the system below 1mK. The more interested readers are referred to the original paper [8]. The calibration depicted in fig.4 is for λ =2.4 Å. The solid curve is the calculated extinction free curve and without the μ-

metal correction, which causes the measured curve not intersepting FR=1 at P_n=0. Once this calibration is done the nuclear polarization, hence the nuclear temperature at given external field, can be determined by measuring the FR.

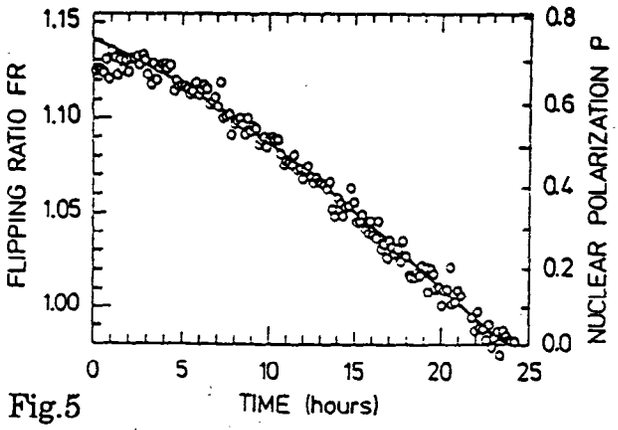

Fig.5

As an application a typical heat leak measurement of the Cu system is shown in fig.5. This measurement was carried out in an external field of 1T and it covers temperatures from 0.5 mK upwards. The curve through the experimental points corresponds to a constant heat leak of $\dot{Q}$=14nW, which describes the experimental data well over the 24 hours. For studies of nuclear ordering such an heat leak measurement is of extreme importance to reduce the heat input to the nuclear stages to a very low level.

To conclude I have picked up two examples to demonstrate the use of the spin dependent part of the nuclear scattering length. Unique and important informations on the nuclear spin system can be obtained. To utilize this possibility neutron scattering at ultra-low temperatures is indispensable.

Acknowledgement
The results described here were obtained in the joint low temperature neutron scattering project with Low Temperature Laboratory at Helsinki University of Technology, Finnland, Neutron Scattering Group at Risø National Laboratory, Denmark and Neutron Scattering Group at Hahn-Meitner-Institut, Berlin. In this context I thank K.N. Clausen, M.T. Huiku, T.A. Jyrkkiö, J.K. Kjems, O.V. Lounasmaa, K. Siemensmeyer and M. Steiner without whose help this contribution could not have been written.

References
[1]: O. Halpern and M.H. Johnson, Phys. Rev., 55 (1939) 898
[2]: C.G. Shull and R.P. Ferrier, Phys. Rev. Lett., 10 (1963) 295
[3]: for review see: S. Kawarazaki and J. Arthur, Physica, 136B (1986) 379
H. Glättli and M. Goldman, "Nuclear Magnetism" in Methods of Experimental Physics, vol.23, Part C, Academic Press, 1987
M. Steiner, Physica Scripta, 42 (1990) 367
[4]: T.A. Jyrkkiö, M.T. Huiku, O.V. Lounasmaa, K. Siemensmeyer, K. Kakurai, M. Steiner, K.N. Clausen and J.K. Kjems, Phys. Rev. Lett., 60 (1988) 2418
[5]: M.T. Huiku and M.T. Loponen, Phys. Rev. Lett., 49 (1982) 1288
[6]: M.T. Huiku, T.A. Jyrkkiö, J.M. Kyynäräinen, M.T. Loponen, O.V. Lounasmaa and A.S. Oja, Jour. Low Temp. Phys., 62 (1986) 433
[7]: A.J. Annila, K.N. Clausen, P.-A. Lindgård, O.V. Lounasmaa, A.S Oja, K. Siemensmeyer, M. Steiner, J.T. Touriniemi and H. Weinfurter, Phys. Rev. Lett., 64 (1990) 1421
[8]: T.A. Jyrkkiö, M.T. Huiku, K.N. Clausen, K. Siemensmeyer, K. Kakurai and M. Steiner, Z. Phys. B - Condensed Matter, 71 (1988) 139

Q(R.Pynn): Do you think there is any possibility of doing inelastic scattering experiments from nuclear ordered systems?

A(K.Kakurai): To be honest, I haven't done any quantitative collection. But it will be difficult because of the following two reasons:

1) Expected low excitation energies in these systems and hence an high energy resolution needed,
2) Low intensities combined with the limited flux available for the measurement.

ICANS-XI International Collaboration on Advanced Neutron Sources
KEK, Tsukuba, October 22-26, 1990

A SUMMARY OF THE WORKSHOP ON NEUTRON SCATTERING DATA ANALYSIS HELD AT THE RUTHERFORD APPLETON LABORATORY IN MARCH 1990

M W Johnson
Rutherford Appleton Laboratory, Chilton, Didcot, Oxon, OX11 0QX, UK

The workshop on neutron scattering data analysis, held at the Rutherford Appleton Laboratory in March 1990, included 22 presentations, 21 of which are included in the IOP Conference Series No 107 to be published in November 1990. Table 1 lists the contributions and their authors. In a talk of this length is is obviously impossible to mention them all, and I have therefore made a personal selection, highlighting those talks which will be of interest to the widest neutron scattering community.

The first is the paper by Ron Ghosh and Adrian Rennie on small angle scattering. They asked the simple question 'Are existing SANS results correct' - bearing in mind the fact that the scattering is assumed to be elastic when it often clearly is not. They answered this question by introducing time-of-flight analysis onto the D17 instrument at the ILL. Figure 1 shows the SANS patterns for perdeuterated polystyrene (PS-d) in hydrogenous toluene, at a series of time-of-flight. The inelastic contribution is quite clear. Analysis using just the elastic channels, Figure 2a, and the total scattering, Figure 2b, show small, but significant, differences. For example, the derived radius of gyration is 24.7Å (elastic scattering) whereas the conventional analysis from the totally scattered neutrons gave 25.9Å. The authors were able to show that, in this example, despite the considerable thermalisation in the sample, the subtraction of the background toluene pattern largely removes the inelastic effects, resulting in substantially correct results. Although only a few percent error is introduced in this example, the authors point out that for models involving greater weight at high Q (Porod's Law) or Fourier transforms the results could be substantially worse.

In reflectometry we had two complementary contributions. Jeff Penfold presented the 'classical' approach of model fitting, illustrating the method with simple examples. Figure 3a shows data from a single 'perfect' surface well fitted by the Fresnel law; 3b shows a 48 layer Langmuir Blodgett film modelled by a single uniform layer of 1186Å with roughness of 20Å at the air-film and film-substrate interfaces; 3c shows that at higher Q a 20 layer Langmuir Blodgett film requires the specific inclusion of the bilayer structure to include the Bragg peak observed at 0.12 $Å^{-1}$.

Davinda Sivia presented some MaxEnt results in which the density profile $\beta(z)$ (β is the average neutron scattering length density, z = depth below surface) is determined by inverting the data using the MaxEnt formulism. A number of striking successes were presented (Figures 4, 5 and 6), which also illustrated the insensitivity of the data to translation (i.e. $\beta(z+a)=\beta(z)$) or inversion $\beta(-z) = \beta(z)$. A clear example was also given of the technique producing quite the wrong answer (Figure 7) which should act as a cautionary note. However, this example was retrieved when further information was supplied (Figure 8). Clearly this method shows promise - but also some additional work in establishing the confidence levels one can place in the result.

In liquids and amorphous diffraction the session was treated to a 'live display' of data analysis using the Reverse Monte Carlo (RMC) technique by Bob McGreevy. In standard Monte Carlo methods, atomic or molecular configurations are determined by minimising an energy cost function, subject to certain constraints, using a weighted sampling procedure. In this case the 'cost function' is derived from theoretical interaction potentials. In RMC the ensemble of atoms

is modified with the aim of reducing χ^2 until it reaches 1. The 'cost function' is now the disagreement between model and observed data. The beauty of the technique lies in its ability to combine different types of data into the analysis. Figure 9 shows the fit of an atomic ensemble to both the X-ray and neutron structure factors for vitreous silica. From this model it is then possible to calculate **three** partial radial distribution functions - from only two measurements! In addition, RMS produces a 3-d structure from which broad angle distributions may be calculated (Figure 10).

Another problem tackled by RMC is liquid sulphur - is the structure based on rings, chains or a mixture, and what happens at the viscous transition? RMC fitting to the structure factor at 423 and 503K (either side of the transition) gives a structure of entangled, broken chains. The average coordination is close to 2, although this comes from 40% 2-coordination + 40% 1 or 3 coordination. The interesting point is that with RMC the model may be constrained - and doing this to produce 92% 2-coordination led to results equally consistent with the data. Examples of high and low 2 coordination are shown in Figure 11.

The crystallographic section of the meeting also produced two excellent presentations on the use of MaxEnt methods. In the first, Papoular and Gillon showed how the limited data from polarised neutron diffraction data may be inverted successfully to determine magnetic structures. In a model example (Figure 12) two positive and two negative magnetic moments are used in a 2-d example. Figures 12a, 12b and 12c show standard Fourier transforms using increasing numbers of reflections, the ME reconstruction (Figure 12d) eliminates truncation effects and quite clearly exhibits the two small negative moments. In a 'real data' case the chemical bonding in tanol suberate was examined. Figure 13 shows the results. Standard Fourier analysis does not resolve the electronic density about the NO group (Figures 13a, 13c) whereas the ME procedure yields clearly resolved features (Figures 13b, 13d) and moreover gives a good value of 3.7 μB for the average magnetisation per unit cell again 3.2 $\pm$ μB obtained from independent, macroscopic measurements.

Another use of ME in crystallography has produced outstanding results. A paper by Bill David (RAL) described how excellent Patterson maps may be obtained using the MaxEnt technique and the results shown to be correct. David has used experimental data from rutile (TiO_2) recorded on the POLARIS spectrometer at ISIS (Figure 14). Using conventional equipartition of overlapping powder lines and Fourier inversion, the maps shown in Figures 15a, 15b and 15c are obtained. Using the criterion of maximising 'Patterson Entropy', the maps in Figures15d, 15e and 15f are obtained - which are certainly sharper. These are not only sharper - but correct - since these Patterson peaks are in excellent agreement with the known interatomic vectors. Confirmation of the validity of the method is also provided by a back-calculation of individual structure factors to obtain a R-factor for the two methods :

$$R_{EQ} = 34\%$$
$$R_{ME} = 14\%$$

This method also holds great promise as the first stage in structure determinations based on Patterson inversions.

In the section on general techniques the meeting was given an excellent review of the subject of simulated annealing. As its name implies, the method attempts to mimic the solidification or annealing process that occurs in solid-liquid transitions to obtain a global minimisation to optimisation problems. The applications are vast ranging from the mathematical (travelling

salesman problems) to engineering (VSLI placement and routing problems) and scientific (structure determination). In fact, the method has been used in a similar way to RMC (which it proceeded) to solve structures directly by minimising the R-factor. More dramatically, it has also been used to determine zeolite crystal structures from crystal-chemistry rules alone.

Finally, two papers on MaxEnt pointed to new future directions in the field. The one by John Skilling introduced the subject to non-experts - but also alluded to the new work on confidence intervals that may be calculated using ME. This new software - MEMSYS III - provides this facility, and this should help make the technique more widely acceptable to the scientific community at large.

The second of these two papers was by Alan Soper (RAL) who dared to raise the question as to whether the ME criterion, while powerful, was sufficient in certain circumstances. He notes the difficulties of ME in inverting certain problems (especially the $S(Q) \rightarrow g(r)$ inversion) and the fact that apparently "noisy" solutions can have the same entropy as 'smooth' solutions, see for example Figure 16.

I would like to conclude with some remarks of my own which were not made at the WONSDA meeting. I believe that the MaxEnt method, at its roots, is perfectly sound - the problem is that the theory has been developed for probability distributions and has been applied without sufficient questioning to spectra. Spectra have some of the attributes of probability distributions, but are not identical. It is in some ways a tribute to the ME method that it has worked so well for spectra.

To illustrate the point I show Figure 17. The data are crosses and two possible 'solutions' are shown by the dotted or dashed lines. Both of these lines have the same χ^2 and entropy, and hence would be equally acceptable to a ME algorithm. The point about a spectrum is that it is an **ordered** series of values, whereas a probability distribution is not. Hence the ME criterion cannot distinguish one solution from another. However, Bayes Theorem has the power to allow us to include a 'desirability' (from Occam's Razor) criterion within the prior to enable these distinctions to be made. Some work now has to be done on the mathematical formulation of Occam's Razor, and its inclusion into a Bayesian/ME formalism.

J Pannetier*	Simulated Annealing: an introduction and a few applications to problems of structure determination
R L McGreevy	Reverse Monte Carlo (RMC) simulation: modelling disordered structures from diffraction data
D A Keen	Determining structural disorder in crystalline materials by Reverse Monte Carlo (RMC) simulation
P Wolfers	MXD: A general least-squares program for non-standard crystallographic refinements
R P Piltz	On the normalization of spallation-source powder diffraction data
M Anne	Real-time neutron powder diffraction study of $MoO_3.2H_2O$ Topotactic Dehydration
C C Wilson	Data analysis of reciprocal space volumes
J Skilling*	Quantified maximum entropy data processing
R J Papoular	Maximum entropy reconstruction of spin density maps in crystals from polarised neutron diffraction data
W I F David	Unscrambling powder diffraction data
D S Sivia	The Bayesian approach to optimal instrument design
A K Soper	An amateur's guide to the pitfalls of maximum entropy – or – a practical solution to two well-known problems in linear inversion of experimental data
M J D Powell*	Radial basis function methods for multivariable approximation
A Smith	Analysis of quasielastic and inelastic scattering data from crystal analyser instruments
H Tietze	Computational aspects in scan performance of the Rotating Analyser Crystal Spectrometer ROTAX
A C Hannon	ATLAS – A package of routines for the analysis of time-of-flight diffraction data from liquid and amorphous samples
F Cilloco	A normalization procedure of liquid diffraction data based on the knowledge of the sample neutron cross section
K M Crennell	NUVU, a program for the visualisation of neutron scattering data based on UNIRAS
C-K Loong*	S(Q,E) analysis for chopper spectrometer data
R Osborn	Multi-phonon and multiple scattering corrections to $S(Q,\omega)$
G J Kearley	CLIMAX – recent extensions
J Penfold*	Analysis of neutron reflectivity data using constrained model fitting
D S Sivia	Maximum entropy analysis of reflectivity data – some preliminary results
C Moreton-Smith	GENIE Version 3: A tool for neutron scattering data analysis and visualisation

Table 1

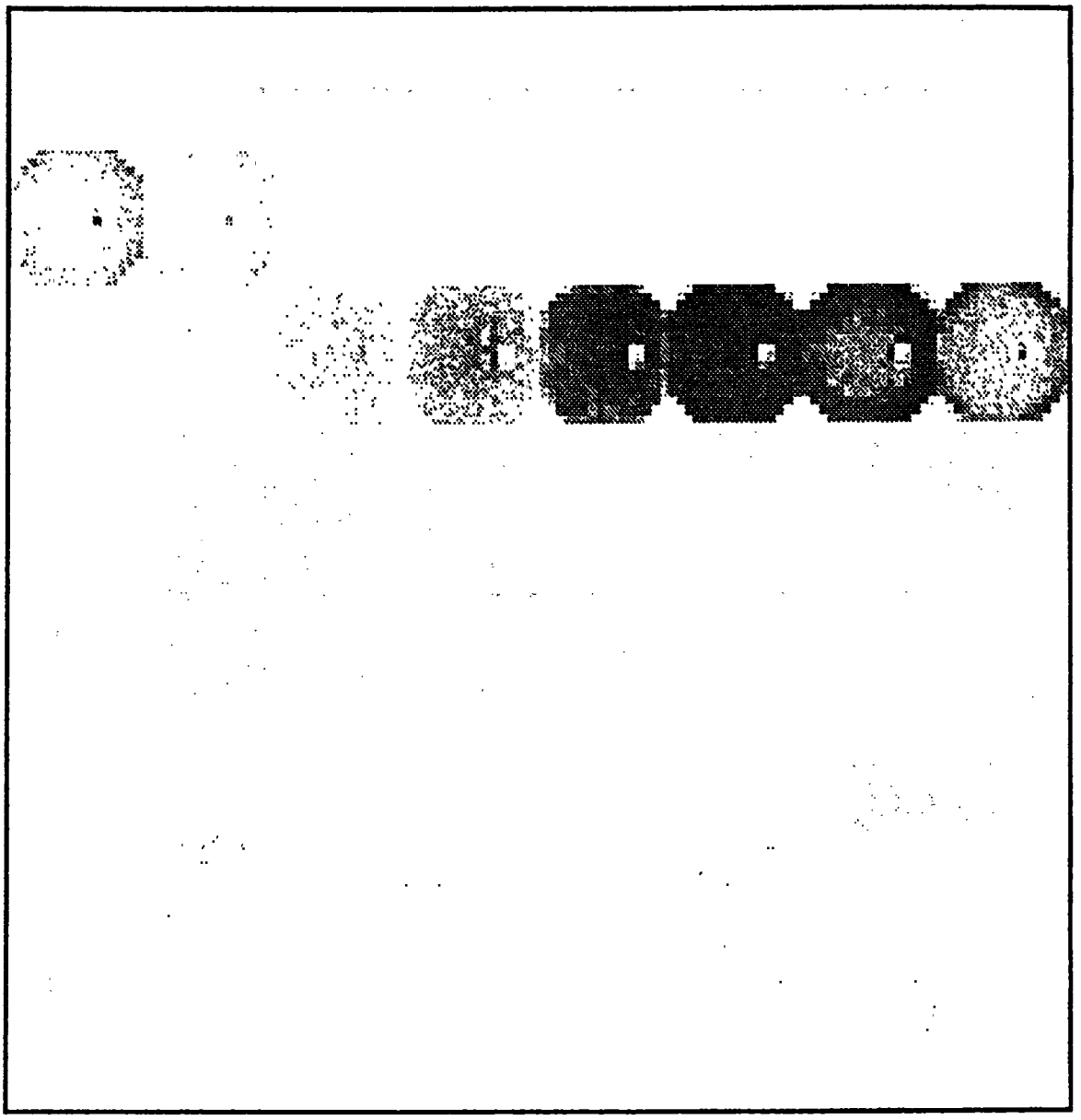

Fig. 1 A set of 64 two-dimensional spectra for 1mm water (25 C) as a function of time-of-flight (raw data). The grey scale goes from light to dark with increasing intensity. The time scale for neutron arrival starts at short times in the bottom left hand corner and increases by rows from left to right and from bottom to top. The most intense signal corresponds to elastic scattering of 12 Å neutrons (time channel 46). The detector is 6 degrees of axis and the beam stop protecting the detector from the incident beam is off-centre showing as a white spot on each frame. The large fraction of inelastically scattered neutrons is evident from the intensity at short times of flight.

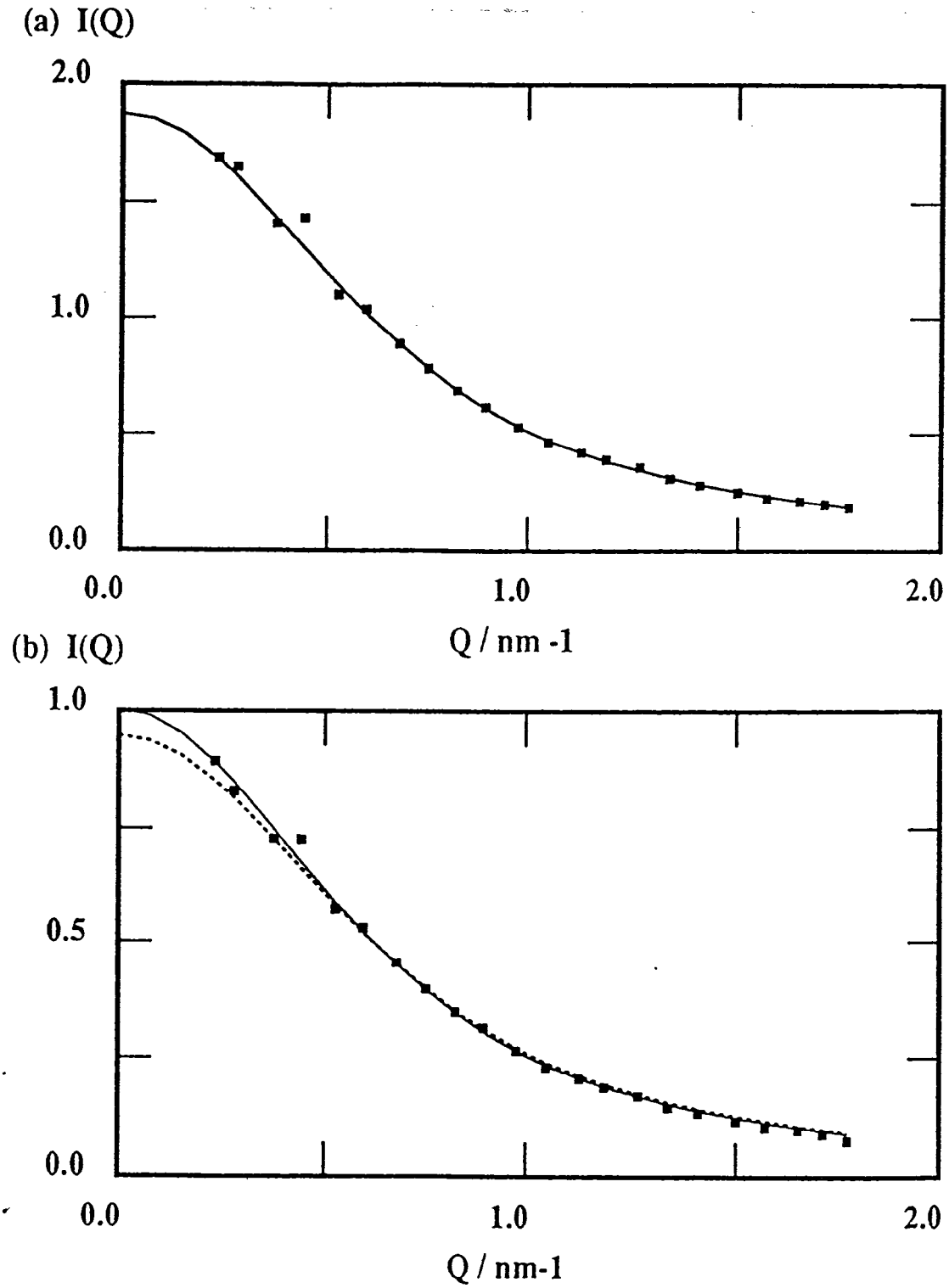

Fig. 2 (a) Elastic scattering for PS-d in toluene with fit of Debye function and (b) total scattering, all time channels, with best fit to data (solid line) and the model fitted to elastic data rescaled (dashes) The latter data show the deviation at large Q values due to an over correction with water.

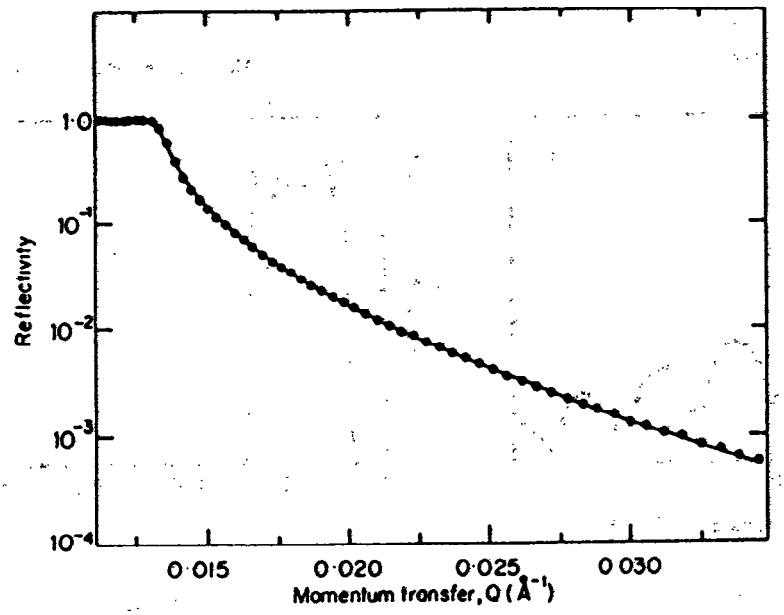
1·0
10^{-1}
10^{-2}
10^{-3}
10^{-4}
Reflectivity
0·015
0·020
0·025
0·030
Momentum transfer, Q (Å^{-1})

a

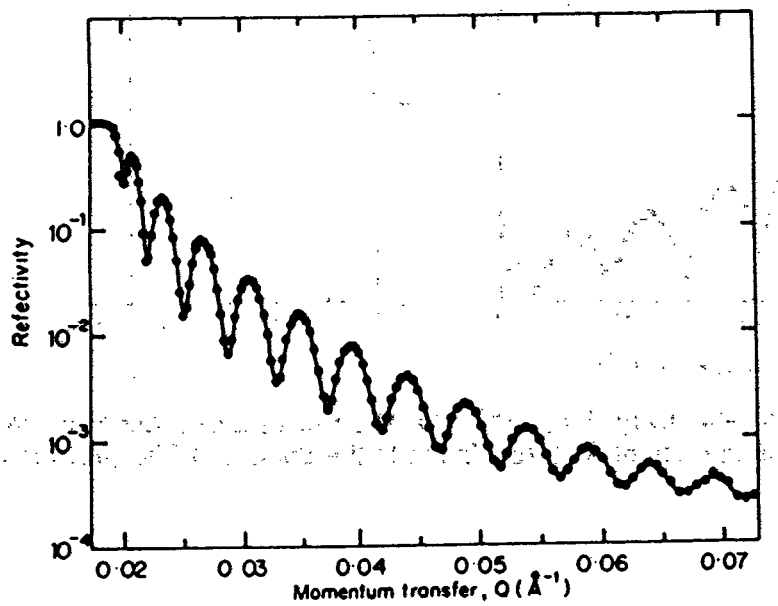
1·0
10^{-1}
10^{-2}
10^{-3}
10^{-4}
Reflectivity
0·02
0·03
0·04
0·05
0·06
0·07
Momentum transfer, Q (Å^{-1})

b

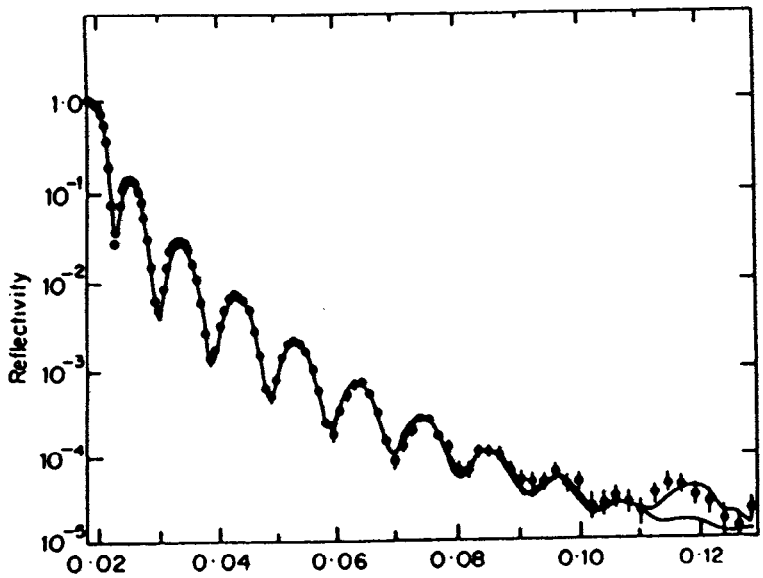
1·0
10^{-1}
10^{-2}
10^{-3}
10^{-4}
10^{-5}
Reflectivity
0·02
0·04
0·06
0·08
0·10
0·12

c

Fig 3

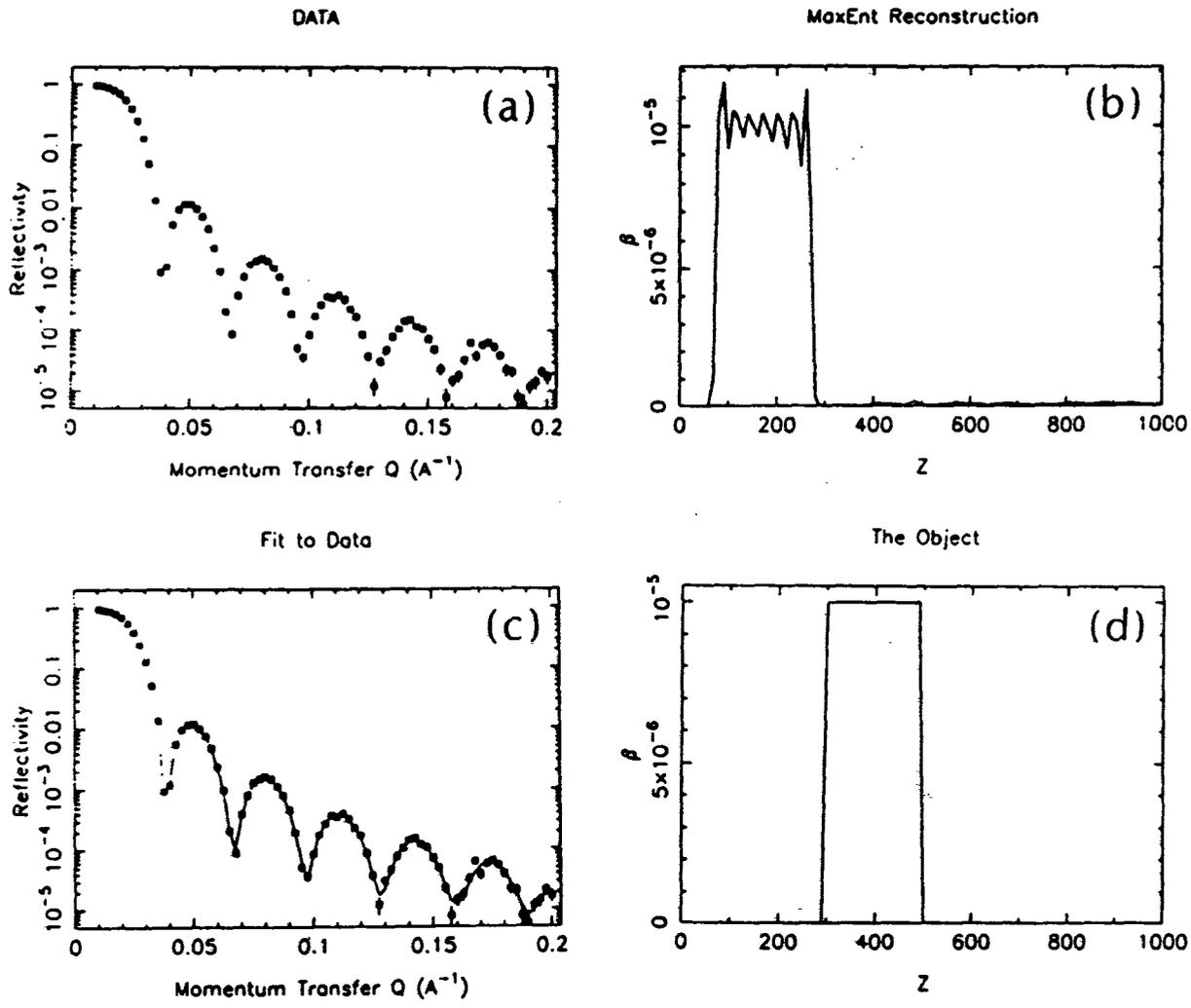

Figure 4 **(a)** Simulated reflectivity data. **(b)** The MaxEnt reconstruction of the depth profile. (z is in units of Å, and β is in units of Å^{-2}.) **(c)** The fit to the data. **(d)** The (true) test profile.

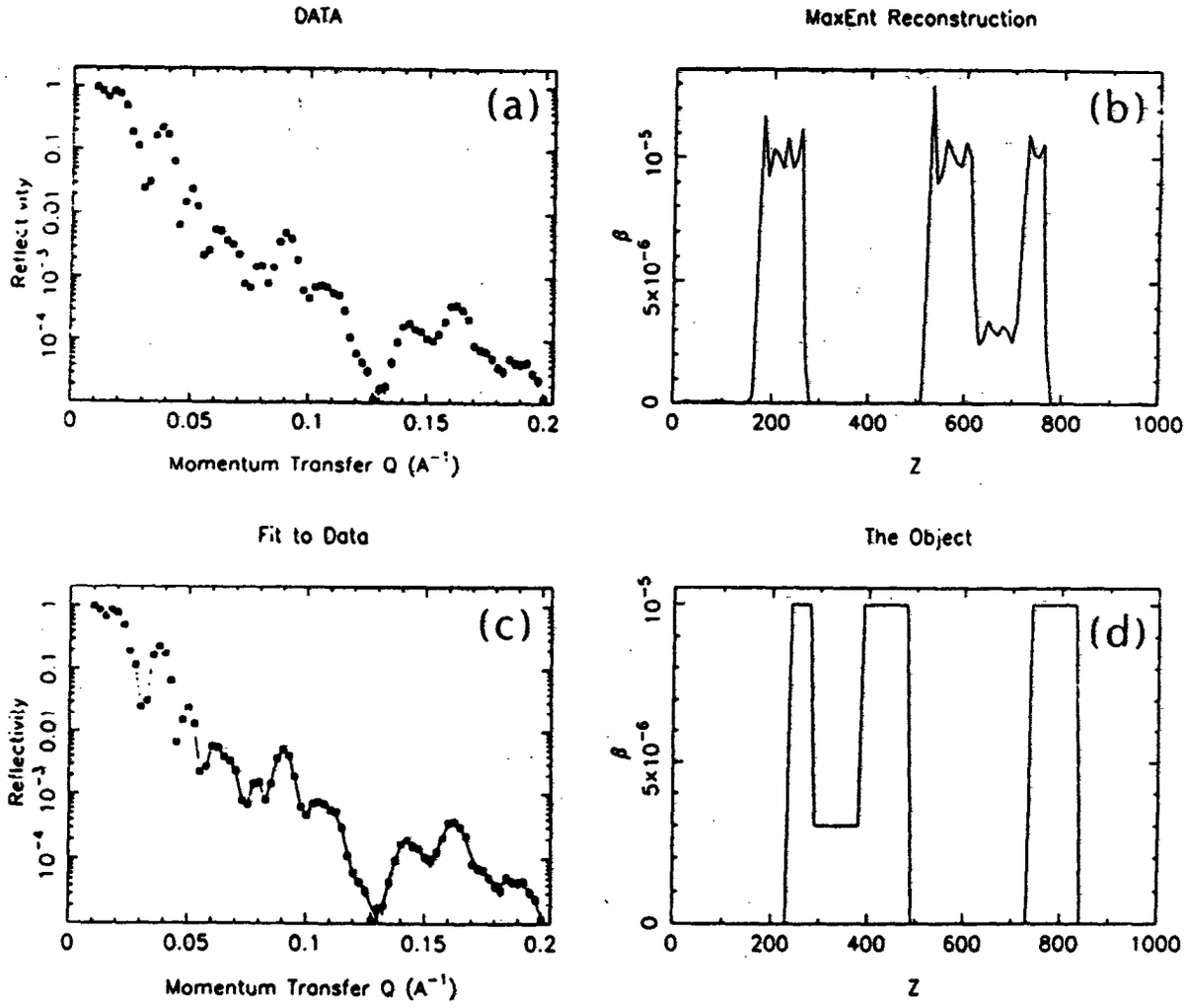

Figure 5 **(a)** Simulated reflectivity data. **(b)** The MaxEnt reconstruction of the depth profile. **(c)** The fit to the data. **(d)** The test profile.

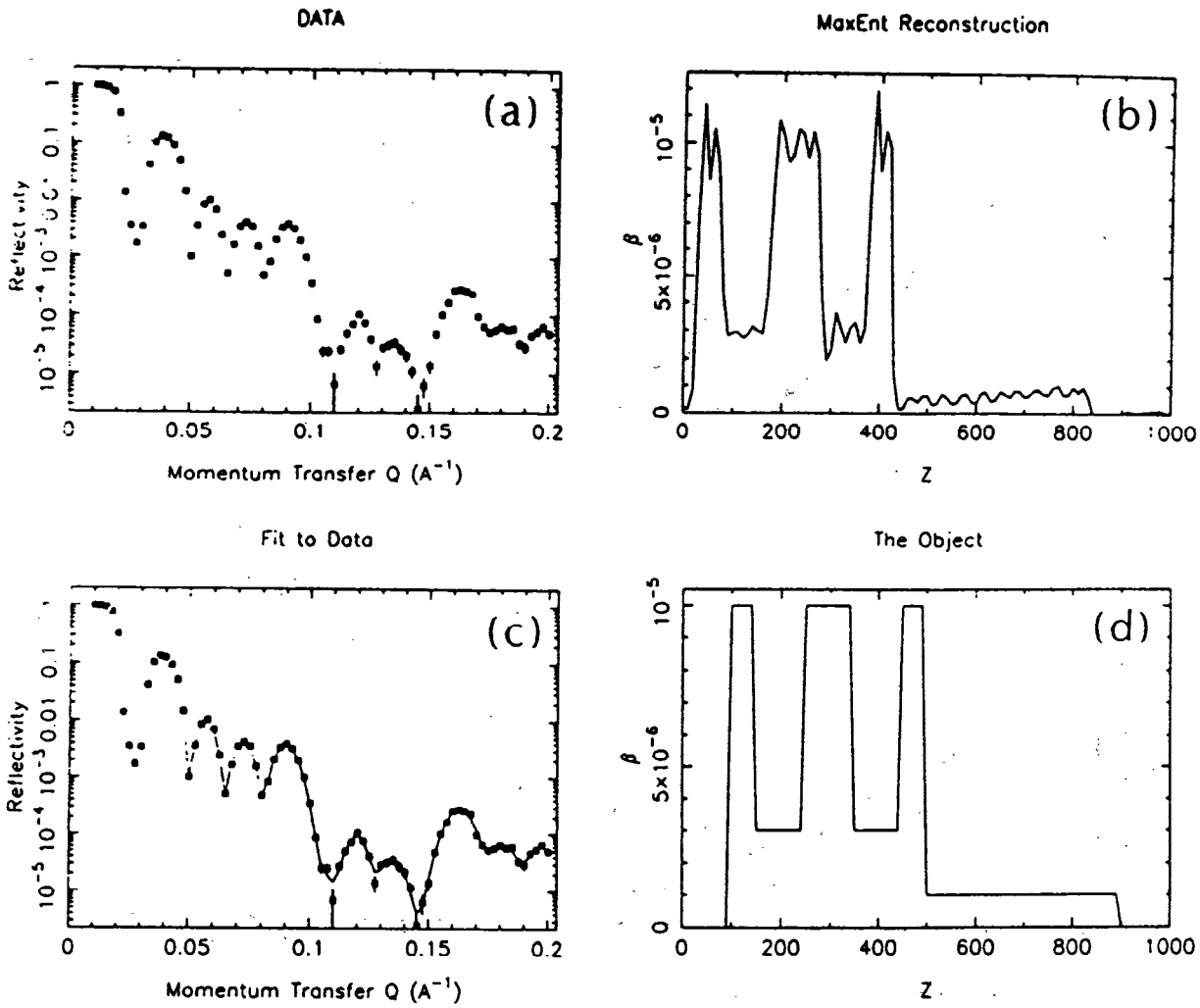

Figure 6 **(a)** Simulated reflectivity data. **(b)** The MaxEnt reconstruction of the depth profile. **(c)** The fit to the data. **(d)** The test profile.

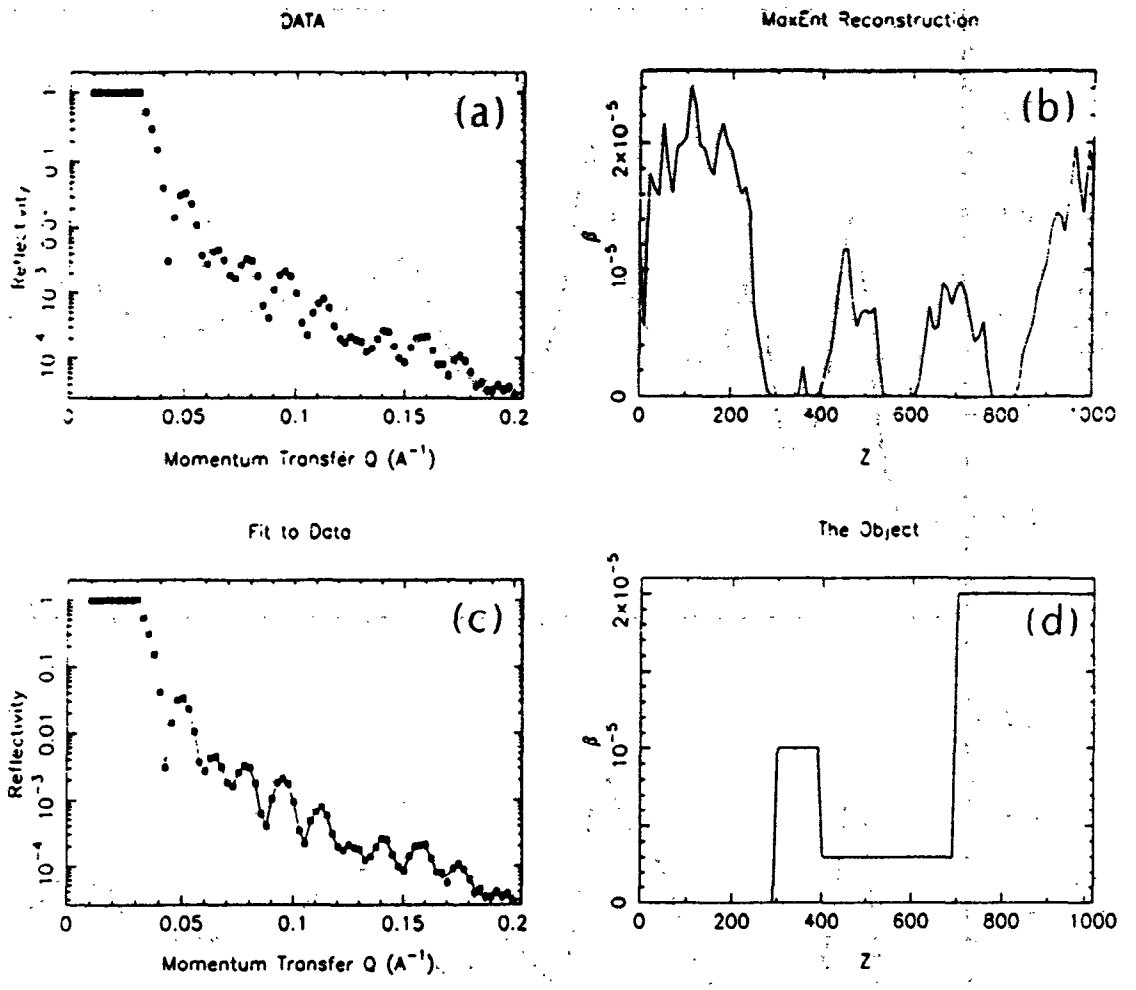

Figure 7 : (a) Simulated reflectivity data. (b) The MaxEnt reconstruction of the depth profile. (c) The fit to the data. (d) The test profile.

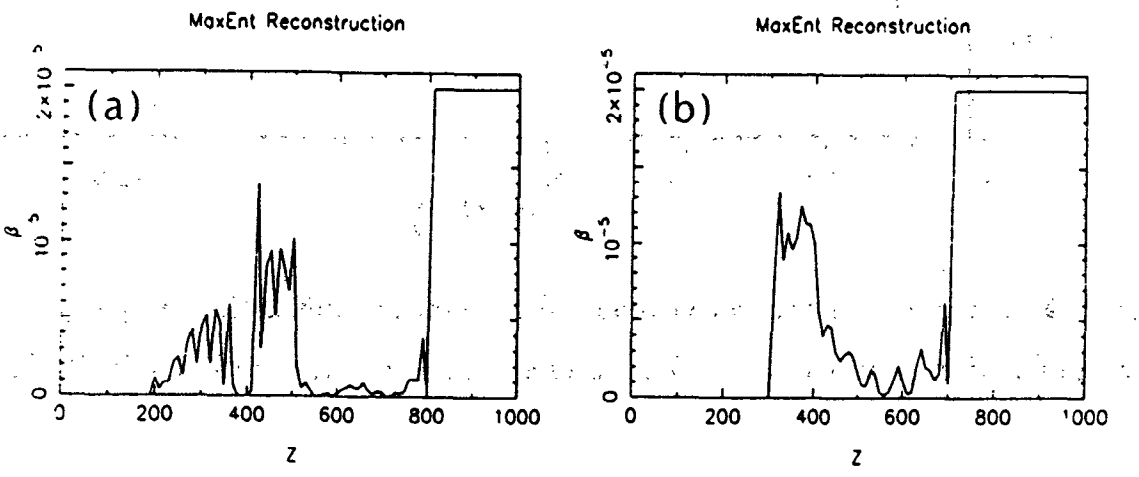

Figure 8 : Analysis of the reflectivity data in Fig. 6(a) using some additional prior knowledge. (a) Given the substrate and that the sample is less than 600Å thick. (b) Given the substrate and that the sample is 400 Å thick.

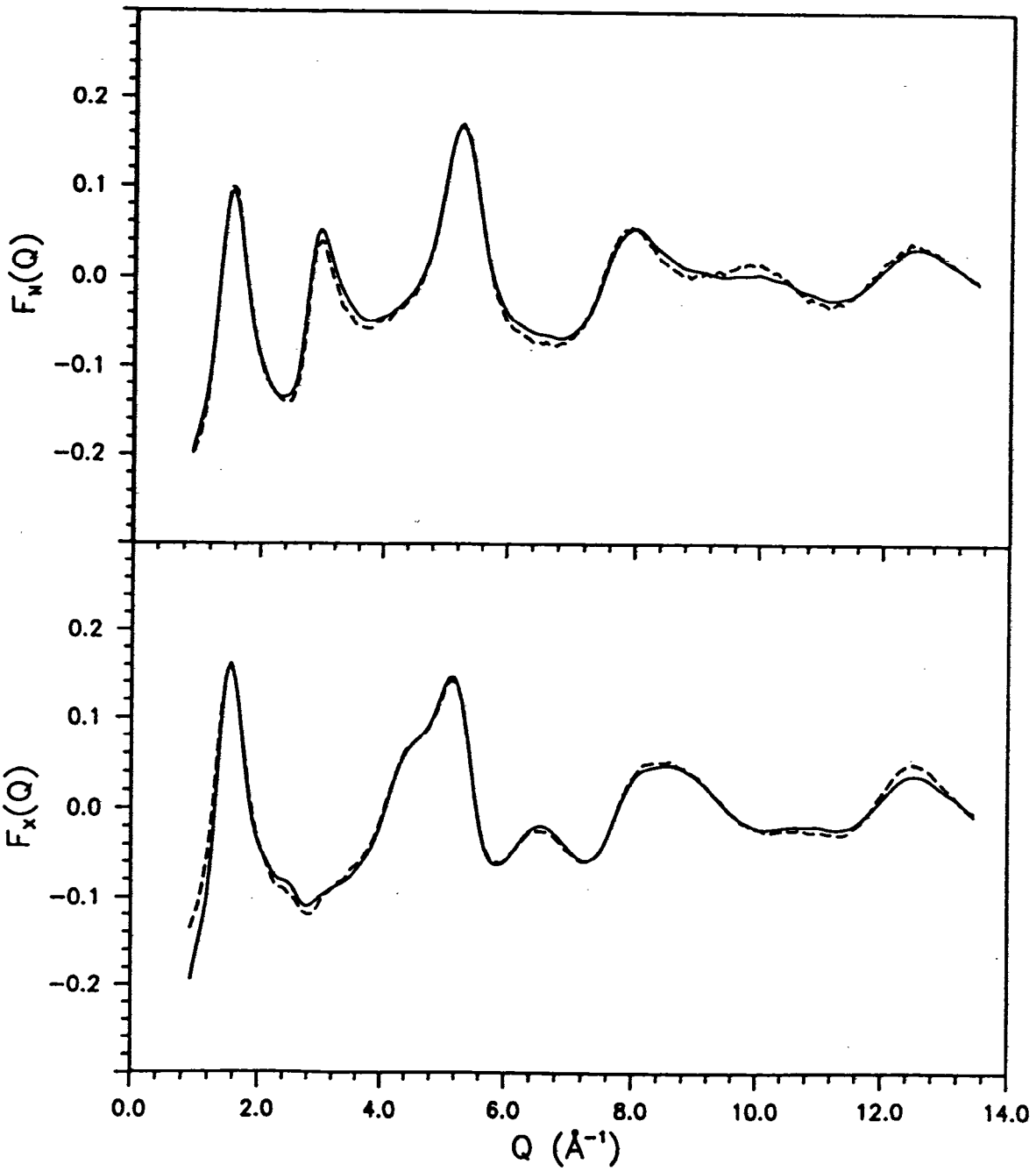

Figure 9. Structure factors for vitreous silica: neutron diffraction (upper graph) and X-ray diffraction (lower graph). Broken line - experiment; solid line - RMC fit.

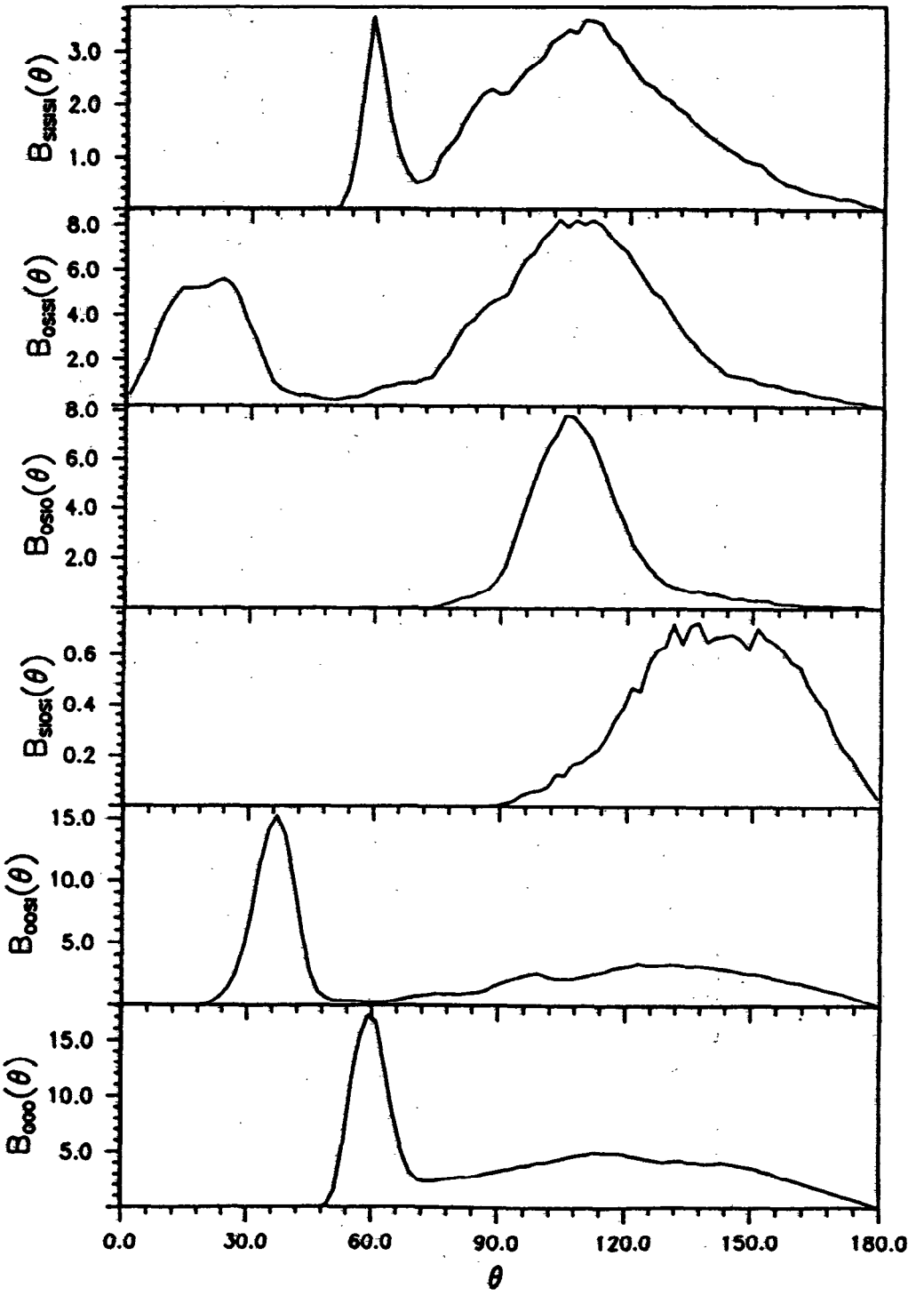

Figure 10 Bond angle distributions for vitreous silica. Maximum bond lengths are defined by the first minima in the appropriate partial radial distribution functions.

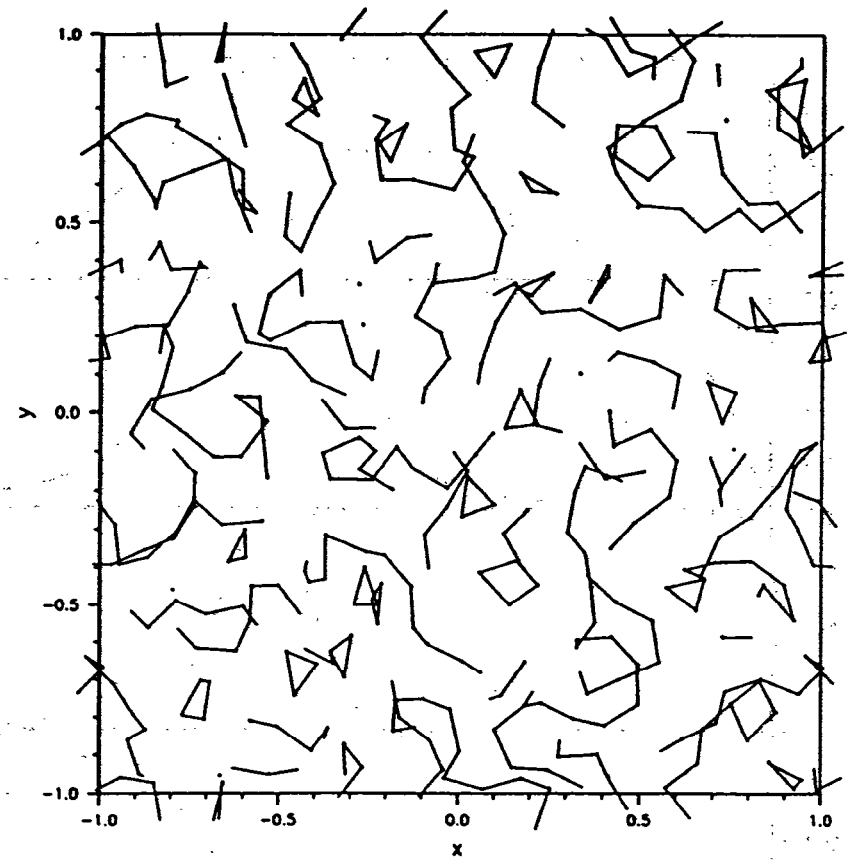

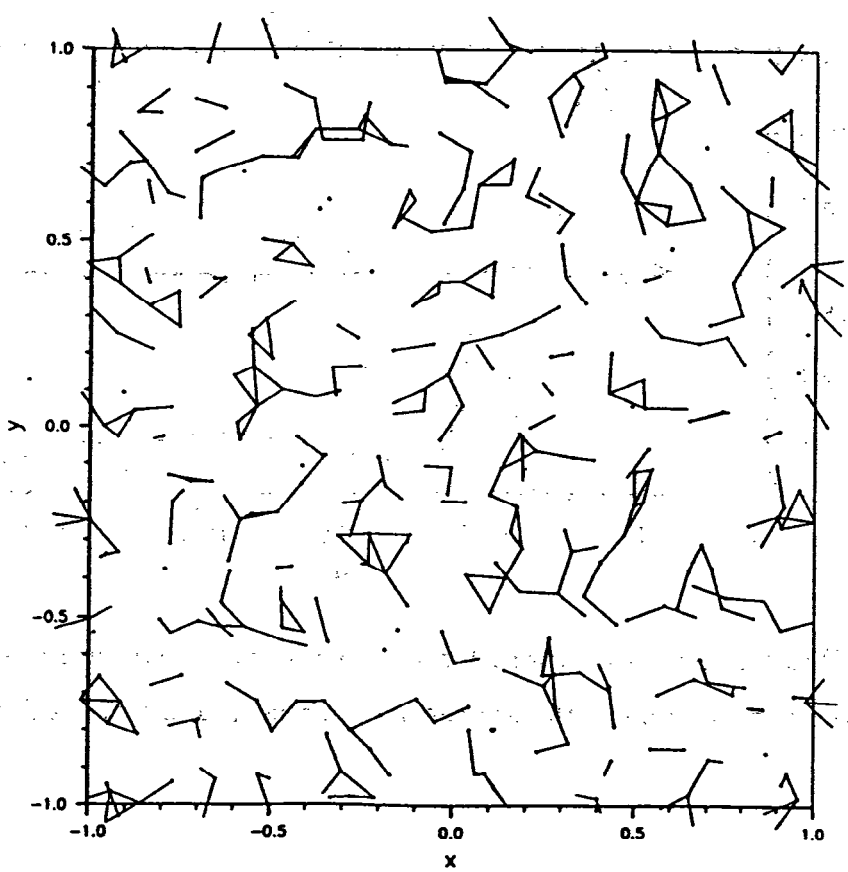

Figure 11 S-S bonds in sections from configurations for liquid sulphur at 423K: high 2-fold coordination (upper graph) and low 2-fold coordination (lower graph).

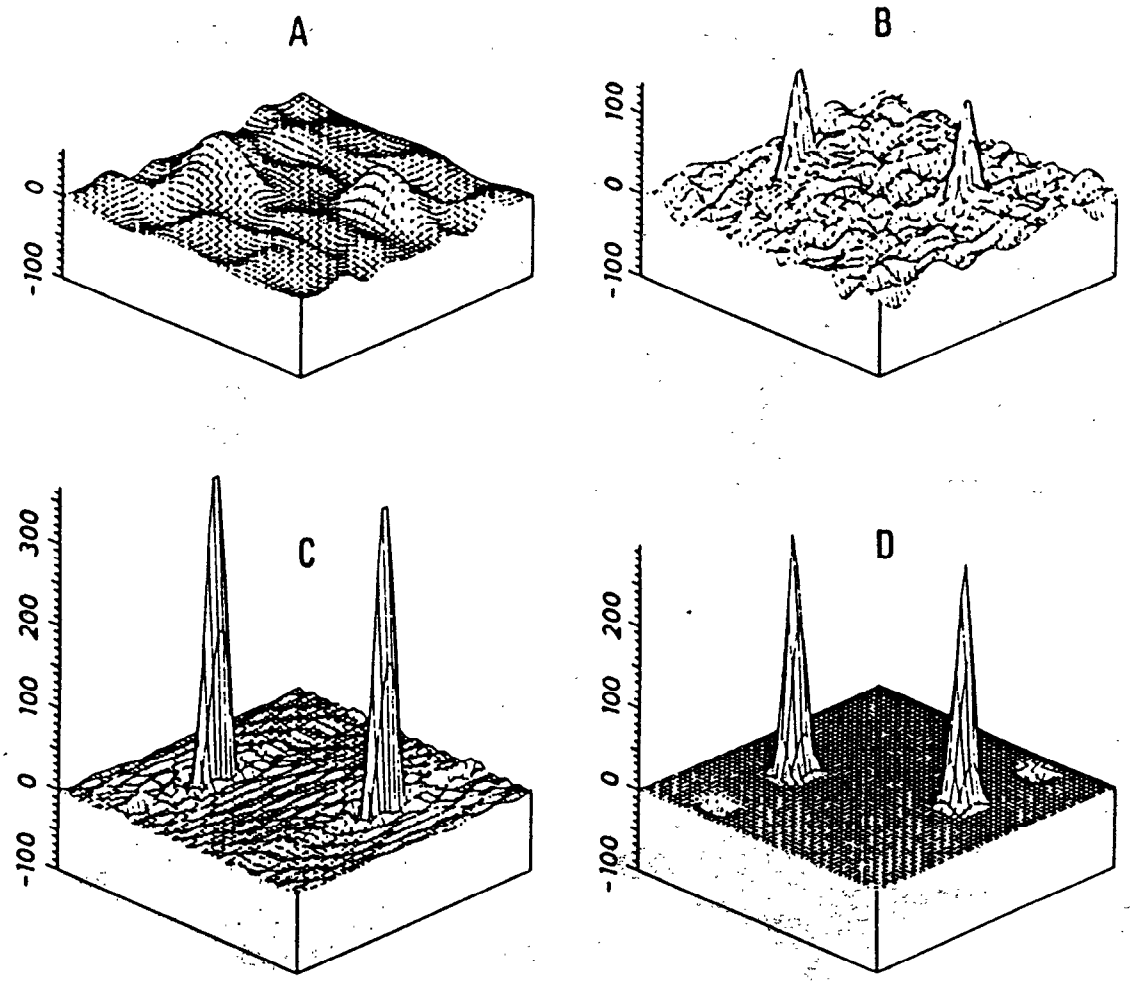

Fig.12 Simulation involving two positive ($+1.25\mu_B$) and two negative ($-0.25\mu_B$) magnetic moments. The unit cell is assumed to be orthorhombic, and the only symmetry operations are the Identity and the Inversion. The projection is taken along the $\vec{a}$ crystallographic axis. The reconstructed magnetisation density is expressed in $\mu_B/\mathring{A}^2$. The size of the image is 50*50 pixels.
Orthographic projections in crystallographic units:
A,B,C : straightforward Inverse Fourier transforms for an increasing number of reflections (23,72, and 262 respectively). Using more Fourier components does not eliminate truncation effects.
D: Maximum Entropy reconstruction using the same 23 reflections as in A. Truncation effects have vanished and the two negative features are now clearly apparent.

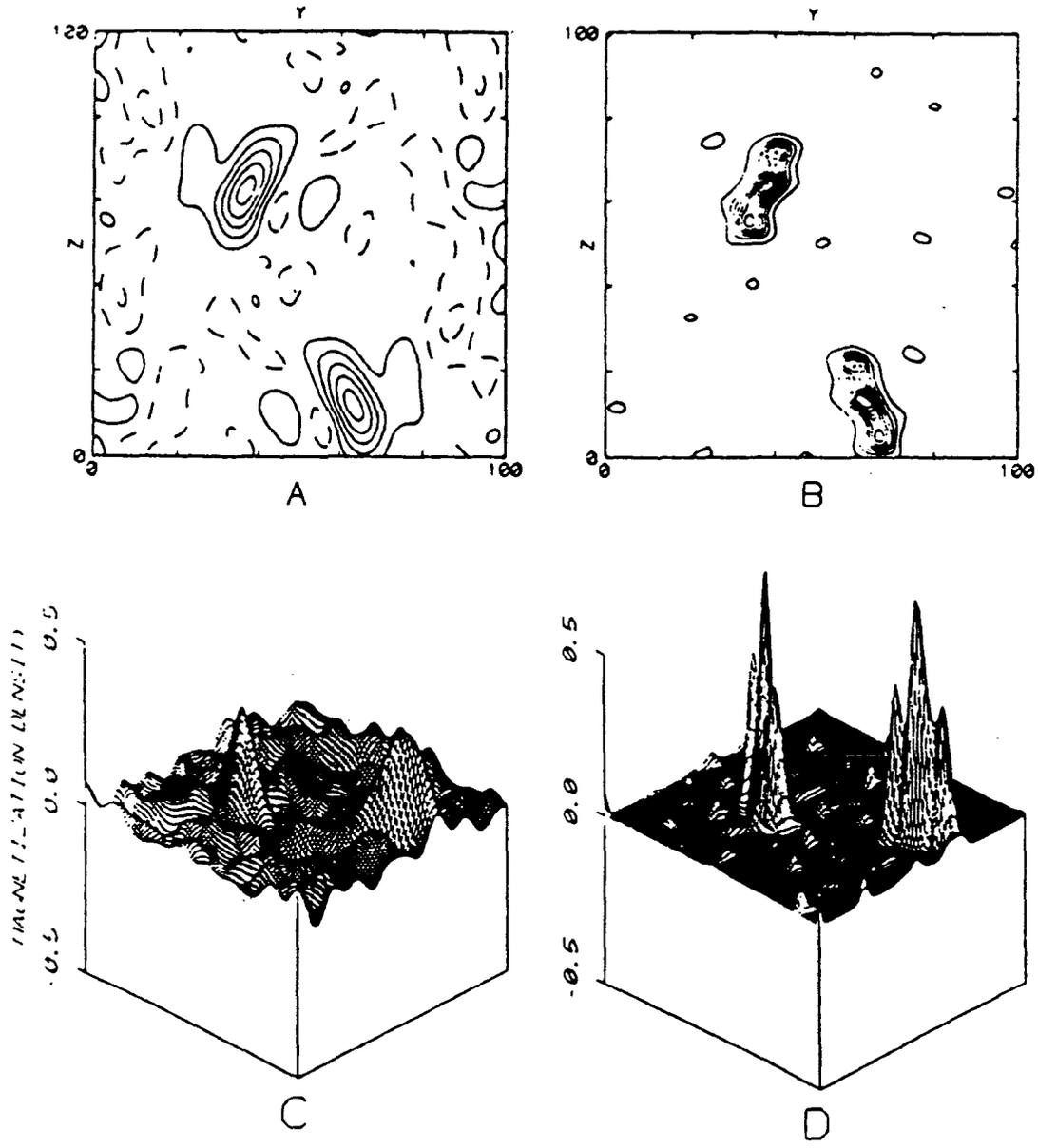

Fig. 13 A real data case: tanol suberate. The magnetisation density is projected along the $\vec{a}$ axis. The data consist of 69 independent Fourier components. The size of reconstructed image is 100*100 pixels.
Above, contour maps. A: Fourier, B: Maximum Entropy. The contour levels are the same in both A and B. The dotted lines refer to negative contours. Levels are $\pm.03, \pm.09, \pm.15, \pm.21 \ldots \mu_B/\mathring{A}^2$. The Maximum Entropy reconstruction clearly resolves the density about the Oxygen and Nitrogen atoms, whereas the Fourier reconstruction does not.
Below, 3-D orthographic projections: C: Fourier, D: Maximum Entropy. The Maximum entropy reconstruction shows that the weight of the p_z orbital for the Oxygen is close to that of the p_z orbital for the Nitrogen. The larger peak results from the overlap of the projections of both orbitals.

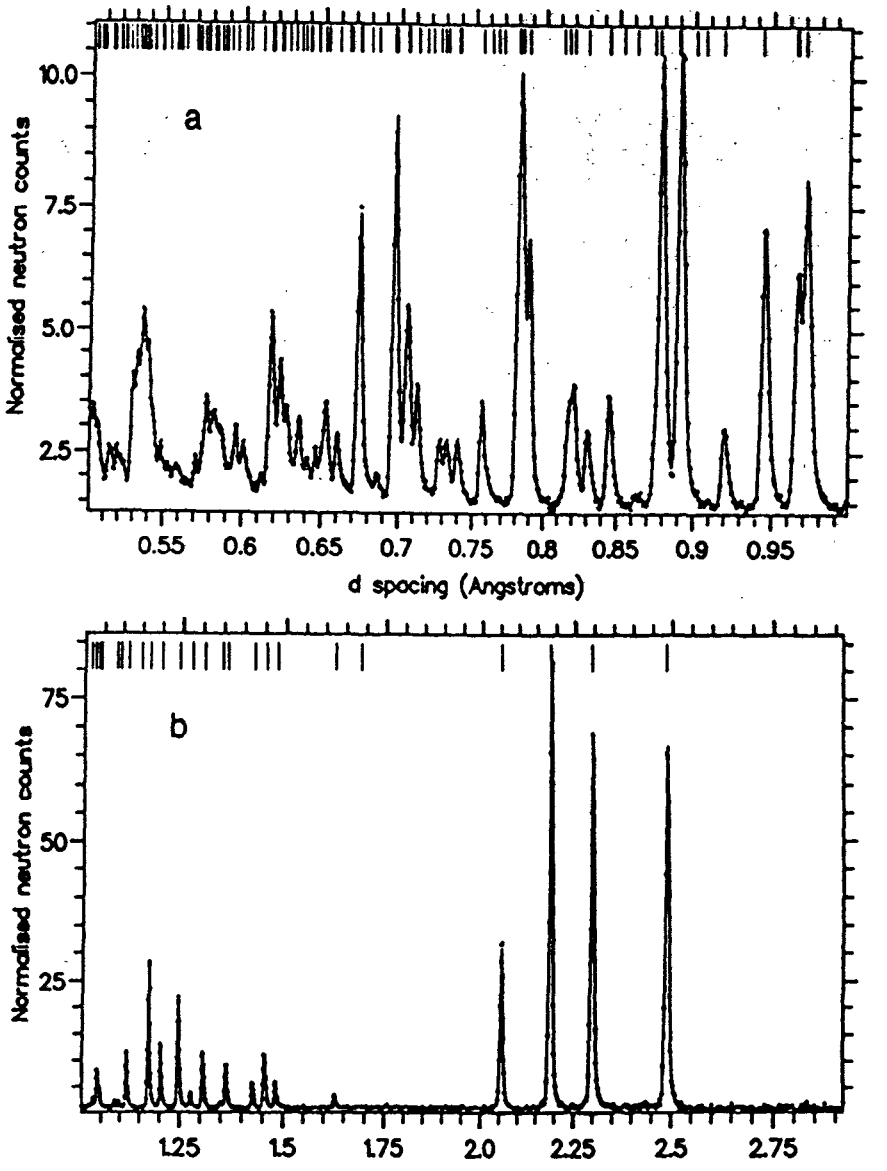

Figure 14

The observed (dots) and calculated (line) profiles for TiO_2 obtained using the POLARIS powder diffractometer at ISIS. The d-spacings range (a) from 0.5Å to 1Å and (b) from 1Å to 2.9Å. The tags mark the positions of Bragg reflections and clearly indicate the severe peak overlap particularly at short d-spacings.

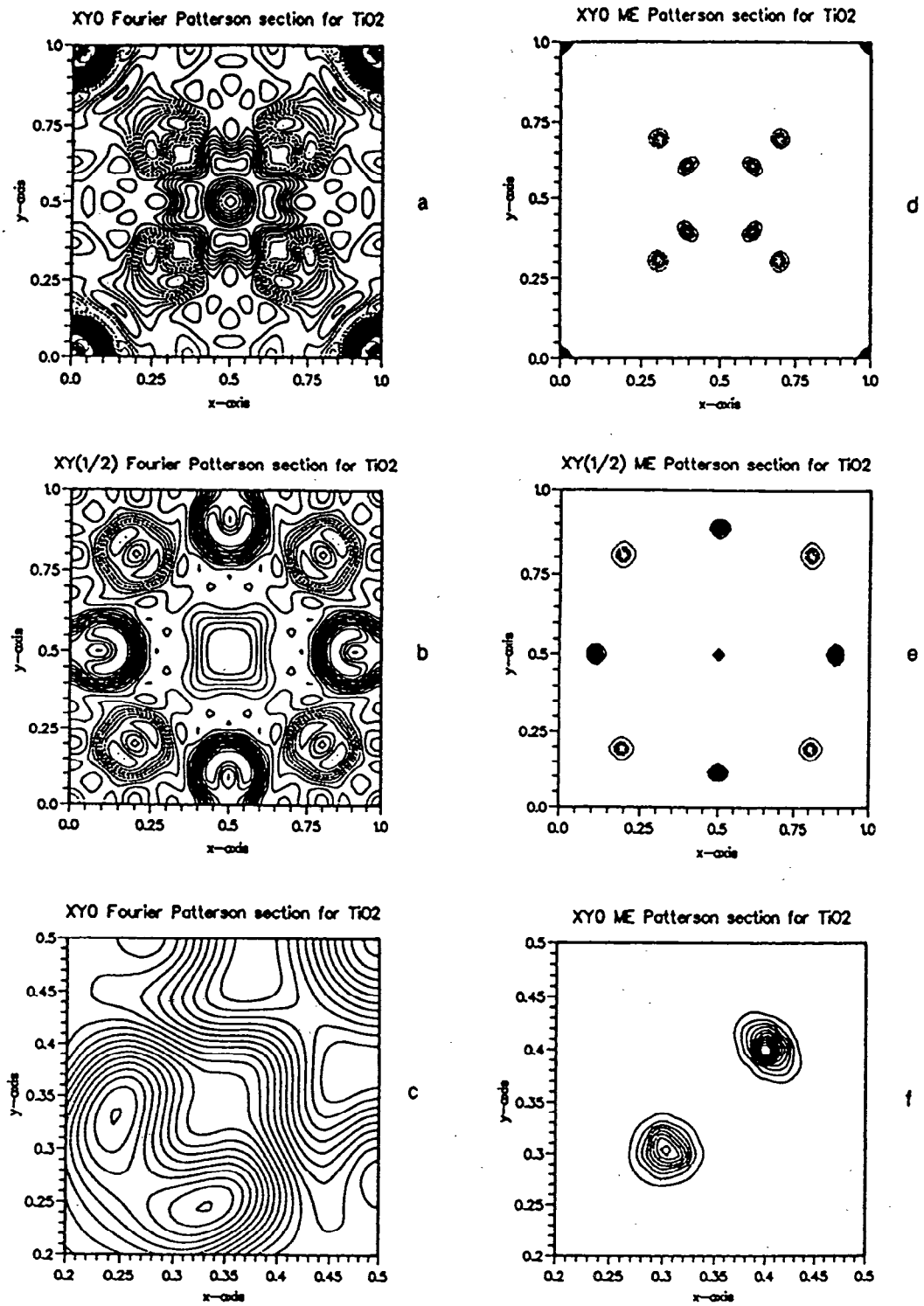

Figure 15

Figures 2a-c: Sections of the Patterson map synthesised by Fourier transformation of the squares of the structure factor magnitudes obtained from the Pawley-type profile refinement of TiO_2 and subsequent averaging of a sphere of diameter 0.5Å. The broad structural features indicate approximate vector positions but are severely distorted by misapportioning of intensities and truncation errors. The first two maps range over the full xy plane at (a) $z=0$ and (b) $z=½$. Figure 2c is a magnification of Figure 2a with $0.2<x<0.5$ and $0.2<y<0.5$. Figures 2d-g: Sections of the Patterson map obtained by maximum entropy reconstruction from the observed clumps of Bragg intensities. The features are extremely sharp and are correctly located at interatomic vector positions. The map ranges in Figures 2d-g correspond to those of Figures 2a-c.

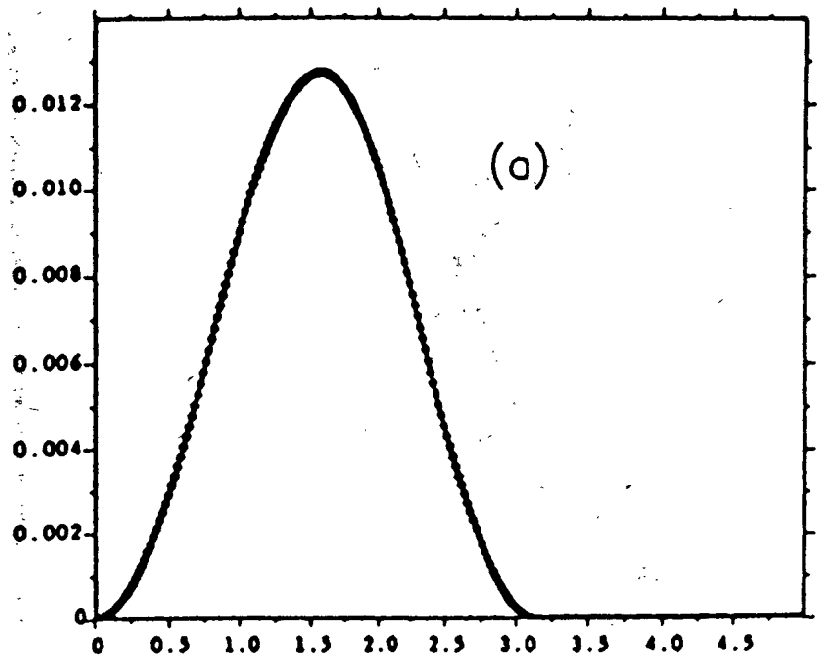
(a)
0.012
0.010
0.008
0.006
0.004
0.002
0
0 0.5 1.0 1.5 2.0 2.5 3.0 3.5 4.0 4.5

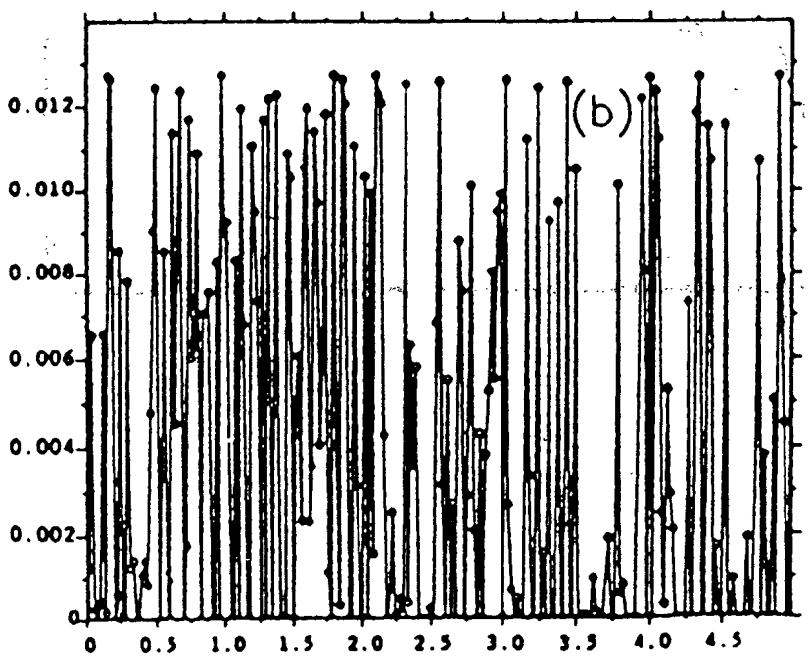
(b)
0.012
0.010
0.008
0.006
0.004
0.002
0
0 0.5 1.0 1.5 2.0 2.5 3.0 3.5 4.0 4.5

Fig 16

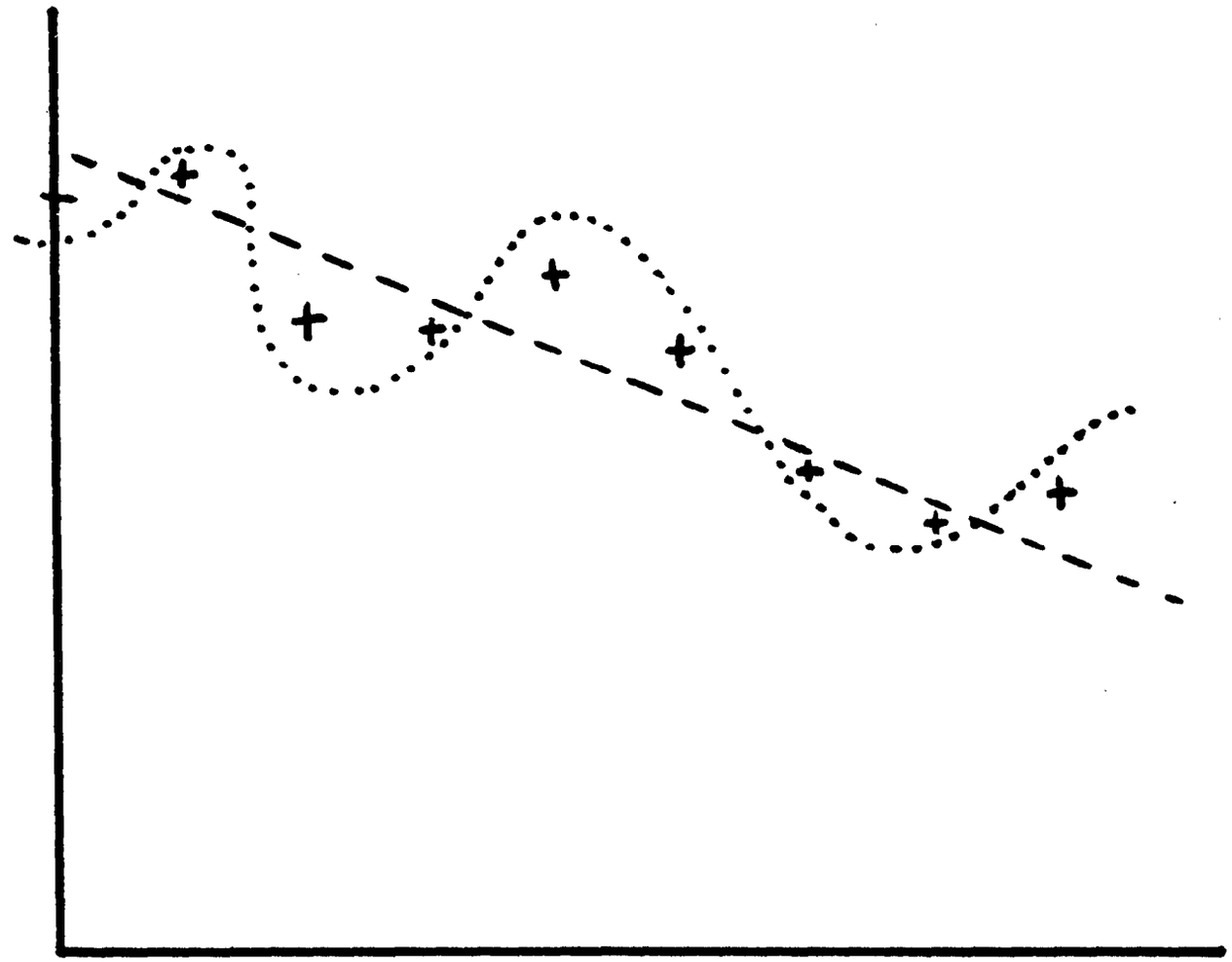

Fig 17

Q(J.B.Hayter): What are the implications of inelastic scattering in SANS experiments performed at pulsed sources? The Rennie-Ghosh experiments indicate that they may be significant, especially at short incident wavelength.

A(M.W.Johnson): Since T.O.F. LOQ experiments record the same Q information at different angles, there is the 'in principle' possibility of disentangling the elastic from the total scattering.

ICANS-XI International Collaboration on Advanced Neutron Sources
KEK, Tsukuba, October 22-26, 1990

The submitted manuscript has been authored by a contractor of the U. S. Government under contract No. W-31-109-ENG-38. Accordingly, the U. S. Government retains a nonexclusive, royalty-free license to publish or reproduce the published form of this contribution, or allow others to do so, for U. S. Government purposes.

RECENT IMPROVEMENTS OF THE PARAMETERIZATION OF BRAGG PEAK PROFILE FUNCTIONS

John M. Carpenter, William C. Dimm[a], and Frank J. Rotella
Intense Pulsed Neutron Source
Argonne National Laboratory
9700 S. Cass Avenue, Argonne, IL 60439

[a]Present Address: Department of Physics, Cornell University, Ithaca, NY

ABSTRACT

The "Jorgensen" profile function conventionally used to describe the shape of observed Bragg peaks in time-of-flight powder neutron diffraction fits individual peaks very well. However, the wavelength or plane spacing variation of the parameters of the components of this function, as they are conventionally represented in Rietveld analysis, is inappropriate for fitting data extending over a wide range of plane spacings, d. We have developed a new representation of the d-dependence of the profile parameters which are generalizations of Pade' approximants, have built-in physically realistic large- and small-d limiting behavior, and provide better fits to parameters derived from individual peak fits than the conventional forms. We report the results of tests of the new parameterization of the profile functions.

I. Introduction

Figure 1 illustrates the Jorgensen profile function[1], which is the sum of truncated rising and falling exponentials normalized to the same value at t=0, convoluted with a Gaussian function. α is the coefficient of the rising exponential, β is the coefficient of the falling exponential, and t_o is the centroid and σ the standard deviation of the Gaussian. All parameters are functions of d, the plane spacing of the reflection presumed to produce the reflection. For detectors at a given scattering angle 2θ, d variation is equivalent to λ variation, since $\lambda = 2d\sin\theta$. We discuss the profile function as a function of time-of-flight, t, the observed variable, with parameters fixed according to the corresponding d (or λ) and θ. Even though the function is of very simple form, experience reveals that it is capable of reproducing the shape of Bragg peaks to quite acceptable accuracy, with only a small systematic deviation near the maximum which is just noticeable in data having better-than-average statistical precision.

The goal of the present work is to develop generally applicable mathematical forms containing wavelength (d spacing) independent parameters specific to instrument and scattering angle, which represent the wavelength (d spacing) dependence of the parameters of the Jorgensen profile function.

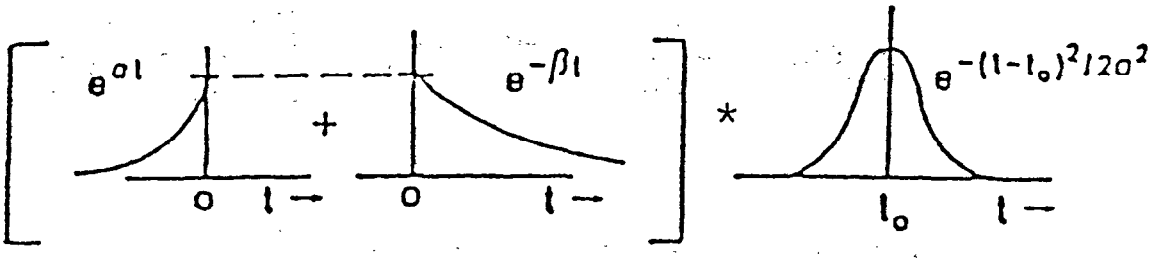

Figure 1. The Jorgensen profile function.

II. Pade' Approximants

Pade' approximants[2] are ratios of polynomials

$$f(x) = x^p \frac{\sum_{i=0}^{i=N_N} a_i x^i}{\sum_{i=0}^{i=N_D} b_i x^i} = x^p \frac{P_N(x)}{P_D(x)} \qquad (1)$$

where a_0 , b_0 , a_{N_N} and b_{N_D} are all different from zero.

The leading terms of a Taylor expansion of (1) are related to the leading terms of a Taylor expansion of f(x) in a simple way.

$$f(x) = \sum_{n=0}^{\infty} f_n x^n \qquad (2)$$

$$a_n = \sum_{k=0}^{n+p} b_{n+p-k} f_k \ , \quad (0 \leq n N_N) . \qquad (3)$$

Similarly, if in a Taylor expansion in y = 1/x,

$$g(y) = \sum_{n=0}^{\infty} g_n y^n \qquad (4)$$

<u>the</u> <u>same</u> polynomials can represent g(y)

$$g(y) = y^q \frac{P_N(1/y)}{P_D(1/y)} \qquad (5)$$

if

$$a_n = \sum_{k=0}^{q+N_D-n} b_{n-q+k} g_k \ , \quad (0 \leq n \leq N_N) . \qquad (6)$$

Equations (3) and (6) can be used to place conditions on the limiting behavior of the function.

The lowest order terms in the Taylor expansions for large and small x are

$$\lim_{x\to\infty} f(x) = \frac{a_{N_N}}{b_{N_D}} x^{(p+N_N-N_D)} \left[1 + \left(\frac{a_{N_N-1}}{a_{N_N}} - \frac{b_{N_D-1}}{b_{N_D}}\right)\frac{1}{x}\right] \tag{7}$$

and

$$\lim_{x\to 0} f(x) = \frac{a_0}{b_0} x^p \left[1 + \left(\frac{a_1}{a_0} - \frac{b_1}{b_0}\right) x\right]. \tag{8}$$

These properties of Pade' approximants, namely the natural way in which limiting behavior required by physical constraints can be built in, led us to choose them for the present purposes. To limit the number of parameters in the functions, we have chosen particular forms of Pade' approximants, namely ones in which most of the disposable a_i's and b_i's are equal to zero. Further, we allow N_N and N_D to have non-integer values, so that in this sense our functions are not properly called Pade' approximants. A necessary constraint on functions in the present context is that the denominator polynomial may have no zeros for real, positive d. When positive-definite quantities appear, we represent them as squares of fitting parameters, respecting the fact that our computer codes operate in the field of real numbers, while the nonlinear least squares routines used for fitting require smooth behavior of the functions with respect to the fitted parameters.

III. Diamond Powder Calibrant

To provide well resolved peaks at the smallest possible wavelengths (d spacings), we use a diamond powder sample with grain size of about 150 μm. (The diamond lattice constant is about 2/3 that of the frequently used silicon powder calibrant.) The grains are purposely large to avoid grain size broadening effects in the measurements, but their large size leads to significant primary extinction effects. The extinction affects the peak intensities, but does not alter the shapes of individual Bragg peaks.

IV. The Coefficient of the Falling Exponential, β

The principal motivation for including a falling exponential in the profile function is to represent the decay of the fundamental eigenfunction in the flux distribution in the moderator. Since the fundamental eigenfunction dominates the energy distribution at long wavelengths, β is expected to approach a constant in the limit of long wavelengths. Experience shows that β approaches the long wavelength limit from shorter wavelengths as (constant)/λ^q, where $q \approx 4$. On these grounds the present Rietveld codes parameterize the d-variation of β in the form (9). This form cannot describe

$$\beta = \beta_o + \beta_1/d^4. \tag{9}$$

the behavior of $\beta(d)$ for small d, where (9) diverges non-physically.
Typically, the profile parameters exhibit several inflection points, because of the complicated wavelength dependence of the moderator pulse shape, so a more complicated form is required.
Noting that the decaying exponential must describe the short wavelength behavior of the moderator pulse, which is of the form

$$\phi(\lambda,t) \propto t^2 e^{-a(\lambda)t} \tag{10}$$

where at short wavelengths, $a(\lambda) \rightarrow (\text{constant})/\lambda$, β must be inversely proportional to λ for short wavelengths,

$$\lim_{\lambda \to 0} \beta(\lambda) = (\text{constant})/\lambda. \tag{11}$$

To the extent that β describes geometric effects, β must also tend to the small-λ limit as $1/\lambda$ $(1/d)$. Thus, the form representing β must be modified from (9) at short wavelengths (small d) in some smooth way. We propose the form

$$\beta(d) = (\beta_o/d)\frac{1 + bd^n}{1 + K^2 d^{n-1}} \tag{12}$$

which has the limiting behavior

$$\lim_{d \to 0} \beta(d) = \beta_o/d \tag{13}$$

and (not quite correctly, but simply)

$$\lim_{d \to \infty} \beta(d) = \beta_o (b/K^2)(1 + 1/bd^n - 1/K^2 d^{n-1}) \tag{14}$$

Figure 2 shows the results of fitting (12) to data from the 150° bank of detectors in the SEPD[1], using the diamond powder sample. The experimental values for β were derived from separate fits to the observed, resolvable peaks.

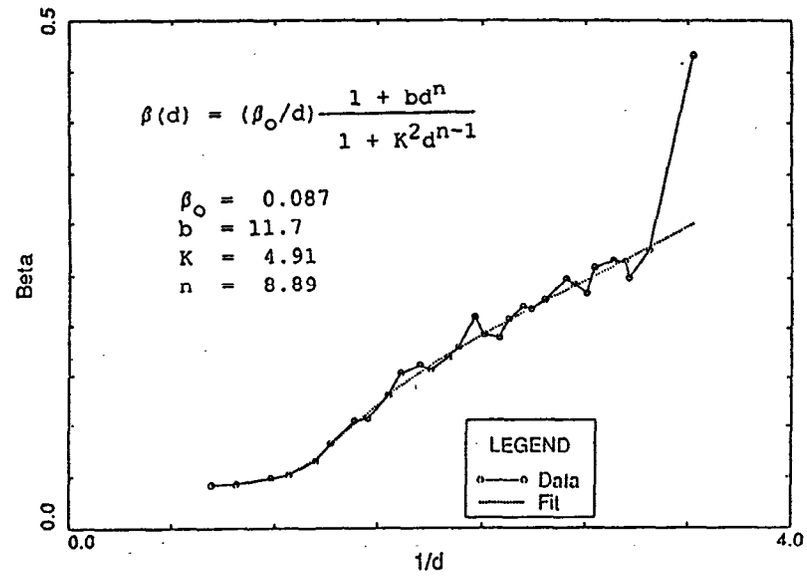

Figure 2. Data and fitted curve, equation (12) for the β parameter describing Bragg peaks measured at 2θ = 150° in the SEPD. The unit of β is μsec^{-1}; the unit of d is Å.

V. The Gaussian Width Parameter

The width of the Gaussian function $\sigma(d)$, must describe the composite of many geometric effects, including the many contributions to the angular distribution of diffracted neutrons, and also must describe the shape of the moderator pulse. Certain sample scattering effects also appear in the Gaussian width function. All these effects add as squares in their contributions to σ^2; this justifies their description as a Gaussian function, according to the central limit theorem. The geometric contributions are strictly proportional to d (or λ). Moderator effects have very complex wavelength dependence, but in the limit of small wavelength, these must contribute to σ as a term proportional to wavelength. It is found empirically that σ behaves as a + bd at long wavelengths, where the constant b is not the same as the slope of σ at small wavelengths.

We have chosen to represent $\sigma(d)$ as

$$\sigma(d) = d \frac{\sigma_o^2 + \sigma_1 d^{n-1} + \sigma_2^2 d^n}{d^n + K^2} \tag{15}$$

Figure 3 shows the resulting fit to data from the 150° bank of detectors in the SEPD, using the diamond powder sample.

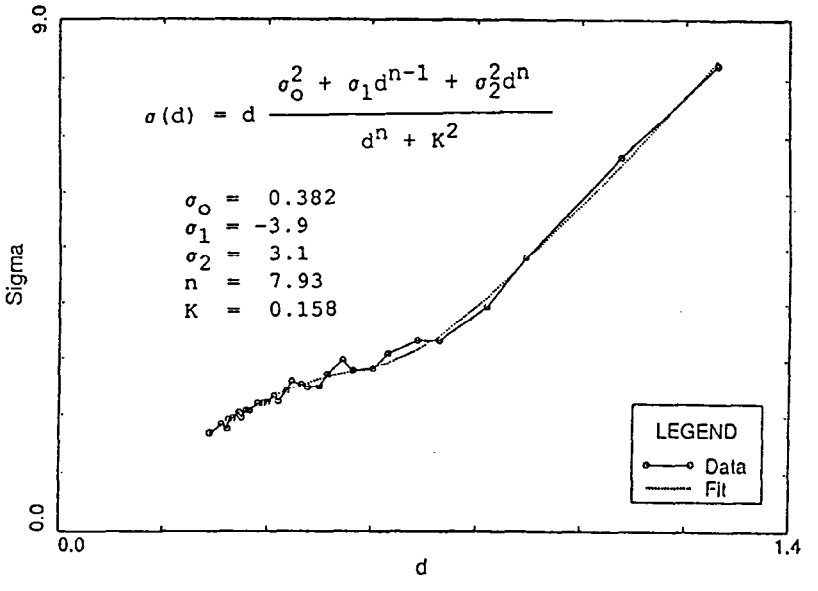

Figure 3. Data and fitted curve, equation (15), for the σ parameter describing Bragg peaks measured at 2θ = 150° in SEPD. The unit of σ is μsec; the unit of d is Å.

VI. The Gaussian Center Time, t_o

The Gaussian center time, t_o, is dominated by the contribution from the total flight path which is proportional to d (or λ), and contains a constant contribution that can be identified with the electronic time delay in the time origin pulse. t_o is not the mean time associated with the Bragg peak, since the rising and falling exponential functions do not in general represent a symmetric function. Furthermore, t_o depends on the shape of the moderator pulse in a complex way. We have chosen to represent $t_o(d)$ as

$$t_o(d) = t_1 + d \frac{t_2^2 + t_3 d^{n-1} + t_4^2 d^n}{d^n + K^2}. \quad (16)$$

Figure 4 shows the results of fitting data from the 150° bank of detectors in the SEPD, using the diamond powder sample.

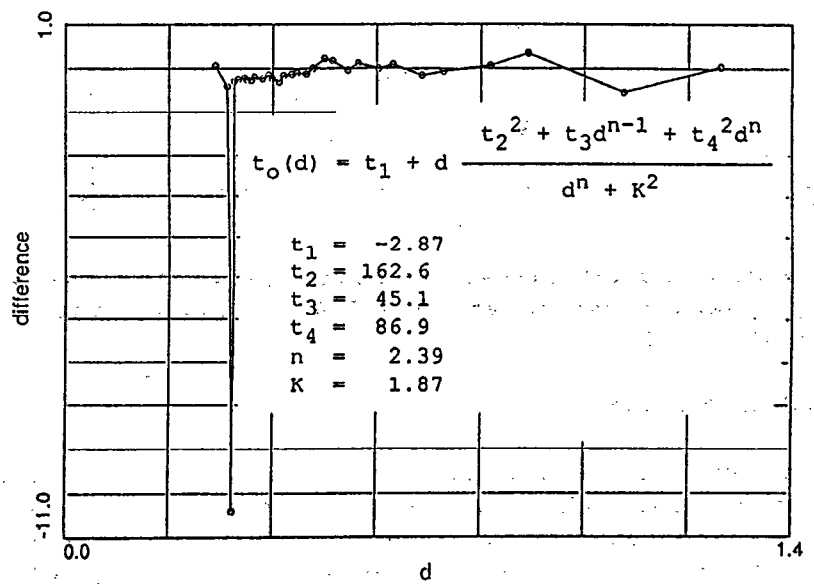

Figure 4. The difference between the data and the fitted curve, equation(16) for the t_o parameter describing Bragg peaks measured at 2θ = 150° in SEPD. The unit of t_o is μsec; the unit of d is Å.

VII. The Coefficient of the Rising Exponential, α

The coefficient of the rising exponential, $\alpha(d)$, represents mostly the effect of detector height (at least at backscattering angles). As such, it describes strictly a geometric effect, and is expected to be simply inversely proportional to λ (or d). Although α is a necessary parameter, the profile functions are not highly sensitive to the value of α, therefore data tend to be poor, but the need for accurate values is correspondingly small. We choose to represent

$$\alpha(d) = \alpha_o/d. \quad (17)$$

Figure 5 shows the results of fitting 150° SEPD data to diamond powder data, using equation (17).

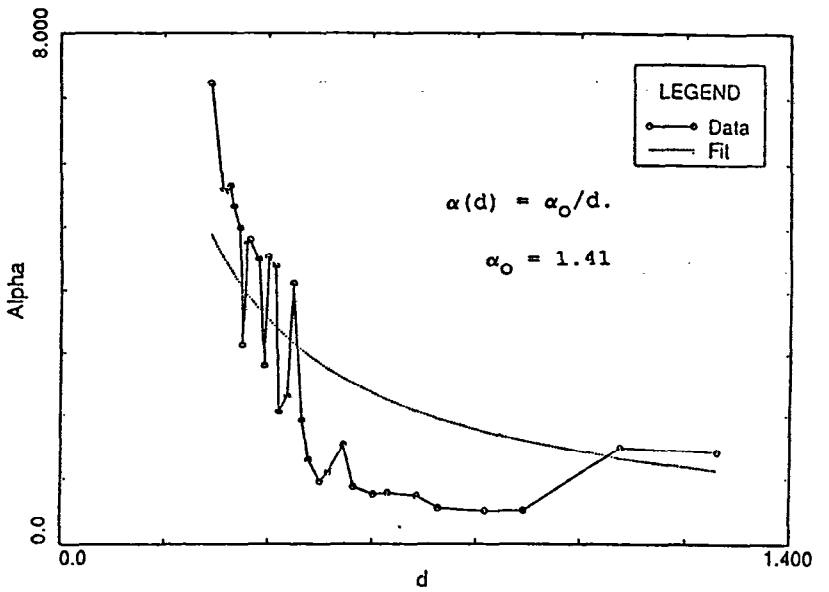

Figure 5. Data and fitted curve, equation (17), for the α parameter describing Bragg peaks measured at 2θ = 150° in SEPD. The unit of α is μsec^{-1}; the unit of d is Å.

VIII. Status and Conclusions

We have conceived and tested a new set of functions having the form of Pade' approximants, to describe the wavelength (d-spacing) variation of the parameters of the Jorgensen profile function. Tests on parameters derived from individual peak fits to data taken from diamond powder at large scattering angles indicate that functions of this form are capable of describing the complicated variation of these parameters, with good accuracy and without requiring an excessively large number of wavelength-independent parameters. This work is really not complete, inasmuch as we have not fully exploited the capabilities of the Pade' approximant forms. Neither have we correctly imposed all the limiting behavior of the profile parameters in the fitting forms, nor been able to recognize which wavelength-independent parameters are related.

Testing of the new functions using the IPNS Rietveld analysis software has begun, addressing questions of refinability, independence of parameters, and the accuracy of Rietveld structure refinement.

We have been able to draw some preliminary conclusions from Rietveld analysis of the 150° SEPD data from the diamond sample in the range $0.2 \leq d \leq 1.3$ Å and from our standard silicon sample in the range $0.3 \leq d \leq 3.3$ Å. The profile fit improves significantly when $\beta(d)$ from the Padé approximant formalism in (12) replaces that described in (9) - e.g., the weighted profile R-factor (R_{wP})[1] reduced from 11.73% to 10.67% in the diamond data analysis. However, virtually no improvement is observed in the fit when the description

for the Gaussian width parameter $\sigma(d)$ in (15) replaces that which is being used at present. We emphasize that these results are preliminary, and in assessing the effects of these functional forms on the accuracy and precision of structural parameters derived from Rietveld analysis, more work on a wider range of standard samples will be required.

Acknowledgements

We express our thanks to J. W. Richardson, R. L. Hitterman, J. D. Jorgensen and K. J. Volin for data collection on GPPD & SEPD. This work was performed under the auspices of the U.S. Department of Energy, Division of Materials Sciences, Office of Basic Energy Sciences, under Contract W-31-109-ENG-38.

References

1. J. D. Jorgensen, J. Faber Jr., J.M. Carpenter, R. K. Crawford, J. R. Haumann, R. L. Hitterman, R. Kleb, G. E. Ostrowski,, F. J. Rotella and T. G. Worlton, J. Appl. Cryst. 22 (1989), 321-333.

2. See for example D. C. Hanscomb, "Methods of Numerical Approximation", Pergamon Press Ltd., Oxford, 1966, p. 99-130.
Messages for figures

3. F. J. Rotella, "User Manual for Rietveld Analysis of Time-of-Flight Neutron Powder Diffraction Data at IPNS", (1988). Argonne National Laboratory, Argonne, IL, USA

ICANS-XI International Collaboration on Advanced Neutron Sources
KEK, Tsukuba, October 22-26, 1990

CORRECTING BEAM MONITOR & DIFFRACTION DATA FOR CHOPPED DELAYED NEUTRON BACKGROUNDS

John M. Carpenter
Intense Pulsed Neutron Source, Argonne National Laboratory
9700 South Cass Avenue, Argonne, IL 60439

David F. R. Mildner
Center for Analytical Chemistry
National Institute of Standards and Technology
Gaithersburg, MD 20899

James W. Richardson, Jr.
and
William C. Dimm[a]
Intense Pulsed Neutron Source, Argonne National Laboratory
9700 South Cass Avenue, Argonne, IL 60439
[a]Present address: Department of Physics, Cornell University, Ithaca, NY

ABSTRACT

Delayed neutron choppers in pulsed source neutron beams serve to reduce the background caused by delayed neutrons in pulsed source instruments. We analyze the effect of a drum chopper placed in an incident pulsed beam which contains delayed neutrons and compute its influence on the detector counting rate. Expressions are found for the time and wavelength dependence of the counting rates for both prompt and delayed neutrons, in both monitor and scattered neutron detectors. On the basis of these results, we suggest an exact, random-phasing method for determining the delayed neutron background for use in measuring the delayed neutron counting rate, and propose a rapidly convergent iterative scheme for computing the correction from normally measured data. We report measurements which confirm the analysis.

I. INTRODUCTION

The ^{235}U enriched booster target provides enhanced neutron fluxes for the IPNS spectrometers[1]. Accompanying the higher pulse intensity is a relatively greater background of delayed neutrons. Methods are needed for describing, assessing and suppressing these backgrounds and applying corrections if necessary.

In order to reduce the delayed neutron backgrounds, drum choppers have been introduced in the incident beam for both SEPD (total flight path length 15.5 meters) and GPPD (21.5 meters)[2]. Figure 1 illustrates the arrangement. These choppers are hollow aluminum drums of 40 cm diameter spinning on a vertical axis, covered with epoxy-boron carbide of 1 cm thickness and 10.5 cm height. They have

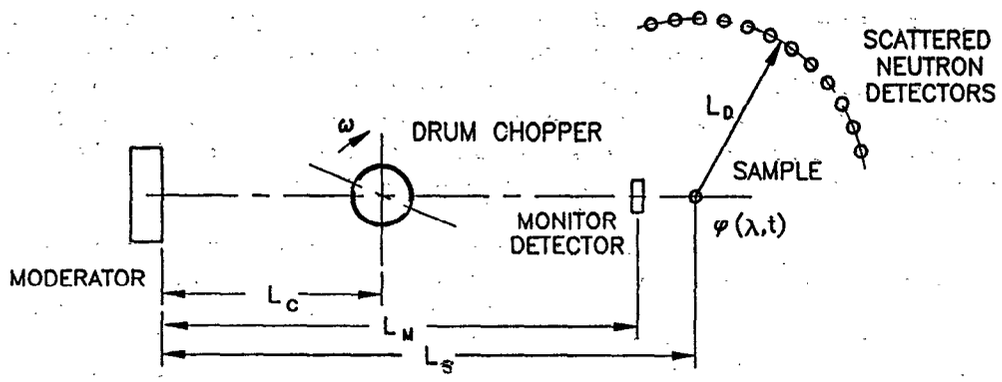

Figure 1. A schematic diagram of a source (moderator) and a drum chopper a distance L_C downstream. The source emits delayed neutrons at a steady rate and also prompt neutrons in periodic, short pulses. $\phi(d, t)$, the flux per unit wavelength at time t, is to be determined at a point L away from the source.

symmetrically placed openings (subtending opening angles measured from the center of 81.8° in SEPD, and 60.7° in GPPD) to allow the passage of the beam. They normally rotate at 15 Hz, driven by hysteresis synchronous motors synchronized at half the frequency of the pulsed source itself and opening twice per revolution. Both choppers are located L_C=6.01 meters from the source (moderator). Appropriately phased, the drum choppers do not significantly affect the transmission of the pulsed beam in the desired wavelength range. Figure 2a is a diagram of the time of arrival of neutrons of different wavelengths vs. distance. Figure 2b shows the corresponding scattered neutron detector counting rate.

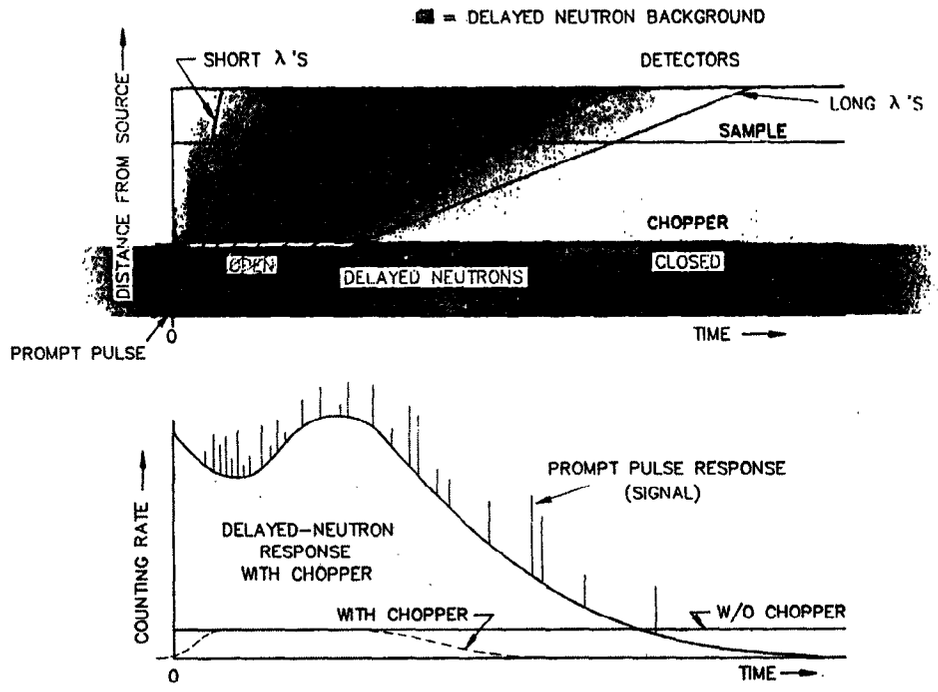

Figure 2a. Time vs. distance diagram ("neutron time schedule") showing the arrival of neutrons from the prompt pulse and of delayed neutrons. In the

absence of the delayed neutron chopper, delayed neutrons arrive at a constant rate. The chopper, shown as either closed (black bar) or open (white), modulates the delayed neutrons, and is phased to reduce the delayed neutron counting rate in the time range when the prompt neutron counting rate is low. The density of shading represents the intensity of delayed neutrons. b. The counting rate distribution corresponding to 2a., showing the prompt response with Bragg peaks, and the delayed neutron counting rate with and without the chopper.

The transmission characteristics and pulse shape of the drum chopper depend on the neutron wavelength, the frequency of rotation of the chopper, the diameter of the chopper, the width of the chopper slot and the width of the incident beam. We define a transmission probability for the chopper $P_c(\lambda,t;\alpha_o)$, that is, the probability that a neutron of wavelength λ which crosses the chopper axis at time t is transmitted through the chopper, where α_o is the phase angle of the chopper at the time of origin of the pulsed beam. In reference (3) we provide full details of the calculation of this probability. Figures 3 and 4 illustrate the transmission probability $P_c(\lambda,t;\alpha_o)=P_c(\lambda,t-\alpha_o/\omega;0)$ for the SEPD and GPPD choppers, respectively.

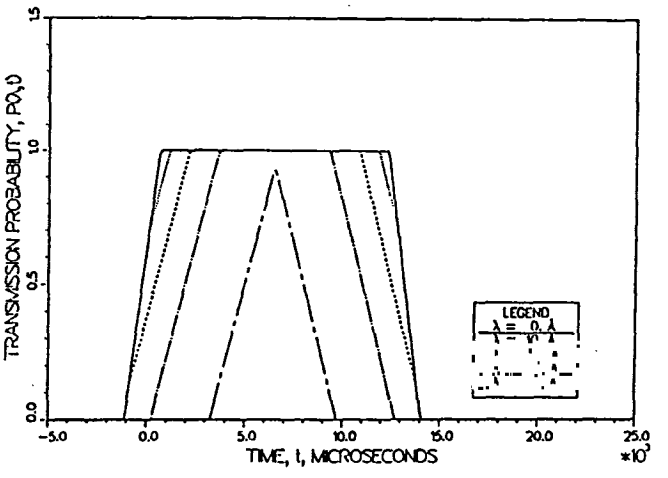

Figure 3. The transmission probability $P_c(\lambda,t;\alpha_o)$ for the SEPD delayed neutron chopper. The nominal opening time $t_o = \alpha_o/\omega$ = 6500 μsec.

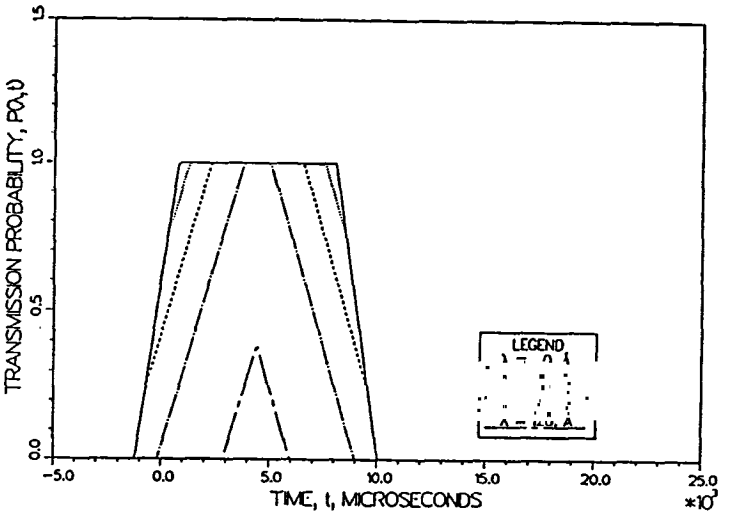

Figure 4. The transmission probability $P_c(\lambda,t;\alpha_o)$ for the GPPD delayed neutron chopper. The nominal opening time $t_o = \alpha_o/\omega$ = 4400 μsec.

In this paper, we derive expressions for the counting rates in both the monitor and the scattered neutron detectors for both the prompt pulse and the delayed neutrons in terms of the chopper transmission probability function. We show that a random phase average counting rate, measured by running the chopper asynchronously with the pulsed source, is directly related to the delayed neutron counting rate. We introduce a rapidly convergent iterative method for calculating the delayed neutron correction from normally measured data. We report measurements of the delayed neutron background taken on two IPNS diffractometers with an incoherently scattering sample, illustrating the random phase operation and the iterative correction calculation.

II. DETECTOR COUNTING RATE

Consider the neutron flux at a distance L from the moderator in a generalized diffraction instrument on a pulsed source, as represented in Figure 1. The flux per unit wavelength at a point a distance L from the moderator and at a time t is given by

$$\phi(\lambda,t)=(1/L^2)\iint dt'dt''i(\lambda,t')P_c(\lambda,t'';\alpha_o)\delta(t-t'-L/v)\delta(t''-t'-L_c/v),$$

$$= (1/L^2)\ i(\lambda,t-L/v)P_c(\lambda,t-(L-L_c)/v;\alpha_o) \tag{1}$$

where $i(\lambda,t')$ is the beam current leaving the moderator per unit wavelength at time t' after one source pulse. The δ-functions relate the times, distances and neutron speeds at the measurement point (t, L and v) and at the chopper (t'', L_c and v) relative to the moderator (t', 0, v). Throughout, $\lambda=(h/m)/v$; $h/m=3955.41$ Å-m/sec. The beam current is composed of a prompt pulse at the time $t'=0$ from the moderator, and a delayed fraction ϵ of neutrons which is assumed to be constant in time and is a known, intrinsic parameter of the source. It is reasonable to assume that the spectral distribution of the delayed neutrons is identical with that of the prompt neutrons. Thus $i(\lambda,t')$ is related to the time-averaged beam current $\bar{I}(\lambda)$ per unit wavelength per unit time by

$$i(\lambda,t') = \bar{I}(\lambda)[(1-\epsilon)\delta(t')/f+\epsilon], \tag{2}$$

where f is the source pulsing frequency.

The counting rate at time t in a monitor detector in the beam is given by

$$C_M(t) = \int d\lambda\phi(\lambda,t)A_M\eta_M(\lambda), \tag{3}$$

where $\phi(\lambda,t)$ is the neutron flux at the monitor detector at a distance L_M from the moderator. A_M is the area of the beam at the monitor and $\eta_M(\lambda)$ is the monitor efficiency, assumed to be time-independent. The counting rate at time t in a neutron detector at a scattering angle θ in a diffraction measurement is similarly

$$C_D(t) = \iint d\lambda du\phi(\lambda,u)\delta(t-u-L_D/v)Nd\sigma/d\Omega(\lambda,\theta)\Delta\Omega_D\eta_D(\lambda), \tag{4}$$

where $\phi(\lambda,u)$ is the neutron flux per unit wavelength at the sample, at a distance L_S from the moderator, at time u. $N\ d\sigma/d\Omega(\lambda,\theta)$ the sample (assumed elastic) scattering cross section. L_D is the distance from the sample to the detector, $\Delta\Omega_D$ is the solid angle subtended by the detector and $\eta_D(\lambda)$ is the detector efficiency.

For the present purposes, we represent the counting rates in both the monitor and the scattered neutron detectors in one generalized expression for the counting rate, which together with (1) and (2) gives results identical in form, which is

$$C(t) = \int d\lambda F(\lambda)[(1-\epsilon)\delta(t-d/v)/f + \epsilon]P_c(\lambda, t-(d-L_c)/v;\ \alpha_o), \tag{5}$$

where

$$F(\lambda) = \begin{cases} \bar{I}(\lambda)A_M\eta_M(\lambda)/L_M^2 & \text{for the monitor measurement} \\ \bar{I}(\lambda)N\ d\sigma/d\Omega(\lambda,\theta)\Delta\Omega_D\eta_D(\lambda)/L_S^2 & \text{for the scattering measurement,} \end{cases} \tag{6}$$

and d is the distance from moderator to monitor (L_M) or detector ($L_S + L_D$) for each measurement. The first term in (5) is the prompt pulse response, the second term is the delayed neutron background, which is a function of the time on account of the presence of the drum chopper, and depends on $\partial\sigma/\partial\Omega(\lambda,\theta)$.

The prompt pulse response is

$$C_p(t) = (1-\epsilon)/f\int d\lambda F(\lambda)\delta(t-d/v)P_c(\lambda, t-(d-L_c)/v-\alpha_o/\omega; 0),$$

$$= [(1-\epsilon)/f]\ (h/md)F(\lambda_t)P_c(\lambda_t,\ L_c t/d-\alpha_o/\omega; 0) \tag{7}$$

where $\lambda_t = (h/m)\ t/d$, and the delayed neutron response is

$$C_d(t) = \epsilon\int d\lambda F(\lambda)P_c(\lambda, t-(d-L_c)/v-\alpha_o/\omega; 0). \tag{8}$$

Crawford [4] has analyzed this same problem using Monte Carlo techniques. The present analytical treatment is appropriate for use in correcting data; the Monte Carlo simulation provides greater insight into "grayness" effects.

III. RANDOM PHASE METHOD FOR DETERMINING DELAYED NEUTRON BACKGROUND

The method proposed here for measuring the delayed neutron response $C_d(t)$ rests upon using the prompt neutrons as a continuous source equivalent to the delayed neutrons. This can be accomplished by operating the chopper very near its normal frequency, but in random phase relative to the source pulse, and analyzing the counting rate as a function of time t_c measured from a time-reference signal derived from the chopper. All phases of the chopper relative to the source are therefore uniformly sampled in the measurement, and both the constant delayed neutron part and the average prompt part accumulate identically as steady sources. (The IPNS delayed neutron chopper drive systems can operate in this mode). Then the random phase counting rate is just proportional to the delayed neutron counting rate in normal operation, with the time scale shifted by an amount equal to the time between the source pulse and the chopper time reference pulse,

$$C_d(t) = \frac{\epsilon\langle C'(t-\alpha_o/\omega)\rangle}{\left(\frac{\omega(1-\epsilon)}{\pi f} + \epsilon\right)}. \tag{9}$$

Only the delayed neutron fraction ϵ and the phase angle (ignoring any small error) α_o need to be known independently to enable $C_d(t)$ to be determined. ϵ follows easily from a separate measurement, and has already been measured[5] for the IPNS booster target, with the result $\epsilon = 0.0283$, $\alpha_o + \alpha_{p0}/\omega$ can be measured by sending the chopper timing signal into a time-of-flight histogram during fixed-phase operation. The phase sampling, which should be uniform to achieve the desired result, can be verified by histogramming source time origin pulses during random-phase operation. The analysis assumes that the detectors operate with time-independent efficiencies.

IV. CALCULATION OF DELAYED NEUTRON COUNTING RATE FROM THE MEASUREMENT

We now explore an iterative approach as an approximate method for determining the relationship of the delayed neutron counting rate to the prompt response. Integrating the expression for the prompt response (equation 8) with respect to wavelength λ, we obtain for either scattered neutron or beam monitor data

$$C_p(t) = [(1-\epsilon)/f](h/md)F((h/m)t/d)\ P_c((h/m)t/d,\ L_c t/d-\alpha_o/\omega;0)\,. \tag{10}$$

The factor P_c represents the reduction of the observed intensity by the chopper, which may be only partially open. Substituting $\lambda = (h/m)t/d$, we obtain from equation (7) the following expression for $F(\lambda)$,

$$F(\lambda) = [f/(1-\epsilon)](md/h)C_p((m/h)\lambda d)/P_c(\lambda, L_c(m/h)\lambda-\alpha_o/\omega;0)\,. \tag{11}$$

We now substitute this expression into that for the delayed neutron response given by equation (8), and obtain

$$C_d(t) = \epsilon f/(1-\epsilon)\int dt' C_p(t')P_c((h/m)t'/d, t-(d-L_c)t'/d-\alpha_o/\omega;0)/$$
$$P_c((h/m)t'/d, L_c t'/d-\alpha_o/\omega;0)\,. \tag{12}$$

This result is exact, and in view of equation (10) the integral always converges, but is unfeasible if the t' integration includes the range where the denominator vanishes but the numerator does not. According to (10), C_p vanishes just when the denominator in (12) vanishes, so (12) is valid everywhere that it is of interest. Of course to produce the result (12), the prompt response $C_p(t)$ must be measured, recorded and available throughout the range where it does not vanish. Figure 5 illustrates this range; there, Δt represents the range of times during which the chopper is open.

Since C_d is in some sense small compared to $C_p(t)$,

$$C_d(t) \approx$$
$$\epsilon f/(1-\epsilon)\int dt' C(t')P_c(0, t-(d-L_c)t'/d-\alpha_o/\omega;0)/P_c(0, L_c t'/d-\alpha_o/\omega;0)\,, \tag{13}$$

Equation (13) suggests an iterative scheme to obtain the delayed neutron counting rate. The nth iteration would give the delayed response $C_{dn}(t)$ from the prompt response $C_{pn}(t)$. That is

$$C_{dn}(t) =$$
$$\epsilon f/(1-\epsilon)\int dt' C_{pn}(t')P_c(0, t-(d-L_c)t'/d-\alpha_o/\omega;0)/P_c(0, L_c t'/d-\alpha_o/\omega;0)\,. \tag{14}$$

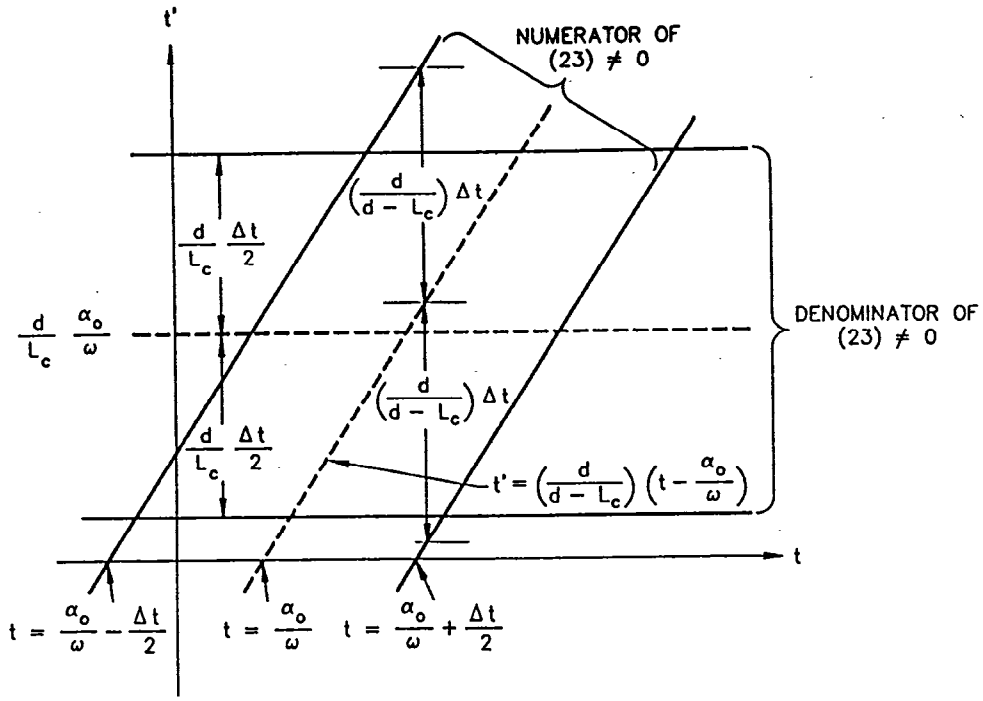

Figure 5. ***A schematic diagram in (t,t′) space showing the region within which the chopper transmission probability $P_c(\lambda,t;0) \neq 0$, where λ is the neutron wavelength, t′ and t are the times when the neutron is at the moderator and at the detector respectively. The chopper rotates at angular speed ω, and the initial phase angle α_o is 0. The lines $t' = (d/L_c)(\alpha_o/\omega \pm \Delta t/2)$ represent the boundaries of the region for which the denominator of (12) is non-zero, and the lines $t' = d/(d-L_c)\ (t - \alpha_o/\omega \pm \Delta t/2)$ represent the boundaries of the region for which the numerator of (12) is non-zero, where $\Delta t(\lambda)$ is the chopper open time.***

This result is used to obtain the $(n+1)^{th}$ value of the prompt response $C_{pn+1}(t)$. That is,

$$C_{pn+1}(t') = C(t') - C_{dn}(t'), \tag{15}$$

where $C(t')$ is the counting rate of the measurement, and $C_{dn}(t')$ is the nth calculation of the correction to it due to delayed neutron background. For the initial calculation we take $C_{d0}(t') = 0$, or $C_{p1}(t') = C(t')$. Such a calculation can be checked against the exact random-phase chopper method of measuring the delayed neutron background. The procedure is a feasible basis for routine correction of scattered neutron and beam monitor data.

V. MEASUREMENTS

We have measured the chopped, delayed neutron counting rate as a function of time in both the GPPD and SEPD diffractometers at IPNS. The source pulsing frequency for these measurements was 15 Hz rather than the usual 30 Hz, in order to provide data at long times when the counting rate due to prompt neutrons is low (this time interval corresponds normally to the "second frame" during normal 30 Hz operation). Delayed neutrons, which represent a fraction ϵ=0.0283 of the total (see equation (2)) then spread over a 66.7 msec interval rather than the normal 33.3 msec interval between pulses. Thus the ratio of the delayed neutron

counting rate to the prompt neutron counting rate is one-half the ratio for normal conditions.

Data were collected in three modes of operation: with the chopper rotating at 15 Hz, opening twice per revolution as during normal operation, and phased as during normal operation (α_0/ω = 6500 μsec for SEPD, 4400 μsec for GPPD); with the chopper rotating at ~15 Hz and asynchronous relative to the source; and with the chopper stopped open. A 6-mm diameter vanadium rod was placed in the sample position. Scattered neutron counting rates were recorded for all scattering angles with time focussing. During random-phase operation, timing signals from the accelerator were recorded which indicated uniform sampling of the source-chopper phase. The moderator was liquid CH_4 at ~105K.

Figure 6 shows the counting rate for detectors at 150° scattering angle for SEPD, (a) with the chopper running and phased with the source, and (b) with the chopper stopped and open; the time origin is the time of the source pulse. Figure 6c shows the counting rate for the same detectors, with the chopper operating at random phase; the time origin is the time of the chopper reference pulse shifted by α_0/ω=6500 μsec. The prompt response dominates the counting rate in the source-phased cases; the chopper has little effect on the prompt response in the interval 0 < t < 30msec. The rise at short times is due to epithermal neutrons. The peak at 6 msec is due to the 130K Maxwellian. The λ-like discontinuities are polycrystalline Bragg edges due to aluminum in the neutron path. Between 30 and 50 msec is the peak due to the second opening of the chopper. The same peak occurs 33 msec earlier, but is small relative to the prompt pulse response. The shape of the delayed neutron counting rate is revealed in Fig. 6c, where, due to the random-phase operation, <u>all</u> neutrons appear to be coming from a steady source. The chopped, delayed neutron peak exactly corresponds to the 30-50 msec peak of Fig. 6a.

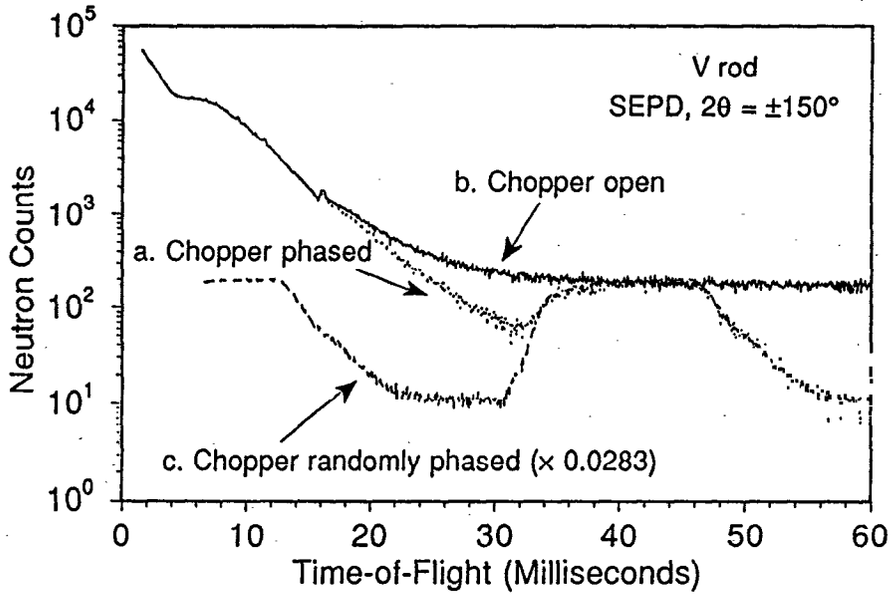

Figure 6. The scattered neutron counting rate from a vanadium rod sample in SEPD detectors at 2θ=150°, normalized to proton current; a) with the chopper running and in phase with the source, b) with the chopper stationary and open, and c) with the chopper operating at random phase relative to the source, normalized by ε=0.0283 (eq. 9) and shifted by α_0/ω=6500 μsec.

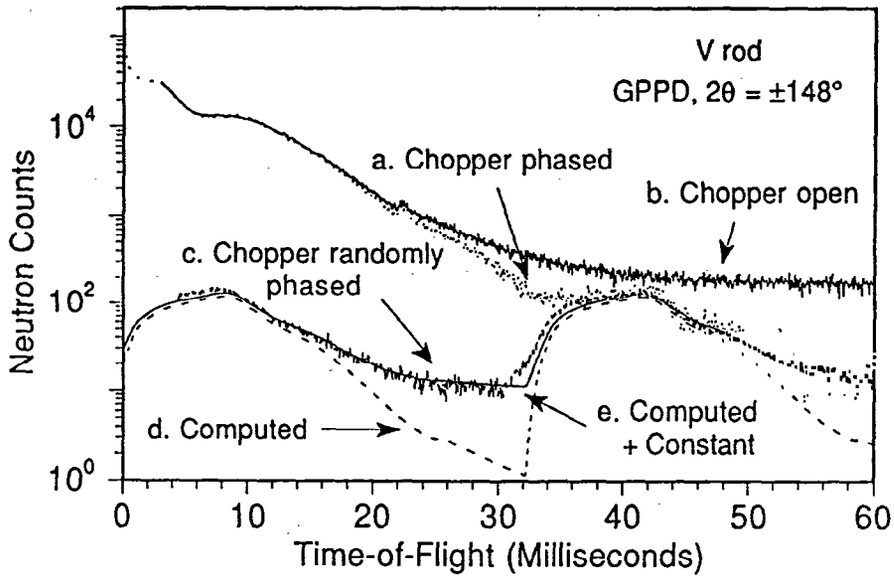

Figure 7. The scattered neutron counting rate from a vanadium rod sample in GPPD detectors at 2θ=148°, normalized to proton current; a) with the chopper running and in phase with the source, b) with the chopper stationary and open, and c) with the chopper operating at random phase relative to the source, normalized by ϵ=0.0283 (eq. 9) and shifted by α_0/ω=4400 μsec. The delayed neutron counting rate computed from a) according to equations (14) and (15), d) without constant correction, e) with constant correction of 10 counts/channel.

Figure 7 shows (a) the chopper-phased, and (b) chopper-stopped-open data, for neutrons scattered by the 6 mm diameter vanadium rod into detectors at 148° scattering angle in GPPD; and Figure 7c shows the corresponding random-phase data. The random phase data are normalized according to equation (9), with f=15 Hz, $\omega/2\pi$=15 Hz, and ϵ=0.0283[5].

We have calculated the delayed neutron background for GPPD from the observed total counting rate distribution for the case of the chopper running and phased to the source, according to equations (14) and (15). The result converged after two iterations. Comparing the result to the random phase data we find a constant contribution of background in addition to the computed chopped background. We have estimated this constant background which is caused by very short wavelength neutrons. These can penetrate the boron carbide of the drum chopper since the black chopper approximation is invalid for short wavelength neutrons (E $\gtrsim$ 65 eV). This background added to the delayed neutron peak is also shown in Figure 7. The discrepancy of the leading edge with the data is caused primarily by the time-focusing of the detectors which results in a uniform smearing of functions of scattered neutron time-of-flight by $\Delta t/t \sim 0.032$ for the GPPD diffractometer.

VI. CONCLUSIONS

Expressions for the pulse shape (transmission probability) and open time functions of drum choppers developed previously[3] have been used for the calculation of the prompt and delayed neutron counting rates in pulsed source diffractometers. An exact method is suggested for determining the delayed neutron counting rate, using the prompt and delayed neutrons with the chopper

operating in random phase with respect to the source. In addition, we have examined three approximate methods by which the delayed neutron response might be determined in terms of the prompt response; these appeal to the calculated pulse shape functions and might be refined iteratively. These approximate methods might be checked using the exact random-phase chopper method. We also report measurements which confirm the analysis of this random-phase chopper method.

VII. ACKNOWLEDGEMENTS

We thank James D. Jorgensen, R. Kent Crawford and Richard L. Hitterman for assistance in the planning and execution of the measurements, and Lawrence I. Donley and George E. Ostrowski for assistance in arranging the random phase operation of the chopper systems. This work was performed under the auspices of the U.S. Department of Energy, Division of Materials Sciences, Office of Basic Energy Sciences, under Contract W-31-109-ENG-38.

VIII. REFERENCES

1. A. E. Knox, J. M. Carpenter, J. L. Bailey, R. J. Armani, R. N. Blomquist, B. S. Brown, D. R. Henley, A. G. Hins, B. A. Loomis, A. W. Schulke and H. R. Thresh, Proc. IXth Meeting of the International Collaboration on Advanced Neutron Sources (ICANS IX), Villigen, Switzerland, 1986. SIN report ISBN 3-907998-01-4 (July 1987) 557-591.

2. J. D. Jorgensen, J. Faber Jr., J. M. Carpenter, R. K. Crawford, J. R. Haumann, R. L. Hitterman, R. Kleb, G. E. Ostrowski, F. J. Rotella and T. G. Worlton, J. Appl. Cryst. 22 (1989), 321-333.

3. J. M. Carpenter and D. F. R. Mildner, "Transmission Probability of a Drum Chopper in a Thermal Neutron Beam". Submitted to Nucl. Instr. & Meth.

4. R. K. Crawford, J. E. Epperson, P. Thiyagarajan and J. M. Carpenter, these proceedings.

5. J. E. Epperson, J. M. Carpenter, P. Thiyagarajan, and B. Heuser, Nucl. Inst. & Meth. A289 (1990) 30-34.

The submitted manuscript has been authored by a contractor of the U. S. Government under contract No. W-31-109-ENG-38. Accordingly, the U. S. Government retains a nonexclusive, royalty-free license to publish or reproduce the published form of this contribution, or allow others to do so, for U. S. Government purposes.

ICANS-XI International Collaboration on Advanced Neutron Sources
KEK, Tsukuba, October 22-26, 1990

Machine Control and Online Data Analysis using PV~Wave[1]

G.S. Smith, W.A. Hamilton, R. O. Nelson and G.P. Cort
Manuel Lujan Jr. Neutron Scattering Center
Los Alamos, New Mexico 87545 USA

ABSTRACT: By combining the commercially available image processing program WAVE with the LANSCE Data Acquisition Command Language (DACL), we have developed a computer program for the LANSCE neutron reflectometer (SPEAR). The instrument specific portion of the program is written in WAVE; whereas, the data acquisition part is composed of generic DACL building blocks. This approach allows one to acquire, archive, and retrieve data just as is done on any other instrument in the facility; however, it also allows one to easily customize the instrument specific program for the special needs of SPEAR. The menu options contained within WAVE are used to call machine operating programs, WAVE based data manipulation routines, and external FORTRAN routines. Several examples will be given which illustrate how the WAVE programs are written and used.

I. INTRODUCTION

One of the problems facing instrument scientists at large experimental facilities is how to minimize the amount of time spent in programming computers for data acquisition. One method is to develop a facility-wide computer program which covers the needs of every instrument. This has the advantage of being a single program written and maintained by a relatively few number of people. By the same token, it quite often has the disadvantage of being so complicated that only those people who wrote it can add any modifications and that even minor changes can be quite involved. On the other hand, a different program for each instrument could be written for data acquisition and online analysis. This gives each instrument scientist the flexibility to add any changes that he wishes without worrying about the consequences these changes may have for other instruments. However, this has the obvious disadvantage that many of the routines developed for a single spectrometer can easily be generalized for use on several instruments and amounts to a duplication of effort.

For the neutron reflectometer (SPEAR) at LANSCE, we have recently developed a program which is partly based on general use routines and partly instrument specific. This is done using two basic building blocks. The first is the LANSCE Data Acquisition Control Language (DACL)[2]. This program was written as a general use program for the control of the LANSCE Fastbus data acquisition hardware which is designed specifically for collection of time-of-flight data. The second portion of the program is specific to SPEAR and is based on the commercial interactive image processing language, PV~WAVE[1].

II. THE SOFTWARE BUILDING BLOCKS

DACL is an extension of Digital Control Language (DCL)[3] written at LANSCE to control the data acquisition hardware and collection process. Using a data base stored in VAX[3] memory, DACL allows the experimenter to configure an ensemble of CAMAC and FASTBUS hardware that controls the data acquisition process, the sample environment, and detector position. Additional commands initialize scalers and time histogramming memories, start and stop data collection, and generate VMS[3] files that save the data base and data histograms from FASTBUS. Each DACL

command generally provides a simple function in a single module, and complex functions are available through DCL[3] procedures.

Although DACL provides an interface between the user and the Fastbus hardware, it is still difficult to master for the casual experimenter. Besides, one wishes to insulate the user from having to learn this language simply to operate the instrument. Also, DACL does not provide a means for on line data inspection and reduction in a way that is useful for every experiment. This is essential for making basic experimental decisions such as when there is enough statistical data. We have found that the software package WAVE provides the necessary features.

"WAVE is an interactive 'language' for navigating through large data sets, selecting important subsets of the data and translating the results into useful charts, scatter plots, contour plots, surfaces, and images."[4] The features of WAVE used in performing these tasks are simple high level commands for plotting data, creating interactive menus and windowing; data manipulation based on vectors and arrays; programing structure which has components of FORTRAN, PASCAL and BASIC; and the ability to link WAVE programs and subprograms to FORTRAN and PASCAL subroutines as well as executing DCL and DACL commands and command files. These WAVE functions give one the ability to visualize data in many ways with a relatively few number of programming commands.

III. REFLECTOMETRY ON SPEAR

To understand the utility of using WAVE for reflectometry data, one must first understand something about the measurements. Fig. 1 is a schematic diagram of SPEAR[5,6]. The neutron beam from the LANSCE target is collimated into two beams within the biological bulk shielding. Either both or each of the shutters for these beams may be used. The beams are inclined at 1 and 1.5 degrees with respect to horizontal for studying either solid or liquid surfaces. At the exit of the bulk shielding, there is a T_0 chopper for reducing the background due to contamination by delayed neutrons produced when the initial flash of high energy neutrons contacts the shielding within the instrument.

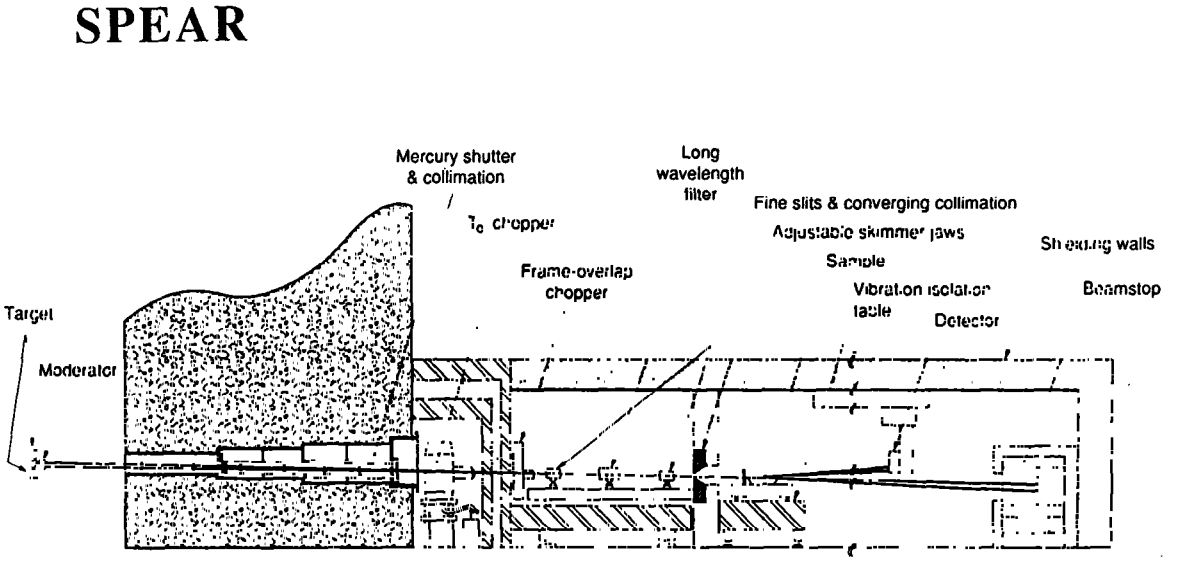

Fig. 1. Schematic diagram of the neutron reflectometer, SPEAR, at LANSCE.

Following the T_0 chopper shielding cave, is the beam handling area. In this room, there is a frame overlap chopper for selecting the wavelength frame (1-16Å or 16-32 Å). Also, there is a set of frame overlap mirrors which filter out long wavelength neutrons (>32Å). It is particularly important to remove these long wavelength neutrons since they will contaminate the low reflectivity measurements of succeeding frames. This entire room is surrounded by shielding walls to prevent any background scattering from reaching the sample and detector.

The paths of the two neutron beams converge to a point at the sample position. The reflected neutrons are then detected by an Ordela[7] model 1202N linear position sensitive detector. Generally, this detector is oriented vertically and, for small angles, its height is adjusted so that it may intercept both the direct and the reflected beams (although during a reflection measurement the direct beam is blocked to prevent damaging the detector). This allows for an accurate determination of the angle of reflection. With this arrangement, the data can be easily visualized by plotting the intensity as a function of time and position on the detector. This is the primary function of our WAVE routines.

IV. THE WAVE PROGRAM

The main WAVE program consists of four major subroutines. The choice of one of these four subroutines is made by clicking on menu options offered whenever the program is first run. These menu items are labeled OPERATION, SETUP, QUICK LOOK, and ANALYZE. Whenever one of these menu items is chosen, a submenu giving the available options is presented. The first main menu items is OPERATION. Its submenu offers the basic machine operation commands RUN, PAUSE, RESUME, END AND SAVE, and END AND DON'T SAVE. By clicking on any one of these options a command file is executed. In this way, the user needn't be troubled with remembering commands or knowing DCL or DACL. Each successful run will begin with the RUN option and end with the END AND SAVE option which automatically archives the data.

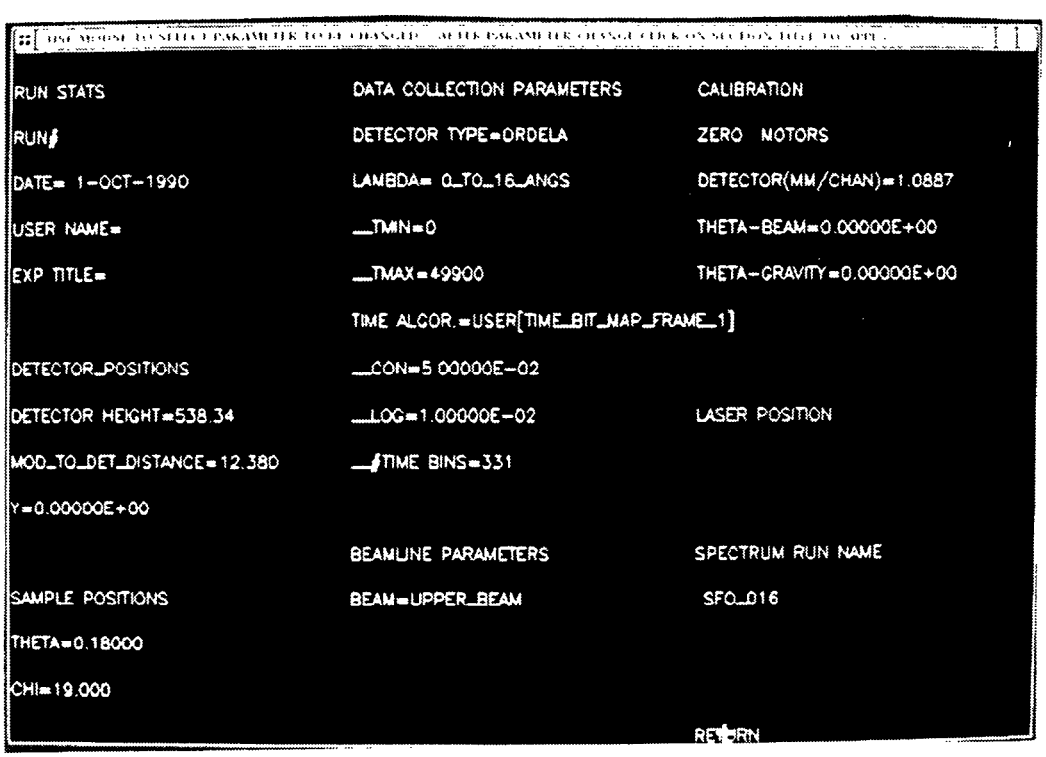

Fig. 2. The SETUP submenu for selecting the instrument running parameters for SPEAR.

Clicking on the second main menu item, SETUP, will cause the display of the setup submenu. As illustrated in Fig. 2, this a 2-dimensional menu which contains many of the instrument configuration parameters which may be selected. The options are grouped by function into titled sections. The main sections are RUN STATS, DETECTOR POSITIONS, SAMPLE POSITIONS, DATA COLLECTION PARAMETERS, BEAMLINE PARAMETERS, CALIBRATION, LASER POSITION, and SPECTRUM RUN NAME. These are used to setup the instrument before a run begins, and typicaly, these only need to be fixed once before beginning a run. If an option in the SETUP submenu is selected, it can be changed using either keyboard input or by another pop-up menu. After changing a parameter, that parameter changes from white to red. The red color indicates that the parameter has been selected for change, but it is not changed. After selecting the parameters in a section, one clicks on the section title to execute those changes.

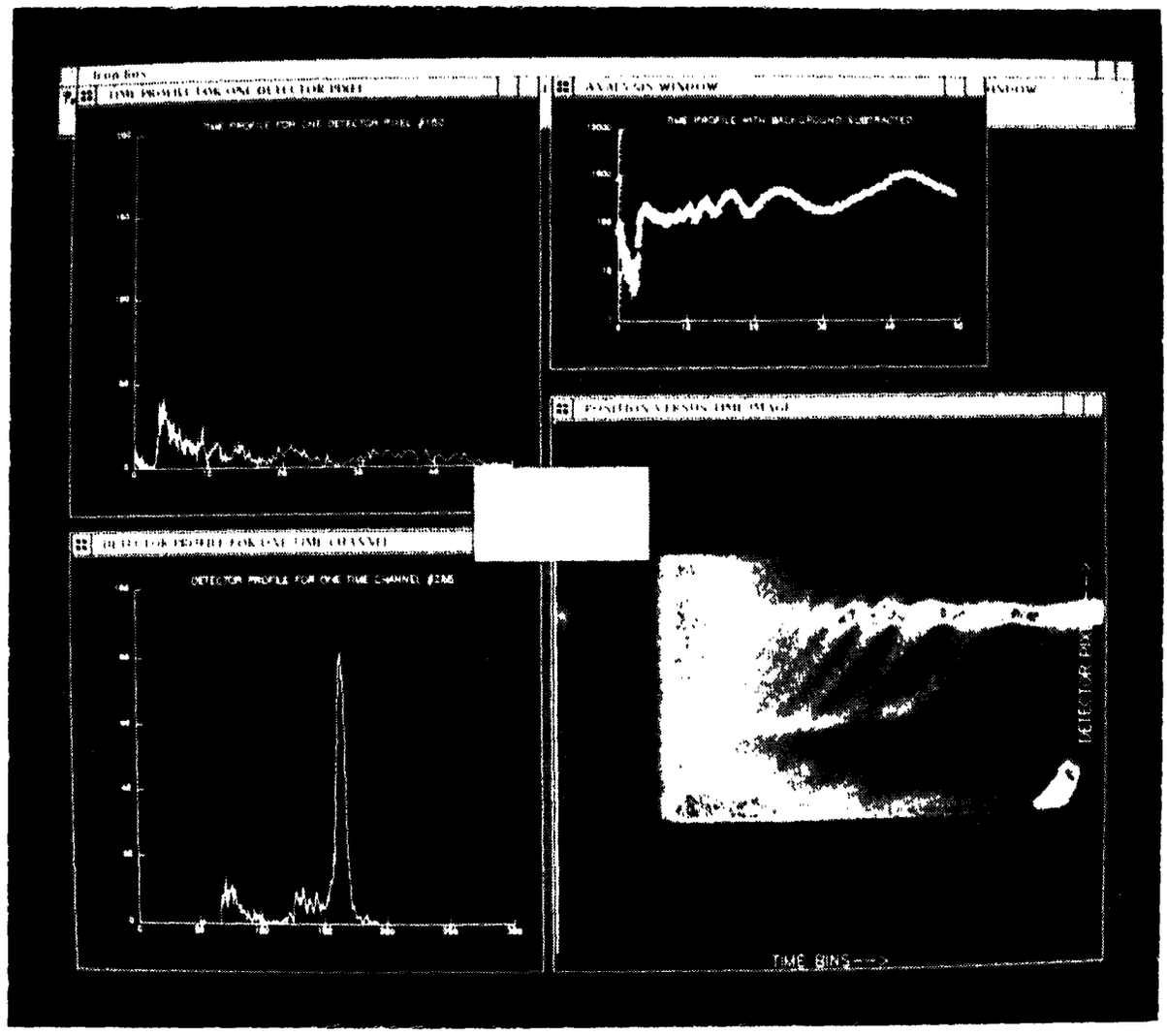

Fig. 3. This is an example of the QUICK LOOK option. Clockwise from the bottom right, we have the data image, a slice through the data image parallel to the detector axis, a slice through the data image parallel to the time axes, and finally a time profile summed over several detector pixels.

The QUICK LOOK main menu item allows one to examine the current data set stored either in the Fastbus hardware memory or the data stored in the data archive. This subroutine is the most important part of the WAVE program used on SPEAR. Upon selecting this option, four windows appear which fill the screen. Immediately afterward, a 3-dimensional plot (referred to as an 'image')[3] of the data appears on the screen where the x-axis is the time channel number, the y-axis is the detector pixel number and the intensities are represented by a blue-green-red color scale. A black and white photograph of this is shown in the lower right corner if Fig. 3. This representation gives the user an instant overall view of the data. As can be seen in the figure, the brightest spot on the right represents the critical edge, and the individual elliptical shapes are the interference fringes. This representation also gives an immediate impression of the amount of diffuse scattering from the sample. The submenu items presented while the QUICK LOOK option is active are intended for reducing the image further. The DETECTOR PROFILE and TIME PROFILE options allow one to plot a slice through a chosen point on the image. The DETECTOR PROJECTION and TIME PROJECTION selections produce plots where all of the data is collapsed onto either the detector or time axes, respectively.

The next QUICK LOOK submenu option is labeled CRUDE ANALYSIS. As this name implies, this is used as a first step in reducing the image plot to a reflectivity curve. The two options in this selection are SUM WITH NO BACKGROUND SUBTRACTION and AUTO BOX. Both of these options allow one to select a minimum and maximum detector pixel value and sum the intensity in each time channel between these detector pixels. In the AUTO BOX option, a linear background defined by the two chosen detector pixels points is subtracted from the data. An example of a SUM WITH NO BACKGROUND SUBTRACTION is plotted in the upper right hand box as shown in Fig. 3. This data can be stored and divided by the incident spectrum to obtain a reflectivity curve.

There are two reasons for the term crude in CRUDE ANALYSIS. First, you can see that the specular peaks have an elliptical shape, this is because the finite resolution of the instrument allows for sampling over a range of incident and exit beam angles. Therefore, at a nominal setting for angle and time (or wavelength) there is a spread of the specularly reflected beam on the detector. At a given time, the spread in angles yields a spread in the values of the normal component of the wave vector, q_z. In fact, the direction of the major axis of each of these ellipses is along the direction of constant q_z all of which converge to $2\Theta/2$ (or the horizon) at time t=0. Since the program doesn't account for this tilt in the spectral peaks, using CRUDE ANALYSIS effectively diminishes the resolution of the instrument, and only a proper conversion of the data into reciprocal space should be used for the final data analysis.

The next QUICK LOOK submenu option is FILTER IMAGE. This is simply a choice of band pass or logarithmic filters to enhance the weak scattering in the image. Following the FILTER IMAGE option, SAVE ANALYZED DATA is used to save either the reduced data set created by CRUDE ANALYSIS or the entire data array can be saved for use in more rigorous analysis. The final option within QUICK LOOK is the PRINT COLOR IMAGE option. This simply calls a WAVE subroutine which creates a color PostScript[8] file to be sent to a color printer. After the data has been examined and reduced using the QUICK LOOK OPTIONS, the final main menu option becomes useful.

The last main menu option is the ANALYSIS option. This calls our WAVE program for plotting 2-dimensional curves. As can be seen in Fig. 4, most of the menu items in this selection are self explanatory. Most often, we use this program to plot the saved, reduced data, plot a second file (the incident spectrum), divide these and normalize the critical edge to one. The other selections such as log-linear plotting, adding error bars, rescaling the axes, changing the color, size, and type of plotting symbol are available for enhancing the plots. Also, using the header information stored in the saved reduced data file, the data can be instantly converted from time-of-flight to wavelength or to q_z in $Å^{-1}$. These plots may be sent to a PostScript printer for hardcopy output.

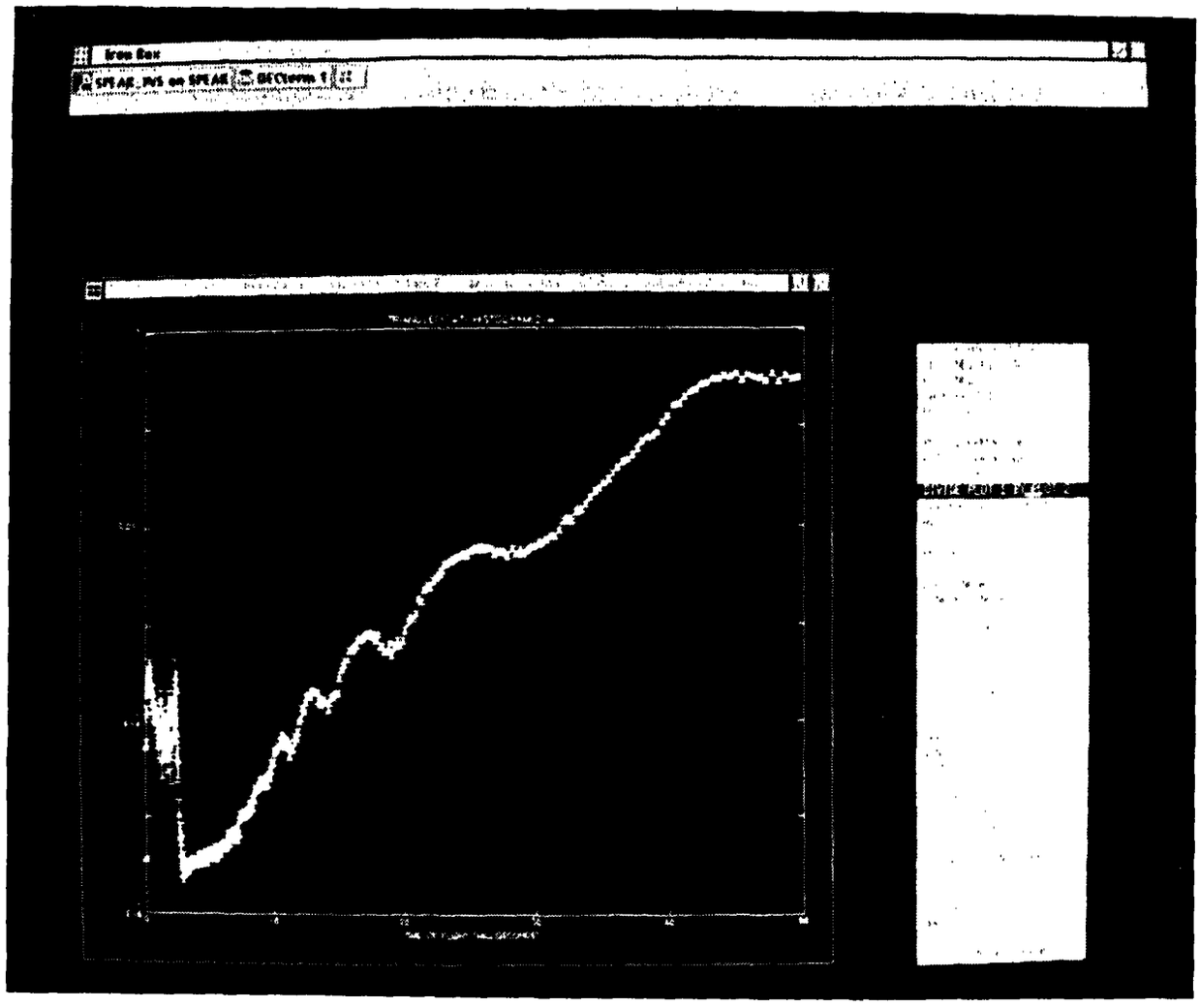

Fig. 4. This is a photograph of the ANALYZE option. In this mode, standard two dimensional manipulations of the data such as dividing by the spectrum, choosing plot axes, and converting to reciprocal space are performed.

V. DISCUSSION

The WAVE language has enabled us to write routines to perform complicated image and data processing with a minimal amount of time invested. We've illustrated several of the functions contained in the WAVE program developed for SPEAR. Using these image processing routines, we get an instant on-line overview of the data. In fact, we have discovered features in the data (especially in the diffuse scattering) that were not apparent using conventional contour and linear plots Fig. 3 (bottom right). The WAVE routines have allowed us to tailor the programs to the needs of the instrument while at the same time the raw data is obtained and stored as it is on any other instrument at LANSCE. Also, the menu options in WAVE have allowed us to present a set of options to our users for operating the instrument and performing the data analysis. Similarly, WAVE routines could be written for use on any of the LANSCE instruments and are especially suited for multi-detector measurements.

References

1. "Precision Visual's Workstation Analysis and Visualization Environment", PV~WAVE is a trademark of Precision Visuals Inc. of Boulder, Colorado.
2. R.O. Nelson, G. Cort, A. Gjovig, J. A. Goldstone, D.E. McMillan, J. Ross, J. Seal, and D.R. Machen, IEEE Transactions on Nuclear Science, **34**, p1017 (1987).
3. VAX, VMS, and DCL are trademarks of Digital Equipment Corporation.
4. "PV~WAVE Overview," Copyright 1988 by Precision Visuals Inc. pp 1-2.
5. "A Neutron Reflectometer for LANSCE?, Report of a Workshop Heald at the Los Alamos National Laboratory November 2-3 1987," ed. D.K. Hyer, Los Alamos National Laboratory Conference Report, LA-11301-C(1988).
6. "Condensed Matter Research at LANSCE," ed D.K. Hyer, Los Alamos National Laboratory Publication, LALP 90-7(1990).
7. Ordela.Inc., Oak Ridge, Tennessee.
8. PostScript is a trademark of Adobe Systems Incorporated.

Q(M.Furusaka): How much is the software? Is it fast?

A(R.Pynn): I haven't heard any complaints about speed. I'm afraid I can't remember the price. It depends somewhat on the number of copies you buy. I suggest you contact the company directly.

ICANS-XI International Collaboration on Advanced Neutron Sources
KEK, Tsukuba, October 22-26, 1990

Future Strategy for Computing at ISIS

W.C.A.PULFORD
ISIS Instrumentation Division,Rutherford Appleton Laboratory

ABSTRACT

This paper initially provides a brief description of the current system together with some of the operational problems encountered during the five years of ISIS running. It then summarizes some of the thoughts of the ISIS computer and electronics groups concerning the best ways for the ISIS data acquisition and analysis systems to evolve. Topics considered include: the increasing use of workstations and windows, the possible future use of UNIX and the next generation of data acquisition electronics.

I am much indebted to the whole IID computing group (Kevin Knowles,Chris Moreton-Smith,Tony Valente,Richard Brodie,Kate Crennell and Scott Robertson) as well as Julian Norris and John Holton of the electronics group, for their contributions to this paper.

Introduction

A powerful and successful pulsed neutron source such as ISIS must be supported by a computer system of high capability. It is clearly of limited value to run this powerful source without the means to progress rapidly and easily from raw data to scientifically interpretible results. The PUlsed Neutron Computer Hierarchy or PUNCH computer system is used for all collection and subsequent analysis of data collected from the neutron diffraction instruments arrayed about the ISIS pulsed neutron source. At present it consists of a Vax8650 computer system, the HUB, connected in a Local Area Vax Cluster (LAVC) to 9 x VaxStation 3200, 6 x MicroVax II , 1 x Vax750 and 3 Vax730 computers. The smaller computers are known as Front End Minicomputers (FEMS) and are responsible for the data acquisition from the ISIS instruments. In addition there are 2 VaxStation 3100, 2 VaxStation 2000 and 12 IBM PC workstations as well as about 130 dumb visual display terminals connected to the network of computers. The whole PUNCH system is displayed schematically in figure 1.

The Data Collection Process

ISIS is a pulsed source of both neutrons and muons. In the former case, single or multidetectors are used to count neutrons scattered by a sample of the material under investigation. In the latter case positrons produced by muon radioactive decay within the sample are counted using multidetector arrays. For both the pulsed nature of ISIS confers a time structure on the detected events. This time structure is reflected in the data collected by storing the counts as a function of their time of occurrence in time bins of width δt (typically 1 μs for neutrons and 20 ns for muons). Consequently a histogram of data is built up for each detector element. These histograms are stored in computer data files whose size is dictated by the product of the number of time bins used and the number of detector elements. Each ISIS instrument is optimised for the investigation of particular types of condensed matter.The sizes and the rates of collection of these 'raw' data files varies considerably. Table 1 gives typical values of these parameters.

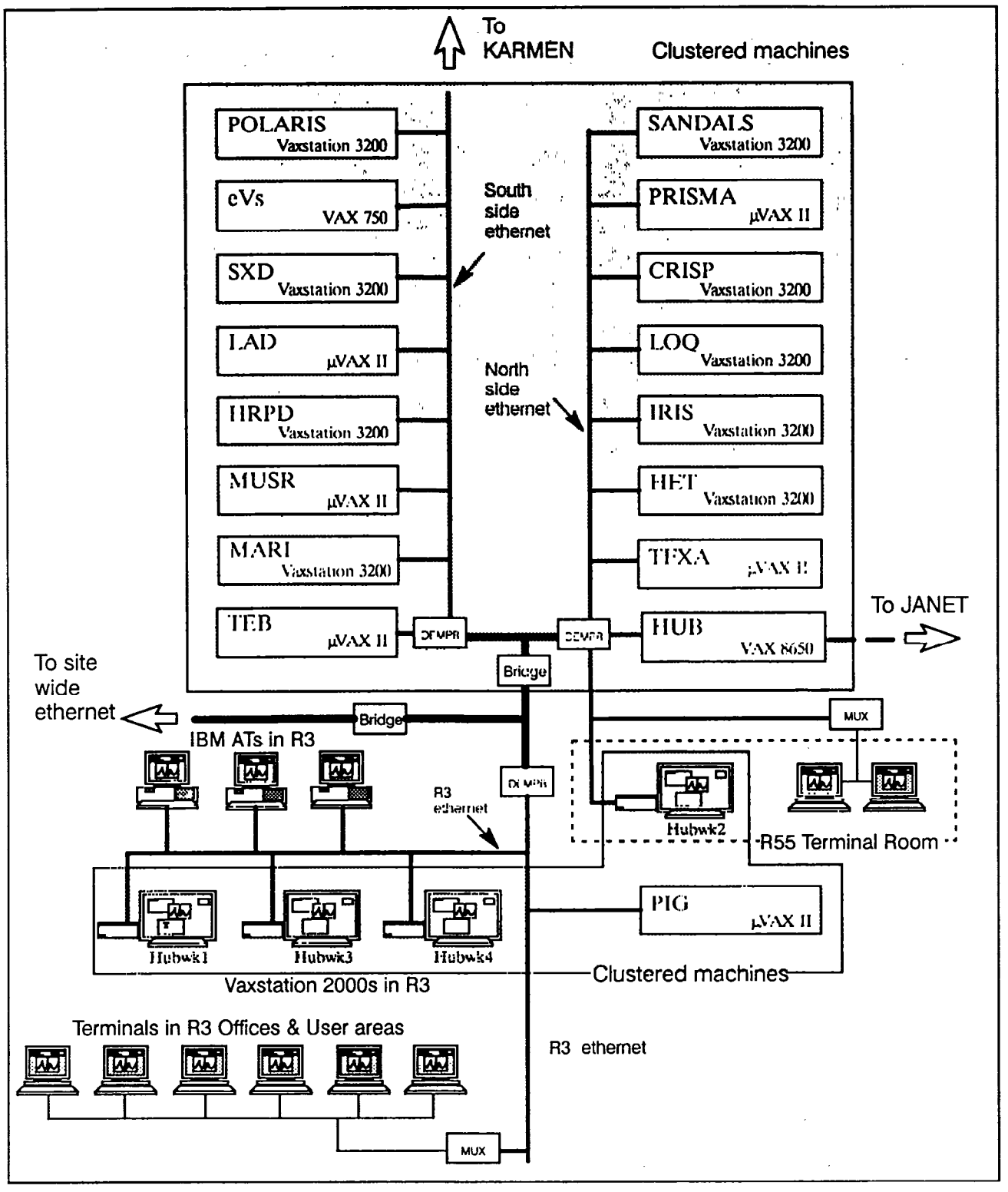

Figure 1 THE PUNCH COMPUTER SYSTEM

Instrument	Number of Runs	Average Data Volume (Kbytes)	Total Data Mbytes	Instrument type (E – Elastic, I – Inelastic)
CRISP	458	50	22	Surface Reflectometer(E)
LOQ	346	1200	415	Low Angle diffractometer(E)
POLARIS	245	330	80	Medium Resolution Powder Diffractometer(E)
HRPD	424	640	272	High Resolution Powder Diffractometer(E)
IRIS	137	180	25	Inelastic High Resolution Spectrometer(I)
LAD	99	790	79	Liquids and Amorphous Diffractometer(E)
PRISMA	153	186	29	Inelastic Excitations Spectrometer(I)
HET	70	1800	132	High Energy Transfer Inelastic Spectrometer(I)
SXD	149	1400	252	Single Crystal Diffractometer(E)
TFXA	30	3200	96	Time Focussed Crystal Analyser(I)

Table 1 – Data Collection Rates for Various Instruments for Cycle 89/7 (duration 4 weeks)

The purpose of the PUNCH computer system must be to archive these data files securely as well as facilitating their analysis to produce physically interpretible results.

Sequence Of Data Processing

Broadly, the sequence of data processing may be described as consisting of the following phases :

1.Setup

Optimum values for the experimental parameters such as the number of time bins and run durations are calculated and then set up for the data collection phase or "RUN". Also such physical parameters as the instrument geometry, sample orientation and temperature are defined at this stage.

2.Run

The progress of the data collection is monitored continuously during this phase by inspecting key run parameters and collection rates. This is important for the early detection of instrument errors or perhaps sample state changes.

3.End of Run

On completion of an experimental RUN the collected histograms are stored in the computer RAW data file. This file is automatically copied from local disk space onto an optical disk jukebox connected to the HUB computer. Details of the data archived in this way are stored in catalogue files for each instrument. This information is sufficient for the archived data to be restored to magnetic disk at a later date.

4.Data Reduction and Analysis

Data Reduction and Analysis – the processing of data varies considerably depending on the instrument and type of material under investigation although most uses a standard program environment called GENIE. A typical sequence of processing might be .

a) Merge histograms collected by detectors at equivalent positions in space such as those diametrically opposite at the same radius on a cylindrically symmetrical instrument.

b) Normalize data. This is basically a process of comparing the data against some collected in the absence of the sample to eliminate any systematic fluctuations in the instrument transmission.

c) Peak fitting. In most cases it is necessary to perform considerable analysis of the histograms in order to determine the exact positions and sizes of features. This may involve processor intensive least squares peak fitting routines, such as in RIETVELDT refinement, or as is becoming increasingly common, the technique of maximum entropy (MAXENT).

d) Model fitting. This depends totally on the type of experiment being performed and whether the probes used are neutrons or muons.

The first category of neutron instrument is that which concentrates on elastic scattering of the incident neutrons. On data collected from these instruments where the neutrons are scattered by the sample with no energy loss, the primary purpose is usually to establish the atomic or molecular structure of the material. In this case further processing involves proposing a model for the structure and using it to calculate the data points expected. These expected data are then compared with the observed data and a new refined model established by a process such as least squares (LSQ). The main line of this type of analysis is structure factor least squares which minimizes the discrepancy between the observed and calculated structure factors of the sample. (The structure factors (fobs) are closely related to observed intensities Iobs = |fobs|**2.) This method tends to be reliable but is a very heavy user of processing power scaling as the number of data observations and the square of the number of scattering elements in the sample. Monte-Carlo techniques tend to replace least squares in model fitting or generation for instruments investigating the properties of liquids and amorphous materials. This is a processor intensive method where the total energies are calculated for a large number of randomly generated models, the most likely model being indicated by that with the lowest energy.

The other major category of neutron instrument is that of inelastic where neutrons exchange some energy with the molecules or atoms of the material under investigation. The observed energy shifts then provide information about the atomic lattice motions or the motions of the atoms themselves. The analysis of this type of experiment tends to involve the calculation of many incident and resultant neutron energies and momenta. Also to appreciate the nature of the molecular motions it may be necessary to compare results obtained from a number of runs.

Muons are fundamental particles which resemble either heavy electrons or positrons depending on their charge. They are produced in large quantities at ISIS by inserting a thin target into the incident proton beam line. The general thrust of the experiments using these probes is to investigate diffusion effects within the solid state or to examine materials during magnetic state transitions, although more recently, considerable effort has been applied to examine the potential of muon catalysed fusion. In each case the computer processing involves the least squares fitting of various exponential functions to the observed data. The most accurate experiments are performed when each of the many detectors on a muon instrument is considered separately. Thus the processing involved scales linearly with the number of detectors.

5.Data Presentation

Once data analysis is complete it is necessary to present the experimental findings. Extensive use of desktop publishing and graphics is made to expedite this process.

The Functions of the PUNCH computers

The configurations of the current PUNCH computers are illustrated in Figures 2 and 3. The FEMs are used primarily for phases 1, 2 and 3 of the data collection process. The FEMs are connected in a peer to peer LAVC where each machine has a separate operating system. This, together with disk capacities ranging from 160 to 768 Mbytes, ensures data collection irrespective of the state of the HUB computer. Nevertheless the HUB computer does fulfil a pivotal role in the PUNCH computer system. This machine performs much of phases 4 and 5 in the data collection process, but its importance extends well beyond this. The HUB computer is the local point for data concentration and storage because it controls a large quantity of magnetic disk space and the 40 Gbyte optical disk jukebox. This latter storage ensures that any data ever collected from the ISIS instrument is available on line. The constantly expanding data storage requirements are illustrated by Figure 4.

It is evident that the data storage requirements continually increase. Indeed, in order to maintain the online status of ISIS data is has been necessary from Cycle 4 1989 to perform processor intensive file compression before archiving.

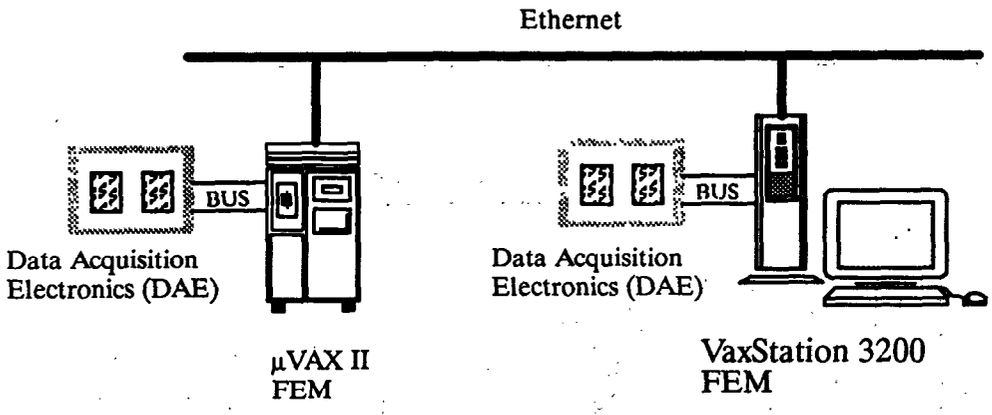

Figure 2 The Two Main Types of FEM

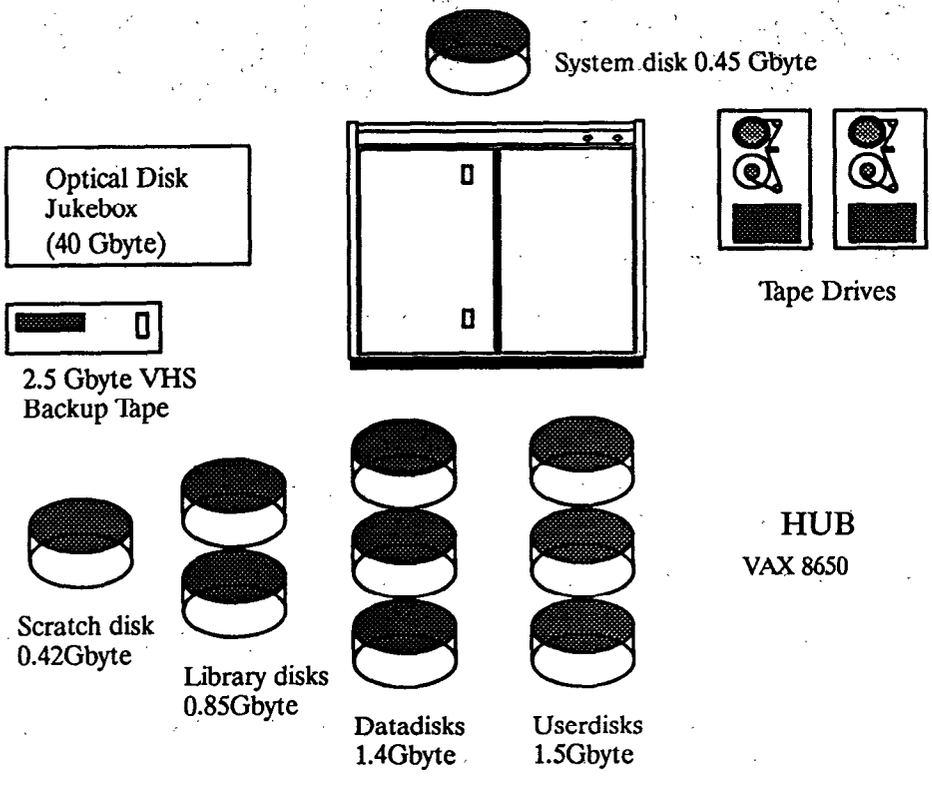

Figure 3 The HUB configuration

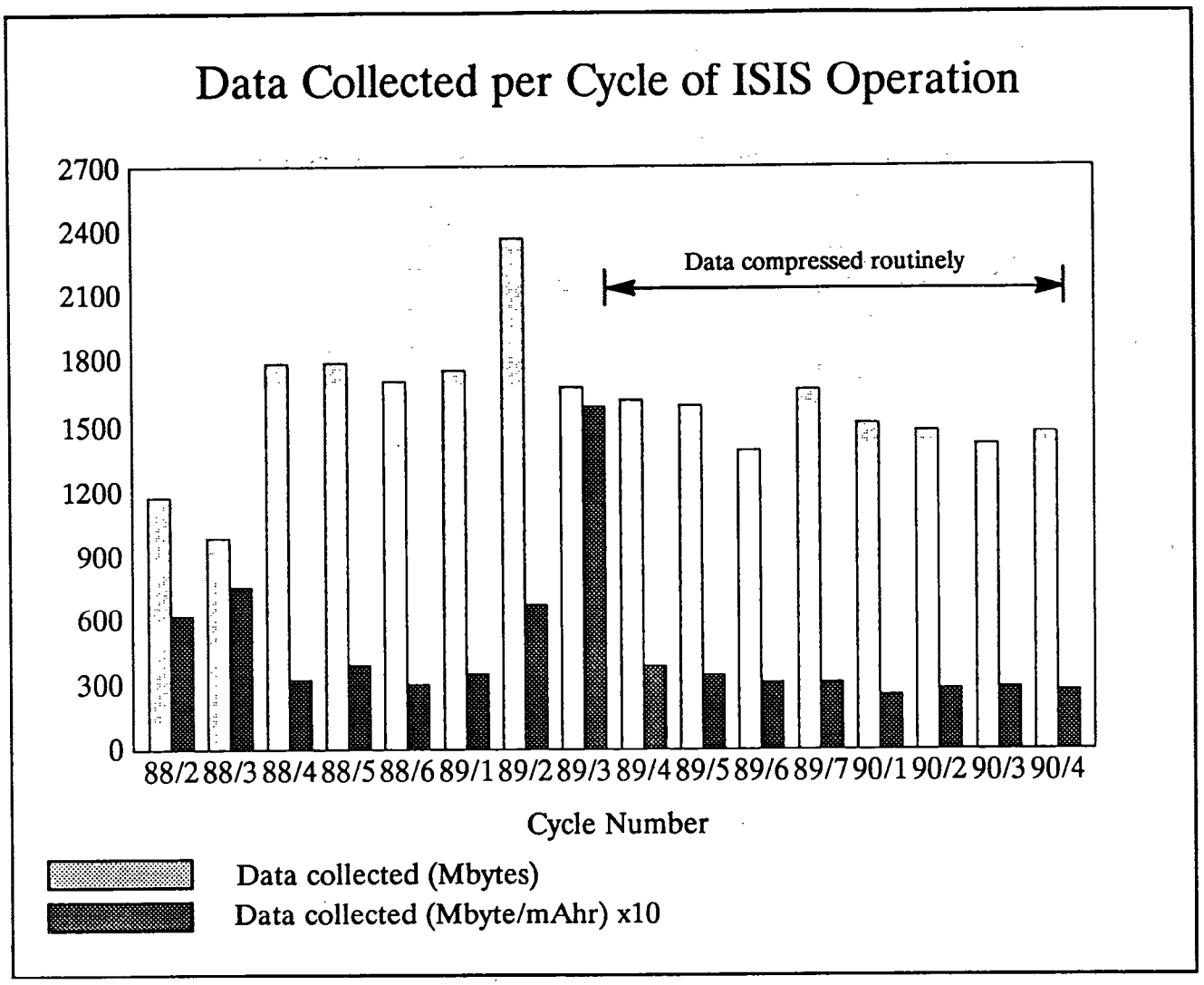

Figure 4

The volume of data collected per proton milliamp hour has remained approximately constant since Cycle 4 in 1989. This can be explained by the following observations:

a) ISIS has been running with a Tantalum target thus reducing the neutron flux by 50%.

b) Fewer more complex experiments are being performed which require longer to setup and longer run durations to improve statistics.

c)There have been no new scheduled instruments during this period. MARI and SANDALS are only now in cycle 90/5 making a significant contribution to the data volumes collected.

The HUB computer provides a broad spectrum of general computing for over 300 registered users. The users perform diverse sets of tasks ranging from editing and word processing through to data analysis often using graphical visualisation techniques. Figure 5 illustrates the typical workload of the HUB processor, the simulations (SI) are performed under the control of a low priority batch queue to use free processing power until pre-empted by any other process. Some reasons why the HUB workload has developed in this way are given below :

a) The HUB computer may perform processing without affecting data collection.

b) It is the only machine within the PUNCH system directly accessible from the UK academic network (JANET).

c) Until recently only the HUB had routine access to the ISIS data catalogues.

d) It is the most powerful computer in the PUNCH system.

e) Many software products are only available on the HUB computer because of their cost and/or storage requirements.

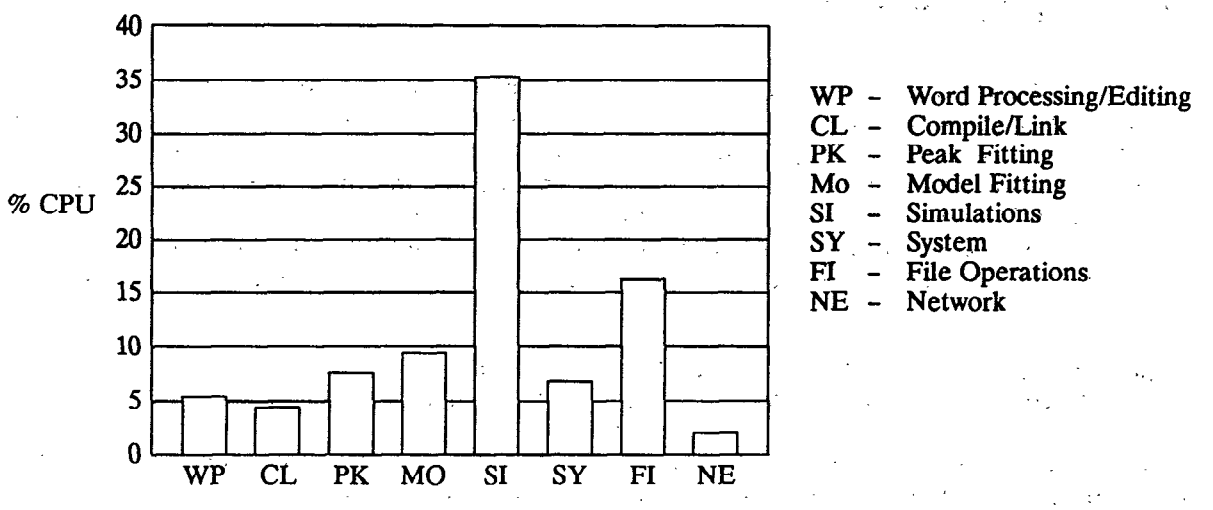

Figure 5 The distribution of HUB processor time between different categories of task

Current Problems With The System

Most of these are concerned with the HUB 8650 computer configuration. It has always been intended that this machine satisfy the interactive needs of a large number of users performing heterogeneous operations. The essence of an interactive machine must be responsiveness, particularly for editing and graphics. Subjectively the response to a typed command should take no longer than 2 seconds but this has deteriorated considerably at peak times over the past 6 months, despite the efforts described below to slow the effect. In order to maintain the interactive response, users are strongly encouraged to run processor intensive tasks in batch mode where they run at lower priority but which the operating system may schedule more efficiently. The scheduling has the unfortunate side effect that few or no batch jobs run during the peak hours between 0900 and 1700 hours daily. Another serious problem is that the HUB is chronically short of both optical and magnetic disk space. Currently the optical disk jukebox has about 8 Gbytes of its 40 Gbyte capacity free and with data accumulating at a rate of about 1.5 Gbyte per 6 week cycle we will no longer be able to maintain all data online from Cycle 6 of 1990. Magnetic disk space is also at a premium, particularly since the poor batch job turn-round tends to extend the duration of data files. By applying stringent disk quotas, the HUB runs constantly with its disks between 85 and 95% full with no spare capacity. In order to run more detailed data analyses the HUB users usually have to compete for the relatively small available space on a scratch disk. A further problem has been HUB downtime caused by a variety of hardware faults. The frequency of these faults can be ascribed to the fact that the 8650 uses 1984 technology which tends to use high current devices to obtain what is by current standards modest performance. This is reflected in the relatively high maintenance cost of about £30,000 per annum.

Remedial Actions

The past year has seen the progressive replacement of the original VAX 11/730 FEMs by VaxStation 3200 workstations. These have about 10 times the central processing speed and 5 times the disk capacity of the older machines. Unfortunately, these workstations, which actually run at about 45% of the 8650 processing speed, are restricted to a maximum of 2 interactive users and can therefore do little to alleviate the interactive load on the

PUNCH system. Nevertheless, connecting these computers in a local area vax-cluster does enable some of this processing power to be exploited by means of cluster-wide accessible batch queues. Any jobs placed in these queues are automatically run on any free cpu in the cluster. This has gone some way to increase the batch processing capacity of the PUNCH system, but it is subject to a law of diminishing returns. Each additional clustered computer does abstract a significant proportion of the HUB processing and disk capacity.

Future Considerations

It is our experience that the computing requirements generated by each instrument double every three years. This observation is shared with the our complementary institute, the Institut Laue Langevin at Grenoble. I believe this assessment of the situation at ISIS to be optimistic. As an example the facility has just received a grant of £2.4M to enable the doubling of the ISIS proton beam current to 200μA. This together with an imminent enhancement to the ISIS target will result in an up to fourfold improvement in neutron flux. Thus purely on the basis of intensity the number of experiments capable of being performed and hence the data collected may well more than double over the next 24-30 months. The problem of this impending data processing bottleneck will be exacerbated by two further factors:

a) Four new instruments MARI,ROTAX,SANDALS and eventually a second muon spectrometer will be commissioned. (MARI and SANDALS in 1990 , ROTAX in 1991 and the new MUSR in 1992)

b) Many of our current instruments (HRPD,POLARIS,CRISP,IRIS,LOQ and SXD) will be equipped with new large detectors with the potential to produce manyfold increases in the data volumes collected.

It is reasonable to assume that not all of this data volume and associated processing will be realized immediately. Much of the increased ISIS intensity will be used to provide better statistics or to enable the prosecution of more ambitious experimental projects possibly involving more complex or more weakly diffracting materials. Nevertheless the combination of these factors must ensure the doubling of the data processing load on PUNCH system within the next 18 months. An important further consideration is that as the complexity of experiments increases so will the need for improved visualization techniques. Visualization is a buzz word which describes the ability to isolate the nuggets of scientific insight from the vast amount of data. In the vernacular, "to see the wood for the trees". The process tends to involve combinations of such techniques as multi-dimensional rotations with hidden line removal, edge detection and maximum entropy. These techniques are very processor-intensive and require graphics workstations to be at their most effective. It is possible that even the most powerful VAX workstation will be insufficient for some needs thus forcing the adoption of the latest ultra-fast RISC based UNIX workstations.

Conclusions

Adopting a computer strategy for the future immediately involves tackling two almost philosophical questions.The first of these is whether our users really need to store all raw data ever collected. Currently the system just copes but with the advent of large area detectors and higher neutron fluxes it will become impossible to transfer the data files by network let alone store them. Thus the answer to the question is definitely not. Instead we must concentrate powerful but flexible and reasonably user-friendly processing power at the point of data collection, that is within the DAE. This would enable much data processing particularly data volume reduction at the earliest opportunity within the PUNCH system and thus avoid the need to transfer and store large amounts of information-sparse data.

The second main philosophical question is a natural consequence of the first. If we make all of this processing power available to the FEM do we still need a HUB computer ? The answer is a most emphatic yes. Even though much raw data processing would be devolved to the FEM systems there remains a requirement for a central file storage and data administration machine. Moreover we must continue to provide a platform for a whole spectrum of more general computing to support all ISIS users irrespective of whether they are actively running an experiment. Indeed the functionality of the HUB computer should be enhanced to provide not only the greater power indicated by the empirical observation made earlier that computing requirements tend to double every three years but also more graphics facilities to aid in the interpretation of scientific results and in the production of high quality publications.The data administration role of the HUB cannot be overstressed. Currently we have about 60,000 ISIS datasets archived and this number is increasing at a rate of about 3000 per 5-week cycle. It has proven to be of great value to be able to access any one or a combination of these automatically within minutes. An example would be to

compare data collected for the same material collected under different conditions and times, even from different instruments. To maintain this facility, we will require not only the HUB as a data concentration point but also a commercially supported high functionality database system such as Digital's Rdb or Compuserve's S1032. Finally the effort involved to reimplement software for a different operating system coupled with the degree of user alienation incurred makes it inconceivible that the new HUB should be any computer than a VAX running VMS.

DAE-II and Enhancements to DAE-I

Considerable thought has been given to the development of the next generation of Data Acquisition Electronics for ISIS. Much of this is described in a previous ICANS paper (Pulford,Quinton,Johnson and Norris, ICANS-X ,pp537-547). As stated earlier, the provision of processing facilities actually within the DAE would enable initial data analysis and compression without moving the data . Moreover it would provide such benefits as real time monitoring of data acquisition and detection of errors. Experience gained in running DAE-I in ISIS instruments as well as some recent technical advances have suggested some additional requirements for the intelligent DAE:

a) The DAE should be connected to the local area network, currently ethernet.This confers great operational flexibility and robustness in that DAE faults would not tend to crash the FEM as they tend to do currently. Also replacing a failed FEM would simply be a matter of using a different caller for the DAE's ethernet address. Moreover FEM's would no longer require a Q-bus and could thus be simpler and cheaper. The potential lower bandwidth available via ethernet rather than by Q-bus should be offset by the lower volume of data output by the intelligent DAE

b) The construction of the component cards within the DAE should be printed circuit rather than wirewrap as used currently. Wirewrap has proven to be very prone to mechanical faults such as broken wires or soldered pins. Also the introduction of programmable logic devices (PLD's) enables increased emphasis to be placed on producing as few different simple cards as possible, thereby improving the maintainablity of the system.

c) Predictably ISIS has been found to be the source of considerable electrical noise. Consequently long multiwire cables such as that connecting the instrument crate, into which the detectors are plugged, and the system crate are undesirable and should be replaced by multiplexed fibre optic cables.

d) As an interim measure the addressing capability of our existing MULTIBUS crates should be upgraded from 24 to 32 bits. This has proven relatively simple and has been accomplished already.

Much progress has been made in implementing this strategy. Figure 6 shows schematically two cards which have been designed and are now under construction. Their first use should be in cycle 91/1. .

Workstations

Technological innovation has brought about a rapid evolution in the capabilities of bit-mapped graphics workstations over the past few years. This coupled with considerable reductions in costs have brought a device which used to be a shared public facility for special applications to the stage where it rivals a dumb terminal in price let alone function. In recognition of this fact, a high percentage of new computer software is now written specifically for workstations. Although dumb terminals are still generally supported the future is clear, and to maintain the highest ability to analyse, visualize and present scientific results, we need to embark upon a program to replace dumb terminals with workstations on as many desks as possible.

Some of the advantages of workstations are:

1) Flexible access to more than one host computer simultaneously.

2) Potential for high quality, high speed graphics.

3) Local processing power available. The amount is generally proportional to the cost of the workstation

4) Great power and flexibility for debugging new applications.

5) Desktop publishing and word-processing.

6) All of this in one box.

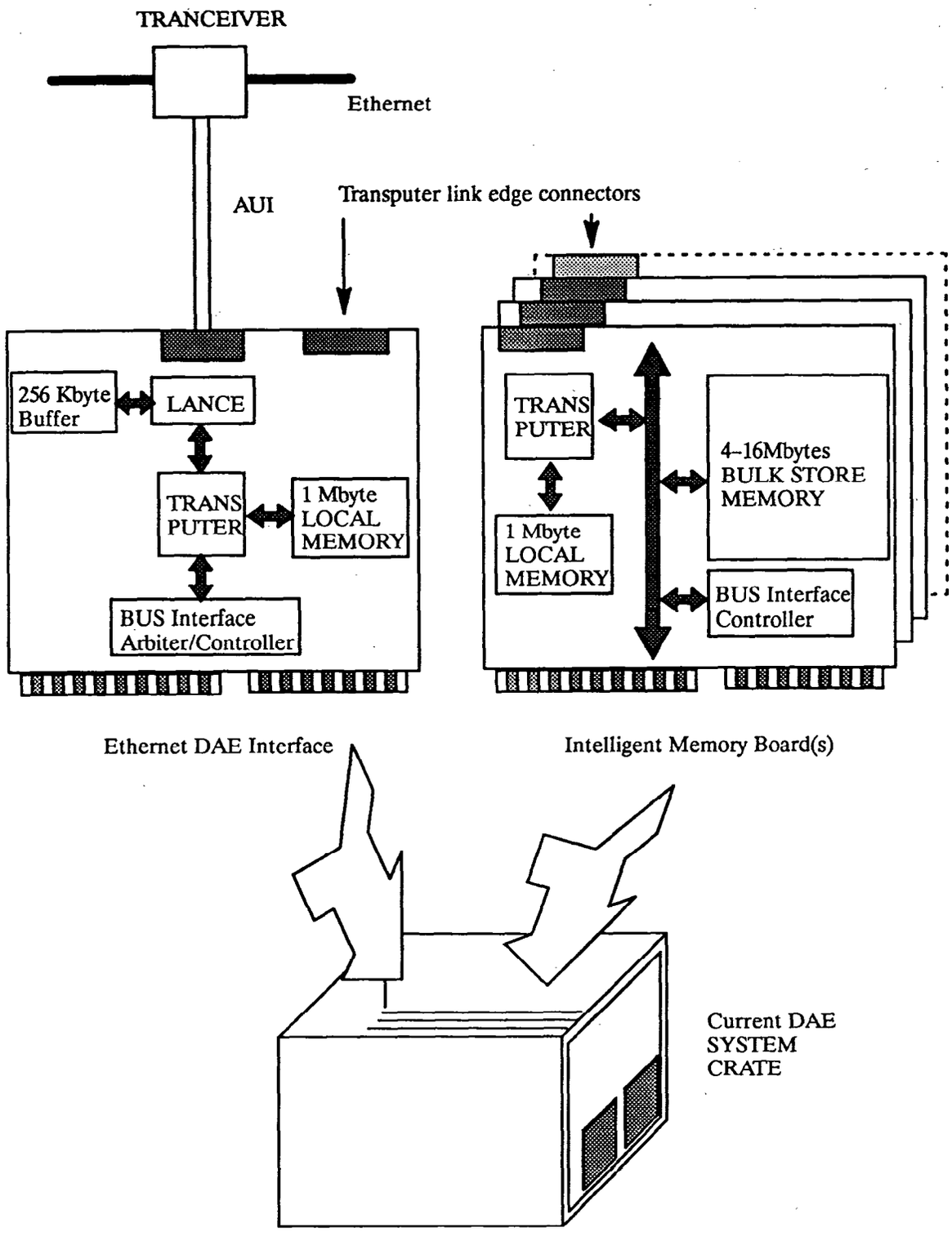

Figure 6 Soon to be available intelligent DAE cards

All of this functionality is useless unless the software controlling the workstation provides a consistent coherent interface for the user. Above all for the power of the workstation to be fully exploited, this interface must speed the interaction between the user and the system and, almost as important, be perceived by the user to do so. The same software must be common to any windowing device that we use. Currently he only viable alternative is X-windows

X windows

X-windows provides a complete working environment for a computer workstation user. Given sufficient processor power and memory it supports the creation and manipulation of any number of areas (i.e. windows) on the workstation screen including managing overlaps and overlays. Any window may occupy the full physical resolution of the workstation screen. Manipulation of the windows is performed using a pointing device such as a mouse with input coming from this device or the keyboard. The major concept behind X-windows is that processes involved with screen handling are logically divorced from the application being run. Consequently running an application breaks down into two processes: a) the X-client which is the core of the application where conventional interactive I/O statements are replaced by X-window subroutine calls ; b) the X-server which is responsible for the window display and interaction. The two communicate using a protocol called X-11 which may be run across any network link. This is illustrated schematically in figure 7a. A natural corollary is that the two processes need not necessarily run on the

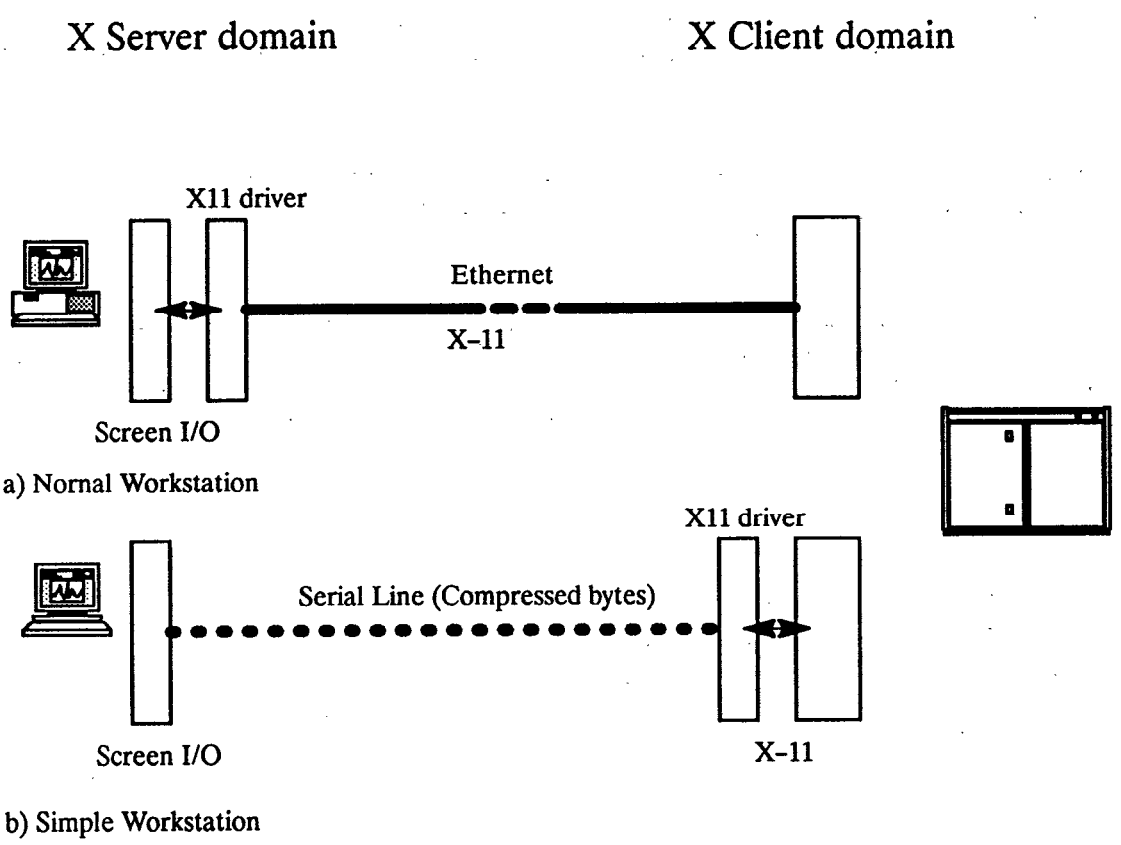

Figure 7 Schematic representation of the operation of X-windows

same computer or even one of the same type. Indeed one workstation may have a number of X-server windows each communicating with X-client processes running on a number of different remote machines. Figure 7b also illustrates a refinement to the system where the X-server software is divided into two components: an X-11 module running on the server computer which decodes the X-11 protocol into compressed bytes ready to be transmitted across a slow link such as an asynchronous serial line, and a remote windows I/O module which maps the bytes to screen operations. This scheme balances the disadvantage of imposing an increased load on the client machine against the fact that the workstation can be made cheaper to buy since it needs neither a relatively expensive ethernet

port nor a large processor capable of decoding the X-11 protocol.This approach should also enable operation of windows over a telephone line. A further interesting advantage to the use of X-windows is that appropriate software (e.g. HELIOS) is available for TRANSPUTER systems. This enables a natural and integrated approach to the control of the intelligent DAE.

A Recommended Solution

The penalty for the enhanced functionality of the X-windows interface is increased demand for processor power and memory. This is illustrated in figure 8 which shows some of the relative resource requirements for two types of X-client process. The first comparison is somewhat unfair since DECwrite has far greater functionality than WPSplus however it does represent the sort of application which will be run increasingly. Figure 8b however has great significance since the running of GENIE is a fundamental requirement for any ISIS computer. The future configuration of the PUNCH system should be that which provides the most cost-effective way to supply these necessary computing resources coupled with the best value workstations.

Broadly workstations divide into three categories:

a) Simple - these provide the minimum necessary the access most X-windows applications. All desks should have one of these at least.

b) Normal - as for simple, but they have some limited processing power in their own rite. Besides running X-client software, these may have some useful dedicated applications. Some examples are IBM 386 PC running spreadsheets or MACintosh II machines running Multifinder.

c) Super - these can be expensive, but they usually provide stunning processing performance and very high resolution screens. These machines are capable of providing all resources necessary for X-windows and may themselves be used as resource providers for category a) and b) workstations.

Details of some currently available workstations are given in Table 2. The prices are approximate and are inevitably out of date. They assume monochrome monitors and no internal disk drives. The usable performance is a number based on VAX780 figures (VUP's); a somewhat arbitrary reduction factor of 0.7 has been applied to non VMS systems to account for the difficulties in exploiting the full performance of alien architecture.

Workstation	Type	Resolution	O.S.	Cost	Usable perf. (VUP)	Network
OPTIMAX	Simple	900 x 500	None	£825	none	Serial
VT1000	Simple	1024 x 864	None	£2000	none	Ethernet
IBM 386 PC	Normal	1024 x 768	MS-DOS	£2200	0.5	Ethernet
Macintosh IICX	Normal	870 x 640	Apple	£5500	1.5	Ethernet
Vaxstation 3100	Normal	1024 x 864	VMS	£6000	3	Ethernet
SUN sparc SLC	Normal	1152 x 900	UNIX	£4500	4	Ethernet
Decstation 3100	Normal	1024 x 864	ULTRIX	£6000	6	Ethernet
Decstation 5000	Super	1280 x 1024	ULTRIX	£15000	12	Ethernet

Table 2 A rough comparison of currently available workstations

The HUB must be capable of supporting a reasonable mix of workstations of types a) and b). Any super workstation will look after themselves. An analysis of figure 8b reveals that X-GENIE requires little extra processor time but considerable extra memory and memory related resources compared with the current version of TEK-GENIE. Consequently to maintain our current level of service we need a HUB computer with perhaps slightly more processor performance but with greater physical memory and large capacity fast disk drives for paging. DEC have recently announced the VAX4000, an ideal machine for this purpose which is particularly optimized for distributed applications such as X-windows. Table 3 gives a brief summary of the major parameters of this system. Clearly in

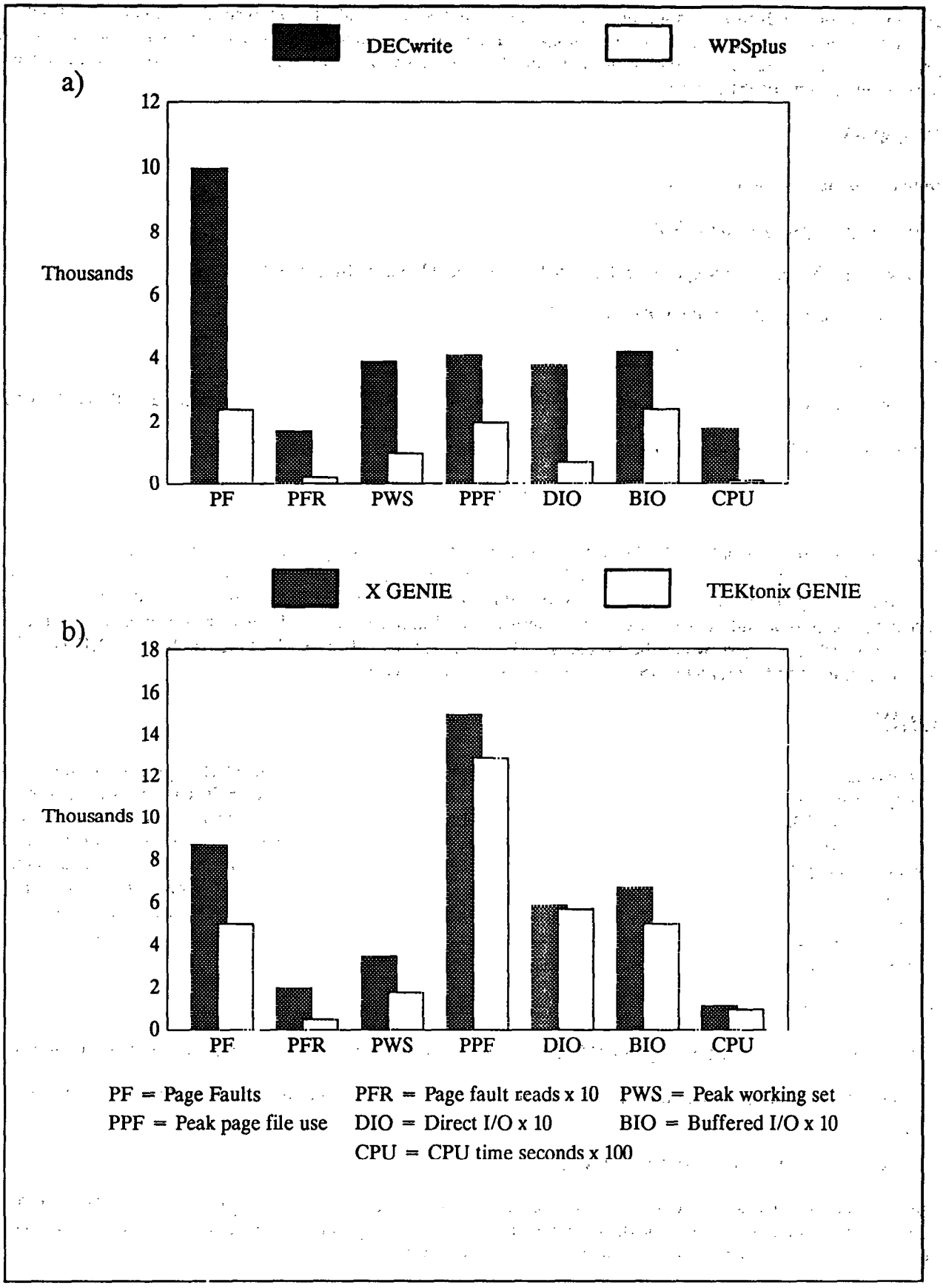

Figure 8 A comparison of the key system parameters with and without X-Windows two applications on a simple workstation

anticipation of our future computing requirements, this system should be duplicated to double the available resources. Judicious choice of disk technology would enable the possibility of disk sharing between the two processors. This in turn leads to considerable fault tolerance, a commodity which has been found to be of value during the running of ISIS up to now.

VAX 4000

Memory 32Mbytes -> 128Mbytes

Disk storage capacity - up to 28Gbyte

Bandwidths - Memory 40 Mbytes/sec, DSSI 8.0Mbytes/sec, Q-bus 3.3Mbytes/sec

CPU performance - 8 x VUP (cf. 8650 6.5VUP)

Power consumption - 0.9kw. (cf. 8650 8kw)

Cost of 1 x VAX 4000 and 5 Gbyte magnetic disk - about £100,000 as as interactive machine, £80000 as SERVER.

Maintenance - about £4500 per annum (cf 8650 £25000 per annum)

Table 3 Introducing the VAX 4000

Figure 9 illustrates a possible PUNCH configuration of the future. The diagram also shows an enhanced central data highway based on the 100Mbits/second FDDI fibre optic token ring. This, although not needed immediately, would be required to provide the necessary bandwidth for future data transfer. The computer configurations within instrument cabins would be associated into groups to avoid unnecessary local network traffic escaping onto the network backbone. These would be probably : a) MUSR,LAD,TEB,MARI b) POLARIS,EVS,SXD,HRPD c) SANDALS,PRISMA,LOQ,ROTAX and d) IRIS,TFXA,HET,CRISP.

UNIX

There is no doubt that the most powerful computers for a given cost are based on the UNIX operating system. As an example, we have found that the ULTRIX based DECstation 5000 gives twice the VAX 8650 processor performance for a portable FORTRAN application. Subjectively UNIX workstations like this also provide very rapid response for windows servers. Unfortunately the UNIX operating system, although much loved by computer scientists and very elegant in many concepts,, cannot be said to be user-friendly and it would be unrealistic to subject our users to it without copious health warnings. The editors are usually powerful and dangerous. Table 4 provides a few example commands and their VMS counterparts to emphasize their abstruse nature. Nevertheless we should incorporate some of these devices into the future PUNCH system to exploit their great processor power. The inclusion of a UNIX machine must be subject to strict criteria:

1) It must run X-windows..

2) Its native compilers, particularly FORTRAN, should compile standard VMS source code without modification

3) It must be possible to submit a job from VMS to the UNIX machine and retrieve the output in a well-defined, simple way.

4) Its speed should make 1,2 and 3 worthwhile.

DEC themselves have acknowledged the potential of UNIX(ULTRIX) computers in producing the VMS-ULTRIX connection software. This enables VMS and UNIX to share files transparently across a network as well providing for shared printer and batch queues. We should make full use of this.

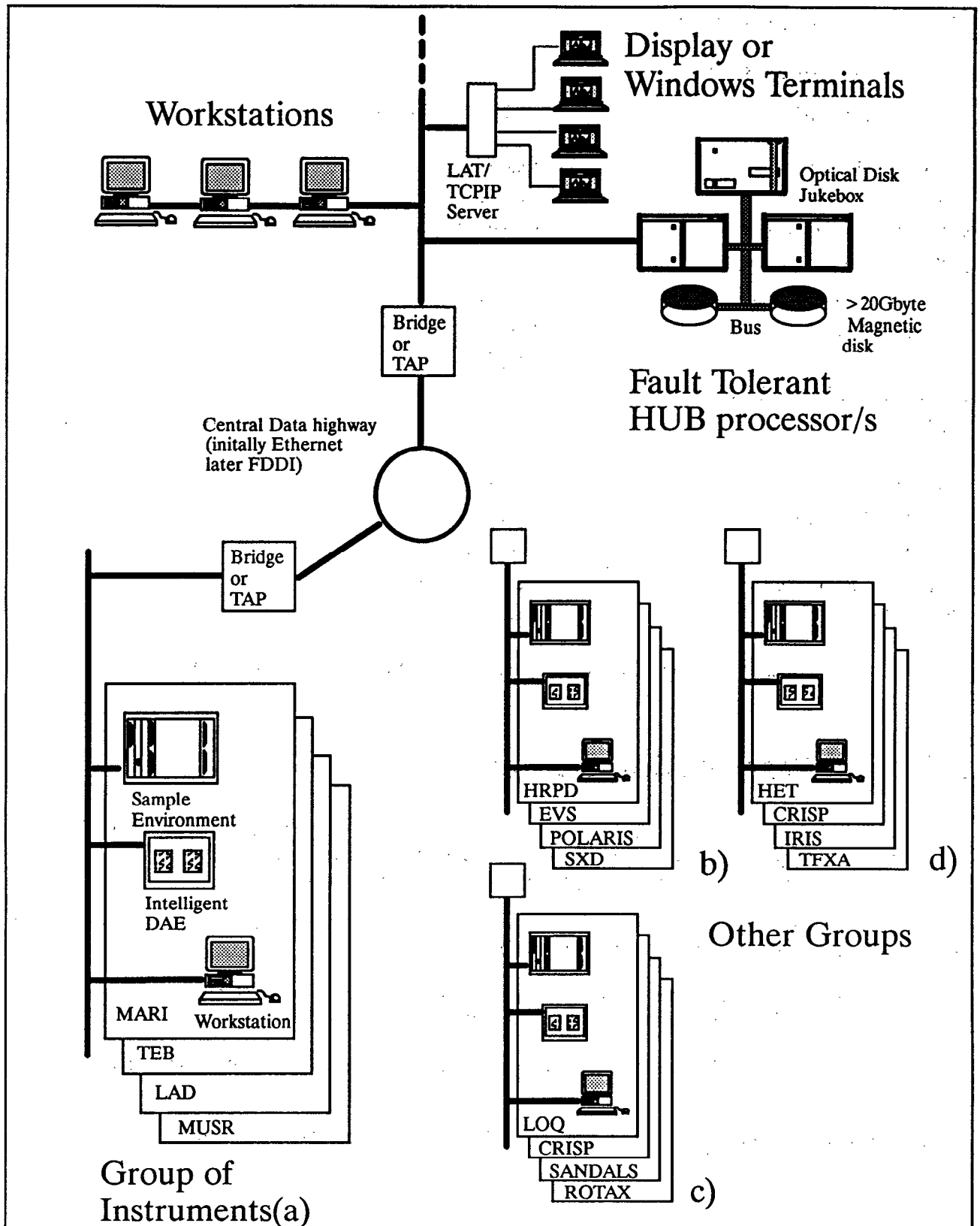

Figure 9 Probable future configuration of PUNCH

UNIX filename *file* - pathname/filename

VMS - DEV:[directory]filename

VMS COMMAND	UNIX COMMAND
$ APPEND *file1 file2*	$ cat *file1* > > *file2*
$ COPY *file1 file2*	$ cp *file1 file2*
$ CREATE/DIR *[dirname]*	$ mkdir *dirname*
$ DELETE *file*	$ rm *file*
$ DELETE/CONFIRM *file*	$ rm -i *file*
$ DIRECTORY	$ ls -a
$ DIR *file*	$ ls *file*
$ DIR/PROTECTION/DATE/SIZE	$ ls -al
$ EDIT *file*	$ ed,ex or vi file (to introduce a powerful unforgiving editor)
$ MAIL	$ mail
$ PRINT *file*	$ print (or lpr or pr) *file*
$ SHOW DEFAULT	$ pwd
$ SHOW PROCESS	$ printenv
$ SHOW TERMINAL	$ stty everything
$ TYPE *file*	$ cat *file*

Table 4 A comparison of some equivalent UNIX and VMS commands

A Future Workstation Screen

The final section of the paper is mainly to provoke thought and discussion. Within 1 year it will be possible given sufficient skilled manpower and resources to produce the underlying applications to format a workstation screen such as that shown in figure 10. The following list of features might be supported:

1) Operations such as changing a sample environment parameter value would be achieved by pointing at the relevant box, clicking a mouse button, and typing the new value on the keyboard.

2) The client applications would run on any one of a number of different hosts. As an example, the real-time picture of the detector would be the output of a process running on the intelligent DAE.

3) Producing wiring tables and any such gemetrical applications would be accomplished by simply pointing using a mouse.

When this notion was presented at a recent meeting of ISIS scientists it provoked a great diversity of response such as:

a) "I'm confused enough as it is!"

b) "It would make the control of instruments much easier for the users"

c) " Just typing a three-letter mnemonic in reply to a terminal prompt is far more efficient"

d) " My arm will get tired!"

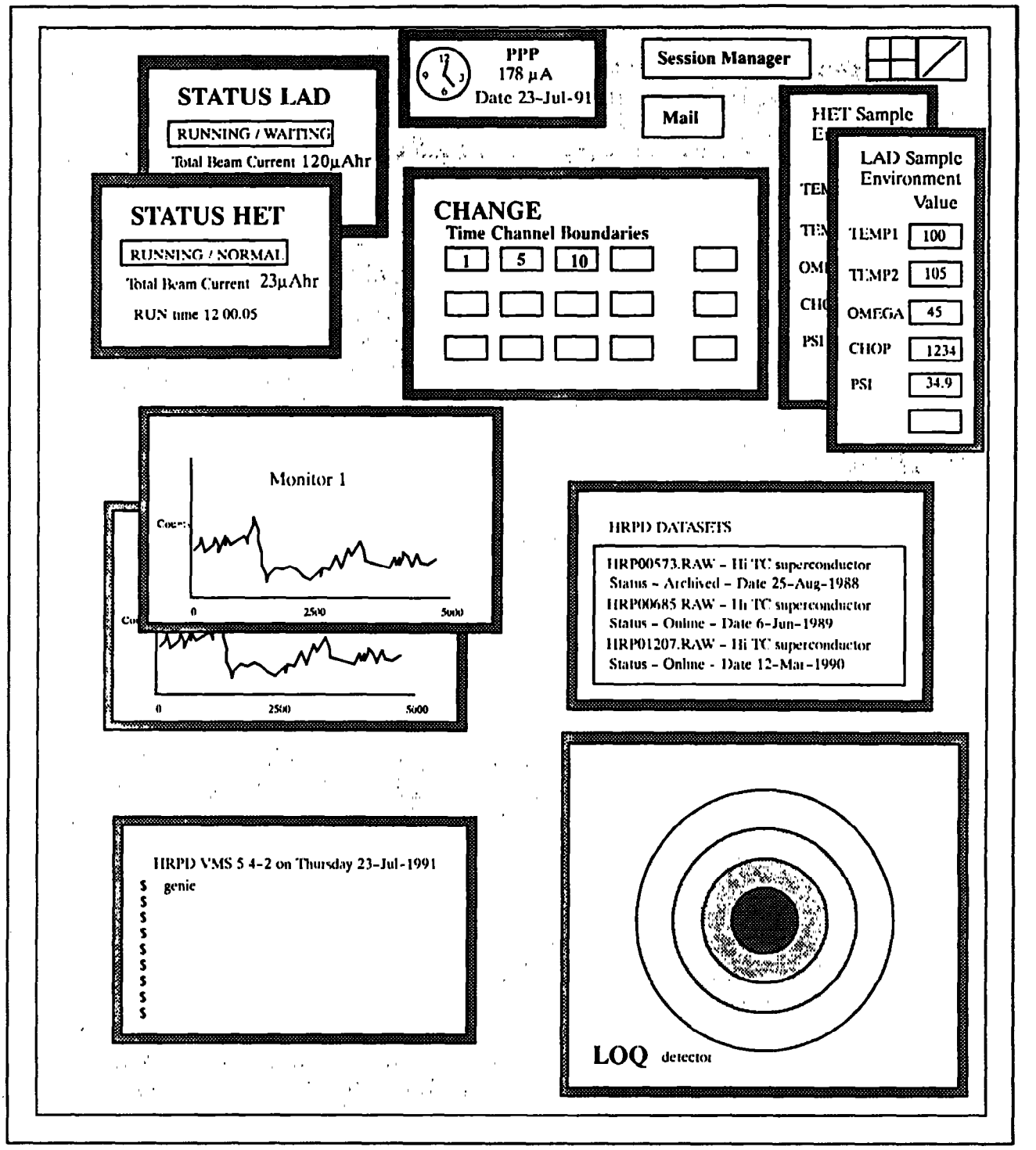
PPP
178 μA
Date 23-Jul-91
Session Manager
Mail
STATUS LAD
RUNNING / WAITING
Total Beam Current 120μAhr
STATUS HET
RUNNING / NORMAL
Total Beam Current 23μAhr
RUN time 12 00.05
CHANGE
Time Channel Boundaries
1
5
10
HET Sample
LAD Sample Environment
Value
TEMP1 100
TEMP2 105
OMEGA 45
CHOP 1234
PSI 34.9
Monitor 1
0
2500
5000
HRPD DATASETS
HRP00573.RAW - Hi TC superconductor
Status - Archived - Date 25-Aug-1988
HRP00685 RAW - Hi TC superconductor
Status - Online - Date 6-Jun-1989
HRP01207.RAW - Hi TC superconductor
Status - Online - Date 12-Mar-1990
HRPD VMS 5 4-2 on Thursday 23-Jul-1991
$ genie
LOQ detector

Figure 10

ICANS-XI International Collaboration on Advanced Neutron Sources
KEK, Tsukuba, October 22-26, 1990

Measurements of two-dimensional antiferromagnetic spin wave by using chopper spectrometer installed in pulsed neutron source

K.Yamada, M.Arai[1], A.D.Taylor[2], S.Hosoya[3], A.Sato, K.Nakajima, K.Ohyama, M.Kohgi, T.Nakane[3], T.Perring[4] and Y.Endoh

Department of Physics, Tohoku University, Sendai
1 National Laboratory for High Energy Physics, Tsukuba, Ibaraki
2 Institute for Materials Science, Tohoku University, Sendai
3 Rutherford Appleton Laboratory, Chilton, DIDCOT
4 Clarendon Laboratory, Oxford

ABSTRACT

Neutron inelastic scattering measurements on the chopper spectrometer MARI installed in the pulsed neutron source ISIS observed a well defined two-dimensional antiferromagnetic spin wave up to the zone boundary of La_2NiO_4 at 124±3 meV.

I.Introduction

Low dimensional antiferromagnetism provides a wide variety of challenging issues such as Haldane's conjecture[1)], the resonating-valence-bonding state[2)] and so on, relating with quantum effects on the spin fluctuations which are enhanced due to the low dimensionality. Two-dimensional antiferromagnetism has been especially put high light after the discovery of the superconductivity in 2D copper oxides because the 2D magnetic interactions between Cu spins have been regarded as one of the candidates for the microscopic interactions to create the Cooper pairs.

Triple-axis neutron scattering measurements first found out unique 2D spin fluctuations in La_2CuO_4 [3)], a mother compound providing a framework for Tc=40 K class oxide superconductor. These techniques also revealed characteristic change of the fluctuations by carrier doping.[4)] In order to prove the correlation of the magnetism with the superconductivity, more quantitative study in a wider q-ω space is necessary because a shift of the energy specrtum in $\chi(q,\omega)$ to higher energies is expected when the superconducting state appears. However, an extention of the energy region by using triple-axis technique is very difficult.

Instead chopper spectrometer coupled with pulsed neutron spallation source has been regarded as one of the better spectrometers in high energy region compared with triple-axis one especially for low dimensional magnetic systems because of the larger detector area, the better energy-resolution and the higher signal-to-noise ratio in high energy region. Therefore pulsed neutron scattering measurements on La_2CuO_4 and the related compound are of great interest not only to study the quantum effects on the 2D spin fluctuations but also to test the capability of the chopper spectrometer. Systematic studies on 2D antiferromagnetic systems with different spin values are also important to clarify the quantum nature of spin fluctuations in 2D antiferromagnets. We believe a series of 2-1-4 compound, La_2CuO_4 with S=1/2, La_2NiO_4 with S=1 and La_2CoO_4 with S=3/2 is the most ideal system to study the spin value dependence of the magnetism.

In the present paper results of pulsed neutron inelastic scattering measurements on single crystal of 2D antiferromagnet La_2NiO_4 are reported. By using chopper spectrometer we first observed a well defined spin-wave up to the zone-boundary and determined the in-plane exchange interaction J.

II.Experimental details

Single crystals of $La_2NiO_{4+\delta}$ with average dimensions of 8 mm$^{\phi}$x 35 mm were grown by a floating zone method in air. As-grown crystals are reduced in a CO_2 mixed with 0.1% CO gas flow at 1100 C for 30 h. This heat treatment reduced the excess oxygens in the as-grown crystals probably to δ~0.02 because the 3D Neel temperature changed from 60 K to 210 K.[5] At room temperature the crystal structure is of two phases, orthorhombic and probably tetragonal phase due to the small amount of excess oxygen. Below around 150 K, the crystal trnsforms into single tetragonal phase with $P_{42/ncm}$ symmetry.

Neutron inelastic scattering measurements were carried out on the chopper spectrometers INC and MARI installed in the spallation neutron sources in the National Laboratory for High Energy Physics and in Rutherford Appleton National Laboratory, respectively. The nominal energy-resolution is about 2.5% for INC and 1% for MARI. In chopper spectrometer coupled with pulsed neutron source, the monochromated incident pulsed beam is provided by a mechanical chopper synchronized with the repetition of the neutron pulse. The energy of incident neutron beam is tunable by changing the phase and/or the frequency of the rotation of the chopper. The scattered neutrons are detected by a large number of ^{3}He detectors aligned in a wide range of scattering angles in both horizontal and vertical directions. In this report we present the data obtained by the low angle-horizontal detector bank in MARI with the scattering angles from 3° to 9°. Other data taken by INC and by vertical detectors which can be used as complementary data will be presented in a separated paper.

For single crystal measurements, crystal orientation is important to extract useful and simple information. In the present study the data were taken by two types of crystal orientations, which are described in the following.

II-1 Orientation with magnetic Bragg lines perpendicular to k_i

In this orientation, hereafter we call type-A configuration, single crystals of La_2NiO_4 were aligned in a direction with the 2D magnetic Bragg lines perpendicular and with the a-axis parallel to the incident neutron momentum k_i as shown in Fig. 1. In time-of-flight (TOF)-scans, which correspond to k_f-scans, detectors pick up magnetic intensities when the scan trajectories cross the 2D spin wave dispersion surfaces. The energy difference in the TOF-scan trajectories of different detectors at the same 2D momentum transfer q_{2D} is less than 2 % for the transferred energies larger than 50% of the incident ones. Since a matching of energy resolution is achieved in this measurement, the intensities picked up by different detectors between at 3° and 9° can be binned up without degradation of the energy resolution. Several incident nuetron energies from 70 meV to 400 meV are carefully

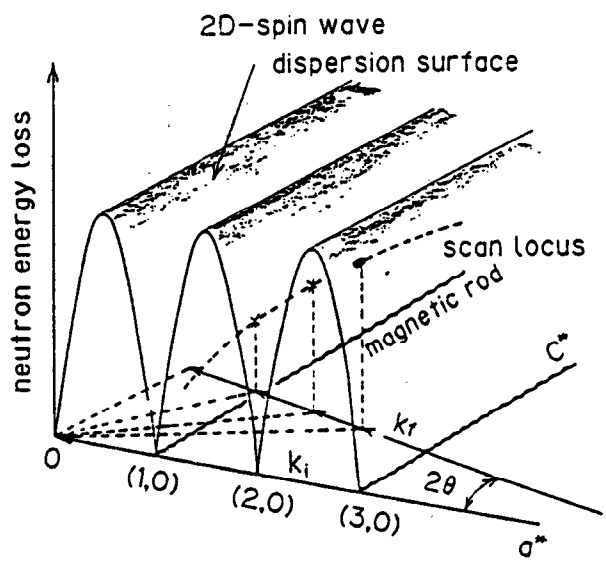

Fig. 1 Type-A orientation

selected to perform proper scans in a wide reciprocal space.

II-2 Orientation with magnetic Bragg lines parallel to k_f

In another orientation, type-B orientation, the crystals are aligned with the 2D magnetic lines parallel and with the a-axis perpendicular to k_f. In this orientation the TOF-scan corresponds approximately to constant q_{2D} scan as shown in Fig. 2. In the figure thick and fine lines denote dispersion curves and scan trajectories, respectively. With this orientation however, neutron counts of a small number of detector can be binned because the scan trajectories are extremely different for different scattering angles compared with type-A orientation.

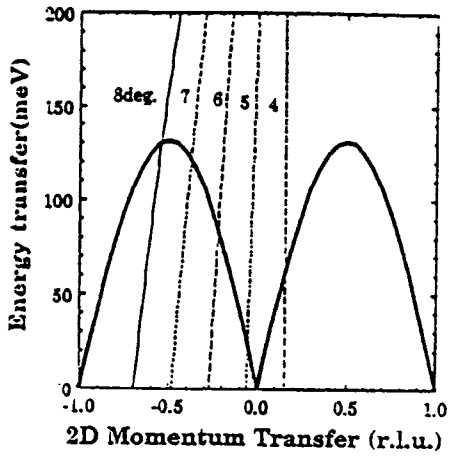

Fig. 2 Type-B orientation

III. Results and Discussion

In Fig. 3 we show a typical spectrum taken by the type-A orientation with an incident energy of 165 meV. The inserted figure shows the expanded one around 100meV. The neutron counts of the 28 horizontal detectors at both left and right hand side are binned in the figure. If observed peaks are originated by spin-wave excitations, they should be mapped on dispersion curves as well. Both TOF trajectories of different incident energies and antiferromagnetic spin-wave dispersion curves are drawn in Fig. 4. Closed circles or ellipsoids on the dispersion curves therefore, represent peak positions of spin-wave. Circles which are not mapped on dispersion curves are considered to be originated by phonon excitations. By changing the incident neutron energies we traced the spin-wave dispersion curves up to the zone-boundary at 124±3 meV. A full width at half maximum of the spin-wave peak at around 117 meV in Fig.3 is about 2.5 % of the transferred energy which is close to the energy-resolution. Due to the high energy-resolution of MARI even the low energy spin-wave peak around 40 meV exhibits a double-peak shape.

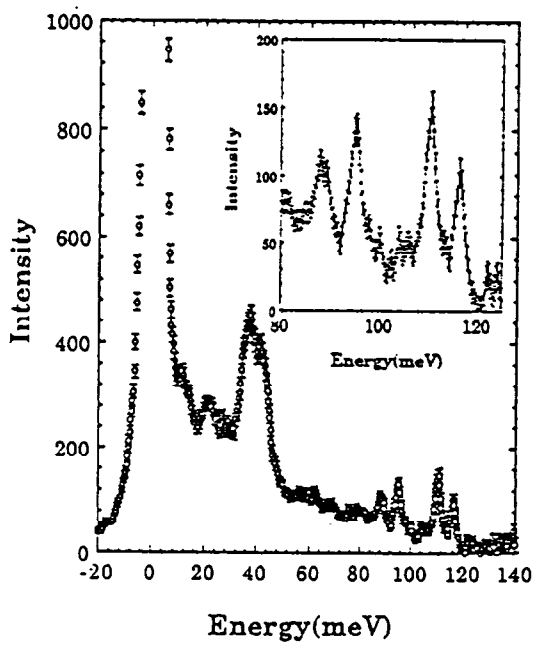

Fig. 3 A typical spectrum taken by type-A orientation

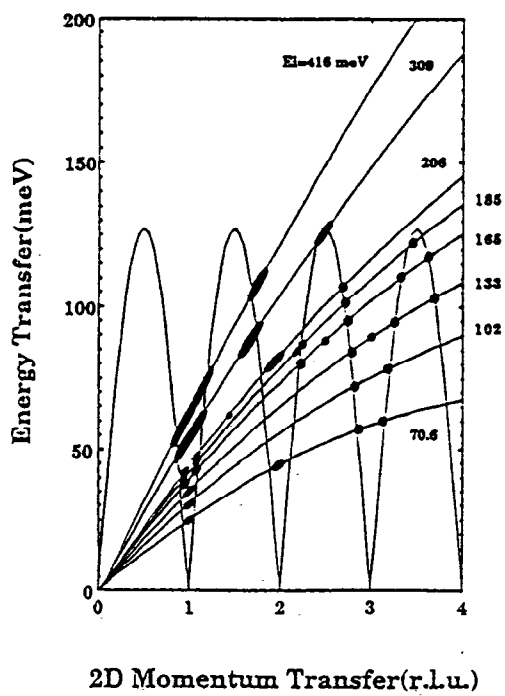

Fig. 4 Dispersion relation and scan trajectories for type-A orientation

A spectrum obtained by the type-B orientation is shown in Fig. 5 where the neutron events detected at the scattering angles between 7° and 8° are binned. Around 125 meV there is a remarkable change in the neutron intensites. As is expected from Fig. 3 and Fig. 4, this energy may correspond to the energy around the zone-boundary. However quality of the data is much worse than that of the type-A orientation due to the smaller number of detectors available in the type-B.

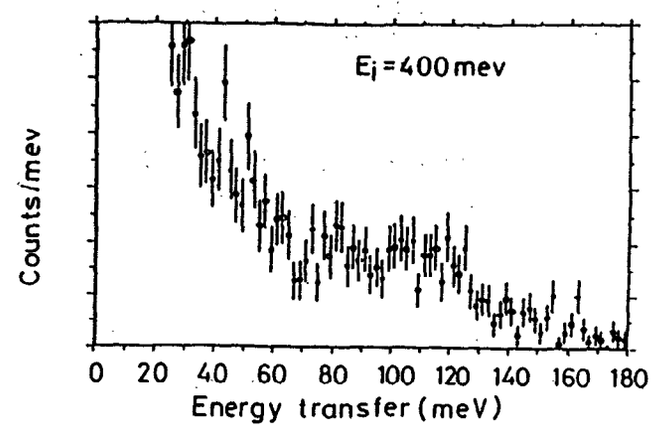

Fig. 5 A typical spectrum taken by type-B orientation

The peak positions of spin-wave observed by the type-A orientation almost perfectly sit on a simple dispersion relation for 2D square-lattice antiferromagnet,

$$\hbar\omega=4SJ\sin(\pi q_{2D}(\text{r.l.u.}))$$

with an in-plane exchange constant J between Ni^{2+} spins of 31± 1 meV. This value is consistent to that of 30 meV obtained from the two-magnon peak observed by Raman measurement [6] where the peak position is predicted to correspond to 6.7J by a spin-wave theory taking into magno-magnon interactions. Therefore within the preliminary data analysis, the observed spin-wave dispersion relation in La_2NiO_4 can be described by a simple spin-wave theory.

Analyses taking into the experimental resolution function will provide more detailed imformations such as the line-widths and the intensities in the magnetic excitations. Although the obtained J value is smaller by factor about three than that is expected in La_2CuO_4, we believe the same technique which is performed here is also well applicable in La_2CuO_4.

Acknowledgement

We would like to thank Z.Bowden and S.Onodera for their excellent technical support.

References

1) F.H.M.Haldane, Phys. Rev. Lett. **61**, 1029 (1988).
2) P.W.Anderson, Phys. Rev. **115**, 2 (1959) : Science **235**, 1196 (1987).
3) G.Shirane, Y.Endoh, R.J.Birgeneau, M.A.Kastner, Y.Hidaka, M.Oda, Y.Enomoto, M.Suzuki, and T.Murakami, Phys. Rev. Lett. 59 (1987), 1613.
4) G.Shirane, R.J.Birgeneau, Y.Endoh, P.Gehring, M.A.Kastner, K.Kitazawa, H.Kojima, I.Tanaka, T.R.Thurston, K.Yamada, Phys. Rev. Lett. **63** (1989), 330.
5) D.J.Buttrey, Ph.D. Thesis, Purdue University, W.Lafayette, Indiana, 1984.
6) S.Sugai, M.Sato, T.Kobayashi, J.Akimitsu, T.Ito, H.Takagi, S.Uchida, S.Hosoya, T.Kajitani, and T.Fukuda, Phys. Rev. B**42** (1990), 1045.

ICANS-XI International Collaboration on Advanced Neutron Sources
KEK, Tsukuba, October 22-26, 1990

Crystal Analyzer Type Spectrometer LAM-D at KENS Spallation Thermal Neutron Source

K. Inoue,[1] T. Kanaya,[2] Y. Kiyanagi,[1] K. Shibata,[3] K. Kaji,[2] S. Ikeda,[4] H. Iwasa,[1] and Y. Izumi[5]

1) Department of Nuclear Engineering, Hokkaido University, Sapporo 060, Japan.
2) Institute for Chemical Research, Kyoto University, Uji, Kyoto-fu 611, Japan.
3) Institute for Material Research, Tohoku University, Sendai, Miyagi-ken 980, Japan.
4) National Laboratory for High Energy Physics, Tsukuba, Ibaraki-ken 305, Japan.
5) Macromolecular Research Laboratory, Faculty of Engineering, Yamagata University, Yonezawa, Yamagata-ken 992, Japan

We constructed the inelastic scattering neutron spectrometer LAM-D covering the energy transfer range up to 300 meV with the resolution $\Delta\varepsilon/E_1$ less than 6%. The basic princile of LAM-D is the same as the quasielastic scattering spectrometers LAM-40 and LAM-80 at KENS.

Introduction

In the previous paper [1], we have reported two crystal analyzer type quasielastic neutron scattering spectrometers LAM-40 and LAM-80 which have been installed at the KENS spallation cold neutron source at the National Laboratory for High Energy Physics (KEK), Tsukuba.[2] LAM-40 with PG analyzer mirrors can cover the energy transfer range up to 10 meV with a conventional energy resolution $\Delta\varepsilon$=0.2 meV at the elastic position. LAM-80 with PG mirrors has a rather high energy resolution of $\Delta\varepsilon$=0.02 meV while the energy transfer range is limited below 0.5 meV. Applying mica crystals, we have recently made a great progress on LAM-80 in the energy resolution. This new machine LAM-80ET has been reported elsewhere.[3]. The energy transfer ranges covered by the two spectrometers are not so narrow compared with other machines which have the same order of the energy resolution.[4] However, it is often essential to measure in a wide energy range up to several hundred meV for some physical phenomena such as molecular vibrations. At the present stage, it is probably impossible to design a single quasi- and inelastic spectrometer covering such a wide energy range with high energy resolution. Therefore, in addition to LAM-40 and LAM-80, we have designed and constructed an inelastic scattering spectrometer (LAM-D) to cover the energy range up to 300 meV with the energy resolution of $\Delta\varepsilon/E_1$

less than 6% through the whole energy range. The basic principle of LAM-D is the same as LAM-40 and LAM-80 while some special considerations have been made on the design of LAM-D for the high energy transfer measurements. Prototype of LAM-D was installed at the KENS thermal neutron beam hole (H-6) in 1982 and the final version is now in practical use on the thermal beam hole (H-9). Combination of the three spectrometers LAM-D, LAM-40 and LAM-80 is very powerful for investigation of dynamics of various molecular systems.

In this paper, we will first recall the basic principle of the LAM-type spectrometer and clarify the characteristics of LAM-D comparing with LAM-40 and LAM-80 in sec.2 and the description and the performance of LAM-D will be given in secs. 3 and 4 including some experimental results.

2. Basic Principle of LAM-type Spectrometer

General layout of the LAM-type spectrometer using a pulsed neutron source is illustrated in Fig.1, which is an inverted geometry quasi- and inelastic spectrometer. Pulsed neutrons with a wide energy distribution emitted from the thermal or cold moderator (H_2O at room temperature and CH_4 at 20K for thermal and cold moderators, respectively, at KENS) are incident on a sample after flying through the first flight path (l_1) and the scattered neutrons with a fixed energy are selected by analyzer mirrors and detected by neutron counters. The distance from the sample to the analyzer mirror is the same as that from the mirror to the detector, which is a half of the second flight path length (l_2). Measurement of energy transfer of neutrons is performed by a time-of-flight (TOF) technique. In the case of TOF measurements, the energy resolution required is attained by selecting an appropriate length of neutron flight path. The energy resolution of the crystal analyzer mirror can be selected by adjusting the Bragg angle. The combination of devices enabled us to design a set of quasi- and inelastic spectrometer with large flexibility of performance.

For the LAM-type spectrometer, the time spectrum of the scattered neutrons from the sample at a scattering angle θ is given by [1,5]

$$\eta(t,\theta) = \mathrm{const}\iint\phi[E_1, t - l_2/(2E_2/m)^{1/2}]\,\sigma(E_1 \rightarrow E_2, q)R(E_2)dE_1dE_2 \qquad (1)$$

where $\phi(E_1,t_1)$ is the incident neutron flux at time t_1 into the sample, $\sigma(E1 \rightarrow E2,\theta)$ is the incoherent differential scattering cross-section, $R(E_2)$ is the energy resolution function of the crystal analyzer mirror, m is the neutron mass, and l_2 is the average flight path length of the scattered neutrons.

The quantities measured are the energy transfer ε and the scattering vector Q defined by

$$\varepsilon = E_1 - E_2 \tag{2}$$

and

$$\mathbf{Q} = \mathbf{k}_1 - \mathbf{k}_2 \tag{3}$$

where $\mathbf{k}_1$ and $\mathbf{k}_2$ are the wave number vectors of the incident and the scattered neutrons, respectively and Q^2 is given by

$$Q^2 = (2m/h^2)[E_1 + E_2 - 2(E_1E_2)^{1/2}\cos\theta\,] \tag{4}$$

The energy resolution of the LAM-type spectrometer is given by [1,5]

$$\Delta\varepsilon = 2E_1[(\Delta t_z{}^2 + \Delta t_1{}^2 + \Delta t_2{}^2)/t_1{}^2 + (E_2/E_1)^2\{(\cot\theta_B\Delta\theta_B)^2 + (\Delta\tau/\tau)^2\}]^{1/2} \tag{5}$$

where Δt_z is the pulse width at half-maximum dependening on the neutron energy and Δt_1 and Δt_2 are the variances of the flight time of neutrons due to the fluctuations of the flight path length l_1 and of the analyzed energy E_2, respectively. θ_B is the Bragg angle of the analyzer mirror and $\Delta\theta_B$ is the angular spread of the Bragg angle. $\Delta\tau$ is the variance of the reciprocal lattice vector τ of the analyzer crystal due to the limitation of the number of lattice planes contributing to the reflection. [5] The first, second and third terms in the right hand side of eq.(5) are the variances in the time-fo-flight measurement and the forth and fifth terms are due to the analyzer mirror resolution. The first term $\Delta t_z/t_1$ was calculated as a function of the incident neutron energy E_1 and the result is shown in Fig.2. In this calculation the first flight path length was taken to be 4.3 m. This term decreases with increasing the incident energy E_1 because the pulse width of neutrons Δt_z decreases with increasing E_1. In the case of high resolution quasielastic machines such as LAM-80, this contribution to the energy resolution is serious so that long flight path is essential to diminish it. The second term which is determined by the sizes of the neutron beam and the sample is small enough compared with other terms in our case as shown in Fig.2. The third term $\Delta t_2/t_1$ was also calculated as a function of E_1, taking l_1 and l_2 as 4.3 m

and 0.6 m, respectively, and the average analyzing energy as 4.4 meV. In contrast to the first term, it increases with E_1. In the case of inelastic spectrometers covering high energy region like LAM-D, this contribution should be diminished without sacrificing the other contributions to the resolution. This term can be rewritten as

$$\Delta t_2/t_1 = (1/2)(l_2/l_1)(E_1/E_2)^{1/2}(\Delta E_2/E_2) \qquad (6)$$

According to eq.(6), in order to achieve higher energy resolution in the high energy region, it is necessary to decrease the second flight path length l_2. Therefor, l_2 of LAM-D was designed to be 0.54 m, which is much shorter than that of LAM-40 and LAM-80 (1.2m). It is necessary to evaluate the spread of the Bragg angle $\Delta\theta_B$ for calculation of the forth term. The resolution function of the analyzer mirror $R(\theta_B)$ can be calculated by the following equation [5],

$$R(\theta_B) = \iiint p(r,\Sigma,S)\ |r-\Sigma|^{-2}\ |\Sigma-S|^{-2} \times \delta[\ \theta_B - \hat{\theta}_B(r,\Sigma,S)\ ]\ drd\Sigma dS \qquad (7)$$

where $\hat{\theta}_B(r,\Sigma,S)$ is the Bragg angle determined by the positions on the sample r, the mirror Σ and the counter S, and $p(r,\Sigma,S)$ is a factor representing efficiency due to the projection of each plane and the mosaicness of the crystals. The integrations are performed with respect to the volume of the sample, the surface of the mirror and the surface of the counter window. $R(\theta_B)$ calculated for the Bragg angle 39 deg is shown in Fig.3. In the calculation, the size of the crystal pieces is 12 mm x 12 mm and 2 mm in thickness with 1.2 deg mosaicness and the total number of the pieces is 56; they are arranged in seven columns. The average second flight path length was taken to be 0.6 m and the cylindrical sample is 14 mm in diameter, 0.1 mm in thickness and 60 mm in height. The window size of the counter is 14 mm in width and 60 mm in height. The spread of the Bragg angle was determined to be 1.1 deg from $R(\theta_B)$ in Fig.3. Using this value, the E_1 dependence of the forth term $(E_2/E_1)\cot\theta_B\Delta\theta_B$ was calculated in Fig.2. The contribution of this term is large in the low energy region while it is not so serious in the high energy region. In the case of LAM-D, the fifth term $(\Delta\tau/\tau)$ is small enough to neglect as compared with the other terms as shown is Fig.2.

Based on the results in Fig.2, we calculated the overall resolution of the spectrometer $\Delta\varepsilon/E_1$ through eq.(5). The results are shown as a function of the

incident energy E_1 in Fig.4 where $\Delta\varepsilon/E_1$ for $l1$=8.6 and 12.9 m are also indicated.

3. Description of the LAM-D Spectrometer

Fig.5 illustrates the configuration of the LAM-D spectrometer. The spectrometer is installed at the H-9 thermal neutron beam hole at KENS, which sees the thermal neutron moderator (H_2O at room temperature). Energy distribution of neutrons from the thermal beam hole is shown in Fig.6. The flight path from the moderator to the sample is evacuated and the length (l_1) is 7.25 m.

Each analyzer mirror is made from 56 pyrolitic graphite (PG) crystal pieces of 12 mm x 12 mm x 2 mm in size with a mosaic spread of 1.2 deg. As seen in Fig.5, two analyzer mirrors are symmetrically mounted at the scattering angle 35 deg and the other two at 85 deg. The 15 cm beryllium (Be) filters, which are cooled by liquid nitrogen, diminish the higher order reflections from the analyzer crystals. The length of the Be filter was determined by Monte Carlo simulation for transmission of neutrons with total atomic-cross section of both σ_t=0.5 and 7.5 barns, which correspond to those below and above the Be cutoff wavelength [6]. The results of the simulation is given in Fig.7.

The set of the mirrors and Be-filters is housed in an evacuated container surrounded by neutron shield made of borated resin and cadmium sheets. Moreover, each analyzer mirror has its own inner shield.

A hollow cylindrical shape was adopted for the sample container to assure identical geometrical conditions for every analyzer mirrors. The typical dimensions of the sample are 14 mm in diameter and 60 mm in height. These dimensions were determined by the optimization condition calculated between the energy resolution and the counting efficiency. The thickness of the sample depends on the scattering and absorbing cross section. It is essential to use a thin sample in order to avoid self-shielding and multiple scattering in the sample . For example, in the case of water, a sample of 0.1 mm thick is desirable. The outer and inner walls are made of aluminum of 0.25 mm in thickness. This container can be also used for measurements on the LAM-40 and LAM-80 spectrometers.

4. Performance

Raw spectra of vanadium measured with LAM-D are shown in Fig.8(a) and (b) for scattering angles of 35 deg and 85 deg, respectively. Each spectrum was obtained by summing up two spectra measured at the symmetrical position with the same scattering angle. The thickness of the vanadium sample is 2 mm and the measureing time is 8 hours. The peak counts are given in the figures which enable us to estimate the intensity performance of the LAM-D spectrometer.

Expanding the spectra in the inelastic region in Fig.8, inelastic scattering from phonons in vanadium is clearly observed. Fig.9 shows the spectrum of vanadium measured with LAM-D without the 15 cm Be-filter. The higher order reflections from the analyzer mirror are very strong in the inelastic region. For example, the second peak is about 5 times larger than the first reflection peak. It is because the intensity of incident neutron at 4.4 meV (elastic energy) is much weaker than that for the second and third reflection as shown in Fig.6. The results indicate that the 15 cm Be-filter works efficiently.

Full-width at hlaf-maximum (FWHM) of the elastic peak evaluated from vanadium spectrum is 0.40 meV, which agrees with the theoretical value in Fig.4. It means that the evaluation of the energy resolution through eq.(5) works very well in the low energy region. However, it is difficult to confirm whether the estimation of resolution in the high energy region is correct or not, since the energy resolution cannot be measured directly in the high energy region. As shown in Fig.2, the resolution is mainly governed by the term $\Delta t_2/t_1$ which is determined by ΔE_2 and by convolution of ΔE_2 and $\Delta t_z/t_1$ in high and low energy regions, respectively. In the low energy region, as shown above, the theoretical evaluation works well. This probably means that we can precisely calculate ΔE_2 and therefor it is expected that the evaluation of the resolution in the high energy region also works well.

Inelastic scattering spectra from trans-1,4-polychloroprene (PCP) at 10 K are shown in Fig.10 where the spectra from the container are also indicated after normalization by the monitor counts. The thickness of the sample is 0.1 mm and the measuring time is 8 hours. These raw spectra make us to conclude that the performance of LAM-D for the S/N ratio is extremely good up to 300 meV. The intense signal below 30 TOF channel is due to fast neutrons with energy higher than Cd cut-off energy. Fortunately, this fast neutron background does not contaminate the sample data below 300 meV. In the PCP spectra we can clearly recognized C-H stretching at 2950 cm^{-1} and some

sharp peaks which agree with the results of normal coordinate calculation for a single chain of PCP.[7]

5. Conclusion

The spectrometer LAM-D with combination of the pulsed thermal neutron source have demonstrated satisfactory performance for the measurements of inelastic scattering in the energy range up to 300 meV. The basic principle of LAM-D is the same as that of the quasielastic spectrometers LAM-40 and LAM-80, so that the data reduction methods developed for LAM-40 and LAM-80 can be applied to data of LAM-D with small modifications. With combination of the three spectrometers, we can cover the energy range form 1μeV to 300 meV. It is very powerful to investigate condensed matter physics.

References

[1] K. Inoue, Y. Ishikawa, N. Watanabe, K. Kaji, Y. Kiyanagi, H. Iwasa and M. Kohgi, *Nucl. Instr. and Meth.*, **A238**, 401(1985).

[2] Y. Ishikawa, *KENS Report-IV*, National Laboratory for High Energy Physics, Tsukuba, Japan (1983).

[3] K. Inoue, T. Kanaya, Y. Kiyanagi, S. Ikeda, K. Shibata, H. Iwasa, T. Kamiyama and Y. Izumi, in the proceedings.

[4] M. Bee, Quasielastic *Neutron Scattering: Principles and Applications in Solid State Chemistry, Biology and Materials Science*, Adam Hilger, Bristol and Philadelphia, 1988.

[5] K. Inoue, Y. Kiyanagi, H. Iwasa and Y. Sakamoto, *Nucl. Instr. and Meth.*, **178**, 459(1980); K. Inoue, Y. Kiyanagi and H. Iwasa, *Nucl. Instr. and Meth.*, **192**, 129(1982).

[6] G. E. Bacon, *Neutron Diffraction*, Clarendon Press, Oxford, 1975.

[7] T. Kanaya, M. Ohkura and K. Kaji, *Bull. Inst. Chem. Res., Kyoto University*, **67**, 68(1989).

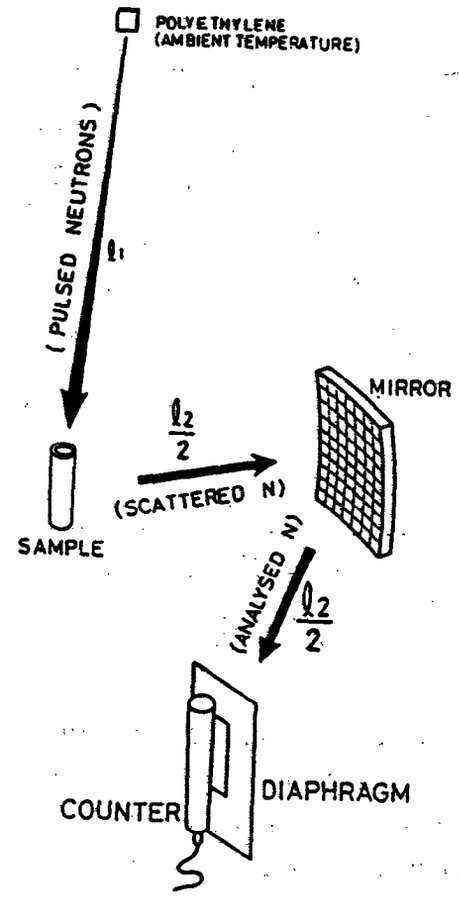

Fig.1. General layout of the LAM-type spectrometer using a pulsed neutron source. It is an inverted time-of-flight quasi- and inelastic scattering spectrometer.

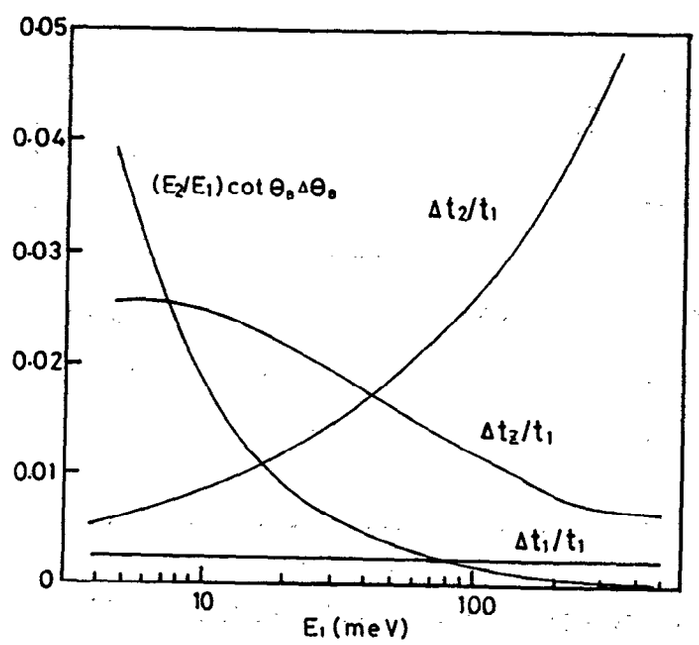

Fig.2. Incident energy dependence of each variance contributing to the enenrgy resolution [see eq.(5)].

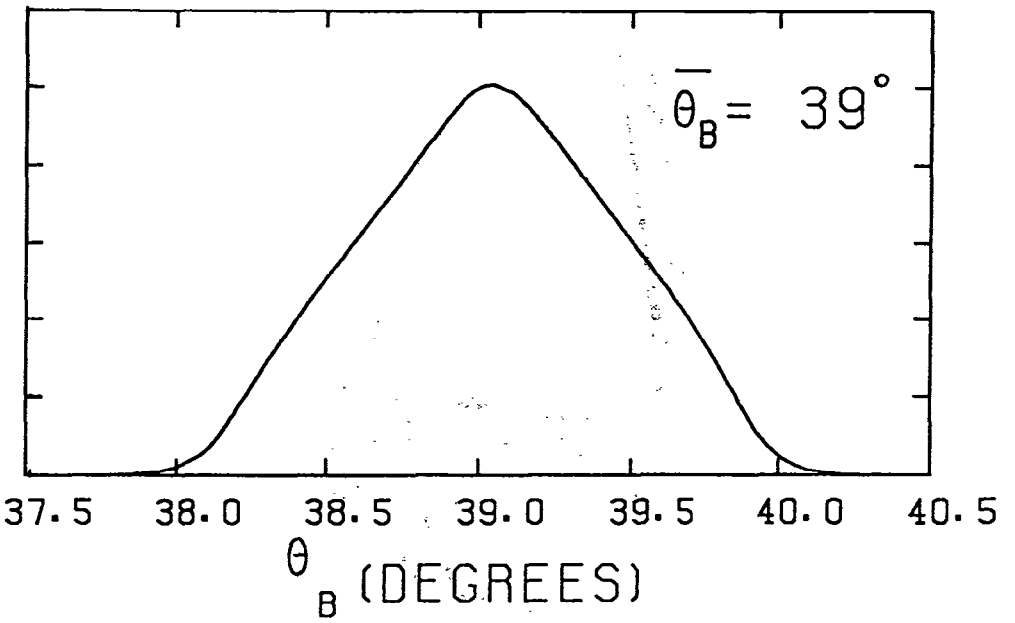

Fig.3. Calculated resolution function of the analyzer mirror for the Bragg angle 39 deg. The size of the sample is 14 mm in diameter, 0.1 mm in thickness and 60 mm in height. The number of the pieces of PG crystals of 12 mm x 12 mm x 2 mm in size is 56. The size of the counter window is 14 mm in width and 60 mm in height.

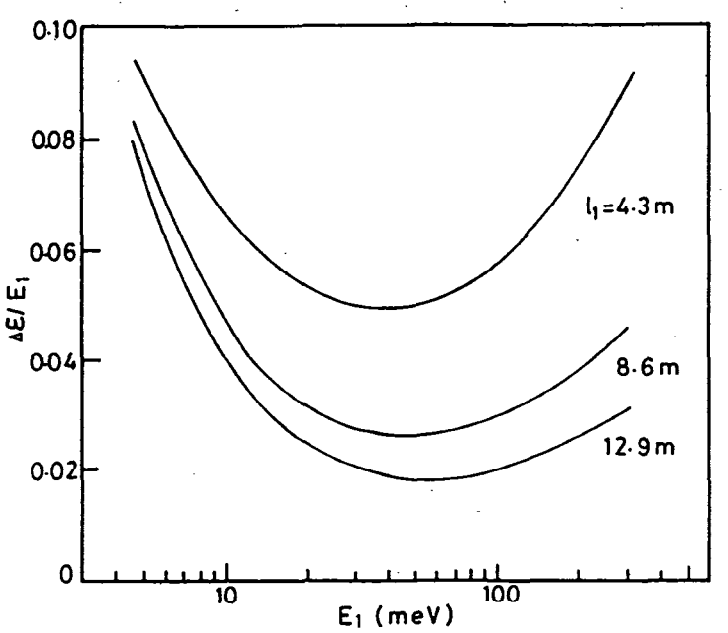

Fig.4. Incident energy dependence of overall resolution of LAM-D calculated for l_1=4.3, 8.6 and 12.9 m. Other parameters are the same as in Fig.2.

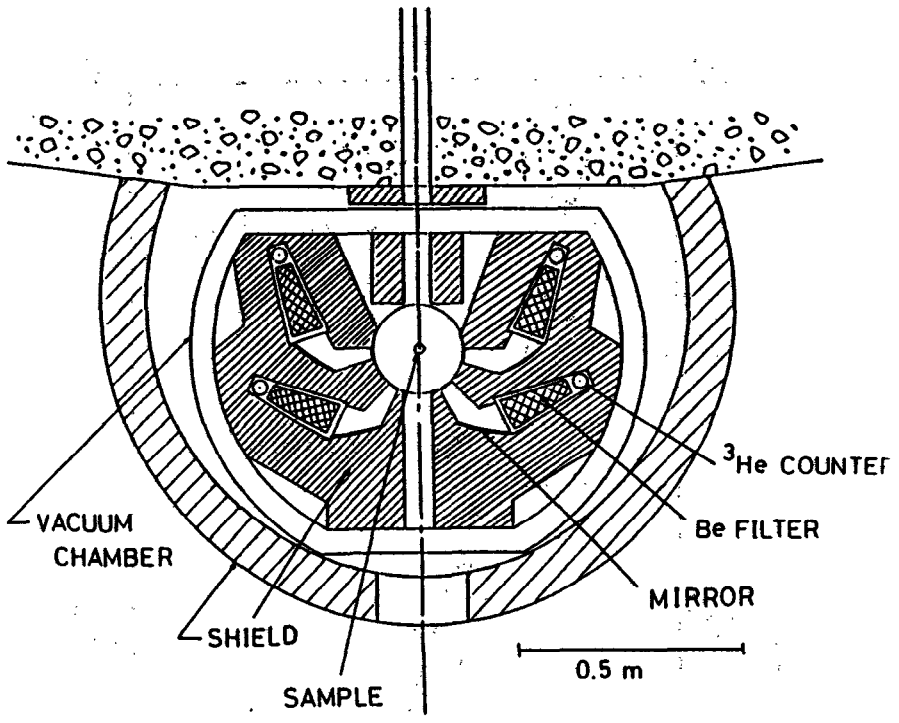

Fig.5. The inelastic spectrometer LAM-D.

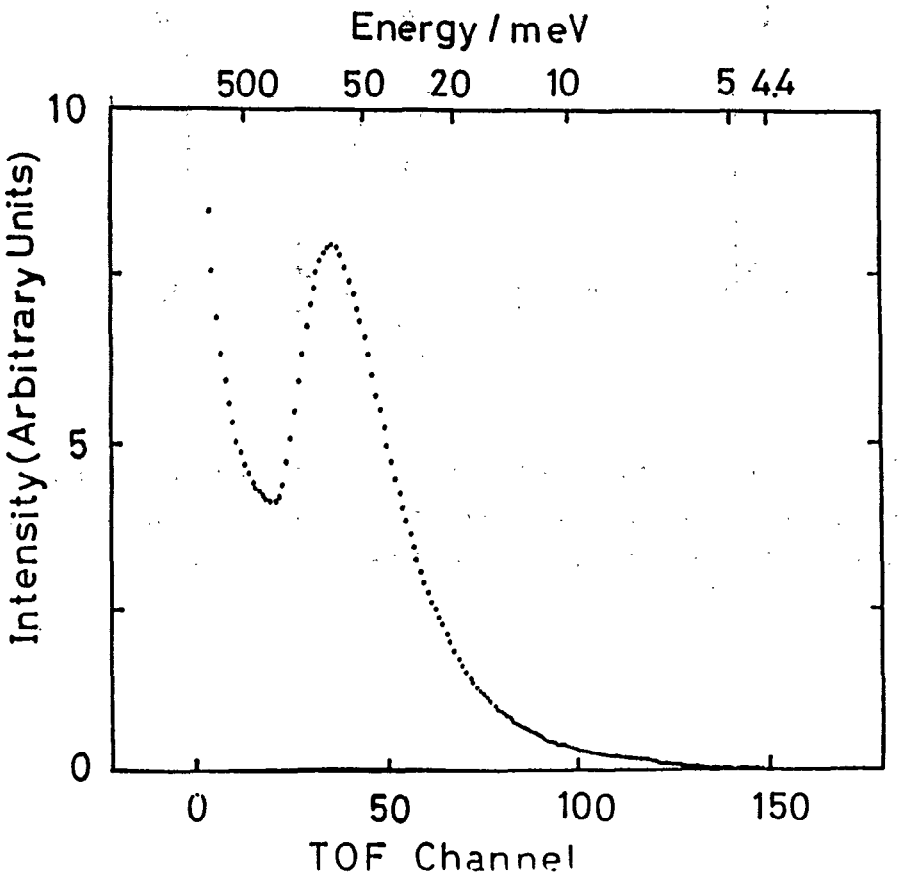

Fig.6. Energy distribution of neutrons from KENS thermal neutron source; H_2O at room temperature.

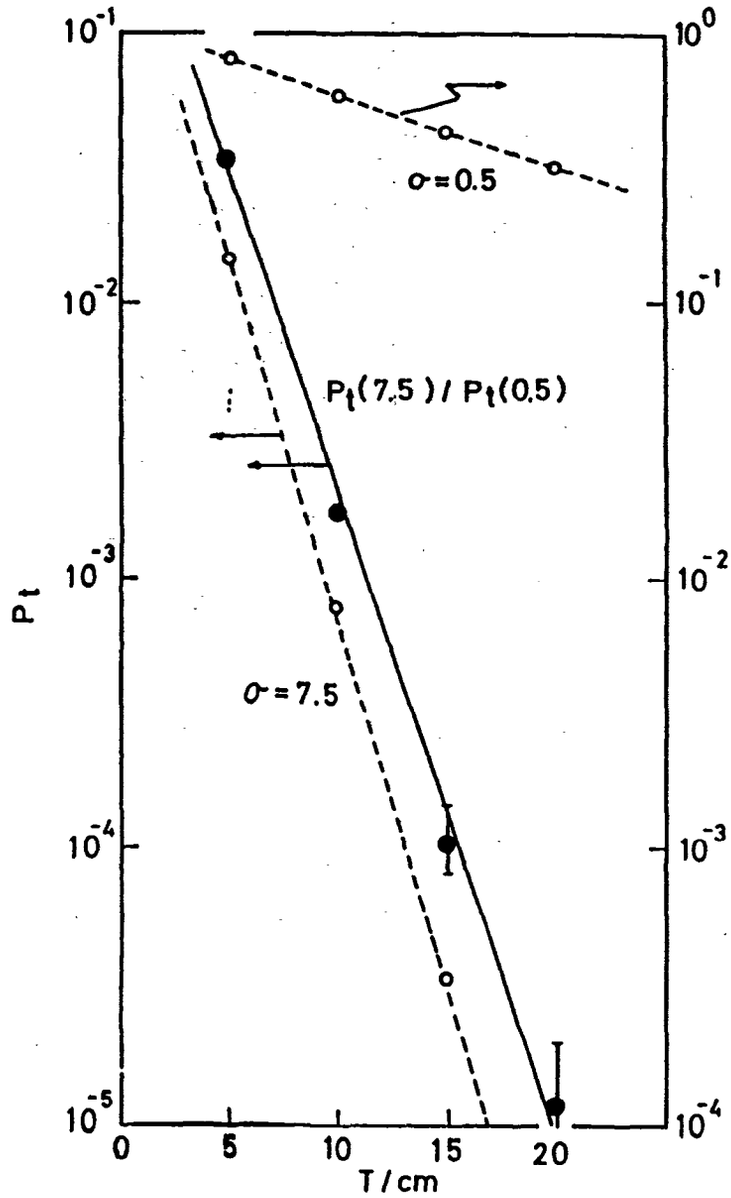

Fig.7. Results of the Monte Carlo simulation for neutron transmission through Be-filter. Calculation was performed for neutrons below and above the Be cutoff wavelength. The corresponding atomic cross sections are 7.5 and 0.5 barns, respectively.

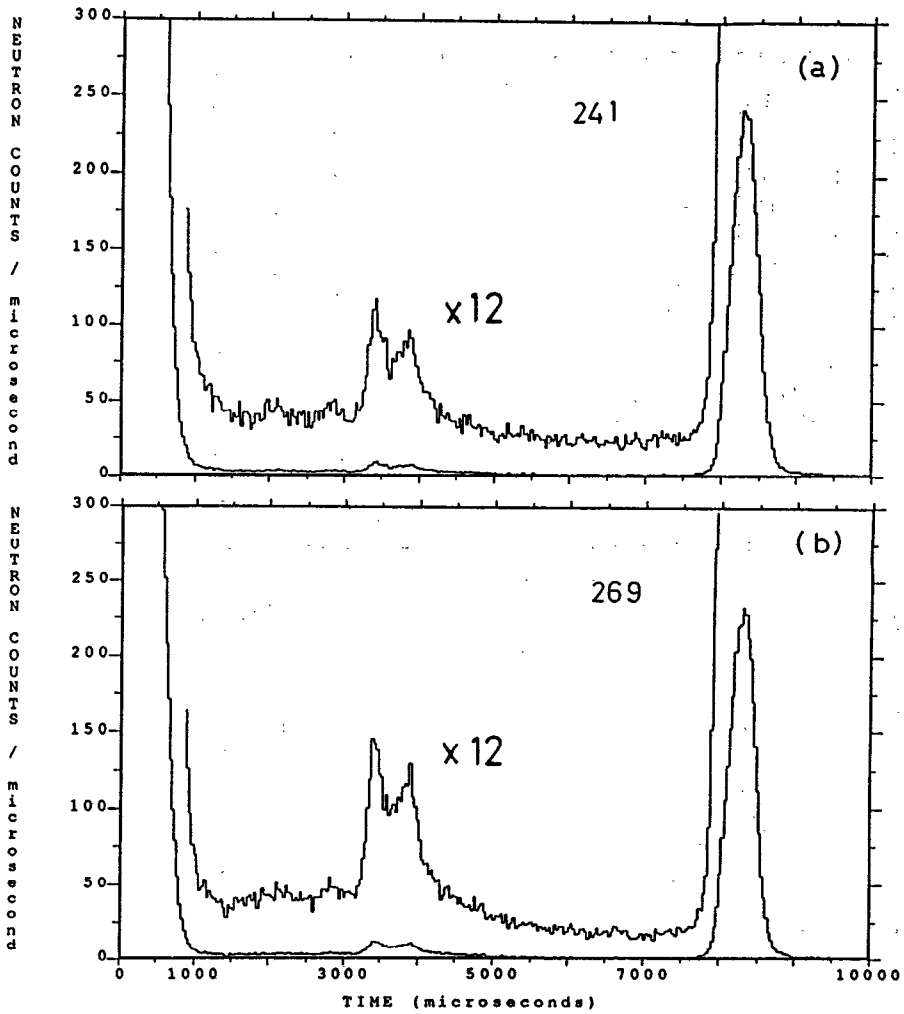

Fig.8. Spectra of vanadium measured by LAM-D. The thickness of the vanadium sample is 2 mm and the measuring time is 8 hrs. (a): the scattering angle 35 deg, (b): 85 deg.

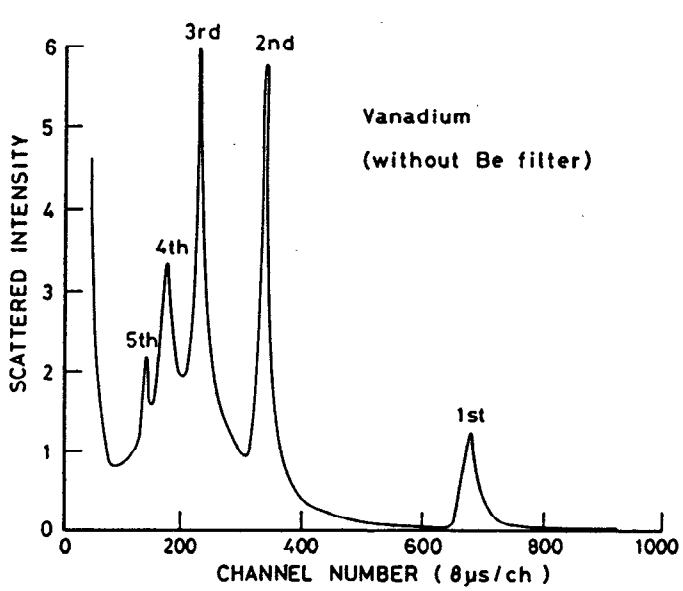

Fig.9. Spectra of vanadium measured LAM-D without the 15 cm Be-filter.

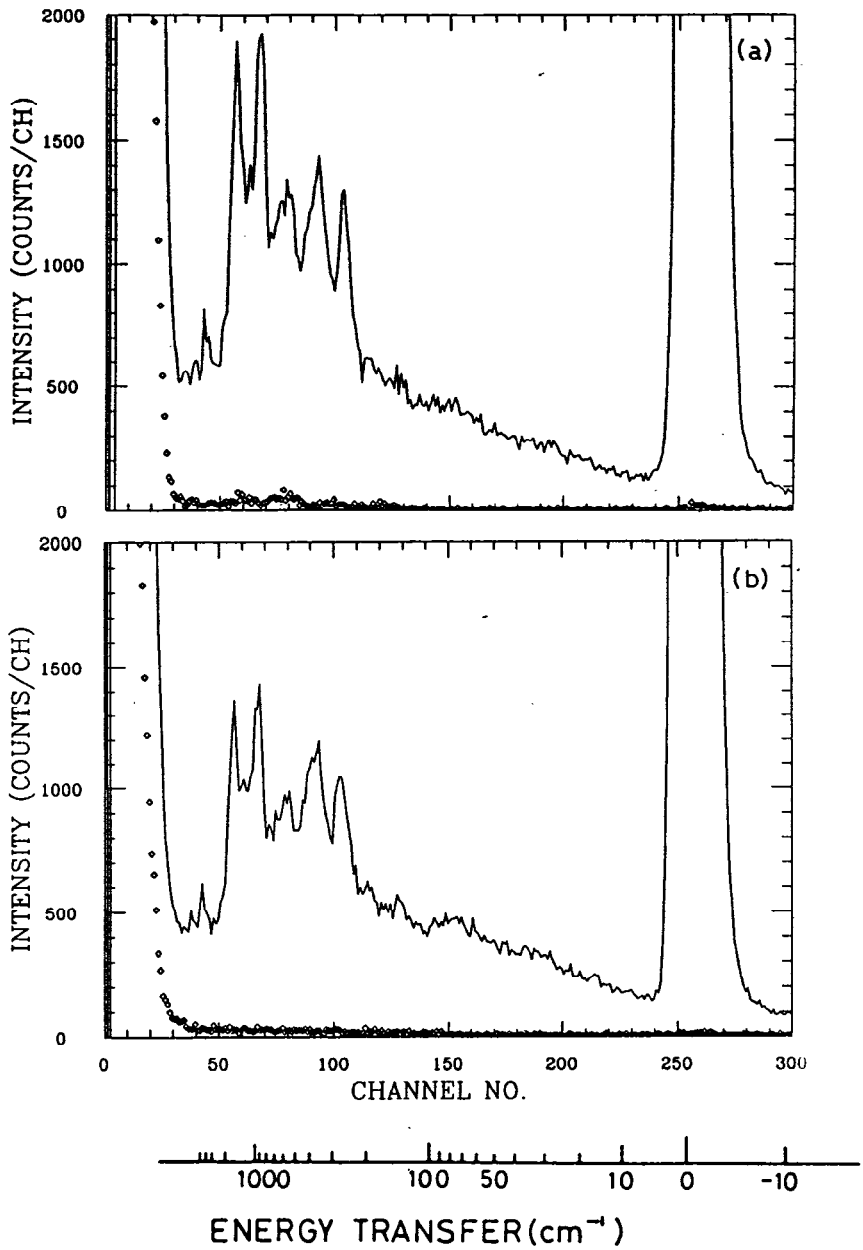

Fig.10. Inelastic scattering spectra of trans-1,4-polychloroprene at 10K and sample container which are normalized by monitor counts. (a): the scattering angle 35 deg, (b): 85 deg.

ICANS-XI International Collaboration on Advanced Neutron Sources
KEK, Tsukuba, October 22-26, 1990

Thermal Neutron Small-Angle Scattering Spectrometer (WIT)

N.NIIMURA, K.AIZAWA*1, M.HIRAI*2, U.SANGAWA*3 AND K.YAMADA*3

Lboratory of Nuclear Science, Tohoku University, Sendai, Mikamine 982, Japan
*1Institute for Materials Research, Tohoku University, Sendai 980, Japan
*2Kanagawa Institute of Technology, Atsugi 234-02, Japan
*3Physics Department, Tohoku University, Sendai 980, Japan

ABSTRACT

This paper describes the configuration and performance of a new time-of-flight (TOF) small-angle neutron scattering (SANS) spectrometer named WIT installed at the pulsed **thermal** neutron source (KENS) at the National Laboratory for High Energy Physics (KEK). We could verify that SANS spectrometer installed at the thermal neutron source could be feasible when adequate instrumental devices such as the slit system for thermal neutrons, the annular glass scintillator detectors, beam line and transmission monitors and a beam stopper were developed. A covered Q-range of WIT is from 0.02 to 0.1 A^{-1}.

I. INTRODUCTION

The SANS spectrometer is a special machine for investigating macro-structures, which is now one of the most important instruments for neutron scattering because of its application to wide scientific fields as solid state physics, chemistry, material science, polymer and biology. The demand for this machine is still increasing and most of the SANS spectrometers are installed at cold neutron sources.The type of TOF-SANS spectrometer installed at the cold neutron source has been already reported and it is working in many places. However, SANS spectrometers installed at the thermal neutron source are few in the world. They might believe as if SANS spectrometer would not work without the cold neutron source. It is true that cold neutrons are of great advantage to SANS. However, if a good collimated thermal neutron source and a high resolution PSD are available, SANS installed at the thermal neutron source might be a match for the one at the cold neutron source. Especially when this is applied for the TOF method where unmonochromated white neutrons are used, a very wide Q range is covered with a simultaneous measurement.

By developing several new instrumental devices such as the slit system for thermal neutrons, the annular glass scintillator detectors and beamline monitors made of scintillators and a special beam stopper, we have constructed a thermal neutron small-angle scattering spectrometer named WIT . The paper describes the overall layout and configuration of the spectrometer in the next section. Some instrumental devices newly developed for this spectrometer, such as the slit system, annular detectors, a beam stopper and data acquisition system, are discussed in this section. Then the performance of the WIT is given in III with experimental results obtained .

II. STRUCTURE OF WIT

The layout of WIT is given in Fig. 1. The spectrometer is installed at the H2 beam hole which is set in the thermal neutron moderator at KENS.

An incident slit system is settled inside the biological shield. We have used a converging pin-hole collimator which was developed in INC spectrometer at KENS . The rectangular holes made by sintered B_4C plates and steels were alternatively placed at about 15cm interval to realize converging condition of focusing on the center of the detector position. The sizes of inlet and exit are 47 mm * 47 mm and 32 mm * 32 mm respectively. The distance between them is 2870 mm.

A specially designed beam monitor is set at the exit of the slit system. It is made of the powder of ^6Li glass scintillators. The size of the beam monitor is 60 mm x 60 mm.

A sample chamber is cylindrical, 500 mm in diameter. It is connected with a vacuum scattering chamber. Another sample container is put inside the sample chamber when it is necessary to carry out the measurement under an atmospheric pressure. A beam window of the sample container is made of a thin aluminum plate, 0.2 mm in thickness.

The scattering chamber is 1 m in diameter and 2.6 m in length. It is surrounded by borated resin of 10 cm in thickness for the shielding of neutrons and the inside wall of the chamber is coated with the B_4C powders in order to remove neutrons scattering from the wall. Moreover, in the chamber three disks which are made of solidified B_4C with resin (1 cm in thickness) and have holes in the center are settled as shown in Fig. 1. In the end of the scattering chamber vacuum is sealed by 2 mm thick aluminum, but at the center (100 mm in diameter) where direct neutrons pass 0.2 mm thick aluminum is used.

A detector house is connected with the scattering chamber. It is surrounded by borated resin of 10 cm in thickness for the shielding of neutrons. In the house light is completely cut off but it is not evacuated. There are two doors at both sides where we can access a beam stopper, a detector system and a transmission monitor in the house.

Annular ^6Li glass scintillators are used for the detector system, since the small-angle scattering pattern on the area detector is annular about the beam center for the case of the isotropic scattering sample. If an annular detector is provided in SANS, the data handling system including electronics becomes extremely simple. Since a large and continuous Q range is required, annular detectors with different radii are preferable. Details of the annular detectors are explained in this Proceedings.

In small-angle neutron scattering experiment, it is very important to measure neutron transmission of a sample, which is used as an absorption correction. In general, scattering and transmission measurement cannot be carried out simultaneously, because the detector system of each measurement is different. In the case of scattering measurement a beam stopper should be placed in front of the center of an area detector to prevent the detector from the damage of direct intense irradiation. In the case of transmission measurement the beam stopper must be removed and an attenuated neutron beam is used not to kill the center of the detector.

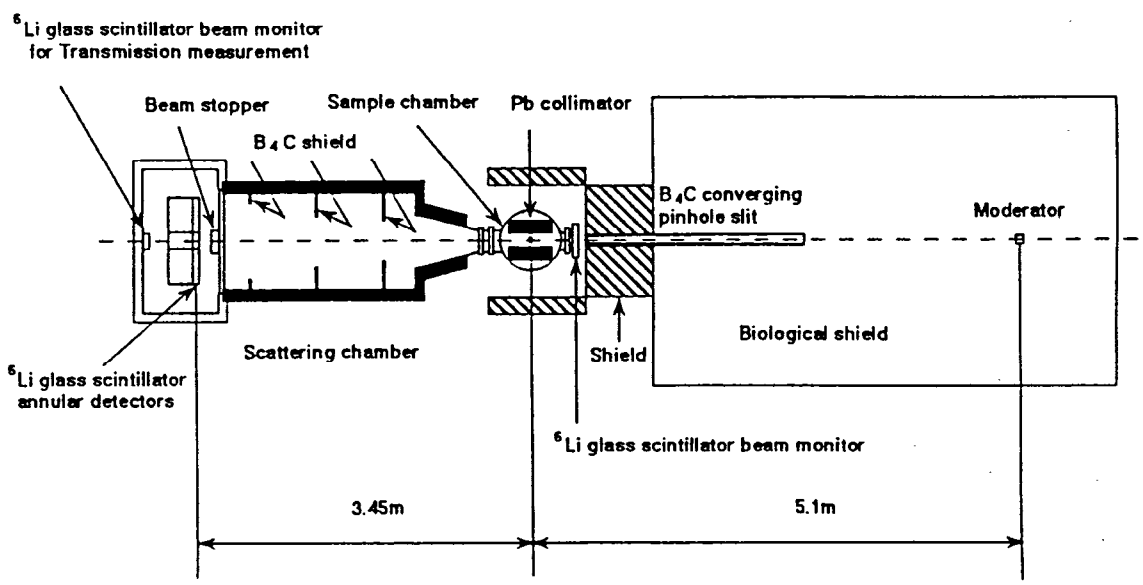

Fig. 1. Overall layout of WIT.

We have specially designed and settled a new beam stopper which enables us to measure both scattering and transmission simultaneously. The schematic layout of the beam stopper is shown in Fig. 2. In the center of a cylinder (155 mm in diameter and 150 mm in length) which is made of B_4C powder solidified by epoxy resin, a hole of 5 mm in diameter is drilled as transmitted neutrons pass through. Moreover, in our case it is not necessary to attenuate incident beams, because the transmitted neutrons are detected with another Li glass scintillator and the dead time of the glass scintillator is estimated to be less than 500 nsec.

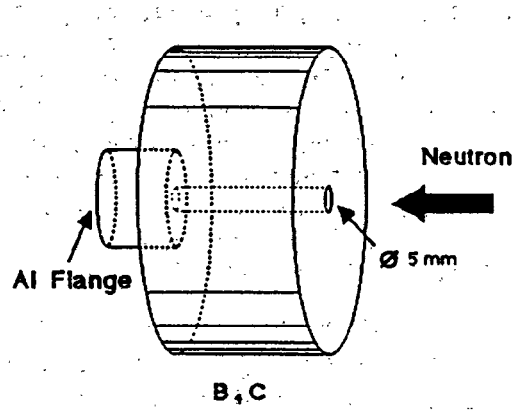

Fig. 2. The schematic layout of the beam stopper.

The wavelength dependences of trnsmission have been measured both with and without the new beam stopper and both results have coinside within statistical errors.

The realization of the simultanious measurements of scattering and transmission provides several benefits, those are,

1) to save the maschine time,
2) to remove the nuisance to mount and then dismount the beam stopper, and
3) to avoid the unexpected change of sample status which might occur while scattering and transmission measurements.

A block diagram of the data processing system for the annular detector is shown in Fig. 3. The signal from the photomultiplier is directed to the amplifiers, and their outputs are fed to a pattern discriminator module, which is specially designed to be applied to the annular detector. The function of the pattern discriminator is as follows: Suppose that the neutron irradiates the scintillator at acertain point, P. Ascintillation event occurs and scintillation photons transmit through the acrylic resin to the neighbouring photomultipliers, for example, A and B as shown in Fig. 4. Since the scitillation event is stochstic, there are several possible combinations of the photomultipliers, for example, A,B,C and H, but there is little possibility that photomultipliers A, B and D accept photons. All the possible combinations of the photomultipliers (called as a pattern) that accept photons simultaneously is written in the read-only-memory (ROM) in the module. This procedure corresponds to a kind of the coincidence among more than two photomultipliers, and this diminishes the electric noise of the photomultipliers.

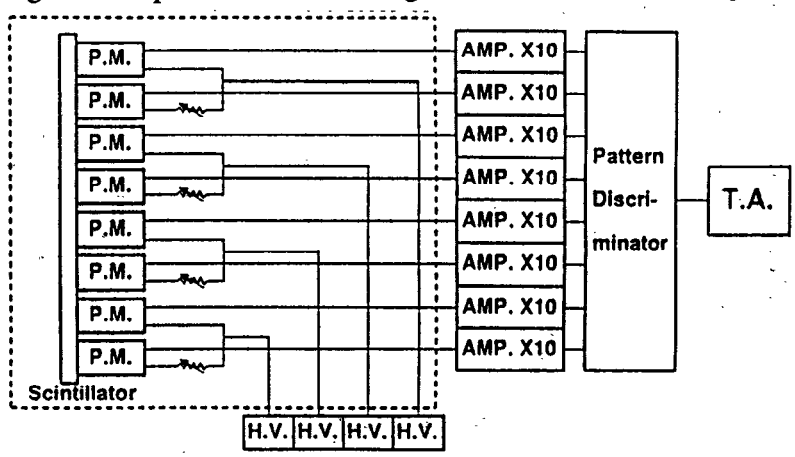

Fig. 3. A block diagram of the data processing system for the annular detector.

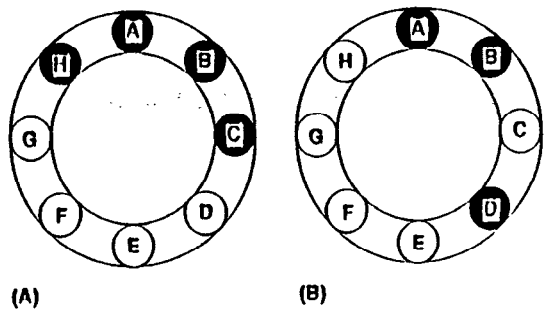

Fig. 4. Illustration how the pattern discriminator works.

A type of the transmission monitor is the same as the one of the beam monitor above mentioned. The transmission monitor can be shifted vertically and horizontally about ± 3 cm in length as to measure beam profiles and to define the beam center.

III. SEVERAL EXPERIMENTAL RESULTS USING WIT

SANS measurement of SiC is a good example to know the qualification of WIT. Fig. 5. shows I(q) of SiC, where the data of different annular detectors were processed separately and overlayed. The agreement among I(Q)'s obtained with different annular detectors is found to be very good. The detailed method how to process raw data will be reported separately elsewhere.

Lysozyme is one of the most typical biological materials as a sample to test a contrast variation method for SANS measurement.

SANS measurement was made for a lysozyme sample in aqueous solution of different D_2O/H_2O ratio i.e. 100%, 90%, 66%, 12% and 0%, where a unit of the ratio is mol%. The mean excess scattering density Γ was determined using $\div I(0)$ vs D_2O/H_2O ratio. The obtained Guinier plots are shown in Fig.6. A radius of gyration R_g of lysozyme is calculated and compared with those reported in the literature. WIT is found to be feasible on the structural study of biological materials.

IV. CONCLUDING REMARKS

The TOF small-angle scattering spectrometer WIT installed at the KENS thermal neutron source has proved to be a feasible machine, having provided good results for the studies of biology and material science.

The authors thank Y.Ishikawa (Deceased) and N. Watanabe for their interest and encouragement in construction. Their thanks are also due to M.Furusaka and M.Arai for their discussion about the slit system.

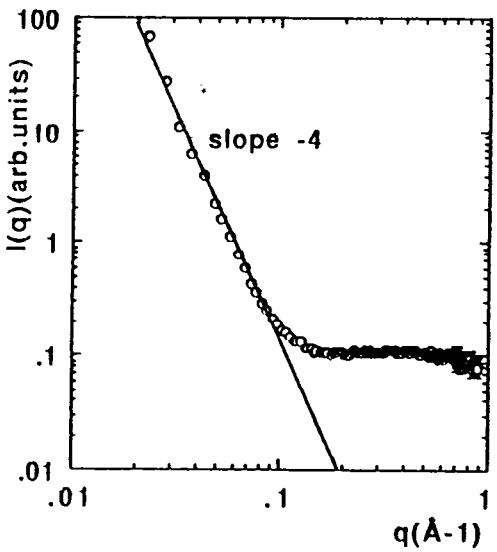

Fig. 5. The obtained I(Q) of SiC.

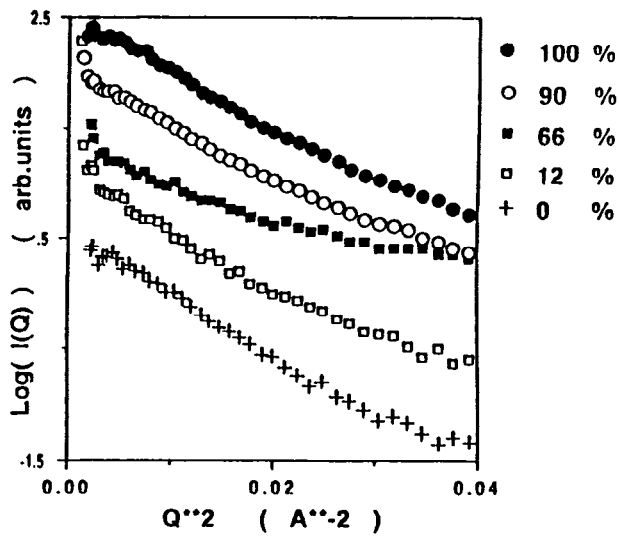

Fig. 6. Guinier plot of lysozyme in aqueous solution at different D_2O/H_2O ratio.

ICANS-XI International Collaboration on Advanced Neutron Sources
KEK, Tsukuba, October 22-26, 1990

Diffuse scattering studies on SXD

C C Wilson, S Hull and D A Keen
ISIS Facility, Rutherford Appleton Laboratory, Chilton, Didcot, Oxon OX11 0QX, UK

ABSTRACT
The application of the ISIS time-of-flight single crystal Laue diffractometer SXD to the study of diffuse scattering is discussed. The ability of such an instrument to access large volumes of reciprocal space in a single measurement is shown to be of great benefit, making the instrument ideal for the observation of such scattering. Examples are given of the use of the instrument in this field and the simultaneous use of diffraction and diffuse scattering data in structural determination discussed.

I. INTRODUCTION

The Single Crystal Diffractometer SXD at ISIS is ideally suited to the study of diffuse scattering. This is a consequence of the instrument being designed as a time-of-flight Laue diffractometer, exploiting the pulsed, polychromatic ISIS beam along with large area detectors to provide continuous coverage of large reciprocal space volumes. The combination of continuos coverage with large detected volume makes SXD an ideal probe for surveying reciprocal space, measuring between the Bragg peaks being as straightforward in this geometry as measuring the Bragg peaks themselves. In addition, it is straightforward on SXD to sample the desired measurement space without the necessity for accurate crystal alignment or complex angular scans of crystal and/or detector. During the actual measurement of a data histogram, all parts of the instrument remain fixed.

The ability to scan on SXD in this way without knowing precisely what one expects to observe is of great benefit in the study of novel systems where the scattering between Bragg peaks may be unknown. In addition, the collection of a large reciprocal space volume of data in a single run is ideally suited to observing changes with temperature etc, which can be achieved without alteration of any other instrument parameters.

In its first year of scheduled operation, a major part of the SXD programme has been devoted to this surveying aspect of the single crystal field, with special emphasis on diffuse scattering. There have been several systems studied successfully, two examples of which are given below to illustrate the technique.

II. DEFECT CLUSTERS IN THE ANION EXCESS FLUORITE $(Ca,Y)F_{2+x}$

Compounds with the fluorite crystal structure provide one of the simplest examples of 'fast-ion' conductors. At temperatures well below the melting point fluorite compounds such as CaF_2 undergo a broad transition to the fast-ion phase, characterised by a rapid increase in the ionic conductivity, and associated with the onset of dynamic disorder within the anion sublattice (Hayes, 1980). The addition of trivalent cations to the halide fluorites introduces excess anion interstitials into the fluorite lattice which maintain electrical neutrality. To understand the profound effect which this doping has on the ionic conductivity (Catlow et al, 1981) it is important to understand the nature of the disordered structure.

Structural information concerning defect clusters within nonstoichiometric compounds can be obtained from both Bragg and diffuse scattering measurements. In a Bragg diffraction experiment the reflection intensities enable the average unit-cell structure to be determined, indicating the atomic positions and occupancies of various crystallographic sites. However, to

obtain direct information concerning the local arrangement of the defect cluster, it is necessary to investigate the coherent diffuse scattering, which often exhibits broad maxima between the Bragg peaks. A single crystal diffractometer on a pulsed neutron source, such as SXD at ISIS, allows large volumes of reciprocal space to be investigated in one crystal orientation. It is possible, therefore, to simultaneously measure a large number of individual Bragg intensities and determine the distribution of the diffuse scattering intensity within reciprocal space.

A combined diffraction and diffuse scattering study has been undertaken, using a single crystal sample of CaF_2 doped with ~5%YF_3, with the aim of constructing a complete, and consistent, model of the defect structure within this anion excess fluorite. Analysis of the experimental data is currently in progress, using defect clusters proposed in the literature on the basis of various experimental and theoretical techniques. To date, the defect cluster which best fits the experimental data for both Bragg intensities and diffuse scattering is that suggested by previous studies using single crystal diffraction alone and is shown in Figure 1. The fluorite lattice can be considered as a simple cubic array of anions, with the cations occupying the alternate cube centres. The excess interstitial F^- anions are then situated at positions (y, –y, 1/4) and (–y, y, 1/4), with respect to the origin on an anion site, and produce relaxations of the two nearest neighbour anions in <111> directions away from the interstitials towards cube centres which are not occupied by cations. These neighbouring relaxed ions cause further, but progressively smaller, relaxations (not shown in Figure 1) of the 6 next nearest neighbours and the 16 3rd nearest neighbours, again in <111> directions towards empty cube centres.

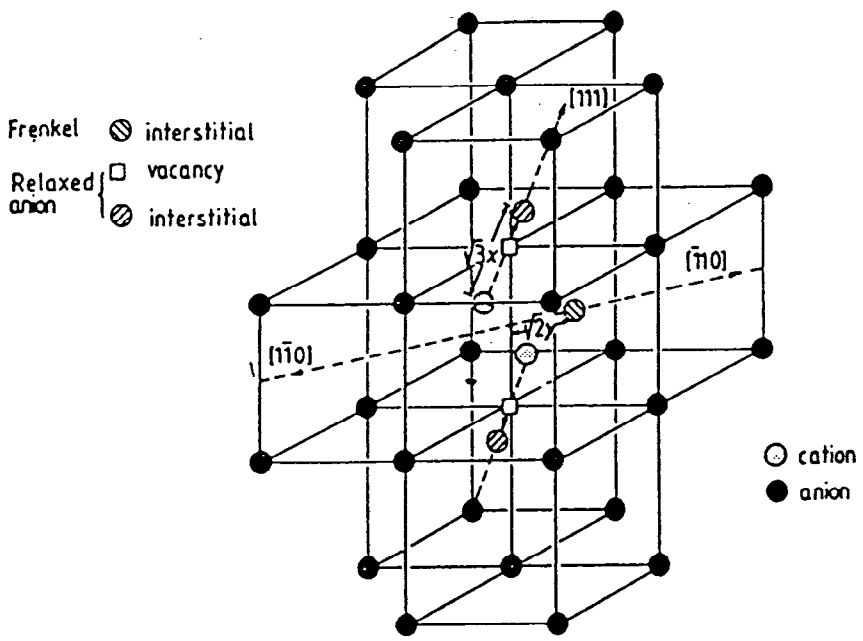

Figure 1 – A model for the defect cluster in $(Ca,Y)F_{2+x}$, showing the interstitial F' ion positions and the relaxed interstitials F".

Values for the positional parameters describing the location of the disordered anions within the defect cluster have been determined by performing a least-squares fit of the diffuse scattering data in the (hhl) plane of reciprocal space using the model described above. Scale and background parameters are also included, plus an overall isotropic temperature factor for the disordered anions. The measured diffuse scattering data and the fitted calculated pattern are shown in Figures 2 and 3. Preliminary refinements of the Bragg intensities support the defect cluster model obtained from the fit to the diffuse scattering data. A comparison of the positional parameters obtained by each approach is shown in Table 1. In view of the encouraging agreement obtained, software for simultaneous least squares refinement of the diffuse and diffraction data is currently being developed at ISIS.

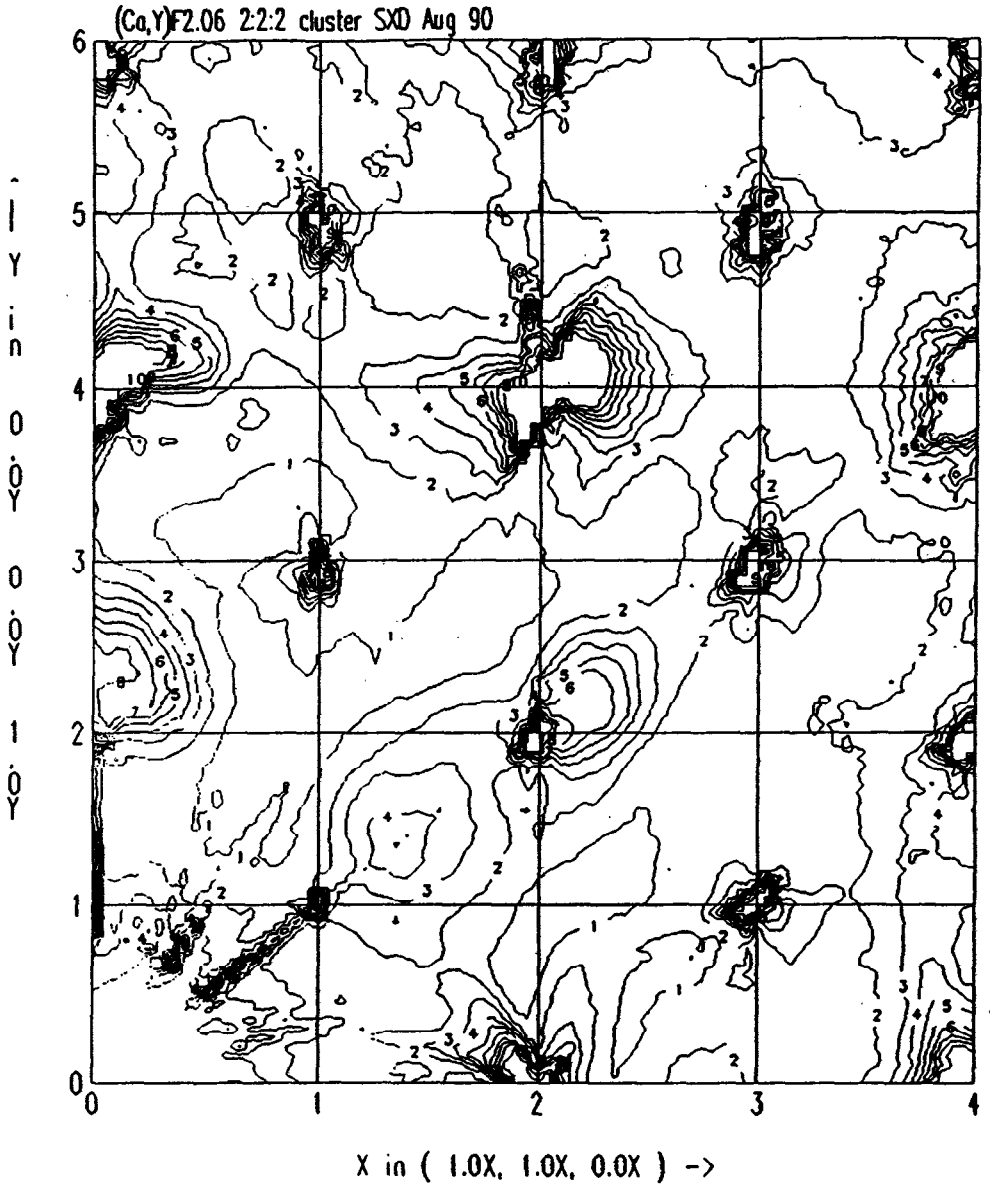

Figure 2 – The Bragg and diffuse scattering data collected on SXD from $(Ca,Y)F_{2.05}$.

TABLE 1 – Refined positional parameters from diffuse and diffraction data refinements

Atom	Position	Parameter	Diffuse	Diffraction
F'	(0.5,a,a)	a	0.442	0.370(9)
F"	(b,b,b)	b	0.419	0.403(11)
F''_b	(c,c,c)	c	0.284	0.266(3)
F''_c	(d,d,d)	d	0.262	0.258(5)

Figure 3 – The observed (top) and calculated (bottom) coherent diffuse scattering in $(Ca,Y)F_2$ from the defect cluster described. The Bragg and thermal diffuse (TDS) scattering have been removed from the observed data in a semi-empirical way, leaving only the diffuse scattering due to the defects.

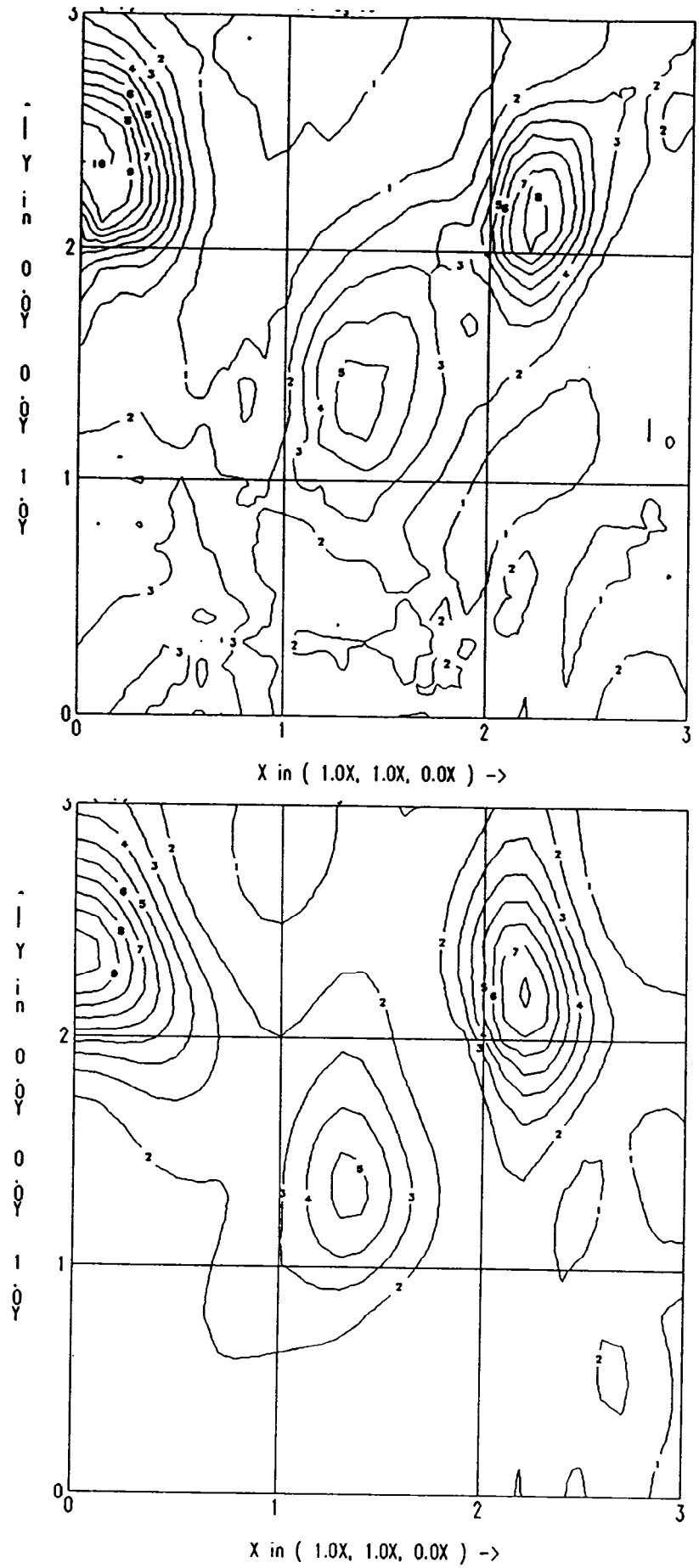

III. PRE-MELTING IN LEAD

Although the solid to liquid transition is familiar to us all, the microscopic mechanism of the melting process is not well understood. Materials which show 'pre-melting' effects, when the solid shows signs of structural disorder prior to melting, have been investigated to try to determine what happens when a solid melts. Lead is one such material, having the advantages of a reasonably low melting point ($T_m = 601K$), a simple fcc structure and readily available single crystals. Conductivity measurements show changes around 60K below T_m which are attributed to the formation of liquid-like defects in the crystal structure. Phonon linewidth measurements also indicate a change in behaviour above 500-550K.

The diffuse neutron scattering has been measured on SXD from a single crystal lead sample at 5K, 293K, 373K and 548K in the (hhl) plane (Figure 4). This scattering shows the development of the thermal disorder in the material as the temperature is increased towards the melting point. There is considerable diffuse scattering even at room temperature, which becomes more pronounced as the temperature is raised still further. At 548K, the high-Q Bragg peaks are barely visible in these plots, demonstrating the high disorder in lead at these high temperatures. The thermal disorder in a crystalline material may be determined via Debye-Waller factors calculated from Bragg scattering (Merisalo, Lehmann and Larsen, 1984). However, in a material where the dominant scattering is diffuse rather than Bragg, this may not be appropriate. Using Reverse Monte Carlo simulation (Keen, Hayes and McGreevy, 1990) the whole structure factor may be modelled and the thermal disorder assessed from both the diffuse and Bragg scattering. The patterns shown here will be analysed in this way.

Having demonstrated that SXD is ideally suited to this sort of measurement, further experiments are planned to measure the diffuse scattering up to the melting point in order to allow the determination of changes in the disordered structure associated with the 'pre-melting' in the material.

References

Hayes W, J. Phys. Coll. C6, 7 (1980)

Catlow C R A, Comins J D, Germano F A, Harley R T, Hayes W and I.B.Owen, J. Phys. C 14, 329 (1981)

Cheetham A K, Fender B E F and Cooper M J, J. Phys. C 4, 3107 (1971)

Keen D A, Hayes W and McGreevy R L J Phys Cond Matter 2, 2773 (1990)

Merisalo M, Lehmann M S and Larsen F K Acta Cryst. A40, 127 (1984)

Figure 4 – Scattering in the (hhl) plane of lead, measured on SXD at 5K, 293K, 373K and 548K. The increasing degree of diffuse scattering between the Bragg peaks as the temperature increases is obvious from these plots. Modelling of the whole pattern in a case such as this obviously has significant benefits over merely refining on Bragg intensities.

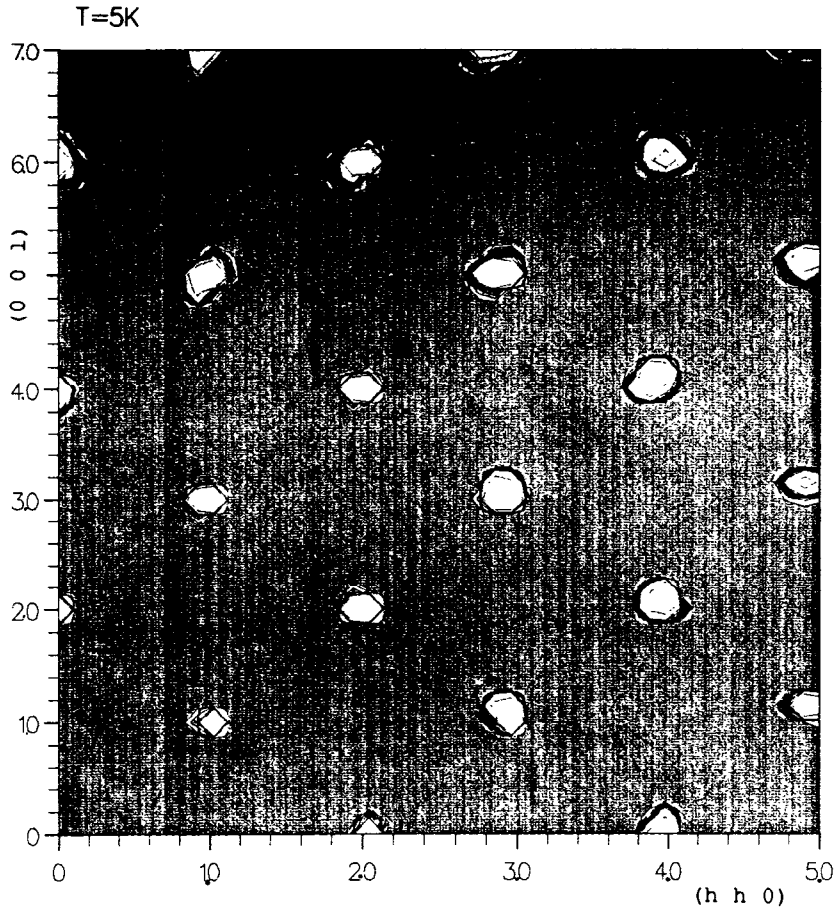

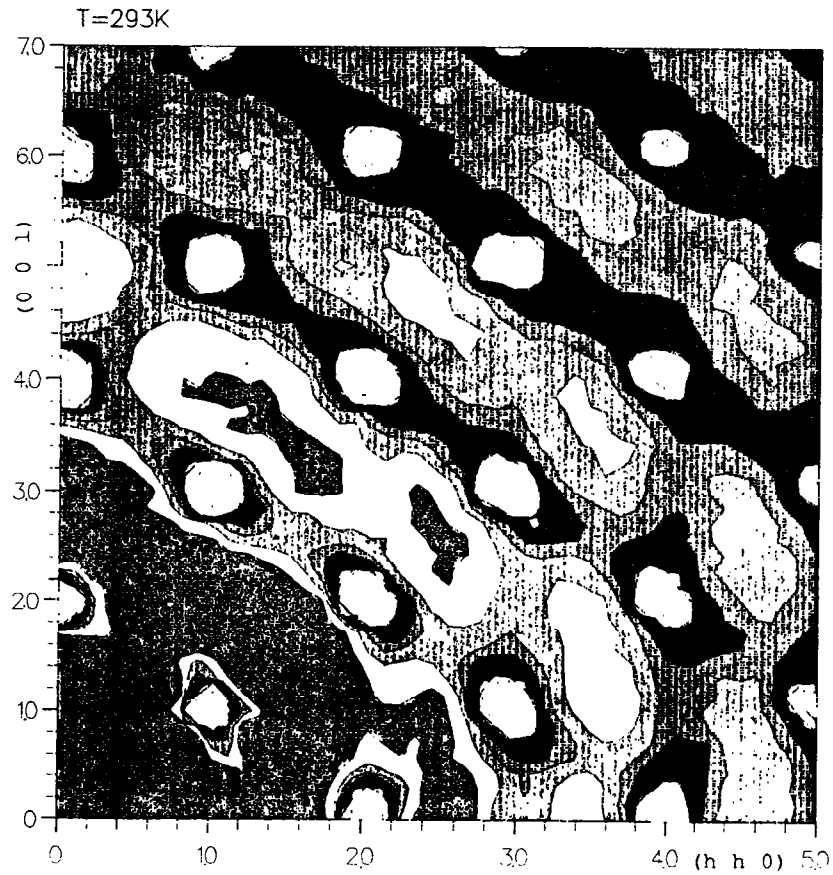

T=373K

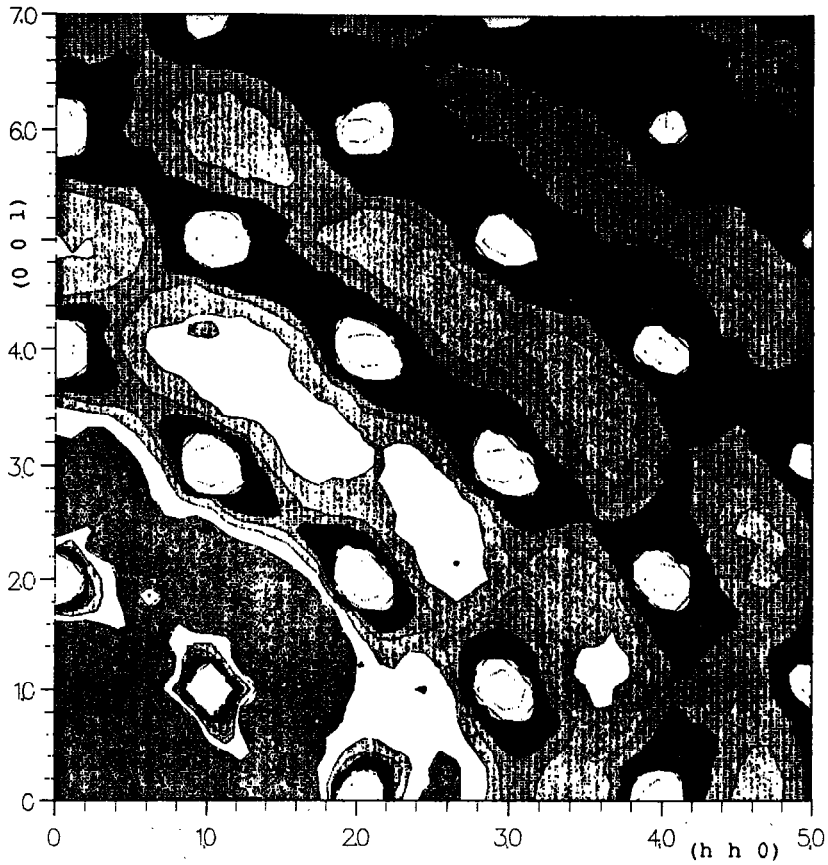
7.0
6.0
(0 0 1)
4.0
3.0
2.0
1.0
0
0
1.0
2.0
3.0
4.0
(h h 0)
5.0

T=548K

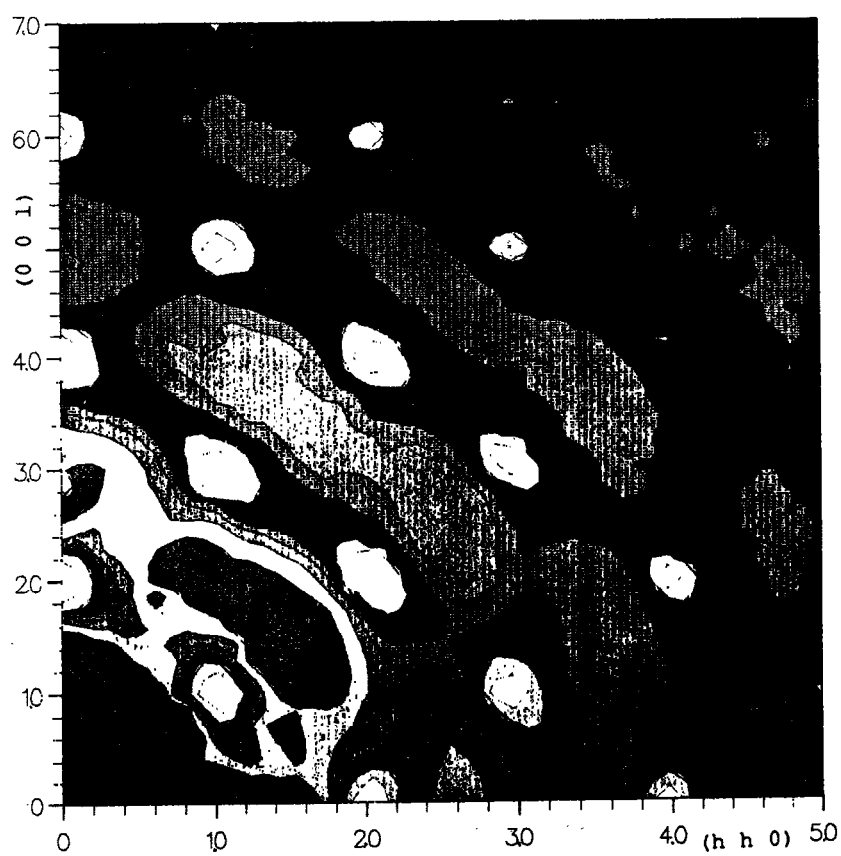
7.0
6.0
(0 0 1)
4.0
3.0
2.0
1.0
0
0
1.0
2.0
3.0
4.0
(h h 0)
5.0

ICANS-XI International Collaboration on Advanced Neutron Sources
KEK, Tsukuba, October 22-26, 1990

High precision structural refinement from time-of-flight single crystal data

C C Wilson
ISIS Facility, Rutherford Appleton Laboratory, Chilton, Didcot, Oxon OX11 0QX, UK

ABSTRACT
The use of time-of-flight single crystal data in structural refinement is discussed. The advantage of variable wavelength and high $\sin\theta/\lambda$ data can lead to significantly more precise and informative refinement information. Reliable and accurate strategies for data reduction are crucial, however, and some of the complexities and possible solutions are mentioned.

I. INTRODUCTION

Pulsed source single crystal diffraction has, by its nature, several features which are of benefit in structural refinement:

(i) The collection of many Bragg reflections simultaneously in the detector allows the accurate determination of crystal cell and orientation from a single data histogram (collected in one fixed crystal/detector geometry). It should also be noted that for some applications this single histogram may be the only data required;

(ii) The white nature of the incident beam enables the straightforward measurement of reflections at different wavelengths. This ability is invaluable in the precise study of wavelength dependent effects such as extinction and absorption;

(iii) The collection of data to the very high $\sin\theta/\lambda$ values accessible on SXD (exploiting the high flux of useful epithermal neutrons from the undermoderated ISIS beams) allows more precise parameters to be obtained, enabling the examination of very subtle structural features.

For many problems in physics, the refinement parameters required are not the normal positional and vibrational parameters, but may be (or may be classed as) second, or higher, order effects. For example, disordered structures, higher order potential terms, incommensurate or satellite peaks, new minority phases etc. In order to be able to extract parameters such as these reliably and precisely, it is necessary both to extract accurate diffraction intensities to very high Q and to apply all necessary corrections to these data in the reduction to a set of structure factors for refinement.

II. DATA EXTRACTION AND REDUCTION

The extraction of structure factor information from an SXD data set proceeds in two stages. Given the provision of an accurate UB matrix from the earlier stages of the data processing procedure, integrated intensities are extracted from the raw data using Wilkinson's modification of the $\sigma(I)/I$ method (Wilkinson, 1986; Wilkinson et al, 1988). This procedure involves fitting variable-shaped ellipsoidal integration volumes around the reflection position as predicted from the crystal UB matrix. Local interpolation of the peak centroid improves the integration accuracy and can also be used to improve the quality of the UB matrix. The "learning" of the shapes of the stronger reflections is exploited by imposing these shapes upon the profiles of weaker reflections occurring in similar regions on the detector. The use of this peak shape library method allows significantly more reliable weak intensities to be extracted, along with the benefit of more accurate strong intensities from the application of the $\sigma(I)/I$ technique. Since

reflections at high Q tend to be rather weak, the availability of data at very high $\sin\theta/\lambda$ values of $>2\text{Å}^{-1}$ on SXD depends strongly on the successful and reliable extraction of weak peak intensities.

Once a reliable set of integrated intensities has been extracted from the raw data, it is necessary to reduce these to structure factors. For this we use the formula of Buras and Gerward (1975)

$$I_h = i_0(\lambda)\, V\, N^2\, |F_h|^2\, \lambda_h^4\, \epsilon(\lambda,\alpha)\, A_h(\lambda)\, E_h(\lambda) \,/\, 2\sin^2\theta_h \qquad (1)$$

where

I_h is the measured intensity of reflection h;
$i_0(\lambda)$ is the incident flux;
V is the crystal volume;
N is the number density of unit cells;
$|F_h|$ is the structure factor magnitude of reflection h;
λ_h is the wavelength at which h is measured (λ^4 is reflectivity);
$\epsilon(\lambda,\alpha)$ is the detector efficiency, a function of wavelength and detector coordinate $[\alpha = \alpha(x,z)]$;
θ_h is the Bragg angle at which h is measured (The term $1/2\sin^2\theta_h$ is the Lorentz correction. It should be noted that in time-of-flight Laue diffraction, the "moving" part to which this correction refers is the contraction of the Ewald sphere (radius $1/\lambda$) during the pulse time frame);
$A_h(\lambda)$ is the absorption correction;
$E_h(\lambda)$ is the extinction correction.

In practice on SXD at present this data reduction is accomplished in three stages :

(i) The detector spatial response correction $\epsilon[\alpha(x,z)]$ is taken account of within the peak integration program;

(ii) In the main reduction program SXDRED, the expression evaluated is

$$|F_h| = \{I_h\, 2\sin^2\theta_h \,/(i_0(\lambda)\, V\, N^2\, \lambda_h^4\, \epsilon(\lambda)) \qquad (2)$$

(iii) In the Cambridge Crystallographic Subroutine Library (CCSL; Brown and Matthewman, 1987) routine TOFEA, the coefficients for the evaluation and subsequent refinement of wavelength and path length dependent absorption and extinction corrections are calculated.

Structure factor refinement is then carried out within the framework of CCSL using the least squares program SFLSQ. In addition, of course, the flexibility of the CCSL system allows special features to be conveniently built in to a refinement, such as bond constraints, relations between variables, magnetic structures etc.

III. FURTHER DATA CORRECTION - THERMAL DIFFUSE SCATTERING

Thermal diffuse scattering (TDS) can be examined in detail using SXD. For a time-of-flight experiment the TDS around an elastic peak displays an appearance characterised by the ratio of the velocity of sound in the crystal to the neutron velocity. Early work on this phenomenon was carried out on HRPD at ISIS in backscattering geometry (Willis et al, 1986) but there are considerable changes in the phonon spectrum as the scattering geometry changes on SXD. Measurements of this effect (Figure 1) are made possible on SXD as a result of the extremely low background close to the Bragg peaks obtained using the ZnS fibre-optic encoded PSDs.

It is hoped that a detailed understanding of such TDS processes and their wavelength and geometry dependence will enable more accurate corrections to be made to intensities collected on SXD. The use of both empirical and analytical models for the TDS under Bragg peaks is being investigated.

Figure 1 – The thermal diffuse scattering around the (004) reflection of SrF_2 as measured on SXD. Note the presence of the one phonon branch and the obvious anisotropy of the correction required for this effect.

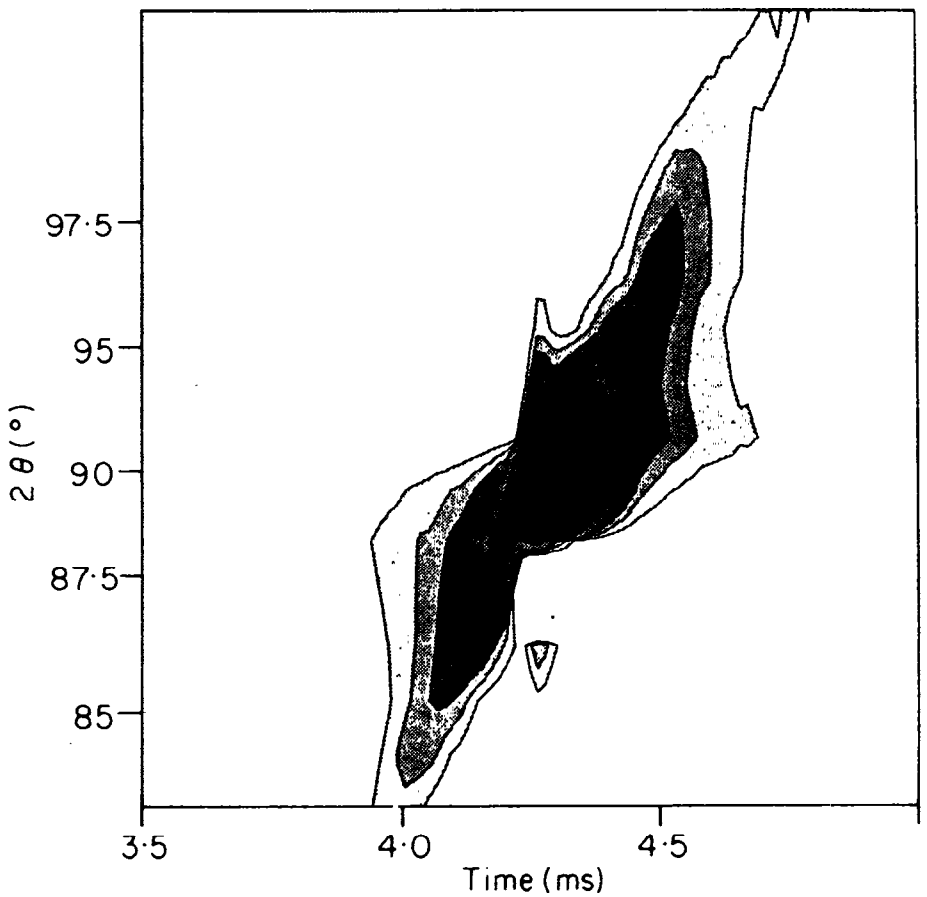

IV. PROFILE EXTRACTION OF INTENSITIES

The question of subtraction of TDS corrections of the type shown in Figure 1 illustrates the desirability of utilising the 3D peak shape information inherently available in time-of-flight single crystal diffraction. Clearly to correct satisfactorily for scattering processes of this type one should do more than simply integrate over some averaged integration volume shape. Ideally one would correct point-by-point in Q-space. Once this is contemplated, the obvious next step is to extract integrated intensities by a full 3D profile fitting procedure, analagous to the Pawley method in powder diffraction (Pawley, 1981), in which detailed peak shape knowledge is used to optimise intensity extraction.

The potential for this method of intensity extraction has been illustrated using the (00l) row of the W-type hexaferrite $Ba(Fe,Co)_2Fe_{16}O_{27}$ (c-axis length = 32.9Å). In this case, accurate intensities were extracted as far as the (0,0,80) reflection, into a region where the diffraction peaks from this material measured on SXD are very significantly overlapped. The high $\sin\theta/\lambda$ values made accessible by this technique should substantially improve the potential resolution of SXD data sets, in addition to allowing detailed Q-dependent corrections to be made. Work on the 2D and 3D profile methods is in progress, especially in relation to intensity extraction from the large unit cell materials intended for study on the proposed biological diffractometer DIBS.

V. STRUCTURAL STUDY OF SrF_2 – EXTINCTION AND ANHARMONICITY

For this experiment (Forsyth, Wilson and Sabine, 1989) a cylindrical sample (height 8mm, diameter 2.5mm) of the fluorite material SrF_2 mounted along $<1\bar{1}0>$ was used. In this case

data were collected solely in the equatorial plane of the instrument, allowing access to (hhl) reflections. The scattering angles for the data collection ranged from 50–110° in 2θ, and the wavelength range from 0.36–6Å. The resulting 101 reflections were used in SFLSQ to refine the structural parameters (Wilson and Forsyth, 1989). It should be noted that not all of these reflections have unique h,k,l values. Since identical reflections measured at different wavelengths remain distinct observations until all wavelength dependent terms are corrected for and since in this case extinction is refined in the least squares program, these reflections are used separately in the refinement data set. Extinction was corrected for using a variable wavelength adaptation of the CCSL extinction correction routine using a Becker–Coppens Gaussian model, with one variable parameter. The refined parameters are shown in Table 1.

TABLE 1 – Refined SrF_2 structural parameters

Scale	9.13
B_{Sr}	0.470(26) Å^2
B_F	0.732(31) Å^2
mosaic spread	1.03(10) 10^{-4} rad^{-1}
R (unweighted)	0.050

On completion of this refinement, however, it was clear that allowance for anharmonic thermal vibrations of the fluorine atoms would significantly improve the quality of the fit. In this model, the thermal vibrations of the tetrahedrally bound fluorine atoms in the SrF_2 structure are defined by the potential

$$V_F(\underline{r}) = V_{0F} + \tfrac{1}{2}\alpha_F(x_F^2 + y_F^2 + z_F^2) + \beta_F(x_F y_F z_F) \qquad (3)$$

where x_F, y_F, z_F are the displacement coordinates for the thermal vibrations of the fluorine atom. It can be shown (Mair and Barnea, 1971) that the third order term β_F has a significant effect on the intensities of reflections where the sum of indices $|h|+|k|+|l| = 4n\pm1$. The ratio of two structure factors of this type can be written as

$$F_+/F_- = 1 - (2b_F/b_{Sr}) \exp\{(B_{Sr}-B_F)[(h^2+k^2+l^2/4a^2)]\} \times (B_F/4\pi a)^3 (\beta_F/kT) [|h_1k_1l_1| + |h_2k_2l_2|] \qquad (4)$$

where

$|F\pm|$ are the structure factors for reflections with $|h|+|k|+|l| = 4n\pm1$;
b_{Sr}, b_F are the scattering lengths of Sr and F;
B_{Sr}, B_F are the isotropic temperature factors;
a is the cubic cell parameter;
k is the Boltzmann constant;
T is the absolute temperature;
β_F is the anharmonicity parameter for fluorine.

It can be seen from this that if one measures pairs of reflections with equal $(h^2+k^2+l^2)$, which in the harmonic approximation have equal intensities, then by (4) some intensity variation can be expected for pairs whose $|h|+|k|+|l| = 4n\pm1$ (see Figure 2). It can also be seen from equation (4) that the effect becomes more pronounced at higher Q – this is where the ability of SXD to exploit the useful ISIS epithermal flux and access the highest resolution data becomes especially valuable. The very high $\sin\theta/\lambda$ attainable on SXD should allow greater precision to be obtained in the determination of the anharmonicity parameter β_F.

To examine this effect, further data were collected on SXD consisting of: 69 (hhl) reflections measured in a full 360° ω scan, with all 4 symmetry equivalent reflections averaged; and 19 further reflections of the $4n\pm1$ type discussed above, which are expected to exhibit the effects of anharmonicity in a pronounced way and were collected at higher statistics. The latter set of reflections do indeed demonstrate significant anharmonic effects, as illustrated in Table 2.

Figure 2 – The $(3,3,\overline{15})$ (top) and $(9\overline{9}\overline{9})$ reflections of SrF_2. In the harmonic approximation these two reflections would have equal intensities. The observed intensity difference is due to the anharmonic thermal vibrations exhibited by the fluorine atoms.

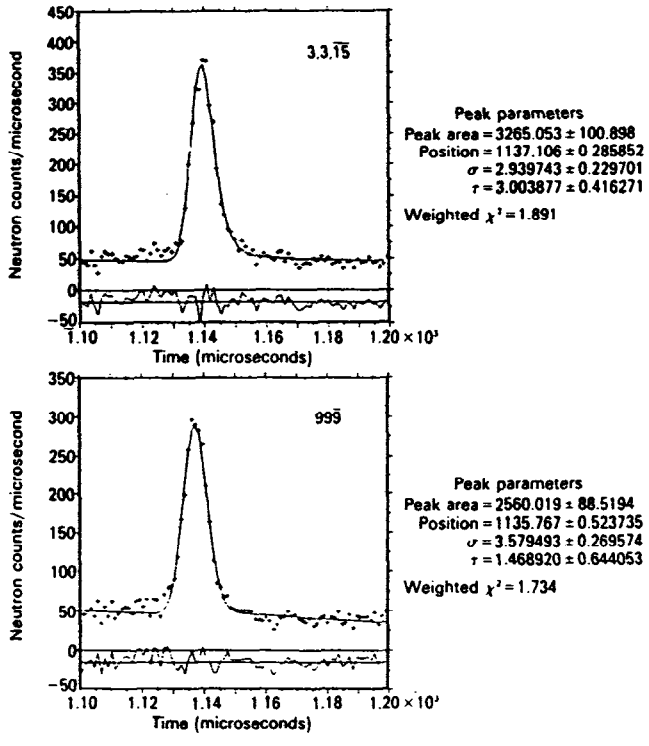

TABLE 2 – Anharmonicity affected pairs of reflections measured for SrF_2

The 'expected' values in this table were calculated using the Cooper and Rouse value of β_F, the 'calculated' values using the refined value from the SXD data.

$\Sigma(h^2+k^2+l^2)$	Pair		RATIO (F_+/F_-) Expected	Measured	Calculated
99	(5 5 7)	(4n+1)	1.045	1.042(4)	1.047
	(3 3 9)	(4n-1)			
	(5 5 7)	(4n+1)	1.039	1.043(5)	1.041
	(7 7 1)	(4n-1)			
123	(1 1 11)	(4n+1)	1.042	0.996(5)	1.045
	(7 7 5)	(4n-1)			
171	(5 5 11)	(4n+1)	1.043	1.032(6)	1.046
	(1 1 13)	(4n-1)			
187	(3 3 13)	(4n-1)	1.000	0.983(8)	1.000
	(9 9 5)	(4n-1)			
219	(7 7 11)	(4n+1)	1.119	1.160(19)	1.126
	(5 5 13)	(4n-1)			
243	(3 3 15)	(4n+1)	1.113	1.107(11)	1.120
	(9 9 9)	(4n-1)			
	(3 3 15)	(4n+1)	1.034	1.044(9)	1.036
	(11 11 1)	(4n-1)			
323	(7 7 15)	(4n+1)	1.205	1.308(31)	1.217
	(11 11 9)	(4n-1)			
363	(11 11 11)	(4n+1)	1.226	1.207(45)	1.240
	(13 13 5)	(4n-1)			
	(1 1 19)	(4n+1)	1.090	1.110(40)	1.095
	(13 13 5)	(4n-1)			

Maximum $\sin\theta/\lambda = 1.696$ Å^{-1} ($Q = 21.2$ Å^{-1})

The anharmonicity refinements were carried out in an adaptation (Mair and Barnea, 1971) of the ORFLS program (Busing, Martin and Levy, 1962), using data pre-corrected for extinction in CCSL. The results of the refinements are summarised in Table 3.

TABLE 3 - Anharmonicity refinements on SrF_2

Reflections used	Anharm Refined	Scale Factor	B_{Sr} (Å2)	B_F (Å2)	β_F (x10^{-19} J.Å^{-3})	R
ALL (88)	NO	1.006(8)	0.454(11)	0.737(16)		0.0425
ALL (88)	YES	1.007(6)	0.457(10)	0.737	-5.0(1.5)	0.0388
4n±1 (16)	NO	1.100(41)	0.539(30)	0.732		0.0441
4n±1 (16)	YES	1.107(9)	0.539	0.732	-4.02(28)	0.0219

The improvements in fit are apparent in both cases, but are of course especially emphasised when only those pairs of reflections exhibiting anharmonicity are used.

The β_F parameter obtained from the refinement should be compared with that obtained from a least squares fit of the observed F_+/F_- ratios (-4.19(30) 10^{-19} J.Å^{-3}) and the previous determination by Cooper and Rouse (1971) (-3.95(46) 10^{-19} J.Å^{-3}) from reactor data. These determinations of the β_F parameter agree well with each other, but it is plain that the *precision* of the SXD determination is higher, reflecting the high $\sin\theta/\lambda$ reached (1.7Å^{-1}) compared with that attained in the earlier study (0.9Å^{-1}).

VI. REFINEMENT OF RELAXED FLUORINE ION POSITIONS IN $(Ca,Y)F_{2.05}$

The doping of 5% YF_3 into CaF_2 introduces interstitial fluorine ions into the lattice. These interstitials cause relaxation of neighbouring fluorine atoms residing on normal tetrahedral fluorite anion sites. The principal interest in the study of these potential fast-ion conduction materials is in the examination of the coherent diffuse scattering caused by the formation of these defect clusters. However, since the relaxation of these ions is, on average, coherent throughout the sample, the diffraction, or structure factor, data also contains information on the geometry of the relaxed ions. It is obvious that the two types of information do not exist in isolation but that the same model ought to be derived from both diffuse and diffraction data.

To this end, in a recent experiment on SXD, two sets of data were collected from the CaF_2-5%YF_3 system, from two crystals grown from the same solid solution. Data from the larger of the two crystals was used in studying the diffuse scattering and diffraction data were accumulated from a smaller, cylindrical crystal (height 10mm, diameter 3mm). Both data sets were collected close to the equatorial plane of SXD from samples mounted along $<1\bar{1}0>$, allowing access to reflections close to the (hhl) plane. A total of 116 $|F_h|$ values were used in these preliminary structural refinements, to a maximum $\sin\theta/\lambda$ of 1.45 Å^{-1}.

The initial model used was based on that of Cheetham et al (1971), with the interstitial fluorine atom F' displaced along the <110> direction and the relaxed F'' ion alone <111> (Figure 3). The diffraction data will of course merely give a crystal average for these relaxations - it is the aim of the diffuse scattering to reveal the local clustering arrangement.

These initial refinements were successful, with values obtained for fluorine positions, thermal parameters and site occupancies which were in good agreement with the previous work (see Table 4). At this stage, however, a more extended model of the cluster was obtained from the diffuse scattering data which introduced further relaxed fluorine ions in two next neighbour positions. From the diffuse scattering data these ions, F''_b and F''_c, both again relaxed along <111>, had coordinates of (0.28,0.28,0.28) and (0.26,0.26,0.26). Such is the nature of the

relaxed ion "tree" introduced by the initial interstitial F' ion, that there are 2 F'' ions, 6 F''_b ions and 16 F''_c ions in this model. The residual F atom occupancy on the original tetrahedral site is now as low as 0.46.

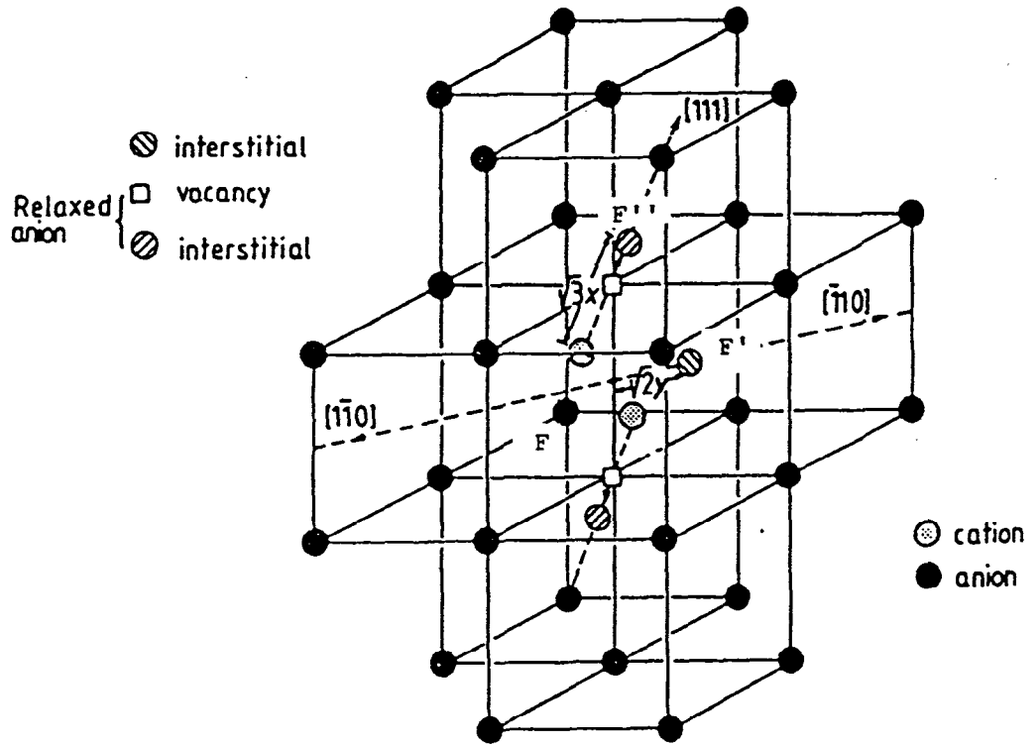

Figure 3 – A model for the defect cluster in $(Ca,Y)F_{2.05}$, showing the interstitial F' ion positions and the relaxed interstitials F''.

TABLE 4 – Preliminary refinement results for CaF_2–5%YF_3
116 observations, 9 variables, R = 6.83%
Scale = 62.5(22), Mosaic Spread = 0.56(9) 10^{-4} rad^{-1}

Atom	x/a	y/b	z/c	B_{iso} ($Å^2$)	Site	F_{2+x}
Ca	0.0	0.0	0.0	0.684(41)		
F	0.25	0.25	0.25	0.881(37)	0.970(18)	1.94(4)
F'	0.5	0.377(4)	0.377(4)	0.65(6)	0.0058(14)	0.070(15)
F''	0.407(16)	0.407(16)	0.407(16)	0.65*	0.0057(14)	0.046(12)

The introduction of this model leads to the refined parameters given in Table 5, and a slightly reduced R-factor of some 6.5%. The data reduction in this case was carried out rapidly on this recently collected data and with care the intensity information should improve. The most impressive aspect of the preliminary refinement, by now involving a highly distorted structure, is the stability of the F''_b and F''_c positional coordinates, which are refined straightforwardly from the data in spite of their small deviations from the tetrahedral site and their rather low occupancies. The refined coordinates for these 2nd and 3rd neighbour relaxed ions agree fairly well with the values obtained from the diffuse scattering data fit. This gives some confidence that the interstitial–relaxed ion model being proposed is fairly close to the true defect cluster.

TABLE 5 - Preliminary refinement results for CaF_2-5%YF_3
Using extended interstitial 'tree', R = 6.52%
Scale = 64.3(11), Mosaic Spread = 0.75(9) 10^{-4} rad^{-1}

Atom	x/a	y/b	z/c	B_{iso} (Å^2)	Site	F_{2+x}
Ca	0.0	0.0	0.0	0.682(34)		
F	0.25	0.25	0.25	0.828(43)	0.464	0.93
F'	0.5	0.370(9)	0.370(9)	0.60(6)	0.0058	0.070
F"	0.403(11)	0.403(11)	0.403(11)	0.60*	0.0057	0.048
F''_b	0.266(3)	0.266(3)	0.266(3)	0.60*	0.0340	0.272
F''_c	0.258(5)	0.258(5)	0.258(5)	0.60*	0.0910	0.728

The use of high Q single crystal diffraction data in this way to obtain fairly precise positional parameters for slightly disordered ions is a good example of structural refinement on SXD. Coupled with the simultaneous measurement of the coherent diffuse scattering pattern, it shows the great power and versatility of the instrument in such studies of total elastic scattering.

References

Brown P J and Matthewman J C, Rutherford Appleton Laboratory Report, RAL-87-010 (1987)
Busing W R and Levy H A, Acta Cryst. 22, 457 (1967)
Cheetham A K, Fender B E F and Cooper M J, J. Phys. C 4, 3107 (1971)
Cooper M J and Rouse K D, Acta Cryst. A27, 622 (1971)
Forsyth J B, Wilson C C, Stringer A M, Howard J A K and Johnson O, J. de Phys. Colloque C5-47, 143 (1986)
Forsyth J B, Wilson C C and Sabine T M, Acta Cryst. A45, 244 (1989)
Pawley G S, J. Appl. Cryst. 14, 357 (1981)
Wilkinson C, J. de Phys. Colloque C5-47, 35 (1986)
Wilkinson C, Khamis H W, Stansfield R F D and McIntyre G J, J. Appl. Cryst. 21, 471 (1988)
Willis B T M, Carlile C J, Ward R C, David W I F and Johnson M W, Europhys. Letts. 2, 767 (1986)
Wilson C C and Forsyth J B, Rutherford Appleton Laboratory Report RAL-89-005 (1989)

ICANS-XI International Collaboration on Advanced Neutron Sources
KEK, Tsukuba, October 22-26, 1990

Powder diffraction at ISIS

W I F David, S Hull, R M Ibberson and C C Wilson
ISIS Facility, Rutherford Appleton Laboratory, Chilton, Didcot, Oxon OX11 0QX, UK

ABSTRACT
The powder diffraction instruments at ISIS are described and examples given of the science performed.

I. INTRODUCTION

The field of powder diffraction at ISIS is well served by the availability of two powerful, complementary, high performance instruments. Both the High Resolution Powder Diffractometer HRPD and the Medium Resolution Powder Diffractometer POLARIS, are used in the performance of vigorous scientific programmes, some examples of which are given below.

II. HRPD - HIGH RESOLUTION POWDER DIFFRACTOMETER

The ISIS high resolution powder diffractometer HRPD (Figure 1) is the highest resolution neutron powder diffractometer in the world. Sitting at the end of a beam line almost 100m in length, and detecting in backscattering geometry, a resolution of $\Delta d/d \sim 5 \times 10^{-4}$ is achieved. Moreover, this resolution is essentially constant over the wide d-spacing range available (currently down to d-spacings of less than 0.3Å) making a much larger number of reflections available - and at higher resolution - than is possible on any other neutron powder instruments.

HRPD has dramatically extended the range of problems that can be tackled by powder diffraction. For example :

- Rietveld profile refinement of more complex structures are possible;
- Hydrogenous samples - often a problem for neutrons because of the high incoherent background - can be tackled;
- Crystal structures can be solved from powders *ab initio*;
- Structure refinements can be performed of a quality which previously required single crystals;
- The high resolution allows sophisticated peak shape analyses enabling the study of, for example, texture and strain.

II.1 Molecular structure of benzene

A fine example of the power of HRPD is given by recent work on benzene, C_6H_6 (David, 1989a). Benzene adopts an orthorhombic structure, space group Pbca (Z=2), with a moderately-sized unit cell (a=7.3550, b=9.3709, c=6.6992Å, V=461.7Å^3) (Figure 2). Although the original structure determination in 1928 located only the carbon atoms, the observed molecular planarity resolved a debate about whether the molecule was puckered, as favoured by a number of eminent scientists including Bragg, or flat.

Successive X-ray single crystal investigations improved the precision and accuracy of structure determination. The use of neutrons as a structural probe confirmed the planarity not only of the

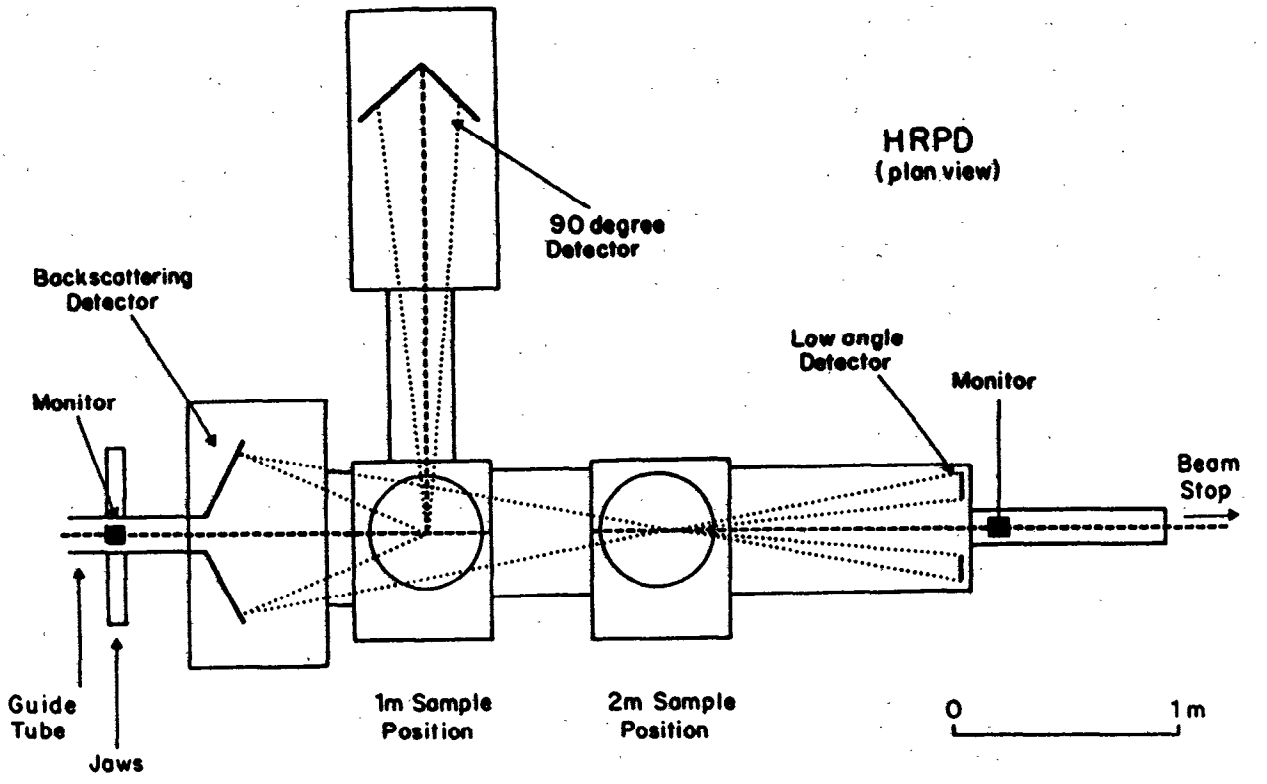

Figure 1 - Plan view of HRPD. The 2m sample position is some 96m from the moderator.

Figure 2 - The crystal structure of benzene.

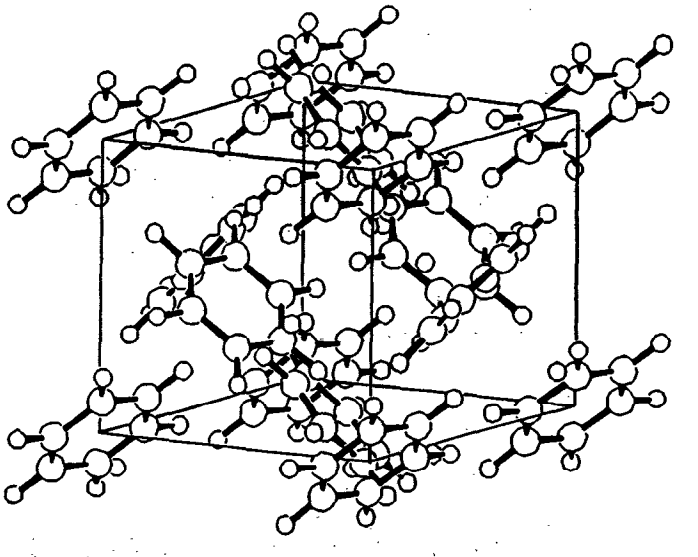

carbon but also the hydrogen atoms. A recent single crystal neutron diffraction investigation on deuterated benzene, C_6D_6 (Jeffrey, Ruble, McMullan and Pople, 1987), sought to investigate any deviations from planarity. In addition to contributing to continued investigations of the nature of the chemical bond, these experimental results have been compared with the latest theoretical calculations to assess the current status both of experimental technique and theoretical calculation. One further justification was given by Jeffrey for performing another single crystal neutron diffraction experiment: benzene "should be repeatedly investigated by each scientific method whenever there is a significant advance with respect to the detail or accuracy that the method can offer". It is therefore fitting that a detailed structural investigation of benzene be performed on HRPD to investigate (i) how well do the best powder diffraction experiments compare with equivalent single crystal studies for moderately complex structures with unit cells of the order of 500Å^3 and (ii) can reliable anisotropic temperature factors be obtained from time-of-flight powder diffraction experiments? The existence of both high precision single crystal data and detailed theoretical calculations provides a very rigorous test for the benzene data collected on HRPD.

Data were collected over a period of approximately nine hours (174 μA-hr). The raw data were corrected for incident flux (using a vanadium calibration), and cryostat and sample attenuation. The last correction was derived from consideration of the transmitted neutron flux and showed significant structure from multiple-scattering self-attenuation effects. Rietveld refinement was performed using the powder diffraction package developed at RAL and based upon the Cambridge Crystallography Subroutine Library. For data in the range 0.606–1.778Å an excellent least-squares fit to the powder diffraction data was obtained (Figure 3). The refined structural parameters included 18 atomic coordinates and 36 anisotropic temperature factors. With the exception of the B_{22} temperature factors for three carbon atoms, there is a remarkably good agreement between the positional and thermal parameters obtained from HRPD and from the single crystal data. More importantly, the anisotropic temperature factors for the deuterium atoms calculated using harmonic lattice dynamical calculations are significantly different from those obtained by both powder and single crystal diffraction techniques. Table 1 lists bond lengths, uncorrected for libration, obtained in the present study and from the work of Jeffrey et al (1987). The agreement is good, with few statistically significant differences, these probably resulting from systematic errors in the powder diffraction data.

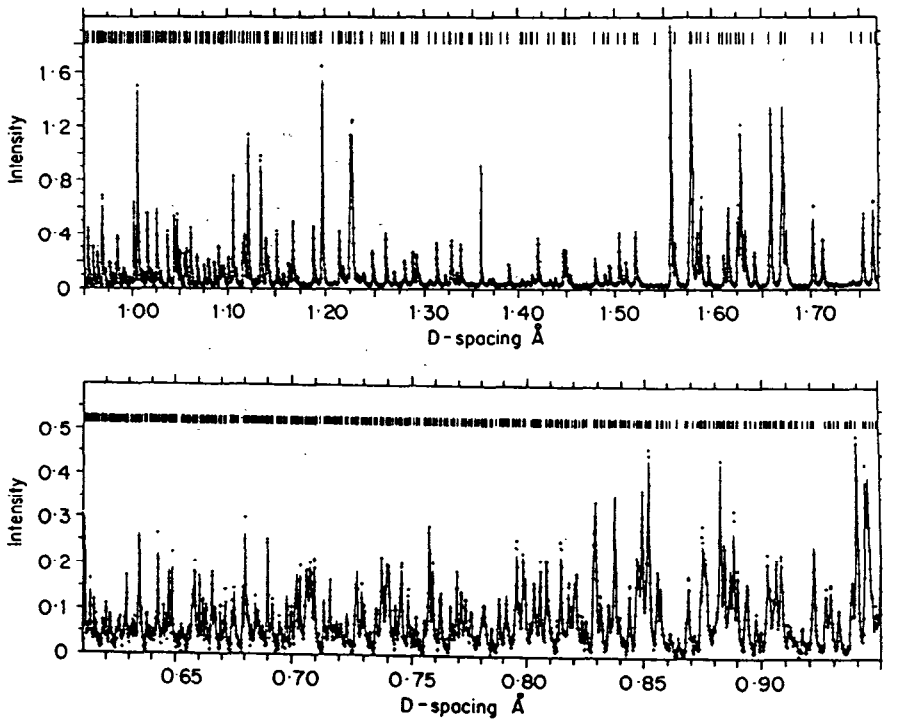

Figure 3 – The final profile fit of the HRPD low temperature benzene data, from which accurate anisotropic temperatures were obtained. The quality of fit is apparent.

TABLE 1 - Benzene : bond lengths in Å (uncorrected for libration)

HRPD data (5K)		Single crystal data (15K)	
C1-C2 = 1.3940(20)	C1-D1 = 1.0825(30)	C1-C2 = 1.3969(7)	C1-D1 = 1.0879(9)
C2-C3 = 1.4047(30)	C2-D2 = 1.0815(30)	C2-C3 = 1.3970(8)	C2-D2 = 1.0869(9)
C1-C3 = 1.3948(20)	C3-D3 = 1.0836(25)	C1-C3 = 1.3976(7)	C3-D3 = 1.0843(8)
mean = 1.3978(15)	mean = 1.0825(20)	mean = 1.3972(5)	mean = 1.0864(7)

At the present stage of analysis it is clear that the end results obtained from refinement of HRPD data are not significantly inferior to the best single crystal data. Both experimental techniques agree closely with each other, and differ from the theoretical calculations, particularly in the values obtained for the anisotropic temperature factors for the deuterium atoms. The powder diffraction experiment thus strongly supports the single crystal study and indicates that further improved theoretical calculations are required. The quality of these powder diffraction results represents present state of the art at ISIS. Further improvements in the normalisation procedure are currently under development and should lead to a precision and accuracy in moderately complex structure determination that is at least as good as the best single crystal results. This indeed represents a very significant advance in the power of powder diffraction.

II.2 Phase transition in Neopentylglycol

Neopentylglycol (NPG) is one of a series of substituted methane compounds of the type $C(CH_3)_4$-n(CH_2OH) (n = 0 to 4). NPG, corresponding to n = 2, exhibits a rigid to plastically-crystalline phase transition at 314.5 K common to all the series, but exhibits an additional low temperature phase transition at 60.4 K. The approximate molecular conformation was obtained (Suga, Matsuo and David, 1990) by a distance-least-squares refinement of atomic positions using a novel combination of chemical constraints. A total of 41 bond length and bond angle constraints define the molecule which when combined with limited single crystal X-ray data collected at room temperature can provide a good starting model for the solution attempt. From such a starting model the structures of the two low temperature phases were obtained using traditional constrained full profile refinement techniques. Both structures were found to be monoclinic, space group $P2_1/n$, with only a 0.2% change in the a, b and c lattice parameters and a 2% change in monoclinic angle, showing the transition to involve very subtle changes in hydrogen bonding. Such detailed knowledge is vital in understanding the inter- and intra-molecular forces which operate to produce the very large enthalpy of this transition, which gives the material potential technical applications as an energy storage material.

II.3 Peak Shape Effects - ferroelastic phase transition in $LaNbO_4$

Many of the diffraction patterns collected on HRPD show peak broadening effects that are dominated not by the instrument but by crystal imperfections within the sample. There is thus a need for a flexible description both of the peak shape function and peak width parameterisation. The final peak shape may be regarded as a multiple convolution of an instrumental resolution function and all the different sample dependent effects such as size, strain and stacking faults. Accordingly a peak shape algorithm based upon the convolution of individual components by fast Fourier transform techniques has been developed. This has the great advantage that, although the final peak shape function is complex, it may be obtained simply as the (inverse) Fourier transform of the product of the simple Fourier transforms of individual peak shape components. This has permitted the inclusion in the overall peak shape description of not only Gaussian and Lorentzian components but also truncated quadratic functions. A further important advance in the Rietveld analysis of HRPD data has been the development of a

program that permits the refinement of crystal structure parameters along with the Lorentzian and Gaussian components of each individual peak in the diffraction pattern. This results in a large number of parameters but has the advantage that one obtains peak widths that are unbiased by the imposition of an *hkl*-dependent peak broadening model. An example of the use of this technique is illustrated in the study of the material $LaNbO_4$.

Rietveld refinement of data collected from $LaNbO_4$ on HRPD at a number of different temperatures (David, 1989b) indicated that the anisotropic broadening resulted from strain rather than size effects (Figure 4). This anomalous behaviour is restricted to the ab plane: no extra broadening is associated with the c axis, with the refined values clearly indicating strain anisotropy within the ab plane.

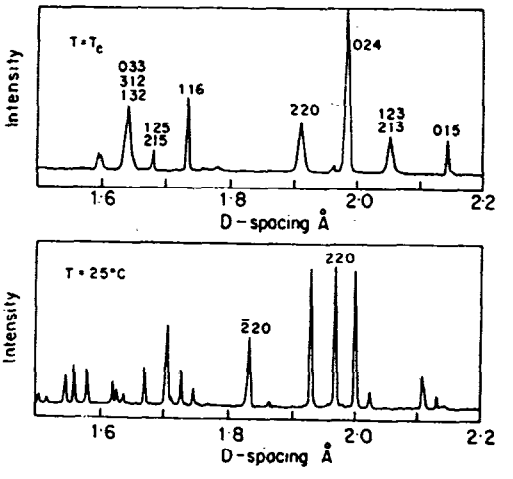

Figure 4 – The differences between diffraction patterns recorded at room temperature and T_c are extremely marked. Note the large anisotropy in peak widths at T_c, with (hk0) peaks being broad whereas predominantly c* reflections remain unaffected by the transition.

The anisotropic broadening of the Bragg peaks (microstrain) in $LaNbO_4$ may, as with the monoclinic lattice distortion (macrostrain), be described in terms of a second rank tensor. The principal axes of the ellipsoid representing the microstrain broadening is rotated by 21° from a*. This agrees to within experimental error (~ 2°) with the orientation of the principal axes of the spontaneous macrostrain hyperbola for all data sets collected between (T_c – 50°) and T_c. The coincidence of the orientation of microstrain (obtained from line broadening considerations) and macrostrain (calculated from peak splittings associated with monoclinic symmetry) was unexpected and is at present unexplained. It indicates, perhaps unsurprisingly, that unit cell and unit cell contents play a coherent role with respect to the phase transition. The importance of strain in the driving mechanism is associated with the fact that $LaNbO_4$ is a proper ferroelastic material – there is a soft acoustic mode but no observed soft optic mode. Further analysis of this phase transition using the structural information is currently underway.

The unexpected discovery of unusual strain broadening in $LaNbO_4$ and its implications for the phase transition mechanism highlights the advantages of high resolution. Although structure refinement involving the traditional Rietveld method is still the mainstay of neutron powder diffraction, there are a growing number of problems in materials science where high resolution has proved invaluable. The diversity of science tackled on HRPD confirms the success and assures the future of high resolution neutron powder diffraction.

III. POLARIS – MEDIUM RESOLUTION POWDER DIFFRACTOMETER

The medium resolution powder diffractometer POLARIS (Figure 5) is an instrument that is in many ways complementary to HRPD. Being situated considerably closer to the ISIS target, it sacrifices some resolution in favour of high count rates. POLARIS thus has the ability to study smaller or more weakly scattering samples. The loss of resolution is important, of course, especially when a material with a large, low symmetry unit cell, and hence many Bragg peaks in

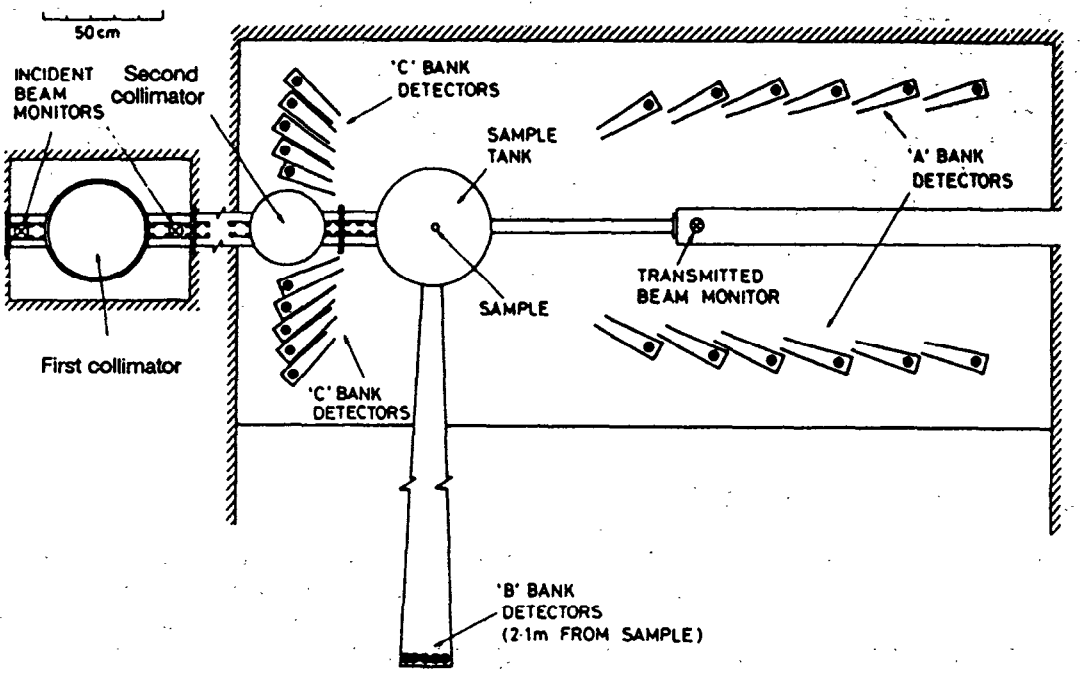

Figure 5 - Layout of POLARIS. The sample position is some 12m from the moderator.

the pattern, is being studied. To some extent, however, this problem is offset by the availability at ISIS of extremely powerful and flexible profile refinement packages.

In addition to having the capability to perform measurements on small samples over normal times, POLARIS also gives the possibility of taking data over very short times on samples of standard size. It is thus an appropriate instrument on which to look in real time at phase changes and solid state chemical reactions. Furthermore, the existence of a large detector bank at 90° allows high quality measurements on samples in pressure cells or other sample environment.

III.1 Measurements of Residual Stress

A knowledge of the residual stress distributions in engineering components is important for predicting their load carrying capabilities, failure characteristics and probable lifetimes. A test experiment has been performed on POLARIS to study the residual stress distribution within an autofrettaged steel ring (Webster and Webster, 1990). The sample was scanned through the beam, using a rig capable of remotely controlled x, y and z translations, together with an ω rotation about the vertical axis. A time-of-flight diffraction instrument, such as POLARIS, has the advantage of measuring the whole diffraction pattern from the individual 'pixels', which allows the lattice parameter a_0 to be obtained by least squares refinement over many reflections. The results are compared in Figure 6 with the values obtained using a fixed wavelength diffractometer at the ILL, where a_0 is determined from measurements of the (211) reflection alone. By measuring a large number of diffraction peaks in the same scattering direction POLARIS can provide additional information on the elastic anisotropy within the illuminated sample volume.

Figure 6 – A comparison between the residual strain measurements of an auto-frettaged ring on POLARIS (o) and D1A (•). Reasonable agreement is achieved except near the edges, probably a consequence of sample volume.

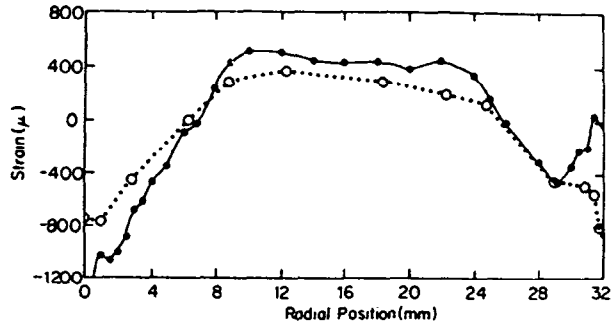

III.2 High pressure diffraction studies

Structural studies of powder samples under hydrostatic pressure are made difficult by the need to surround the sample by pressure transmitting components of the pressure cell. The fixed scattering geometry of a time-of-flight diffraction instrument allows collimation of the incident and scattered beams which eliminate spurious Bragg reflections from these components. One of the first successful experiments on samples under hydrostatic pressure on POLARIS, using the 'McWhan' clamped cell constructed at ISIS, is illustrated elsewhere (Hull, David, Ibberson and Wilson, this volume).

Figure 7 – Equation of state of LiD measured on POLARIS using the McWhan (•) and Paris (▪) pressure cells. The dashed line represents previous measurements. It can be seen that the POLARIS measurements differ appreciably from these, but agree very well with recent calculations (solid line).

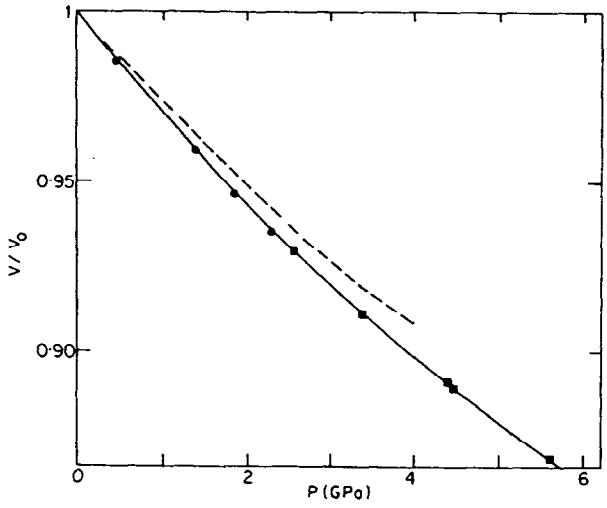

The collaborative project with the Universities of Paris and Edinburgh to develop a clamped cell for very high pressure neutron studies has also made significant progress, and is also detailed (Hull, David, Ibberson and Wilson, this volume). The equation of state of the quantum solid LiD has been measured to 70 kbar (Figure 7; Besson et al, 1991), the first time a sample volume of 100 mm3 has been studied above ~40 kbar. Future modifications, including the replacement of tungsten carbide anvils by sintered diamond, are now confidently expected to allow structural refinements to be performed in the pressure range above 100 kbar previously unexplored by neutrons.

III.3 Powder diffraction studies of the mechanism of battery discharge

Manganese dioxide, MnO_2, is widely used as the cathode material in alkaline batteries. Despite considerable research effort over the past 20 years, the processes which occur within the cathode of a cell during discharge are still not fully understood. In particular, it is unclear how the MnO_2 lattice accommodates protons during operation and how the structural behaviour is related to the ultimate failure of the cell. POLARIS has been used to obtain powder diffraction spectra of samples of MnO_2, taken from batteries at various stages of discharge (Figure 8; Clark, David and Hull, 1989).

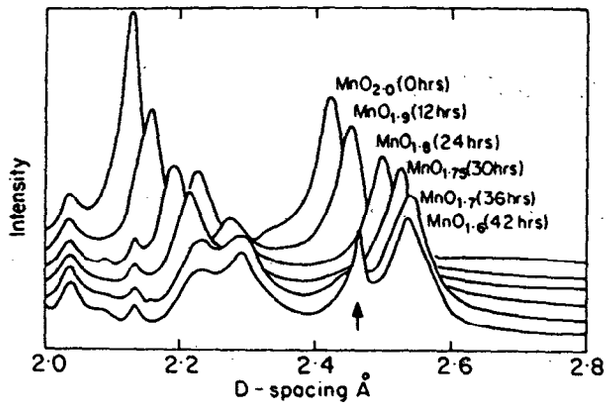

Figure 8 – Powder diffraction spectra taken from batteries at various stages of discharge. Indicated is the position of an additional Bragg peak, attributed to the formation of an ordered Mn–O–H phase. The appearance of this phase coincides closely with the point of battery failure.

Structural investigations of MnO_2 are made difficult by the poorly crystalline nature of the samples and the many, essentially similar, allotropic forms adopted by MnO_2, which comprise different arrangements of MnO_6 octahedra. Simulations of the powder diffraction spectra have been performed, using the known structures of the most common crystalline forms, pyrolusite (single chains of edge-sharing MnO_6 octahedra) and ramsdellite (alternating double chains of linked MnO_6 octahedra). These are found to differ significantly from the diffraction pattern measured from the MnO_2 in its undischarged state. It is possible, therefore, to discount these structures, plus that of γ–MnO_2, which comprises an irregular intergrowth of pyrolusite and ramsdellite layers. Surprisingly, adequate agreement is achieved by adopting the little known ϵ–MnO_2 structure, with hexagonal close packed O^{2-} ions and half the octahedral sites occupied by Mn^{4+}.

It is clear from Figure 8 that significant structural changes occur during battery discharge, including the expansion of the lattice associated with the intercalation of protons. These results give the first direct experimental evidence of proton insertion into MnO_2. Preliminary analysis suggests that the protons are accommodated randomly within the remaining empty octahedra in the ϵ–MnO_2 lattice. There is also evidence of additional broad diffraction peaks which appear after about 36 hours discharge. This coincides closely with the point of battery failure. These extra Bragg peaks are attributable to the formation of ordered Mn–O–H phases which essentially hinder proton diffusion through the MnO_2 lattice.

References

Besson J M, Weill G, Nelmes R J, Loveday J S and Hull S, High Pressure Research, submitted (1991)

Clark J W, David W I F and Hull S, ISIS 1989 Annual Report, RAL-89-050, 68 (1989)

David W I F, ISIS 1989 Annual Report, RAL-89-050, 43 (1989a)

David W I F, ISIS 1989 Annual Report, RAL-89-050, 47 (1989b)

Jeffrey G A, Ruble J R, McMullan R K and Pople J A, Proc. Roy. Soc. Lond. A414, 47 (1987)

Suga H, Matsuo T and David W I F, ISIS 1990 Annual Report, RAL-90-050, A31 (1990)

Webster G A and Webster P J, ISIS 1990 Annual Report, RAL-90-050, A63 (1990)

ICANS-XI International Collaboration on Advanced Neutron Sources
KEK, Tsukuba, October 22-26, 1990

HELIUM-3 NEUTRON POLARISERS

W G Williams, ISIS Science Division, Rutherford Appleton Laboratory, Chilton, Didcot, Oxon, OX11 0QX, UK

1. INTRODUCTION

The attractive features of polarised ^{3}He as a broad-band polarising filter for thermal and epithermal neutrons has been recognised for over two decades (1). The cross-section for neutron capture σ_c is large (5327b atom^{-1} at 25.3 meV, decreasing inversely with neutron velocity), and the ratio of the cross-section for antiparallel spin capture to the total cross-section has been experimentally determined to be 1.010 + 0.032 (2). In common with all other resonance absorption polarising filters (3), the properties of polarised ^{3}He are dominated by the capture cross-section, and any non-resonant capture and scattering can be ignored.

The most obvious method for polarising solid ^{3}He is to cool the nuclear moments in a large applied magnetic field ('Brute Force' polarisation). In principle a ^{3}He nuclear polarisation P_{He-3} ~ 55% is achievable at 10mK in a 10T field, however the neutron beam heating due to capture makes this method non-viable in high flux beams (4). The recent resurgence of interest in using polarised ^{3}He as a neutron polariser follows the discovery of an optical pumping method which can provide high nuclear polarisations (P_{He-3} ~ 70%) in high pressure gaseous samples (5). This new technique utilises the spin transfer from optically pumped Rb vapour, and is undergoing extensive development in the USA and France. The interest for the neutron scattering community is twofold: a cell containing highly polarised ^{3}He can be used as an efficient broad-band polarising filter at neutron energies up to 1eV and beyond, and there is also the possibility of combining the polarisation and detection properties of ^{3}He to provide a spin analyser-detector as a single instrument component.

The main objective of this paper is to examine the polarised ^{3}He cell parameters, ie polarisation and gas pressure, required for the neutron polariser and spin analyser-detector applications. Optimised values for the design parameters are derived and used to calculate the neutron energy dependences of various efficiency parameters which define the effectiveness of the polariser and spin analyser-detector.

2. DYNÁMIC POLARISATION IN Rb/^{3}He MIXTURES

High pressure polarised ^{3}He gas is most readily achieved in gas mixtures containing an alkali metal vapour where the ^{3}He nuclei are polarised by spin exchange with the laser-pumped alkali metal vapour. The alkali metal, normally Rb, contains a fully polarised valence electron spin, and the spin exchange is a consequence of the hyperfine interaction between this electron spin and the ^{3}He nuclear spin during binary collisions. In the experimental set-up of Coulter et a (5), ^{3}He gas at pressures up to several atmospheres was contained in a glass cell together with a Rb droplet and ~100 Torr of nitrogen as a buffer gas to assist the optical pumping process. The cell was heated to approximately 200°C and the Rb component of the gas first polarised by illumination with D_1 resonance light (795nm). The ^{3}He-Rb spin exchange probabilities were sufficiently large to produce ^{3}He polarising times of a few hours, with ^{3}He polarisation relaxation times of about 40 hours. ^{3}He polarisations greater than 70% were achieved in a volume of 6cm3 at a density of 3×10^{20} at cm^{-3} (10 atm at STP).

3. NEUTRON POLARISER PARAMETERS

In this section we define the parameters of a polarised ^{3}He cell which determine its effectiveness as both a neutron polarising filter and as a spin analyser-detector. The underlying principle by which they operate is the large difference in the neutron capture cross-sections for neutron spins parallel (σ_+) and antiparallel (σ_-) to the nuclear polarisation, which, for the pure (I-½) resonance absorption in ^{3}He is given by

$$\sigma_\pm = \sigma_c (1 \mp P_{He-3}) \tag{3.1}$$

where σ_c is the unpolarised beam capture cross-section, and P_{He-3} is the ^{3}He nuclear polarisation. The transmittances $T_\pm$ of ($\pm$) spin neutrons are given by exp-($\sigma_\pm$ Nt), where Nt is the ^{3}He atomic thickness (at.cm^{-2}), and these have a significant neutron energy dependence consequential to the energy dependence of the capture cross-section σ_c.

3.1 Neutron Polarisers

The three relevant polarising filter parameters are the polarising efficiency:

$$P = (T_+ - T_-)/(T_+ + T_-) = \tanh (\sigma_c P_{He-3} Nt), \tag{3.2}$$

the unpolarised beam transmittance,

$$T = (T_+ + T_-)/2 = \exp(-\sigma_c Nt)\cosh(\sigma_c P_{He\text{-}3} Nt) \tag{3.3}$$

and the polariser quality factor

$$Q = P\,T^{1/2} \tag{3.4}$$

3.2 Spin Analyser-Detectors

The corresponding quantities which determine the effectiveness of spin analyser-detectors are the spin analyser efficiency:

$$\begin{aligned} P_A &= (T_- - T_+)/[2-(T_+ + T_-)] \\ &= \sinh(\sigma_c P_{He\text{-}3} Nt)/[\cosh(\sigma_c P_{He\text{-}3} Nt) - \exp(\sigma_c Nt)], \end{aligned} \tag{3.5}$$

the detector efficiency for unpolarised neutrons,

$$\eta = 1 - T \tag{3.6}$$

and the spin analyser-detector quality factor,

$$Q_A = P_A \eta^{1/2} \tag{3.7}$$

In contrast to the polariser, the analyser efficiency decreases with increasing atomic thickness Nt and a further useful spin analyser parameter is its maximum efficiency $P_A(Max)$ which is given by the $\sigma_c Nt \rightarrow 0$ approximation of eqn (3.5):

$$P_A(Max) = (\sigma_+ - \sigma_-)/(\sigma_+ + \sigma_-) = -P_{He\text{-}3} \tag{3.8}$$

3.3 Commmon Relationships

For polarised ^{3}He neutron polarisers P, T and η are always positive whereas P_A is negative, and these are interrelated as follows:

$$PT = -P_A\eta \tag{3.9}$$

In discussing spin analyser efficiencies and quality factors we shall generally simply use their moduli $|P_A|$ and $|Q_A|$.

These efficiencies are related to the quality factors as follows:

$$|Q/Q_A| = |P/P_A|^{1/2} = (\eta/T)^{1/2} \tag{3.10}$$

4. PERFORMANCE OF ^{3}He NEUTRON POLARISERS AND SPIN ANALYSERS

The most useful starting point for discussing the properties of filter polarisers and spin analysers is to use the defining equations given in section 3 to calculate universal 'constant polarisation' curves (6). For ^{3}He neutron polarisers, once P is fixed, $\sigma_c Nt$ and P_{He-3} are related through eqn (3.2), and the complete series of polariser and analyser parameters are calculable as a function of P_{He-3} (or $\sigma_c Nt$). In this section we present two sets of polariser and analyser parameter curves for ^{3}He neutron polarisers with widely different polarising efficiencies. We then proceed to use the results of these calculations to evaluate the neutron energy dependences of the efficiency parameters for ^{3}He polarisers and spin analysers with optimised values for the ^{3}He atomic thickness Nt and nuclear polarisation P_{He-3}.

4.1 Universal Curves

Figure 1 shows the polariser transmittance T, spin analyser polarising efficiency $|P_A|$, and analyser detection efficiency η for a ^{3}He filter with constant polarising efficiency P = 0.95 (or equivalently $\sigma_c P_{He-3} Nt = 1.832$), as a function of the helium polarisation P_{He-3} and absorption parameter $\sigma_c Nt$. These are suitable design parameters for a ^{3}He filter used as a polariser in neutron scattering experiments where the need for a high polarising efficiency is extremely important. The polariser transmittance rises sharply as P_{He-3} increases, and combining this with the requirement that any effective polarising filter should ideally have $T > 0.3$, we conclude that for the polariser application we need an optically polarised ^{3}He cell with nuclear polarisation $P_{He-3} \simeq 0.80$ and absorption parameter $\sigma_c Nt \simeq 2.3$. Neutron scattering applications require the filter to operate at neutron energies $\sim$ 1eV (and beyond), where $\sigma_c \sim$ 830b atom^{-1}, and this determines the ^{3}He atomic thickness to be $Nt \sim 2.76 \times 10^{21}$ atom cm^{-2}. This atomic thickness can, for example, be achieved with a 10 atm (at 300K) ^{3}He cell which has a length $t \simeq 11.3$cm. The specification compares reasonably favourably with the currently achievable $P_{He-3} \simeq 0.70$ in a 10 atm cell of length 5cm.

The spin analyser efficiency $|P_A|$, in contrast to P, rises sharply with decreasing absorption parameter $\sigma_c Nt$, and the values in Fig 1 fall significantly short of the diagonal line representing $|P_A(Max)| = P_{He-3}$. We conclude that the behaviour of a filter with absorption parameters $\sigma_c Nt$ in the 2-10 range departs significantly from the low $\sigma_c Nt$ limit represented by eqn (3.8), and that this filter is too absorbent for the spin analyser application, unless ^3He polarisations in excess of 95% can be achieved.

To produce an effective spin analyser we therefore require a lower atomic thickness Nt, but must retain a usefully large absorption parameter to give an acceptable detector efficiency. Figure 2 shows the filter parameters T, $|P_A|$, and η where $\sigma_c Nt$ has been reduced to one tenth of the values of Figure 1; these curves correspond to constant polarisation curves where $P = 0.181$, or $\sigma_c P_{He-3} Nt = 0.183$. It is immediately evident that $|P_A|$ now approaches $|P_A(Max)|$, and is in fact within 90% of $|P_A(Max)|$ for all P_{He-3} values greater than ~ 0.5. It is also clear that there is a significant increase in $|P_A|$ towards larger P_{He-3} values, and we conclude that for the spin analyser-detector application it is important to achieve ^3He polarisations approaching unity.

The data of Figure 1 and 2 have also been used to calculate universal curves for the polariser quality factor Q and spin analyser quality factor $|Q_A|$; these are shown in Figure 3. The plots confirm a) that the polariser application requires the more absorbent filter ($\sigma_c P_{He-3} Nt = 1.832$) and b) that for ^3He polarisations up to $\sim$ 75%, the lower density filter has the more effective performance as a spin analyser. It is also apparent that the spin analyser quality factors $|Q_A|$ will in general always be lower than the best polariser quality factors Q obtained with a highly absorbing filter.

4.2 Neutron Energy Dependences

Universal curves provide a powerful method for assessing the properties of neutron polarising filters and polarisation analysers. In practice, however, an operational filter always has a fixed P_{He-3} (ie the maximum value attainable) and a fixed atomic thickness Nt chosen by the filter designer to optimise the performance over the neutron energy range (or equivalently the σ_c range) corresponding to the demands of the neutron experiments. For condensed matter physics scattering experiments we can regard the useful neutron energy band to be 0-1 eV. The neutron experimentalist requires good filter characteristics over as large a part of this energy range as possible, and it is essential to know how the filter parameters vary over this energy band.

We now present calculated values of the neutron energy dependences of P, T, $|P_A|$ and η for two gaseous polarised ^3He filters. The filter parameters were chosen on the basis of the results

described in Section 4.1; the first is suitable as a filter polariser and the second as a spin analyser-detector. For the polariser we have selected a filter with $P_{He-3} = 0.80$, ^3He atomic density $N = 2.45 \times 10^{20}$ atom cm^{-3} (this corresponds to 10 atmospheres of gas pressure at 300K), and a thickness t = 5cm; this is designated Filter A. For the spin analyser-detector we have retained the ^3He polarisation value $P_{He-3} = 0.80$, but have reduced the atomic density to $N = 0.49 \times 10^{20}$ atom cm^{-3} (ie $\sim$ 2 atmos. gas pressure at 300K) and the cell thickness to t = 2.5cm; this is designated Filter B.

The neutron energy dependences of the polarising efficiency P, transmittance T, and polariser quality factor Q for Filter A are shown in Figure 4. The overall performance is very satisfactory over the entire 10-1000meV range; note that the polarising efficiency at energies less that 100 meV is essentially 100%, and that the lowest polarising efficiency is P = 0.67 at 1eV.

The neutron energy dependences of the spin analyser efficiency $|P_A|$, detector efficiency η, and analyser quality factor $|Q_A|$ for Filter B are shown in Figure 5. The overall performance of this filter as a spin-analyser is very good over the whole energy range, however it should be noted that $|P_A|$(Filter B) < P(Filter A) and $|Q_A|$(Filter B) < Q (Filter A) over most of this range. Thus, in general, a filter of this type will have a better performance as a polariser than as a spin analyser.

5 CONCLUSIONS

Generalised curves have been presented to illustrate the performances of gaseous polarised ^3He cells when they are used as neutron polarisers and spin analyser-detectors. The efficiency parameters of the devices are strongly dependent on the ^3He polarisation and atomic thickness in both applications. The main conclusions are that for neutron scattering experiments in the 0.01-1 eV energy range:

a) it is important to improve the currently achievable ^3He polarisation from $P_{He-3} = 0.70$ to $P_{He-3} = 0.80$ (or greater),

b) it is necessary to increase the effective area of the cell to accommodate $\sim 6\ cm^2$ beams in the case of the polariser and $\sim 10 cm^2$ scattered beams for the spin analyser, and

c) there is no compelling reason to develop the optical pumping technique to accommodate gas pressures in excess of 10 atmospheres; the recommended optimum gas pressures are $\sim$10 atmos in a cell length $\sim$ 5cm for the polariser, and $\sim$ 2 atmos in a cell length $\sim$ 2.5 cm

for the spin analyser. The shorter cell thickness of the spin analyser is necessary to preserve resolution in neutron time-of-flight experiments, e.g. when it is used as a detector in a pulsed neutron source spectrometer.

REFERENCES

1. H. Postma, 'Polarised neutrons on polarised targets' Proc 3rd Int Symp on Polarisation Phenomena in Nuclear Reactions, ed. H H Barschall and W Haeberli, Madison (1970) 373.
2. L Passell and R I Schermer, Phys Rev **150** (1966) 146
3. R Cywinski, J Mayers and W G Williams, 'Resonance absorption polarising filters for epithermal neutrons'. Rutherford Appleton Laboratory Report RL-81-043 (1981).
4. F Tasset 'The Polarised ^{3}He gas filter; A promising polarisation method for hot neutron beams' Troixeime Souffle Workshop, Institut Laue Langevin, August 1989.
5. K P Coulter, A B McDonald, W Happer, T E Chupp and M E Wagshul, Nucl Instr Meth *A270* (1988) 90.
6. W G Williams 'Polarised Neutrons', Oxford Science Publications, Oxford University Press (1988).

FIGURE CAPTIONS

Figure 1

Universal curves showing the polariser and spin analyser parameters for a polarised ^{3}He filter with $P=0.95$ or $\sigma_c P_{He-3} Nt = 1.832$, as a function of ^{3}He polarisation and the absorption parameter $\sigma_c Nt$.

Figure 2

Universal curves showing the polariser and spin analyser parameters for a polarised ^{3}He filter with $P=0.181$ or $\sigma_c P_{He-3} Nt = 0.183$, as a function of ^{3}He polarisation and the absorption parameter $\sigma_c Nt$.

Figure 3

Universal curves for the quality factors Q and $|Q_A|$ of the polarised ^{3}He filters described in Figs 1 and 2 as a function of ^{3}He polarisation.

Figure 4

Neutron energy dependences of the polariser parameters P, T, and Q for a polarised ^{3}He filter with 80% ^{3}He polarisation and atomic thickness $Nt = 1.225 \times 10^{21}$ at.cm^{-2}.

Figure 5

Neutron energy dependences of the spin analyser-detector parameters $|P_A|$, η, and $|Q_A|$ for a polarised ^{3}He filter with 80% ^{3}He polarisation and atomic thickness $Nt = 1.225 \times 10^{20}$ at.cm^{-2}.

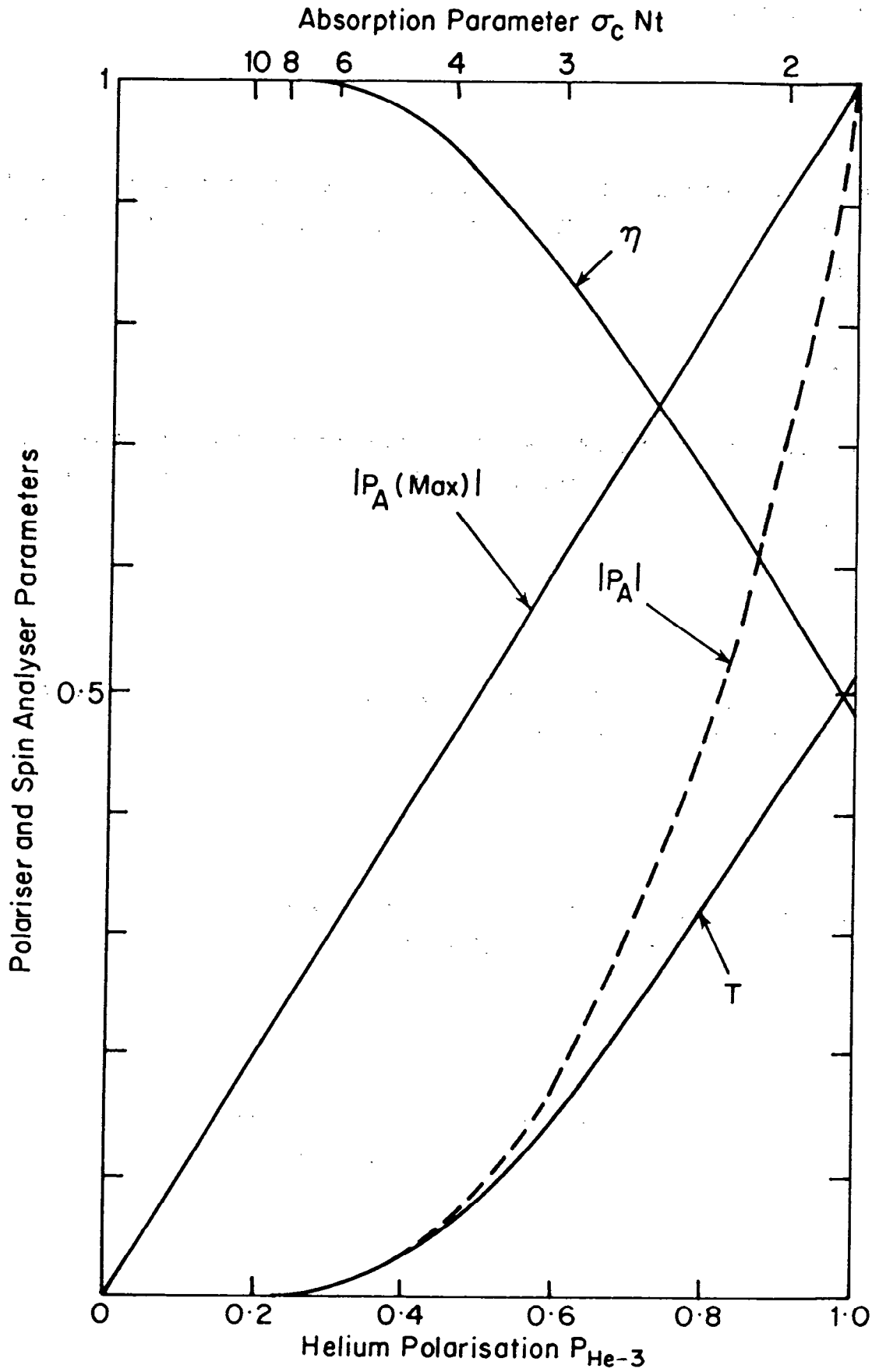
Absorption Parameter σ_c Nt
10 8 6 4 3 2
1
0·5
0
0·2
0·4
0·6
0·8
1·0
Polariser and Spin Analyser Parameters
Helium Polarisation P_{He-3}
η
$|P_A(Max)|$
$|P_A|$
T

Fig. 1

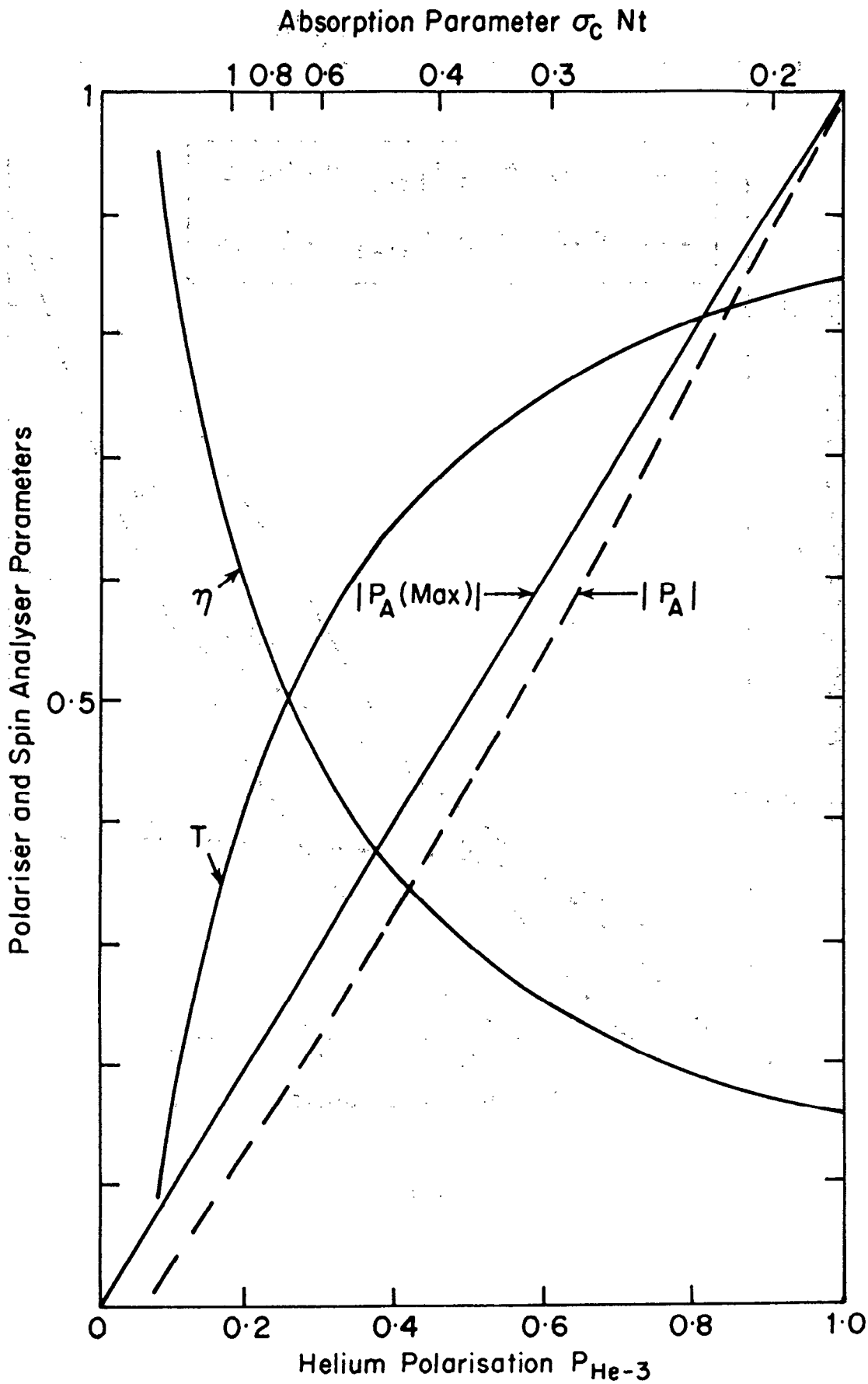
Absorption Parameter σ_c Nt
1 0·8 0·6 0·4 0·3 0·2
1
0·5
0
0·2
0·4
0·6
0·8
1·0
Polariser and Spin Analyser Parameters
Helium Polarisation P_{He-3}
η
T
$|P_A(Max)|$
$|P_A|$

Fig.2

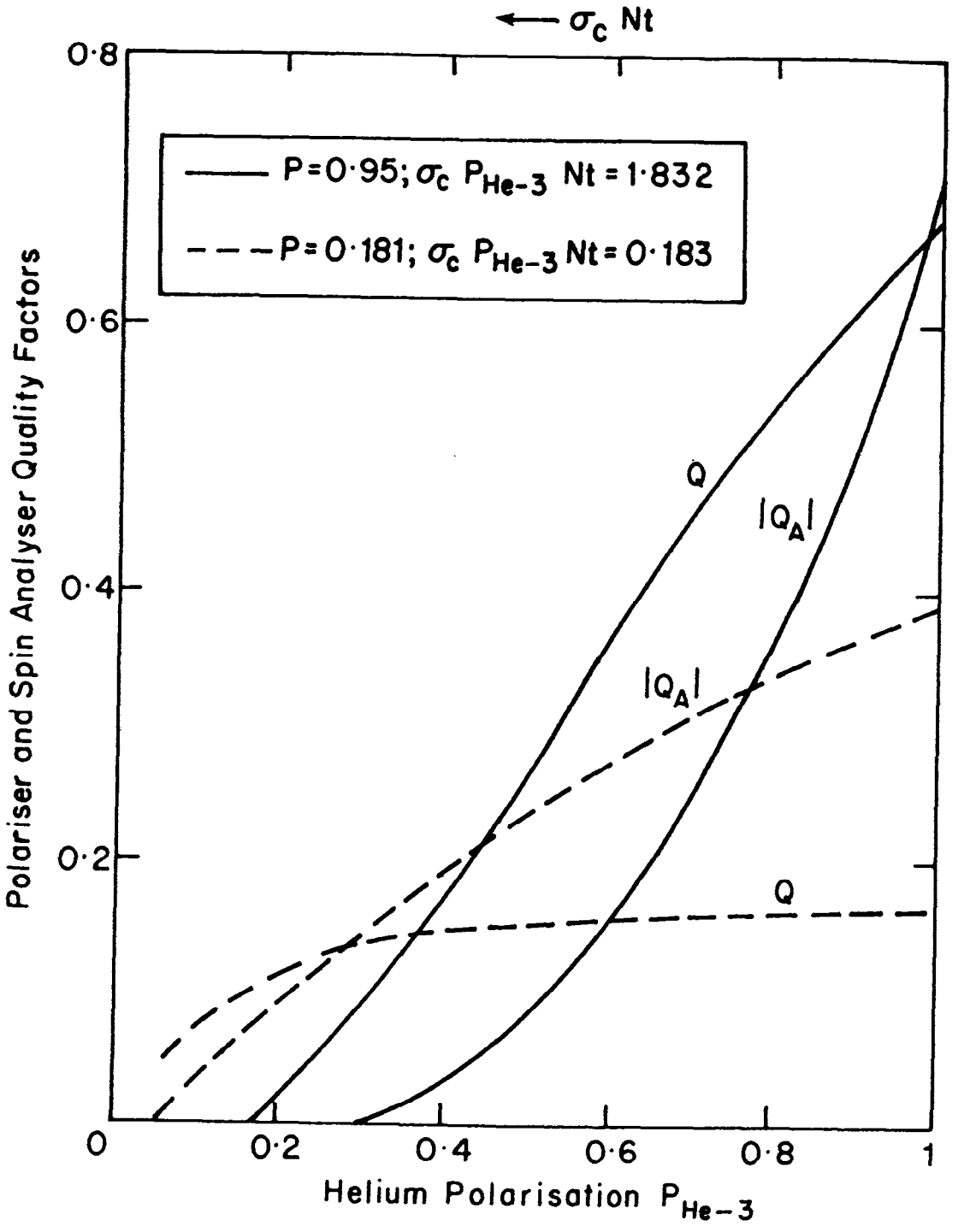
← σc Nt
P=0·95; σc PHe-3 Nt = 1·832
P=0·181; σc PHe-3 Nt = 0·183
Q
|QA|
|QA|
Q
0·8
0·6
0·4
0·2
0
0·2
0·4
0·6
0·8
1
Polariser and Spin Analyser Quality Factors
Helium Polarisation PHe-3

Fig.3

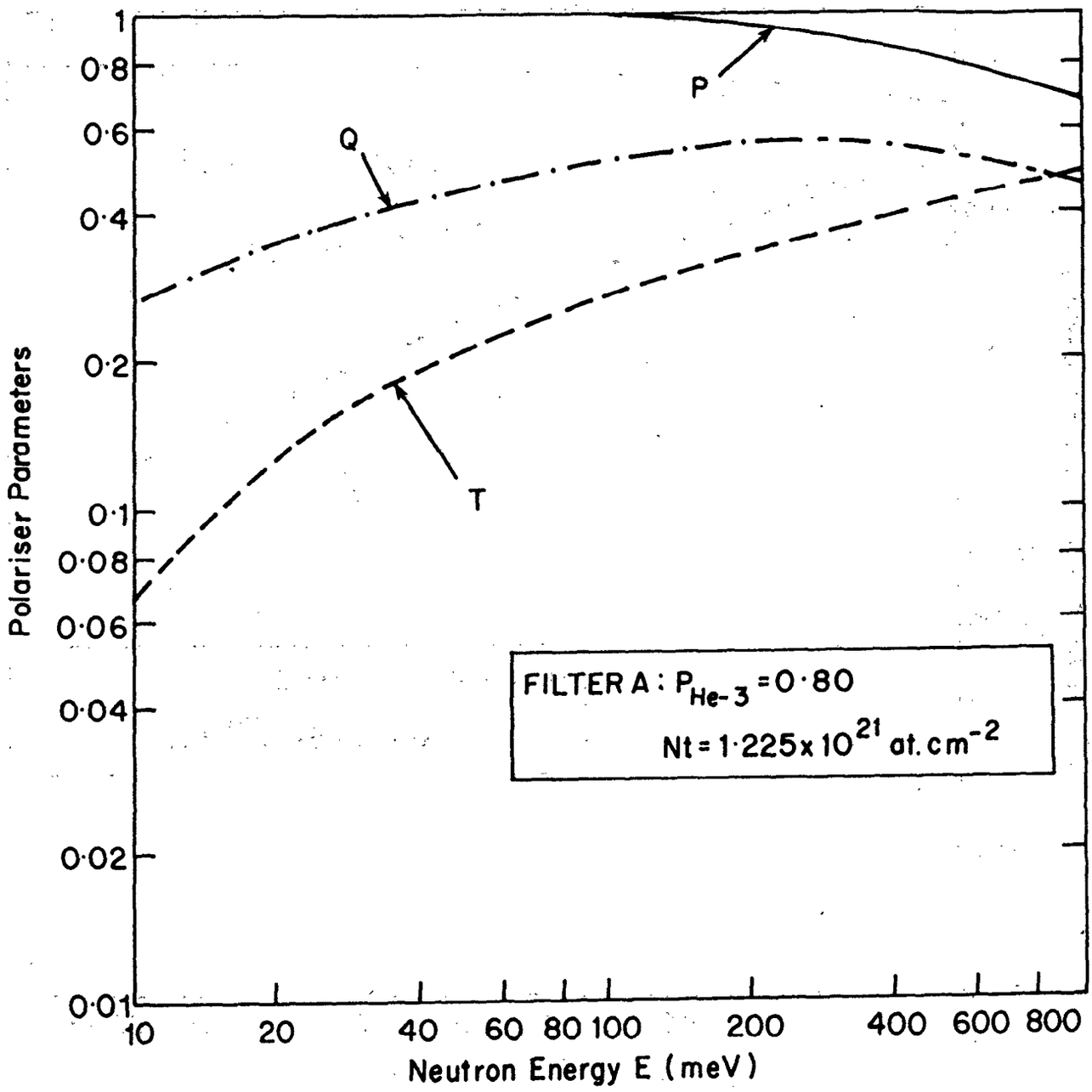
Polariser Parameters
1
0·8
0·6
0·4
0·2
0·1
0·08
0·06
0·04
0·02
0·01
P
Q
T
FILTER A : P_{He-3} = 0·80
Nt = 1·225 x 10^{21} at. cm^{-2}
10
20
40
60
80
100
200
400
600
800
Neutron Energy E (meV)

Fig. 4

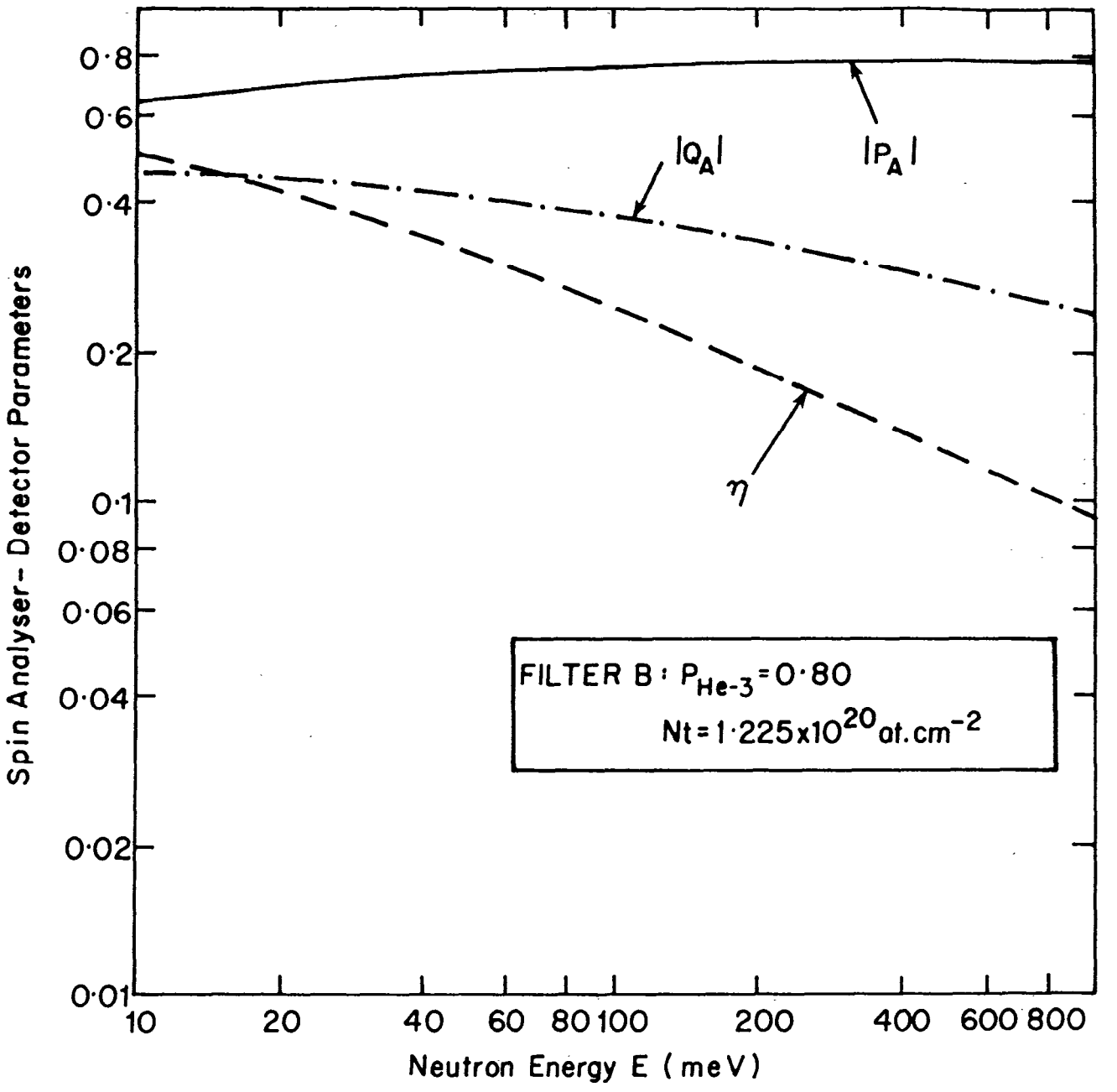
0·8
0·6
0·4
0·2
0·1
0·08
0·06
0·04
0·02
0·01
Spin Analyser- Detector Parameters
|Q_A|
|P_A|
η
FILTER B : P_He-3 = 0·80
Nt = 1·225x10^20 at.cm^-2
10
20
40
60
80
100
200
400
600
800
Neutron Energy E (meV)

Fig.5

ICANS-XI International Collaboration on Advanced Neutron Sources
KEK, Tsukuba, October 22-26, 1990

A new polarized target for structure studies on biomolecules at GKSS

M. Hirai[1], W. Knop[2], H.-J. Schink[2], H.B. Stuhrmann[2], R. Wagner[2], J. Zhao[2], O. Schärpf[3], R.R. Crichton[4], M. Krumpole[5], K. Nierhaus[6], T.O. Niinikoski[7] and A.Rijllart[7]

1 Kanagawa Inst. Technology, Atsugi-shi, Kanagawa-ken 243-02, Japan
2 GKSS Forschungszentrum, D-2054 Geesthacht, Germany
3 Inst. Laue Langevin, F-38042 Grenoble, France
4 Unité be Biochemie, Université Catholique de Louvain, B-1318 Louvain-la-Neuve
5 Department of Chemistry, University of Illinois, Chicago, USA
6 Max-Planck-Inst. fur Molekulare Genetik, Berlin, Germany
7 CERN-EP, Geneva, Switzerland

ABSTRACT

The Small-Angle Neutron Scattering instrument (SANS-1) which has been designed for the fields of molecular biology and polymer research has been put into operation in the new experimental hall for neutron scattering at the research reactor FRG-1 equipped with a Cold Neutron Source and a beryllium reflector at the GKSS Research Center. SANS-1 has been equipped with a polarized target station for the measurement of polarized neutron scatterings, which is mainly dedicated to the use of nuclear spin contrast variation method. The nuclear spins of protons and deuterons in most polymers and biological macromolecules can be almost aligned by dynamic nuclear polarization (DNP) with respect to an external magnetic field of 2.5 tesla at temperatures below 1 K in the presence of paramagnetic centers via 4 mm microwave irradiation, where one of them can be depolarized selectively by irradiation of their proper nuclear resonance frequency. First experiments using SANS-1 have been carried out with apoferritin and deuterated large subunit of E.coli ribosomes.

I. INTRODUCTION

During the last three years, a Cold Neutron Source using GH_2 with 1.5 kW cooling power has been installed in the research reactor FRG-1 (5MW light water swimming-pool reactor). At the same time, new experimental facilities for neutron scattering have been constructed in the enlarged new experimental hall. This hall has five cold neutron guides and eleven spectrometers one third of which utilize polarized neutrons. One of the

small-angle scattering spectrometer, SANS-1, has been equipped with a polarized target station.

The first measurements of the scattering of polarized proton spin clusters of various proteins in deuterated medium confirmed the predicted concept of the nuclear spin contrast variation method in macromolecular structure research (Knop et al., 1986,1989). First experiments using SANS-1 has shown the feasibility of this method owing to the increase of the gain in neutron scattering by a factor of 10^3 compared to earlier experiments. A more detailed report of this study will be published (Knop et al.).

II. METHOD

II-1 Concept of spin contrast variation

Spin contrast variation is a most convenient method for in site structure determination. This method is a kind of isotopic label method using the dependency of scattering amplitude on the nuclear spin polarization. At first we will summarize its concept (Stuhrmann et al., 1986, Boulin et al., 1988).

The interest in polarized targets is due to the spin-dependent neutron scattering showed by Abragam et al. (1982). The Fermi scattering amplitude operator for a free nucleus is given by

$$a = b + 2B\mathbf{I}\cdot\mathbf{s} \qquad \text{..... (1)}$$

where s and I are the spin operators of the neutron and the nucleus, respectively. The constants b and B are expressed as a function of the two eigenvalues b_+ and b_- which correspond to the two different coupling channels I+1/2 and I-1/2.

$$b = [(I+1)b_+ + Ib_-] / (2I + 1), \quad B = (b_+ - b_-) / (2I + 1) \qquad \text{..... (2)}$$

When we assume that neutrons impinge on a collection of scattering centers at position r_i and that the nuclear spins have a polarization P with no correlation and that neutrons have a polarization P_n parallel to that of the nuclei, neutron differential cross section of this cluster is given by the following expression (Abragam and Goldmann, 1982):

$$\begin{aligned} d\sigma/d\Omega &= \sum_i \langle|a_i|^2\rangle + \sum_{i\neq j}\langle a_i a_j^* \exp[-i\mathbf{Q}\cdot(\mathbf{r}_i-\mathbf{r}_j)]\rangle \\ &= \sum_i [\langle|a_i|^2\rangle - \langle a_i a_j\rangle_{i\neq j}] + \langle a_i a_j^*\rangle_{i\neq j} \sum_{i,j} \exp[-i\mathbf{Q}\cdot(\mathbf{r}_i-\mathbf{r}_j)] \\ &= (d\sigma/d\Omega)_{inc.} + (d\sigma/d\Omega)_{coh.} \end{aligned}$$

whence

$$(d\sigma/d\Omega)_{inc.} = \sum_i B_i^2[I_i(I_i + 1) - P_n P_i I_i - P_i^2 I_i^2] \qquad \text{..... (3)}$$

$$(d\sigma/d\Omega)_{coh.} = |U(Q)|^2 + 2P_nRe[U(Q)V(Q)] + |V(Q)|^2 \quad \text{..... (4)}$$

where < > means the spin variable average in the target, Q is the momentum transfer, U(Q) and V(Q) are the coherent scattering amplitudes obtained by the Fourier transforms of the invariant part u(r) and the polarization-dependent part v(r), respectively. These terms are defined as

$$U(Q) = \sum_i b_i exp(-iQ\cdot r_i) = F\{\sum_i b_i\delta(r - r_i)\} = F\{u(r)\} \quad \text{..... (5)}$$

$$V(Q) = \sum_i B_i I_i P_i exp(-iQ\cdot r_i) = F\{\sum_i B_i I_i P_i \delta(r - r_i)\} = F\{v(r)\} \quad \text{..... (6)}$$

Under the conditions that the cluster with no preferred orientation has only one nuclear species with non zero spin, the coherent scattering intensity per cluster can be obtained as follows.

$$I(Q) = <|U(Q)|^2> + 2P_n<Re[U(Q)V(Q)]> + <|V(Q)|^2>$$

$$\equiv I_u(Q) + P_nPI_{uv}(Q) + P^2I_v(Q) \quad \text{..... (7)}$$

where < > means the average of scattering intensity in momentum space. According to Eq. (7) it is clear that each of the basic scattering functions, $I_u(Q)$, $I_{uv}(Q)$ and $I_v(Q)$, can be obtained easily by a series of measurements of I(Q) at different P and P_n, that is, $I_u(Q)$ from P = 0, $I_{uv}(Q)$ from the difference between P_nP = 1 and -1, $I_v(Q)$ from the sum of P_nP = 1 and -1.

In the case of small-angle scatterings from the dissolved molecules in the solvent with a mean scattering amplitude density $_{solvent}\bar{\rho}_u + {}_{solvent}\bar{\rho}_v$, the use of the definition of the scattering density is more convenient. So we can get the reformulation of Eq. (7) for P_n=1 at zero angle as follows.

$$I(0) = V^2[\bar{\rho}_u^2 + 2(\bar{\rho}_u\bar{\rho}_v) + \bar{\rho}_v^2] = V^2(\bar{\rho}_u + \bar{\rho}_v)^2$$

$$= V^2(\bar{\rho}_u + P\bar{\rho}'_v)^2 \equiv V^2\bar{\rho}^2 \quad \text{..... (8)}$$

where V is the volume of the particle, $\bar{\rho}_u$ and $\bar{\rho}_v$ are the mean excess scattering densities with respect to the solvent per unit volume, which correspond to the invariant and polarization-dependent parts, respectively. Here $\bar{\rho}$, $\bar{\rho}_u$ and $\bar{\rho}_v$ are termed so-called contrast of the whole cluster, isotope contrast and nuclear spin contrast, respectively. Those notations are defined in the same manner as is well-known isotope contrast variation method.

$$\bar{\rho}_u \equiv \sum b_i/V - {}_{solvent}\bar{\rho}_u, \qquad \bar{\rho}_v \equiv NBIP/V - {}_{solvent}\bar{\rho}_v \equiv P\bar{\rho}'_v \quad \text{..... (9)}$$

N is the number of atoms in the cluster which have a nuclear spin-dependent scattering amplitude.

II-2 Dynamic polarization and selective depolarization

In the presence of paramagnetic centers, as which we used sodium bis(2-ethyl-2-hydroxybutyrato)oxochromate(V) monohydrate (abbreviated EHBA-Cr(V): Krumpolc et al., 1985), the nuclear spins of protons and deuteron in macromolecules can be polarized by the use of dynamic polarization method (Abragam and Goldmann, 1982). The polarizations P_H, P_D and the spin temperatures T_H, T_D are related by Brillouin functions:

$$P_H = \tanh(h\nu_H / 2kT_H) \qquad \text{..... (10)}$$

$$P_D = 4\tanh(h\nu_D / 2kT_D) / (3 + \tanh^2(h\nu_D / 2kT_D)) \qquad \text{..... (11)}$$

where ν_H and ν_D are the Larmor frequencies of protons and deuterons, respectively. Assuming equal-spin-temperature, $T_H = T_D$, a unique temperature T can substitute for the different temperatures. After a high steady state of the nuclear spin polarizations is attained by microwave injection, one of the spins, protons or deuterons, is saturated by suppling RF of ν_H or ν_D, instead of microwave. In order to attain a high steady state, the temperature must be reached as low as possible. For this purpose the concentration of Cr(V) complex must be also controlled to reduce dipole-dipole interaction in paramagnetic electrons and to have a appropriate dipole-dipole interaction between nucleus and paramagnetic electron, simultaneously.

Following simulated results, Fig.1-5, base on equal-spin-temperature hypothesis of two different spin systems, i.e., proton spin system and deuteron spin one at thermal contact. Fig. 1 and 2 show the dependencies of deuteron polarization and of

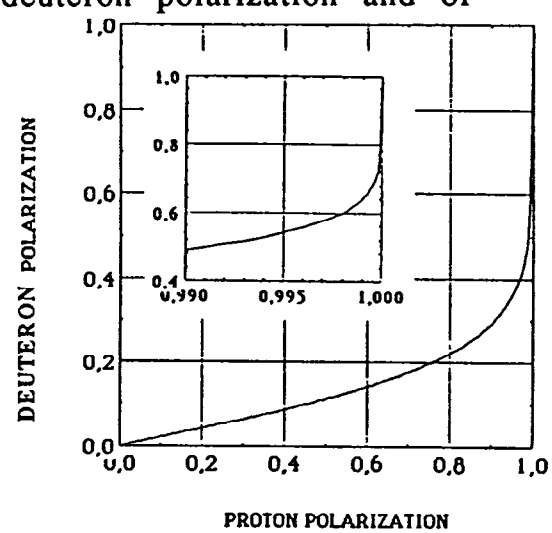

Fig. 1 Deuteron polarization vs. proton polarization

Fig. 2a

Fig. 2b

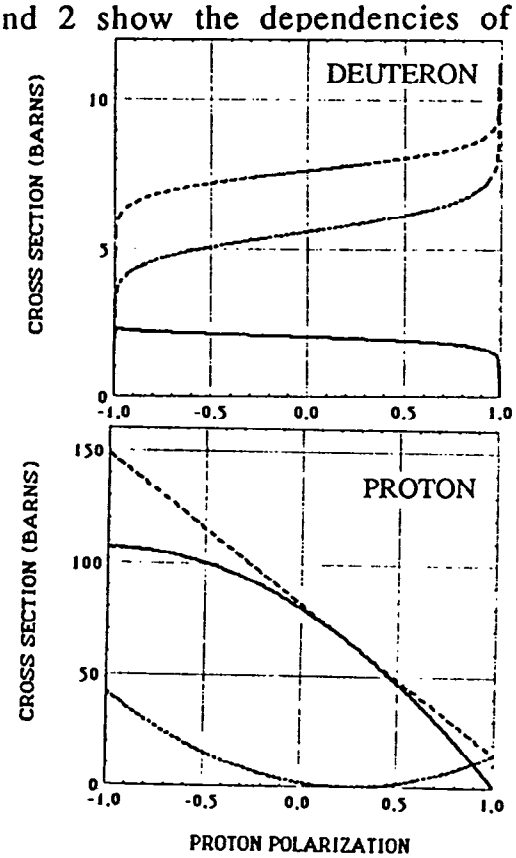

Fig. 2a & 2b The dependency of cross section on proton polarization: ---- σ_{total}, ·····$\sigma_{coh.}$, ––– $\sigma_{inc.}$

scattering cross sections on proton polarization (at $P_N = 1$). In Fig. 3 we see how great experimental improvement for signal to noise ratio defined by (zero scattering int.)/(incoherent back ground scattering int.). In Fig. 4 and 5 (at $P_N = 1$) so-called contrast is given by the difference between solvent and solute scattering densities. A contrast matching proton polarization is obtained from a point of intersection of both lines. For each simulation corresponding to Fig. 2-5, the concentration of solute is 2 wt% Urease and the deuteration ratios of solute, glycerol & water are 0%, 98.5% & 99.5%, respectively. The effect of H-D exchange is also considered.

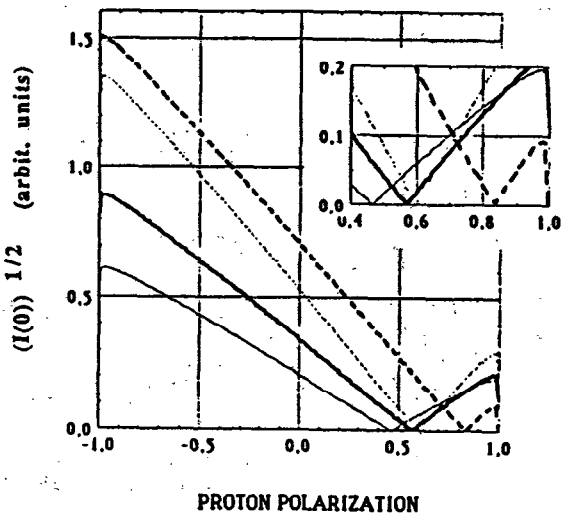

Fig. 4 Zero angle scattering int. vs. proton polarization: —— protein, – – – DNA, ---- lipid head, ---- lipid alkyl.

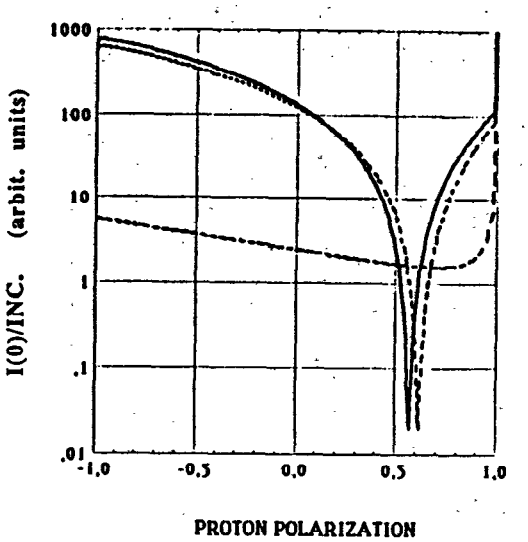

Fig. 5 Signal to Noise ratio of solution : —— in D_2O, ---- in H_2O, ····· in D_2O + D-glycerol (1:1).

III. EXPERIMENTAL

III-1 Materials

Apoferritin was prepared from horse spleen ferritin by the method described elsewhere (Jin and Crichton, 1987). This sample solution which contained 1.7 wt% apoferritin, 53 wt% deuterated glycerol, 45 wt% D_2O, 0.72 wt% EHBA (1.2 x $10^{19}/cm^3$) and 2 wt% H_2O was quenched rapidly in a copper block cooled by liquid nitrogen and formed the frozen sample with the dimensions 17 x 17 x 2 mm^3.

The sample solution of deuterated large subunit of E.coli ribosomes contained 0.55 wt% subunit and almost the same amounts of other components as the apoferritin sample had. After quenching treatment was also same. The deuteration ratio of the subunit, 83%, was deduced from zero-angle scattering intensities. At this deuteration ratio, the scattering amplitude density of the subunit (at P=0) is slightly more than half of that of the solvent. For sample preparation the rapid quenching and the existence of glycerol in solution is so important that we can eliminate the effect on solute molecular structure caused by the precipitation of water crystallites.

In the sample cell, two pieces of the frozen samples were alined perpendicular to incident neutrons with the effective sample path length 4 mm.

III-2 Polarized target

The surroundings of the target and the inside view of the sample cell are shown schematically in Fig. 6. This target station for polarized neutron scattering has been developed by CERN (Niinikoski et al., 1976, 1982). The sample is immersed in a liquid ^{4}He bath so as to be transparent to incident neutrons and cooled by thermal couple to the mixing chamber of the ^{3}He/^{4}He dilution refrigerator. This refrigerator has 20 mM/s maximum circulation rate

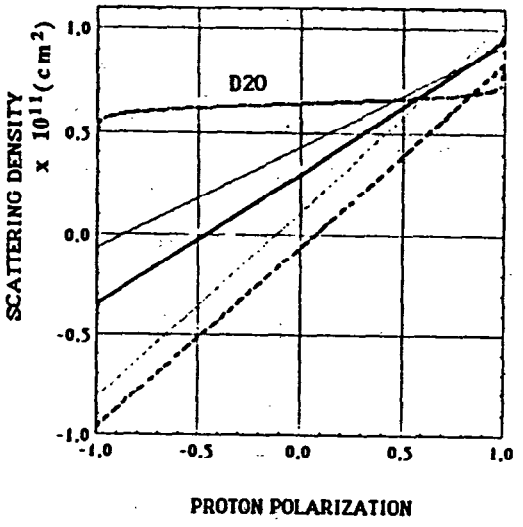

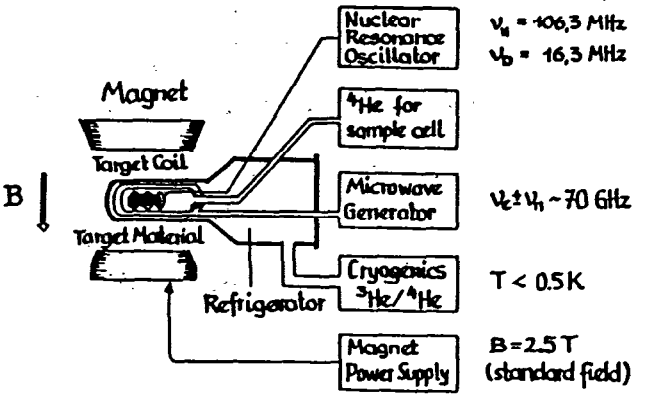

Fig. 6

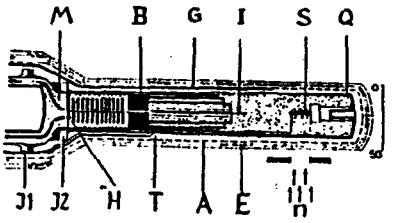

Fig. 5 Scattering length density vs. proton polarization: —— protein, —— DNA, ---- lipid head, ---- lipid alkyl.
Fig. 6 Schematic view of the target and its surroundings: mixing chamber M; heat exchanger B; sample S; quarz cell Q; inner vacuum chamber A; indium joints J1,J2; liquid ^{4}He path I; microwave guide G; heat shield E (50Φ).

of ^{3}He and 1 mW cooling power at the sample position at T = 200 mK. The procedure of the target cooling is as follows. The sample holder fixing the sample with a framework made of Teflon and fine ceramics is inserted in the quartz cell which is connected to the top of the refrigerator. After one hour pre-cooling by the use of liquid N_2, cooling with liquid ^{4}He is started down to 20 K and continued with ^{4}He gas exchange in the inner vacuum chamber. It takes four hour to reach 1K. Further cooling with more ^{3}He circulation is still continued to reach 100 mK. Under 2.5 tesla magnetic field, the rate of the proton spin polarization by 69.1 GHz microwave irradiation is high enough, for instance, 20 %/min at the beginning. The maximum polarization of proton with water/glycerol solvent is 95 %.

The polarization of the target is monitored by the CW-NMR with a Q-meter circuit. Its absolute value is obtained by the calibration using the value of the proton spin polarization at 1k and 2.5 tesla. The accuracy of this calibration, mainly depending on that of the temperature measurements, is

better than 1 %. The depolarization of proton or deuteron is also done by irradiating appropriate modulated RF, ν_H or ν_D, through the NMR coil.

III-3 Small-angle scattering spectrometer (SANS-1)

Fig. 7 shows the side view of SANS-1. Neutrons emerging from the reactor FRG-1 enter the H_2-gas Cold Source with a flat bottle shape at 25 K through light water moderator and are reflected to the curved neutron guides by the beryllium reflector. At the end of the neutron guide (NG-1) 10^8 n/cm^2/s is registered. The peak wavelength of Maxwell's distribution of neutrons is 6 Å. This neutron beam is monochromatized by the helical slot velocity selector with a band pass about 10 %. We have used the neutrons with the wavelength of 8.5 Å. After the monochromatization, the super mirror polarizer passes the neutrons with one spin direction through itself. Inside the movable neutron guide sections there are the collimator system and the Mezei type flat coil spin flipper for the inversion of the orientation of polarized neutrons. The magnetic guide field is applied for the polarized neutrons all the way from the polarizer to the sample. Under 2 m collimation condition, 10^5 polarized neutrons/cm^2/s enter the sample. In the evacuated scattering chamber, the position sensitive area counter with 55 x 55 cm^2 sensitive area and 0.7 x 0.7 cm^2 effective pixel size can be moved from 0.7 m to 8 m distance from the sample.

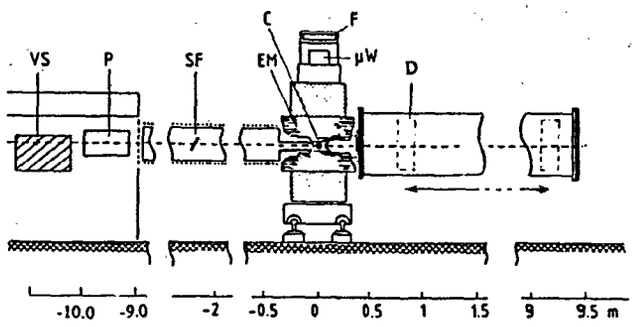

Fig. 7 The side view of SANS-1: velocity selector VS; polarizer P; spin flipper SF; electromagnet EM; nose of horizontal dilution refrigerator C; microwave generator μW; microwave frequency counter F; movable area detector D. The length L of collimation is 2,3,5,7 & 9 m. The sample-detector distance is 0.7-8 m.

IV. RESULTS AND DISCUSSIONS

Apoferritin, whose structure was well-defined by several authors (Stuhrmann et al., 1976), has been used as a standard sample to demonstrate the superiority of spin contrast variation over other methods (Stuhrmann, 1989). The polarized neutron scattering profiles at several proton polarizations are shown in Fig. 8. The scattering intensity of the apoferritin sample is minimized near P_H = 0.6, so-called at contrast matching point of apoferritin. According to the scheme in the preceding sections, each of the basic scattering functions is obtained as shown in Fig. 9. As those profiles coincide with one another, we can confirm that the homogeneous proton spin polarization has proceeded in fact. This result is very important for the feasibility of spin contrast variation in macromolecular research.

Using the same sample selective depolarization of protons and deuteron were carried out. The depolarization process was monitored by polarized

neutron scattering. The process of proton spin depolarization by RF irradiation ν_H = 106.5 MHz for 8 min. is shown in Fig. 10, which is explained by the change of spin-dependent scattering density $\bar{\rho}_V$ (see in the figure caption). The experiments of the deuteron spin saturation with three samples: the preceding apoferritin solution, a 3 wt% bovine serum albumin solution and pure solvent (water glycerol mixture including 5 wt% H_2O), were also done at 300 mK to measure the proton- deuteron thermal mixing time τ_{HD}. τ_{HD} depending on the proton concentration were 20 h, 50 h and 250 h for those samples, respectively.

The experiment of deuterated large ribosomal subunit was the first one in a series of the planned studies. In Fig. 10 three basic scattering functions are all different, in contrast to Fig. 9. This result is reasonable. Because large

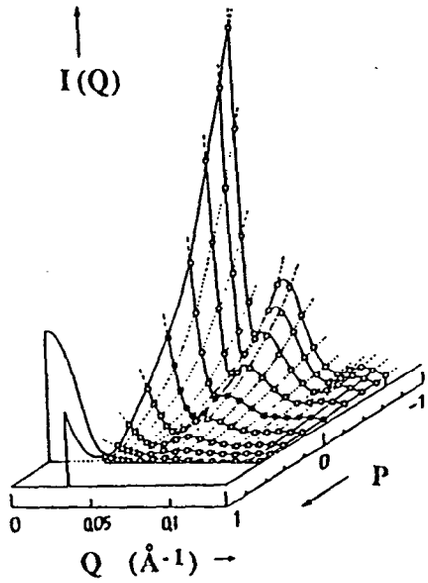

Fig. 8 (on the left side) Polarized netron scattering I (Q) of apoferritin. Contrast minimum is at P=0.6.

Fig. 9 (on the right side) The basic scattering functions of apoferritin: $I_u(Q)$ o ; $I_{uv}(Q)$ o ; $I_v(Q)$ •.

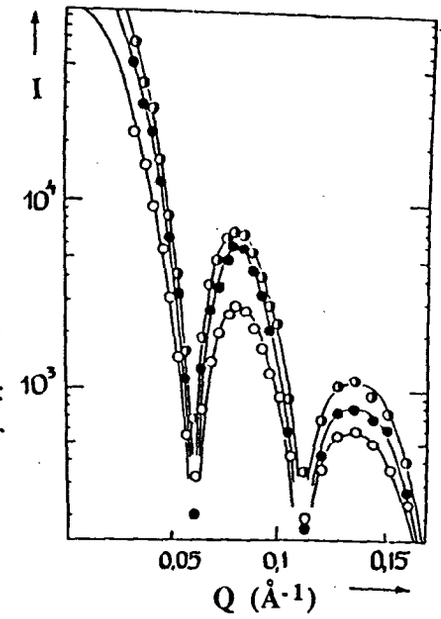

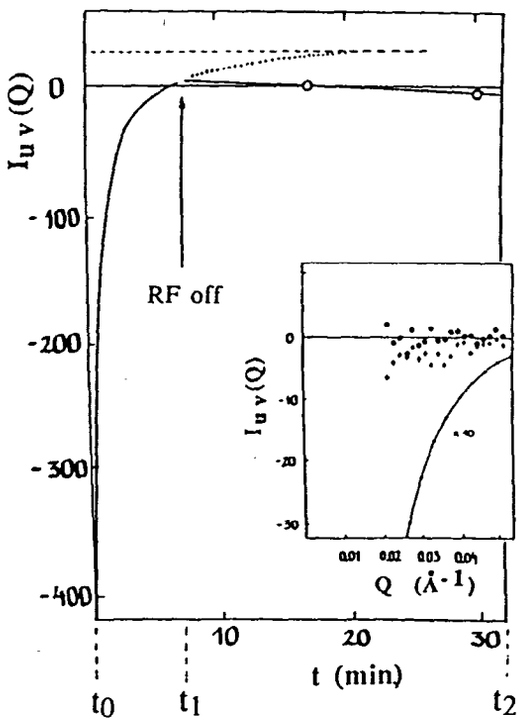

Fig. 10 Proton depolarization measurement of apoferritin. The sign of I_{uv} at each time is determined by the contrasts $\bar{\rho}_u$ and $\bar{\rho}_v$: at t_0 and t_2, ($\bar{\rho}_u < 0$, $\bar{\rho}_v > 0$); at t_1, ($\bar{\rho}_u < 0$, $\bar{\rho}_v < 0$). The insert shows the I_{uv} at 17' and 30'.

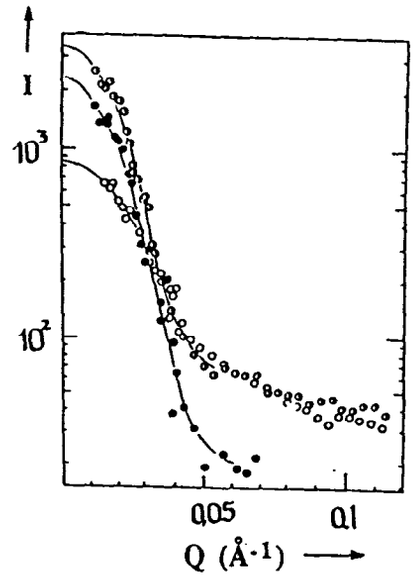

Fig. 11 The basic scattering functions of deuterated ribosomal subunit: $I_u(Q)$ o ; $I_{uv}(Q)$ o ; $I_v(Q)$ •.

ribosomal subunit consists of two different species, i.e., protein and rRNA, the difference of the density of protons between these species results in unequal basic scattering function. More detailed results and discussions including these results will be done in another report (Knop et al.).

References

Abragam, A., & Goldman, M., Nuclear Magnetism: Order and Disorder, edited by J.A. Krumhansl, W. Marshal & D.A. Wilkinson, Oxford: Clarendon Press, (1982).

Abragam, A., Bacchella, G.L., Coustham, J., Glättli, H., Fourmond, M., Malinovski, A., Meriel, P., Pinot, P. & Roubeau, P., Journal de Physique 44,

Boulin, C., Büldt, G., Dauvergne, F., Gabriel, A., Goerigk, G., Knop, W., Krumpolc, M., Munk, B., Nierhause, K.H., Niinikoski, T.O., Nowotny, V., Rieubland, M., Rijlart, A., Schärpf, O., Schink, H.-J., Wagner, R. & Stuhrmann, H.B., Makromol. Chem., Macromol. Symp. 15, 19-49 (1988).

Jin, Y. & Crichton, R.R., FEBS Letts. 215, 41-46 (1987).

Knop, W., Nierhaus, K.H., Nowotny, V., Niinikoski, T.O., Krumpolc, M., Rijlart, A., Schärpf, O., Schink, H.-J., Stuhrmann, H.B. & Wagner, R., Helv. Phys. Acta 50, 741-746 (1986).

Knop, W., Schink, H.-J., Stuhrmann, H.B., Wagner, R., Wenkow-Es-Souni, M., Schärpf, O. W., Krumpolc, M., Niinikoski, T.O., Rieubland, M. & Rijlart, A., J. Appl Cryst. 22, 352-362 (1989).

Knop, W., Hirai, M., Schink, H.-J., Stuhrmann, H.B., Wagner, R., Zhao, J., Schärpf, O. W., Crichton, R.R., Krumpolc, M., Nierhaus, K.H., Niinikoski, T.O., & Rijlart, A., submitted to J. Appl. Cryst. .

Krumpolc, M., Rocek, J., Inorganic Chemistry 24, 617-621 (1985)

Niinikoski, T.O. & Udo, F., Nucl. Instrum. Methods 134, 219-233 (1976).

Niinikoski, T.O., & Rijlart, A., Nucl. Instrum. Methods 199, 485-489 (1982).

Stuhrmann, H.B., Schärpf, O. W., Krumpolc, M., Niinikoski, T.O., Rieubland, M. & Rijlart, A., Eur. Biophys. J. 14, 1-6 (1986).

Stuhrmann, H.B., Physica B 156 & 157, 444-451 (1989).

ICANS-XI International Collaboration on Advanced Neutron Sources
KEK, Tsukuba, October 22-26, 1990

ENGINEERING STRAIN MEASUREMENTS using the NPD at LANSCE

M. A. M. Bourke, J. A. Goldstone, K. J. Lovell.
LANSCE
Los Alamos National Laboratory
New Mexico, 87545
USA

Abstract

The presence of residual stress in engineering components can affect their mechanical properties and structural integrity. Neutron diffraction is the only measuring technique which can provide spatially resolved non-destructive strain measurements in the interior of a component. By recording the change in the interplanar spacings elastic strains can be measured for individual lattice reflections. Also on a pulsed source, where all lattice reflections are recorded, profile refinement is an option which allows the strain to be obtained from changes in the lattice parameter. Measurements made at LANSCE demonstrate the potential for stress measurements on a pulsed source and indicate the advantages and disadvantages over measurements made on a reactor.

Introduction

Measurements of macroscopic residual stress in engineering components were first made in the early eighties on reactor sources (refs. 1,2). However it is only recently that pulsed sources like ISIS and LANSCE have produced sufficient neutron intensities to make measurements in components which may involve neutron path lengths in a specimen of several centimeters. Engineering strain measurements necessitate positioning of samples to accuracies of 0.1mm relative to precisely defined neutron beams. Different positions are examined by translating the specimen through a defined volume. The strain in different directions is measured by reorienting the specimen with respect to the detectors. Thus the main requirements are a multi-axis manipulation system and precise, repeatable collimation of both the incident and exit beams. On the NPD at LANSCE or POLARIS at ISIS the collimation and manipulators must be placed in a sample can of diameter less than 1m which limits the range of travel available and complicates the positioning of specimens. The approach taken on the NPD at LANSCE is to independently mount both the apertures and translators on a frame which can be placed precisely in the sample can using cone locators. This has proved effective since the specimens can accurately be aligned optically prior to insertion of the apparatus into the vacuum can.

Definition of a sampling volume

On most neutron powder diffractometers or spectrometers the incident beam cross section is several cm^2. However stress fields near crack tips or due to severe processing may vary over distances comparable to a millimeter. Thus the sampling volumes required for strain examination by neutron

diffraction are typically between 10 and 60mm^3. Definition of a sampling volume is achieved by masking the incident and diffracted neutron beams to produce a single intersection from which neutrons can reach the detectors. The optimal scattering angle is 90° since this gives the best spatial resolution in the specimens.

The manipulation system which has been developed for use on the NPD (neutron powder diffractometer) at LANSCE provides 360° rotation about a vertical axis, XY horizontal travel of 35cm and a vertical range of 45cm. It can carry components up to 50kg. The NPD has four detector banks at ±90° and ±148° which potentially offer four simultaneous strain measurements during each measurement. However at this time exit collimation has only been installed on the 90° banks. The collimating apertures are supported from optical benches and may be moved on radii from the centre of the sample can. Positional adjustment is achieved using microcontrol manual adjusters. The masks were machined from commercially obtained boron nitride (cost ~$1000US/1000cm^2 at 1.3cm thick). Boron is used as the active component for collimation on pulsed sources since (unlike cadmium) it remains opaque to neutrons with wavelengths less than 0.5 Å. Boron nitride proved to be easy to machine and a variety of precise aperture shapes were fabricated.

The NPD lies 32m from a tungsten target and the divergence of the incident beam at the sample position is small. Consequently the distance between the incident aperture and the specimen is not critical to the definition of a sampling volume. The defocussing at the sample position due to the inherent beam divergence for a 2mm square placed 50mm from the specimen is only ~0.2mm in each dimension. Collimation of the diffracted beams is more sensitive to the position of the exit aperture (more so than on a reactor source) because there is no inherent collimation between the sample position and the detectors. Consequently the spatial resolution along the incident beam decreases with increasing distance of the exit aperture from the incident beam. The time of flight operation of a pulsed source means that to make measurements in acceptable times care must be taken not to achieve exit collimation at the expense of obscuring too large a solid angle of the detectors.

By assuming sharp cut-offs at the edges of the exit slits the angle of the 90° detector visible at different positions along the incident beam can be evaluated. The parameters which can be altered for the exit apertures are their width (d), thickness (t) and distance (l) from the specimen (fig 1). Many specimens possess plate geometries which are placed at 45° to the incident beam for simultaneous in-plane and normal strain measurements using the 90° detectors. Some apertures have been fabricated with slits at 45° to the surface. This permits the aperture to be placed adjacent to the specimen surface (i.e. closer to the incident beam than a flat aperture) which improves the resolution along the incident beam. This is illustrated in figure 2.

Calibration measurements were made by translating a vertical 4mm diameter steel pin through the sampling volume defined for different aperture sizes and positions. The diffracted intensity was noted as the pin was moved parallel and normal to the incident beam. The dimensions of the sampling volume normal to the incident beam direction showed sharp cut-offs indicating that it could be treated as parallel sided. Scans parallel to the incident beam demonstrated the sensitivity of the resolution along the incident beam path to the position of the exit aperture. It was shown that the resolution could be calculated for different exit mask arrangements from geometric considerations.

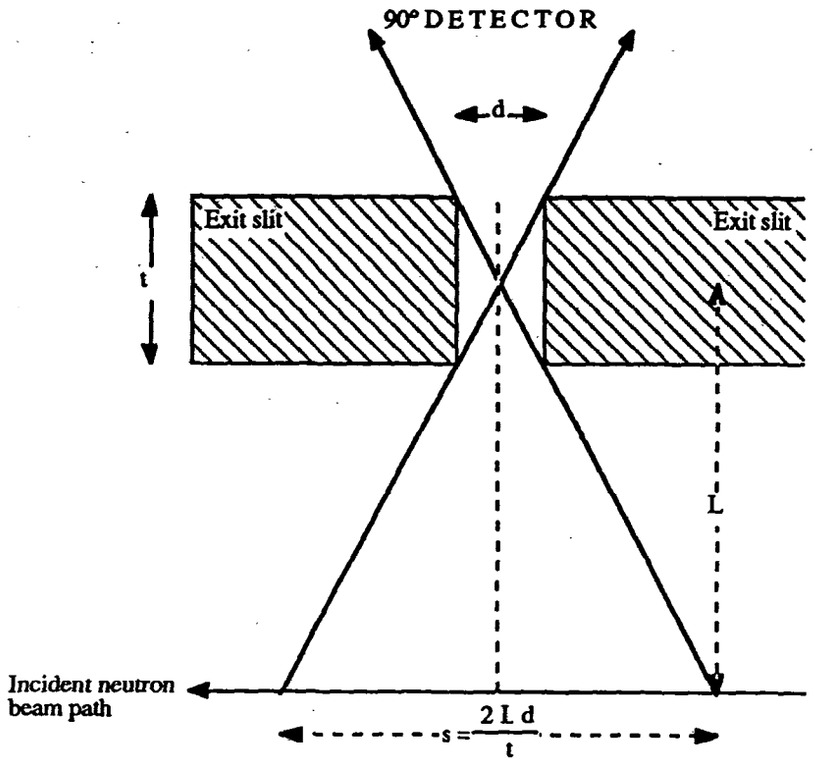

Figure 1: Shows the spatial resolution (s) along the beam path (not including the finite angle subtended by the detectors).

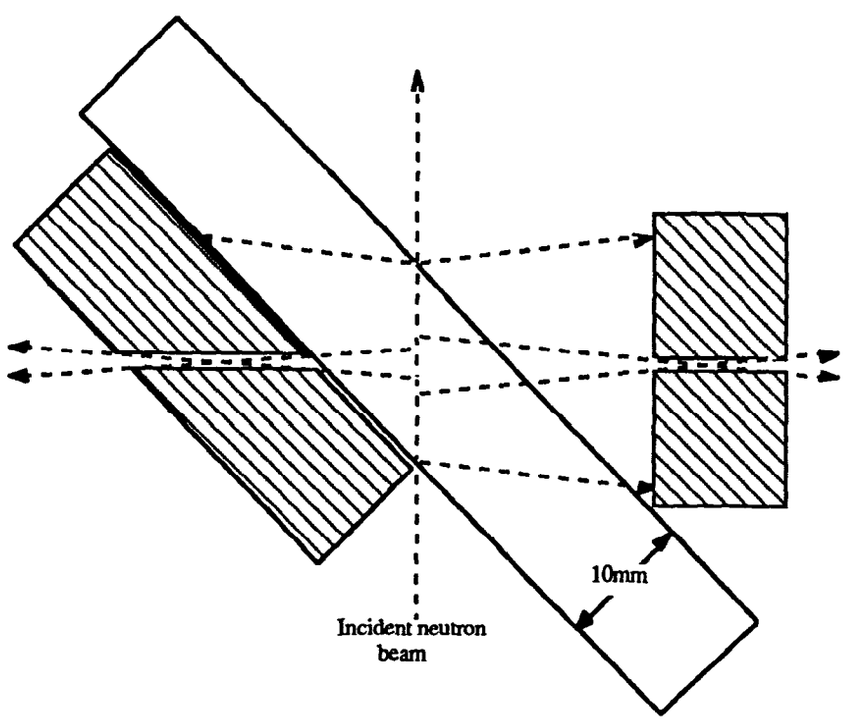

Figure 2 : Comparison of the spatial resolution for the normal and 45° exit apertures.

Data analysis

Measurement of grain interaction stresses has already been performed on pulsed sources (ref 3) however the measurements made at LANSCE represent the first attempt to define small gauge volumes within components to investigate the variation of macroscopic residual stress variations through a component. Consequently there is uncertainty concerning minimum count times to obtain specified strain accuracies for different materials, specimen geometries and aperture geometries. Measurements performed at ISIS on a thin autofrettaged ring (with no exit collimation) demonstrated that profile refinement of spectra obtained from different regions in a component permits the strain to be obtained from changes in the lattice parameter (ref 4). This is important since count times for each measurement may be reduced if the strain is obtained from the lattice parameter instead of from individual lattice reflections. This approach is attractive from an engineering standpoint since it averages any anisotropic variations due to differences in elastic compliance offering a strain value which might, in the absence of preferred orientation, be assumed to represent a bulk average. If detailed information concerning the strains for grains in specific orientations is required then count times must be increased in order to obtain adequate statistical accuracy for individual peak fits.

The two 90° detectors on NPD at LANSCE each consist of sixteen ^{3}He tubes which subtend an angle of 11° at the sample position. Each individual tube collects a spectrum corresponding to a unique strain direction in the specimen. However single tubes can take many hours to provide adequate spectra which is unacceptably long. Consequently all the detectors in each 90° bank are added together giving a combined spectrum corresponding to a spread in the scattering vector (and thus of the strain measuring directions) of 5.5° (fig 3). In addition the backscattering detectors also give an indication concerning the texture of the material and strain measurements but with poorly defined sampling volumes.

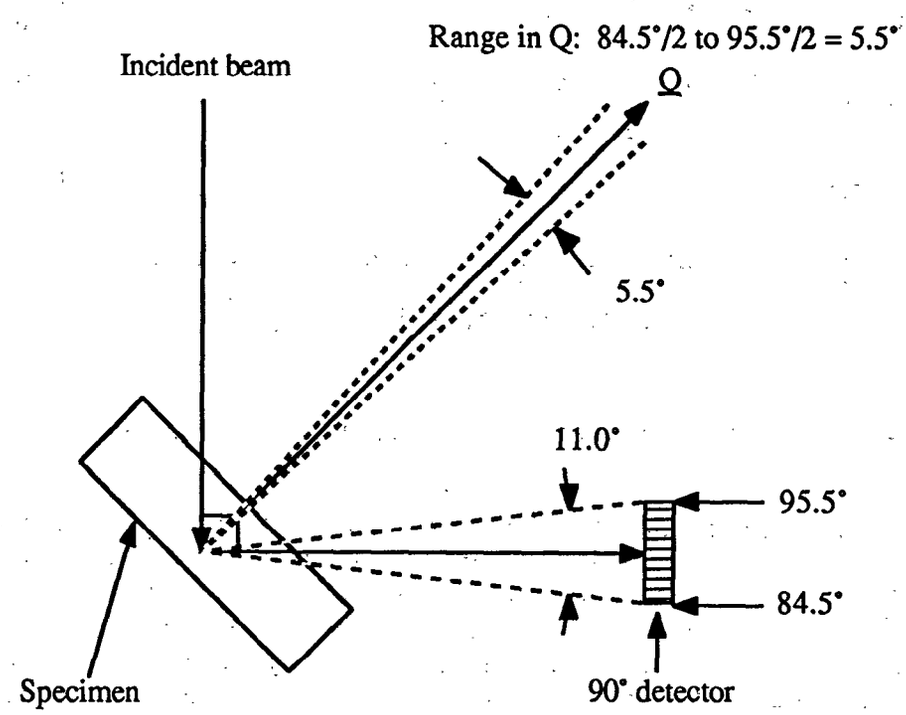

Figure 3: Range in scattering vector resulting from addition of all spectra obtained from 90° detector.

Preliminary Results

To evaluate the capability of making residual strain measurements with restricted sampling volumes, in collaboration with Tom Holden of AECL, we examined a deformed stainless steel ring which has been modelled by detailed finite element calculations and has been previously studied at Chalk River National Laboratory, Canada (ref 5). The ring is approximately 76mm ID, 127mm OD, and 13mm thick and was compressed along a diameter. Our measurements were along a radius in a section of the ring at 90 degrees from the applied stress point. Using a sampling volume of 40 mm^3 with a beam current of ~75μA two strain directions were measured at each position every 4 hours. The accuracy for strong reflections was <±80μstrain. Three strain components, tangential, radial and axial were measured on the 90° detectors by using two orientations of the ring. Figure 4 shows the tangential strain data available from many of the reflections observed. The trend in the strain is evident in all reflections and these data agree with the (111) and (200) reflections measured at Chalk River and the calculations.

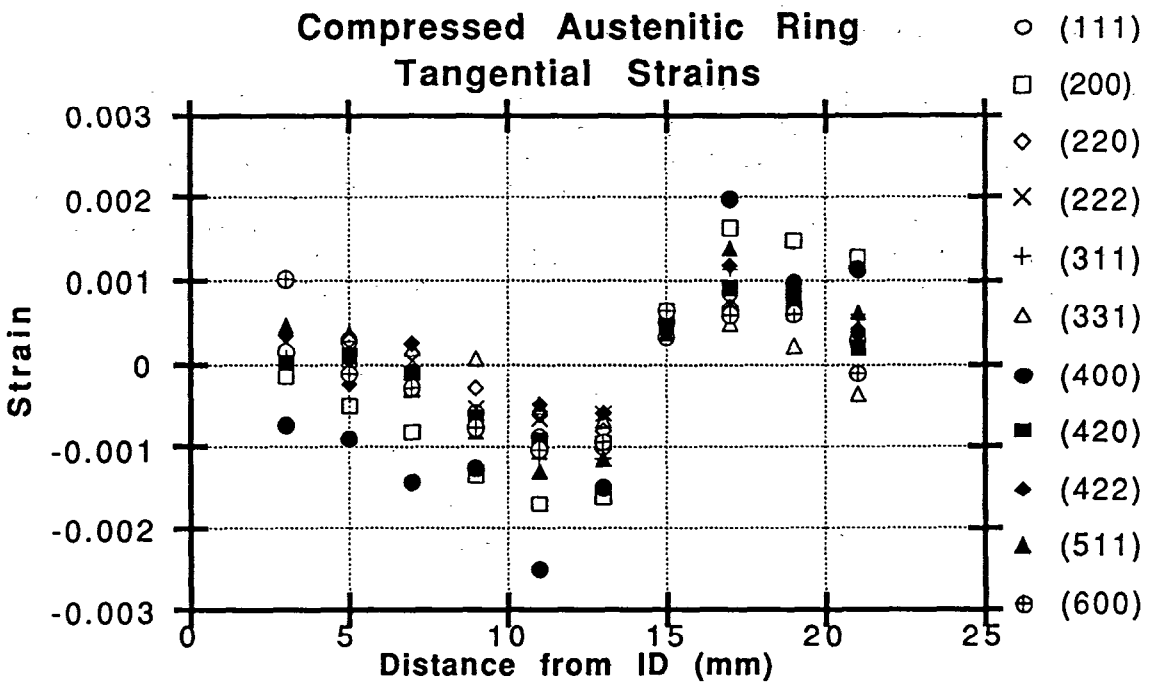

Figure 4: Tangential strain measurements for selected (hkl) reflections.

An advantage of a pulsed source is that strain information can be obtained for all lattice reflections in each measurement. The anisotropic strain response is illustrated in figure 5. The strains at a single measuring position are plotted for each reflection against the anisotropy factor A_{hkl} (= $[h^2k^2 + k^2l^2 + l^2h^2]/[h^2 + k^2 + l^2]$). In principle the relationship between the strain and A_{hkl} is given by $\varepsilon_{hkl} = \sigma[S_{11}-2SA_{hkl}]$, where $S = S_{11}-S_{12}-S_{44}/2$ (ref 2). Using the single crystal compliance values, the slope and intercept give an estimate of the elastic stress in the material. Deviations from the elastic model or the inappropriateness of using the single crystal compliances will appear as inconsistencies in stress computed from the different strain components

Other samples examined include whisker and particulate reinforced Al-SiC composites, multipass welds, and a compacted powder. The Al-SiC metal-matrix composite specimens did not require a small sample volume because the strains of interest were assumed to be uniform throughout the samples.

Uniaxial tension or compression specimens were deformed to differing levels of plastic deformation and then released. The residual strain states of the two components in the composites were then examined. Neutron diffraction is a valuable tool for studies of this nature because the matrix and reinforcement can be examined simultaneously and non-destructively. This basic study of the composite response to stress was complimented by the examination of a composite automobile component.

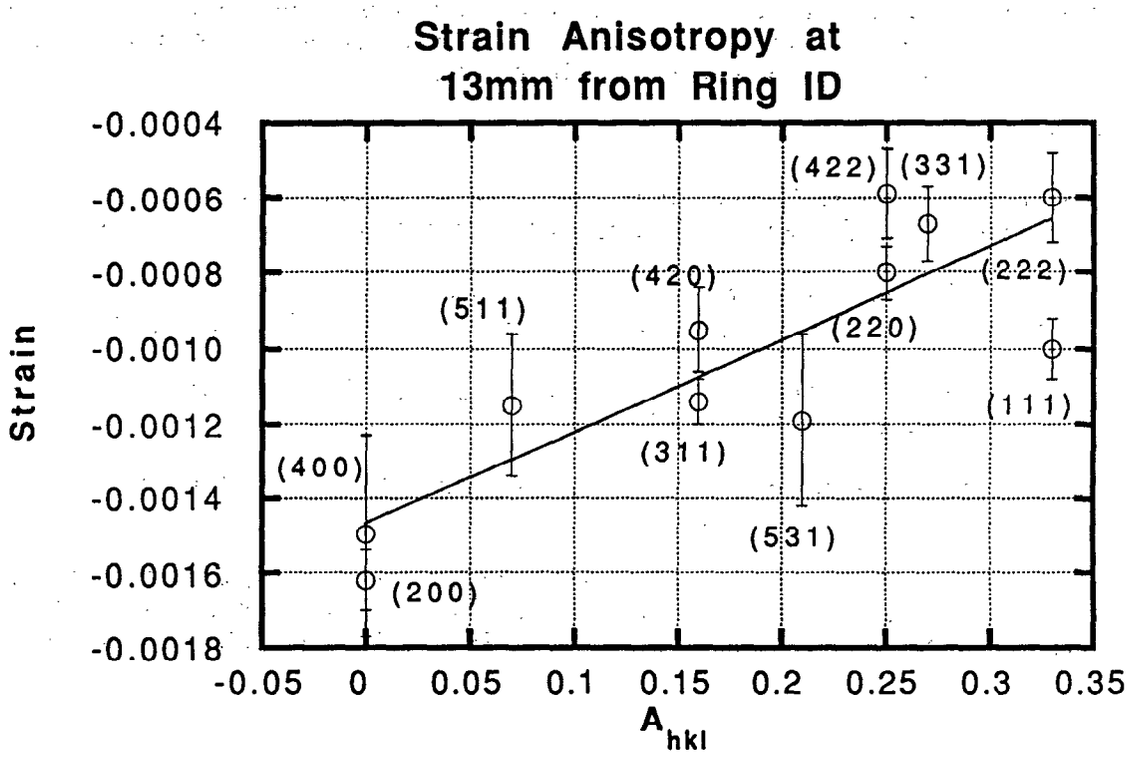

Figure 5: Anisotropic strain for selected (hkl) reflections at 13mm from the ring ID.

The multipass welds were in 2.5 cm thick stainless plates (30cm x 30cm). They represented a severe test concerning the maximum path length ($2.5\sqrt{2}$ cm) in steel over which the neutrons can pass while still giving representative strain measurements in reasonable time scales. The weld was scanned from the top surface to the bottom of the weld vee using an extended sampling volume to take advantage of the symmetry along the weld direction. Data were taken to evaluate the nature of residual strain developed by different weld methods. In compacted metal powders, the integrity of the part is strongly affected by the residual strains from processing. We began a basic study of the strains in a cylindrical ejected compacted powder sample, looking at the strains through a diameter and in the corner of the specimen. Results will help improve models of the strain state.

Conclusions

A manipulation and collimation system has been installed on the NPD at LANSCE. Components up to 50kg can be moved within the confines of the sample tank. Sampling volumes as small as $10mm^3$ have been achieved for thin flat samples. However for complicated specimen geometries unless the exit collimation can be placed within 30mm of the incident beam it is impossible to define small ($<20mm^3$) sampling volumes and make individual strain measurements in less than a day.

Although collimation has only been installed on the ±90° detectors strains are recorded on all detectors, and "bonus information" is collected in the backscattered directions. Using the two 90° banks two strain measurements (normal to each other) with well defined sampling volumes are obtained in each measurement. Consequently when measuring triaxial stress distributions there may be duplication of measurement in one direction which provides a check and calibration of the experiment.

The presence of all the lattice reflections in each spectrum provides information concerning the overall stress state of the material at a granular level. This is important in understanding grain interaction stresses, slip processes in polycrystals and will help to calibrate measurements on reactor sources where strains are usually inferred from only one or two Bragg reflections.

References

1. *Measurement of residual stresses by neutron diffraction*, Stacey, A., MacGillivray, H.J., Webster, G.A., Webster, P.J. & Ziebeck,K.R.A. Journal of strain analysis, **1985a**, Vol. 20, No 2, 93-100.

2. *Neutron diffraction methods for the study of residual stress fields*, ,Allen, A.J., Hutchings, M.T., Windsor, C.G. & Andreani, C, Advances in physics, **1985**, Vol. 34, No4, 445-473.

3. *The use of time of flight neutron diffraction to study grain interaction stresses*, MacEwen, S.R., Faber, J. & Turner, P.L., Acta metall, **1983**, Vol 31, No 5, 657-676.

4. *Residual stress measurement in engineering components by neutron diffraction*, Bourke, M.A.M., PhD Thesis, University of London **1990**.

5. *A comparison of finite element analysis with neutron and X-ray measurements of residual strains in stainless steel*, Flower, E.C., MacEwen, S.R., Holden, T.M., Hosbons, R.R., Proceedings of the international conference on residual stresses, **1989b**, Nancy (1988), pbld by Elsevier.

Participants List

Participants List

T. ADACHI
BSF
National Laboratory for High Energy Physics
1-1 Oho,
Tsukuba-shi 305
JAPAN
Tel. 0298-64-1171
Fax. 0298-64-3202

K. AIZAWA
Institute for Materials Research
Tohoku University
2-1-1 Katahira, Aoba-ku,
Sendai-shi 980
JAPAN
Tel. 022-229-6200
Fax. 022-264-7984

H. ASANO
Institute of Materials Science,
University of Tsukuba
1-1, Tennodai,
Tsukuba-shi 305
JAPAN
Tel. 0298-53-5122
Fax. 0298-55-7440

G. I. BATSKIKH
Moscow Radiotechnikal Institute,
USSR
Warshavskoye chaussee 132
Moscow, 113519
USSR
Tel. 311-43-12
Fax. (007)-095-196-1632

G. S. BAUER
Paul Scherrer Institute
CH-5232 Villigen, PSI
Switzerland
Tel. 056-99-2524
Fax. 056-98-2327

P. BONI
Paul Scherrer Institute
CH-5232 Villigen, PSI
Switzerland
Tel. 056-99-2518
Fax. 056-98-2635

B. S. BROWN
IPNS
Argonne National Laboratory
9700 South Cass Avenue
Argonne, Illinois, 60439
USA
Tel. 708-972-4999
Fax. 708-972-4163

J. M. CARPENTER
IPNS
Argonne National Laboratory
9700 South Cass Avenue
Argonne, Illinois, 60439
USA
Tel. 708-972-5519
Fax. 708-972-4163

R. K. CRAWFORD
IPNS
Argonne National Laboratory
9700 South Cass Avenue
Argonne, Illinois, 60439
USA
Tel. 708-972-7769
Fax. 708-972-4163

M. DUBS
Paul Scherrer Institute
CH-5232 Villigen, PSI
Switzerland
Tel. 056-99-2546
Fax. 056-98-2327

T. EBISAWA
Research Reactor Institute,
Kyoto University
Kumatori-cho, Sennan-gun,
Osaka 590-04
JAPAN
Tel. 0724-52-0901
Fax. 0724-53-5810

P. A. EGELSTAFF
Department of Physics
University of Guelph
Guelph Ontario
N1G 2W1
CANADA
Tel. 519-824-4120
Fax. 519-836-9967

Y. ENDOH
Faculty of Science
Tohoko University
Aoba, Aramaki, Aoba-ku,
Sendai-shi 980
JAPAN
Tel. 022-222-1800
Fax. 022-225-1891

J. L. FINNEY
ISIS Science Division
Rutherford Appleton Laboratory
Chilton, Didcot, Oxfordshire
OX11 OQX
UK
Tel. 235-44-6287
Fax. 235-44-5720

T. FUKUDA
Institute for Nuclear Study,
University of Tokyo
3-2-1 Midori-cho,
Tanashi-shi 188
JAPAN
Tel. 0424-61-4131
Fax. 0424-68-5845

T. FUKUNAGA
School of Engineering,
Nagoya University
Furo-cho, Chikusa-ku,
Nagoya-shi 464
JAPAN
Tel. 052-781-5111
Fax. 052-782-2129

S. FUNAHASHI
Department of Physics,
Japan Atomic Energy Research Institute
Tokai-mura, Naka-gun,
Ibaraki-ken 319-11
JAPAN
Tel. 0292-82-6093
Fax. 0292-82-5927

M. FURUSAKA
BSF
National Laboratory for High Energy Physics
1-1, Oho,
Tsukuba-shi 305
JAPAN
Tel. 0298-64-1171
Fax. 0298-64-3202

Participants List

I. S. K. GARDNER
ISIS AD Division
Rutherford Appleton Laboratory
Chilton, Didcot, Oxfordshire
OX11 OQX
UK
Tel. 235-82-19002
Fax. 235-44-5720

M. I. GRACHEV
Neutron Laboratory
Institute of Nuclear Research USSR
Academy of Sciences
60th October Anniversary Prospect
7a 117312 Moscow
USSR
Tel. 334-01-91
Fax.

J. B.HAYTER
Advanced Neutron Source Project
Oak Ridge National Laboratory
FEDC/MS-8218, P.O. Box 2009,
Oak Ridge, TN 37831
USA
Tel. 615-576-9300
Fax. 615-576-3041

M. HIRAI
Kanagawa Institute of Technology
1030,Shimo-ogino
Atsugi-shi 243-02
JAPAN
Tel. 0462-41-1211
Fax. 0462-42-3737

M. HOLDING
ISIS Science Division
Rutherford Appleton Laboratory
Chilton, Didcot, Oxfordshire
OX11 OQX
UK
Tel. 235-82-1900
Fax. 235-44-5720

H. IKEDA
BSF
National Laboratory for High Energy Physics
1-1, Oho,
Tsukuba-shi 305
JAPAN
Tel. 0298-64-1171
Fax. 0298-64-3202

S. IKEDA
BSF
National Laboratory for High Energy Physics
1-1, Oho,
Tsukuba-shi 305
JAPAN
Tel. 0298-64-1171
Fax. 0298-64-3202

Y. IRIE
BSF
National Laboratory for High Energy Physics
1-1, Oho,
Tsukuba-shi 305
JAPAN
Tel. 0298-64-1171
Fax. 0298-64-3202

T. ISHIGAKI
Institute of Materials Science,
University of Tsukuba
1-1, Tennodai,
Tsukuba-shi 305
JAPAN
Tel. 0298-53-5476
Fax. 0298-55-7440

S. ITOH
BSF
National Laboratory for High Energy Physics
1-1, Oho,
Tsukuba-shi 305
JAPAN
Tel. 0298-64-1171
Fax. 0298-64-3202

Y. IZUMI
Macromolecular Research Laboratory
Faculty of Engineering,
Yamagata University
4-3-16 Jyonan
Yonezawa-shi 992
JAPAN
Tel. 0238-22-5181
Fax. 0238-22-5362

M. W. JOHNSON
ISIS Science Division
Rutherford Appleton Laboratory
Chilton, Didcot, Oxfordshire
OX11 OQX
UK
Tel. 235-44
Fax. 235-44-5720

K. KAKURAI
Faculty of Science
Tohoko University
Aoba, Aramaki, Aoba-ku,
Sendai-shi 980
JAPAN
Tel. 022-222-1800
Fax. 022-225-1819

T. KAMIYAMA
Institute of Materials Science,
Univesity of Tsukuba
1-1, Tennodai,
Tsukuba-shi 305
JAPAN
Tel. 0298-53-5030
Fax. 0298-55-7440

T. KAMIYAMA
Institute for Materials Research
Tohoku University
2-1-1 Katahira, Aoba-ku,
Sendai-shi 980
JAPAN
Tel. 022-227-6200
Fax. 022-264-7984

T. KANAYA
Institute for chemical Research,
Kyoto University
Gokasho, Uji-shi 611
JAPAN
Tel. 0774-32-3111
Fax. 0774-33-1247

Y.KANEKO
Director of Reactor Engineering
Department Japan Atomic Energy Research Institute
Tokai-mura, Naka-gun,
Ibaraki-ken 319-11
JAPAN
Tel. 0292-82-5517
Fax. 0292-82-6122

I. KANNO
Department of Physics,
Japan Atomic Energy Research Institute
Tokai-mura, Naka-gun,
Ibaraki-ken 319-11
JAPAN
Tel. 0292-82-6093
Fax. 0292-82-5927

Participants List

K. KATOH
National Laboratory for High Energy Physics
1-1, Oho,
Tsukuba-shi 305
JAPAN
Tel. 0298-64-1171
Fax. 0298-64-1993

T. KAWAI
Research Reactor Institute,
Kyoto University
Kumatori-cho, Sennan-gun,
Osaka 590-04
JAPAN
Tel. 0724-52-0901
Fax. 0724-53-1043

T. KAWAKUBO
National Laboratory for High Energy Physics
1-1, Oho,
Tsukuba-shi 305
JAPAN
Tel. 0298-64-1171
Fax. 0298-64-3182

M. KIHARA
National Laboratory for High Energy Physics
1-1, Oho,
Tsukuba-shi 305
JAPAN
Tel. 0298-64-1171
Fax. 0298-64-3182

Y. KIYANAGI
Faculty of Engineering
Hokkaido University
Kita-13-jyou, Nishi-8-choume,
Kitaku Kita, Sapporo 060
JAPAN
Tel. 011-716-2111
Fax. 011-717-4745

M. KOHGI
Department of Physics,
Faculty of Science,
Tohoko University
Aoba, Aramaki, Aoba-ku,
Sendai-shi 980
JAPAN
Tel. 022-222-1800
Fax. 022-225-1891

K. KURODA
Faculty of Science
Tohoko University
Aoba, Aramaki, Aoba-ku,
Sendai-shi 980
JAPAN
Tel. 022-222-1800
Fax. 022-225-1891

M. KUROSAWA
Japan Atomic Energy Research Institute
Tokai-mura, Naka-gun,
Ibaraki-ken 319-11
Japan
Tel. 02928-2-5111
Fax.

R. E. LECHNER
Hahn-Meitner-Institut Berlin
Glienicker Strasse 100
D-1000 Berlin 39
Germany
Tel. 30-80092780
Fax. 30-80092181

R. J. MACEK
Los Alamos National Laboratory
Meson Physics Division
MS H848
Los Alamos, NM 87545
USA
Tel. 505-667-8877
Fax. 505-665-1712

Y. MAEDA
Research Reactor Institute,
Kyoto University
Kumatori-cho, Sennan-gun,
Osaka 590-04
JAPAN
Tel. 0724-52-0901
Fax. 0724-53-1043

Y. MASUDA
BSF
National Laboratory for High Energy Physics
1-1, Oho,
Tsukuba-shi 305
JAPAN
Tel. 0298-64-1171
Fax. 0298-64-3202

M. MATSUDA
Faculty of Science
Tohoko University
Aoba, Aramaki, Aoba-ku,
Sendai-shi 980
JAPAN
Tel. 022-222-1800
Fax. 022-225-1891

K. MIKAMI
Laboratory of Nuclear Science,
Faculty of Science
Tohoku University
1-2-1 Mikamine, Taihaku-ku
Sendai-shi 982
JAPAN
Tel. 022-245-2151
Fax. 022-243-0965

M. MISAWA
BSF
National Laboratory for High Energy Physics
1-1, Oho,
Tsukuba-shi, 305
JAPAN
Tel. 0298-64-1171
Fax. 0298-64-3202

S. MITSUDA
Institute for Solid State Physics,
The University of Tokyo
7-22-1, Roppongi,
Minato-ku 106
JAPAN
Tel. 03-478-6811
Fax. 03-402-9449

T. MOCHIKU
Institute of Materials Science,
University of Tsukuba
1-1, Tennodai,
Tsukuba-shi 305
JAPAN
Tel. 0298-53-5476
Fax. 0298-55-7440

Y. MORI
National Laboratory for High Energy Physics
1-1, Oho,
Tuskuba-shi 305
JAPAN
Tel. 0298-64-1171
Fax. 0298-64-3182

Participants List

Y. MORII
Department of Physics
Japan Atomic Energy Research Institute
Tokai-mura, Naka-gun,
Ibaraki-ken 319-11
JAPAN
Tel. 0292-82-5477
Fax. 0292-82-5927

M. MOTOKAWA
Department of Physics,
Faculty of Science,
Kobe University
Rokkodai, Nada,
Kobe 657
JAPAN
Tel. 078-881-1212
Fax. 078-881-7593

Y. NAKAHARA
Department of Reactor Engineering,
Japan Atomic Energy Research Institute
Tokai-mura, Naka-gun
Ibaraki-ken 319-11
JAPAN
Tel. 02928-2-5361
Fax. 0292-82-6122

Y. NAKAI
Institute of Materials Science,
University of Tsukuba
1-1, Tennoudai,
Tsukuba-shi 305
JAPAN
Tel. 0298-53-5476
Fax. 0298-55-7440

K.NAKAJIMA
Faculty of Science
Tohoko University
Aoba, Aramaki, Aoba-ku,
Sendai-shi 980
JAPAN
Tel. 022-222-1800
Fax. 022-225-1891

T. NAKAMURA
Cyclotron and Radioisotope Center
Tohoku University
Aoba, Aramaki, Aoba-ku,
Sendai-shi 980
JAPAN
Tel. 022-263-5929
Fax. 022-263-5356

T. NAKANE
Institute for Materials Research
Tohoku University
2-1-1 Katahira, Aoba-ku,
Sendai-shi 980
JAPAN
Tel. 022-227-6200
Fax. 022-264-7984

N. NIIMURA
Laboratory of Nuclear Science,
Faculty of Science
Tohoku University
1-2-1 Mikamine,
Taihaku-ku, Sendai-shi 982
JAPAN
Tel. 022-245-2151
Fax. 022-243-0965

S. NINOMIYA
National Laboratory for High Energy Physics
1-1 Oho,
Tsukuba-shi 305
JAPAN
Tel. 0298-64-1171
Fax. 0298-64-3182

N. NISHIDA
Department of Physics,
Faculty of Science,
Kobe University
Rokkodai, Nada,
Kobe 657
JAPAN
Tel. 078-881-1212
Fax. 078-881-7593

T. NISHIDA
Reactor Engineering Department,
Japan Atomic Energy Research Institute
Tokai-mura, Naka-gun,
Ibaraki-ken 319-11
JAPAN
Tel. 0292-82-5362
Fax. 0292-82-6122

A. NODA
Institute for Nuclear Study,
University of Tokyo
3-2-1, Midori-cho
Tanashi-shi 188
JAPAN
Tel. 0424-61-4131
Fax. 0424-68-5845

H. NOJIRI
Department of Physics,
Faculty of Science,
Kobe University
Rokkodai, Nada,
Kobe 657
JAPAN
Tel. 078-881-1212
Fax. 048-881-7593

C. OHMORI
Institute for Nuclear Study,
University of Tokyo
3-2-1 Midori-cho,
Tanashi-shi 188
JAPAN
Tel. 0424-61-4131
Fax. 0424-68-5845

K. OHOYAMA
Faculty of Science
Tohoko University
Aoba, Aramaki, Aoba-ku,
Sendai-shi 980
JAPAN
Tel. 022-222-1800
Fax. 022-225-1891

T. OSAKABE
Faculty of Science
Tohoko University
Aoba, Aramaki, Aoba-ku,
Sendai-shi 980
JAPAN
Tel. 022-222-1800
Fax. 022-225-1891

M. OSAWA
Institute of Materials Science,
University of Tsukuba
1-1, Tennodai,
Tsukuba-shi 305
JAPAN
Tel. 0298-53-5476
Fax. 0298-55-7440

W. C. A. PULFORD
ISIS Science Division
Rutherford Appleton Laboratory
Chilton, Didcot, Oxfordshire
OX11 OQX
UK
Tel. 235-82-1900
Fax. 235-44-5720

R. PYNN
Los Alamos National Laboratory
Lansce, MS H805
Los Alamos, NM 87545
USA
Tel. 505-
Fax. 505-665-2676

G. H. REES
Rutherford Appleton Laboratory
Chilton, Didcot, Oxfordshire
OX11 OQX
UK
Tel. 235-82-1900
Fax. 235-44-5720

G. J. RUSSELL
Los Alamos National Laboratory
LANSCE MS H805,
Los Alamos, NM 87545
USA
Tel. 505-667-2937
Fax. 505-665-2676

U. SANKAWA
Laboratory of Nuclear Science,
Faculty of Science
Tohoku University
1-2-1 Mikamine, Taihaku-ku
Sendai-shi 982
JAPAN
Tel. 022-245-2151
Fax. 022-243-0965

H. SASAKI
National Laboratory for High Energy Physics
1-1, Oho,
Tuskuba-shi 305
JAPAN
Tel. 0298-64-1171
Fax. 0298-64-3202

E. P. SHABALIN
Joint Institute for Nuclear Research,
Laboratory of Neutron Physics
Dubna, Head Post Office
P.O. Box 79
101000 Moscow
USSR
Tel.
Fax.

K. SHIBATA
Institute for Materials Research
Tohoku University
2-1-1 Katahira, Aoba-ku,
Sendai-shi 980
JAPAN
Tel. 022-227-6200
Fax. 022-264-7984

T. SHIBATA
Institute for Nuclear Study,
University of Tokyo
3-2-1 Midori-cho,
Tanashi-shi 188
JAPAN
Tel. 0424-61-4131
Fax. 0424-67-9159

N. SHIKAZONO
Japan Atomic Energy Research Institute
Tokai-mura, Naka-gun,
Ibaraki-ken 319-11
JAPAN
Tel. 02928-2-5015
Fax. 0292-82-6111

K. SHIN
Department of Nuclear Engineering,
Kyoto University
Sakyo-ku, Kyoto 606
JAPAN
Tel. 075-753-5825
Fax. 075-753-5845

G. SHIRANE
Department of Physics
Brookhaven National Laboratory
Upton, Long Island
New York, 11973
USA
Tel.
Fax. 516-282-2739

S. F. SIDORKIN
Neutron Laboratory
Institute of Nuclear Research USSR
Academy of Sciences
60th October Anniversary Prospect
7a 117312 Moscow
USSR
Tel. 334-01-91
Fax.

K. SOYAMA
Japan Atomic Energy Research Institute
Tokai-mura, Naka-gun,
Ibaraki-ken 319-11
JAPAN
Tel. 02928-2-5639
Fax. 0292-82-5258

Y. Y. STAVISSKY
Neutron Laboratory
Institute of Nuclear Research USSR
Academy of Sciences
60th October Anniversary Prospect
7a 117312 Moscow
USSR
Tel. 334-01-91
Fax.

U. STEIGENBERGER
Neutron Science Division
Rutherford Appleton Laboratory
Chilton, Didcot, Oxfordshire
OX11 OQX
UK
Tel. 235-44-5145
Fax. 235-44-5720

M. SUGIYAMA
Research Reactor Institute,
Kyoto University
Kumatori-cho, Sennan-gun,
Osaka 590-04
JAPAN
Tel. 0724-52-0901
Fax. 0724-53-1043

J. SUZUKI
Faculty of Science
Tohoko University
Aoba, Aramaki, Aoba-ku,
Sendai-shi 980
JAPAN
Tel. 022-222-1800
Fax. 022-225-1891

K. SUZUKI
Institute for Materials Research
Tohoku University
2-1-1 Katahira, Aoba-ku,
Sendai-shi 980
JAPAN
Tel. 022-227-6200
Fax. 022-264-7984

Participants List

T. SUZUKI
Institute of Physics,
Tsukuba University
1-1, Tennoudai
Tsukuba-shi, 305
JAPAN
JAPAN
Tel. 0298-53-4035
Fax.

T. SUZUKI
National Laboratory for High Energy Physics
1-1, Oho,
Tsukuba-shi 305
JAPAN
Tel. 0298-64-1171
Fax. 0298-64-3182

K. SUZUYA
Institute for Materials Research
Tohoku University
2-1-1 Katahira, Aoba-ku,
Sendai-shi 980
JAPAN
Tel. 022-227-6200
Fax. 022-264-7984

K. TAJIMA
Faculty of Science and Technology
KeioUniversity
3-14-1, Hiyoshi
Kohoku-ku
Yokohama-shi 223
JAPAN
Tel. 045-563-1141
Fax. 045-563-1761

H. TAKADA
Reactor Engineering Department,
Japan Atomic Energy Research Institute
Tokai-mura, Naka-gun,
Ibaraki-ken 319-11
JAPAN
Tel. 0292-82-5362
Fax. 0298-82-6122

M. TAKAHASHI
Faculty pf Science,
Ochanomizu Universitty
2-1-1, Otsuka,
Bunkyo-ku, 112
JAPAN
Tel. 03-943-3151
Fax. 03-942-2815

Y. TAKEDA
Paul Scherrer Institute
CH-5232 Villigen, PSI
Swizerland
Tel. 056-99-3568
Fax. 056-99-3294

T. TAKIZUKA
OMEGA Program Team,
Japan Atomic Energy Research Institute
Tokai-mura, Naka-gun,
Ibaraki-ken 319-11
JAPAN
Tel. 0292-82-6434
Fax. 0292-82-6438

K. TANAKA
National Laboratory for High Energy Physics
1-1, Oho,
Tuskuba-shi 305
JAPAN
Tel. 0298-64-1171
Fax. 0298-64-2580

A. D. TAYLOR
Rutherford Appleton Laboratory
Chilton, Didcot, Oxfordshire
OX11 OQX
UK
Tel. 235-44
Fax. 235-44-5720

I. M. THORSON
Tri-Univ. Meson Facility
4004 Wesbrook Mall
Vancouver BC V6T 2A3
CANADA
Tel.
Fax. 604-222-1074

H. TIETZE
Institute of Physics
University of Wurzburg
Am Hubland, D-8700
Wurzburg
Germany
Tel. 931-888-5797
Fax. 931-706297

Y. TODATE
Faculty pf Science,
Ochanomizu Universitty
2-1-1, Otsuka,
Bunkyo-ku, 112
JAPAN
Tel. 03-943-3151
Fax. 03-942-2815

M. UTSURO
Research Reactor Institute,
Kyoto University
Kumatori-choSennan-gun,
Osaka 590-04
JAPAN
Tel. 0724-52-0901
Fax.

Y. UWAMINO
Institute for Nuclear Study,
University of Tokyo
3-2-1 Midori-cho,
Tanashi-shi 188
JAPAN
Tel. 0424-61-4131
Fax. 0424-67-9159

R. G. VASSILKOV
Moscow Radiotechnikal Institute,
USSR
Warshavskoye chaussee 132
Moscow, 113519
USSR
Tel. 311-43-12
Fax. (007)-095-196-1632

W. WAGNER
Paul Scherrer Institute
CH-5232 Villigen, PSI
Switzerland
Tel. 056-99-2517
Fax. 056-98-2635

N. WATANABE
BSF
National Laboratory for High Energy Physics
1-1, Oho,
Tsukuba-shi, 305
JAPAN
Tel. 0298-64-1171
Fax. 0298-64-3202

T. WATANABE
Faculty of Science
Tohoko University
Aoba, Aramaki, Aoba-ku,
Sendai-shi 980
JAPAN
Tel. 022-222-1800
Fax. 022-225-1891

W. G. WILLIAMS
ISIS Science Division
Rutherford Appleton Laboratory
Chilton, Didcot, Oxfordshire
OX11 OQX
UK
Tel. 235-44-5599
Fax. 235-44-5720

C. C. WILSON
Rutherford Appleton Laboratory
Chilton, Didcot, Oxfordshire
OX11 OQX
UK
Tel. 235-44
Fax. 235-44-5720

K. YAMADA
Faculty of Science
Tohoko University
Aoba, Aramaki, Aoba-ku,
Sendai-shi 980
JAPAN
Tel. 022-222-1800
Fax. 022-225-1891

Y. YAMADA
Institute for Solid State Physics,
University of Tokyo
7-22-1, Roppongi,
MInato-ku 106
JAPAN
Tel. 03-478-6811
Fax. 03-402-9449

S. YAMAGUCHI
Institute for Materials Research
Tohoku University
2-1-1 Katahira, Aoba-ku,
Sendai-shi 980
JAPAN
Tel. 022-227-6200
Fax. 022-264-7984

Y. YAMAGUCHI
Institute for Materials Research
Tohoku University
2-1-1 Katahira, Aoba-ku,
Sendai-shi 980
JAPAN
Tel. 022-227-6200
Fax. 022-264-7984

I. YAMANE
National Laboratory for High Energy
Physics
1-1, Oho,
Tsukuba-shi 305
JAPAN
Tel. 0298-64-1171
Fax. 0298-64-3182

Y. YAMAZAKI
National Laboratory for High Energy
Physics
1-1, Oho,
Tsukuba-shi 305
JAPAN
Tel. 0298-64-1171
Fax. 0298-64-3182

Y. YANO
BSF
National Laboratory for High Energy
Physics
1-1 Oho,
Tsukuba-shi 305
JAPAN
Tel. 0298-64-1171
Fax. 0298-64-3202

H. YOKOBORI
Department of Physics,
Japan Atomic Energy Research
Institute
Tokai-mura, Naka-gun,
Ibaraki-ken 319-11
JAPAN
Tel. 0292-82-6076
Fax. 0292-82-6122

H. YOSHIKI
National Laboratory hor High Energy
Physics
1-1, Oho,
Tsukuba-shi 305
JAPAN
Tel. 0298-64-1171
Fax. 0298-64-4402

H. YOSHIZAWA
The Institute for Solid State
Physics,
University of Tokyo
7-22-1, Roppongi
Minato-ku 106
JAPAN
Tel. 03-478-6811
Fax. 03-402-9449